frontiers | Research Topics

Pre-earthquake observations and methods for earthquake forecasting and seismic hazard reduction

Edited by
Giovanni Martinelli, Yuanyuan Fu, Ying Li and Filippos Vallianatos

Published in
Frontiers in Earth Science
Frontiers in Environmental Science

ISSN 1664-8714
ISBN 978-2-83251-544-0
DOI 10.3389/978-2-83251-544-0

About Frontiers

Frontiers is more than just an open access publisher of scholarly articles: it is a pioneering approach to the world of academia, radically improving the way scholarly research is managed. The grand vision of Frontiers is a world where all people have an equal opportunity to seek, share and generate knowledge. Frontiers provides immediate and permanent online open access to all its publications, but this alone is not enough to realize our grand goals.

Frontiers journal series

The Frontiers journal series is a multi-tier and interdisciplinary set of open-access, online journals, promising a paradigm shift from the current review, selection and dissemination processes in academic publishing. All Frontiers journals are driven by researchers for researchers; therefore, they constitute a service to the scholarly community. At the same time, the *Frontiers journal series* operates on a revolutionary invention, the tiered publishing system, initially addressing specific communities of scholars, and gradually climbing up to broader public understanding, thus serving the interests of the lay society, too.

Dedication to quality

Each Frontiers article is a landmark of the highest quality, thanks to genuinely collaborative interactions between authors and review editors, who include some of the world's best academicians. Research must be certified by peers before entering a stream of knowledge that may eventually reach the public - and shape society; therefore, Frontiers only applies the most rigorous and unbiased reviews. Frontiers revolutionizes research publishing by freely delivering the most outstanding research, evaluated with no bias from both the academic and social point of view. By applying the most advanced information technologies, Frontiers is catapulting scholarly publishing into a new generation.

What are Frontiers Research Topics?

Frontiers Research Topics are very popular trademarks of the *Frontiers journals series*: they are collections of at least ten articles, all centered on a particular subject. With their unique mix of varied contributions from Original Research to Review Articles, Frontiers Research Topics unify the most influential researchers, the latest key findings and historical advances in a hot research area.

Find out more on how to host your own Frontiers Research Topic or contribute to one as an author by contacting the Frontiers editorial office: frontiersin.org/about/contact

Pre-earthquake observations and methods for earthquake forecasting and seismic hazard reduction

Topic editors

Giovanni Martinelli — National Institute of Geophysics and Volcanology, Section of Palermo, Italy

Yuanyuan Fu — Institute of Earthquake Forecasting, China Earthquake Administration, China

Ying Li — Institute of Earthquake Forecasting, China Earthquake Administration, China

Filippos Vallianatos — National and Kapodistrian University of Athens, Greece

Citation

Martinelli, G., Fu, Y., Li, Y., Vallianatos, F., eds. (2023). *Pre-earthquake observations and methods for earthquake forecasting and seismic hazard reduction*. Lausanne: Frontiers Media SA. doi: 10.3389/978-2-83251-544-0

Table of contents

frontiers | Frontiers in Earth Science

TYPE Editorial
PUBLISHED 16 March 2023
DOI 10.3389/feart.2023.1150414

OPEN ACCESS

EDITED AND REVIEWED BY
Jeroen Van Hunen,
Durham University, United Kingdom

*CORRESPONDENCE
Giovanni Martinelli,
giovanni.martinelli15@gmail.com

SPECIALTY SECTION
This article was submitted to Solid Earth Geophysics, a section of the journal Frontiers in Earth Science

RECEIVED 24 January 2023
ACCEPTED 20 February 2023
PUBLISHED 16 March 2023

CITATION
Martinelli G, Fu Y, Li Y and Vallianatos F (2023), Editorial: Pre-earthquake observations and methods for earthquake forecasting and seismic hazard reduction.
Front. Earth Sci. 11:1150414.
doi: 10.3389/feart.2023.1150414

Editorial: Pre-earthquake observations and methods for earthquake forecasting and seismic hazard reduction

Giovanni Martinelli[1,2]*, Yuanyuan Fu[3], Ying Li[3] and Filippos Vallianatos[4]

[1]Department of Palermo, INGV Istituto Nazionale di Geofisica e Vulcanologia, Palermo, Italy, [2]Northwest Institute of Eco-Environment and Resources, Chinese Academy of Sciences, Lanzhou, China, [3]Institute of Earthquake Forecasting, China Earthquake Administration, Beijing, China, [4]Department of Geophysics and Geothermy, National and Kapodistrian University of Athens, Athens, Greece

KEYWORDS

earthquake preparation process, earthquake source physics, earthquake forecasting, seismic hazard reduction, earthquake forecasting policies

Editorial on the Research Topic
Pre-earthquake observations and methods for earthquake forecasting and seismic hazard reduction

Introduction

Understanding the governing principles, which include long-term tectonic loading, sluggish nucleation, and rapid fracture propagation, enables estimation of the stress level and change during geophysical observations in seismically active locations. The first step in earthquake forecasting is the identification of those factors whose space-time dynamics can be linked to the crustal deformations that precede earthquakes. Significant progresses have been made in analysing earthquake spatial-temporal correlations, clustering, and the development of seismicity patterns, paving the way for the possibility of earthquake prediction. In addition, earthquake physics addresses fundamental questions in seismology, such as how earthquakes form, how seismic rupture begins, propagates, and ends, what role long-term and short-term processes play in earthquake triggering, what role fluids play in earthquake triggering, and what relationship exists between fault dynamics, energy, friction, and other physical parameters of the focal zone. Recent advances in seismological and non-seismological observations have resulted in a variety of data, which have significantly increased our ability to investigate earthquake-related processes at multiple scales. In addition to established earthquake occurrence patterns and probabilistic models, a wealth of newly accessible non-seismological data gathered on a global scale has opened new roads for systematic study and model validation. Ground-based or satellite-based geophysical and geochemical observations, ranging from ground deformation patterns to pre-earthquake changes (geochemical, electromagnetic, hydrogeological, geodetic, etc.), may be related to stress variations in the lithosphere preceding a large earthquake. A critical reevaluation of proposed techniques in

conjunction with state-of-the-art and original observations has been carried out in this volume with the purpose to identify most promising future research directions. The primary objective of the Frontiers in Earth Sciences Research Topic on Pre-Earthquake Observations and Methods for Earthquake Forecasting and Seismic Hazard Reduction is to provide an up-to-date view of the processes preceding earthquake occurrence that can be applied to the design of earthquake forecasting experiments aimed at validating their accuracy in desirable Test Site areas. The growing number of articles and Research Topic devoted to earthquake forecasting, attests to a new attitude towards earthquake forecasting. New observables are constantly proposed, taking advantage from the large amount of data provided by new Earth observation systems and from increased computational power. Nonetheless, efforts to convert such elusive data into precisely defined ones are still limited. Operational earthquake forecasting methods, in particular, should be testable and confirmed by evidence. The set of errors, namely, the rates of failure and the space-time extent of alarms, in comparison to those obtained from the same number of random guess trials, allows for the evaluation of the effectiveness of the forecasting method. A necessary emphasis has been devoted on continuous statistical testing of the relevance and confidence of the precursors in order to evaluate and continue to improve the performance of the forecasts. Observations and physical models suggest that several processes in the lithosphere of the Earth are predictable, but only after extensive averaging and up to a certain limit. Consequently, earthquake forecasting necessitates a holistic approach and should be posed as an integrated, multi-scale process, narrowing the magnitude range, expected territory, and time of occurrence within the constraints imposed by physics and data uncertainties. Understanding governing laws, ranging from long-term tectonic loading and slow nucleation to rapid rupture propagation, can aid in estimating the stress state and temporal evolution of geophysical observables in seismically active regions. Reducing the space-time uncertainty of forecasts requires the use of additional, independent, and trustworthy information, which can be provided by multidisciplinary observations and recording of natural observables at various space-time scales. With this Research Topic, we present the current state of research Pre-Earthquake Observations and Methods for Earthquake Forecasting and Seismic Hazard Reduction, with a particular emphasis on:

a) Systematic analysis, physical interpretation, and modeling of pre-earthquake processes; Yun Zhou, Lisheng Xu, Jianping Wu, Chunlai Li, Lihua Fang, and Pan Pan, Seismicity of the repeating earthquake clusters in the northern Xiaojiang fault zone and its implications.
Jing Zhao, Zhengyi Yuan, Jinwei Ren, Zaisen Jiang, Qi Yao, Zhihua Zhou, Chong Yue, Jun Zhong, and Anfu Niu, Acceleration of deep slip along the Longmenshan fault plane before the 2008 M8.0 Wenchuan earthquake.

b) Model validation and statistical assessment of proposed physical-based precursors; Zhiwei Zhang, Chuntao Liang, Feng Liong, Min Zhao, and Di Wang, Spatiotemporal Variations of Focal Mechanism Solutions and Stress Field of the 2019 Changning Ms6.0 Earthquake Sequence.

c) Statistical methods and issues in earthquake forecast validation; Renata Rotondi and Elisa Varini, Temporal variations of the probability distribution of Voronoi cells generated by earthquake epicenters.
Chong Yue, Ping Ji, Yali Wang, Huaizhong Yu, Jin Cui, Chen Yu, and Yuchuan Ma, Evolution characteristics and mechanism of the Load/Unload Response Ratio based on strain observation before the Jiuzhaigou MS7.0 earthquake.

d) Analysis of input data and requirements for real-time model testing; Jinhan Xie, Shanshan Yong, Xi'an Wang, Zhenyu Bao, Yibin Liu, Xing Zhang, and Chunjiu He, Weekly earthquake prediction in a region of China based on an intensive precursor network AETA.

e) Time-dependent seismic hazard assessment based on space-time characterization of impending earthquakes; Aybige Akinci, Irene Munafò, and Luca Malagnini, S-wave Attenuation Variation and its impact on Ground Motion Amplitudes during 2016–2017 Central Italy Earthquake Sequence.

f) Geophysical interpretation of non-seismological parameters associated with crustal deformation processes Yang Xing, Zhang Tie-bao, Lu Qian, Long Feng, Liang Ming-Jian, Wu Wei-Wei, Gong Yue, Wei Jia-Xi, and Wu Jia, Variation of thermal infrared brightness temperature anomalies in the Madoi earthquake and associated earthquakes in the Tibetan Plateau (China);
Jinhan Xie, Shanshan Yong, Xi'an Wang, Zhenyu Bao, Yibin Liu, Xing Zhang, and Chunjiu He
Mehdi Akhoondzadeh, Angelo De Santis, Dedalo Marchetti, and Xuhui Shen, Swarm-TEC satellite measurements as a potential earthquake precursor together with other Swarm and CSES data: the case of Mw7.6 2019 Papua New Guinea seismic event.
Pan Xiong, Cheng Long, Huiyu Zhou, Roberto Battiston, Angelo De Santis, Dimitar Ouzounov, Xuemin Zhang, and Xuhui Shen, Pre-earthquake ionospheric perturbation identification using CSES data *via* transfer learning.

g) Time series analysis of geophysical and geochemical parameters; Chenhua Li, Xiaocheng Zhou, Jingchao Li, Lei Liu, Hejun Su, Ying Li, Miao He, Jinyuan Dong, Jiao Tian, Huiling Zhou, Gang Gao, Caiyan Zhang, and Zhixin Luo, Hydrogeochemical Characteristics of Thermal Springs in the Qilian-Haiyuan Fault Zone at northeast Tibetan Plateau: Role of fluids and seismic activity.

h) Modeling of pressure fluctuation in deformation processes; Wei Shi, Hanchao Jiang, G. Ian Alsop, and Guo Wu, A continuous 13.3-ka paleoseismic record constrains major earthquake recurrence in the Longmen Shan collision zone.

i) Slow-slip geodetic precursors; Jiangtao Qiu, Lingyun Ji, Liangyu Zhu, and Qingliang Wang, Present-day tectonic deformation partitioning across south Tianshan from satellite geodetic imaging.

j) Modeling of chemical and physical parameter variations in faulted regions; Guo Guangmeng, On the relation between anomalous clouds and earthquakes in Italian land.

k) Spatial and temporal variation of geochemical and hydrogeological features in seismic areas and their relationship to faults and seismic activity Mingbo Yang, Guiping Liu, Zhe Liu, Jingchen Ma, Zhiguo Wang, Peixue Hua, Xiaoru Sun, Kongyan Han, Bowen Cui, and Xiaodong Wu, Geochemical Characteristics of Geothermal and Hot Spring Gases in Beijing and Zhangjiakou-Bohai Fault Zone.

l) How possible scientific results on earthquake forecasting may be provided to decision-makers in a useful way
Xia Chaoxu, Nie Gaozhong, Li Huayue, Fan Xiwei, Zhou Junxue, Yang Rui, and Zeng Xun, Research on lethal levels of buildings based on historical seismic data.

Conclusion

This volume addresses the physical processes that occur in the Earth's crust before the initiation of earthquakes with the purpose to set up methods oriented to earthquake forecasting and to seismic hazard reduction. Numerous newly available seismological and non-seismological data collected on a global scale, present new opportunities for systematic study and model validation. Several geophysical and geochemical measurements obtained by ground-based or satellite-based methods, ranging from ground-associated deformation patterns to pre-seismic alterations, may be associated with stress variations in the lithosphere prior to an eventual large earthquake. We believe that an objective reevaluation of the proposed methods, along with state-of-the-art and novel observations, can aid in elucidating most promising research avenues. The primary objective of the Frontiers in Earth Sciences Research Topic on Pre-Earthquake Observations and Methods for Earthquake Forecasting and Seismic Hazard Reduction is to provide a current view of current knowledge of processes preceding earthquake occurrence, which can be used to set up earthquake forecasting experiments to test their accuracy in large and small Test Site areas.

Author contributions

All authors listed have made a substantial, direct, and intellectual contribution to the work and approved it for publication.

Conflict of interest

The authors declare that the research was conducted in the absence of any commercial or financial relationships that could be construed as a potential conflict of interest.

Publisher's note

frontiers in Environmental Science

ORIGINAL RESEARCH
published: 04 November 2021
doi: 10.3389/fenvs.2021.779255

Pre-Earthquake Ionospheric Perturbation Identification Using CSES Data *via* Transfer Learning

*Pan Xiong[1], Cheng Long[2], Huiyu Zhou[3], Roberto Battiston[4,5], Angelo De Santis[6], Dimitar Ouzounov[7], Xuemin Zhang[1] and Xuhui Shen[8]**

[1]Institute of Earthquake Forecasting, China Earthquake Administration, Beijing, China, [2]School of Computer Science and Engineering, Nanyang Technological University, Singapore, Singapore, [3]School of Computing and Mathematical Sciences, University of Leicester, Leicester, United Kingdom, [4]Department of Physics, University of Trento, Trento, Italy, [5]National Institute for Nuclear Physics, The Trento Institute for Fundamental Physics and Applications, Trento, Italy, [6]Istituto Nazionale di Geofisica e Vulcanologia, Rome, Italy, [7]Center of Excellence in Earth Systems Modeling & Observations, Chapman University, Orange, CA, United States, [8]National Institute of Natural Hazards, Ministry of Emergency Management of China, Beijing, China

During the lithospheric buildup to an earthquake, complex physical changes occur within the earthquake hypocenter. Data pertaining to the changes in the ionosphere may be obtained by satellites, and the analysis of data anomalies can help identify earthquake precursors. In this paper, we present a deep-learning model, SeqNetQuake, that uses data from the first China Seismo-Electromagnetic Satellite (CSES) to identify ionospheric perturbations prior to earthquakes. SeqNetQuake achieves the best performance [F-measure (F1) = 0.6792 and Matthews correlation coefficient (MCC) = 0.427] when directly trained on the CSES dataset with a spatial window centered on the earthquake epicenter with the Dobrovolsky radius and an input sequence length of 20 consecutive observations during night time. We further explore a transferring learning approach, which initially trains the model with the larger Electro-Magnetic Emissions Transmitted from the Earthquake Regions (DEMETER) dataset, and then tunes the model with the CSES dataset. The transfer-learning performance is substantially higher than that of direct learning, yielding a 12% improvement in the F1 score and a 29% improvement in the MCC value. Moreover, we compare the proposed model SeqNetQuake with other five benchmarking classifiers on an independent test set, which shows that SeqNetQuake demonstrates a 64.2% improvement in MCC and approximately a 24.5% improvement in the F1 score over the second-best convolutional neural network model. SeqNetSquake achieves significant improvement in identifying pre-earthquake ionospheric perturbation and improves the performance of earthquake prediction using the CSES data.

Keywords: earthquake, pre-earthquake anomalies, CSES and DEMETER satellites, ionospheric plasma, transfer deep learning, physical mechanisms

OPEN ACCESS

Edited by:
Giovanni Martinelli, National Institute of Geophysics and Volcanology, Italy

Reviewed by:
Mukesh Gupta, Catholic University of Louvain, Belgium
Jinyun Guo, Shandong University of Science and Technology, China

****Correspondence:***
Xuhui Shen
shenxh@seis.ac.cn

Specialty section:
This article was submitted to Environmental Informatics and Remote Sensing, a section of the journal Frontiers in Environmental Science

Received: *18 September 2021*
Accepted: *21 October 2021*
Published: *04 November 2021*

Citation:
Xiong P, Long C, Zhou H, Battiston R, De Santis A, Ouzounov D, Zhang X and Shen X (2021) Pre-Earthquake Ionospheric Perturbation Identification Using CSES Data via Transfer Learning. Front. Environ. Sci. 9:779255. doi: 10.3389/fenvs.2021.779255

INTRODUCTION

Earth observation by satellites offers several advantages such as wide coverage, short repeat observation period, fast data update, and non-restriction by ground conditions, which makes up for the shortcomings of conventional ground-based observations that cannot attain large-area, dynamic, and continuous earthquake precursor information (Shen et al., 2013). Among such

observation satellites, the China Seismo-Electromagnetic Satellite (CSES) (Shen et al., 2018) [as known as ZhangHeng-1 (ZH-1)] and DEMETER (Detection of Electromagnetic Emissions Transmitted from Earthquake Regions) (Parrot, 2006) were launched in February 2018 and June 2004, respectively, which have been designed to detect variations in the electromagnetic environment in space to support earthquake monitoring and research. These satellites have accumulated a wealth of scientific data and enabled many research achievements over the years of their continuous operation.

Ionospheric anomalies related to earthquakes are typically investigated via case studies and statistical analyses. Two magnitude 6.9 and 7.4 earthquakes struck the area of Kii-Peninsula (Lat = 33.05°N, Long = 136.78°E) on September 5, 2004 at 10.07.07 and 14.57.18 UT, respectively, were the first for which many ionospheric perturbations were identified as earthquake precursors using the DEMETER data (Parrot et al., 2006a). It was discovered by Zhang et al. (2009) that the ion density dropped suddenly 3 days before the Wenchuan earthquake struck on May 12, 2008, and that the ion density dropped to its lowest level 3 days before the earthquake. About a month before the earthquake, the equatorial ionosphere started to exhibit anomalies, and it peaked 8 days before the mainshock (Ryu et al., 2014b). Píša et al. (2011) showed that the plasma density increased remarkably before an earthquake in Chile. Many studies have confirmed that ionospheric perturbations recorded by DEMETER can detect anomalies related to earthquakes with good sensitivity, including the 2007 Pu'er earthquake (Mofiz and Battiston, 2009; He et al., 2011), and earthquakes in L'Aquila (Bertello et al., 2018) and Haiti (Athanasiou et al., 2011). The CSES data have also recorded perturbations in ionospheric plasma parameters before large earthquakes. The first earthquake with Ms > 7.0 recorded by CSES was the Ms 7.1 earthquake in Mexico on February 17, 2018; disturbances in low-frequency electromagnetic waves and ionospheric plasma were found 1 day before the earthquake (Shen et al., 2020). Yan et al. (2018b) analyzed the electron density observed by the Langmuir probe (LAP) on the CSES before the Ile Hunter M7.1 earthquake on August 29, 2018, and found that the electron density (Ne) near the epicenter suddenly increased 12 and 9 days before the event. The 6.9-magnitude 2018 Bayan earthquake has also been studied in detail for co-seismic and precursor phenomena (Piersanti et al., 2020b) using CSES, ERA-5, and ground data. Vertical Total Electron Content (VTEC) precursor anomalies were detected starting 5.3 h before the earthquake, accompanied by a sharp, temporary decrease of the Frequency Resonance Line (FLR) 6 h before the earthquake and followed by a similar co-seismic FLR decrease. Marchetti et al. (2020) investigated ionosphere disturbances associated with the Ms 7.5 earthquake in Indonesia on September 28, 2018, by analyzing the electron density and magnetic data from the CSES during a quiet geomagnetic period and found that anomalies were concentrated around 2.7 months before the quake. In addition, there are many techniques used to detect pre-earthquake ionospheric anomalies, such as Global Navigation Satellite System (GNSS), Constellation Observing System for Meteorology, Ionosphere, and Climate (COSMIC), etc. Shi et al. (2021) investigated ionospheric anomalies in the F2 region (Nmf2), vertical structure (GNSS radio occultation profile) and multi-height (electron density) pre-earthquake anomalies for the Concepcion, Chile, earthquake (February 27, 2010, Mw 8.8). The findings indicate that there were evident local Nmf2 disturbances in the epicenter region for up to 5 h on the 21st and 25th of February. The perturbations of the radio occultation profiles, as well as the interaction of other layers of the ionosphere, indicated the presence of fluctuation signals with significant long-wavelength fluctuations >50 km in the F layer. Total electron content (TEC) and oblique electron content (STEC) data from GNSS sites near the April 25, 2015 Mw7.8 earthquake in Nepal (Shi et al., 2020) and the January 23, 2018 Mw7.9 earthquake in Alaska (Zhang et al., 2021), after processing and analysis by the singular spectrum analysis (SSA) method, revealed a large-scale TEC anomaly in the epicenter and conjugate region.

Statistical research is a way for studying pre-earthquake ionospheric anomalies. Němec et al. (2008,2009) conducted statistical research using electric-field data up to 10 kHz, and the statistics show a significant reduction in wave intensity of 4–6 dB in several hours before the earthquake. Similar but less prominent (only two sigmas) results were also found by Píša et al. (2012,2013). The correlation between the equatorial anomalies observed by DEMETER and seismic activities have been analyzed based on electric-field measurements (Hobara et al., 2013) and equatorial plasma density (Ryu et al., 2014a). Further, other statistical analyses using the complete DEMETER dataset have shown that the number of disturbances first increases and then gradually decreases during earthquakes (Li and Parrot, 2013; Yan et al., 2017; Parrot and Li, 2018; Xiong et al., 2020). De Santis et al. (2019c) used 2.5 years of data from the Swarm satellite to analyze magnetic field and electron density data for months before and after the 12 strong earthquakes. They discovered significant concentrations of electron density and magnetic anomalies that occurred 2 months to a few days before the earthquakes and magnetic anomalies that occurred after the earthquakes. De Santis et al. (2019b) then used more Swarm three-satellite data (4.7 years) to confirm the findings. The CSES team has examined strong earthquakes with Ms > 6.0 in China and earthquakes of Ms > 7.0 worldwide since the CSES launch and explored the characteristics and mechanisms of ionospheric disturbances characteristics before and after earthquakes (Shen et al., 2020).

However, most existing studies have only examined pre-earthquake ionospheric anomalies in the context of specific earthquakes; the lack of consistent analysis methods and anomaly evaluation metrics may lead to inconsistent analysis results for the same earthquakes. Therefore, suitable and generalizable research methods must be developed. In this study, we proposed and tested an efficient analysis method for pre-earthquake ionospheric perturbations discrimination using electromagnetic satellite data accumulated over many years by utilizing deep-learning techniques widely used in recent earthquake studies (Rouet-Leduc et al., 2018; Bergen et al., 2019; Gulia and Wiemer, 2019; Ross et al., 2019; Xiong et al., 2020).

Pre-earthquake perturbation identification using LAP data (Lebreton et al., 2006; Yan et al., 2018a) with electron temperature and electron density data from the CSES and DEMETER datasets was explored using a sequence-to-sequence architecture based on deep transfer learning; these data covered earthquakes worldwide. As CSES has only accumulated a few years of data since its launch, and thus, has covered relatively less earthquakes, the analysis of these data may not be robust. An extensive database containing more than 6 years of data from DEMETER and the transfer-learning technique (Pan and Yang, 2010) was used to overcome this limitation. First, we employed the DEMETER data to train an ensemble model combined with a convolutional neural network (CNN) and a bidirectional long short-term memory (Bi-LSTM) network. We then further trained the model with a small set of CSES data. The proposed method, known as SeqNetQuake, is a deep-learning method based on a sequence-based classification neural network for pre-earthquake perturbation identification, and its performance is compared to that of other state-of-the-art techniques. Finally, the method's results allowed us to perform a test of hypothesis regarding the physical mechanisms of earthquake-induced ionospheric perturbations.

DATA AND PROCESSING

Dataset

CSES and DEMETER satellites were both launched specifically with the purpose of monitoring earthquakes. The DEMETER satellite was launched in 2004 by France and ceased data collection at the end of 2010, with an operating time of 6.5 years (Parrot, 2006). Data along more than 30,000 orbits were obtained, which provided a solid data foundation for the research in earthquake monitoring and ionospheric physics. During the operation of the DEMETER satellite, preliminary preparations for the CSES program were initiated and successfully launched on February 2, 2018 (Shen et al., 2020). However, compared to DEMETER, CSES is designed for a lower orbit altitude of 507 km, which is closer to the ionospheric peak region; the lifting and lowering nodes are at 14:00 and 02:00 local time, also known as day-side or night-side orbits, and the day-side observation time is when the peak ionospheric electron density occurs; the satellite revisiting time is set to 5 days, which is denser than the 16 days revisiting time of the DEMETER satellite.

Of the scientific payloads on CSES, the LAP is the *in situ* space plasma detection device (Liu et al., 2018). LAP can measure electron density (Ne) in the range of 5×10^2–1×10^7 cm^{-3}, and electron temperature (Te) in the range of 500–10,000 K, with a relative accuracy of 10%, allowing the analysis of Ne and Te to study space plasma physical phenomena and ionospheric changes caused by earthquakes, magnetic storms, and other events. CSES data, including LAP electron density and electron temperature from August 1, 2018 to June 22, 2020, were utilized in this study. During this period, 6004 EQs with magnitudes ≥4.8 were recorded (USGS: http://www.usgs.gov). Due to the impact of the magnetic storm and the Sumatra earthquake from November to December 2004, we excluded the data from the DEMETER satellite in 2004 and started our study using the data from 2005 onwards. The DEMETER data used in this study included LAP electron density and electron temperature from 2005 to the end of 2010. During this period (about 6 years), 20,727 EQs with magnitudes ≥4.8 were recorded. The K_p index was referenced to avoid the effect of solar and magnetic activities ($K_p > 3$) in this paper.

Data Processing

To avoid mixing pre-and post-seismic effects, we deleted the aftershocks from the list of earthquakes in this study (Yan et al., 2017). In our study, all the seismic events in the area of $2^\circ \times 2^\circ$ centered on the epicenter and within 15 days after the given earthquake were considered aftershocks. The choice of 15 days as the largest anticipation time of the pre-earthquake anomaly was made for convenience; otherwise, we could not exclude dependence on the impending earthquake magnitude (De Santis et al., 2019b). We first sorted the list of seismic events by time, selecting and removing the aftershocks for an earthquake (given earthquake) in the list in turn. After these operations, we dropped 3013 and 11,815 aftershocks for CSES and DEMETER data analysis. Finally, 2991 (CSES) and 8912 (DEMETER) independent earthquakes remained on the list, respectively. Additionally, we also deleted the data corresponding to the aftershocks.

To validate the dependability of machine learning technologies and to enhance their robustness, we generated the same number of artificial non-seismic events as real earthquakes, randomizing and shifting times and locations to avoid overlapping with the real earthquakes. We randomly sampled time, latitude, and longitude within the selected spatio-temporal range, following the given constraints: 1) the longitude or latitude is not within 10° before and after the longitude or latitude of a real earthquake, and 2) the time is not within 15 days before and after a real earthquake.

The operational modes of the Langmuir Probe onboard CSES include survey mode and burst mode (Yan et al., 2018a). As the sweeping period of the two modes is different, we used simple linear interpolation to interpolate the data in the survey mode so that the time resolution of the two modes was 1.5 s.

METHODS

The continuously observed satellite data is susceptible to errors caused by satellite payload interference, space environment, and other factors. To avoid such errors, we used fixed-length sliding windows (also called "sequences") to partition continuous observation data and used them as inputs to our proposed model. Moreover, because time series data is a strongly auto-correlated series of values, we segmented the data as continuous, but not overlapping, sliding windows. To ensure that the data in each time window were continuous, we carefully checked the time difference between the first and the last data points sorted by time in each time window and deleted time series windows with unreasonable time differences (i.e., gaps). Then, we formulated the pre-earthquake ionospheric perturbation discrimination task

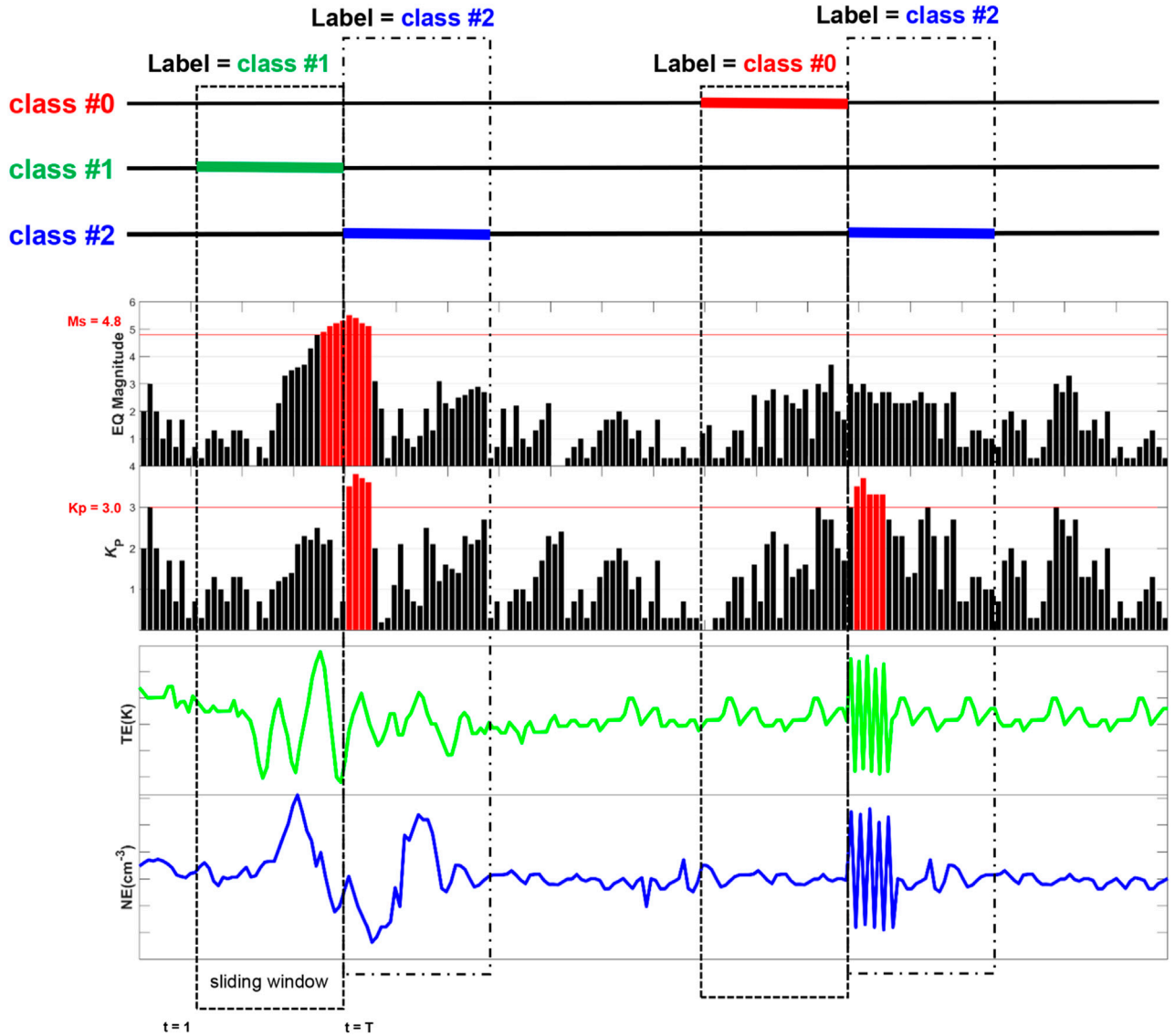

FIGURE 1 | Sequence labeling after segmenting the data with a sliding window. Consecutive observations of Ne and Te are segmented by non-overlapping sliding windows. T is the length of the window. Non-seismic data are labeled as 0 (class #0), seismic-related data are labeled as 1 (class #1), and data with a K_p index >3 are labeled as 2 (class #2), regardless of whether or not they are related to an earthquake.

as a multiclass multivariate time series classification problem, where the non-seismic-related data were labeled as 0, seismic-related data were labeled as 1, and the data with a K_p index greater than 3 (regardless of whether the data were related to an earthquake) were labeled as 2, which indicated density perturbations due to solar and magnetic activity (Parrot et al., 2006b), as depicted in **Figure 1**. The labeled sequence data are well illustrated in **Supplementary Figure S1**, which show real cases of different labels. The red dashed boxes in **Supplementary Figure S1** indicate non-seismic data with labeled 0. The green dashed boxes indicate seismic-related data with labeled 1 before the Chile M_s 8.8 earthquake on February 27, 2010. The blue dashed boxes are synchronous perturbations (labeled as 2) with large fluctuations in the data during the large magnetic storm on May 15, 2005.

The Earth's magnetic field experiences temporal fluctuations and displays known trends associated with the movement of the poles, and time series data have strong autocorrelation properties. Each dataset was rigorously divided into two contiguous parts: the first 80% (chronologically) of the data were used for model training, and the last 20% for testing and final evaluation. Specifically, the DEMETER dataset was divided into TR0 (training set) and TS0 (test set), and the CSES dataset was divided into TR1 (training set) and TS1 (test set). We first trained the deep-learning models with the DEMETER dataset; its architecture is shown in **Figure 2**. Then, we further tuned the models with the CSES dataset for transfer learning.

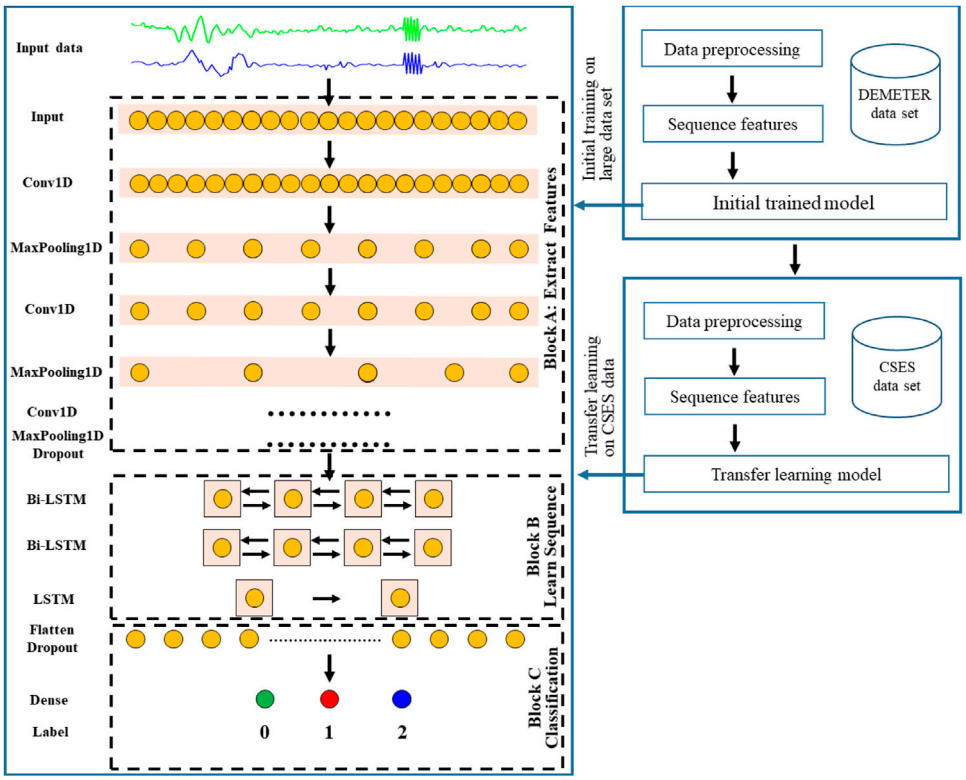

FIGURE 2 | Generalized model architecture of SeqNetQuake and the transfer learning process. Conv1D: 1-D convolutional neural network; MaxPooling1D: 1-D max-pooling layer; Dropout: drop-out layer; Bi-LSTM: bidirectional long short-term memory layer. "Flatten" and "Dense" are the names of the functional layers.

Deep Neural Networks

In our study, we combined a CNN and Bi-LSTM to train our proposed model SeqNetQuake (**Figure 2**). The model's architecture is composed of one-dimensional convolutional layers, a one-dimensional Bi-LSTM structural layer, and a fully connected (FC) block. The SeqNetQuake model employs CNN layers to extract features from the input data and Bi-LSTMs for sequence prediction. SeqNetQuake reads subsequences of the main sequence as blocks, extracts features from each block, and then allows the LSTM layer to interpret the extract features. To enable the same CNN model to read each subsequence in the window, the whole CNN model is wrapped in a TimeDistributed layer. After flattening the retrieved features, they are forwarded to the Bi-LSTM layer for reading, and further features are extracted. Conceptually, the 1D convolutional layers are used to extract the data features, after which the Bi-LSTM structures optimize the feature extraction in the sequential data. Finally, an FC layer is employed to generate a classification probability. The loss function was categorical cross-entropy, and the optimization was performed using the Adam method (Kingma and Ba, 2014).

The suggested model was developed using the Keras (v 2.3.0) interface with TensorFlow 2.0 (Abadi et al., 2016). To facilitate fast training, all models were built on a server equipped with two Intel Xeon E5-2650 v4 CPU processors, 128 GB of RAM, and an NVIDIA GeForce RTX 2080 Ti graphics processing unit (GPU) (Oh and Jung, 2004). As the proposed method is sensitive to the selected parameters, Bayesian hyperparameter tuning (Snoek et al., 2012) was utilized to determine the parameters that provide the best performance, and the Hyperopt Python package (Bergstra et al., 2013) was used to implement it. In this process, the negative of the F-measure (F1) was used as the return value (loss) of the objective function. The process selects the most promising hyperparameters based on their ability to minimize an objective function by building a probability model based on the past evaluation results. Thus, this study can better perform with fewer iterations than the required efforts to conduct random and grid searches. **Supplementary Table S2** provides the information on the search space for the significant parameters of SeqNetQuake. The maximum number of iterations for each model was set to 100. Supplemental Dataset S1 provides the hyperparametric optimization trial results for all the datasets passed through SeqNetQuake and other benchmarking classifiers when we train the model.

Transfer Learning

Transfer learning describes when a complex model that has been trained using a large dataset for a specific task is further trained for a related task with limited data (Pan and Yang, 2010). We used the training data from the large DEMETER dataset (TR0) for initial training, the test data of the large DEMETER dataset (TS0) was used for testing the initial model, and then transfer learning was employed using the small CSES training dataset (TR1)

(**Figure 2**). All the weights/parameters that were learned using TR0 were retrained for TR1. We trained all the model weights without freezing any layer during transfer learning, as this approach provides better results (Hanson et al., 2020). The small CSES test dataset (TS1) was used as an independent test set during transfer learning, and the hyperparameters used were the same as those employed when we train the models on the TS0 dataset.

Performance Evaluation

The DEMETER and CSES datasets are often class imbalanced where the number of the samples representing non-seismic class is much higher than the number of the samples in the other classes (Japkowicz and Stephen, 2002). In this case, a trivial classifier that predicts each sample as the majority class can obtain very high accuracy, and therefore, the overall classification accuracy is not accurate to evaluate the performance. Therefore, we use the F-measure (F1) evaluation model, which considers the correct classification of each class to be equally important. The F1-score is a metric that combines precision and recall. It is usually described as the harmonic mean of both. Thus, the class imbalance is countered by weighting different classes according to their sample proportions.

Beyond the metric mentioned above, which emphasize the positives, the Matthews correlation coefficient (MCC) (Matthews, 1975) is also adopted.

Further, receiver operating characteristic (ROC) curves, plots of the true positive rate (TPR) against the false-positive rate (FPR), were used to evaluate the classifier's output quality in this study. ROC curves are typically used in binary classification contexts to evaluate the output of a classifier. To extend the ROC curve and ROC area for multiclass classification, the output is binarized, and one ROC curve can be drawn and used to evaluate classifier quality per class. In addition, we calculated the area under the ROC curve, termed as AUC, which is used to distinguish different models. Higher AUC values were considered to be indicative of superior methods for the identification of pre-earthquake ionospheric perturbations.

Finally, to visually demonstrate the classification performance of each class, ternary probability diagrams and confusion matrixes were used to show the probability distributions for each input class of the test data and the distribution of the predictions and actual values.

Comparison of the Methods

Five state-of-the-art methods were benchmarked for the study task: the gradient boosting machine (GBM) (Friedman, 2001), deep neural network (DNN) (LeCun et al., 2015), random forest (RF) (Geurts et al., 2006), CNN (Krizhevsky et al., 2012), and LSTM (Hochreiter and Schmidhuber, 1997) models. These methods were implemented in Python (v 3.6) with scikit-learn (v 0.20.0) and Keras (v 2.3.0). As the investigated models are sensitive to parameter selection, we chose parameters that yielded the best performance using Bayesian hyperparameter tuning, as described above. After optimal parameters were determined for each method, the performances of the different methods were compared.

RESULTS

Direct Training Using CSES Data

We first directly trained the proposed SeqNetQuake model using the CSES dataset, which was further contiguously divided into a training set (TR1) and a test set (TS1). Given that there is no universal standard for the lengths of the input sequence and the spatial window, we initially configured the data with 10 consecutive observations as the input sequence length, a spatial window centered at the epicenter, a deviation of 3°, and nighttime data in the initial configuration (DataSet 01 in **Supplementary Table S1**).

As shown in **Supplementary Figure S2**, ROC curves are adopted as a performance metric, as they depict relative trade-offs between true positives (benefits) and false positives (costs) for each class; the model's performance using nighttime data is displayed for three classes. **Supplementary Figures S2A–C** demonstrates that the AUC values of classes 0 and 1 are higher than 0.7, indicating that the model can roughly identify the time series related to earthquakes and non-seismic events, but the AUC of class 2 is only 0.6128, indicating that the model's accuracy in identifying space weather such as magnetic storms is not high. This may be attributed to the smaller number of samples used to train class 2, which could have led the model to fail to extract the features of this class. **Supplementary Figure S2D** shows the bar plot curves of MCC, F1 score, and accuracy, which reflect the model's overall performance. The results are similar to those implied by the ROC curves, indicating that the model can distinguish, to some extent, earthquakes, non-seismic, and space events. In general, the performance of the model based on the initial configuration was reasonable but relatively weak. Therefore, we explored whether combining datasets with different temporal and spatial features or different models may offer better performance.

Nighttime vs. Daytime Data

Data acquisition time may impact pre-earthquake electromagnetic perturbation identification. A daytime dataset (DataSet 02 in **Supplementary Table S1**) was generated to demonstrate the influence of data acquisition time. As shown in **Figure 3** and **Table 1**, benchmarking datasets collected during the daytime and nighttime were used to compare SeqNetQuake's results with different data acquisition times. We employed AUC, MCC, F1, and accuracy metrics to evaluate the model's performance.

In general, we discovered that the use of the nighttime datasets (DataSet 01 in **Supplementary Table S1**) leads to better classification performance than the daytime dataset for the same spatial and temporal features (**Table 1**). The ROC curves of SeqNetQuake for both datasets are shown in **Figures 3A–C**, and we can see that the AUC curve of SeqNetQuake with the nighttime data is a little higher than that with the daytime data, with about 8, 8, and 10% improvements in AUC for the three classes. When all the classes are considered, the F1 score of SeqNetQuake increases from 0.5963 to 0.6238 when the nighttime data are used, compared to those when the daytime data are used, and MCC improves by 33% (**Table 1**). **Figure 3D** compares the daytime and nighttime MCC, F1 score, and accuracy values, all of which show better performance with the nighttime data. These findings may represent a small number of significant changes in daytime data, since ionospheric conditions are

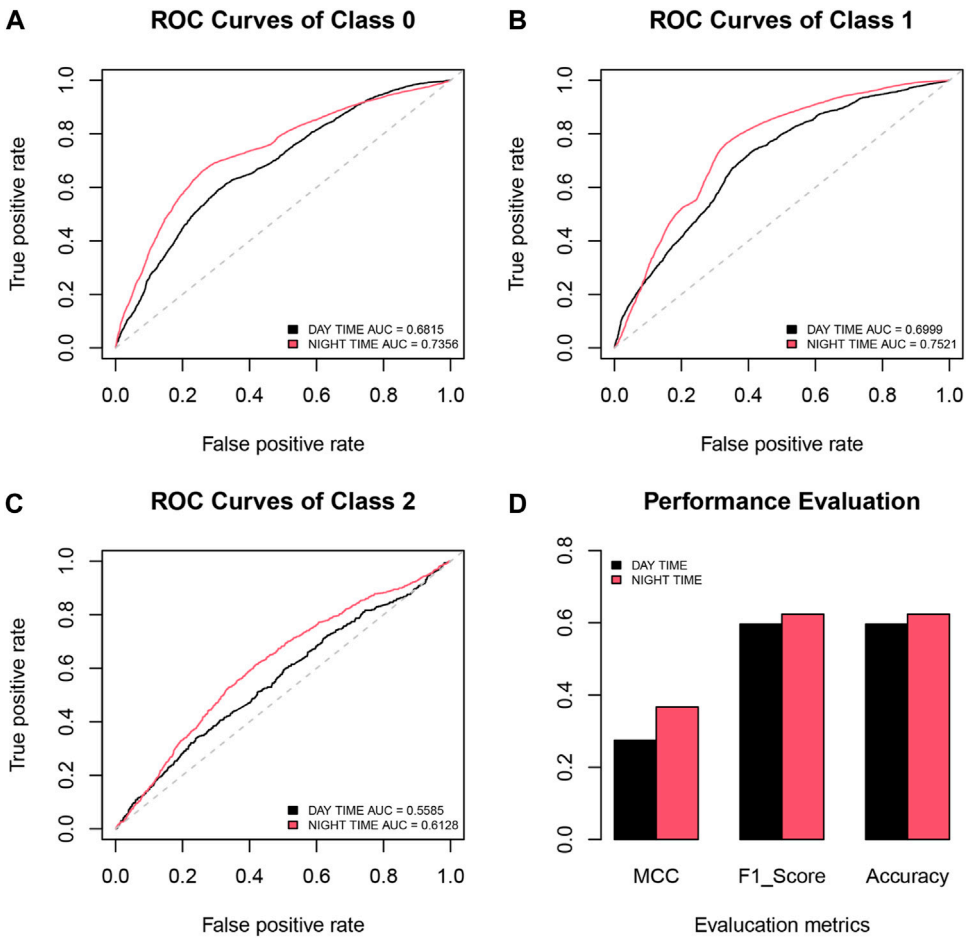

FIGURE 3 | Receiver operating characteristic (ROC) curves displaying the performance comparison between model use in the nighttime and daytime data for **(A)** class 0, **(B)** class 1 and **(C)** class 2. **(D)** Bar plot curves of Matthews correlation coefficient (MCC), F1 score, and accuracy comparing model performance for nighttime and daytime data use.

often more disrupted during the day, making identification of seismic electromagnetic impacts more challenging. This conclusion is consistent with statistical findings on electromagnetic disturbances associated with earthquake activity (De Santis et al., 2019b; Němec et al., 2008,2009; Píša et al., 2012,2013).

Effect of Input Sequence Length

We observed that using the dataset with 10 consecutive observations (DataSet 01) per sliding window as the input sequence length yields good classification performance. To further study whether the SeqNetQuake method can identify pre-earthquake perturbations using different input sequence lengths, datasets with an input sequence length of 20 consecutive observations (DataSet 03), 30 consecutive observations (DataSet 04), 40 consecutive observations (DataSet 05), and 50 consecutive observations (DataSet 06) were generated (**Supplementary Table S1**).

Figure 4 shows the ROC curves and MCC, F1 score, and accuracy bar plot curves for the datasets with different input sequence lengths. **Table 1** shows the classification performance measures using SeqNetQuake. As shown in **Table 1**, the overall F1 scores range from 0.5959 to 0.6658, and the MCC ranges from 0.2629 to 0.3875 for different datasets; these values are also demonstrated in performance comparison in **Figure 4D**. When the input sequence length increases, the model's performance fluctuates; the best performance is achieved using the dataset with the input sequence length of 20 consecutive observations (DataSet 03). The ROC curves shown in **Figures 4A–C** also suggest that SeqNetQuake provides satisfactory performance for each class using DataSet 03. However, SeqNetQuake's performance becomes worse if the input sequence length increases by more than 20. We infer from these findings that the length of the input sequence has an impact on the results of the SeqNetQuake model and that the best performance is achieved with an input sequence of 20 consecutive observations.

Effect of Different Spatial Windows

SeqNetQuake performed well for a circular region centered at the epicenter with a deviation of 3° (DataSet 03). To further explore

TABLE 1 | Performance of SeqNetQuake on the test set after direct training, initial training, and transfer learning. Data from DEMETER were divided into a training set (TR0) and test set (TS0), and data from CSES were divided into TR1 (training set) and TS1 (test set).

Method	Traning set	Test set	F1	MCC	Accuracy	AUC of class 0	AUC of class 1	AUC of class 2
Direct training	TR1-01	TS1-01	0.6238	0.3667	0.6238	0.7356	0.7521	0.6128
	TR1-02	TS1-02	0.5963	0.2749	0.5963	0.6815	0.6999	0.5585
	TR1-03	TS1-03	0.6658	0.3857	0.6658	0.7508	0.7890	0.6163
	TR1-04	TS1-04	0.5989	0.2868	0.5989	0.6971	0.7143	0.5606
	TR1-05	TS1-05	0.6023	0.2859	0.6023	0.6926	0.7141	0.6106
	TR1-06	TS1-06	0.5959	0.2629	0.5959	0.6909	0.6939	0.5913
	TR1-07	TS1-07	0.6792	0.427	0.6792	0.7638	0.7564	0.6269
	TR1-08	TS1-08	0.6636	0.2812	0.6636	0.6896	0.6724	0.5747
	TR1-09	TS1-09	0.6532	0.2935	0.6532	0.6861	0.6681	0.5802
	TR1-10	TS1-10	0.6289	0.2309	0.6289	0.6605	0.6409	0.5643
Initial training	TR0	TS0	0.7002	0.3763	0.7002	0.7393	0.7177	0.6254
Transfer learning	TR0	TS1-07	0.7607	0.5523	0.7607	0.8329	0.8519	0.6323

the influence of different spatial windows on the model's performance, satellite datasets using spatial windows with Dobrovolsky radius (DataSet 07), a deviation of 5° (DataSet 08), 7° (DataSet 09), and 12° (DataSet 10) were generated (**Supplementary Table S1**).

Rows 6 to 10 in **Table 1** show the SeqNetQuake's performance using the five datasets, and **Figure 5** shows the ROC curves and MCC, F1 score, and accuracy bar plot curves. SeqNetQuake attains the best performance using the dataset with the spatial window radius given by the Dobrovolsky's formula (DataSet 07), achieving an F1 score of 0.6792 and an MCC of 0.427. Comparing the results from **Figure 5D** and **Table 1** reveals a slight increase in the overall performance achieved when the spatial windows are larger. This trend is also shown in the ROC curves in **Figures 5A–C**, and the AUC value of DataSet 07 is the best among the datasets. Though the explanation for these results is unclear, it might concern the fact that, geometrically, a disturbance traveling upward from the earth surface may alter the ionosphere's characteristics, and the radius of the affected region matches the radius estimated using Dobrovolsky's formula.

Initial Training on DEMETER Data and Transfer Learning on CSES Data

A DEMETER dataset was generated based on the optimal spatio-temporal feature configuration for the CSES data (DataSet 11 in **Supplementary Table S1**). In this study, deep transfer learning, although it is first applied to DEMETER to be transferred to CSES, considers the properties and features of CSES data. In other words, it is shaped/adapted to CSES data features.

We first trained the SeqNetQuake model using the full DEMETER dataset, which was contiguously divided into a training set (TR0) and test set (TS0). Using TR0 for training, TS0 for testing, and the sliding sequences as model input, we trained deep-learning models with its architecture shown in the left panel of **Figure 2**. The performance of the best model using TS0 is shown in **Table 1**. The F1 score of 0.7002 and MCC of 0.3763 for TS0 suggest the robustness of the trained model.

The model obtained using the DEMETER data was further trained using the CSES data employing TR1 (training set) and TS1 (test set), which corresponds to a transfer-learning process. The TS1 set was independent of the training data (TR0 and TR1). **Table 1** and **Figure 6D** further illustrate the performance of the initial training and transfer training. The F1 score improved by 8% from 0.7002 to 0.7607, and MCC increased from 0.3763 to 0.5523 using TR0 for training, confirming the robustness of the model trained using the larger DEMETER dataset. The ROC curves in **Figures 6A–C** provide a visual performance comparison of each class and further demonstrate the result.

Comparison Between Transfer Learning and Direct Learning

We selected the model with the best performance in direct learning, the SeqNetQuake model trained on Dataset 07 (called SeqNetQuake-DT), and compared it with the model trained using transfer learning (called SeqNetQuake-TL). **Table 2** compares the performance of the two approaches, and **Figure 6D** shows the bar plot of the performance metrics. **Figures 6A–C** compares the ROC curves yielded by direct training and transfer learning for the independent test set TS1.

The performance of direct learning was significantly lower than that of transfer learning, yielding a 10% reduction in the F1 score and a 23% reduction of the MCC value. These results confirm the difficulty of using small training data sets (TR1) for direct learning and the need to use large data sets that can effectively exploit the capabilities of the deep-learning networks.

To further confirm the performance of transfer learning, ternary probability diagrams and a confusion matrix were used to indicate the distribution of the predicted and true values and allow more profound insight into the classification performance of the models. **Supplementary Figure S3** and **Figure 7** show the ternary probability diagrams and the confusion matrix for the three classes obtained from SeqNetQuake-DT and SeqNetQuake-TL, respectively.

The ternary probability diagrams allow a qualitative evaluation of the classification results. The number of the correctly classified samples in class 0 increases significantly, as evidenced from **Supplementary Figure S3A** and **Figure 7A**; the

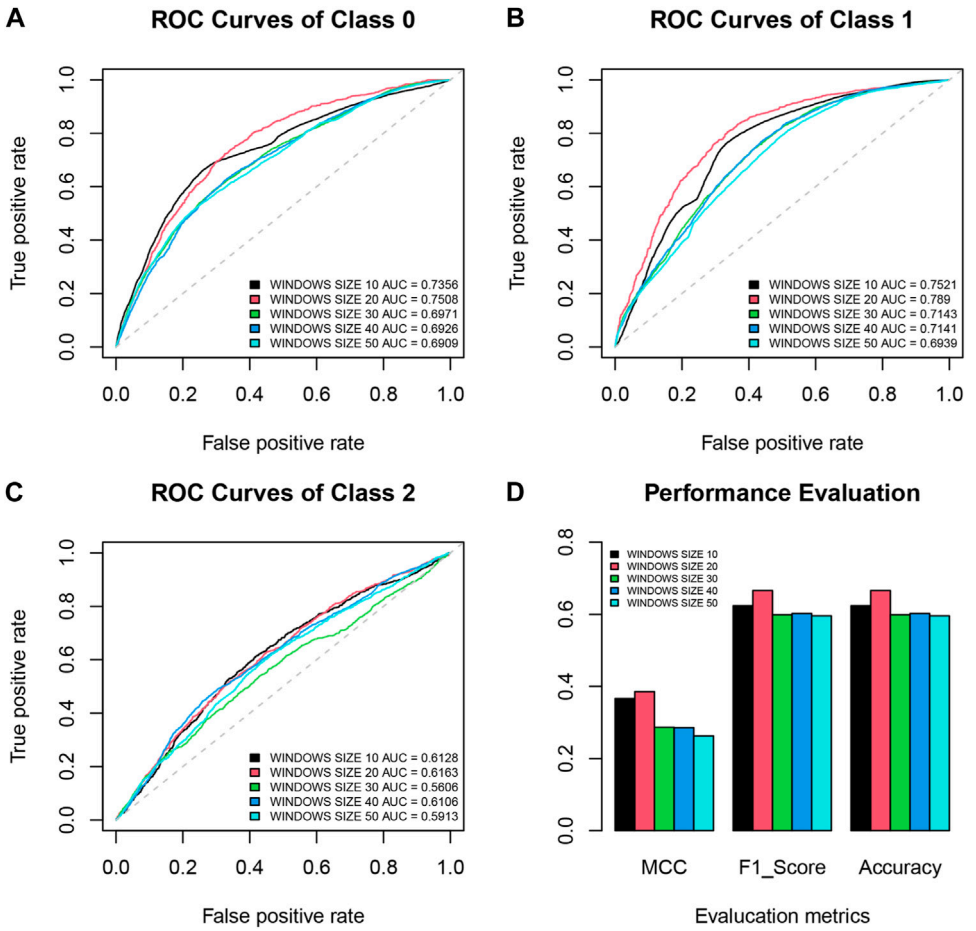

FIGURE 4 | Receiver operating characteristic (ROC) curves comparing model performance with window sizes of 10, 20, 30, 40, and 50 for **(A)** class 0, **(B)** class 1 and **(C)** class 2. **(D)** Bar plot curves of Matthews correlation coefficient (MCC), F1 score, and accuracy with window sizes of 10, 20, 30, 40, and 50.

same trend also appears in the qualitative comparison of class 1 in **Supplementary Figure S3B** and **Figure 7B**. For class 2, the direct training results (**Supplementary Figure S3B**) show that the probability that the model would discriminate the true class is generally only around 0.4. With transfer learning, the probability is significantly improved and is typically higher than 0.5 (**Figure 7C**). As class 2 only represents 10.5% of samples, far less than the proportions of the other two classes (which are 45.3 and 44.1%, respectively), the model likely fails to fully learn the features of this class, causing a higher error rate.

The confusion matrixes shown in **Supplementary Figure S3D** and **Figure 7D** show significant improvements in precision regarding class 2, from 75.3% before transfer learning to 95.2% after. Further, transfer learning achieves 9 and 13.06% improvements in precision for classes 0 and 1, respectively. Therefore the misclassification rate of each class drops significantly after transfer learning. Transfer learning achieves satisfactory results in the classification of classes 0 and 1, and the probability distributions for each class of the test data (**Figure 7D**) show that 77.9 and 85.1% of the input samples, respectively, are correctly classified (recall).

Comparison With Other Classifiers

Table 2 and **Figure 8D** report the performance of our transfer-learning model (SeqNetQuake-TL) with five other benchmarking classifiers for the independent test set TS1-07. The performance of the existing methods ranges from F1 = 0.5757 to 0.7607 and MCC = 0.2365 to 0.552. However, SeqNetQuake-TL offers the best performance, improving MCC by 64.2% MCC and F1 by about 24.5% over those for the next-best CNN model. **Figures 8A–C** compares the ROC curves obtained for the SeqNetQuake-TL model with those of the five other classifiers, and SeqNetQuake-TL again demonstrates the best performance with a 14.5% improvement in AUC for class 0 and a 12.2% improvement for class 1 over the second-best CNN model and a 4.4% improvement in AUC for class 2 over the second-best LSTM model.

Excellent neural network architecture may explain why SeqNetQuake outperforms all the other predictors. First, SeqNetQuake's CNN network layers allows us to extract local parallel features. Then, the Bi-LSTM layer (composed of multiple memory modules with a two-cell topological structure) extracts long-distance dependent features and performs sequence

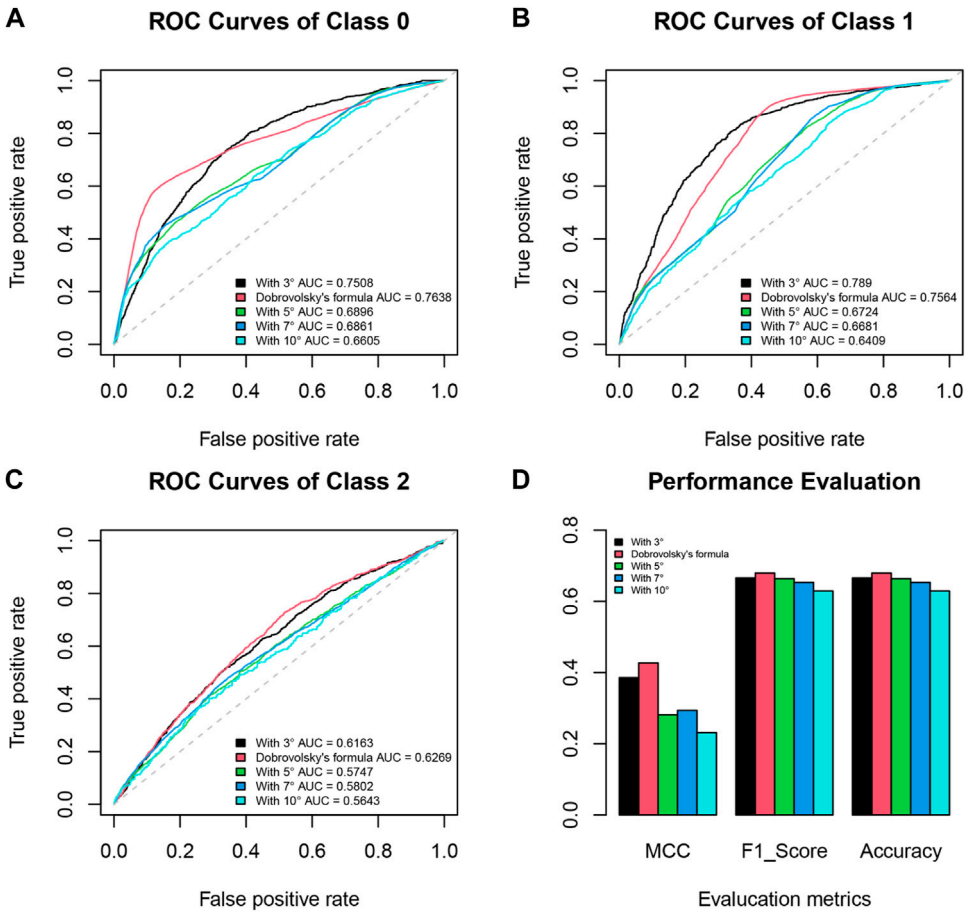

FIGURE 5 | Receiver operating characteristic (ROC) curves comparing model performance with different spatial window radii (3°, Dobrovolsky's formula, 5°, 7°, and 10° for **(A)** class 0, **(B)** class 1, and **(C)** class 2. **(D)** Bar plot curves of Matthews correlation coefficient (MCC), F1 score, and accuracy.

learning, thereby mitigating the influence of the front and back features of each attribute feature point. Finally, the model obtains the classification results through the FC layer and the Softmax classifier, improving SeqNetQuake's accuracy and reducing false positives. Notably, the DNN, CNN, and LSTM models performed better than the RF and GBM models, suggesting that the deeper neural network models are much more efficient in computation and the number of the parameters.

Possible Physical Mechanisms of Earthquake-Induced Ionospheric Perturbations

Lithospheric-ionospheric coupling is a topic that has been qualitatively discussed in several papers. Several studies have investigated the physical mechanisms of ionospheric pre-earthquake perturbations (Hayakawa et al., 2010; Pulinets and Ouzounov, 2011; Wu et al., 2012; Ouzounov et al., 2018; De Santis et al., 2019a; De Santis et al., 2020; Freund et al., 2021). Hypotheses regarding these mechanisms were presented by Pulinets et al. (2015) and Kuo et al. (2014), who proposed complex lithosphere–atmosphere–ionosphere coupling as the physical basis of the generation of short-term earthquake precursors. Recently, a detailed mathematical model providing a quantitative description of the Magnetospheric-Ionospheric-Lithospheric-Coupling (MILC) was introduced and successfully tested with data from individual earthquakes (Piersanti et al., 2020a). A key feature of the MILC model is based on the development of an Acoustic Gravity Wave (AGW) (Carbone et al., 2021) interacting mechanically with the ionosphere and then electromagnetically with the magnetosphere. The AGW coupling mechanism is quite general and can provide for both co-seismic and precursor lithospheric-ionospheric coupling. In the case of co-seismic coupling, the AGW is generated by ground surface motion (solid, liquid). In contrast, in the case of precursor coupling, the AGW can be generated by phenomena which modifying the temperature or the electrical properties of the atmospheric column above the EQ preparation zone.

One example of such mechanisms is radon release following by its radioactive decay, emitting alpha particles of 5.2 MeV, a large value used in comparison to the ionization energy required for the dissociation of an atmospheric molecule (32 eV). One alpha particle is sufficient to generate 150,000 pairs of positive and negative ions, thereby creating an excess

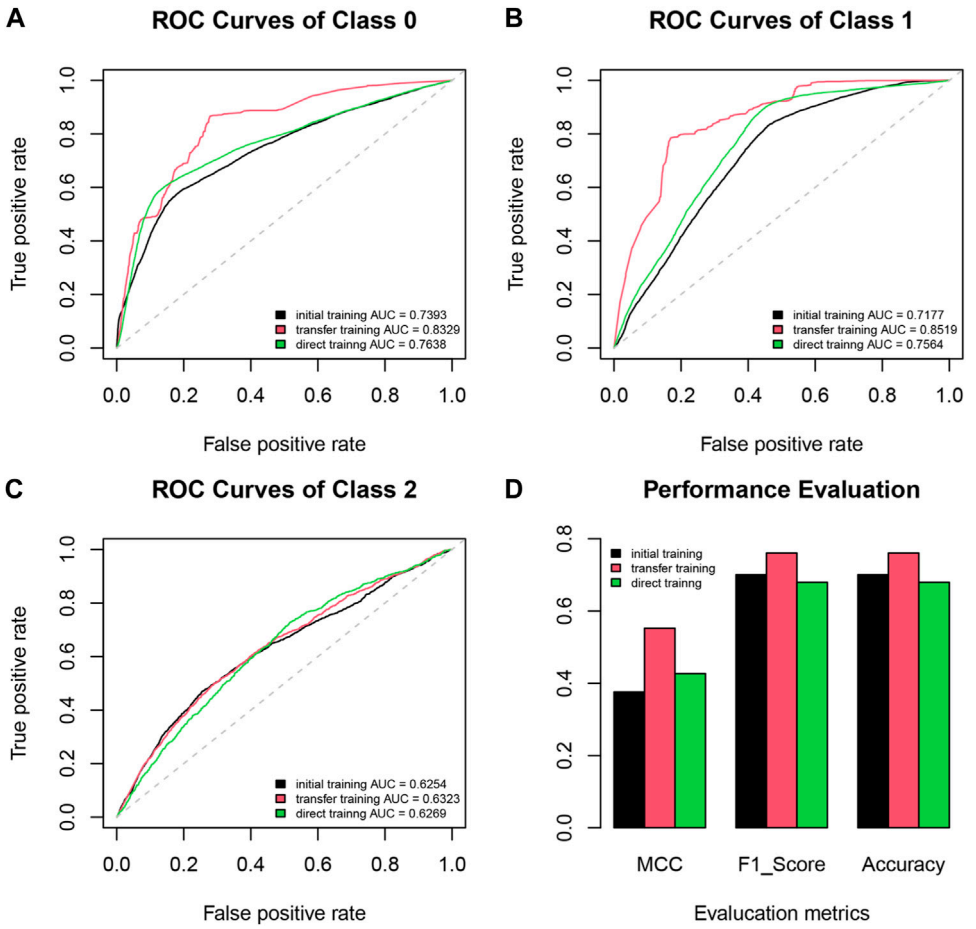

FIGURE 6 | Receiver operating characteristic (ROC) curves comparing the performance of initial training, transfer training, and direct training for **(A)** class 0, **(B)** class 1 and **(C)** class 2. **(D)** Bar plot curves of Matthews correlation coefficient (MCC), F1 score, and accuracy.

TABLE 2 | Performance of all classifiers on the test set TS1. Data from DEMETER were divided into a training set (TR0) and test set (TS0), and data from CSES were divided into TR1 (training set) and TS1 (test set). SeqNetQuake-TL, SeqNetQuake-IT, and SeqNetQuake-DT indicate the SeqNetQuake model trained via transfer learning, initial training, and direct training.

Method	Traning set	Test set	F1	MCC	Accuracy	AUC of class 0	AUC of class 1	AUC of class 2
SeqNetQuake-TL	TR0	TS1-07	0.7607	0.5523	0.7607	0.8329	0.8519	0.6323
SeqNetQuake-IT	TR0	TS0	0.7002	0.3763	0.7002	0.7393	0.7177	0.6254
SeqNetQuake-DT	TR1-07	TS1-07	0.6792	0.427	0.6792	0.7638	0.7564	0.6269
Random Forest	TR1-07	TS1-07	0.5757	0.2365	0.5757	0.6883	0.6755	0.5399
GBM	TR1-07	TS1-07	0.5845	0.2553	0.5845	0.7027	0.6959	0.5477
CNN	TR1-07	TS1-07	0.611	0.3364	0.611	0.7274	0.7591	0.5913
LSTM	TR1-07	TS1-07	0.6061	0.2973	0.6061	0.6979	0.7134	0.6055
DNN	TR1-07	TS1-07	0.5928	0.2896	0.5928	0.6901	0.7059	0.5947

of positive airborne ions near the Earth's surface, which can influence the ionosphere. Radon gas accumulates with time in the lower crust and upper mantle and can exhibit large-scale distribution in the rocks. During the preparation phase of an earthquake, these gas domains can become hydrostatically unstable and force their way upward through the lithosphere. The rapid lithospheric degassing followed by radon atoms radioactive decays would trigger several atmospheric processes near Earth's surface, leading to changes in air conductivity and temperature and therefore changes to the near-ground atmospheric electric field (Ouzounov et al., 2018; Pulinets and Ouzounov, 2018).

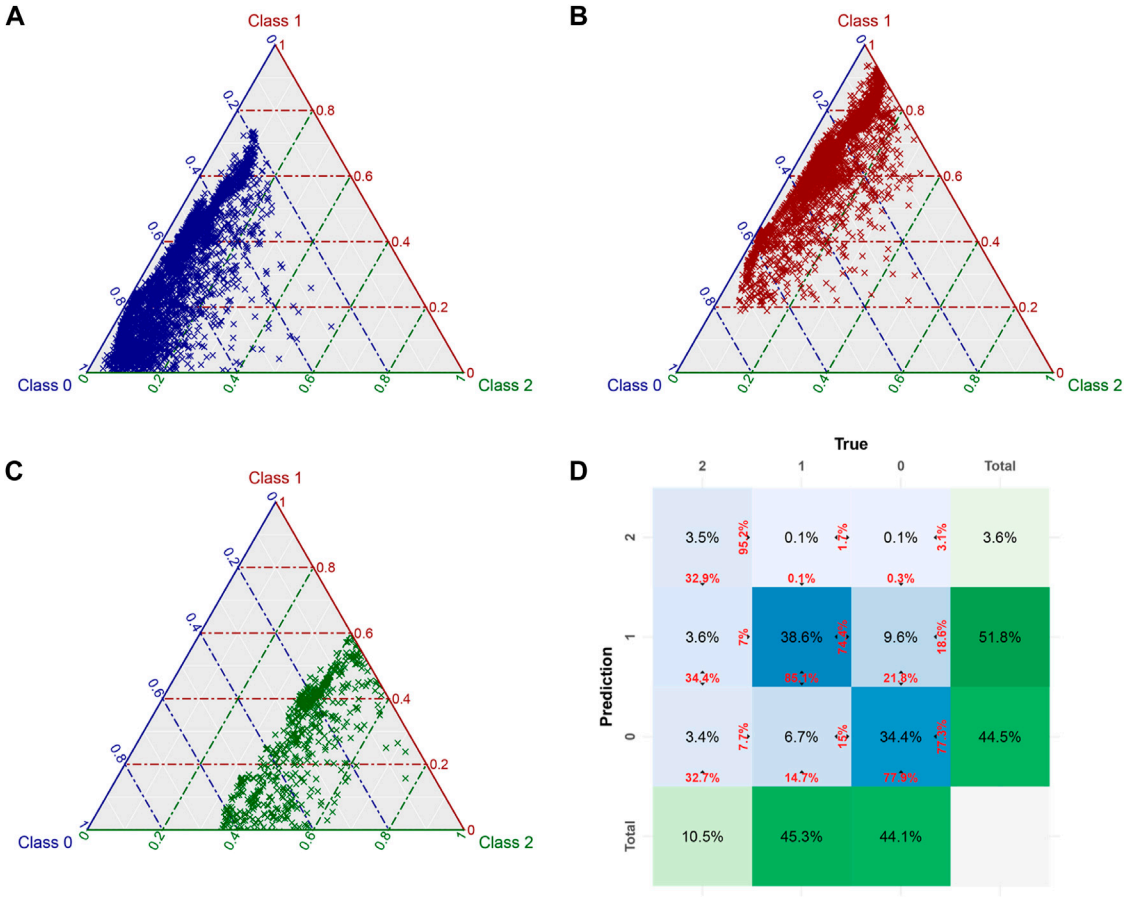

FIGURE 7 | Ternary probability diagrams showing transfer learning results for **(A)** class 0, **(B)** class 1, and **(C)** class 2 using the test data. Class 0, class 1, and class 2 are shown in blue, red, and green, respectively; the color of the dot itself represents the real class, and the distance projected from each dot to each class axis represents the probability of that class in the model prediction. **(D)** Confusion matrix indicating the distribution of the predicted and true values. The normalized count (overall percentage) is shown in the center of each tile. The column percentage is shown at the bottom of each tile, and the row percentage is shown on the right. Sum tiles to the right and bottom of the plot show the overall distribution of predictions and targets. Note that the color intensity is based on the counts.

Crustal strain measurements typically fail to detect any unusual changes before earthquakes (Soter, 1999), while radon outgassing has been observed before the earthquake (Gold and Soter, 1985; Riggio and Santulin, 2015; Fu et al., 2019), and they are considered as a possible EQ precursor.

DISCUSSION AND CONCLUSION

Previous studies have applied machine learning with the DEMETER data for earthquake prediction and pre-earthquake perturbation analysis. Li et al. (2020) statistically investigated seismo-ionospheric influencing factors; however, the FPR of the statistical results reached 50.2%. The relationship between earthquakes and ultralow frequency (ULF) wave activity in the nighttime ionosphere was investigated by Ouyang et al. (2020). According to their research, the accuracy of detecting electromagnetic pre-earthquake disturbances was 34%. Xu et al. (2010) used a back-propagation neural network to predict seismic events in 2008 with DEMETER data and achieved an accuracy of 69.96%. Finally, Wang et al. (2014) adopted the frequent itemset algorithm to predict earthquakes of M_s > 5.0 in Taiwan, China, and achieved a maximum sensitivity of 70.01%.

When the performance of these models was compared, the SeqNetQuake method outperformed the others. SeqNetQuake offers three main advantages over those existing methods. First, hyperparametric optimization is applied for all the engaged methods, allowing researchers to identify the most suitable parameters at each step. Therefore, technology can be selected with high confidence, and the selection of a robust method is assured. Second, a more advanced deep-learning architecture is used than that in traditional statistical and data-mining methods. Finally, the majority of existing techniques are verified using a limited sample size; this includes the method proposed by Wang et al. (2014), which may exhibit a significant bias toward results covering a wider geographic region or a longer time period. However, in the present study, SeqNetQuake was trained with all the DEMETER data and nearly 2 years of the CSES data worldwide, and global features were learned during the training process. Hence,

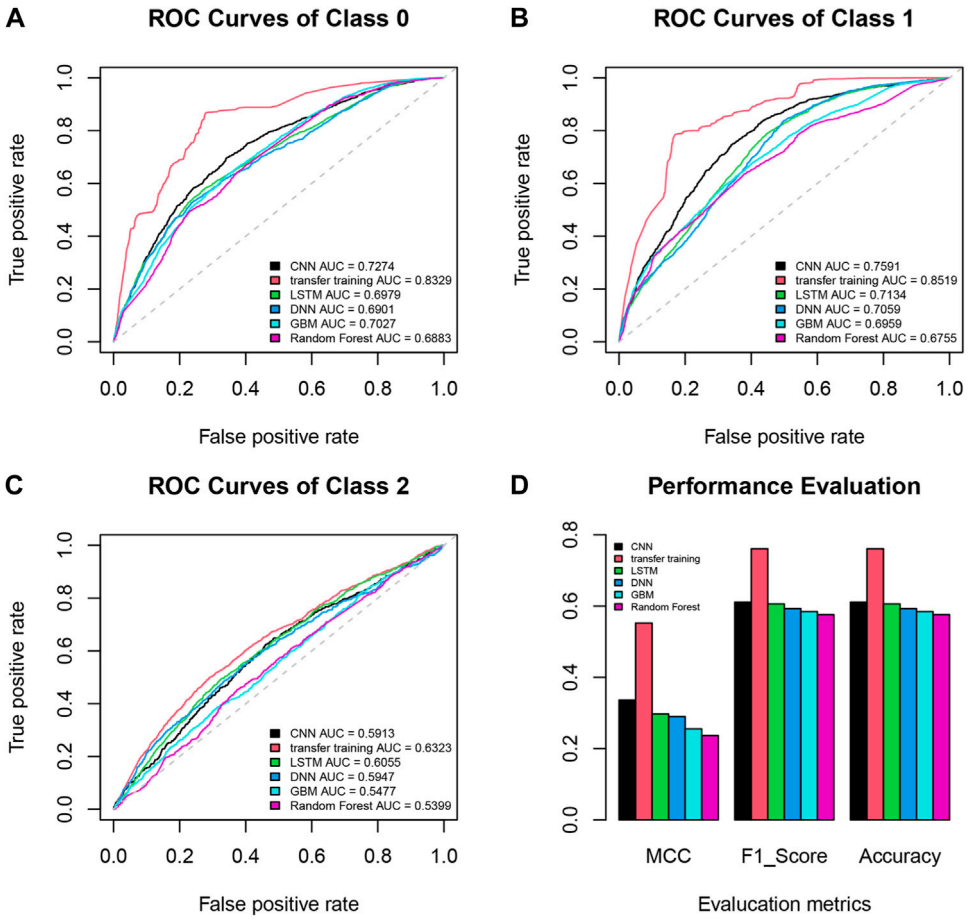

FIGURE 8 | Receiver operating characteristic (ROC) curves displaying the performance comparison of SeqNetQuake-TL, gradient boosting machine (GBM), deep neural network (DNN), random forest (RF), convolutional neural network (CNN), and long short-term memory (LSTM) models for **(A)** class 0, **(B)** class 1 and **(C)** class 2. **(D)** Bar plot curves of Matthews correlation coefficient (MCC), F1 score, and accuracy.

SeqNetQuake has strong generalizability. One limitation of SeqNetQuake, however, is its significant computational complexity owing to its complex network architecture. This issue may be resolved by increasing the number of processing resources available, such as additional CPUs or GPUs.

Recent research (Ikuta et al., 2020; Eisenbeis and Occhipinti, 2021) showed that claimed TEC anomalies were actually artifacts. However, their negative response is mainly based on the criticisms to some previous papers (Heki, 2011; Heki and Enomoto, 2015; He and Heki, 2017). In this paper, we do not define anomalies in the same way the criticized papers define the TEC anomalies. On the other hand, most seismologists will say that tectonic plates are always in a state of stress, and the stress is always present because the tectonic system constantly adjusts to a state of self-organized criticality, which theoretically would indicate that when and where the earthquake occurred are inherently unpredictable (Bak et al., 1987). Nevertheless, Ramos et al. (2009) proved that earthquakes are preceded by continuous and detectable changes in the interior of the earth's crust, and these changes can be monitored and have been achieved for prediction purposes: this argument was also confirmed by De Santis et al. (2019b) and Varotsos et al. (2020), with statistical and theoretical arguments, respectively.

In our paper, we proposed the use of deep learning for pre-earthquake ionospheric perturbations identification using the SeqNetQuake model and identifying optimal training regimes and parameter settings. The proposed model offers better performance than five state-of-the-art models. Finally, our analysis results verify the hypothesis regarding the physical mechanisms of earthquake-induced ionospheric perturbations. These results also support that the use of big satellite data analytics and transfer learning can successfully improve the pre-earthquake ionospheric perturbation identification performance. The SeqNetQuake algorithm is useful in the analysis of precursor effects in electromagnetic satellite data.

DATA AVAILABILITY STATEMENT

The CSES data can be acquired from the website (www.leos.ac.cn), and DEMETER data can be accessed through the website https://cdpp-archive.cnes.fr/. The used K_p indices were provided

from the World Data Center for Geomagnetism, Kyoto (http://wdc.kugi.kyoto-u.ac.jp/wdc/Sec3.html).

AUTHOR CONTRIBUTIONS

PX, HZ, RB, AS, DO, and XS: Conceptualization, Methodology, Software. PX and XZ: Data curation, Writing-Original draft preparation. HZ, RB, and AS: Visualization, Investigation. RB and XS: Supervision. PX, CL, and HZ: Software, Validation: PX, CL, HZ, RB, AS, and DO: Writing- Reviewing and Editing.

FUNDING

This work is funded by the National Key Research and Development of China under Grant No. 2018YFC1503505. This work is also supported by the LIMADOU-Science under Grant No. 2020-31-HH.0, a project funded by the Italian Space Agency (ASI), and INGV Further and MiUR Pianeta Dinamico-Working Earth Project.

SUPPLEMENTARY MATERIAL

The Supplementary Material for this article can be found online at: https://www.frontiersin.org/articles/10.3389/fenvs.2021.779255/full#supplementary-material

Supplementary Figure S1 | Electron density (Ne) and electron temperature (Te) sequence labels from real cases.

Supplementary Figure S2 | Receiver operating characteristic (ROC) curves demonstrating the performance of SeqNetQuake using nighttime data.

Supplementary Figure S3 | Ternary probability diagrams showing the results of SeqNetQuake-DT.

Supplementary Table S1 | Datasets with different features generated using DEMETER and CSES data.

Supplementary Table S2 | Search space of parameters for the SeqNetQuake model.

REFERENCES

Abadi, M., Barham, P., Chen, J., Chen, Z., Davis, A., Dean, J., et al. (2016). Tensorflow: A System for Large-Scale Machine Learning. Paper presented at the 12th {USENIX} symposium on operating systems design and implementation ({OSDI} 16)

Athanasiou, M. A., Anagnostopoulos, G. C., Iliopoulos, A. C., Pavlos, G. P., and David, C. N. (2011). Enhanced ULF Radiation Observed by DEMETER Two Months Around the strong 2010 Haiti Earthquake. *Nat. Hazards Earth Syst. Sci.* 11 (4), 1091–1098. doi:10.5194/nhess-11-1091-2011

Bak, P., Tang, C., and Wiesenfeld, K. (1987). Self-organized Criticality: An Explanation of the 1/fnoise. *Phys. Rev. Lett.* 59 (4), 381–384. doi:10.1103/physrevlett.59.381

Bergen, K. J., Johnson, P. A., de Hoop, M. V., and Beroza, G. C. (2019). Machine Learning for Data-Driven Discovery in Solid Earth Geoscience. *Science* 363 (6433). Available at: https://www.ncbi.nlm.nih.gov/pubmed/30898903. doi:10.1126/science.aau0323

Bergstra, J., Yamins, D., and Cox, D. D. (2013). "Making a Science of Model Search: Hyperparameter Optimization in Hundreds of Dimensions for Vision Architectures," in Paper presented at the Proceedings of the 30th International Conference on International Conference on Machine Learning, ICML 2013, Atlanta, GA, USA, 16–21 June 2013, 28, 115–123.

Bertello, I., Piersanti, M., Candidi, M., Diego, P., and Ubertini, P. (2018). Electromagnetic Field Observations by the DEMETER Satellite in Connection with the 2009 L'Aquila Earthquake. *Ann. Geophys.* 36 (5), 1483–1493. doi:10.5194/angeo-36-1483-2018

Carbone, V., Piersanti, M., Materassi, M., Battiston, R., Lepreti, F., and Ubertini, P. (2021). A Mathematical Model of Lithosphere-Atmosphere Coupling for Seismic Events. *Sci. Rep.* 11 (1), 8682, 2021 . Available at: https://www.ncbi.nlm.nih.gov/pubmed/33883652. doi:10.1038/s41598-021-88125-7

De Santis, A., Abbattista, C., Alfonsi, L., Amoruso, L., Campuzano, S. A., Carbone, M., et al. (2019a). Geosystemics View of Earthquakes. *Entropy (Basel)* 21 (4). Available at: https://www.ncbi.nlm.nih.gov/pubmed/33267126. doi:10.3390/e21040412

De Santis, A., Marchetti, D., Pavón-Carrasco, F. J., Cianchini, G., Perrone, L., Abbattista, C., et al. (2019b). Precursory Worldwide Signatures of Earthquake Occurrences on Swarm Satellite Data. *Sci. Rep.* 9 (1), 20287, 2019b . Available at: https://www.ncbi.nlm.nih.gov/pubmed/31889060. doi:10.1038/s41598-019-56599-1

De Santis, A., Marchetti, D., Spogli, L., Cianchini, G., Pavón-Carrasco, F. J., Franceschi, G. D., et al. (2019c). Magnetic Field and Electron Density Data Analysis from Swarm Satellites Searching for Ionospheric Effects by Great Earthquakes: 12 Case Studies from 2014 to 2016. *Atmosphere* 10 (7), 371. doi:10.3390/atmos10070371

De Santis, A., Cianchini, G., Marchetti, D., Piscini, A., Sabbagh, D., Perrone, L., et al. (2020). A Multiparametric Approach to Study the Preparation Phase of the 2019 M7.1 Ridgecrest (California, United States) Earthquake. *Front. Earth Sci.* 8, 540398. doi:10.3389/feart.2020.540398

Eisenbeis, J., and Occhipinti, G. (2021). The TEC Enhancement before Seismic Events Is an Artifact. *J. Geophys. Res. Space Phys.* 126 (4), e2020JA028733. doi:10.1029/2020ja028733

Freund, F. T., Heraud, J. A., Centa, V. A., and Scoville, J. (2021). Mechanism of Unipolar Electromagnetic Pulses Emitted from the Hypocenters of Impending Earthquakes. *Eur. Phys. J. Spec. Top.* 230 (1), 47–65. doi:10.1140/epjst/e2020-000244-4

Friedman, J. H. (2001). Greedy Function Approximation: A Gradient Boosting Machine. *Ann. Stat.* 29 (5), 1189–1232. Available at: http://www.jstor.org/stable/2699986. doi:10.1214/aos/1013203451

Fu, C.-C., Lee, L.-C., Yang, T. F., Lin, C.-H., Chen, C.-H., Walia, V., et al. (2019). Gamma Ray and Radon Anomalies in Northern Taiwan as a Possible Preearthquake Indicator Around the Plate Boundary. *Geofluids* 2019, 1–14. doi:10.1155/2019/4734513

Geurts, P., Ernst, D., and Wehenkel, L. (2006). Extremely Randomized Trees. *Mach Learn.* 63 (1), 3–42. journal article. doi:10.1007/s10994-006-6226-1

Gold, T., and Soter, S. (1985). Fluid Ascent through the Solid Lithosphere and its Relation to Earthquakes. *Pure Appl. Geophys. PAGEOPH* 122 (2-4), 492–530. doi:10.1007/BF00874614

Gulia, L., and Wiemer, S. (2019). Real-time Discrimination of Earthquake Foreshocks and Aftershocks. *Nature* 574 (7777), 193–199. Available at: https://www.ncbi.nlm.nih.gov/pubmed/31597971. doi:10.1038/s41586-019-1606-4

Hanson, J., Litfin, T., Paliwal, K., and Zhou, Y. (2020). Identifying Molecular Recognition Features in Intrinsically Disordered Regions of Proteins by Transfer Learning. *Bioinformatics* 36 (4), 1107–1113. Available at: https://www.ncbi.nlm.nih.gov/pubmed/31504193. doi:10.1093/bioinformatics/btz691

Hayakawa, M., Kasahara, Y., Nakamura, T., Muto, F., Horie, T., Maekawa, S., et al. (2010). A Statistical Study on the Correlation between Lower Ionospheric Perturbations as Seen by Subionospheric VLF/LF Propagation and Earthquakes. *J. Geophys. Res. Space Phys.* 115 (A9), n/a. doi:10.1029/2009ja015143

He, L., and Heki, K. (2017). Ionospheric Anomalies Immediately before M W 7.0-8.0 Earthquakes. *J. Geophys. Res. Space Phys.* 122 (8), 8659–8678. doi:10.1002/2017ja024012

He, Y., Yang, D., Qian, J., and Parrot, M. (2011). Anomaly of the Ionospheric Electron Density Close to Earthquakes: Case Studies of Pu'er and Wenchuan Earthquakes. *Earthq Sci.* 24 (6), 549–555. doi:10.1007/s11589-011-0816-0

Heki, K., and Enomoto, Y. (2015). M W Dependence of the Preseismic Ionospheric Electron Enhancements. *J. Geophys. Res. Space Phys.* 120 (8), 7006–7020. doi:10.1002/2015ja021353

Heki, K. (2011). Ionospheric Electron Enhancement Preceding the 2011 Tohoku-Oki Earthquake. *Geophys. Res. Lett.* 38 (17), n/a. doi:10.1029/2011gl047908

Hobara, Y., Nakamura, R., Suzuki, M., Hayakawa, M., and Parrot, M. (2013). Ionospheric Perturbations Observed by the Low Altitude Satellite DEMETER and Possible Relation with Seismicity. *J. Atmos. Electr.* 33 (1), 21–29. doi:10.1541/jae.33.21

Hochreiter, S., and Schmidhuber, J. (1997). Long Short-Term Memory. *Neural Comput.* 9 (8), 1735–1780. Available at: https://www.ncbi.nlm.nih.gov/pubmed/9377276. doi:10.1162/neco.1997.9.8.1735

Ikuta, R., Hisada, T., Karakama, G., and Kuwano, O. (2020). Stochastic Evaluation of Pre-Earthquake TEC Enhancements. *J. Geophys. Res. Space Phys.* 125 (11), e2020JA027899. doi:10.1029/2020ja027899

Japkowicz, N., and Stephen, S. (2002). The Class Imbalance Problem: A Systematic Study1. *Intell. Data Anal.* 6 (5), 429–449. doi:10.3233/ida-2002-6504

Kingma, D. P., and Ba, J. (2014). Adam: A Method for Stochastic Optimization. arXiv preprint arXiv:1412.6980

Krizhevsky, A., Sutskever, I., and Hinton, G. E. (2012). "Imagenet Classification with Deep Convolutional Neural Networks," in *Paper Presented at the Advances in Neural Information Processing Systems 25 (NIPS 2012): 26th Annual Conference on Neural Information Processing Systems* (United States: Morgan Kaufmann Publishers, Inc).

Kuo, C. L., Lee, L. C., and Huba, J. D. (2014). An Improved Coupling Model for the Lithosphere-Atmosphere-Ionosphere System. *J. Geophys. Res. Space Phys.* 119 (4), 3189–3205. doi:10.1002/2013ja019392

Lebreton, J.-P., Stverak, S., Travnicek, P., Maksimovic, M., Klinge, D., Merikallio, S., et al. (2006). The ISL Langmuir Probe experiment Processing Onboard DEMETER: Scientific Objectives, Description and First Results. *Planet. Space Sci.* 54 (5), 472–486. doi:10.1016/j.pss.2005.10.017

LeCun, Y., Bengio, Y., and Hinton, G. (2015). Deep Learning. *Nature* 521 (7553), 436–444. Available at: https://www.ncbi.nlm.nih.gov/pubmed/26017442. doi:10.1038/nature14539

Li, M., and Parrot, M. (2013). Statistical Analysis of an Ionospheric Parameter as a Base for Earthquake Prediction. *J. Geophys. Res. Space Phys.* 118 (6), 3731–3739. doi:10.1002/jgra.50313

Li, M., Shen, X., Parrot, M., Zhang, X., Zhang, Y., Yu, C., et al. (2020). Primary Joint Statistical Seismic Influence on Ionospheric Parameters Recorded by the CSES and DEMETER Satellites. *J. Geophys. Res. Space Phys.* 125 (12), e2020JA028116. doi:10.1029/2020ja028116

Liu, C., Guan, Y., Zheng, X., Zhang, A., Piero, D., and Sun, Y. (2018). The Technology of Space Plasma Iin-Ssitu Measurement on the China Seismo-Electromagnetic Satellite. *Sci. China Technol. Sci.* 62 (5), 829–838. doi:10.1007/s11431-018-9345-8

Marchetti, D., De Santis, A., Shen, X., Campuzano, S. A., Perrone, L., Piscini, A., et al. (2020). Possible Lithosphere-Atmosphere-Ionosphere Coupling Effects Prior to the 2018 Mw = 7.5 Indonesia Earthquake from Seismic, Atmospheric and Ionospheric Data. *J. Asian Earth Sci.* 188, 104097. doi:10.1016/j.jseaes.2019.104097

Matthews, B. W. (1975). Comparison of the Predicted and Observed Secondary Structure of T4 Phage Lysozyme. *Biochim. Biophys. Acta (Bba) - Protein Struct.* 405 (2), 442–451. . Available at: https://www.ncbi.nlm.nih.gov/pubmed/1180967. doi:10.1016/0005-2795(75)90109-9

Mofiz, U. A., and Battiston, R. (2009). Possible Ion-Acoustic Soliton Formation in the Ionospheric Perturbations Observed on DEMETER before the 2007 Pu'er Earthquake. *Earthq Sci.* 22 (3), 257–262. journal article. doi:10.1007/s11589-009-0257-1

Němec, F., Santolík, O., Parrot, M., and Berthelier, J. J. (2008). Spacecraft Observations of Electromagnetic Perturbations Connected with Seismic Activity. *Geophys. Res. Lett.* 35 (5), L05109. doi:10.1029/2007GL032517

Němec, F., Santolík, O., and Parrot, M. (2009). Decrease of Intensity of ELF/VLF Waves Observed in the Upper Ionosphere Close to Earthquakes: A Statistical Study. *J. Geophys. Res. Space Phys.* 114 (A4), n/a. doi:10.1029/2008JA013972

Oh, K.-S., and Jung, K. (2004). GPU Implementation of Neural Networks. *Pattern Recognition* 37 (6), 1311–1314. Available at: http://www.sciencedirect.com/science/article/pii/S0031320304000524. doi:10.1016/j.patcog.2004.01.013

Ouyang, X. Y., Parrot, M., and Bortnik, J. (2020). ULF Wave Activity Observed in the Nighttime Ionosphere above and Some Hours before Strong Earthquakes. *J. Geophys. Res. Space Phys.* 125 (9), e2020JA028396. doi:10.1029/2020ja028396

Ouzounov, D., Pulinets, S., Tiger Liu, J.-Y., Hattori, K., and Han, P. (2018). "Multiparameter Assessment of Pre-Earthquake Atmospheric Signals," in *Pre-Earthquake Processes* (Hoboken, NJ, USA; Washington, D.C.: John Wiley & Sons, Inc.; American Geophysical Union), 339–359. doi:10.1002/9781119156949.ch20

Pan, S. J., and Yang, Q. (2010). A Survey on Transfer Learning. *IEEE Trans. Knowl. Data Eng.* 22 (10), 1345–1359. doi:10.1109/tkde.2009.191

Parrot, M., and Li, M. (2018). "Statistical Analysis of the Ionospheric Density Recorded by the DEMETER Satellite during Seismic Activity," in *Pre-Earthquake Processes* (Hoboken, NJ, USA; Washington, D.C.: John Wiley & Sons, Inc.; American Geophysical Union), 319–328. doi:10.1002/9781119156949.ch18

Parrot, M., Berthelier, J. J., Lebreton, J. P., Sauvaud, J. A., Santolik, O., and Blecki, J. (2006a). Examples of Unusual Ionospheric Observations Made by the DEMETER Satellite over Seismic Regions. *Phys. Chem. Earth, Parts A/B/C* 31 (4-9), 486–495. doi:10.1016/j.pce.2006.02.011

Parrot, M., Buzzi, A., Santolík, O., Berthelier, J. J., Sauvaud, J. A., and Lebreton, J. P. (2006b). New Observations of Electromagnetic Harmonic ELF Emissions in the Ionosphere by the DEMETER Satellite during Large Magnetic Storms. *J. Geophys. Res.* 111, A08301. doi:10.1029/2005ja011583

Parrot, M. (2006). Special Issue of Planetary and Space Science 'DEMETER'. *Planet. Space Sci.* 54 (5), 411–412. doi:10.1016/j.pss.2005.10.012

Piersanti, M., Materassi, M., Battiston, R., Carbone, V., Cicone, A., D'Angelo, G., et al. (2020a). Magnetospheric–Ionospheric–Lithospheric Coupling Model. 1: Observations during the 5 August 2018 Bayan Earthquake. *Remote Sensing* 12 (20), 3299. doi:10.3390/rs12203299

Piersanti, M., Pezzopane, M., Zhima, Z., Diego, P., Xiong, C., Tozzi, R., et al. (2020b). Can an Impulsive Variation of the Solar Wind Plasma Pressure Trigger a Plasma Bubble? A Case Study Based on CSES, SWARM and THEMIS Data. *Adv. Space Res.* 67 (1), 35–45. doi:10.1016/j.asr.2020.07.046

Píša, D., Parrot, M., and Santolík, O. (2011). Ionospheric Density Variations Recorded before the 2010 Mw 8.8 Earthquake in Chile. *J. Geophys. Res. Space Phys.* 116, A08309. doi:10.1029/2011JA016611

Píša, D., Němec, F., Parrot, M., and Santolík, O. (2012). Attenuation of Electromagnetic Waves at the Frequency ~1.7 kHz in the Upper Ionosphere Observed by the DEMETER Satellite in the Vicinity of Earthquakes. *Ann. Geophys.* 55 (1), 157–163. doi:10.4401/ag-5276

Píša, D., Němec, F., Santolík, O., Parrot, M., and Rycroft, M. (2013). Additional Attenuation of Natural VLF Electromagnetic Waves Observed by the DEMETER Spacecraft Resulting from Preseismic Activity. *J. Geophys. Res. Space Phys.* 118 (8), 5286–5295. doi:10.1002/jgra.50469

Pulinets, S., and Ouzounov, D. (2011). Lithosphere–Atmosphere–Ionosphere Coupling (LAIC) Model – an Unified Concept for Earthquake Precursors Validation. *J. Asian Earth Sci.* 41 (4-5), 371–382. doi:10.1016/j.jseaes.2010.03.005

Pulinets, S., and Ouzounov, D. (2018). "The Possibility of Earthquake Forecasting: Learning from Nature," in *Learning from Nature* (Bristol, UK: IOP Publishing). doi:10.1088/978-0-7503-1248-6

Pulinets, S. A., Ouzounov, D. P., Karelin, A. V., and Davidenko, D. V. (2015). Physical Bases of the Generation of Short-Term Earthquake Precursors: A Complex Model of Ionization-Induced Geophysical Processes in the Lithosphere-Atmosphere-Ionosphere-Magnetosphere System. *Geomagn. Aeron.* 55 (4), 521–538. doi:10.1134/S0016793215040131

Ramos, O., Altshuler, E., and Måløy, K. J. (2009). Avalanche Prediction in a Self-Organized Pile of Beads. *Phys. Rev. Lett.* 102 (7), 078701, 2009 . Available at: https://www.ncbi.nlm.nih.gov/pubmed/19257719. doi:10.1103/PhysRevLett.102.078701

Riggio, A., and Santulin, M. (2015). Earthquake Forecasting: a Review of Radon as Seismic Precursor. *Bollettino di Geofisica Teorica Ed. Applicata* 56 (2), 95–114. doi:10.4430/bgta0148

Ross, Z. E., Trugman, D. T., Hauksson, E., and Shearer, P. M. (2019). Searching for Hidden Earthquakes in Southern California. *Science* 364 (6442), 767–771.

Available at: https://www.ncbi.nlm.nih.gov/pubmed/31000593. doi:10.1126/science.aaw6888

Rouet-Leduc, B., Hulbert, C., and Johnson, P. A. (2018). Continuous Chatter of the Cascadia Subduction Zone Revealed by Machine Learning. *Nat. Geosci* 12 (1), 75–79. doi:10.1038/s41561-018-0274-6

Ryu, K., Lee, E., Chae, J. S., Parrot, M., and Pulinets, S. (2014a). Seismo-ionospheric Coupling Appearing as Equatorial Electron Density Enhancements Observed via DEMETER Electron Density Measurements. *J. Geophys. Res. Space Phys.* 119 (10), 8524–8542. doi:10.1002/2014ja020284

Ryu, K., Parrot, M., Kim, S. G., Jeong, K. S., Chae, J. S., Pulinets, S., et al. (2014b). Suspected Seismo-Ionospheric Coupling Observed by Satellite Measurements and GPS TEC Related to the M7.9 Wenchuan Earthquake of 12 May 2008. *J. Geophys. Res. Space Phys.* 119 (12), 10,305–310,323. doi:10.1002/2014ja020613

Shen, X., Zhang, X., Hong, S., Jing, F., and Zhao, S. (2013). Progress and Development on Multi-Parameters Remote Sensing Application in Earthquake Monitoring in China. *Earthq Sci.* 26 (6), 427–437. doi:10.1007/s11589-013-0053-9

Shen, X., Zong, Q.-G., Zong, Q.-G., and Zhang, X. (2018). Introduction to Special Section on the China Seismo-Electromagnetic Satellite and Initial Results. *Earth Planet. Phys.* 2 (6), 439–443. doi:10.26464/epp2018041

Shen, X., Zhima, Z., Shigeng, Y., Jianping, D., Jianping, H., Xinghong, Z., et al. (2020). The CSES Mission and its Preliminary Results. *Aerospace China* 21 (1), 5–18. doi:10.3969/j.issn.1671-0940.2020.01.001

Shi, K., Guo, J., Liu, X., Liu, L., You, X., and Wang, F. (2020). Seismo-ionospheric Anomalies Associated with Mw 7.8 Nepal Earthquake on 2015 April 25 from CMONOC GPS Data. *Geosci. J.* 24 (4), 391–406. doi:10.1007/s12303-019-0038-3

Shi, K., Guo, J., Zhang, Y., Li, W., Kong, Q., and Yu, T. (2021). Multi-Dimension and Multi-Channel Seismic-Ionospheric Coupling: Case Study of Mw 8.8 Concepcion Quake on 27 February 2010. *Remote Sensing* 13 (14)–2724. doi:10.3390/rs13142724

Snoek, J., Larochelle, H., and Adams, R. P. (2012). Practical Bayesian Optimization of Machine Learning Algorithms. Paper presented at the Advances in neural information processing systems

Soter, S. (1999). Macroscopic Seismic Anomalies and Submarine Pockmarks in the Corinth–Patras Rift, Greece. *Tectonophysics* 308 (1-2), 275–290. doi:10.1016/s0040-1951(99)00090-6

Varotsos, P. A., Sarlis, N. V., and Skordas, E. S. (2020). Self-organized Criticality and Earthquake Predictability: A Long-Standing Question in the Light of Natural Time Analysis. *EPL (Europhysics Letters)* 132 (2), 29001. doi:10.1209/0295-5075/132/29001

Wang, Y. D., Pi, D. C., Zhang, X. M., and Shen, X. H. (2014). Seismo-ionospheric Precursory Anomalies Detection from DEMETER Satellite Data Based on Data Mining. *Nat. Hazards* 76 (2), 823–837. doi:10.1007/s11069-014-1519-3

Wu, L.-x., Qin, K., and Liu, S.-j. (2012). GEOSS-based Thermal Parameters Analysis for Earthquake Anomaly Recognition. *Proc. IEEE* 100 (10), 2891–2907. doi:10.1109/jproc.2012.2184789

Xiong, P., Long, C., Zhou, H., Battiston, R., Zhang, X., and Shen, X. (2020). Identification of Electromagnetic Pre-Earthquake Perturbations from the DEMETER Data by Machine Learning. *Remote Sensing* 12 (21), 3643. doi:10.3390/rs12213643

Xu, F., Song, X., Wang, X., and Su, J. (2010). "Neural Network Model for Earthquake Prediction Using DMETER Data and Seismic Belt Information," in Paper presented at the 2010 Second WRI Global Congress on Intelligent Systems.

Yan, R., Parrot, M., and Pinçon, J.-L. (2017). Statistical Study on Variations of the Ionospheric Ion Density Observed by DEMETER and Related to Seismic Activities. *J. Geophys. Res. Space Phys.* 122, 12,421–12,429. doi:10.1002/2017ja024623

Yan, R., Guan, Y., Guan, Y., Shen, X., Huang, J., Zhang, X., et al. (2018a). The Langmuir Probe Onboard CSES: Data Inversion Analysis Method and First Results. *Earth Planet. Phys.* 2 (6), 1–10. doi:10.26464/epp2018046

Yan, R., Shen, X., Shen, X., Huang, J., Wang, Q., Chu, W., et al. (2018b). Examples of Unusual Ionospheric Observations by the CSES Prior to Earthquakes. *Earth Planet. Phys.* 2 (6), 515–526. doi:10.26464/epp2018050

Zhang, X., Shen, X., Liu, J., Ouyang, X., Qian, J., and Zhao, S. (2009). Analysis of Ionospheric Plasma Perturbations before Wenchuan Earthquake. *Nat. Hazards Earth Syst. Sci.* 9 (4), 1259–1266. Available at: https://www.nat-hazards-earth-syst-sci.net/9/1259/2009/. doi:10.5194/nhess-9-1259-2009

Zhang, Y., Liu, X., Guo, J., Shi, K., Zhou, M., and Wang, F. (2021). Co-Seismic Ionospheric Disturbance with Alaska Strike-Slip Mw7.9 Earthquake on 23 January 2018 Monitored by GPS. *Atmosphere* 12 (1)–83. doi:10.3390/atmos12010083

Conflict of Interest: The authors declare that the research was conducted in the absence of any commercial or financial relationships that could be construed as a potential conflict of interest.

Publisher's Note: All claims expressed in this article are solely those of the authors and do not necessarily represent those of their affiliated organizations, or those of the publisher, the editors and the reviewers. Any product that may be evaluated in this article, or claim that may be made by its manufacturer, is not guaranteed or endorsed by the publisher.

frontiers in Earth Science

ORIGINAL RESEARCH
published: 07 January 2022
doi: 10.3389/feart.2021.797907

Spatiotemporal Variations of Focal Mechanism Solutions and Stress Field of the 2019 Changning *Ms* 6.0 Earthquake Sequence

Zhiwei Zhang[1,2]*, *Chuntao Liang*[1]*, *Feng Long*[2], *Min Zhao*[2] *and Di Wang*[2]

[1]Key Laboratory of Earth Exploration and Information Technology of Ministry of Education (Chengdu Universtiy of Technology), Chengdu, China, [2]Sichuan Earthquake Administration, Chengdu, China

The June 17, 2019, M_S 6.0 Changning earthquake is the largest recorded event in the Sichuan basin, spatiotemporal variations of stress field may shed light on the seismogenic mechanism of the earthquake. We determined the focal mechanism solutions (FMSs) of 124 earthquakes with $M_S \geq 3.0$ occurring in the Changning area from April 1, 2007, to February 29, 2020, and analyzed changes of FMSs and stress field before and after Changning earthquake. The Changning aftershocks were predominantly thrust fault earthquakes, followed by strike slip. The *P*-axis azimuths of the aftershock FMSs were oriented predominantly in the *NEE* direction, notably differing from the *NWW*-oriented *P*-axis azimuths of pre-earthquake FMSs; it shows the rotation of local stress field before and after the Changning earthquake, it is speculated that the change of stress field in Changning area may be caused by long-term water injection and salt mining activities. From the southeast to the northwest of the aftershock zone, the azimuths of principal compressive stress (S_1) change from *NEE* to near-EW in both horizontal and vertical planes. Significant changes occurred in the FMS types and stress field of the aftershock zone following the Changning earthquake, the FMSs became diverse, the S_1 azimuth of the Changning area changed from *NWW* to *NEE*, and then EW, the plunge and stress tensor variances increased, it reflects that the stress field of the Changning area adjusts continually with time.

Keywords: the MS 6.0 changning earthquake, focal mechanism solution, stress field, principal compressive stress, spatiotemporal variation

OPEN ACCESS

Edited by:
Ying Li,
China Earthquake Administration, China

Reviewed by:
Bin Zhou,
Earthquake Bureau of the Guangxi Zhuang Autonomous Region, China
Libo Han,
China Earthquake Administration, China

***Correspondence:**
Zhiwei Zhang
zzw1983107@163.com
Chuntao Liang
liangchuntao12@cdut.cn

Specialty section:
This article was submitted to Solid Earth Geophysics, a section of the journal Frontiers in Earth Science

Received: *19 October 2021*
Accepted: *14 December 2021*
Published: *07 January 2022*

Citation:
Zhang Z, Liang C, Long F, Zhao M and Wang D (2022) Spatiotemporal Variations of Focal Mechanism Solutions and Stress Field of the 2019 Changning Ms 6.0 Earthquake Sequence. Front. Earth Sci. 9:797907. doi: 10.3389/feart.2021.797907

INTRODUCTION

The Changning *Ms* 6.0 earthquake is the largest recorded earthquake in the Sichuan Basin. It occurred at 22:55:43.3 on June 17, 2019 in the Changning County of Yibin City in Sichuan Province according to the China Earthquake Networks Center. The epicenter was located at 28.34°N 104.90°E, with a focal depth of 16 km. The source parameters were computed by scientists worldwide shortly after the earthquake. The FMSs of the main shock show a set of nodal planes with the strike of (102°–135°) which is similar to that of the axis of the Changning anticline. The dip angles are 45°–61°. The azimuth/dip angles of P-axis are 70°–76° and 7°–10°, respectively. The dislocation type of the main shock is thrust and strike-slip, and the focal depths are relatively shallow (only 3 km). The reported moment magnitude is of 5.68–5.79 (Lei et al., 2019; Yi et al., 2019; Liang et al., 2020; Liu & Zahradník, 2020; Hu et al., 2021).

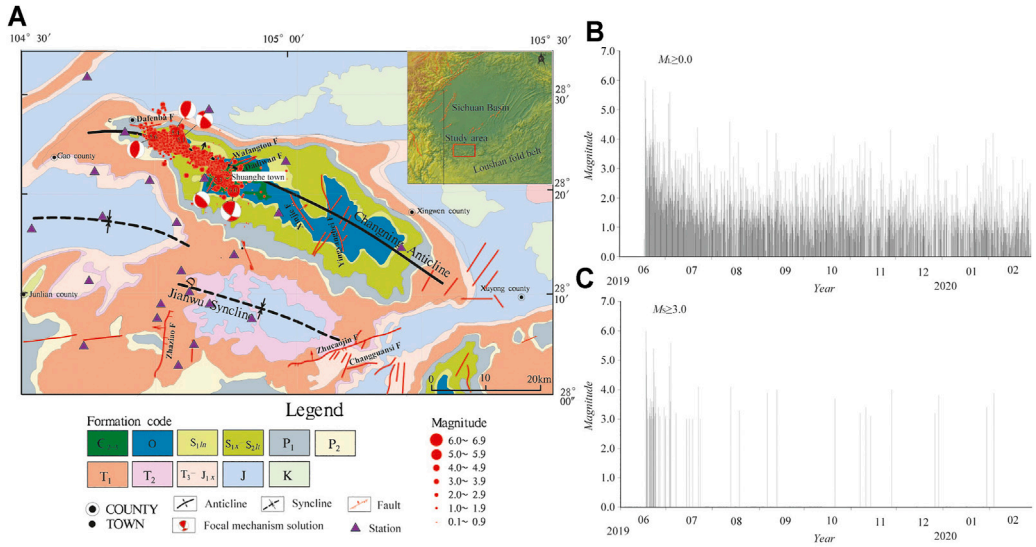

FIGURE 1 | Tectonic map of the Changning earthquake source area and its aftershock sequence. **(A)** Tectonic map and distribution of aftershocks. The upper right insert map shows the structural background of the study area in the red box. Beach ball is the FMSs of the Changning main shock and four $M_S \geq 5.0$ aftershocks. The red dots represent aftershocks. The aperture of the seismic array (The purple triangle) is approximately 10 km. **(B)** *M–t* graph of $M_L \geq 0.0$ aftershocks; and **(C)** *M–t* graph of $M_S \geq 3.0$ aftershocks.

The relocated Changning earthquake sequence showed that the aftershocks followed the *NW–SE* striking axis of the Changning anticline. The aftershocks started at the Shuanghe anticline (in the middle of the Changning anticline) and ended at the Baixiangyan–Shizitan anticline (in the northernmost part of the Changning anticline). The ruptures unilaterally occurred along the NW direction and the focal depths become deeper progressively to the NW (Lei et al., 2019; Yi et al., 2019; Sun et al., 2021). The seismic location and FMSs of the aftershocks indicate that they were probably related to the Baixiangyan–Shizitan segment and the Shuanghe segment of the Changning anticline and their associated fault activities (Yi et al., 2019). He et al. (2019) determined that the earthquakes of the Changning anticline usually occur on its southern wing. These moderate earthquakes are associated with the activities in the footwall ramp of the basement fault.

To a certain degree, FMSs in different stages reflect variations of stress field in the process of strong earthquake preparation, the FMSs of earthquake sequence can provide important clues about the seismogenic process and stress state (Zheng et al., 2009; Luo et al., 2010; Diao et al., 2011). Previous studies focus on focal mechanism of main shock and several larger aftershocks (Yi et al., 2019; Liang et al., 2020; Hu et al., 2021), owing to data limitations, the varying characteristics of stress field before and after the Changning earthquake have not yet been analyzed. To fill this gap, Base on the FMSs of 124 earthquakes with $M_S \geq 3.0$ in the Changning area from April 1, 2007, to February 29, 2020, we analyze the spatiotemporal variation of FMSs and stress field before and after the Changning earthquake. Our findings enable a thorough understanding of the seismogenic process and seismogenic mechanism of the Changning earthquake.

DATA AND METHODS

Data

The study area is located at the junction between the Sichuan basin and the Loushan fold belt (**Figure 1A**: Red box), the tectonic structure is the result of multiple tectonic movements, which include the Caledonian, Haixi, Indosinian, Yanshanian, and Himalayan movements. The structure of its surface comprises an alternating series of gentle anticlines and synclines with a few surface faults (Li and Zeng, 1994; Wang, 2014). The *NW–SE* striking Changning anticline is the major geological structure in the region where the Changning earthquake occurred. This anticline passes through the Shuanghe town to Gao County in the northwest and extends to Xuyong County in the southeast. The anticline is wider in the southeast and narrower in the northwest, and its outcrops comprise Cambrian rocks at the core, followed by Ordovician, Silurian, Permian, Triassic, and Jurassic rocks toward the periphery. The main faults in the aftershock zone include the *NEE*-trending Wafangtou and Dadiwan faults and the near-*EW*-striking Dafenba fault (**Figure 1A**). The mean stress field of the Sichuan–Yunnan region indicates that the principal compressive stress axis of the Sichuan Basinis oriented in a *NWW* direction (Cheng et al., 2003; Zhong and Cheng, 2006).

Up to February 29, 2020, a total of 9,861 aftershocks with $M_L \geq 0.0$ have been recorded after the Changning earthquake, including 67 events of M_S 3.0–3.9, ten of M_S 4.0–4.9, and four of M_S 5.0–5.9. The $M_S \geq 5.0$ aftershocks include the M_S 5.1 earthquake in Gong County on June 17, 2019, the M_S 5.3 event in Changning on June 18, 2019, the M_S 5.4 event in Gong County on June 22, 2019, and the M_S 5.6 event in Gong County on July 4,

2019. The aftershock activity follows the axis of the Changning anticline (i.e., in a NW–SE direction), and they cover an area of approximately 25 km × 5 km (**Figure 1A**). The aftershock swarm is characterized by strong and frequent aftershocks (**Figure 1B**). Most of the $M_S \geq 3.0$ aftershocks occurred between June 17, 2019, and July 4, 2019, after which the aftershock sequence decayed rapidly (**Figure 1C**).

Method to Invert for FMS and Stress Field

Among the various methods to compute FMS, Compared with the P-wave first-motion method (Chen et al., 2001), the inversion of body waves (Fan and Wallace, 1991; Dreger and Helmerger, 1993) and the inversion of surface waves (Patton, 1980; Thio and Kanamori, 1995), the "cut and paste" (CAP) method (Zhao and Helmberger, 1994; Zhu and Helmberger, 1996) can be regarded as a full waveform inversion method. It has the advantages of requiring fewer stations, and the inversion results are relatively independent of the selected velocity model and the lateral variations in the crustal structure (Tan et al., 2006; Zheng et al., 2009; Luo et al., 2015; Zhang et al., 2015a; Zhao et al., 2021). The CAP method can also constrain the focal depth using the surface wave amplitudes in the waveforms, thereby yielding a reliable focal centroid depth (Luo et al., 2015).

Estimating stress field based on FMSs is useful for investigating crustal dynamics and earthquake physics. In most methods, it is assumed that the stress field is spatially uniform (Angelier, 1979; Gephart and Forsyth, 1984; Michael, 1984; Cui and Xie, 1999; Yang et al., 2017; Yang et al., 2018). However, to determine the stress field characteristics of spatially heterogeneous, Michael (1991) proposed the superposition stress inversion (SSI) method. In this method, the distribution of heterogeneous stress fields is approximated by superimposing perturbations onto homogeneous stress fields to obtain the orientations of S_1 (most compressive principal stress), S_2 (intermediate principal stress), and S_3 (tensile principal stress) and inversion variance. The variance is a quantitative metric for the consistency between the focal stress field of an earthquake and the tectonic stress field of the region (Michael, 1987; Michael, 1991). A variance lower than 0.1 implies that the observed FMS can be explained by a single stress tensor and that the stress field of the region is homogeneous. In contrast, a variance greater than 0.2 suggests that the stress field of the region is spatially and temporally heterogeneous or that there are complex focal mechanisms (Lu et al., 1997). The stress field obtained using this approach has been demonstrated experimentally to be reliable, and the method has been employed in many studies worldwide (Michael, 1991; Wiemer et al., 2002).

RESULTS

Based on the one-dimensional velocity model in Changning area (Yi et al., 2019), the FMSs and focal centroid depth of $M_S \geq 3.0$ events in the Changning earthquake sequence were inverted by selecting high signal-to-noise ratio and broadband waveform records of stations within 250 km from the epicenter (**Figure 1**). In the calculation, the source function duration of the Changning M_S 6.0 earthquake was set as 5 s, and that of the other events were set as 1 s. The length of the body wave and surface wave window was set as 30 and 60 s, respectively, and the corresponding bandpass filter bandwidth was 0.05–0.2 Hz and 0.05–0.1 Hz, respectively. The search step for fault plane parameters (strike, dip angle and slip angle) was 5°, and the depth step was 1 km. The optimal FMS is the solution that minimizes the error function, with a depth corresponding to the centroid depth.

Focal mechanism solutions and waveform fitting for the Changning M_S 6.0 main shock and M_S 3.9 aftershock are shown in **Figure 2**. The fitting errors of the FMSs at different focal depths are shown in **Figures 2A,C**, the fitting errors are minimized at a focal depth of 3 and 8 km, the corresponding FMSs are optimal solutions. **Figures 2B,D** show the fitting results between the synthetic (red line) and observed (black line) seismic waveforms of the data used for CAP inversion. The figure indicates that the phases and amplitudes of the observed and synthetic waveforms of both the Changning M_S 6.0 main shock and M_S 3.9 aftershock are in good agreement. The FMS of main shock shows that the strike, dip, and rake angles of the fault are 124°, 60°, and 22°, respectively, which implies that the dislocation is a thrust and strike-slip fault, it was consistent with that of other studies (Lei et al., 2019; Yi et al., 2019; Liang et al., 2020).

The Focal Mechanism Characteristics of Changning Aftershocks

The FMSs of 81 aftershocks with $M_S \geq 3.0$ in Changning sequence from June 17, 2019 to February 29, 2020 were obtained by using CAP method, including 15 earthquakes with $M_S \geq 4.0$ and 66 earthquakes with $3.0 \leq M_S \leq 3.9$. The FMSs of the Changning aftershocks were classified by comparing the plunge of three principal axes using the classification criteria by Zoback (1992) (**Table 1**). The FMSs (or stress regime) can be divided into five types, namely normal fault type (NF), normal and strike-slip type (NS), strike-slip type (SS), thrust and strike-slip type (TS) and thrust fault type (TF). Considering the dominant type of an earthquake, this study only divides into three types: normal fault, strike-slip and thrust fault. The NS type dominated by normal fault is classified into normal fault type, and the TS type dominated by thrust fault is classified into thrust fault type for analysis.

Figure 3A shows the spatial distribution of the FMS types and the overall stress field. A summary of the analysis results is presented in **Table 2**. The $M_S \geq 3.0$ aftershocks are predominantly thrust fault earthquakes (TF:48), followed by strike-slip earthquakes (SS:24), and then normal fault earthquakes (NF:9). These types of earthquakes account for 59, 30, and 11% of the aftershocks, respectively (**Table 2**), and they show distinct differences in spatial distribution. The thrust fault earthquakes are mainly located on the southern and northern parts of the aftershock zone, whereas the strike-slip earthquakes mostly occurred in the central-northern part of the

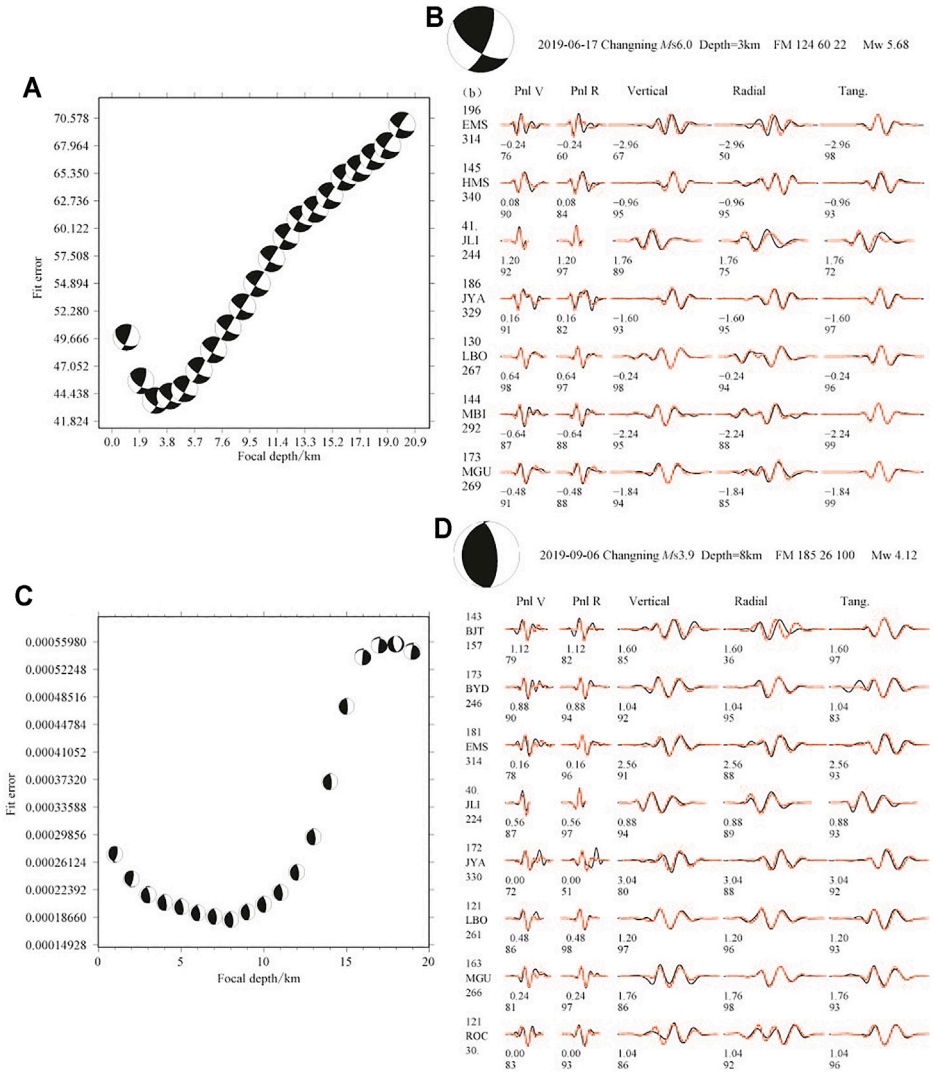

FIGURE 2 | FMSs of the Changning M_S 6.0 main shock (up) and M_S 3.9 aftershock (down). **(A)** and **(C)** The fitting error versus depth. **(B)** and **(D)** The fitting results between synthetic (red line) and observed (black line) waveforms. The station names are given on the left, the numbers above and below the names are epicentral distance (in km) and azimuth (in degree). Numbers below the traces are the time shifts (in second) of the synthetic relative to the observations and the corresponding cross-correlation coefficients (in percentage).

TABLE 1 | Classification criteria of focal mechanism solutions and stress regime.

FMS type/Stress Regime	Plunge of Axes/(°)		
	P-axis/S_1	B-axis/S_2	T-axis/S_3
NF	$Pl \geq 52°$	—	$Pl \leq 35°$
NS	$40° \leq Pl < 52°$	—	$Pl \leq 20°$
SS	$Pl < 40°$	$Pl \geq 45°$	$Pl \leq 20°$
	$Pl \leq 20°$	$Pl \geq 45°$	$Pl < 40°$
TS	$Pl \leq 20°$	—	$40° \leq Pl < 52°$
TF	$Pl \leq 35°$	—	$Pl \geq 52°$

aftershock zone. Normal fault earthquakes are scattered across the zone. The stress field of the Changning aftershock zone shows that, the azimuth/plunge of the S_1, S_2, and S_3 axes were 83°/7.4°, 175°/15.7°, and 329°/72.5°, respectively. Therefore, the aftershock zone had a thrust stress regime with low S_1 and S_2 plunge (Pl ≤ 35°) and a high S_3 plunge (Pl ≥ 52°).

To a certain extent, medium and small earthquakes occur randomly. Therefore, to ensure that the conclusions drawn from our data are reasonable and objective, a large number of medium and small earthquakes FMSs were analyzed statistically to obtain the average nodal plane, stress axis, and dislocation types. A rose diagram of the nodal plane and stress axis parameters of the aftershock FMSs are shown in **Figure 3B**.

The strikes of the nodal planes were relatively scattered, there are not only strikes in NW which are consistent with the direction of Changning anticline, but also strikes nearly in NS direction which deviates from the striking of the anticline. The dip angles of

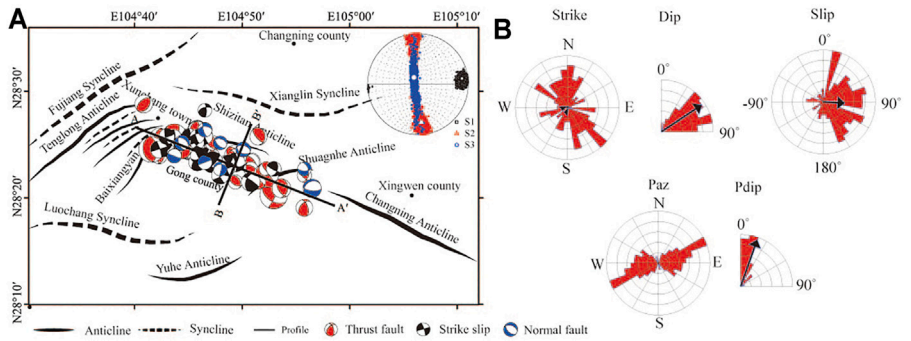

FIGURE 3 | (A) FMS distribution of the Changning aftershocks. Beach ball are FMSs, different colors represent different focal mechanism types, among which red beach ball is thrust fault type, black beach ball is strike slip type, blue beach ball is normal fault type. The circular is spherical projection of principal stress axis, the small black squares, red triangles, and blue circles in the ball diagrams represent the projections of S_1, S_2, and S_3, respectively, while the larger square, triangle, and circle represent their mean values. **(B)** The rose diagram of FMS nodal plane and stress axis parameters, including the strike, dip angle and slip angle of the nodal planes, and the azimuth and dip angle of the *P*-axis.

TABLE 2 | FMS types of the Changning aftershocks and the stress field of the aftershock zone.

Number of FMS	FMS types			S_1		S_2		S_3		Stress regime
	TF (%)	SS (%)	NF (%)	Az (°)	*Pl* (°)	Az (°)	*Pl* (°)	Az (°)	*Pl* (°)	
81	48 (59%)	24 (30%)	9 (11%)	83	7.4	175	15.7	329	72.5	Thrust

nodal plane ranged from 40° to 90°, and this wide range may be indicative of spatial complexity for fault planes. The slip angle indicated that the aftershocks were dominantly thrust earthquakes. Based on the FMSs of 16 Changning $M_S \geq 3.6$ aftershocks, Yi et al. (2019) also found that the strikes of nodal planes are scattering. Thus, the Changning earthquake sequence is complicated by the seismicity of with various faults associated with the Changning anticline. The azimuths of *P*-axis (P_{az}) of the FMSs are consistently oriented in the *NEE* direction, and this is similar to the *P*-axis azimuth of the main shock (75°) and the S_1 azimuth of the aftershock zone. However, this direction differs somewhat from the orientation of the Sichuan basin's stress field (*NW–NWW*), and the dip angle of the *P*-axis (P_{dip}) is close to horizontal (generally within 20°). Therefore, it can be concluded that the Changning aftershocks were controlled by a local near-horizontal *NEE*-oriented stress field.

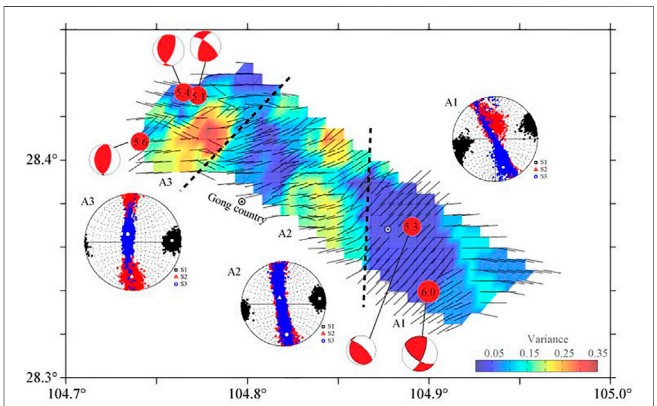

FIGURE 4 | The distribution of S_1 and stress tensor variance in the Changning aftershock zone. The black dotted lines divide the aftershock zone into A1, A2, and A3 segments, and the black solid lines represent the S_1 azimuths. Beach ball are FMSs, the circular is spherical projection of principal stress axis, the details are shown in **Figure 3**.

The Stress Field Characteristics of Aftershock Zone.

Based on the FMSs of 81 aftershocks with $M_S \geq 3.0$, the region with a relatively high density of aftershock FMSs was divided into 0.005°× 0.005°grids. Subsequently, we employed the SSI method (Michael, 1991) to obtain the stress tensor of every node, using minimum of eight FMSs at and around each node. ZMAP software (Wiemer, 2001) was adopted to compute the S_1 azimuth of each node in the aftershock zone. Based on these results, a consistency parameter of FMSs was computed at each node in the aftershock zone, and using the variance of the stress tensor to show the heterogeneity of the stress field (**Figure 4**).

To depict the spatial distribution of stress field in the aftershock zone, three segments (A1–A3) were divided along the Changning anticline from the southeast to the northwest. The projection of the principal stress axis in each of these segments from their FMSs, the detailed parameters such as azimuth and plunge of three principal stress axes, variance and stress regime

TABLE 3 | Stress field in the different segments of the Changning aftershock zone.

Segment	Number of FMS	S_1		S_2		S_3		Variance	Stress regime
		Az (°)	*Pl* (°)	Az (°)	*Pl* (°)	Az (°)	*Pl* (°)		
A1	17	254	0.2	345	69.3	164	20.6	0.11	Strike Slip
A2	28	81	8.0	328	70.1	174	18.1	0.16	Strike Slip
A3	36	88	11.6	182	18.4	327	65.0	0.17	Thrust

are listed in **Table 3**. The S_1 azimuths of the aftershock zone were found to vary significantly in different sub-zones. In A1 segment (the southern part of the aftershock zone and the initial rupture area of the Changning earthquake), the average S_1 was oriented in a *NEE* direction with an azimuth of 254°, according to classification criteria of stress regime (Zoback, 1992), the plunge of S_1 is less than 20°, the plunge of S_2 is more than 45°, and the plunge of S_3 is less than 40°, it is indicative of a strike-slip stress regime. The A2 segment is located in the middle of the aftershock zone. The S_1 azimuth is dominantly oriented in *NEE* direction with some EW distributed in local area. The average azimuth of S_1 in A2 segment is 81°, the plunge of S_1 is less than 20°, the plunge of S_2 is more than 45°, and the plunge of S_3 is less than 40°, the sub-zone is controlled by a strike-slip stress regime. The A3 segment is located in the northern part of the aftershock zone, and a near-EW was noted in this sub-zone. The azimuth of S_1 is 88°, the plunge of S_1 is less than 35°, the plunge of S_3 is more than 52°, indicating a thrust-fault stress regime in this sub-zone.

In summary, local variations of stress field were found in the Changning aftershock zone. From the southeast to the northwest, the S_1 azimuths change from *NEE* (254°) to near-EW azimuths (88°), whereas the plunge of S_1 gradually increases from 0.2° to 11.6°. Based on changning coseismic slip distribution (Li et al., 2021), the relationship between coseismic slip and stress regime is analyzed. The results show the strike-slip stress regime is in region with a large amount of slip, the thrust stress regime is in a small amount of slip.

Together with the distribution of Changning M_S≥5.0 aftershock, this study analyzes the relationship between strong aftershocks and the spatial distribution of stress tensor variance (background color in **Figure 4**). The results showed that the stress tensor variance of the aftershock zone was relatively small, but they differed between segments. For example, the lowest stress tensor variance (0.11) was found in the A1 segment, this indicated that the stress field of the initial rupture area was relatively homogeneous, and the June 18 M_S 5.3 aftershock occurred in this area with a low stress tensor variance. The stress tensor variance in A2 segment was found to be significantly lower on its western side than its eastern side, which indicated that the stress field was more homogeneous on the western side than the eastern side. However, the stress tensor variance of A3 segment was significantly lower at the northern end than at the southern end. The June 17 M_S 5.1 and June 22 M_S 5.4 Gong county earthquakes both occurred at the northern end of A3 segment. These findings are consistent with studies of the Wenchuan and Lushan earthquakes (Zhang et al., 2015a), where it was also observed that strong aftershocks generally occur at or near areas with low stress tensor variances.

Depth Cross-Sectional Characteristics of FMS and Stress Field

The depth cross-sectional characteristics of FMS and the stress field were analyzed along the long A-A′ and short B-B′ axes of the region (**Figure 3A**). **Figure 5** shows the depth distributions of the FMSs corresponding to $M_S \geq 3.0$ and $M_S \geq 4.0$ aftershocks, which were projected onto the A-A′ and B-B′ cross-sections. It is worth noting that the focal depths of earthquakes were obtained by using CAP method, the spatial locations of the earthquakes were determined by double-difference earthquake location algorithm (Waldhauser and Ellsworth, 2000). To probe the stress states, the stress tensors of the A-A′ cross-section were inverted from the FMSs, and the trend of S_1 axis was projected onto the cross-section. Owing to the symmetry of the stress axes, the angle between the trend of S_1 axis and the cross-section was limited to 0°–180°. The depth distributions of the FMSs for the $M_S \geq 3.0$ and $M_S \geq 4.0$ aftershocks along the A-A′ cross-section are shown in **Figures 5A,C**, respectively. These results show that the compressive stress in each segment of the aftershock zone also exist depthwise-variation. For instance, the depths of earthquakes in the central-southern segment are generally less than 5 km, the angle between the S_1 azimuths and the strike of Changning anticline varies between 30° and 60° in the southern segment and 60°–90° in the central segment. In the northern segment, the focal depths become gradually deeper, even exceeding 10 km, and the angle between the S_1 azimuth and the strike of the Changning anticline varies from 90° up to 120°. From southeast to northwest, the angles between the S_1 azimuths and the strike of the Changning anticline become gradually larger with depth. And the shallow, *NE*-oriented compressive stress changes to deep, *NW*-oriented compressive stress (**Figure 5A**). The angle between the strike of Changning anticline and the *P*-axis orientations of the $M_S \geq 4.0$ aftershock FMSs also varies from one segment to another (**Figure 5C**). The phenomenon differs to those of the Lushan earthquake, where the *P*-axis orientations of the $M_S \geq 4.0$ aftershocks were all perpendicular to the trend of the Longmenshan fault (Zhang et al., 2015b). Again, this shows the complexity of the stress field of the Changning aftershock zone.

The depth distribution of the FMSs of the $M_S \geq 3.0$ and $M_S \geq 4.0$ aftershocks along the B-B′ cross-section is shown in **Figures 5B,D**, respectively. The black line (**Figure 5B**)is the inferred fault (Fx), which were identified by the seismic relocation and focal

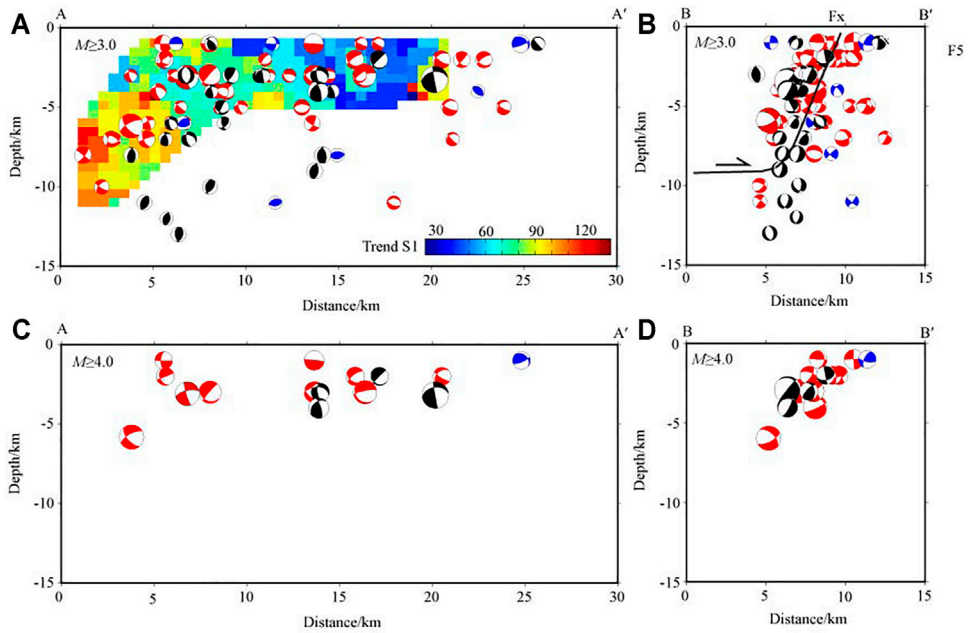

FIGURE 5 | The focal mechanism projection along the A-A′ and B-B′ cross-sections. **(A, B)** are the depth distribution of the FMSs of the $M_S \geq 3.0$ aftershocks along the A-A′ and B-B′ cross-section respectively. **(C)** and **(D)** are the depth distribution of the FMSs of the $M_S \geq 4.0$ aftershocks along the A-A′ and B-B′ cross-section respectively. The different colors represent the angles between S_1 azimuths and the cross-sections in **(A)**. The black line is the inferred fault (Fx) in **(B)**.

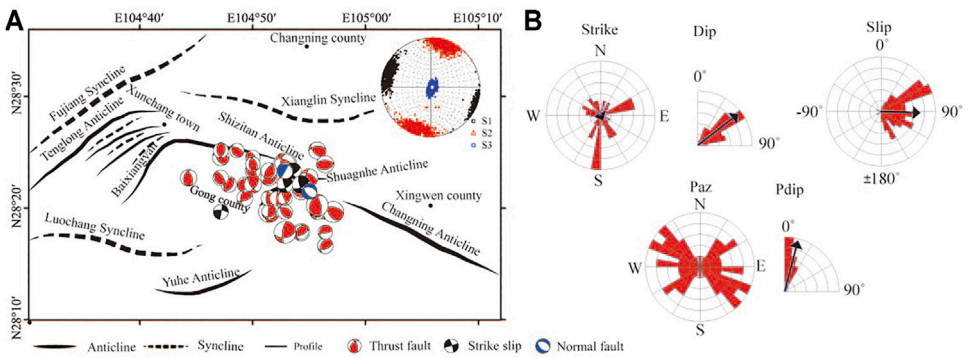

FIGURE 6 | (A) FMS distribution of the pre-earthquake and the spherical projection of principal stress axis. The details of FMSs and principal stress axis are shown in **Figure 3**. **(B)** The rose diagram of FMSs nodal plane and stress axis parameters, including the strike, dip angle and slip angle of the nodal planes, and the azimuth and dip angle of the *P*-axis.

mechanism solutions. It is speculated that the tendency of fault plane is *SW*, the dip angle is steep, the inferred fault is consistent with the results of Yi et al. (2019), we think the activation of the basement fault in the depth of ~10 km in Changning anticline driven by regional stress field.

DISCUSSION

To probe the seismogenic mechanisms of the Changning earthquake, a comparison of the FMSs before and after the Changning earthquake was conducted. The CAP method was used to invert the FMSs of 43$M_S \geq 3.0$ earthquakes from April 1, 2007 to June 16, 2019. In accordance with the method used previously, the FMS types and the parameters of the nodal planes and stress axes were computed, and the pre-earthquake stress field was also inverted (**Figure 6**). The results are summarized in **Table 4**.

The spatial distribution of the pre-earthquake FMSs is shown in **Figure 6A**. Among the 43 earthquakes included in this analysis, there are 37 thrust fault earthquakes, four strike-slip earthquakes, and two normal fault earthquakes, accounting for 86, 9, and 5% of the total, respectively (see **Table 4**). The pre-earthquake stress field shows that the azimuths/plunge of S_1, S_2,

TABLE 4 | FMS types and stress field after the Changning earthquake.

Number of FMS	FMS types			S_1		S_2		S_3		Stress regime
	TF (%)	SS (%)	NF (%)	Az (°)	*Pl* (°)	Az (°)	*Pl* (°)	Az (°)	*Pl* (°)	
43	37 (86%)	4 (9%)	2 (5%)	280	3.2	190	0.8	86	86.6	Thrust

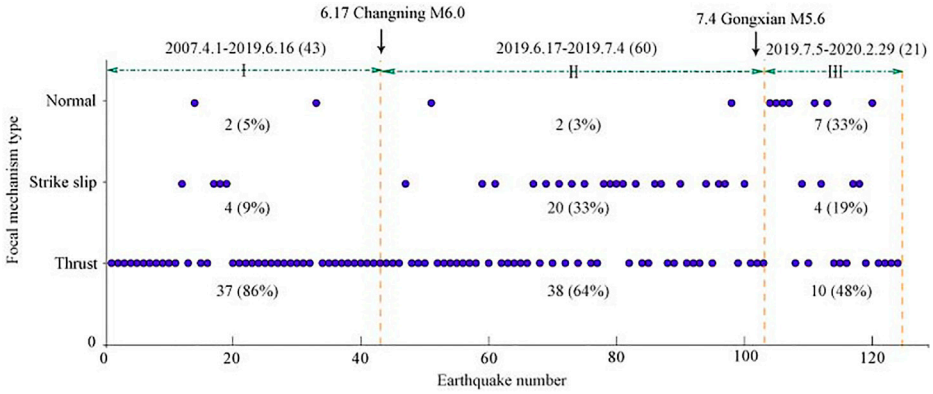

FIGURE 7 | The change characteristic of focal mechanism type with time.

and S_3 were 280°/3.2°, 190°/0.8°, and 86°/86.6°, respectively. The pre-earthquake and post-earthquake stress regimes were all thrust fault, with low S_1 and S_2 plunge (Pl ≤ 35°) and a high S_3 plunge (Pl ≥ 52°). However, the S_1 azimuth rotated 17° anticlockwise after the Changning earthquake. **Figure 6B** shows that the nodal plane strikes of the pre-earthquake FMSs are quite scattered, mostly in the NS direction, deviating from the strike of the Changning anticline. The dip angles of the nodal planes were 40–60°, which were smaller than the post-earthquake dip angles. The *P*-axis azimuths of the pre-earthquake FMSs were oriented predominantly in the *NWW* direction, notably differing from the *NEE*-oriented *P*-axis azimuths of the aftershock FMSs; but similar to the orientation of the Sichuan basin's stress field (*NW–NWW*). The dip angles of *P*-axis ranged between 0° and 20°, which is consistent with the horizontal stress field of southwestern China (Kan et al., 1977). These results indicate that the seismicity of this region was controlled mainly by the near-horizontal stress field of the Sichuan Basin before the Changning earthquake.

The temporal evolution of the FMSs before and after the Changning earthquake was analyzed by dividing the research period into three time periods. Including the pre-earthquake period (I: April 1, 2007, to June 16, 2019), the active post-earthquake period (II: June 17, 2019, to July 4, 2019), and the decaying post-earthquake period (III: July 5, 2019, to February 29, 2020). The numbers and percentages of earthquake types during these periods were shown in **Figure 7**. The 43 earthquakes occurred in Period I, of which thrust earthquakes accounted for 86% and strike-slip earthquakes and normal fault earthquakes accounted for only 9 and 5%, respectively. This result showed that the FMS types in this region were highly consistent before the Changning earthquake. According to Diao et al. (2011), stress accumulation prior to an earthquake in a source area with a thrust regime may induce similar transformations in the local stress field. Moreover, after the stress field has transformed into a stress state identical to that of the main shock, the stress near the source area are extremely high. In Period II, the 60 earthquakes were still dominated by thrust earthquakes (64%); the number of thrust earthquakes declined by 22%, whereas the strike-slip earthquakes increased by 24% (up to 33%) compared with those in Period I. Significant change was not detected in the number of normal fault earthquakes. The FMS types of the aftershocks that occurred shortly after the Changning earthquake were similar to those of the main shock with thrust fault type. Afterward, the number of strike slip earthquakes increased significantly, whereas the number of thrust fault earthquakes decreased gradually over time. This finding indicates a significant adjustment of the stress field during the active post-earthquake period. In Period III, 21 earthquakes were detected, and their FMS types were significantly different from those of Period II. Thrust fault and strike slip earthquakes decreased by 16 and 14%, respectively, whereas normal fault earthquakes increased by 30%. The evolution of FMS types in the Changning earthquake resembled that of the M_S 7.0 Lushan earthquake (Zhang et al., 2015b). For both events, the FMS types were consistent prior to the earthquake but became more diverse following it. The changes in the FMS types can be interpreted as perturbation of the stress field of the source area induced by the main shock (Diao et al., 2011).

The stress fields of the source area during each period were inverted, as shown in **Figure 8**. The detailed parameters of stress field are listed in **Table 5**. It is evident that the parameters of the stress field changed significantly over time. The S_1 azimuths/plunges in periods I, II, and III were

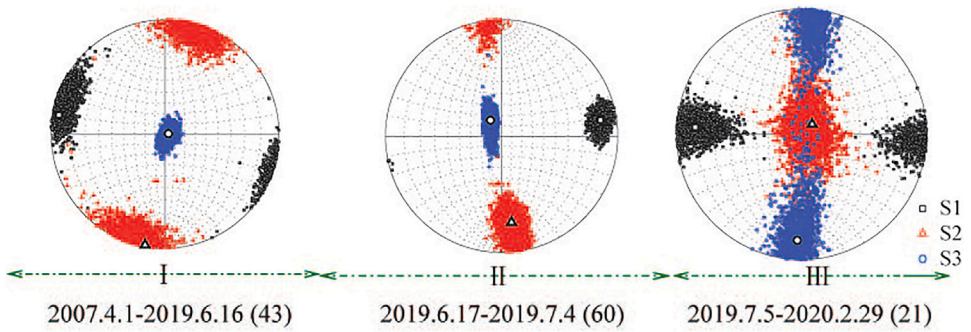

FIGURE 8 | The stress field with time in Changning source area The detail of principal stress axis is shown in **Figure 3**.

TABLE 5 | The stress field in different periods in the Changning source area.

Period	Number of FMS	S_1		S_2		S_3		Variance	Stress regime
		Az (°)	*Pl* (°)	Az (°)	*Pl* (°)	Az (°)	*Pl* (°)		
I	43	280	3.2	190	0.8	86	86.6	0.14	Thrust
II	60	81	8.5	173	16.7	325	71.1	0.12	Thrust
III	21	274	9.1	47	76.7	182	9.5	0.24	Strike Slip

280°/3.2°, 81°/8.5°, and 274°/9.1°, respectively. Therefore, the S_1 azimuth changed from *NWW* in Period I to *NEE* in Period II, and then to *EW* in Period III, with the plunges gradually increasing over time. The stress tensor variance is a quantitative metric of the stress field homogeneity of the study area (Wan, 2011). The variances were 0.14, 0.12, and 0.24 in periods I, II and III, respectively. The gradual increase in variance over time is the result of the increasing diversity of the FMSs and the increasing heterogeneity of the local stress field. In periods I and II, the plunge of S_1 is less than 35°, the plunge of S_3 is more than52°. In periods III, the plunge of S_1 is less than 20°, the plunge of S_2 is more than 45°, and the plunge of S_3 is less than 40°, the stress regime of the source area during periods I and II indicated a thrust regime, which changed dramatically into a strike-slip regime in Period III. Previous studies have suggested that industrial production activities associated with salt mining, hydraulic fracturing, or geothermal exploitation can induce pore pressure and stress field changes (Li, et al., 2021). Earlier studies reported that large-scale human activities like wastewater reinjection and salt mining have been ongoing for a long time in the Zigong-Longchang and Changning areas (Ruan et al., 2008; Zhang et al., 2012; Sun et al., 2017; Lei et al., 2019). The stress fields in these two areas have similar characteristics, and the analysis shows that the local stress fields in these areas have been altered by wastewater reinjection and salt mining activities. In other regions around the world, rotations of principal stress axes have also been observed in geothermal reservoirs, correlated with large fluid injections (e.g., Martínez-Garzón et al., 2013; Dreger et al., 2017). For two injection episodes in the Geysers geothermal field in California, Martínez-Garzón et al. (2013) found that the usually vertical S_1 axis rotated to a shallower plunge by 15–20°, while the usually horizontal S_2 and S_3 axes plunged more steeply. They also observed a horizontal rotation of ~20° during one injection interval. All of these rotations were followed by back rotations to the initial stress state when the injection subsided. During another injection episode at the Geysers, Dreger et al. (2017) observed a ~15° horizontal rotation, accompanied by a transition from a pure strike slip to a transtensional stress state.

CONCLUSION

Based on the FMSs of 124 earthquakes with $M_S \geq 3.0$ occurring in the Changning area from April 1, 2007 to February 29, 2020, the spatiotemporal variations of FMSs and stress field before and after the Changning M_S 6.0 earthquake were analyzed.

The Changning M_S 6.0 earthquake is a thrust and strike-slip dislocation type with a focal depth of 3km, which is controlled by a *NEE* near-horizontal local stress. The Changning aftershocks were predominantly thrust fault earthquakes, followed by strike slip earthquakes and then normal fault earthquakes. The *P*-axis azimuths (*NEE*) of the aftershocks were different from the *NWW* orientations of the pre-earthquake.

The principal compressive stress (S_1) and stress tensor variances of the Changning aftershock zone varied significantly with space. Tracing the aftershock zone from its southeastern end to its northwestern, the S_1 azimuths change from *NEE* to near-EW in the horizontal plane, and plunges had also gradually increased. Furthermore, the stress regime has changed from a strike-slip regime into a thrust regime. The stress tensor variance in the southern segment was significantly lower than the central and

northern segment; strong aftershocks generally occur at or near areas with small stress tensor variances.

The principal compressive stress (S_1) of the aftershock zone also varied in the depth dimension. The angle between the S_1 azimuths and the strike of Changning anticline varies between 30° and 60° in the southern segment, 60°–90° in the central segment and 90°–120° in the northern segment. The angles gradually transformed from the shallow, *NEE*-oriented to deep, *NWW*-oriented.

Significant changes occurred in the FMS types and stress field of the aftershock zone following the Changning earthquake. The FMS types were highly consistent before the Changning earthquake, and became increasingly diverse after the earthquake. The S_1 azimuth also changed from *NWW* to *NEE*, and *EW*. The plunge and stress tensor variances increased over time. Furthermore, the pre-earthquake stress field of the aftershock zone transformed from a homogeneous stress field into a heterogenous stress field following the Changning earthquake.

The stress field of a large regional block is usually stable and uniform, although it is possible for anomalies to appear in small localized areas (Zhang et al., 2012). According to Seeber and Armbruster (2000), earthquakes can be signs of stress change, and their spatial and temporal distribution is very sensitive to stress changes. Crustal stress states can be affected by a variety of processes, which include natural processes such as fault creep or magma injection, or human activities such as dam impoundment, salt mining and hydraulic fracturing. It is speculated that the change of stress field in Changning area may be caused by long-term water injection and salt mining activities.

AUTHOR'S NOTE

ZZ, Master, associate professor, mainly engaged in seismicity and digital seismology research

DATA AVAILABILITY STATEMENT

The original contributions presented in the study are included in the article; further inquiries can be directed to the corresponding authors.

AUTHOR CONTRIBUTIONS

ZZ mainly completed the writing of the manuscript. CL mainly formed the idea of the manuscript and supported the completion of the manuscript. FL mainly completed the data processing. MZ and DW participated worked for the manuscript. All authors contributed to the article and approved the submitted version.

FUNDING

The research was supported by the Special Project of Central Government Guiding Local Development (2020ZYD026) and Sichuan-Yunnan national Earthquake Monitoring and Prediction Experimental Site Project (2016CESE0101, 20150115).

ACKNOWLEDGMENTS

We acknowledge the Sichuan seismic station for providing earthquake observation data. We thank Prof. Zhu lupei of San Luis University of the United States for providing the CAP program. Some figures are generated using the Generic Mapping Tools (GMT) software (Wessel and Smith, 1998). We are very grateful to the editors and reviewers for their constructive comments and thoughtful suggestions.

REFERENCES

Angelier, J. (1979). Determination of the Mean Principal Directions of Stresses for a Given Fault Population. *Tectonophysics* 56 (3–4), T17–T26. doi:10.1016/0040-1951(79)90081-7

Chen, T. C., Horiuchi, S., and Zheng, S. H. (2001). Earthquake Focal Mechanisms and Stress Field in Sichuan-Yunnan Area Determined Using P Wave Polarity and Short Period P and S Wave Form Data. *Acta Seismologica Sinica* 23 (4), 436–440. doi:10.1007/s11589-001-0125-0

Cheng, W. Z., Diao, G. L., Lü, Y. P., Zhang, Y. J., Li, G. F., and Chen, T. C. (2003). Focal Mechanisms, Displacement Rate and Mode of Motion of the Sichuan-Yunnan Block. *Seismology Geology.* 25 (1), 71–87. doi:10.3969/j.issn.0253-4967.2003.01.008

Cui, X. F., and Xie, F. R. (1999). Preliminary Research to Determine Stress Districts from Focal Mechanism Solutions in Southwest China and its Adjacent Area. *Acta Seismologica Sinica* 21 (5), 513–522. doi:10.1007/s11589-999-0056-8

Diao, G. L., Xu, X. W., Chen, Y. G., Huang, B. S., Wang, X. S., Feng, X. D., et al. (2011). The Precursory Significance of Tectonic Stress Field Transformation before the Wenchuan Mw7.9 Earthquake and the Chi-Chi Mw7.6 Earthquake. *Chin. J Geophys* 54 (1), 128–136. doi:10.3969/j.issn.0001-5733.2011.01.014

Dreger, D. S., Boyd, O. S., and Gritto, R. (2017). "Automatic Moment Tensor Analyses, *In-Situ* Stress Estimation and Temporal Stress Changes at the Geysers EGS Demonstration Project," in Proc. 42nd Workshop Geotherm, Stanford, Calif, Feb. 13-15 2017 (Reserv. Eng., Stanford Univ).

Dreger, D. S., and Helmberger, D. V. (1993). Determination of Source Parameters at Regional Distances with Three-Component Sparse Network Data. *J. Geophys. Res.* 98 (B5), 8107–8125. doi:10.1029/93jb00023

Fan, G., and Wallace, T. (1991). The Determination of Source Parameters for Small Earthquakes from a Single, Very Broadband Seismic Station. *Geophys. Res. Lett.* 18 (8), 1385–1388. doi:10.1029/91gl01804

Gephart, J. W., and Forsyth, D. W. (1984). An Improved Method for Determining the Regional Stress Tensor Using Earthquake Focal Mechanism Data: Application to the San Fernando Earthquake Sequence. *J. Geophys. Res.* 89 (B11), 9305–9320. doi:10.1029/jb089ib11p09305

He, D. F., Lu, R. Q., Huang, H. Y., Wang, X. S., Jiang, H., and Zhang, W. K. (2019). Tectonic and Geological Background of the Earthquake Hazards in Changning Shale Gas Development Zone. *Pet. Exploration Develop.* 46 (5), 993–1006. doi:10.11698/PED.2019.05.00

Hu, X. P., Cui, X. F., Zhang, G. W., Wang, G. J., Zang, A., Shi, B. X., et al. (2021). Analysis on the Mechanical Causes of the Complex Seismicity in Changning Area, China. *Chin. J Geophys* 64 (1), 1–17. doi:10.6038/cjp2021O0232

Kan, R. J., Zhang, S. C., Yan, F. T., and Yu, L. S. (1977). Present Tectonic Stress Field and its Relation to the Characteristics of Recent Tectonic Activity in Southwestern China. *ACTA GEOPHUSICA SINICA* 20 (2), 96–109.

Lei, X., Wang, Z. W., Wang, Z., and Su, J. (2019). Possible Link between Long-Term and Short-Term Water Injections and Earthquakes in Salt Mine and Shale Gas Site in Changning, South Sichuan Basin, China. *Earth Planet. Phys.* 3, 510–525. doi:10.26464/epp2019052

Li, T., Sun, J., Bao, Y., Zhan, Y., Shen, Z.-K., Xu, X., et al. (20212021). The 2019 Mw 5.8 Changning, China Earthquake: A cascade Rupture of Fold-Accommodation Faults Induced by Fluid Injection. *Tectonophysics* 801, 228721. doi:10.1016/j.tecto.2021.228721

Li, Y., and Zeng, Y. F. (1994). On the Sedimentary Response to Thrusting of Longmenshan Thrust belt in Chengdu basin. *J. Mineralogy Petrol.* 14 (1), 58–66.

Liang, S. S., Xu, Z. G., Sheng, S. Z., Zhang, G. W., Zhao, B., and Zou, L. H. (2020). Focal Mechanism Soltions and Strress Field of the 2019 Changning, Sichuan Mainshock and its Moderate-strong aftershocks(Ms≥4.0). *Seismology Geology.* 42 (3), 547–561. doi:10.3969/j.issn.0253-4967.2020.03.001

Liu, J., and Zahradník, J. (2020). The 2019 M W 5.7 Changning Earthquake, Sichuan Basin, China: A Shallow Doublet with Different Faulting Styles. *Geophys. Res. Lett.* 47, e2019GL085408. doi:10.1029/2019GL085408

Lu, Z., Wyss, M., and Pulpan, H. (1997). Details of Stress Directions in the Alaska Subduction Zone from Fault Plane Solutions. *J. Geophys. Res.* 102 (B3), 5385–5402. doi:10.1029/96jb03666

Luo, Y., Ni, S., Zeng, X., Zheng, Y., Chen, Q., and Chen, Y. (2010). A Shallow Aftershock Sequence in the north-eastern End of the Wenchuan Earthquake Aftershock Zone. *Sci. China Earth Sci.* 53 (6), 1655–1664. doi:10.1007/s11430-010-4026-8

Luo, Y., Zhao, L., Zeng, X., and Gao, Y. (2015). Focal Mechanisms of the Lushan Earthquake Sequence and Spatial Variation of the Stress Field. *Sci. China Earth Sci.* 58, 1148–1158. doi:10.1007/s11430-014-5017-y

Martínez-Garzón, P., Bohnhoff, M., Kwiatek, G., and Dresen, G. (2013). Stress Tensor Changes Related to Fluid Injection at the Geysers Geothermal Field, California. *Geophys. Res. Lett.* 40, 2596–2601. doi:10.1002/grl.50438

Michael, A. J. (1984). Determination of Stress from Slip Data: Faults and Folds. *J. Geophys. Res.* 89 (B13), 11517–11526. doi:10.1029/jb089ib13p11517

Michael, A. J. (1991). Spatial Variations in Stress within the 1987 Whittier Narrows, California, Aftershock Sequence: New Techniques and Results. *J. Geophys. Res.* 96 (B4), 6303–6319. doi:10.1029/91jb00195

Michael, A. J. (1987). Use of Focal Mechanisms to Determine Stress: A Control Study. *J. Geophys. Res.* 92 (B1), 357–368. doi:10.1029/jb092ib01p00357

Patton, H. (1980). Reference point Equalization Method for Determining the Source and Path Effects of Surface Waves. *J. Geophys. Res.* 85, 821–848. doi:10.1029/jb085ib02p00821

Ruan, X., Cheng, W. Z., Zhang, Y. J., Li, J., and Chen, Y. (2008). Research of the Earthquake Induced by Water Injections in Salt Mines in Changning, Sichuan. *Earthquake Res. China* 24 (3), 226–234. doi:10.3969/j.issn.1001-4683.2008.03.004

Seeber, L., and Armbruster, J. G. (2000). Earthquakes as Beacons of Stress Change. *Nature* 407 (6800), 69–72. doi:10.1038/35024055

Sun, Q., Pei, S. P., Su, J. R., Liu, Y. B., Xue, X. T., Li, J. W., et al. (2021). Three-dimensional Seismic Velocity Structure across the 17 June 2019 Changning Ms6.0 Earthquake, Sichuan, China. *Chin. J Geophys* 64 (1), 36–53. doi:10.6038/cjg2021O0246

Sun, X., Yang, P., and Zhang, Z. (2017). A Study of Earthquakes Induced by Water Injection in the Changning Salt Mine Area, SW China. *J. Asian Earth Sci.* 136, 102–109. doi:10.1016/j.jseaes.2017.01.030

Tan, Y., Zhu, L., Helmberger, D. V., and Saikia, C. K. (2006). Locating and Modeling Regional Earthquakes with Two Stations. *J. Geophys. Res.* 111, B11. doi:10.1029/2005JB003775

Thio, H. K., and Kanamori, H. (1995). Moment-tensor Inversions for Local Earthquakes Using Surface Waves Recorded at TERRAscope. *Bull. Seis Soc. Amer* 85 (4), 1021–1038. 10.1785/BSSA0850041021.

Waldhauser, F., and Ellsworth, W. L. (2000). A Double-Difference Earthquake Location Algorithm: Method and Application to the Northern Hayward Fault, California. *Bull. Seismological Soc. America* 90 (6), 1353–1368. doi:10.1785/0120000006

Wan, Y. G. (2011). Contemporary Tectonic Stress Field in China. *Translated World Seismology* 3, 18–29.

Wang, S. Z. (2014). *The Tectonic Characteristics of Changning Area, South of Sichuan and Crack Characteristics of Longmaxi Formation of Silurian System*. Chengdu: Chengdu University of Technology.

Wessel, P., and Smith, W. H. F. (1998). New, Improved Version of Generic Mapping Tools Released. *Eos Trans. AGU* 79, 579. doi:10.1029/98EO00426

Wiemer, S. (2001). A Software Package to Analyze Seismicity: ZMAP. *Seismological Res. Lett.* 72 (2), 373–382. doi:10.1785/gssrl.72.3.373

Wiemer, S., Gerstenberger, M., and Hauksson, E. (2002). Properties of the Aftershock Sequence of the 1999 Mw 7.1 Hector Mine Earthquake: Implications for Aftershock Hazard. *Bull. Seismological Soc. America* 92 (4), 1227–1240. doi:10.1785/0120000914

Yang, Y., Liang, C., Fang, L., Su, J., and Hua, Q. (2018). A Comprehensive Analysis on the Stress Field and Seismic Anisotropy in Eastern Tibet. *Tectonics* 37, 1648–1657. doi:10.1029/2018TC005011

Yang, Y., Liang, C., Li, Z., Su, J., Zhou, L., and He, F. (2017). Stress Distribution Near the Seismic gap between Wenchuan and Lushan Earthquakes. *Pure Appl. Geophys.* 174, 2257–2267. doi:10.1007/s00024-016-1360-6

Yi, G. X., Long, F., Liang, M. J., Zhao, M., Wang, S. W., Gong, Y., et al. (2019). Focal Mechanism Solutions and Seismogenic Structure of the 17 June 2019 Ms6.0 Sichuan Changning Earthquake Sequence. *Chin. J Geophys* 62 (9), 3432–3447. doi:10.6038/cjg2019N0297

Zhang, Z. W., Cheng, W. Z., Liang, M. J., Wang, X. S., Long, F., Xu, Y., et al. (2012). Study on Earthquakes Induced by Water Injection in Zigong-Longchang Area, Sichuan. *Chines J. Geophys.* 55 (5), 1635–1645. doi:10.6038/j.issn.0001-5733.2012.05.021

Zhang, Z. W., Zhou, L. Q., Cheng, W. Z., Ruan, X., and Liang, M. J. (2015b). Focal Mechanism Solutions of Lushan Mw6.6 Earthquake Sequence and Stress Field for Aftershock Zone. *Earth Science-Journal China Univ. Geosciences* 40 (10), 1710–1722. doi:10.3799/dqkx.2015.154

Zhang, Z. W., Zhou, L. Q., Long, F., and Ruan, X. (2015a). Spatial and Temporal Characteristic of Stress Field for Wenchuan Ms8.0 and Lushan Ms7.0 Earthquake Sequence. *Seismology Geology.* 37 (3), 804–817. doi:10.3969/j.issn.0253-4967.2015.03.011

Zhao, L. S., and Helmberger, D. V. (1994). Source Estimation from Broadband Regional Seismograms. *Bull. Seismol Soc. Amer* 84 (1), 91–104.

Zhao, M., Long, F., Yi, G., Liang, M., Xie, J., and Wang, S. (2021). Focal Mechanism and Seismogenic Structure of the MS 5.1 Qingbaijiang Earthquake on February 3, 2020, Southwestern China. *Front. Earth Sci.* 9, 644142. doi:10.3389/feart.2021.644142

Zheng, Y., Ma, H. S., Lü, J., Ni, S. D., Li, Y. C., and Wei, S. J. (2009). Source Mechanism of Strong Aftershocks (M_S≥5.6) of the 2008/05/12 Wenchuan Earthquake and the Implication for Seismotectonics. *Sci. China (Series D)* 39 (4), 413–426. doi:10.1360/zd2009-39-4-413

Zhong, J. M., and Cheng, W. Z. (2006). Determination of Directions of the Mean Stress Field in Sichuan-Yunnan Region from a Number of Focal Mechanism Solutions. *Acta Seismologica Sinia* 28 (4), 337–346. doi:10.1007/s11589-004-0359-y

Zhu, L., and Helmberger, D. V. (1996). Advancement in Source Estimation Techniques Using Broadband Regional Seismograms. *Bull. Seismol Soc. Amer* 86 (5), 1634–1641. doi:10.1785/bssa0860051634

Zoback, M. L. (1992). First- and Second-Order Patterns of Stress in the Lithosphere: The World Stress Map Project. *J. Geophys. Res.* 97 (B8), 11703–11728. doi:10.1029/92jb00132

Conflict of Interest: The authors declare that the research was conducted in the absence of any commercial or financial relationships that could be construed as a potential conflict of interest.

Publisher's Note: All claims expressed in this article are solely those of the authors and do not necessarily represent those of their affiliated organizations, or those of the publisher, the editors and the reviewers. Any product that may be evaluated in this article, or claim that may be made by its manufacturer, is not guaranteed or endorsed by the publisher.

frontiers in Earth Science

ORIGINAL RESEARCH
published: 10 February 2022
doi: 10.3389/feart.2021.793890

Present-Day Tectonic Deformation Partitioning Across South Tianshan From Satellite Geodetic Imaging

Jiangtao Qiu[1,2], *Lingyun Ji*[2]*, *Liangyu Zhu*[2] *and Qingliang Wang*[2]

[1]Institute of Geology, China Earthquake Administration, Beijing, China, [2]The Second Monitoring and Application Center, China Earthquake Administration, Xi'an, China

The Tianshan orogenic belt has intense crustal deformation and shortening in the near north-south direction. We processed ascending and descending Sentinel-1A/B [1]synthetic aperture radar (SAR) data to obtain the first line-of-sight deformation field over South Tianshan (75–78 E), and combined with GPS velocity data to construct the current three dimensions surface velocity fields with high quality and high spatial resolution. The results show that: 1) deformation is not evenly distributed in the study area. The convergence across the Tianshan ranges is approximately 15–24 mm/yr; the deformation gradient in the junction area between South Tianshan and Pamir is the largest, and adjusts ~68% of the total convergence deformation. South Tianshan is relatively stable without sharp gradients, and ~58% of the deformation is distributed in the intermontane faults and basin systems in the north of South Tianshan. 2) Thrust slip of faults, uplift of folds, and slippage of décollement jointly play important roles in accommodating regional strain. The Maidan fault, which is the boundary between South Tianshan and Tarim Basin, has strike-slip and thrust characteristics, and is the root fault of the slip partitioning system. Our results can provide effective kinematic boundary constraints for the study of Asian crustal movement models.

Keywords: South Tianshan, GPS/InSAR, 3D surface deformation, deformation partitioning, fault slip

OPEN ACCESS

Edited by:
Ying Li,
China Earthquake Administration, China

Reviewed by:
Alexis Rigo, UMR8538 Laboratoire de Géologie de l'Ecole Normale Supérieure (LG-ENS), France
Hua Wang, Guangdong University of Technology, China

***Correspondence:**
Lingyun Ji
dinsar010@163.com

Specialty section:
This article was submitted to Structural Geology and Tectonics, a section of the journal Frontiers in Earth Science

Received: *12 October 2021*
Accepted: *29 December 2021*
Published: *10 February 2022*

Citation:
Qiu J, Ji L, Zhu L and Wang Q (2022) Present-Day Tectonic Deformation Partitioning Across South Tianshan From Satellite Geodetic Imaging. Front. Earth Sci. 9:793890. doi: 10.3389/feart.2021.793890

INTRODUCTION

The Tianshan orogenic belt (TSOB) is one of the most active regions in Eurasia. The long-range effect of the collision between the Indian plate and the Eurasian plate in the late Cenozoic led to the reactivation of the TSOB and the occurrence of intracontinental orogeny. At the same time, the TSOB expanded to the foreland basins on both sides, forming multiple rows of décollement- and fault-related fold belts in the basin-mountain boundary zone (Yin et al., 1998; Burchfiel et al., 1999; Deng et al., 2003). Global Positioning System (GPS) observations around longitude ~76° show that the crustal shortening rate in the north-south direction across the Tianshan Mountains is at least ~20 mm/yr (Wang et al., 2000; Yang S. et al., 2008; Zubovich et al., 2010). However, the distribution of deformation in the tectonics of the TSOB is controversial.

Abbreviations: SAR, Sythetic aperture radar; InSAR, Interferometric synthetic aperture radar; TSOB, Tianshan orogenic belt; GPS, Global Positioning System; LOS, line-of-sight; SLC, single look complex; HRES-ECMWF, high-resolution European Center for Medium-Range Weather Forecasts;GACOS, Generic Atmospheric Correction Online Service; WKPT, western Kunlun piedmont thrust.

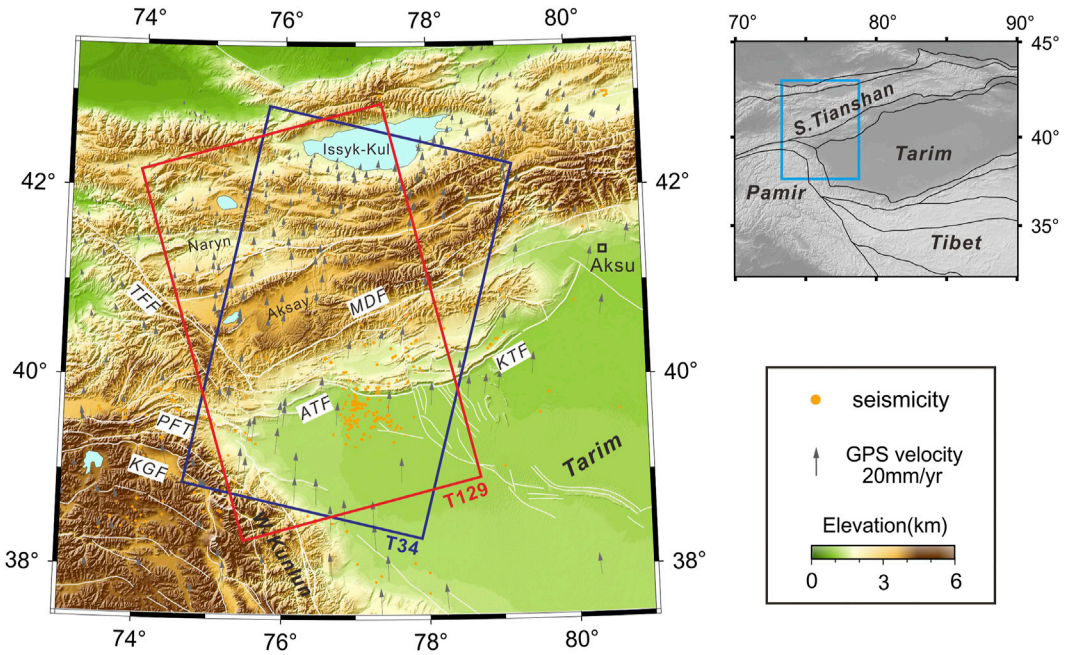

FIGURE 1 | Topographic and tectonic map of the study area superimposed on Digital Elevation Model of the Shuttle Radar Topography Mission (SRTM DEM). Gray vectors represent the GPS velocities with respect to stable Eurasia plate (Wang and Shen, 2020). White lines represent fault traces from http://www.activefault-datacenter.cn. Orange dots are the locations of M > 4.5 earthquakes since 1992. Blue and red rectangles delimit the extents of Sentinel-1A/B radar imagery on ascending (129) and descending tracks (34). ATF: Atushi fault, MDF: Maidan fault, KTF: kepingtag fault, KGF: Kongur fault, PFT: Pamir front thrust, TFF: Taras-Fergana fault.

One point of view is that the basins on the north and south of the Tianshan Mountains are compressed into the mountain along the main root faults on both sides, causing the nappe structure at the basin-mountain junction to absorb most of the deformation in Tianshan (Yang S. et al., 2008; Wang and Shen, 2020). The intermountain basins in Tianshan also have significant tectonic deformation, therefore, the strain accumulation is distributed evenly throughout the Tianshan Mountains (Thompson et al., 2002; Zhang et al., 2003). In addition, certain researchers have shown that fold-thrust belts are the most intensely deformed areas in the TSOB (Abdrakhmatov et al., 1996; Zhang et al., 1996; Burbank et al., 1999), and the expansion and uplift of active folds play an important role in regulating regional strain in the southern Tianshan-Tarim collision zone (Bufe et al., 2017; Li et al., 2020). Therefore, in the study of tectonic deformation partitioning in this area, if only faults are considered and active folds are disregarded, the deformation of faults will be overestimated.

Interferometric synthetic aperture radar (InSAR) has yielded numerous results with respect to obtaining the deformation characteristics of fault zones (e.g., Jolivet et al., 2008; Wang and Wright, 2012; Daout et al., 2016; Liu et al., 2018; Wang et al., 2019; Ji et al., 2020). Unlike the station information observed by GPS, InSAR observes continuous area information, which can determine the fine variations in the shortening deformation of the Tianshan Mountains. This provides a new way of studying the fine deformation of the Tianshan orogenic belt. However, owing to the challenges in data processing, only a few studies have attempted to investigate the regional deformation field in the southern Tianshan-Tarim collision zone (He et al., 2015; Qiao et al., 2017). In this study, we focus on the central part of South Tianshan between longitudes 75°and 78° (**Figure 1**). We processed two ascending and descending Sentinel-1 tracks from Issyk-Kul Lake to the northwest of the Tarim Basin based on the time-series InSAR technology, thereby, yielding a line-of-sight (LOS) velocity map covering a 250 × 420 km region. Combining GPS data, a velocity decomposition of crustal movement with high spatial resolution in Tianshan was obtained, elucidating the present-day tectonic deformation partitioning across southern Tianshan. We further discussed the tectonic kinematics and strain distributions in the study area.

GEOLOGIC SETTING

Owing to its intense crustal deformation and shortening in the near north-south direction, the TSOB is a natural experimental field for the study of intraplate deformation and continental dynamics. Numerous active faults and folds are developed in the Tianshan Mountains and in the basin-mountain junction zone, which are important components for adjusting the compressive strain and controlling the uplift of the Tianshan Mountains. Among them, the Pamir-South Tianshan-Tarim collision zone is the strongest uplift area of the TSOB (**Figure 1**).

The compression of the TSOB, Pamir Plateau, and Tarim Basin has resulted in the complex and unique structural features

of the central part of South Tianshan. The fold-thrust belts in the front of South Tianshan are merged into the main décollement plane at the bottom of the sedimentary caprock in the deep, forming typical thin-skin structures (Zhang et al., 1996; Chen et al., 2001). The Keping nappe structure in the east of our study area is composed of rows of EW-trending reverse fault-anticline belts, which are fan-shaped. The main bodies of these anticlines are composed of Paleozoic strata, which are formed by the fault slope caused by the uplift of the décollement plane. The décollement of the Keping nappe structure is divided by the Piqiang fault, which plane exists at ~9 km depth in the west, and at ~5 km depth in the east. The nappe slopes gently to the north until it converges with the Maidan fault, which is the root of South Tianshan (Yin et al., 1998; Tian et al., 2006; Yang X. et al., 2008). In the southernmost front edge of the Keping nappe, the Kepintag fault is one of the most recent active faults, and many M ≥ 6 earthquakes have occurred on this fault.

In the west of our study area, deformation along the Main Pamir Thrust appears to have ceased for the most part (Chen et al., 2011) and moved northward, where it interferes with southern Tianshan, and the Cenozoic fold-thrust belt at the Kashi area is composed of three to four rows of anticlines. From north to south, the Muziduke anticline and the Tashipisake anticline are controlled by the north-dip thrust fault, whereas the western and eastern parts of the Atushi anticline are controlled by the north-dip thrust fault and the south-dip thrust fault, respectively, and the Kashi anticline is controlled by a south-dip thrust fault (Miao et al., 2007). In contrast to the Keping nappe structure, the Kashi fold-thrust belt has been active at a significantly later time and is currently more active, and most of the deformation occurs on the young fold anticlines (Chen et al., 2011). An M $8^1/_4$ earthquake occurred in the Toth Goubaz fault on the north side of the Atushi anticline in 1902 (Shen J. et al., 2001).

As the boundary fault between South Tianshan and Tarim basin, the root fault of the Kashi fold-thrust belt and the Keping nappe, the Maidan fault is nearly 400 km long. Starting from Aheqi to the east, the Maidan fault and the several surrounding peripheral faults together form a complex fault zone, with a maximum width of 17 km. Geological and seismic data have shown that thrust is the main activity of the fault at present (Chen et al., 2001; Gao et al., 2005). However, certain researches believe that apart from thrust movement, the Maidan fault has evident left-lateral strike-slip characteristics and is a large-scale left-lateral compression-torsion fault (Shen Z.-K. et al., 2001; Li et al., 2015; Wu et al., 2019).

INSAR PROCESSING

We acquired Sentinel-1A/B data (ascending track: 129; descending track: 34) from the European Space Agency (ESA) between November 2014 and December 2019 covering a 420 km long and 250 km wide range of South Tianshan (**Figure 1**). We constructed 108 ascending interference pairs and 91 descending interference pairs based on commercial Gamma software (Wegnüller et al., 2016) and the permanent scatterer InSAR method (**Supplementary Figures S1, S2** in the Supporting Information show all the epochs and baselines of the processed pairs). InSAR time series analysis was performed using the StaMPS package (Hooper et al., 2004; Hooper et al., 2007). The long-wavelength and elevation-dependent atmospheric errors from each interferogram are reduced using the TRAIN package (Bekaert et al., 2015) and GACOS data (Yu et al., 2018; Yu et al., 2020).

Decrease Decoherence

As InSAR measures one-dimensional areal displacements in the direction of radar line-of-sight (LOS), it is prone to shrinkage, overlap, and shadows in areas with high terrain gradients, leading to high decorrelation and a corresponding low coherence of deformation signals. The PSInSAR method was used to obtain the time series deformation of the study area and to limit the signal decoherence. Single look complex (SLC) images were computed from the raw radar data in a common mean Doppler geometry. After the SLC images were co-registered, the linear ramp within range was corrected to account for orbital errors and clock drift (Zhang et al., 2014; Daout et al., 2018). Interferograms are formed with one range look and one azimuth look to obtain finer differential interferograms. The finer the resolution, the fewer the scatterers contained within each resolution pixel, and the greater the chance that the pixel is dominated by one scatterer. This reduces the probability that the high-coherence pixel is averaged by the surrounding decorrelation noise, and the pixel is more easily recognized as a permanent scatter (PS) pixel. Subsequently, we used a robust power spectrum filter (Goldstein and Werner, 1998) to further reduce the phase noise thus improving the quality of the interferogram.

Finally, we used StaMPS to select and filter PS pixels. StaMPS selects PS candidates based on the spatial correlation of the interferogram phase, which does not rely on thresholding pixel amplitude dispersion over time and does not require prior knowledge of temporal variations in the deformation rate (Hooper et al., 2004; Hooper et al., 2007). Therefore, a certain number of PS pixels can be found in the low-amplitude area. We obtained 48,655,102 PS candidates for the ascending track (A129) and 44,340,642 PS candidates for the descending track (D34). The pixels that were mistakenly selected were removed based on phase analysis, and 316,079 PS for A129 and 318,066 PS for D34 were finally screened out, which completely covered the study area.

Atmospheric Delay Correction

Spatial and time variations in temperature, pressure, and relative humidity in the atmosphere caused a delay in the radar signal in the propagation path, and this delay information was finally integrated into the interferometric phase, which is known as the atmospheric delay error. The atmospheric delay can be split into hydrostatic and wet components. For C-band SAR data, the proportion of hydrostatic delay to the total delay can reach 15% in areas with significant relief and spatial variation areas (Jolivet et al., 2014), which can be attenuated by differential and stacking InSAR technology. In contrast with hydrostatic signals, the magnitude of wet delays, which are caused by the lateral

variation in water vapor, is several times smaller (Hanssen, 2001), whereas the spatial pattern is significantly more variable and is not related to topography. Therefore, if the interferometric phase is in a flat or mountainous area, the wet delay may conceal the slight surface deformation information.

At present, there are two types of atmospheric delay estimation approaches (Bekaert et al., 2015; Shen et al., 2019). One entails correcting the atmosphere using external data, such as GPS data and atmospheric models (ERA5, WRF, etc.). The other entails empirically determining the phase/elevation relationship using the interferometric phase. Different approaches have different sensitivities to hydrostatic and wet delay components, and have unique advantages and disadvantages.

Here, to reduce the atmospheric delay effects of Sentinel-1 data covering South Tianshan, we use the toolbox for reducing atmospheric InSAR noise (TRAIN) to estimate the atmospheric delay maps using the Generic Atmospheric Correction Online Service (GACOS; Yu et al., 2018; Yu et al., 2020) product. The GACOS analysis product integrates the surface pressure, temperature, and humidity from the latest high-resolution European Center for Medium-Range Weather Forecasts (HRES-ECMWF), with a significantly higher spatial resolution (0.1°) and time resolution (6 h), which could be beneficial for describing smaller-scale variations in atmospheric delays. Both hydrostatic and wet delay components to the phase delay are taken into account in this approach. As shown in **Supplementary Figures S3, S4**, the atmospheric delay phase ranges of A129 and D34 are −13.9–18.3 rad and −16.3–19.1 rad, respectively, which shows that the atmospheric noise in the study area is severe.

Combine GPS and InSAR Velocity Data

Monitoring the intense N-S shortening in Tianshan is a significant challenge. Restricted by the polar-orbit flight and side-view imaging of SAR satellite, InSAR can only monitor the one-dimensional projection of surface deformation in LOS, and is insensitive to the north-south deformation. Therefore, InSAR LOS deformation is very likely to result in the misinterpretation of crustal movement in South Tianshan. Considering that GPS can provide high-precision crustal horizontal movement information, even reach the sub-millimeter level. However, its spatial resolution of the GPS network is very low, which can only provide the deformation of a few discrete points. The technical characteristics of InSAR and GPS are complementary; therefore, information on surface deformation in the study area can be developed by combining GPS velocities and InSAR LOS rate data.

After the InSAR LOS deformation field (**Figure 2**) was produced, we used the method developed by Shen and Liu (2020) to integrate GPS and InSAR data. The GPS data were obtained from the study performed by Wang and Shen (2020). They found that 28 CMONOC I (phase I of the Crustal Movement Observation Network of China) campaign sites located in the eastern TianShan region showed abnormal displacements before 2008, and speculated that the problem may be attributed to systematic biases caused by the use of different receiver/antenna units between surveys, particularly certain substandard antennas. Therefore, they removed the troublesome epochs of data in the derivation of the velocities for the affected sites. The uniformly distributed GPS sites in the study area can be used to perform remarkable horizontal calibration of the InSAR data of the two tracks (A129 and D34).

We interpolated the discrete GPS data points to generate a 2-dimensional continuous velocity field on the grid covered by InSAR data. In the algorithm of Shen and Liu (2020), the GPS data and their interpolated values are needed in the estimate and remove offset/ramp of InSAR LOS measurements to stabilize the inversion at the first step. The offset and/or ramp were globally estimated for all the images to minimize data misfit, particularly in regions where the data overlap. To combine the interpolated GPS data with InSAR data, the GPS velocities uncertainties are estimated from the interpolation to be used as data weighting in the combination. The uniform smoothing method is adopted to ensure that the estimated uncertainty can consistently reflect the strength of the measured data and is not affected by uneven smoothing. We set 2 mm/yr as cutoff uncertainty of InSAR data and 3 as the weighting thresholds for GPS data interpolation in the GPS/InSAR combination. At the location with InSAR and interpolated GPS data, the weighted least squares method is used to solve the optimal 3-dimensional component. Finally, we obtained a horizontal continuous deformation field from spatially limited GPS and dimensionally limited InSAR data (**Figure 3**). Owing to the lack of a GPS vertical velocity constraint, the vertical deformation combination effect in the non-overlapping areas of A129 and D34 was not good (**Figure 3C**). The data post-fit residuals and solution uncertainties are shown in **Supplementary Figures S6**. As Shen and Liu (2020) suggested, for a GPS network with a spacing of ~30 km, the GPS data can provide significantly greater constraints for the solution of continuous horizontal deformation than InSAR. However, because the spatial resolution of GPS is not as high as that of InSAR, there may be exceptions at places with localized deformation sources, for example, Kashi.

Positive motion is toward the satellite. Black lines represent fault traces. Pink dashed contours (A1–A6) are caused by nontectonic activities. The intersecting black and white arrows indicate satellite flight and look directions, respectively. P1,P2,P3,P4, P5 denote five velocity profiles locations described in **Supplementary Figures S5, S6, S7, S8** and **Figure 7**.

profiles P1,P2,P3,P4, P5 as in **Figure 2**. The red dotted line box is the common coverage area of tracks 129 and 34. YJSF:Yingjisha fault, KSF: Kashi fault, ATF: Atushi fault, TGF: Toth Goubaz fault, MDF: Maidan fault, KKGF:kerkeigel fault, ODF:Oinak-Djar fault, SNF:South Naryn fault, SIKF:South Issyk-Kul lake fault,TSF: Toshgan fault, KLTKF: Kalatieke fault, KPF: Kepingtag fault.

ANALYSIS OF DEFORMATION FIELD

The final LOS surface velocity maps (**Figure 2**) show, for the first time, an almost continuous view of the surface displacement field across South Tianshan. **Figure 2** shows that deformation

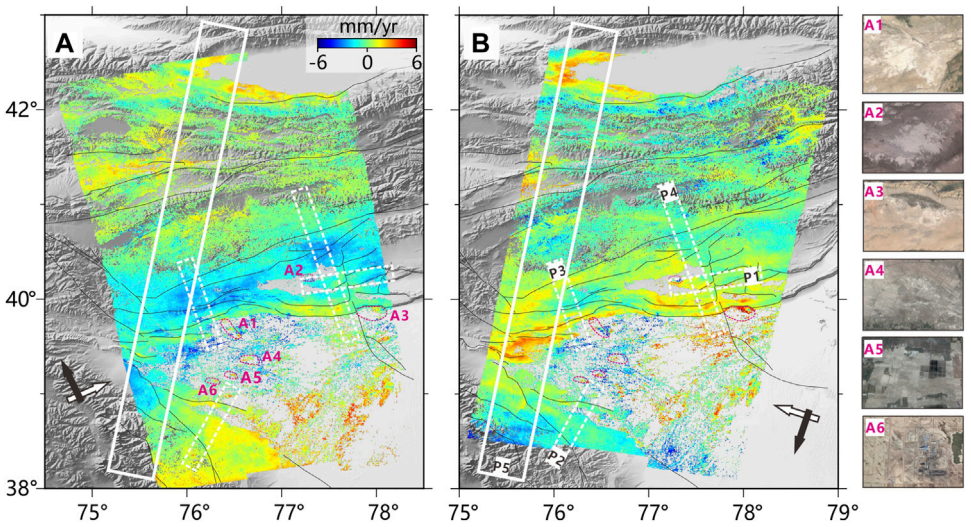

FIGURE 2 | Line-of-sight (LOS) velocity map of the tracks 129 **(A)** and 34 **(B)**.

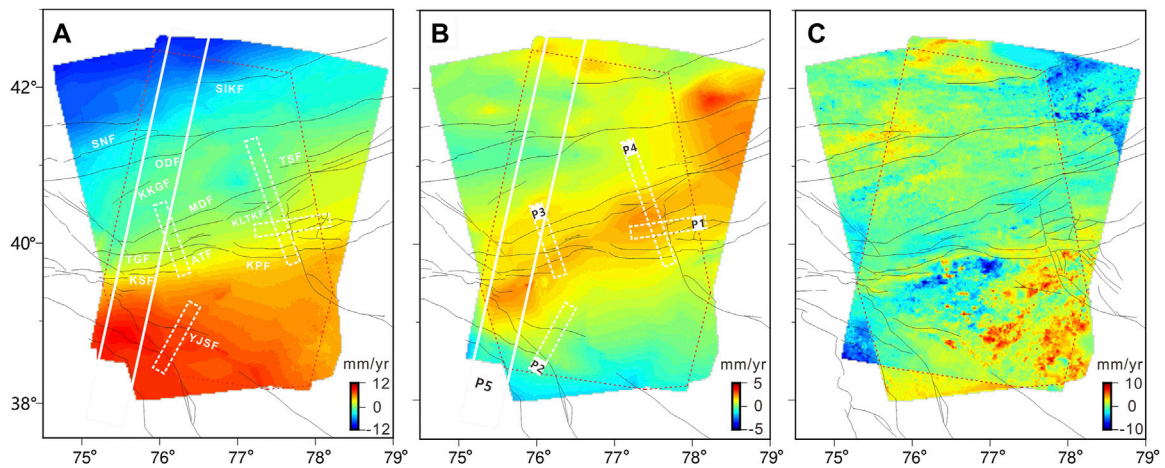

FIGURE 3 | horizontal deformation map. **(A)** deformation for the north-south component and positive toward north. **(B)** deformation for the east-west component and positive toward east. **(C)** deformation for the vertical component and positive toward up.

information is only lacking in these marginal or local areas, such as grasslands and deserts in the Tarim basin, and high-altitude snow areas in South Tianshan. There are six significant deformation signals in the Kashi region (A1–A6, dashed boxes in **Figures 2A,B**). According to the field survey, these abnormal deformation signals are caused by nontectonic activities, including salt mining (A1, A2, A3), farmland reclamation (A4, A5), and oil and gas exploitation (A6). Excluding the influence of these nontectonic activities, the overall depression in the Kashi region, which is bounded by the Atushi fault in the north, the Pamir front thrust in the southwest, and the Tarim Basin in the southeast is clearly visible relative to the surrounding area. As shown in **Figure 2**, the LOS deformation in the Kashi depression is negative in both ascending and descending tracks (blue tones, away from the satellite). **Figure 3C** shows that the vertical subsidence deformation is approximately 2–10 mm/yr. The most severe depression was north of Jiashi County (7–10 mm/yr) and Kashi City (5–10 mm/yr). The fold-thrust belt and Keping nappe structure in the periphery of the Kashi region have evident uplift.

The horizontal deformation maps (**Figure 3**) show that the deformation was not evenly distributed throughout the study area. The clear feature of the N-S velocity field (**Figure 3A**) is that the north and south sides of the Tianshan are strongly compressed, and the N-S convergence rate across the Tianshan is approximately 15–24 mm/yr. The largest deformation among these is in the collision area between South Tianshan and Pamirs; the deformation is mainly distributed in the Pamir front thrust (PFT) and Cenozoic fold-fault belts. The central section of South Tianshan is relatively

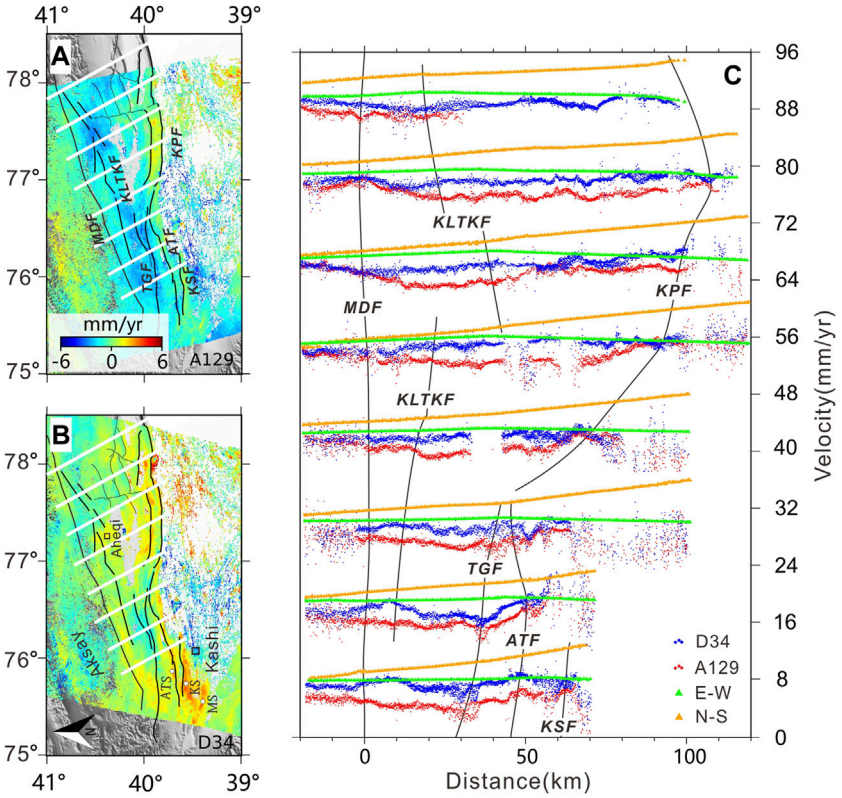

FIGURE 4 | Deformation data profiles across the south of southern Tianshan. **(A)** and **(B)** indicate LOS velocity map of the tracks 129 (A129) and 34 (D34),respectively. The white lines are 8 profiles locations **(C)** velocity profile from D34 (blue dots), A129 (red dots), E-W (green triangle)and N-S (yellow triangle). The black lines are fault tracks. KSF: Kashi fault, ATF: Artux fault, TGF: Toth Goubaz fault, MDF: Maidan fault, KPF: Kepingtag fault, KLTKF: Kalatieke fault. MS: Mushi fold, KS: Kashi fold, ATS: Atushi fold.

stable, with very slight deformation. These results are consistent with previous GPS research results (Niu et al., 2007; Yang S. et al., 2008; Li et al., 2015; Wang and Shen, 2020). This shows that the crust in Tianshan has undergone intense shortening deformation due to the push of the Indian plate, and the crustal deformation gradually weakens from west to east and from south to north with increased proximity from Pamirs. As shown in **Figure 3B**, there is a steep gradient across the fold area between South Tianshan and Tarim basins, which shows the overall eastward movement of the fold area with respect to South Tianshan and Tarim basins. The W-E movement rate of the fold area is approximately 1–3 mm/yr, and exhibits obvious segmentation in Kashi and Keping.

For the rather complex deformation field of South Tianshan, we created a series of velocity profiles to examine the regional deformation fields. These profiles clearly show the deformation gradients on various structural faults and the distribution of crustal deformations throughout southern Tianshan.

Kashi Fold-Thrust Belt

The Kashi fold-thrust belt is located in a narrow area where the Pamir collides with South Tianshan, and is currently the most active place in this area. From the LOS deformation field (**Figures 2**, **4**), the deformation is mainly concentrated on a series of folds: the Mushi, Kashi, and Atushi folds and the faults between folds: the Kashi, Atushi, and Toth Goubaz faults. Among these folds, the LOS deformation gradually attenuated from south to north. The Mushi fold and Kashi fold had the highest surface uplift rate: ~ 6 mm/yr; followed by the Atushi fold: ~ 2 mm/yr. The peak surface uplift rates on the folds were all near their adjacent faults. Structures to the north of these folds appear to be mostly inactive.

From the north-south component of the horizontal deformation field (**Figure 3A**), the N-S deformation rate of the Kashi fold-thrust belt is approximately 10 mm/yr. Among them, the kashi fault is approximately 4 mm/yr, the Atushi fault is approximately 2 mm/yr, and the Toth Goubaz fault is approximately 2 mm/yr. The remaining convergence and shortening occurred on the folds, resulting in the uplift and growth of the folds. From the east-west deformation field (**Figure 3B**), we can see that the fold region has an entire eastward movement relative to South Tianshan and Tarim, and the movement rate is approximately 4 mm/yr at most. This discovery is consistent with the geological conclusion that these folds have the growth characteristics of lateral extension from east to west. However, the E-W deformation of the Atushi, Toth Goubaz, and Kashi faults is not clear, and exhibits thrust characteristics.

Maidan Fault

We can see from the LOS deformation fields (**Figures 2**, **4**) that, as the boundary fault between South Tianshan and Tarim basins,

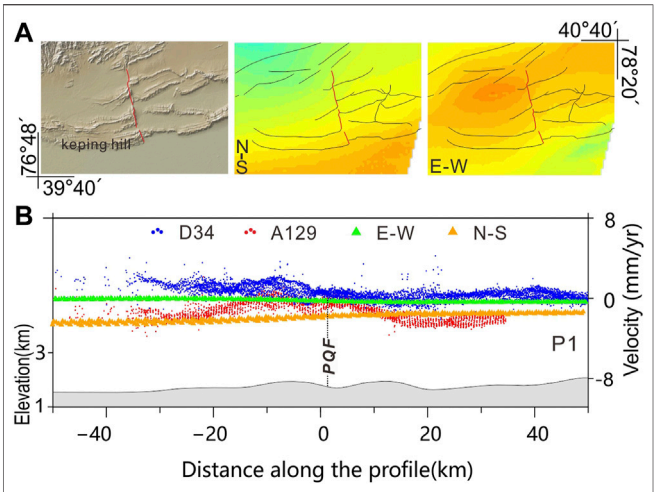

FIGURE 5 | (A) Enlargements of shaded elevation, the N-S and E-W velocity maps overing Piqiang fault, the color bar is the same as **Figure 3**. **(B)** Deformation data profile across Piqiang fault (PQF). See **Figures 2**, **3** for P1 location.

the positive and negative deformations on both sides of the Maidan fault are at opposite positions in ascending and descending deformation fields, indicating that the present tectonic deformation of the Maidan fault has a strike-slip component. From the horizontal deformation field (**Figure 3**), the tectonic deformation of the Maidan fault seems segmented. In the segment between the Talas-Fergana fault and eastern Aheqi (75.8–77.0E), the Maidan fault shows slight left-lateral strike-slip and thrust deformation. In Aheqi eastward to Wushi (77.0–78.8E), the N-S deformation of the Maidan fault is strengthened.

To better determine the deformation variation of the Maidan fault and its deformation partitioning relationship with adjacent folds and nappes, we selected eight profiles of LOS and horizontal deformation from west to east across the front of South Tianshan (**Figure 4**). From **Figure 4**, we observed that the strike-slip of the Maidan fault gradually weakened from west to east, and the E-W and N-S deformations are approximately 1.0–2.0 mm/yr and approximately 1.0–1.5 mm/yr, respectively. Especially after the Kalatieke fault, strike-slip deformation mostly occurred on the fault. This shows that the Maidan fault is still active today, and has absorbed part of the tectonic deformation of the Tianshan orogeny with the adjacent faults.

Keping Nappe

The Keping nappe is bounded by the Kalatieke fault, and folds appear in the nappe from north to south. Among them, the profiles in **Figure 5** show that the deformation difference in N-S and E-W on both sides of the Karatike fault is approximately 2.0 mm/yr and 1.0 mm/yr, respectively, showing a left-lateral strike-slip pattern. Considering the Piqiang fault as the dividing line, the Keping nappe is divided into the eastern and western parts, and the two parts show different tectonic deformations. As shown in **Figures 5A,B**, in the western part, the deformation is mainly concentrated on the Keping hill and Kepingtag fault in the front of the nappe, where the N-S and E-W deformation of kepingtag fault are approximately 2.5 mm/yr and approximately 1.0 mm/yr respectively. In the eastern part, the N-S deformation of the front of the nappe is reduced to approximately 1.5 mm/yr and distributed on the Kepingtag fault and other folds and faults. This shows that as the front edge of the Keping nappe, the tectonic deformation of the Keping Tage fault is segmented in the Piqiang fault.

Figures 2, **3** show that the LOS deformation and N-S deformation on the east and west sides of the Piqiang fault are evidently different, and gradually become clear from south to north. The velocity profile across the middle of the Piqiang fault (**Figure 5**) shows that the fault is a left-lateral strike-slip, with an average rate of ~1.5 mm/yr.

West Kunlun Piedmont Thrust

From the LOS deformation maps (**Figure 2**) and the N-S horizontal deformation map (**Figures 3A**, **6**), the western Kunlun piedmont thrust (WKPT) located in the south of the Kashi depression also exhibits deformation. Influenced by the significant northward movement and rotation of the Pamirs in the Cenozoic, the WKPT and its periphery developed in an arc shape (Cheng et al., 2012). The main fault in the middle of the WKPT is the Kusilafu fault, and the front fault is the Yingjisha fault. The deformation profile across the WKPT (**Figure 6**) shows that the Kusilafu fault has the characteristics of right-lateral strike-slip and thrust, showing deformation gradients in the N-S and E-W directions, indicating that it is affected by regional right-lateral strike-slip stress in addition to northward thrust. There is an N-S deformation gradient on the Yingjisha fault. Therefore, the Kusilafu and Yingjisha faults, as the boundary faults between the WKPT and Tarim Basin continue to accommodate the pushing movement of the Pamirs on the Tarim Basin. Owing to the difference in the positions of the deformed fronts on the east and west sides of the fault, the Kusilafu fault's right lateral compression and torsion are formed.

Northern Basins of South Tianshan

As seen in the LOS deformation maps (**Figures 2**, **7**) and the horizontal deformation map (**Figure 3**), the deformation in the north of South Tianshan is dispersed in a series of intermountain active structures and the depression basins, unlike in the south side, where the deformation is mainly concentrated on the thrust folds.

There is an evident deformation gradient in the northwestern Aksay Basin, involving the Kerkeigel fault and a previously unresearched fault, which we named the Aksay fault here. The deformation profiles in **Figure 7C** show that the N-S convergence rates on the two faults are approximately 1.5 mm/yr, and W-E deformations are slight but show left-lateral slip. There is a subsidence area between the Kerkeigel fault and the At-Bashi range, where there is a lake. This shows that there is a local squeeze and subsidence deformation inside South Tianshan. From **Figure 7C**, the N-S convergence of Oinak-Djar fault in At-Bashi Basin is approximately 1.0 mm/yr, with slight W-E deformation of <0.5 mm/yr.

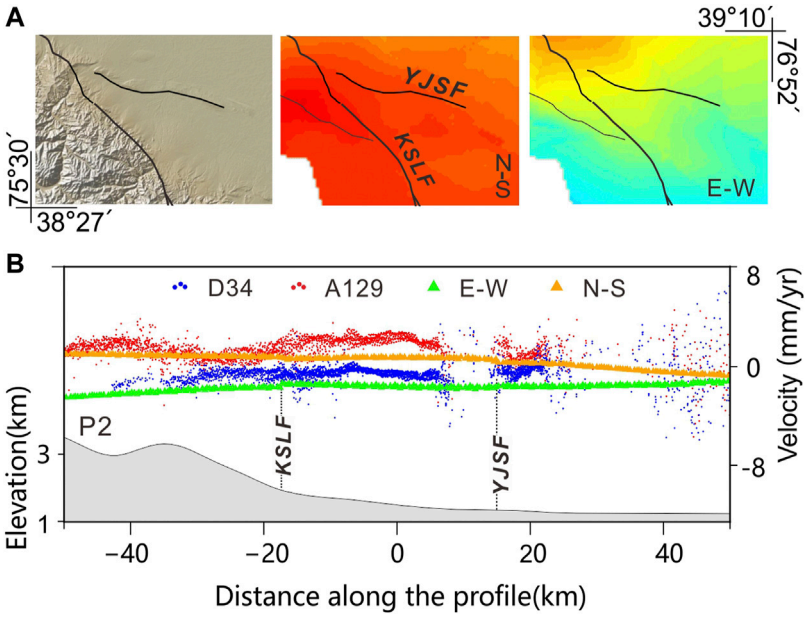

FIGURE 6 | (A) Enlargements of shaded elevation, the N-S and E-W velocity maps overing the western Kunlun piedmont thrust belt, the color bar is the same as **Figure 3**. **(B)** Deformation data profile across the western Kunlun piedmont thrust belt. See **Figures 2**, **3** for P2 location. KSLF:kusilafu fault, YJSF:Yingjisha fault.

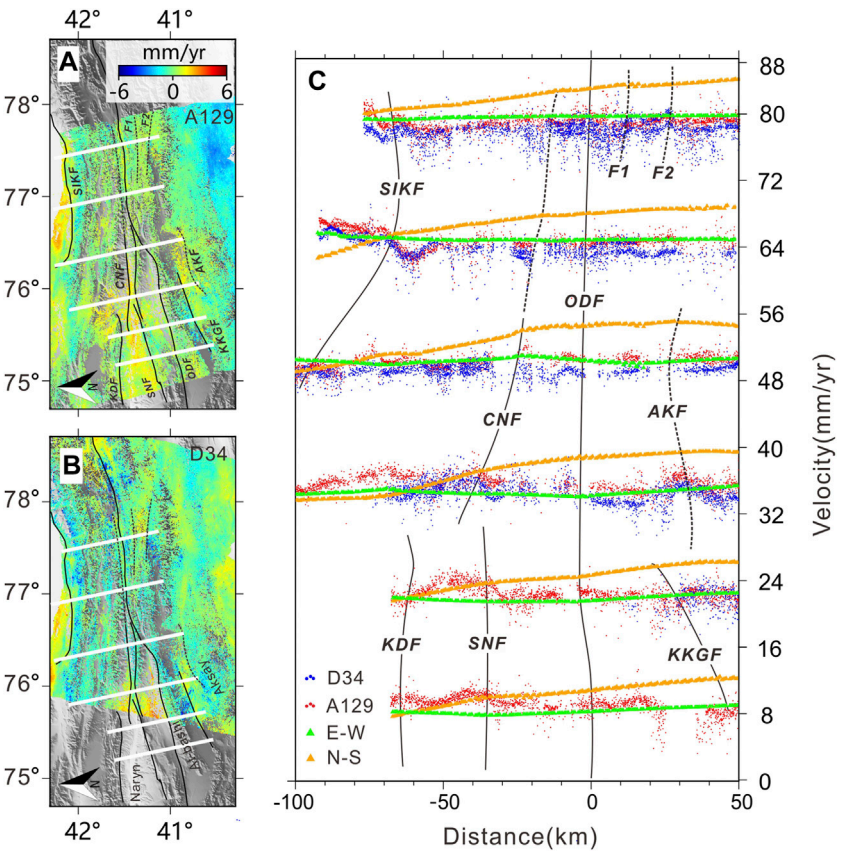

FIGURE 7 | Deformation data profile across the north of the South Tianshan. **(A,B)** indicate LOS velocity map of the tracks 129 (A129) and 34 (D34),respectively. The white lines are 6 profiles locations **(C)** velocity profile from D34 (blue dots), A129 (red dots), E-W (green triangle)and N-S (yellow triangle). KKGF, kerkeigel fault; AKF, Aksay fault; ODF, Oinak-Djar fault; SNF, South Naryn fault; KDF, Kadierty fault; CNF, Central Naryn fault; SIKF, South Issyk-Kul lake fault.

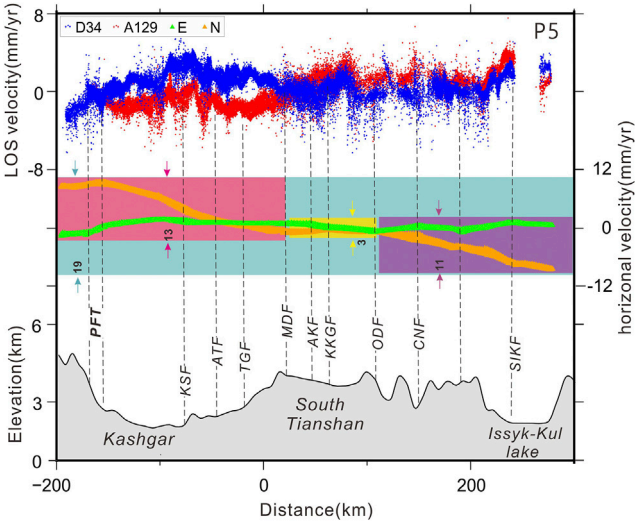

FIGURE 8 | Deformation data profile across the South Tianshan. See **Figures 2**, **3** for location.

Naryn Valley is one of the largest intermontane basins in the Kyrgyz Tian Shan and contains abundant evidence of Quaternary shortening (Burbank et al., 1999; Thompson et al., 2002; Jobe et al., 2017). Located in the northern margin of the basin, the Kadjerty fault has N-S convergence of approximately 2.0 mm/yr and E-W deformation of approximately 0.5 mm/yr. In the middle of the basin, the central Naryn fault has N-S convergence of 2.0 mm/yr, and the deformation extends eastward along the intermountain valley. At 76.3°, it is close and approximately parallel to the Oinak–Djar fault, and the deformation decreased.

We also observed uplift deformation distributed around Issyk-Kul Lake. The South Issyk-Kul lake fault has an N-S convergence deformation of approximately 2.0–3.0 mm/yr. There are deformations on multiple faults between the southern edge of the Issyk-Kul and Maidan faults. Among them, the deformation gradient zone involves two faults that have not been studied before. We temporarily refer to them as F1 and F2; there is almost no W-E deformation on these two faults, but N-S convergences of approximately 2.0 and 1.0 mm/yr are accommodated, respectively. This indicates that the internal tectonic faults and basins north of South Tianshan have played a role in accommodating the current crustal movement.

DISCUSSION

Present Tectonic Deformation Partitioning Across South Tianshan

The collision and compression of the TOSB, Pamir Plateau, and Tarim basin caused complex and intense tectonic movements. The relative movements among the three were accommodated by diverse structures. Based on the first LOS velocity maps (**Figure 2**) and horizontal velocity fields (**Figure 3**) over South Tianshan (75–78 E), continuous across high-relief areas and sedimentary basins, we quantitatively analyzed the present tectonic deformations across South Tianshan. As some previous studies suggested, one of the most intriguing features of crustal deformation across South Tianshan is that both sides of the entire TOSB are strongly compressed in the N-S direction. In this study, we include deformation information which are more than that have been used in all of the previous studies. Our 3D surface deformations shown that the narrow collide area between the Pamir Plateau and South Tianshan is the most active place at present, as the deformation profile in **Figure 8** shows, the deformation in this area accounts for ~68% (13/19) of the total N-S convergence across South Tianshan, and the deformation is mainly concentrated on the PFT and Cenozoic folds-faults.

We found that the strongest deformation occurred on the front edge folds of both the Kashi fold-fault belt and the western part of the Keping nappe. In the Kashi fold-fault belt, the Mushi and Kashi anticlines had the highest surface uplift rates. In the Keping Nappe, the Keping hill had the highest surface uplift rate. This shows that, among the crustal movements of South Tianshan, the uplift deformation of active folds occupies a major proportion. We believe that this significant fold uplift may be related to the development of décollement in the region. According to geological suggestion, the existence of the décollement provides a regional weak layer for the extension of Pamir and South Tianshan to the foreland region, which is beneficial for the formation of a foreland thrust fault-fold belt (Chen et al., 2011).

For deformation within the north of South Tianshan, our observation in this study is the deformation is dispersed in a series of intermountain active structures and depression basins. Compared with the southern piedmont fault of the South Tianshan, the E-W strike-slips of faults in this area are clearer. Thompson et al. (2002) and Zubovich et al. (2010) discussed these faults across the Naryn Basin of the range slipping at 3–4 mm/yr, and other more minor faults. Zubovich et al. (2010) also discussed another of ~5–6 mm/yr between the southern and northern edges of Issyk-Kul and the large basin that it occupies. Our profiles P5 show a difference of ~11 mm/yr across the north of South Tianshan between 100 and 300 km on the profile (**Figure 8**), and the deformation in this area accounts for ~58% (11/19) of the total N-S convergence across South Tianshan.

In addition, we found that the fold belts at the Pamir-South Tianshan junction and the nappes at the Tarim-South Tianshan junction move eastward relative to South Tianshan. The northern boundary of the movement is the Maidan fault. This indicates that the Maidan fault is still active, indicating sinistral strike-slip and thrust. Compared with the previously known tectonic pattern of the Maidan fault (Wu et al., 2019), the high spatial resolution surface deformation field shows that tectonic deformation of the Maidan fault is weakened from west to east. This weakening is closely related to the activity of adjacent faults. This indicates that the tectonic deformation in South Tianshan area is not completely concentrated in the piedmont fault-anticline belts, and the root faults of Tianshan accommodate a part of the deformation.

Furthermore, separated by the Piqiang fault, the eastern and western parts of the Keping nappe show different structural deformations. The deformation gradient is mainly concentrated at the front edge of the western nappe, but the

deformation is diffusely distributed on the front edge and inner folds of the eastern nappe. As a result, the deformation of the Kepingtage fault at the front edge of the nappe suddenly decreases east of the Piqiang fault. This indicates that the Piqiang fault may not only be a separation line in the geological structure, but also an important separation line of tectonic movement to regulate the unequal crust shortening in the Tianshan.

Tectonic Kinematic Model of the South Tianshan Foreland

Under the stress environment of compression in the N-S direction, the TOSB has uplifted mountains and shortened and thickened the crust. In its eastern part, the Tarim Basin is inserted under South Tianshan from south to north; in its western part, the Fergana Basin is inserted under South Tianshan from north to south (Zhao et al., 2008). There must be a transition zone between the western and eastern subduction zones. The south Tianshan foreland in our study area is located at this transition zone, which is geologically considered to be a typical thin-skin structure, involving thrust-folds and décollement. To understand the tectonic kinematics and the partitioning of the deep-secular motion in this area, we established two 2-dimensional motion models by using the Bayesian inversion tool developed by Daout et al. (2016). We explored various fault geometries in agreement with the observed displacements along two data profiles (P3 and P4 in **Figures 2**, **3**) of LOS and horizontal velocity across the Kashi fold belt and the Keping nappe. Based on the research results of seismology and geology (Chen et al., 2001; Turner et al., 2010; Liu 2011; Wu et al., 2019; Li et al., 2020), we modeled the flat décollement in profile P3 by a horizontal semi-infinite dislocation, limited to the north by the Maidan fault, with oblique motion (both strike-slip and dip-slip). In profile P4, a composite structure comprising two triple junctions and one frontal ramp was modeled. See Supporting Information 4 for the specific model settings.

For the western profile P3 (**Supplementary Figures S7, S9A**), the model suggests a depth of 21.6 km for the décollement, H1, and sets the tip of the shallow ramp, H2, at 5.5 km. Our estimates also indicate a well-constrained width, D, of 45 km, corresponding to a dip angle of 20.1° below the Kashi fold-thrust belt, with a dip-slip rate of 6.2 mm/yr. The left-lateral slip rate on the western section of the Maidan Fault is 2.2 mm/yr, and the strike-slip rate of the Atushi fault is 0.7 mm/yr. The mean shortening rate across the entire system is 6.0 mm/yr. The geometry of the inverted model is consistent with the geometry inferred from seismic reflection studies (Liu, 2011; **Figure 9A**).

For eastern profile P4 (**Supplementary Figures S8, S9B**), the model suggests that the left-lateral slip rate in the eastern section of the Maidan fault is 1.3 mm/yr, and the locking depth, H1, is 35.0 km. On the Toshigan fault, the dip-slip rate is -0.8 mm/yr, the left-lateral strike-slip rate is 0.3 mm/yr, and the locking depth, H2, is 7.0 km. On the Kalatieke fault, the dip-slip rate is 0.8 mm/yr, the right-lateral strike-slip rate is 1.2 mm/yr, and the locking depth, H3, is 20.0 km. On the Ozgeltawu fault in the north of Keping hill, the left-lateral strike-slip rate is 1.2 mm/yr, and the locking depth, H4, is 10.0 km. On Kepingtag fault on the south of Keping hill, the right-lateral strike-slip rate is 1.4 mm/yr, and the locking depth, H5, is 5.2 km. The dip-slip rate on the Keping hill ramp is 6.4 mm/yr. The mean shortening rate across the entire system is only 1.1 mm/yr.

The slip rate of the Maidan fault in the west and east sections is consistent with the geological results (Wu et al., 2019). The dip-slip rates of the Atushi and Kepingtag faults were very high, which indicates that the active fold is very intense and plays an important role in regulating the relative movements of Pamir-Tianshan and Tarim-Tianshan. The structural deformation has been partitioned into low-angle thrust-folds along the foreland and sinistral reverse faulting along the high-angle range front of the Maidan fault. The dip-slip rate on the décollement will result in the accumulation of elastic deformation, which we supposed will eventually be transformed by intermittent seismic activity into permanent strain of these parallel thrust faults in the overlying layer.

Strain Partitioning in South Tianshan

The velocity field can reflect the evident structural difference movement characteristics in the study area most visualized, but cannot effectively reflect the relationship between deformation and the dynamic mechanism. To further discuss the dynamic background of the structural deformation across south Tianshan and the strain distribution on both sides of the Tianshan, we derived a continuum strain rate field (**Figure 10**) by using the method developed by Shen et al. (2015) and constrained by the horizontal deformation field. From **Figure 10**, fine strain rate fields show the same features as those of the previous studies (Zheng et al., 2017; Wang and Shen, 2020). the TSOB is mainly dominated by N-S compression, with the largest shear and convergence occurring in the contact area between Pamirs and south Tianshan, with N-S convergence of approximately 120–150 nanostrain/yr, and a dilatation rate of approximately 50–80 nanostrain/yr, corresponding to the rapid shortening of the crust of the thrust-fault zone in the northern margin of Pamirs, where earthquakes are most likely to occur. However, we found that the principal strain rates of the thrust fault zone are mainly in the NW-SE direction, which is consistent with the strike of the Talas-Fergana fault. The convergence and shear deformation front is located at the contact zone between the Pamir and Alai Valley, where the distributed thrust strike-slip fault system includes the Pamir Frontal Thrust and Main Pamir Thrust. In the south of the high compressive strain area, near-W-E extensional deformation occurs in the Kongur tensile system.

The results in **Figure 10** also show a few interesting strain zones. 1) From the east of the Talas-Fergana fault, the direction of the principal strain rate in the collision zone between South Tianshan and Tarim basin is mainly in the N-S direction, which differs from that in the thrust-fault zone on the northern edge of Pamir. From west to east, the rates tend to decrease. This indicates that the tectonic stress field in this area is complex and restricted by several tectonics such as faults and folds. 2) The dilatation rate showed strong areal contraction, up to 100 nanostrain/yr, along the South Tianshan-Pamir-Talimu collision zone (**Figure 10B**). Assuming that the volume of this area is conserved, this means that the crust under the thrust fault-fold belts shortens and/or thickens. Considering the robust fold structure in this case, we can expect that the growth of active folds may play an important role in regulating regional strain.3) In the Keping nappe,

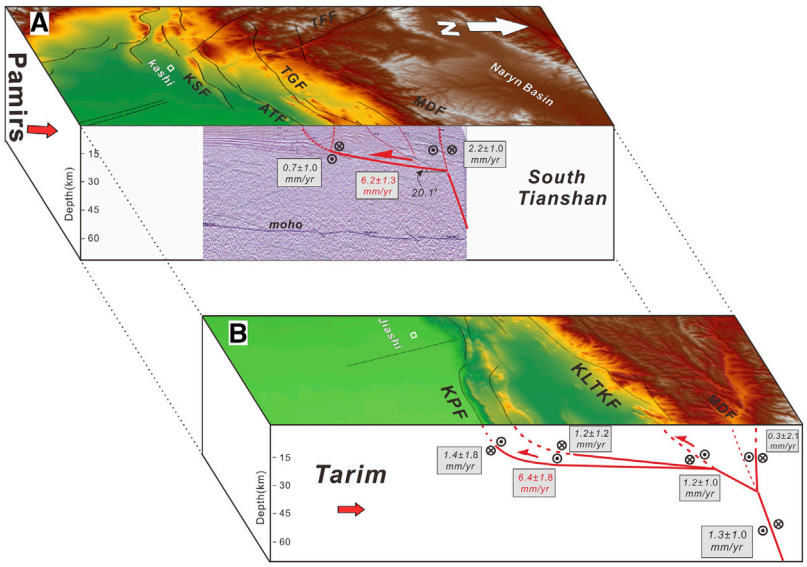

FIGURE 9 | Three-dimensional schematic tectonic model across the South Tianshan-Tarim junction zone (Deep seismic reflection profile is from Liu Jinkai, 2011), and interpreted active faults summarizing the average interseismic strike-slip (back font) and dip-slip (red font) rates extracted from the Bayesian exploration.

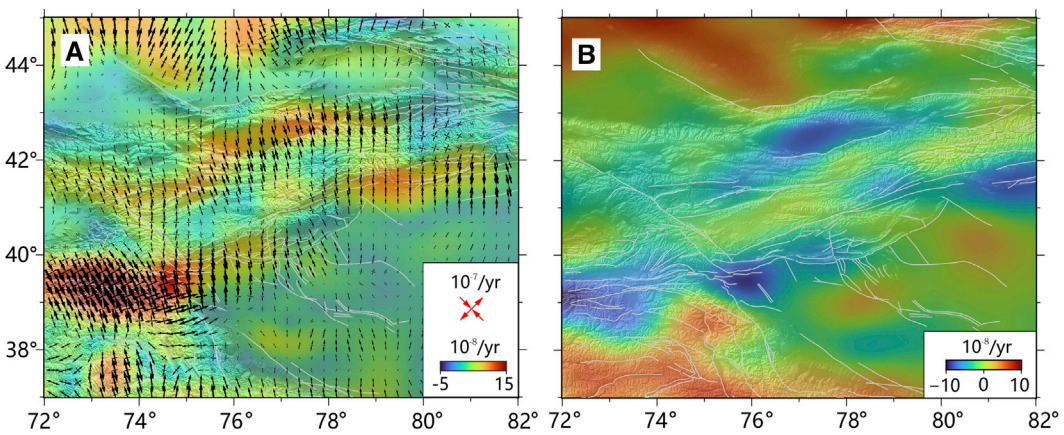

FIGURE 10 | Continuum deformation field of Tianshan derived from horizontal velocities. **(A)** Strain rates. Maximum shear strain rate is shown in background color and principal strain rates are shown as vector pairs. **(B)** Dilatation rate.

separated by the Piqiang fault, the eastern and western parts of the nappe show opposite shear strain rates and different dilatation rates. This corresponds to the different tectonic deformation between the eastern and western parts, and also corresponds to the different depths of the detachment plane under the Keping nappe, which is approximately 9 km in the west and 5 km in the east (Yin et al., 1998; Tian et al., 2006; Yang X. et al., 2008). The reason may be that the Pamirs pushed northward along with the Tarim, which was mainly pushed by Pamirs in the west of Piqiang, and the Tarim basin in the east of Piqiang. The Piqiang fault is a transition boundary of regional stress. 4) The principal strain rates are very low in south Tianshan, and high in the Naryn Basin and Issyk-Kul Lake in the north of South Tianshan. Approximately 20–60 nanostrain/yr shear strain and approximately 50 nanostrain/yr dilatation indicate that Naryn Basin and Issyk-Kul Lake experience crustal thickening caused by compression on both the north and south, especially in Issyk-Kul Lake. This may be attributable to the existence of small-scale mantle convection in this area (Wolfe and Vernon, 1998; Tian et al., 2010), or the shearing effect between the lithosphere and asthenosphere on a regional scale (Li and Chen, 2006).

CONCLUSION

We produced the LOS velocity fields from two Sentinel-1 tracks by PSInSAR and horizontal velocity fields by combining GPS data reported by Wang and Shen (2020)

across South Tianshan. Adequate coverage of the velocity fields significantly improved the spatial resolution of the present-day crustal deformation in southern Tianshan, leading to the following conclusions:

(1) The TSOB is strongly compressed by the Eurasian plate and Indian plate on the north and south sides respectively, and the deformation across South Tianshan is not evenly distributed. The contact area between Pamirs and south Tianshan is currently the most active area, which accommodates the total N-S convergence by ~68%. The deformation field at the center of South Tianshan is stable, and deformation is observed in local places. Approximately 58% of the total N-S convergence deformation is continuously distributed in active faults and basin systems in the north of South Tianshan.
(2) The deformation of the Pamir-South Tianshan-Tarim collision zone is gradually attenuated from west to east and from south to north as the distance from the Pamir Plateau increases. This indicates that the pushing of the Indian plate is the main driving force for the intense shortening deformation of the crust in this area.
(3) Thrust strike-slip of structural faults, uplift deformation of active folds, and slippage of décollement play important roles in regulating regional strain. As a root fault in South Tianshan, the Maidan fault continues to exhibit strike-slip and thrust, and its strike-slip is gradually attenuated from west to east, which together with adjacent faults has part of tectonic deformation in the Tianshan orogeny. The shallow flat décollement in the south Tianshan foreland was modeled, and the dip-slip rate ranged 6.2–6.4 mm/yr.
(4) The strain rate field shows that the N-S convergence of approximately 120–150 nanostrain/yr and dilatation rate of approximately 50–80 nanostrains/yr occurred in the collision area between the Pamir Plateau and South Tianshan, where rapid shortening of the crust and earthquakes are most likely to occur.

DATA AVAILABILITY STATEMENT

Publicly available datasets were analyzed in this study. This data can be found here: All Sentinel-1 data were obtained from the ESA (https://scihub.copernicus.eu/).

AUTHOR CONTRIBUTIONS

JQ: Data curation, Visualization, Investigation, Writing—Original draft preparation. LJ: Conceptualization, Writing—Reviewing, Supervision. LZ: Writing—Reviewing and Editing. QW: Software.

FUNDING

This work was supported by the National Natural Science Foundation of China (No. 41904007) and the Spark Programs of Earthquake Sciences granted by the China Earthquake Administration (XH20083).

ACKNOWLEDGMENTS

We appreciate Prof. Jianbao Sun for giving detailed guidance in using StaMPS. All Sentinel-1 data were obtained from the ESA. Figures were drawn by using Generic Mapping Tools.

SUPPLEMENTARY MATERIAL

The Supplementary Material for this article can be found online at: https://www.frontiersin.org/articles/10.3389/feart.2021.793890/full#supplementary-material

REFERENCES

Abdrakhmatov, K. Y., Aldazhanov, S. A., Hager, B. H., Hamburger, M. W., Herring, T. A., Kalabaev, K. B., et al. (1996). Relatively Recent Construction of the Tien Shan Inferred from GPS Measurements of Present-Day Crustal Deformation Rates. *Nature* 384, 450–453. doi:10.1038/384450a0

Bekaert, D. P. S., Walters, R. J., Wright, T. J., Hooper, A. J., and Parker, D. J. (2015). Statistical Comparison of InSAR Tropospheric Correction Techniques. *Remote Sensing Environ.* 170, 40–47. doi:10.1016/j.rse.2015.08.035

Bufe, A., Bekaert, D. P. S., Hussain, E., Bookhagen, B., Burbank, D. W., Thompson Jobe, J. A., et al. (2017). Temporal Changes in Rock Uplift Rates of Folds in the Foreland of the Tian Shan and the Pamir from Geodetic and Geologic Data. *Geophys. Res. Lett.* 44, 10977–10987. doi:10.1002/2017GL073627

Burbank, D. W., McLean, J. K., Bullen, M., Abdrakhmatov, K. Y., and Miller, M. M. (1999). Partitioning of Intermontane Basins by Thrust-related Folding, Tien Shan, Kyrgyzstan. *Basin Res.* 11, 75–92. doi:10.1046/j.1365-2117.1999.00086.x

Burchfiel, B. C., Brown, E. T., Qidong, D., Xianyue, F., Jun, L., Molnar, P., et al. (1999). Crustal Shortening on the Margins of the Tien Shan, Xinjiang, China. *Int. Geology. Rev.* 41, 665–700. doi:10.1080/00206819909465164

Chen, J., Li, T., Li, W. Q., and Yuan, C.-D. (2011). Late Cenozoic and Present Tectonic Deformation in the Pamir Salient, Northwestern China. *J. Seismology Geology.* 33 (2), 241–259. (in Chinese with English abstract). doi:10.3969/j.issn.0253-4967.2011.02.001

Chen, J., Lu, Y. C., and Ding, G. Y. (2001). Records of Late Cenozoic Mountain Building in Western Tarim Basin: Molasses, Growth Strata and Growth Unconformity. *J. Quat. Sci.* 21 (6), 528–539. (in Chinese with English abstract). doi:10.3321/j.issn:1001-7410.2001.06.009

Cheng, X. G., Huang, Z. B., Chen, H. L., Du, C., Li, K., and Shi, J. (2012). Fault Characteristics and Division of Tectonic Units of the Thrust belt in the Front of the West Kunlun Mountains. *J. Acta Petrologica Sinica* 28 (8), 2591–2601. (in Chinese with English abstract).

Daout, S., Doin, M.-P., Peltzer, G., Lasserre, C., Socquet, A., Volat, M., et al. (2018). Strain Partitioning and Present-Day Fault Kinematics in NW Tibet from Envisat SAR Interferometry. *J. Geophys. Res. Solid Earth* 123, 2462–2483. doi:10.1002/2017JB015020

Daout, S., Jolivet, R., Lasserre, C., Doin, M.-P., Barbot, S., Tapponnier, P., et al. (2016). Along-strike Variations of the Partitioning of Convergence across the Haiyuan Fault System Detected by InSAR. *Geophys. J. Int.* 205, 536–547. doi:10.1093/gji/ggw028

Deng, Q., Zhang, P., Ran, Y., Yang, X., Min, W., and Chen, L. (2003). Active Tectonics and Earthquake Activities in China. *J. Earth Sci. Front.* 10, 66–73. (in Chinese with English abstract). doi:10.3321/j.issn:1005-2321.2003.z1.012

Gao, G., Wen, H., and Nie, X. (2005). Analysis of Focal-Mechanism Solution of Moderately strong Earthquakes in Xinjiang from 1991 to 2002. *J. Earthquake.* 25 (1), 81–87. (in Chinese with English abstract).

Goldstein, R. M., and Werner, C. L. (1998). Radar Interferogram Filtering for Geophysical Applications. *Geophys. Res. Lett.* 25, 4035–4038. doi:10.1029/1998GL900033

Hanssen, R. F. (2001). *Radar Interferometry: Data Interpretation and Error Analysis (Remote Sensing and Digital Image Processing)*. New York, United States: Springer.

He, P., Wen, Y., Xu, C., Liu, Y., and Fok, H. S. (2015). New Evidence for Active Tectonics at the Boundary of the Kashi Depression, China, from Time Series InSAR Observations. *Tectonophysics* 653, 140–148. doi:10.1016/j.tecto.2015.04.011

Hooper, A., Segall, P., and Zebker, H. (2007). Persistent Scatterer Interferometric Synthetic Aperture Radar for Crustal Deformation Analysis, with Application to Volcán Alcedo, Galápagos. *J. Geophys. Res.* 112, B07407. doi:10.1029/2006JB004763

Hooper, A., Zebker, H., Segall, P., and Kampes, B. (2004). A New Method for Measuring Deformation on Volcanoes and Other Natural Terrains Using InSAR Persistent Scatterers. *Geophys. Res. Lett.* 31, 1–5. doi:10.1029/2004GL021737

Ji, L., Zhang, W., Liu, C., Zhu, L., Xu, J., and Xu, X. (2020). Characterizing Interseismic Deformation of the Xianshuihe Fault, Eastern Tibetan Plateau, Using Sentinel-1 SAR Images. *Adv. Space Res.* 66, 378–394. doi:10.1016/j.asr.2020.03.043

Jobe, J. A. T., Li, T., Chen, J., Burbank, D. W., and Bufe, A. (2017). Quaternary Tectonic Evolution of the Pamir-Tian Shan Convergence Zone, Northwest China. *Tectonics* 36, 2748–2776. doi:10.1002/2017TC004541

Jolivet, R., Agram, P. S., Lin, N. Y., Simons, M., Doin, M. P., Peltzer, G., et al. (2014). Improving InSAR Geodesy Using Global Atmospheric Models. *J. Geophys. Res. Solid Earth* 119 (3), 2324–2341. doi:10.1002/2013jb010588

Jolivet, R., Cattin, R., Chamot-Rooke, N., Lasserre, C., and Peltzer, G. (2008). Thin-Plate Modeling of Interseismic Deformation and Asymmetry across the Altyn Tagh Fault Zone. *Geophys. Res. Lett.* 35 (2), L02309. doi:10.1029/2007gl031511

Li, A., and Chen, C. (2006). Shear Wave Splitting beneath the central Tien Shan and Tectonic Implications. *Geophys. Res. Lett.* 33, L22303. doi:10.1029/2006GL027717

Li, A., Ran, Y., Gomez, F., Thompson Jobe, J. A., Liu, H., and Xu, L. (2020). Segmentation of the Kepingtage Thrust Fault Based on Paleoearthquake Ruptures, Southwestern Tianshan, China. *Nat. Hazards* 103, 1385–1406. doi:10.1007/s11069-020-04040-6

Li, J., Qiao, X. J., Yang, S. M., Nie, Z. S., Wang, D. J., Zou, R., et al. (2015). Detachment Fault Model Characterized for the 3D Surface Displacement Field in the Southwestern Tian Shan. *Chin. J. Geophys.* 58 (10), 3517–3529. (in Chinese with English abstract). doi:10.1002/cjg2.20184

Liu, C., Ji, L., Zhu, L., and Zhao, C. (2018). InSAR-Constrained Interseismic Deformation and Potential Seismogenic Asperities on the Altyn Tagh Fault at 91.5-95°E, Northern Tibetan Plateau. *Remote Sensing* 10 (6), 943. doi:10.3390/rs10060943

Liu, J. K. (2011). *Fine Data Processing and Pre-stack Imaging of the Deep Seismic Reflection Profile of the Contact Zone between the Southern Tianshan and Tarim basin*. China, Beijing: D. Chinese Academy of Geological Sciences. (in Chinese with English abstract).

Miao, J., Jia, C., Hou, X., Wang, Z., Zou, C., Tang, L., et al. (2007). Structural Analysison Cenozoic Fold and Thrust Belts in Kashi Area, Western Tarim basin. *J. Chin. J. Geology.* 42 (4), 740–752. (in Chinese with English abstract). doi:10.3321/j.issn:0563-5020.2007.04.009

Niu, Z., You, X., and Yang, S. (2007). Analysis of Contemporary Crustal Deformation Characteristics with GPS Data of Tianshan Mountain. *J. J. Geodesy Geodynamics* 27 (002), 1–9. (in Chinese with English abstract). doi:10.5194/sed-7-3179-2015

Qiao, X., Yu, P., Nie, Z., Li, J., Wang, X., Kuzikov, S. I., et al. (2017). The Crustal Deformation Revealed by GPS and InSAR in the Northwest Corner of the Tarim Basin, Northwestern China. *Pure Appl. Geophys.* 174, 1405–1423. doi:10.1007/s00024-017-1473-6

Shen, J., Wang, Y., Zhao, R., Jei, C., and Guosheng, Q. (2001). Propagation of Cenozoic Arcuate Structures in Northeast Pamir and Northwest Tarim basin. *J. Seismology Geology.* 23 (3), 381–389. (in Chinese with English abstract). doi:10.3969/j.issn.0253-4967.2001.03.005

Shen, L., Hooper, A., and Elliott, J. (2019). A Spatially Varying Scaling Method for InSAR Tropospheric Corrections Using a High-Resolution Weather Model. *J. Geophys. Res. Solid Earth* 124, 4051–4068. doi:10.1029/2018JB016189

Shen, Z.-K., Wang, M., Li, Y., Jackson, D. D., Yin, A., Dong, D., et al. (2001). Crustal Deformation along the Altyn Tagh Fault System, Western China, from GPS. *J. Geophys. Res.* 106, 30607–30621. doi:10.1029/2001jb000349

Shen, Z. K., and Liu, Z. (2020). Integration of GPS and InSAR Data for Resolving 3-Dimensional Crustal Deformation. *Earth Space Sci.* 7, e2019EA001036. doi:10.1029/2019EA001036

Shen, Z. K., Wang, M., Zeng, Y., and Wang, F. (2015). Optimal Interpolation of Spatially Discretized Geodetic Data. *Bull. Seismological Soc. America* 105 (4), 2117–2127. doi:10.1785/0120140247

Thompson, S. C., Weldon, R. J., Rubin, C. M., Abdrakhmatov, K., Molnar, P., and Berger, G. W. (2002). Late Quaternary Slip Rates across the central Tien Shan, Kyrgyzstan, central Asia. *J. Geophys. Res.* 107, 7–1. doi:10.1029/2001jb000596

Tian, Q., Ding, G., and Hao, P. (2006). Seismotectonic Study on West Part of the Interaction Zone between Southern Tianshan and Northern Tarim. *J. Seismology Geology.* 28 (002), 213–223. (in Chinese with English abstract).

Tian, X., Zhao, D., Zhang, H., Tian, Y., and Zhang, Z. (2010). Mantle Transition Zone Topography and Structure beneath the central Tien Shan Orogenic Belt. *J. Geophys. Res.* 115, B1030. doi:10.1029/2008JB006229

Turner, S. A., Cosgrove, J. W., and Liu, J. G. (2010). Controls on Lateral Structural Variability along the Keping Shan Thrust belt, SW Tien Shan Foreland, China. *Geol. Soc. Lond. Spec. Publications* 348 (1), 71–85. doi:10.1144/sp348.5

Wang, H., Wright, T. J., Liu-Zeng, J., and Peng, L. (2019). Strain Rate Distribution in South-Central Tibet from Two Decades of InSAR and GPS. *Geophys. Res. Lett.* 46 (10), 5170–5179. doi:10.1029/2019gl081916

Wang, H., and Wright, T. J. (2012). Satellite Geodetic Imaging Reveals Internal Deformation of Western Tibet. *Geophys. Res. Lett.* 39 (7), 7303. doi:10.1029/2012gl051222

Wang, M., and Shen, Z. K. (2020). Present-Day Crustal Deformation of Continental China Derived from GPS and its Tectonic Implications. *J. Geophys. Res. Solid Earth* 125, e2019JB018774. doi:10.1029/2019JB018774

Wang, Q., Ding, G., Qiao, X., Wang, X., and You, X. (2000). The Rapid Crustal Shortening and the Relative Movement with the north and South Blocks in the Tianshan. *J. Chin. Sci. Bull.* 45 (14), 1543–1547. (in Chinese). doi:10.1007/bf02909695

Wegnüller, U., Werner, C., Strozzi, T., Wiesmann, A., Frey, O., and Santoro, M. (2016). Sentinel-1 Support in the GAMMA Software. *Proced. Comput. Sci.* 100, 1305–1312. doi:10.1016/j.procs.2016.09.246

Wolfe, C. J., and Vernon, F. L. (1998). Shear-wave Splitting at central Tien Shan: Evidence for Rapid Variation of Anisotropic Patterns. *Geophys. Res. Lett.* 25, 1217–1220. doi:10.1029/98GL00838

Wu, C., Zheng, W., Zhang, P., Zhang, Z., Jia, Q., Yu, J., et al. (2019). Oblique Thrust of the Maidan Fault and Late Quaternary Tectonic Deformation in the Southwestern Tian Shan, Northwestern China. *Tectonics* 38, 2625–2645. doi:10.1029/2018TC005248

Yang, S., Li, J., and Wang, Q. (2008). Study on the Present Deformation and Fault Activity of Tianshan by GPS. *J. SCIENTIA SINICA Terrae* 38 (7), 872–880. (in Chinese). doi:10.1007/s11430-008-0090-8}

Yang, X., Deng, Q., Zhang, P., and Xu, X.-W. (2008). Crustal Shortening of Major Nappe Structcrus on the Front Margins of the Tianshan. *J. Seismology Geology.* 30 (1), 111–131. (in Chinese with English abstract).

Yin, A., Nie, S., Craig, P., Harrison, T. M., Ryerson, F. J., Xianglin, Q., et al. (1998). Late Cenozoic Tectonic Evolution of the Southern Chinese Tian Shan. *Tectonics* 17, 1–27. doi:10.1029/97TC03140

Yu, C., Li, Z., Penna, N. T., and Crippa, P. (2018). Generic Atmospheric Correction Model for Interferometric Synthetic Aperture Radar Observations. *J. Geophys. Res. Solid Earth* 123, 9202–9222. doi:10.1029/2017JB015305

Yu, C., Li, Z., and Penna, N. T. (2020). Triggered Afterslip on the Southern Hikurangi Subduction Interface Following the 2016 Kaikōura Earthquake from InSAR Time Series with Atmospheric Corrections. *Remote Sensing Environ.* 251, 112097. doi:10.1016/j.rse.2020.112097

Zhang, L., Ding, X., Lu, Z., Jung, H.-S., Hu, J., and Feng, G. (2014). A Novel Multitemporal Insar Model for Joint Estimation of Deformation Rates and Orbital Errors. *IEEE Trans. Geosci. Remote Sensing* 52, 3529–3540. doi:10.1109/TGRS.2013.2273374

Zhang, P., Deng, Q., Xu, X. W., Peng, S. Z., Feng, X. Y., Yang, X. P., et al. (1996). Late Cenozoic Tectonic Deformation and Mechanism along the Tianshan Mountain, Northwestern China. *J. Earthquake Res. China* 12 (2), 127–140. (in Chinese with English abstract).

Zhang, P., Deng, Q., Zhang, G., Ma, J., Gan, W., Min, W., et al. (2003). Strong Seismicity and Active Block in Chinese Mainland. *J. SCIENTIA SINICA Terrae* 33, 12–20. (in Chinese). doi:10.3321/j.issn:1006-9267.2003.z1.002

Zhao, J., Cheng, H., Pei, S., Liu, H., Zhang, J., Liu, B., et al. (2008). Deep Structure in the Northern Margin of Tarim basin. *J. Chin. Sci. Bull.* 053 (008), 946–955. (in Chinese). doi:10.1007/s11434-008-0117-8

Zheng, G., Wang, H., Wright, T. J., Lou, Y., Zhang, R., Zhang, W., et al. (2017). Crustal Deformation in the India-Eurasia Collision Zone from 25 Years of GPS Measurements. *J. Geophys. Res. Solid Earth* 122, 9290–9312. doi:10.1002/2017JB014465

Zubovich, A. V., Wang, X. Q., Scherba, Y. G., Schelochkov, G. G., Reilinger, R., Reigber, C., et al. (2010). GPS Velocity Field for the Tien Shan and Surrounding Regions. *Tectonics* 29 (6), TC6014. doi:10.1029/2010tc002772

Conflict of Interest: The authors declare that the research was conducted in the absence of any commercial or financial relationships that could be construed as a potential conflict of interest.

Publisher's Note: All claims expressed in this article are solely those of the authors and do not necessarily represent those of their affiliated organizations, or those of the publisher, the editors and the reviewers. Any product that may be evaluated in this article, or claim that may be made by its manufacturer, is not guaranteed or endorsed by the publisher.

frontiers in Earth Science

ORIGINAL RESEARCH
published: 23 February 2022
doi: 10.3389/feart.2022.820189

Swarm-TEC Satellite Measurements as a Potential Earthquake Precursor Together With Other Swarm and CSES Data: The Case of Mw7.6 2019 Papua New Guinea Seismic Event

Mehdi Akhoondzadeh[1], *Angelo De Santis*[2]*, *Dedalo Marchetti*[2,3] and *Xuhui Shen*[4]

[1]Photogrammetry and Remote Sensing Department, School of Surveying and Geospatial Engineering, College of Engineering, University of Tehran, Tehran, Iran, [2]Istituto Nazionale di Geofisica e Vulcanologia, Roma, Italy, [3]The College of Instrumentation and Electrical Engineering, Jilin University, Changchun, China, [4]Space Observation Research Center, National Institute of Natural Hazards, MEMC, Beijing, China

OPEN ACCESS

Edited by:
Giovanni Martinelli, National Institute of Geophysics and Volcanology, Italy

Reviewed by:
J. R. K. Kumar Dabbakutti, K L University, India
Vyacheslav Pilipenko, Institute of Physics of the Earth (RAS), Russia

***Correspondence:**
Angelo De Santis
angelo.desantis@ingv.it

Specialty section:
This article was submitted to Geohazards and Georisks, a section of the journal Frontiers in Earth Science

Received: *22 November 2021*
Accepted: *11 January 2022*
Published: *23 February 2022*

Citation:
Akhoondzadeh M, De Santis A, Marchetti D and Shen X (2022) Swarm-TEC Satellite Measurements as a Potential Earthquake Precursor Together With Other Swarm and CSES Data: The Case of Mw7.6 2019 Papua New Guinea Seismic Event. Front. Earth Sci. 10:820189. doi: 10.3389/feart.2022.820189

On May 14, 2019, a strong M_w = 7.6 shallow earthquake occurred in Papua New Guinea. This paper explores for the first time the analysis of total electron content (TEC) products measured for 6 months by GPS antenna onboard Swarm satellites, to detect possible seismo-ionospheric anomalies around the time and location of the above-mentioned earthquake. The night-time vertical total electron content (VTEC) time series measured using Swarm satellites Alpha and Charlie, inside the earthquake Dobrovolsky's area show striking anomalies 31 and 35 days before the event. We successfully verified the possible presence of concomitant anomalous values of *in situ* electron density detected by the new Chinese satellite dedicated to search for electromagnetic earthquake precursors [China Seismo-Electromagnetic Satellite (CSES)-01]. On the other hand, the analysis of VTEC night time measured by Swarm Bravo shows gradual and abnormal increase of the VTEC parameter from about 23 days before the earthquake, which descends 3 days before the earthquake and reaches its lowest level around the earthquake day. We also analyzed the time series and tracks of other six *in situ* parameters measured by Swarm satellites, electron density from CSES, and also GPS-TEC measurements. As it is expected from the theory, the electron density anomalous variations acknowledge the Swarm VTEC anomalies, confirming that those anomalies are real and not an artifact of the analysis. The comparative analysis with measurements of other Swarm and CSES sensors emphasizes striking anomalies about 2.5 weeks before the event, with a clear pattern of the whole anomalies typical of a critical system as the earthquake process is for Earth. A confutation analysis outside the Dobrovolsky area and without significant seismicity shows no anomalies. Therefore based on our study, the VTEC products of Swarm satellites could be an appropriate precursor aside from the other measured plasma and magnetic parameters using Alpha, Bravo, and Charlie Swarm and CSES satellites that can be simultaneously analyzed to reduce the overall uncertainty.

Keywords: earthquake precursors, ionosphere, swarm satellites, TEC, CSES

INTRODUCTION

Since the seismological community generally emphasizes the great difficulty of earthquake prediction by analyzing seismic data (e.g., Matsumura, 2009), or even the impossibility of such an enterprise (e.g., Geller, 1997), many researchers have dedicated their efforts to search for alternative non-seismic precursors. Up to now, many papers and reports have been released to emphasize the importance of this kind of earthquake precursors. It seems that the results of ionospheric precursors have been more reliable than lithospheric and atmospheric ones (Parrot, 1995; Hayakawa and Molchanov, 2002; Pulinets and Boyarchuk, 2004; Freund, 2009; Pulinets and Ouzounov, 2011; Sorokin and Pokhotelov, 2014; Guo et al., 2015; Piscini et al., 2017; Liu, 2018; Cianchini et al., 2020; Ouzounov et al., 2021). The seismo-ionospheric anomalies might be observed in the D, E, and F layers around the time and location of the event. Therefore, remote sensing satellite sensors could be good tools to gather and monitor ionospheric precursors above seismic-prone areas (Akhoondzadeh et al., 2010; De Santis et al., 2015).

Swarm mission (launched on 22 November, 2013) is a constellation of three identical satellites, Alpha (A), Bravo (B), and Charlie (C), placed in quasi-polar orbits at an altitude between 440 (Alpha and Charlie) and 510 km (Bravo) (Friis-Christensen et al., 2006). These satellites include magnetic and plasma sensors: 1) an absolute scalar magnetometer (ASM), which measures the strength of the magnetic field and provides scalar measurements of the magnetic field to calibrate the vector field magnetometer; 2) a vector field magnetometer (VFM), which makes high-precision measurements of the intensity and direction of the magnetic field; and 3) the EFI instrument, which is composed of the Langmuir probe and thermal ion imager. The Langmuir probe provides plasma data such as electron density, Ne, electron temperature, Te, and spacecraft electric potential, V (Haagmans et al., 2013).

To date, some papers have investigated plasma and magnetic field parameters around the time and location of some strong earthquakes using Swarm satellites' data (De Santis et al., 2017; Akhoondzadeh et al., 2018; Marchetti and Akhoondzadeh, 2018; Akhoondzadeh et al., 2019; Marchetti et al., 2019a; Marchetti et al., 2019b). A very recent paper has established the statistical significance of the anomalies of these parameters observed by Swarm satellites as anticipating strong earthquakes all over the world for the last 5 years of data (De Santis et al., 2019).

However, there has not yet been any scientific report indicating the Swarm vertical total electron content (VTEC) data analysis as possibly associated with powerful earthquakes.

The Global Navigation Satellite System (GNSS) transmits signals, while the ground receivers and the one mounted on the Swarm satellites receive them. By the analysis of transmission delays, it is possible to infer the total amount of electrons in the ionospheric path crossed by the signals. Therefore slant total electron content (STEC), which is defined as the integrated electron density along the line of sight from the ground or Swarm receivers to GNSS satellites, is estimated by analyzing the mentioned delay (Swarm Level 2 Processing System, 2019). This means that Swarm-TEC data contain information about the integrated electron density from about 400 km above Swarm satellites (Swarm Expert Support Laboratories, 2017), so analogous to what happened with the CHAMP satellite (Noja et al., 2013).

Relative STEC can be estimated by the following equation:

$$STEC = \frac{f_1^2 \times f_2^2}{f_1^2 - f_2^2} \times \frac{L_1 - L_2}{K} \quad (1)$$

where f_1 and f_2 are carrier frequencies of GNSS signals, L_1 and L_2 are ambiguity-corrected carrier phase observations, and $K \approx 40.3\ m^3 s^{-2}$ is a conversion factor. By considering the elevation angle of the GNSS satellite as seen from ground or Swarm GPS receivers (and also altitude of the Swarm satellite in this case), VTEC is calculated from STEC (Foelsche and Kirchengast, 2002; Yizengaw et al., 2006; Noja et al., 2013) only for allowable elevation angles (Swarm Level 2 Processing System, 2019). When the Swarm satellites are close to the edge of Dobrovolsky area, to VTEC, satellite data also contribute to the electron density data from a little outside the Dobrovolsky area. However, we think that this effect is very little and can be neglected with respect to most data that are inside the Dobrovolsky area.

This paper presents for the first time the results of Swarm-TEC data analysis for a specific large earthquake. In detail, we analyzed the Swarm data during the period of January 01 to June 30, 2019 inside the Dobrovolsky's area (Dobrovolsky et al., 1979; see also *Swarm-TEC Data*) of the Papua New Guinea earthquake. The mentioned earthquake had a magnitude M_w = 7.6 and took place at 12:58:25 UTC (LT = UTC+$\lambda_{epicenter}$/15 = 23:08:48) on May 14, 2019, 46 km SSE of Namatanai in Papua New Guinea (4.051°S, 152.597°E) at an estimated shallow depth of about 10 km (**Figure 1**). The region where the event occurred is critical from a tectonical point of view: the Australian plate moves in East–North East direction with respect to the Pacific plate, and many microplates are involved in the plate boundary. In particular, the main event of May 14, 2019 occurred in the boundary between South Bismark and Manus microplates. The estimated rupture of the fault was about $50 \times 10\ km^2$, with a peak slip of about 25 m (Chen et al., 2019). In the past, in the same location, other several big earthquakes already occurred (for example, M8.0 on November 16, 2000 localized at 3.980S 152.169E, 33 km depth).

Figure 1 shows that the seismic events with a magnitude greater than or equal to 4.5 occurred in the area investigated in this period from January 01 to June 30, 2019 (USGS catalogue; https://earthquake.usgs.gov/earthquakes). We underline a particular strong event of Mw = 7.1 that occurred on May 06, 2019 at 21:19:37 UTC localized at 6.975°S 146.449°E at a depth of about 146 km. Despite the relative great depth of this event, it is not possible to exclude any coseismic effect in the ionosphere when the results are discussed.

OBSERVATIONS

Solar and Geomagnetic Data

To exclude the solar geomagnetic disturbances in the analysis of potential seismo-ionospheric precursors, the a_p and D_{st} magnetic indices and the solar radio flux (i.e., F10.7) are checked, defining quiet solar geomagnetic conditions such as a_p < 25 nT, |Dst| ≤

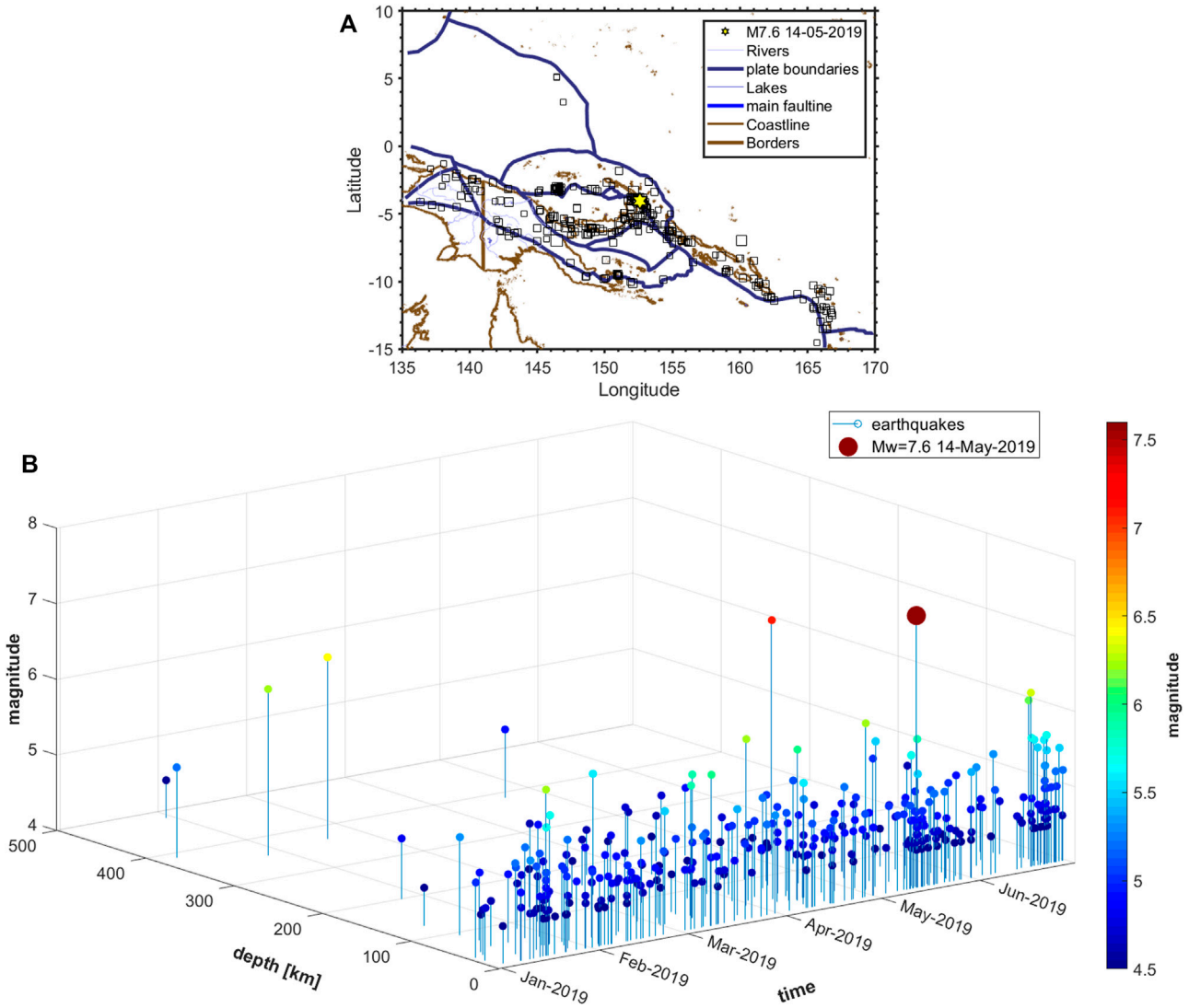

FIGURE 1 | Representation of the M4.5+ earthquakes that occurred inside the Dobrovolsky area of the Mw = 7.6 May 14, 2019 Papua New Guinea earthquake from January 01 to June 30, 2019 retrieved from USGS catalogue (https://earthquake.usgs.gov/earthquakes). **(A)** Geographical map of the seismic events with the geographical features and main faults. The epicenter is depicted by a yellow star. **(B)** Graph of the temporal, depth, and magnitude of the selected M4.5+ events. The main shock has been evidenced by the largest circle.

20 nT, and F10.7 < 120 SFU. **Figure 2** illustrates the variations of a_p, D_{st} and F10.7 indices, and solar wind and IMF intensity during the period of January 01 to June 30, 2019. A star symbol shows the earthquake time. The *x*-axis indicates the day relative to the earthquake day. The *y*-axis represents the universal time in a) and b), the F10.7 (SFU) value in c), and the values of solar wind speed (in km/s) and IMF intensity (in nT) in d). In addition, to monitor the space weather conditions for what concerns the Interplanetary Magnetic Field (IMF), we retrieved the data by the solar satellite observatory Advanced Composition Explorer (ACE), placed in the Sun–Earth L1 Lagrangian point (at 1.4 million kilometers from Earth), have been investigated. In particular, in **Figure 2D**), the intensity of IMF from the magnetometer and the alpha-particle solar wind speed from the solar wind ion composition spectrometer instrument are represented. Thus, the eventual anomalies in the ionosphere detected during high solar wind speed and IMF are excluded by the analysis because they are more likely the effects of an ionosphere–magnetosphere coupling rather than lithosphere–atmosphere–ionosphere coupling. The identification of high solar activity has been evaluated by characterizing two investigated physical observables (a vector of the interplanetary magnetic field defined by the components IMF_X, IMF_Y, IMF_Z, and its intensity IMF_F and the intensity of alpha-particle solar wind) by median and interquartile over the analyzed 6-month data, and defining a high activity when one of the investigated solar quantities (i.e., IMF_X, IMF_Y, IMF_Z, IMF_F, and alpha-particle solar wind) overpasses the median by 1.5 times

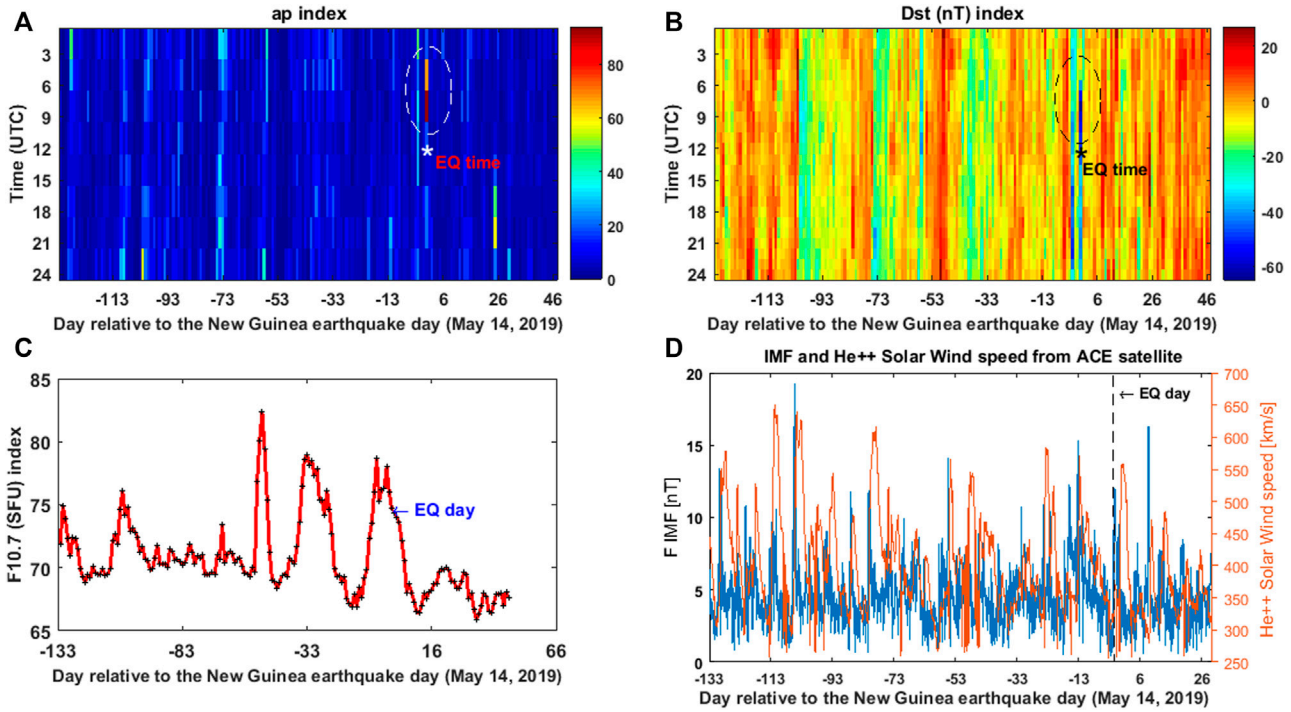

FIGURE 2 | (A–D) show the variations of a_p, D_{st}, and solar radio flux (F10.7) indices and two parameters (magnetic field scalar intensity and He^{2+} solar wind speed) of the IMF recorded from ACE satellite, respectively, during the period of January 01 to June 30, 2019.

the interquartile range, which corresponds to the thresholds of 7.59 nT for IMF_F (scalar intensity of IMF) and 524 km/s for solar wind speed. These conditions have been applied, taking into account two ways of possible magnetosphere–ionosphere coupling: one is the impact of solar wind onto the ionosphere, and the other is the electromagnetic field coupling. For the former, the time of flight of the particles from ACE satellite to Swarm or CSES has been estimated for the specific time while for the latter, it requires about 5 s so it can be considered instantaneous for this work. Consequently, our basic hypothesis is that the detected remaining anomalous variations of ionospheric parameters in quiet solar geomagnetic conditions might be associated with seismic activities.

High geomagnetic activity is clearly seen on the earthquake date, when the a_p index reaches the unusual values of 67 nT and 94 nT between 04:00 and 09:00 UTC. The unusual variations of the a_p index are also seen 3 days before the earthquake (**Figure 2A**).

In addition, abnormal D_{st} values are observed 2 days before, on the earthquake date, and 1 day after the event. This parameter exceeds the lower boundary value (i.e., −20 nT) and reaches the value of −65 nT at 18:00 UTC on the earthquake day, −51 nT at 8: 00 on 2 days before, and −43 nT at 7:00 on the day after the event (**Figure 2B**). The times of earthquake day with high geomagnetic activities have been distinguished using dotted ellipsoids in **Figure 2**. **Figure 2C**) shows the normal variations of solar activities during the studied period.

Figure 3 shows the variations of magnetic vectors measured by the Kakadu (KDU) magnetometer station during the period from January 01 to June 30, 2019. The geographic location of this magnetometer is 12.69°S, 132.47°E that is one of the closer geomagnetic observatories of INTERMAGNET network to the earthquake epicenter outside the Dobrovolsky's area. **Figure 3A** shows striking anomalies around the earthquake time. We noted that such anomalies occurred during geomagnetic perturbed conditions (indicated by "P" in the graph). The occurrence of the earthquake during or just after disturbed geomagnetic perturbation is confirmed by Marchitelli et al. (2020) who made a controversial suggestion that the solar activity could be a possible trigger of seismic events.

Swarm-TEC Data

The size of the affected area by an impending earthquake can be estimated with the formula $R = 10^{0.43M}$, where R is the radius in kilometers of the earthquake preparation zone, supposed circular and centered at the earthquake epicenter, and M is its magnitude (Dobrovolsky et al., 1979). Therefore, to detect the potentially seismo-ionospheric anomalies, we only considered all tracks of satellites A, B, and C crossing the Dobrovolsky's region, i.e., within R ~ 1,850 km from the New Guinea earthquake epicenter during the period of January 01 to June 30, 2019.

For every day, the median of the VTEC values in Dobrovolsky's area was calculated and, finally, the time series of the median values were constructed. Due to the nonlinear variations of VTEC, a polynomial of degree 4 was fitted to the

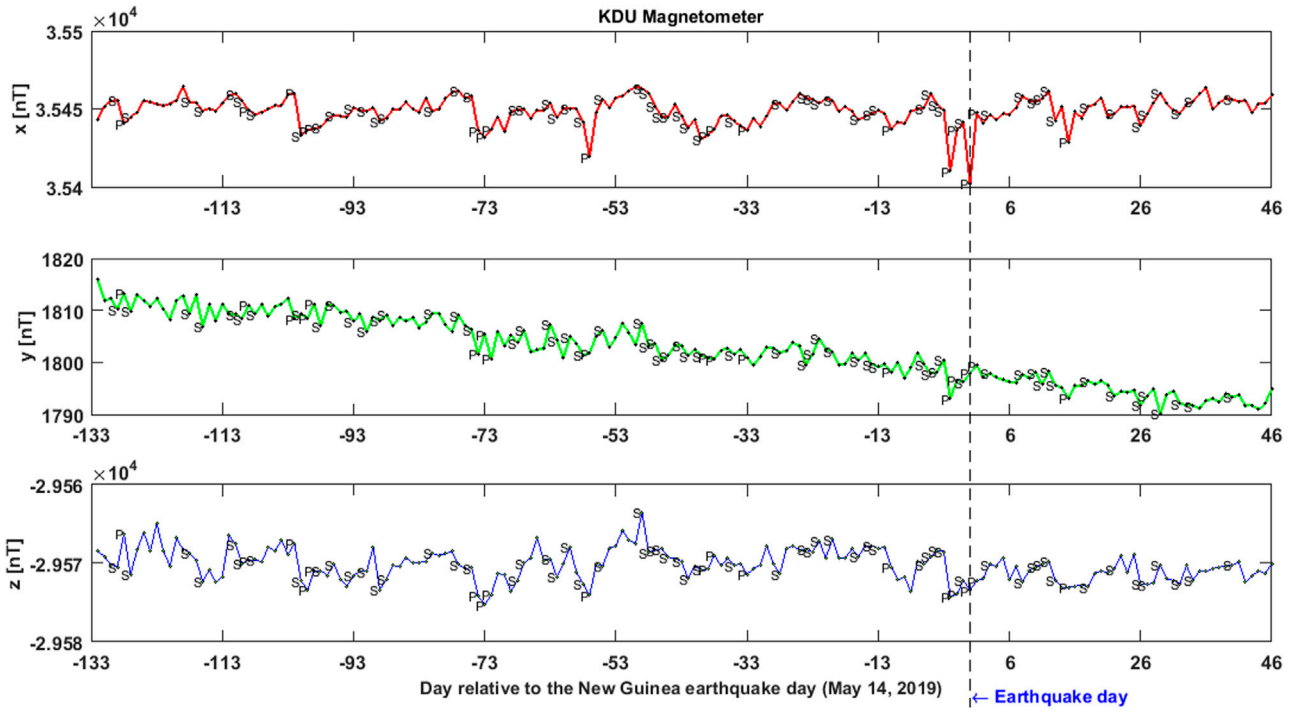

FIGURE 3 | KDU magnetometer (12.69°S, 132.47°E) measurements **(A)** x, **(B)** y, and **(C)** z during the period from January 01 to June 30, 2019. The earthquake day is indicated by a dashed black vertical line.

time series and the residuals between the two curves were considered as a new time series. For convenience, we will still use the name VTEC for the *y*-axis but we are adding the term "detrend" to intend that actually, what is plotted is the VTEC detrended by the polynomial fit.

Figure 4, **Supplementary Figures S1, S2** show the night-time VTEC residual variations of Swarm A, B, and C satellites during the period from January 01 to 30 June 30, 2019, respectively. The abscissa indicates the day relative to the earthquake day. The vertical dotted line represents the earthquake date. Median higher and lower bounds are drawn as blue and green horizontal lines, respectively. The pre-defined allowed ranges are $\boldsymbol{m} \pm 1.5 \times \boldsymbol{Iqr}$ in which m and Iqr are the median and the inter-quartile range statistical parameters, respectively. In the case of Gaussian residuals, this threshold would correspond to around two times the standard deviation from the mean. In this figure, the perturbed days with high geomagnetic activities are shown with the "P" symbol ("P" stands for "perturbed") and the ones with high solar activity are shown with the "S" symbol ("S" stands for "solar"). It should be noted that the values of the median and the allowed bounds were calculated using only the quiet geomagnetic days (i.e., those points without "P" indication), taking into account the magnetic indices, F10.7, and the ACE solar wind parameters.

Figure 4 shows a striking anomaly when the VTEC night-time variations measured by Swarm A exceed the higher bound with the value of 311.03%, 35 days before event. This time series indicates other unusual variations 4, 13, and 31 days before the earthquake with the deviation values of 8.27%, 29.32%, and −74.68%, respectively. The VTEC night-time variations measured by Swarm C acknowledge the observed anomalies by Swarm A on 31 and 35 days prior to the earthquake (**Supplementary Figure S1**).

Supplementary Figure S2 regards the VTEC parameter measured by Swarm B in night time: it shows the gradual and abnormal increase from about 23 days before the earthquake that descends 3 days before the earthquake and reaches its lowest level around the earthquake day. VTEC variations exceed the lower bound with the value of 19.19%, 1 day before the earthquake during normal solar and geomagnetic activity.

It is observed that the anomalous value of the VTEC parameter on the day of the earthquake coincides with the high geomagnetic activity on this day (**Figure 2**) and we encounter a complex situation. Two days present significant anomalies preceding 13 and 7 days of the earthquake occurrence with the values of 26.90% and 48.33% above the threshold, respectively. Also, the night-time VTEC values on 20 and 23 days before the earthquake slightly exceed the upper boundary.

It seems that from 23 to 7 days, there are some spots–increase of the oscillation of electron content in the ionosphere–mainly toward positive values overpassing the threshold, and on the day before the earthquake, there is a precipitation of electrons in the lower layers of the same ionosphere or the chemical composition of the ionosphere changed and so enhanced the recombination rate. Even if we propose a link of this depletion of electrons with the impending earthquake, we need to note that it happened

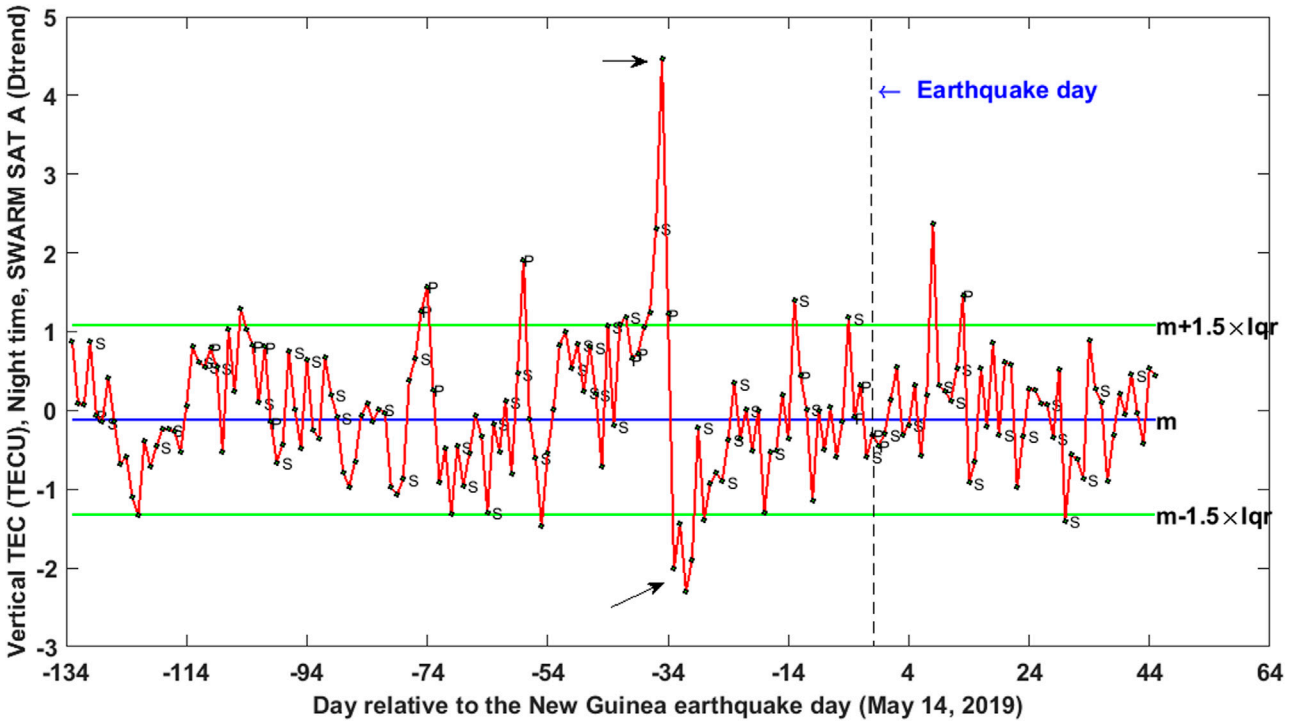

FIGURE 4 | Results of Swarm A night time VTEC data analysis for the Papua New Guinea (May 14, 2019) from January 01 to June 30, 2019. The symbols "P" and "S" indicate disturbed magnetic days ("P" according to magnetic indices, "S" according to solar parameters).

between two geomagnetically disturbed periods, so even an external perturbation of the ionosphere can be the source of this phenomenon. **Supplementary Figure S3** shows the Swarm B satellite day-time VTEC residual variations during the period of January 01 to June 30, 2019. This figure confirms the anomalous VTEC variations on 20 days preceding the earthquake when VTEC exceeds the upper bound with the value of 90.59%.

Swarm Magnetic Field Anomalies

In order to make a comparative analyses, six other parameters measured by satellites A, B, and C including scalar and vectors' (X, Y, Z) magnetic components, electron density, and electron temperature were analyzed during the period from January 01 to June 30, 2019, inside the Dobrovolsky's area.

For anomaly detection in the magnetic field components, at the first step, the difference between the measured parameter in nominal satellite conditions and the predicted value using the IGRF-12 (International Geomagnetic Reference Field) (Thébault, et al., 2015) model was computed. Afterwards, the median of the residuals of magnetic values of each track inside the Dobrovolsky's area separately for day and night was calculated and finally, the time series of the magnetic field median values during the period from January 01 to June 30, 2019 was created. It should be noted that to obtain residual curves of magnetic components using the IGRF model, all tracks of Swarm satellite inside a square centered in earthquake epicenter with a diagonal equals to two times of Dobrovolsky's radius were considered (the use of a square instead of a circular area of investigation was motivated to have analyzed tracks with the same length). To remove the seasonal variations and all variations not predicted by the IGRF, a polynomial of degree 4 was fitted to the time series and the residual values were finally calculated. A threshold value is defined as $\boldsymbol{m} \pm 1.50 \times \boldsymbol{Iqr}$. Therefore, we select those residual values of the observed parameter if they exceed the pre-defined threshold in geomagnetically quiet conditions ($|Dst| \leq 20$ nT, $a_p < 25$ nT and F10.7 < 120). Further checking of the identified anomalies is made that also takes into account the external conditions evaluated by IMF and solar wind speed as specified in 2.1 "*Solar and geomagnetic data*" section. The final selected anomalies are then regarded as an anomaly candidate, i.e., a potential seismic anomaly.

Figure 5 illustrates the day-time Y magnetic field values measured by satellite B during the study period. Striking anomalies are seen on 26, 20, and 7 days and 1 day before the earthquake occurrence with the values of 11.22%, −42.45%, −8.55%, and −25.77% of the allowable bounds in geomagnetically quiet conditions, respectively. The Swarm Bravo magnetic Y component time series during night time is not shown as it does not contain any apparent anomaly.

Figure 6A presents the recorded track of satellite B close to the New Guinea earthquake epicenter on 14 May, half an hour before the earthquake time. The residual of the time series of the first derivatives of the measured magnetic fields scalar and vectors (X, Y, Z) values and a cubic spline are shown in **Figures 6A–D**, respectively. The vertical axis represents the geomagnetic latitude. An unusual variation in the time series of the residual curve of the

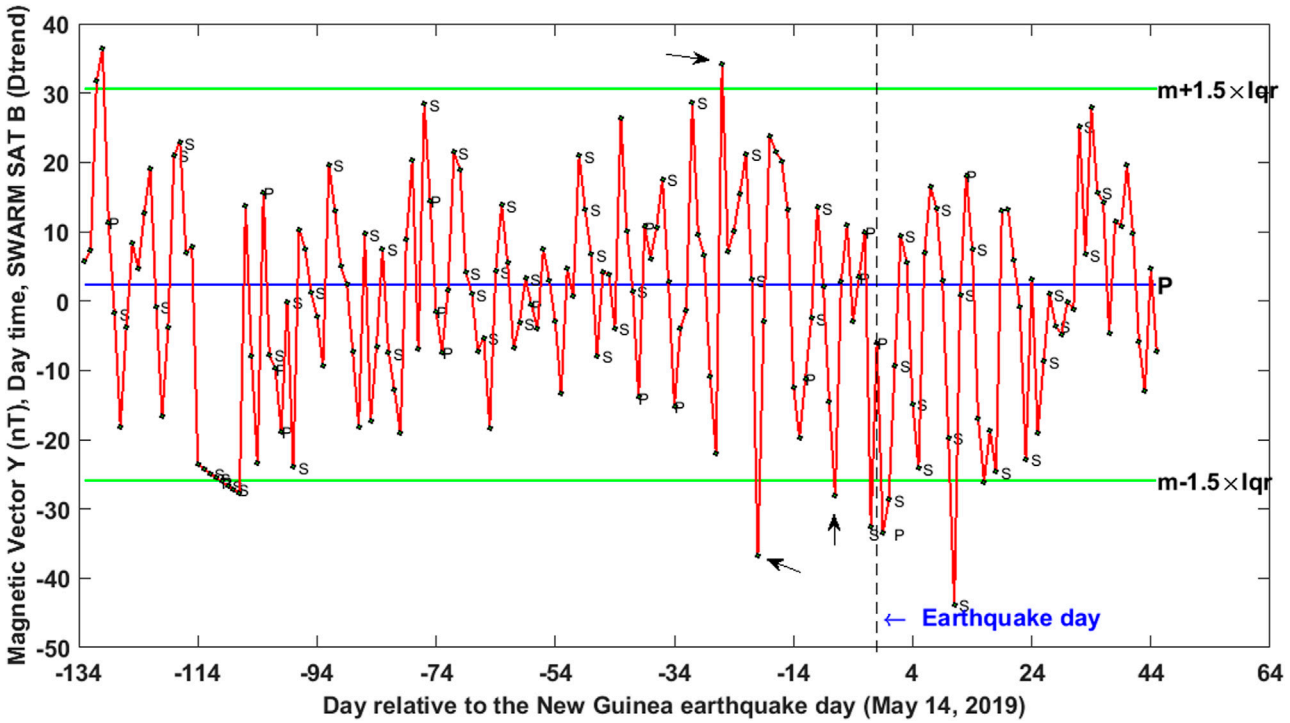

FIGURE 5 | Results of Y magnetic field data analysis from Swarm B for the New Guinea earthquake (May 14, 2019) from January 01, to June 30, 2019 at day time. The symbols "P" and "S" indicate disturbed magnetic days ("P" according to magnetic indices, "S" according to solar parameters).

X, Y, and Z components of the magnetic field is clearly seen around the earthquake location (the red arrows in **Figure 6**). We note another smaller perturbation in the southern position but, with respect to the underlined one, it is very short, and it is probably due to moderate geomagnetic activity.

Supplementary Figure S4 shows the track of satellite B crossing the Dobrovolsky's area 20 days before the main shock. Anomalous variations are clearly seen in the time series of the residual curves of the vectors X, Y, and Z of the magnetic field around the earthquake location.

We noted that the Y component is a little more disturbed than X and Z for anomalies depicted in **Figure 6** and **Supplementary Figure S4**.

Although the time series analysis does not underline any anomaly in the mean night-time Y daily values of magnetic field, a single track analysis shows some anomalies also in this period. **Figure 7** and **Supplementary Figure S5** show the two candidates of pre-earthquake anomalies that preceded the main seismic event by about 2 days and 1 month. Both tracks were acquired during geomagnetic quiet conditions and show a clear anomaly around the future epicentral coordinates (indicated by a red circle). The FFT of Y component of **Figure 7** shows a peak centered at a frequency of 0.13 Hz that corresponds to a period of 7.4 s. In **Supplementary Figure S5**, the identified anomaly is more evident in the Y component, supporting the hypothesis of an internal source for this signal. It is worth noting that the epicentral latitude corresponds to the southern peak of the equatorial ionospheric anomaly (EIA): this implies that we cannot completely exclude that the underlined anomalies are intrinsic phenomena of the ionospheric response to the solar diurnal activity. However, in the cases shown in **Figure 7** and **Supplementary Figure S5**, the night local time would exclude a typical EIA on that occasion: these anomalies are also called absolute ionospheric precursors (Pulinets and Ouzounov, 2018). In addition, all other tracks did not show these kinds of anomalies at −15° of geomagnetic latitude, deposing more for a transient phenomenon in the two cases shown in **Figure 7** and **Supplementary Figure S5**.

Supplementary Figure S6 shows the night-time Z magnetic field values measured by satellite B during the study period. Unusual variation is seen on 29 days before the event with the values of 3.12% of the higher bound in geomagnetically quiet conditions.

Supplementary Figures S7 illustrates the night-time Y magnetic field values measured by satellite C. Clear anomaly is seen on 5 days before the event with the values of 5.36% of the higher bound in geomagnetically quiet conditions; nevertheless, it presents some solar activity, so its origin could be likely due to an external source, i.e., the Sun.

Swarm Electron Density and Temperature Anomalies

For every track inside the Dobrovolsky's area at every day, the median of each parameter including the electron density and the electron temperature separately for day and night were obtained

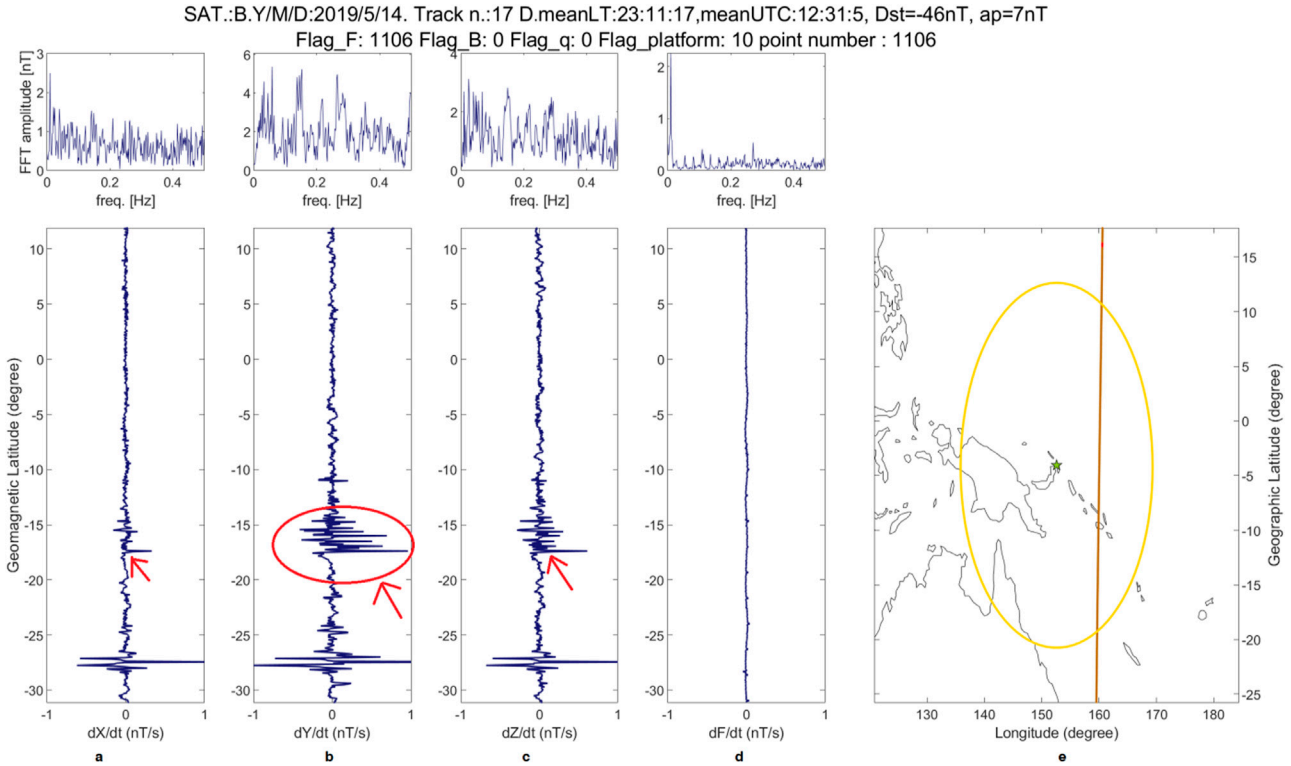

FIGURE 6 | Results of Swarm B track analysis for the New Guinea earthquake (May 14, 2019) on earthquake day. **(E)** A map of the region with the longitude in horizontal axis and latitude in vertical one is represented. A green asterisk, a brown line, and a yellow circle represent the earthquake epicenter, the track, and Dobrovolsky's area, respectively. The track crossed the Dobrovolsky's area between the 12:27:12 and 12:35:03 UTC. **(A–D)** The residuals of the time series of the derivatives of the measured scalar magnetic field (X, Y, Z) components and F, respectively, along this track. The vertical axis represents the geomagnetic latitude. Above each analysis, the FFT spectra are represented too.

and finally, the time series of the median values, for day and night during the studied period, were created. However, since the variations of the plasma parameters are affected by nonlinear variations, a polynomial of degree 4 fitted to the time series and the residuals between the two curves as a new time series was calculated.

Figure 8 and **Supplementary Figure S8** show the Swarm A satellite electron density residual variations during the period from January 01 to June 30, 2019 for night and day times. Two striking anomalies are seen on 32 and 35 days before the event when the parameter variations exceed the higher bound with the values of 229.84% and 236.21%, respectively.

Supplementary Figure S9 shows the Swarm B satellite night-time electron density residual variations during the period of January 01 to June 30, 2019.

It is interesting that this figure confirms the results deduced from **Supplementary Figure S2**, which indicated night-time VTEC variations. It is seen that electron density variations encounter with a rising trend from about 20 days before the event and then fall in day earthquake similar to VTEC variations. It exceeds the upper bound on −7 days before the earthquake with a value of 253.42%.

Figure 9 shows the track of satellite B on 7 days before the earthquake (May 07) inside the Dobrovolsky's area. To look for possible seismo-anomalies, a polynomial of degree 12 along this track has been fitted and subtracted. The residuals of the measured electron density/temperature are shown in **Figures 9B,C**. The vertical axis represents the geomagnetic latitude. Unusual variations of the electron density and electron temperature in the residual time series are clearly seen close to the earthquake location (the red arrows in **Figure 9**).

It should be noted that the detected anomalies in the measured parameters using Swarm A can be compared by the corresponding measured parameters in Swarm C due to the same orbit altitude and also the close distance (about 1.4° longitudinal separation) between two satellites. For this reason, we decided to apply a similar technique used by Zaxapros et al. (2019) to study the variation of Ne associated with a typhoon in Pacific Ocean. **Figure 10** and **Supplementary Figure S10** show the variations of differences between gradients of electron density values measured by Swarm A and C at night and day, respectively, clear anomalies are seen on 34 days before the event.

Supplementary Figure S11 shows the Swarm C satellite night-time electron temperature residual variations during the period from January 01 to June 30, 2019. It is interesting that the latter figure confirms the results deduced from Swarm A. Clear anomalies are seen between 20 and 32 days before the

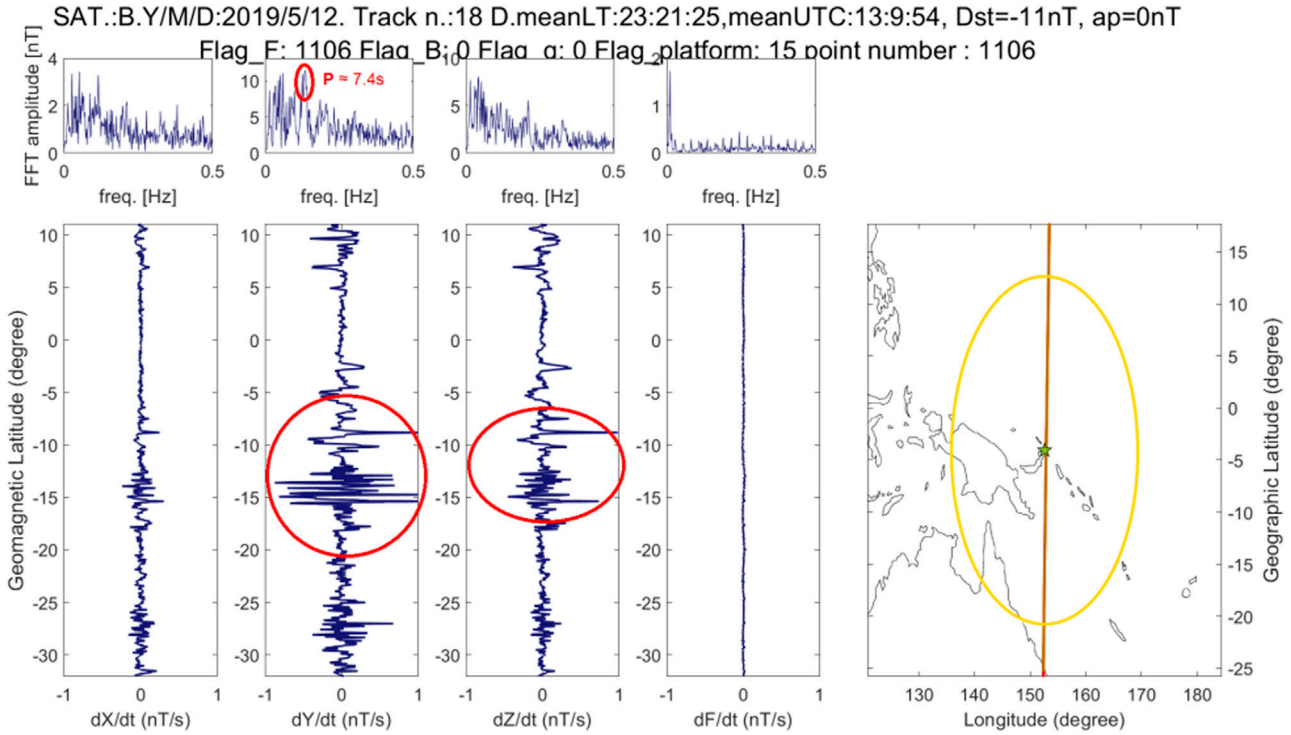

FIGURE 7 | Swarm B night-time data analysis of the track that preceded the earthquake by about 2 days (−1.99 days). The same elements of **Figure 8** are shown, and, in addition, the FFT of the signal inside the Dobrovolsky area is reported for each magnetic field component and total intensity. For Y magnetic field component, the FFT evidences a peak at 7.4 s.

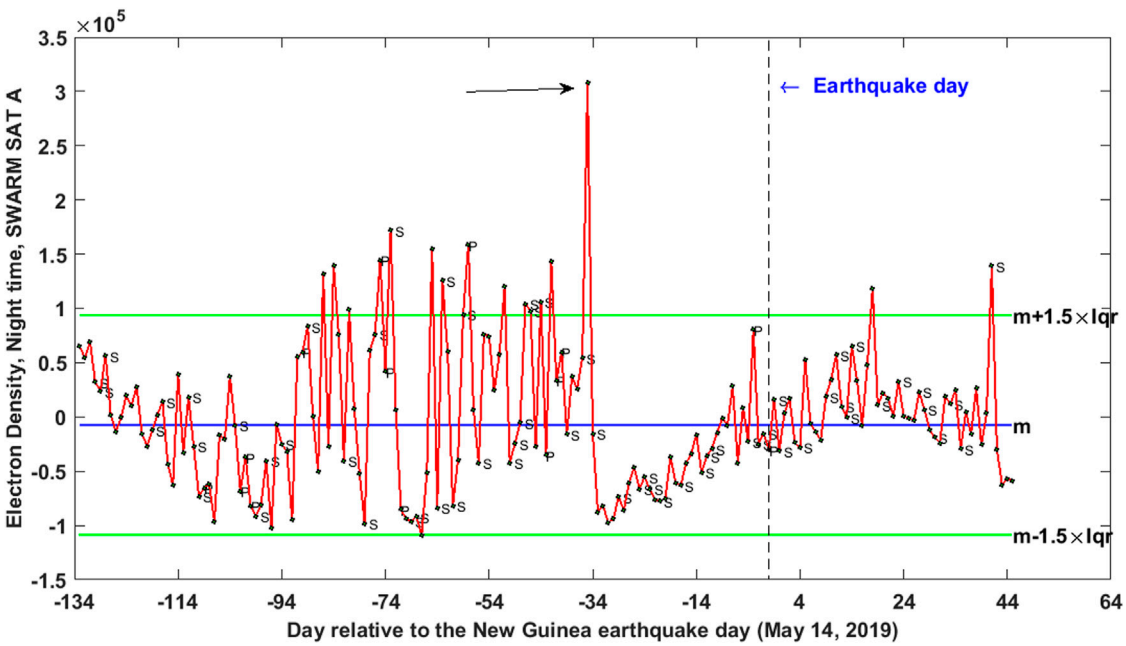

FIGURE 8 | Results of Swarm A electron density data analysis for the New Guinea earthquake (May 14, 2019) from January 01 to June 30, 2019 at night time. The symbols "P" and "S" indicate disturbed magnetic days ("P" according to magnetic indices, "S" according to solar parameters).

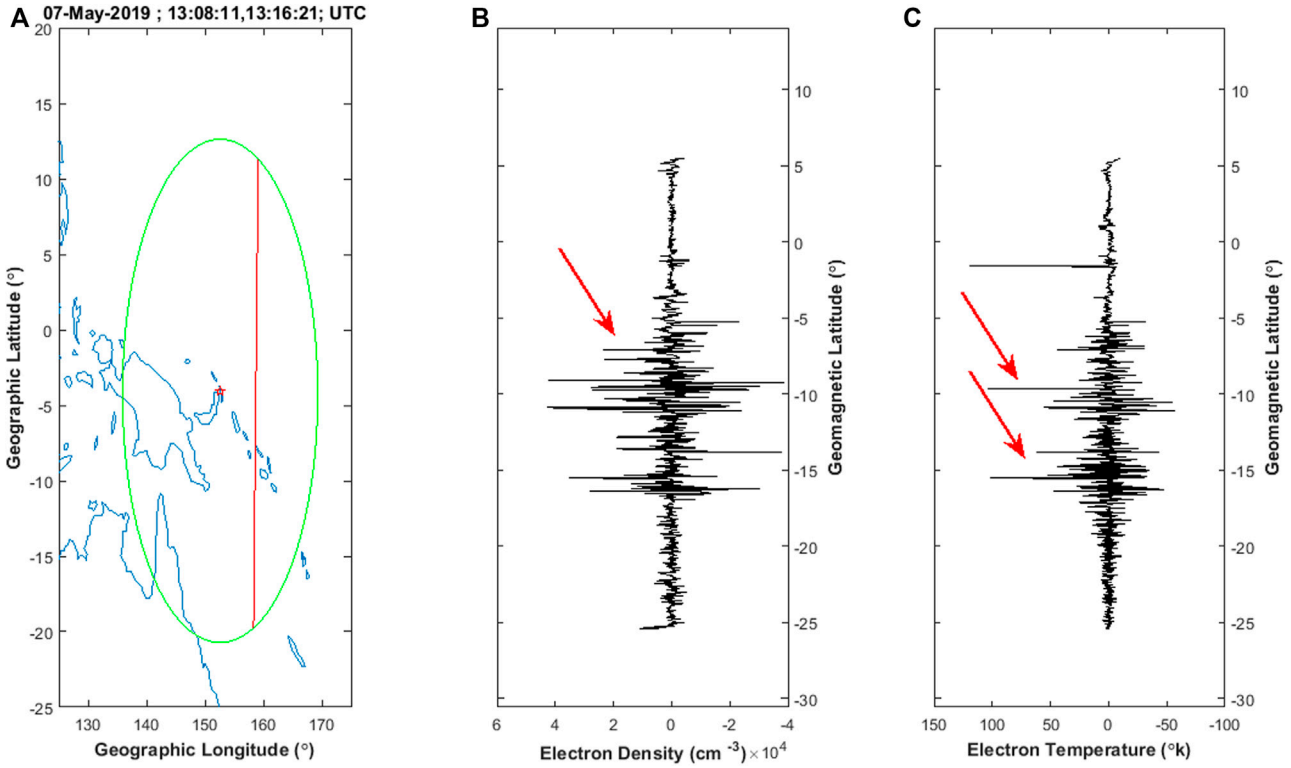

FIGURE 9 | Results of Swarm B track analysis for the New Guinea earthquake (May 7 , 2019), 7 days before earthquake day. **(A)** A map of the region with the longitude in the horizontal axis and latitude in vertical one is represented. A red asterisk, a brown line, and a yellow circle represent the earthquake epicenter, the track, and Dobrovolsky's area, respectively. The track crossed the Dobrovolsky's area between the 13:08:11 and 13:16:21 UTC. **(B,C)** show the differences between the time series of the measured electron density and temperature and a polynomial of degree 20 fitted along the same track. The vertical axis represents the geomagnetic latitude.

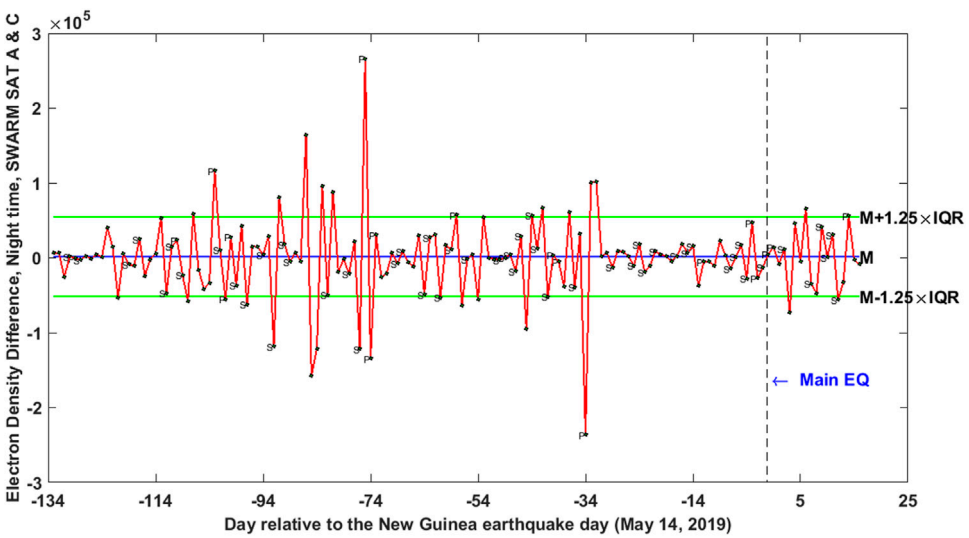

FIGURE 10 | Differences between gradients of electron density values measured by Swarm A and C from January 01 to June 30, 2019 at night time. The symbols "P" and "S" indicate disturbed magnetic days ("P" according to magnetic indices, "S" according to solar parameters).

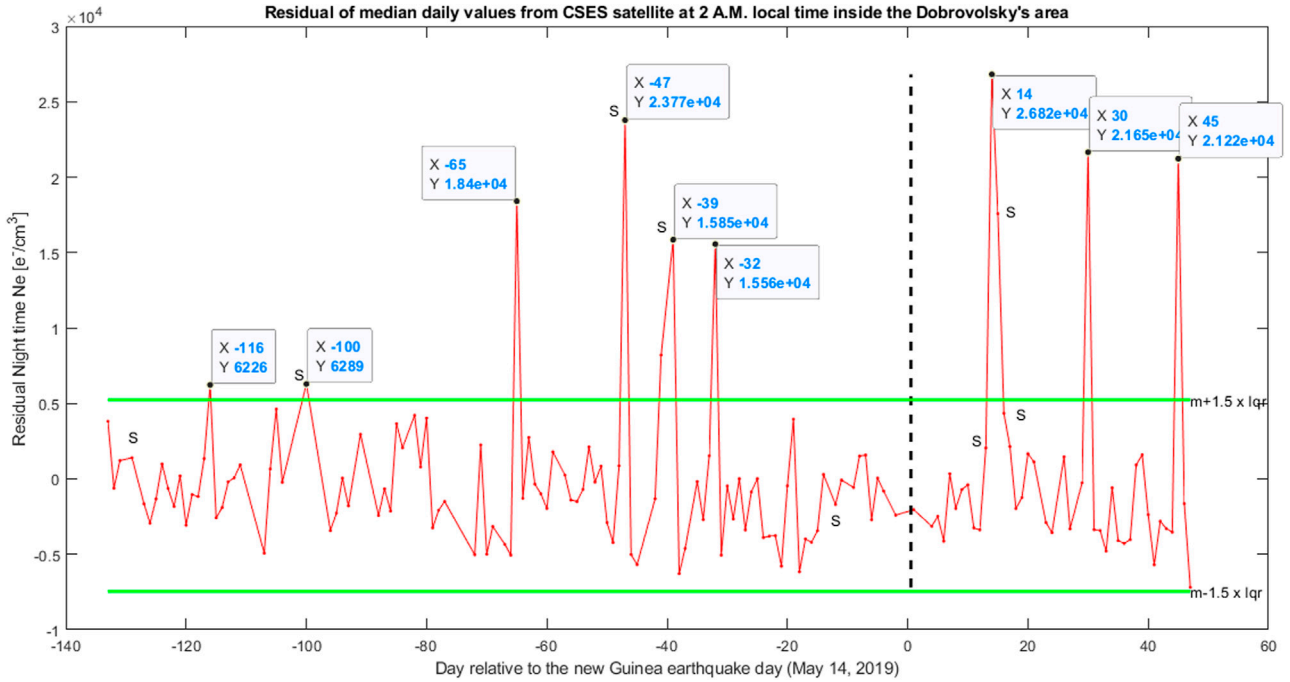

FIGURE 11 | CSES daily median electron density during night time (2:00 a.m.). Only data acquired during geomagnetic quiet time (|Dst| ≤ 20 nT and a_p ≤ 10 nT) has been shown. Days with high solar activity are depicted by "S."

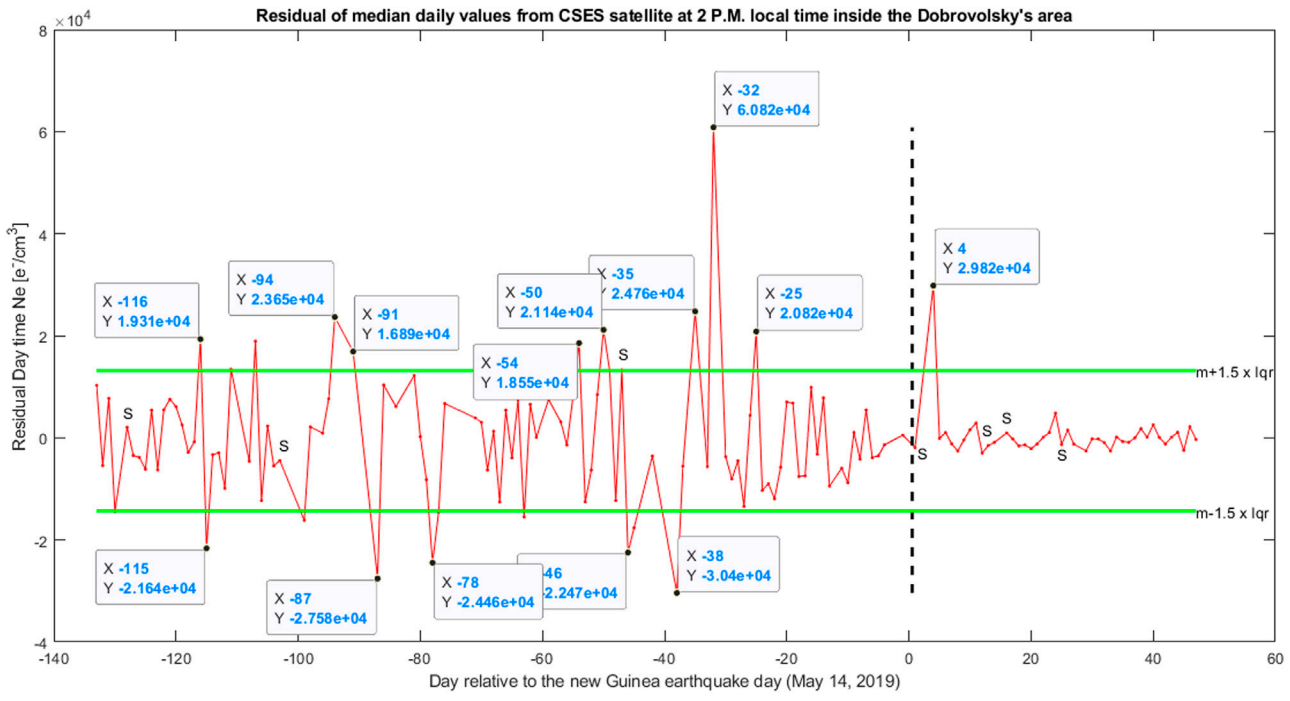

FIGURE 12 | CSES daily median electron density during day time (2:00 p.m.). Only data acquired during geomagnetic quiet time (|Dst| ≤ 20 nT and a_p ≤ 10 nT) has been shown. Days with high solar activity are depicted by "S."

TABLE 1 | A summary of the detected anomalies in the investigated period. The anomalies are sorted following these criteria: satellite that detects, night and day, before and after the earthquake occurrence, and finally, in chronological order. The anomalies detected during high magnetic or solar activity are not listed. Also, TEC and Ne negative anomalies are not included.

Parameter	Day	Time (LT)	Anomaly value
Vertical TEC (VTEC), Swarm A satellite	−105	Night	25.64%
	−37	Night	20.38%
	−35	Night	318.38%
	10	Night	161.19%
Vertical TEC (VTEC), Swarm B satellite	−85	Night	87.84%
	−84	Night	96.17%
	−83	Night	99.26%
	−81	Night	14.86%
	−7	Night	12.16%
	10	Night	92.62%
	22	Night	134.48%
	46	Night	36%
	−79	Day	65%
	−77	Day	64%
	−51	Day	45%
	−23	Day	70%
	−20	Day	224%
	11	Day	20%
Vertical TEC (VTEC), Swarm C satellite	−51	Night	40.05%
	−37	Night	61.50%
	−35	Night	278.80%
Electron density, Swarm A satellite	−86	Night	57%
	−84	Night	49.03%
	−65	Night	92%
	−51	Night	40%
	−42	Night	74%
	−35	Night	318%
	20	Night	37%
	−33	Day	34%
	−32	Day	256.05%
	−31	Day	94%
	−30	Day	80%
	−16	Day	35%
	−15	Day	33%
Electron density, Swarm B satellite	−84	Night	60%
	−81	Night	8%
	−80	Night	30%
	−32	Night	208%
	−19	Night	236%
	−14	Night	11%
	−7	Night	301%
	46	Day	14%
Electron temperature, Swarm C satellite	−122	Night	11.96%
	−32	Night	196.23%
	−30	Night	179.84%
	−19	Night	213.93%
Magnetic field, Y component, Swarm B satellite	−130	Day	18.75%
	−26	Day	11.22%
	−20	Day	−42.45%
	−7	Day	−8.55%
Magnetic field, Z component, Swarm B satellite	−44	Night	−19.22%
	−29	Night	3.12%
Electron Density, CSES-01	−116	Night	18.88%
	−65	Night	251.35%
	−47	Night	353.89%
	−32	Night	197.12%
	−116	Day	46.29%
	−94	Day	79.17%
	−32	Day	360.76%
	−25	Day	125.91%
TEC, GPS	−32	06:00	21.34%
		07:00	35.97%
		08:00	44.12%
		16:00	9.69%
		17:00	8.32%
		18:00	3.34%
	−31	10:00	4.38%

earthquake, especially on 30 days prior to the event with a value of 179.84%.

CSES Satellite Data Analysis

As we noticed that in the analyses of the electron density, some trends still remain that could be due to the Swarm local time precession, we decided to perform a similar analysis with the data from China Seismo-Electromagnetic Satellite (CSES, also known as CSES-01 or Zhangheng-01) that has a fixed local time at ~2: 00 a.m. for night time and ~2:00 p.m. for day time (Shen et al., 2018). The median electron density of the samples acquired inside the Dobrovolsky's area during only geomagnetic quiet time ($|Dst| \leq 20$ nT and $a_p \leq 10$ nT) have been computed separately for day-time tracks and night-time tracks. The seasonal trend has been removed by a 3rd degree and 7th degree polynomial for night and day time, respectively. **Figures 11**, **12** show the residual trends for night and day time as well as the median values plus or minus 1.5 times the interquartile range of the same series. The points outside the given threshold, i.e., the anomalous ones, have been underlined by datatips with the indication of the day with respect to the earthquake and the residual value of electron density in e^-/cm^3.

DISCUSSION

The characteristics and temporal evolution of the detected anomalies in the variations of discussed parameters are listed in **Table 1**. This table shows the day of anomaly occurrence with respect to the earthquake, the night or day local time, and the anomaly value with respect to the median; all the anomalies are identified in quiet geomagnetic times, i.e., when the geomagnetic indices and the solar activity, as detected by ACE, were both low. The same day can be indicated with and without solar activity because we take into account the specific time that the satellite crossed the Dobrovolsky area and the solar activity can change during the day. In this table, only the positive anomalies of TEC and electron density have been listed because the earthquakes are expected to increase the ionospheric electron density (e.g., He and Heki, 2017 with the model described by Enomoto, 2012). In general, it appears that electron density and VTEC are the most sensitive quantities to the earthquake preparation phase (both with 20 anomalies before the earthquake occurrence), while the magnetic field is the least sensitive (only 7 anomalies).

We noted that the local time of Swarm Alpha and Charlie around 34 days before the earthquake was close to sunrise and sunset (6:00 a.m. and 6:00 p.m., respectively). So, the anomalies (especially in VTEC and Ne) recorded around this day need to be further discussed to understand better if their origin could be linked to the local time of the satellite or real special ionospheric conditions. A further analysis made use of TEC recorded by the ground station for 24 h on the day, presented in the following paragraph that will address this issue.

Figure 13A shows GNSS-TEC variations deduced from GIM data and the closest grid node (5°S, 150°E) to the epicenter during the period from April 01 to June 30, 2019. Unusual GNSS-TEC variations are sharply seen on 32 and 31 days prior to the earthquake. **Figure 13B** shows variations of DTEC ($DTEC = \frac{TEC - Median}{Interquartile}$). **Figure 13C** shows anomalous TEC values detected using the median method when $|DTEC| > 1.5$. After considering only quiet solar and geomagnetic conditions (ap < 25 nT, $|Dst| \leq 20$ nT, and F10.7 < 120 SFU), **Figure 13D** indicates striking TEC anomalies 32 days before the event between 06:00 and 08:00 UTC and also between 16:00 and 18: 00 UTC. The DTEC value has an increase of the order of 44.12%, from the normal state at 08:00 UTC.

From this analysis, it is evident that the anomaly recorded 31 days before the earthquake occurrence is not an artefact of the local time covered by Swarm as the ground station has a full coverage. From **Figure 13A**, we can even infer that the recorded TEC anomalies are mainly an increase of the crests of the equatorial ionospheric anomalies that is a phenomenon that has been previously found for several earthquakes mainly by the DEMETER satellite (e.g., Li and Parrot, 2012).

A final check of the most anomalous day in night Swarm Bravo VTEC data before the earthquake occurrence is presented. **Figure 14** shows the TEC map around the earthquake on May 7, 2019 at 13:00 UTC. The Swarm Bravo track projections have been displayed over by red lines and the right one between 13:06 and 13:17 UTC is the one where the GNSS Swarm receiver found the VTEC anomaly of the May 7, 2019. The map confirms that inside the Dobrovolsky, there is an enhancement of TEC as seen by Swarm B VTEC. Moreover, the map also shows that the TEC anomaly is well inside the Dobrovolsky area and with this highest value close to the future epicenter (a bit shifted North-East).

We noticed that the most anomalous VTEC value occurred 35 days before the earthquake, as expected for the strict physical link between TEC and Ne; in the same day also, the *in situ* electron density shows an anomalous increase of its value. Furthermore, this anticipation time is very close to the ones found for an increase of electron density before the M7.5 Indonesia 2018 (40 days) and M7.1 California Ridgecrest 2019 (33 days) earthquakes (Marchetti et al., 2019b; De Santis et al., 2020). It is interesting to note that these events have a similar earthquake magnitude, and one of them even occurred in different region/tectonic settings (i.e., Ridgecrest). So, it would be interesting in future studies to further verify whether the ionosphere could respond 30–40 days before earthquakes with this magnitude. This fact would confirm the validity of Rikitake law (1987) as recently established also for satellites by De Santis et al. (2019).

The sequence of all anomalies, taken from all Swarm satellite observables (i.e., VTEC, electron density, electron temperature, and Y, Z magnetic field components) has been finally considered in their whole by constructing the cumulative number of anomalous days. The anomalies that are due to an increase of solar activity checked on the data measured by the ACE satellite from 2 h before the anomaly to its occurrence have been excluded from this cumulate. If the ionospheric anomaly preceded the IMF ones it is not excluded as the magnetosphere coupling can be immediate or needs some delay that the solar wind can impact the ionosphere from the observation point of ACE (about 1.4 millions of kilometers away from Earth) but not precede. **Figure 15** shows the cumulative number of anomalous days with

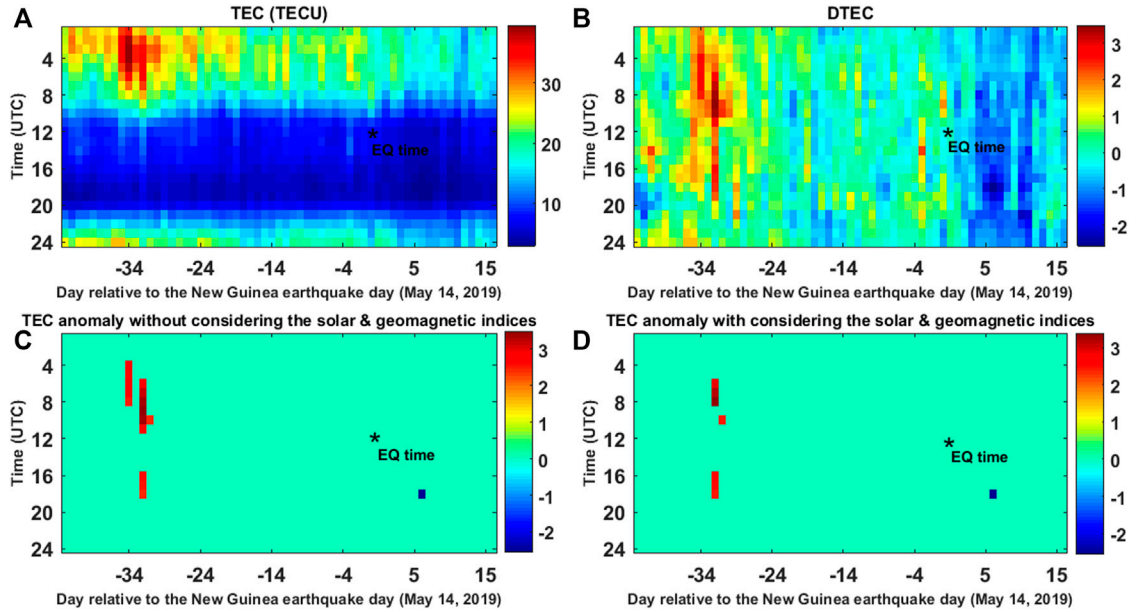

FIGURE 13 | Summary of TEC analysis results using median method for the Papua New Guinea (May 14, 2019) from April 01 to June 30, 2019. The *y*-axis represents the time UTC (LT = UTC – 5:00). **(A)** TEC variations, **(B)** DTEC variations calculated by formula of $DTEC = \frac{TEC - Median}{Interquartile}$, **(C)** detected TEC anomalies when |DTEC| = > 1.5, and **(D)** detected TEC anomalies when ap < 20 nT, Dst > −20 nT, Dst < 20 nT and F10.7 < 120, and ~|DTEC| = > 1.5.

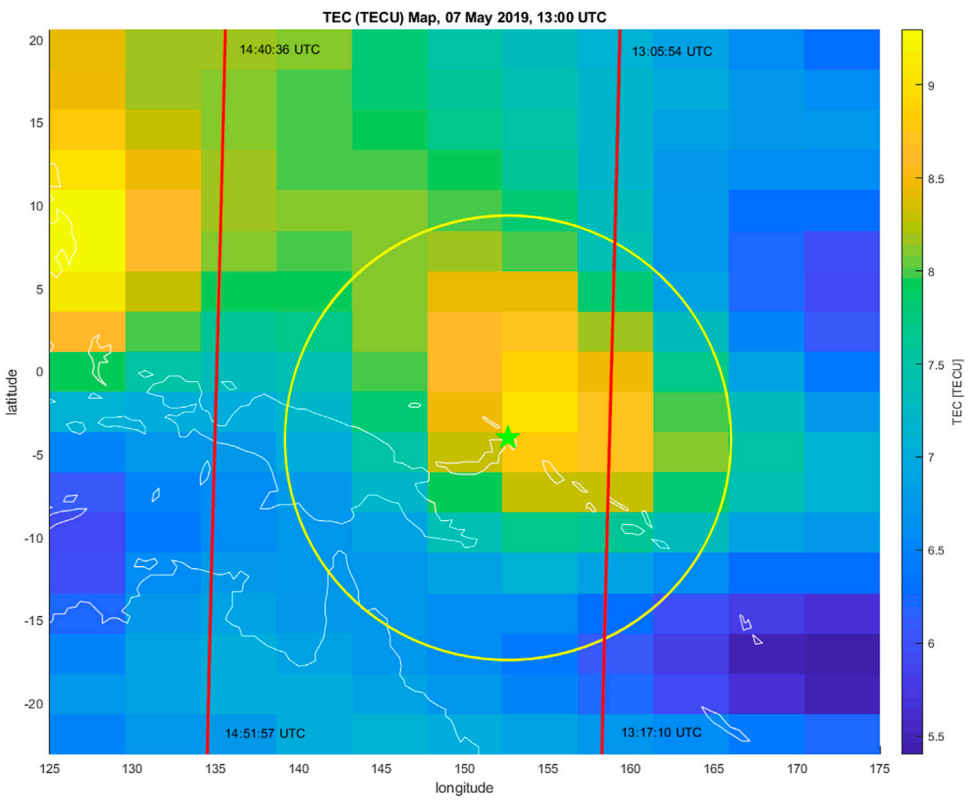

FIGURE 14 | TEC map around the M7.6 Papua New Guinea (May 14, 2019) earthquake on May 7, 2019 at 13:00 UTC. The epicenter is represented as a green star; its Dobrovolsky area is shown by a yellow circle. The red lines represent the Swarm Bravo projection of the track in the same area and time.

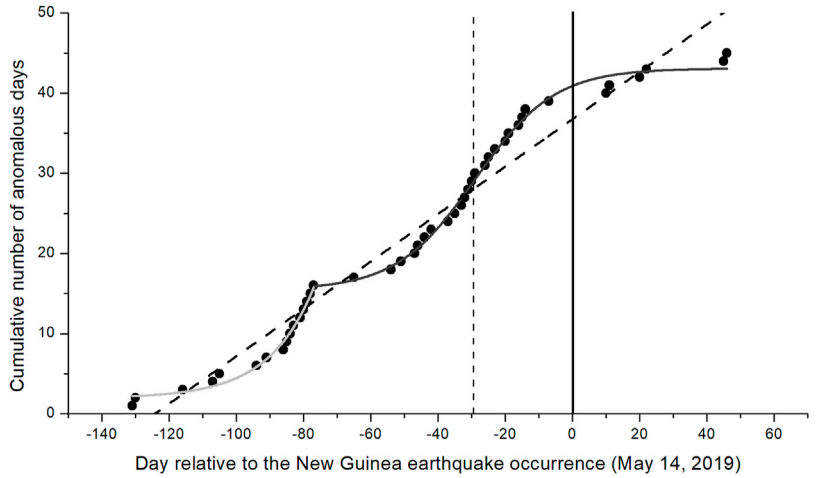

FIGURE 15 | Cumulative number of anomalous days (considering all the Swarm satellites and presented time series) with respect to the day of occurrence of the Papua New Guinea mainshock (negative days before the earthquake occurrence, positive after). Anomalies are shown as black circles, while dark- and light-gray curves are sigmoidal (Boltzmann) fits over two subsequent intervals; the dashed line is the linear fit. The vertical black line is the time of the earthquake, while the vertical dashed line is the inflection of the sigmoidal dark-gray curve.

respect to the day of the earthquake (here placed as time zero), weighting each anomalous day for the same unitary amount. The dark- and light-gray curves are two sigmoidal (Boltzmann) fits over two distinct parts of the points (see **Figure 15**; the first fit is partial for the early analyzed period, while the second one comprises some data before and after the earthquake occurrence), the linear fit is given by a dashed (oblique) line, over all detected anomalies. It is evident that there are two accelerations of anomalies before the earthquake, and for this reason the data have been divided into two time intervals separated at −77 days. The two intervals have been fitted by sigmoidal curves shown in light and dark gray with adjusted R^2 = 0.980 and R^2 = 0.992 (both are better than the linear fit with R^2 = 0.958). The second curve, i.e., the one from −77 to +60 days with respect to the earthquake day, is the one with better statistical indications, and it indicates a turning point of the system (the inflection point of the full sigmoidal curve indicated as vertical dashed black line) at about −29 days, i.e., the ionosphere showed a critical behavior about 1 month before the mainshock. Furthermore, a first increase of anomaly has been depicted at about 80 days before the earthquake and this seems to be a typical anticipation time for ionospheric disturbances as extensively (on more than 1,000 earthquakes) analyzed by De Santis et al. (2019).

A confutation analysis was finally performed to acknowledge the potentially detected anomalies in VTEC variations measured by Swarm B. **Supplementary Figure S12** shows the results of Swarm B night time VTEC data analysis for the location of 4.051°S, 85°E, outside the Doborovolsky's area from January 01 to June 30, 2019. According to the USGS catalogue, no significant (M > 6) earthquake was recorded in this area during the analyzed time. Some minor events have been localized, in particular an M6.0 on February 02, 2019 and its aftershocks, but we underline that such events are not significant when compared with the tectonic of the region that potentially can generate M7.5+, or even greater events, as it is in the interaction plate boundary between Sunda and Indian plates. In addition, no Swarm anomalies are seen from about 100 days before the main event to the earthquake occurrence day, providing evidences that the identified anomalies for Papua New Guinea are confined inside the Dobrovolsky's area.

Therefore the all of implemented comparative and confutation analyses, reduce the uncertainty about the source of the observed anomalies and lead to make a robust decision about the observed anomalies in VTEC time series measured using Swarm satellites.

CONCLUSION

This paper presents the first study concerning the Swarm-TEC data analysis to detect seismo-ionospheric anomalies. In order to make some robust comparative analyses, other six measured plasma and magnetic field parameters from Swarm satellites and GNSS-TEC measurements were also investigated, together with the electron density of CSES. Results show clear anomalies on the earthquake day and some days before the main seismic event, with significant concentrations (acceleration) of anomalies on around 80 and 30 days before the mainshock. We were careful to detect the anomalies during low geomagnetic activity, so those anomalies could be considered potentially as pre-seismic anomalies. Interesting enough, we find that a sigmoidal fit represents well the behavior of part or all anomalies toward the time of main earthquake occurrence: in particular, the sigmoid closer to the earthquake occurrence shows the inflection point about 1 month before the earthquake, supporting an underlying critical system pointing toward a critical point. Moreover, the electron density variations acknowledge the VTEC variations, better supporting the found results. Our

finding shows that, for the present case study, the magnetic field component Y appears to be the most sensitive component to ionospheric anomalies with respect to X, Z, and total intensity but the least one with respect to the other analyzed ionospheric parameters.

Therefore, Swarm-TEC measurements could be used as one of the main data sources for studies on earthquake precursors, especially in combination with electron density and magnetic field *in situ* satellite observations. This reinforces the multi-precursors analysis, which remains the most favored approach to study the preparation phase of large earthquakes with non-seismic data.

DATA AVAILABILITY STATEMENT

Publicly available datasets were analyzed in this study. This data can be found in the following: The European Space Agency (ESA) for the Swarm data at HTTP or FTP (anonymous login) server: swarm-diss.eo.esa.int, NASA NOAA for the solar and geomagnetic indices at https://www.ngdc.noaa.gov/geomag/indices/indices.html. The China Earthquake Administration, China National Space Administration and Italian Space Agency for the data of CSES-01 available upon request and formal approval at www.leos.ac.cn. Ground magnetic field measurements are freely available at www.intermagnet.org.

AUTHOR CONTRIBUTIONS

MA, AD, DM, and XS: Conceptualization, Methodology, Software. MA, AD, and DM: Data curation, Writing-Original draft preparation, Writing- Reviewing and Editing.

FUNDING

Part of this work has been funded by the SAFE (Swarm for Earthquake Study) project (ESA) and by LIMADOU-Science+ Project (Italian Space Agency). Partial funds were also provided by FURTHER (INGV) Project, "Pianeta Dinamico-Working Earth" Project (Italian Ministry of University and Research—project code: D53J19000170001), "Research on anomaly extraction technology of seismic electromagnetic satellite data based on blind source separation" project (National Natural Science Foundation of China, Grant number 41974084), and project "Research on multiparametric anomalies in Lithosphere-Atmosphere-Ionosphere before the earthquakes" (Grant number: 2021M691190) funded by the China Postdoctoral Science Foundation.

ACKNOWLEDGMENTS

The authors would like to acknowledge the European Space Agency (ESA) for the Swarm data, NASA Jet Propulsion Laboratory for the solar and geomagnetic indices. We also thank "Geoscience Australia (GA)", for supporting its operation and INTERMAGNET for promoting high standards of magnetic observatory practice (www.intermagnet.org). Some of the results presented in this paper rely on the data collected at "Kakadu."

SUPPLEMENTARY MATERIAL

The Supplementary Material for this article can be found online at: https://www.frontiersin.org/articles/10.3389/feart.2022.820189/full#supplementary-material

REFERENCES

Akhoondzadeh, M., Parrot, M., and Saradjian, M. R. (2010). Electron and Ion Density Variations Before Strong Earthquakes (M>6.0) Using DEMETER and GPS Data. *Nat. Hazards Earth Syst. Sci.* 10, 7–18. doi:10.5194/nhess-10-7-2010

Akhoondzadeh, M., De Santis, A., Marchetti, D., Piscini, A., and Cianchini, G. (2018). Multi Precursors Analysis Associated with the Powerful Ecuador (MW= 7.8) Earthquake of 16 April 2016 Using Swarm Satellites Data in Conjunction with Other Multi-Platform Satellite and Ground Data. *Adv. Space Res.* 61, 248–263. doi:10.1016/j.asr.2017.07.014

Akhoondzadeh, M., De Santis, A., Marchetti, D., Piscini, A., and Jin, S. (2019). Anomalous Seismo-LAI Variations Potentially Associated with the 2017 Mw = 7.3 Sarpol-E Zahab (Iran) Earthquake from Swarm Satellites, GPS-TEC and Climatological Data. *Adv. Space Res.* 64, 143–158. doi:10.1016/j.asr.2019.03.020

Chen, K., Milliner, C., and Avouac, J. P. (2019). The Weitin Fault, Papua New Guinea, Ruptured Twice by M W 8.0 and M W 7.7 Earthquakes in 2000 and 2019. *Geophys. Res. Lett.* 46, 12833. 833–12,840, 12840. doi:10.1029/2019GL084645

Cianchini, G., De Santis, A., Di Giovambattista, R., Abbattista, C., Amoruso, L., Campuzano, S. A., et al. (2020). Revised Accelerated Moment Release under Test: Fourteen Worldwide Real Case Studies in 2014–2018 and Simulations. *Pure Appl.Geoph.* 177 (9), 4057–4087. doi:10.1007/s00024-020-02461-9

De Santis, A., Balasis, G., Pavón-Carrasco, F. J., Cianchini, G., and Mandea, M. (2017). Potential Earthquake Precursory Pattern from Space: the 2015 Nepal Event as Seen by Magnetic Swarm Satellites. *Earth Planet. Sci. Lett.* 461, 119–126. doi:10.1016/j.epsl.2016.12.037

De Santis, A., Cianchini, G., Marchetti, D., Piscini, A., Sabbagh, D., Perrone, L., et al. (2020). A Multiparametric Approach to Study the Preparation Phase of the 2019 M7.1 Ridgecrest (California, United States) Earthquake. *Front. Earth Sci.*, 8. doi:10.3389/feart.2020.540398

De Santis, A., De Franceschi, G., Spogli, L., Perrone, L., Alfonsi, L., Qamili, E., et al. (2015). Geospace Perturbations Induced by the Earth: the State of the Art and Future Trends. *Phys. Chem. Earth, Parts A/B/C* 85-86, 17–33. doi:10.1016/j.pce.2015.05.004

De Santis, A., Marchetti, D., Pavón-Carrasco, F. J., Cianchini, G., Perrone, L., Abbattista, C., et al. (2019). Precursory Worldwide Signatures of Earthquake Occurrences on Swarm Satellite Data. *Sci. Rep.* 9, 20287. doi:10.1038/s41598-019-56599-1

Dobrovolsky, I. P., Zubkov, S. I., and Miachkin, V. I. (1979). Estimation of the Size of Earthquake Preparation Zones. *Pageoph* 117, 1025–1044. doi:10.1007/bf00876083

Enomoto, Y. (2012). Coupled Interaction of Earthquake Nucleation With Deep Earth Gases: A Possible Mechanism for Seismo-Electromagnetic Phenomena. *Geophys.* 191 (3), 1210–1214. doi:10.1111/j.1365-246X.2012.05702.x

Foelsche, U., and Kirchengast, G. (2002). A Simple "geometric" Mapping Function for the Hydrostatic Delay at Radio Frequencies and Assessment of its Performance. *Geophys. Res. Lett.* 29 (10), 111–1. doi:10.1029/2001GL013744

Freund, F. (2009). Stress-activated Positive Hole Charge Carriers in Rocks and the Generation of Pre-earthquake Signals. *In Electromagnetic Phenomena Associated with Earthquakes*, Ed. By M. Hayakawa, Transworld Research Network, Trivandrum, 41–96.

Friis-Christensen, E., Lühr, H., and Hulot, G. (2006). Swarm: A Constellation to Study the Earth's Magneticfield. *Earth Planets Space* 58, 351–358. doi:10.1186/BF03351933

Geller, R. J. (1997). Earthquake Prediction: a Critical Review. *Geoph. J. Inter.* 131 (3), 425–450. doi:10.1111/j.1365-246x.1997.tb06588.x

Guo, J., Li, W., Liu, X., Wang, J., Chang, X., and Zhao, C. (2015). On TEC Anomalies as Precursor Before MW 8.6 Sumatra Earthquake and MW 6.7 Mexico Earthquake on April 11, 2012. *Geosci. J.* 19, 721–730. doi:10.1007/s12303-015-0005-6

Haagmans, R., Bock, R., and Rider, H. (2013). Swarm; ESA's Magnetic Field mission. Available at: https://earth.esa.int/documents/700255/1805948/ESA+magnetic+field+mission/36942f02-b2d4-4787-af81-eb19efb74265.

Hayakawa, M., and Molchanov, O. A. (2002). *Seismo- Electromagnetics: Lithosphere-Atmosphere-Ionosphere Coupling*. Tokyo: Terra Scientific Publishing Co, 477.

He, L., and Heki, K. (2017). Ionospheric anomalies immediately before Mw 7.0–8.0 earthquakes. *J. Geophys. Res. Space Phys.* 122, 8659–8678. doi:10.1002/2017JA024012

Li, M., and Parrot, M. (2012). Real Time Analysis of the Ion Density Measured by the Satellite DEMETER in Relation With the Seismic Activity. *Nat. Hazards Earth Syst. Sci.* 12, 2957–2963. doi:10.5194/nhess-12-2957-2012

Liu, J. Y. (2018). "Seismo-ionospheric Precursors of the 2017 M7.3 Iran-Iraq Border Earthquake and the 2018 M5.9 Osaka Earthquake Observed by FORMOSAT-5/AIP," in EMSEV 2018, International Workshop Integrating Geophysical Observations from Ground to Space for Earthquake and Volcano Investigations Potenza (Basilicata: Italy), 17–21.

Marchetti, D., and Akhoondzadeh, M. (2018). Analysis of Swarm Satellites Data Showing Seismo-Ionospheric Anomalies Around the Time of the strong Mexico (Mw = 8.2) Earthquake of 08 September 2017. *Adv. Space Res.* 62, 614–623. doi:10.1016/j.asr.2018.04.043

Marchetti, D., De Santis, A., D'Arcangelo, S., Poggio, F., Piscini, A., A. Campuzano, S., et al. (2019a). Pre-earthquake Chain Processes Detected from Ground to Satellite Altitude in Preparation of the 2016-2017 Seismic Sequence in Central Italy. *Remote Sensing Environ.* 229, 93–99. doi:10.1016/j.rse.2019.04.033

Marchetti, D., De Santis, A., Shen, X., Campuzano, S. A., Perrone, L., Piscini, A., et al. (2020b). Possible Lithosphere-Atmosphere-Ionosphere Coupling Effects Prior to the 2018 Mw = 7.5 Indonesia Earthquake from Seismic, Atmospheric and Ionospheric Data. *J. Asian Earth Sci.* 188, 104097. In Press. doi:10.1016/j.jseaes.2019.104097

Marchitelli, V., Harabaglia, P., Troise, C., and De Natale, G. (2020). On the Correlation between Solar Activity and Large Earthquakes Worldwide. *Sci. Rep.* 10, 11495. doi:10.1038/s41598-020-67860-3

Matsumura, S. (2009). Trends and Problems in Earthquake Prediction Research. *Sci. Tech. Trends Q. Rev.* 31, 65–84.

Noja, M., Stolle, C., Park, J., and Lühr, H. (2013). Long-term Analysis of Ionospheric Polar Patches Based on CHAMP TEC Data. *Radio Sci.* 48, 289–301. doi:10.1002/rds.20033

Ouzounov, D., Pulinets, S., Davidenko, D., Rozhnoi, A., Solovieva, M., Fedun, V., et al. (2021). Transient Effects in Atmosphere and Ionosphere Preceding the 2015 M7.8 and M7.3 Gorkha-Nepal Earthquakes. *Front. Earth Sci.* 9, 757358. doi:10.3389/feart.2021.757358

Parrot, M. (1995). Use of Satellites to Detect Seismo-Electromagnetic Effects, Main Phenomenological Features of Ionospheric Precursors of strong Earthquakes. *Adv. Space Res.* 15 (11), 1337–1347. doi:10.1016/0273-1177(95)00072-m

Piscini, A., De Santis, A., Marchetti, D., and Cianchini, G. (2017). A Multi-Parametric Climatological Approach to Study the 2016 Amatrice-Norcia (Central Italy) Earthquake Preparatory Phase. *Pure Appl. Geophys.* 174, 3673–3688. doi:10.1007/s00024-017-1597-8

Pulinets, S., and Boyarchuk, K. A. (2004). *Ionospheric Precursors of Earthquakes*. Berlin: Springer.

Pulinets, S., and Ouzounov, D. (2011). Lithosphere-Atmosphere-Ionosphere Coupling (LAIC) Model - an Unified Concept for Earthquake Precursors Validation. *J. Asian Earth Sci.* 41, 371–382. doi:10.1016/j.jseaes.2010.03.005

Pulinets, S., and Ouzounov, D. (2018). *The Possibility of Earthquake Forecasting. Learning from Nature*. Bristol: IOP Publ.

Swarm Level 2 Processing System (2019). *Swarm Level 2 Processing System* Available at: https://earth.esa.int/eogateway/missions/swarm/product-data-handbook/level-2-product-definitions.

Shen, X., Zhang, X., Yuan, S., Wang, L., Cao, J., Huang, J., et al. (2018). The State of-the-art of the China Seismo-Electromagnetic Satellite Mission. *Scie. China Technol.* 61, 634–642. doi:10.1007/s11431-018-9242-0

Sorokin, V. M., and Pokhotelov, O. A. (2014). Model for the VLF/LF Radio Signal Anomalies Formation Associated with Earthquakes. *Adv. Space Res.* 54 (12), 2532–2539. doi:10.1016/j.asr.2013.11.048

Thébault, E., Finlay, C. C., Beggan, C. D., Alken, P., Aubert, J., Barrois, O., et al. (2015). International Geomagnetic Reference Field: the 12th Generation. *Earth Planets Space* 67 (79), 1–19. doi:10.1186/s40623-015-0228-9

Yizengaw, E., Moldwin, M. B., Komjathy, A., and Mannucci, A. J. (2006). Unusual Topside Ionospheric Density Response to the November 2003 Superstorm. *J. Geophys. Res.* 111, A02308. doi:10.1029/2005JA011433

Zakharov, V. I., Pilipenko, V. A., Grushin, V. A., Khamidullin, A. F., et al. (2019). Impact of Typhoon Vongfong 2014 on the Ionosphere and Geomagnetic Field According to SWARM Satellite Data: 1. Wave Disturbances of Ionospheric Plasma. *Solar-Terrestrial Phys.* 5 (114), N2–N123. doi:10.12737/szf-52201914

Conflict of Interest: The authors declare that the research was conducted in the absence of any commercial or financial relationships that could be construed as a potential conflict of interest.

Publisher's Note: All claims expressed in this article are solely those of the authors and do not necessarily represent those of their affiliated organizations, or those of the publisher, the editors and the reviewers. Any product that may be evaluated in this article, or claim that may be made by its manufacturer, is not guaranteed or endorsed by the publisher.

frontiers in Earth Science

ORIGINAL RESEARCH
published: 25 February 2022
doi: 10.3389/feart.2022.812540

On the Relation Between Anomalous Clouds and Earthquakes in Italian Land

*Guo Guangmeng**

Remote Sensing Center, Nanyang Normal University, Nanyang, China

In 1997 Russian scientist Morozova found some cloud anomalies possibly related to active fault systems and earthquakes. Now, 24 years later, the correlation between clouds and earthquakes is still controversial, and in this paper we checked systematically the satellite images in Italy from 2010 to 2013. The correlation between earthquakes and cloud anomalies was statistically examined by assuming different various leading times and magnitudes. The result showed that when the leading time interval was set to $23 \leq \Delta T \leq 45$ days and the magnitude is bigger than or equal to M4.7, 70% of earthquakes were preceded by cloud anomalies. Poisson random test showed that anomaly appearance rate (AAR) and earthquake occurrence rate (EOR) was much higher than those derived in a random situation, which means it is nearly impossible to deny the correlation between cloud anomaly and land earthquakes in Italy. Error matrix analysis showed this method provides 75% overall accuracy for the 52 total cases. Analysis also showed that cloud method provides a very high AAR value and similar EOR value compared with other earthquake prediction methods based on ionospheric or skin temperature data. The physical mechanism of cloud anomaly was likely caused by electric field, which linked active fault, atmosphere circuit conduction current, and cloud anomaly, and thus provides a reasonable hypothesis of cloud anomaly.

Keywords: cloud anomaly, earthquake, EOR, AAR, satellite

OPEN ACCESS

Edited by:
Giovanni Martinelli,
National Institute of Geophysics and Volcanology, Italy

Reviewed by:
Lixin Wu,
Central South University, China
Angelo De Santis,
Istituto Nazionale di Geofisica e Vulcanologia (INGV), Italy
Nilgun Sayil,
Karadeniz Technical University, Turkey

***Correspondence:**
Guo Guangmeng
guogm@igsnrr.ac.cn

Specialty section:
This article was submitted to Environmental Informatics and Remote Sensing, a section of the journal Frontiers in Earth Science

Received: *10 November 2021*
Accepted: *25 January 2022*
Published: *25 February 2022*

Citation:
Guangmeng G (2022) On the Relation Between Anomalous Clouds and Earthquakes in Italian Land. Front. Earth Sci. 10:812540. doi: 10.3389/feart.2022.812540

INTRODUCTION

Clouds are very common in the atmosphere, and they are always considered to be related to weather change. In 1997 Russian scientist Morozova (1997) reported some unusual linear clouds above land fracture regions. This was the first report about cloud anomaly possibly related to active fault systems. Shou (1999) reported some unusual clouds which looked like they emitted from a point source 5 days prior to the 26 December 2003, M6.6 Bam, Iran, earthquake. Guo and Wang (2008) studied M6.0 and M6.4 Iran strong earthquakes and found that some linear clouds appeared about 2 months before these earthquakes. Wu et al. (2009) reported two linear clouds which pointed to the epicenter prior to the 12 May 2008, M7.9 Wenchuan earthquake of China. Guo and Yang (2013) observed an anomalous linear cloud over Italy on April 23, 2012, and predicted that an M5.5–M6.0 earthquake would hit Italy in the next month. An M6.1 earthquake hit north Italy on 20 May 2012, and verified this prediction (**Figure 1**). Mansouri Daneshvar et al. (2014) found abnormal cloud circulation 1 week prior to the 2013 Iran M7.8 earthquake. Some scientists tried to construct models or use laboratory experiments to explain the mechanism of cloud anomaly (Freund, 2010; Harrison et al., 2014; Pulinets et al., 2015), while the correlation between clouds and earthquakes was still

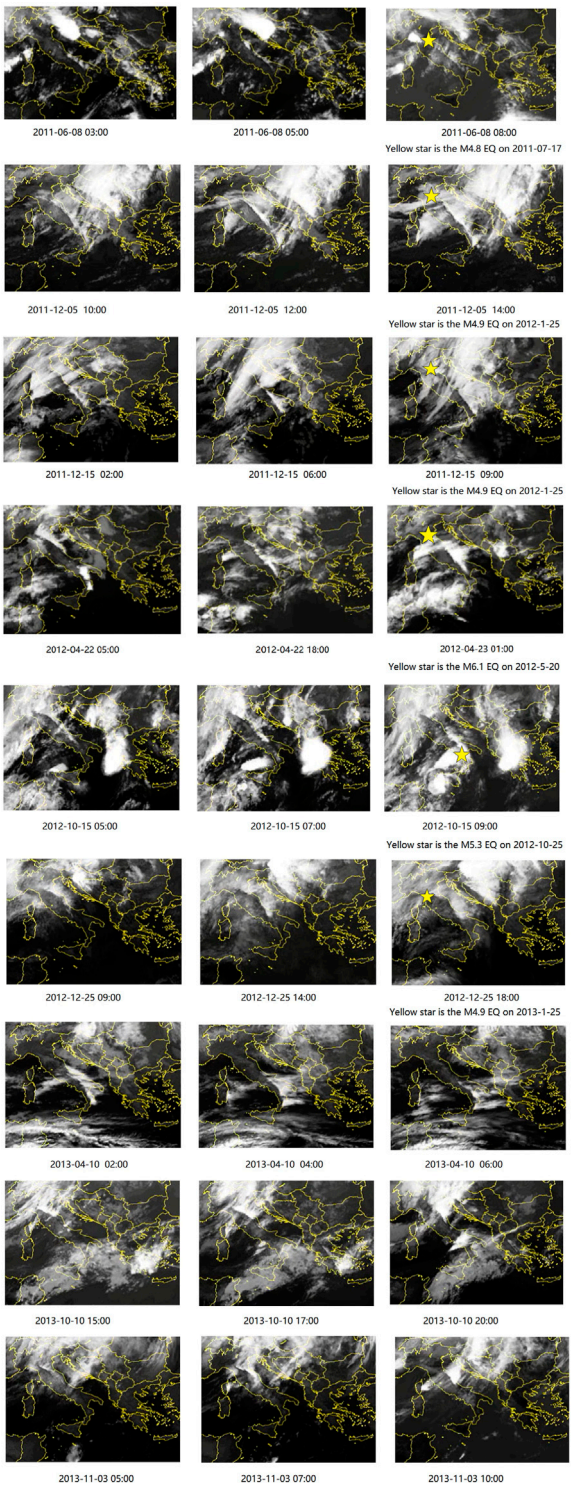

FIGURE 1 | Typical satellite cloud anomalies appeared over Italy main fault systems. The yellow star means the earthquake following the cloud anomaly. Note some cloud anomalies has no earthquake that followed.

controversial, for example, Thomas et al. (2015) studied the M > 5.0 earthquakes and clouds anomaly in Italy and considered there was no significant relation between them. A problem of their research was that they just studied M > 5.0 earthquakes and did not study > M4.0, >M4.5, >M5.5, and >M6.0 earthquakes respectively. It is well known that there are hundreds of small earthquakes in Italy, and few M > 6 earthquakes in 2010–2013, and if a bigger or a smaller threshold is selected, there will be too few or too many earthquakes; this will of course lead to insignificant relation. Guo (2021) introduced just one case study: in particular, it showed how to predict the Emilia M6.1 earthquake with a cloud anomaly. In the present paper, we made instead rigorous statistics to check the relation between earthquakes with different magnitudes and cloud anomalies in 4 years, and we compared with other types of earthquake prediction methods, presenting a significant step forward to earthquake precursor research.

DATA AND METHOD

The cloud data is derived from Thomas et al. (2015) and the sat24 website (**Table 1**). All the stationary clouds which stayed bigger than 3 h are selected as candidate anomalies. Some typical clouds are listed in **Figure 1** and others are listed in supplement files which derived from EUMETSAT. Earthquake data is derived from EMSC (**Table 2**). First we defined two parameters, EQ (earthquake) occurrence rate (EOR) and the anomaly appearance rate (AAR). AAR is defined by the number of EQs which occurred within the leading time interval ΔT after cloud anomaly appearance divided by the total number of EQs, whereas EOR is the number of cloud anomalies which preceded EQs within the same leading time interval ΔT divided by the total number of cloud anomalies. Note that AAR and EOR are equivalent to the alarm rate and success rate in earthquake prediction (Orihara et al., 2012).

TABLE 1 | Cloud anomalies in Italy and their duration in 2010–2013.

Group no	No	Date	Year	Approximate duration (hours)
1	1	June 8	2011	7
2	2	Dec. 5	2011	16
3	3	Dec. 14	2011	18
	4	Dec. 15	2011	12
4	5	April 21–23	2012	34
5	6	May 5–6	2012	9
6	7	Sept. 24–25	2012	13
	8	Sept. 27	2012	22
7	9	Oct. 14–15	2012	12
8	10	Dec. 25	2012	16
9	11	April 10	2013	6
10	12	May 29	2013	9
11	13	Aug. 7–8	2013	10
12	14	Oct. 10	2013	10
	15	Oct. 13	2013	6
13	16	Oct. 28–29	2013	12
14	17	Nov. 3	2013	13
	18	Nov. 4	2013	12
15	19	Nov. 9–10	2013	19
16	20	Nov. 20	2013	6
17	21	Dec. 29	2013	4

TABLE 2 | Earthquakes in 2010–2013 with M ≥ 4.7 in the land area of Italy.

Date and time (UTC)	Latitude (°N)	Longitude (°E)	Magnitude	Depth (km)	Area
2011-07-17 18:30:27	45.01	11.37	M4.8	8	Northern Italy
2012-1-25 8:06:37	44.87	10.51	M4.9	29	Northern Italy
2012-1-27 14:53:12	44.52	10.01	M5.0	72	Northern Italy
2012-5-20 2:03:50	44.90	11.26	M6.1	10	Northern Italy
2012-10-25 23:05:24	39.88	16.02	M5.3	6	Southern Italy
2013-1-25 14:48:18	44.16	10.45	M4.9	20	Northern Italy
2013-2-16 21:16:09	41.71	13.57	M4.9	17	Central Italy
2013-6-21 10:33:56	44.13	10.14	M5.3	7	Northern Italy
2013-7-21 1:32:24	43.51	13.72	M5.0	8	Central Italy
2013-12-29 17:08:43	41.40	14.43	M5.2	20	Southern Italy

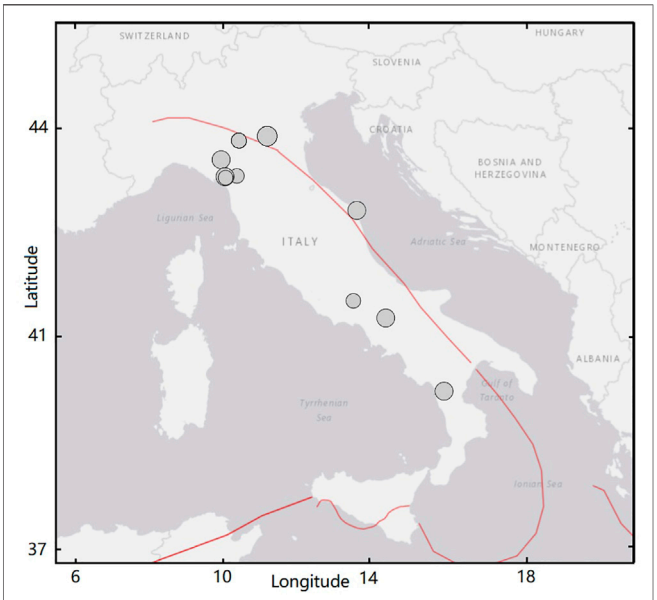

FIGURE 2 | Map of the 10 earthquakes that happened in land of Italy from 2010 to 2013 with M ≥ 4.7. The red line is the main fault systems of Italy.

Second we calculated EOR and AAR for the earthquakes in Italy. Tronin (2000) and Tronin et al. (2002) studied AVHRR satellite thermal infrared data and found thermal anomalies 6–24 days before earthquakes with magnitude bigger than or equal to M4.7. All of the earthquakes bigger than or equal to M4.7 in Italy land area in 2010–2013 were selected from EMSC (http://www.emsc-csem.org). In this period, some events in the Corsica Sea and Ionian Sea were excluded because this study concerns only the land earthquakes. Finally we got the 10 earthquakes listed in **Table 2**, and their epicenters are reported in **Figure 2**.

STATISTICAL ANALYSIS

The aftershocks for the M6.1 earthquake occurred on 20 May 2012, were clustered into one group with the main shock. Similarly we clustered cloud anomalies within three consecutive days into one group and finally got 17 groups of cloud anomalies. **Figure 3** shows the time series of cloud anomalies and earthquakes.

To prove that AAR was not obtained by chance, we compared the actual values of AAR with that of temporally randomly generated EQs. In this study 10 EQs were randomly inserted into 1,461 days (namely 365 × 4 + 1), and 10,000 catalogues were generated by the Mersenne Twister algorithm (Matsumoto et al., 1998). Then AAR was calculated for the randomly generated catalogue for a different leading time interval, and the result is shown in **Figure 4** (top). It was clear that the actual values of AAR were much higher than those expected by chance except $\Delta T \leq 30$ days. For the case of $23 \leq \Delta T \leq 45$ days, it used the minimum time interval, namely 23 days, and got the maximum AAR 70%.

As for EOR, the EQ dates were fixed, 17 cloud anomalies were randomly inserted into 1,461 days, and finally 10,000 model sets were generated by the Mersenne Twister algorithm. The calculated EOR values for these sets for different ΔT are shown in **Figure 4** (bottom). It was also clear that the actual values were much higher than those for random models except $\Delta T \leq 30$ days. For the case of $23 \leq \Delta T \leq 45$ days, it used the minimum time interval, namely 23 days, and got EOR 41.2%. Thus it was statistically demonstrated that the relation between cloud anomaly and Italy land EQs was nearly impossible to be obtained by chance, and some correlation should exist.

We noticed that nearly all the earthquakes of **Table 2** were preceded at least by one anomaly from 23 to 45 days before their occurrence, except three events happened on 2013-1-25, 2013-2-16, and 2013-7-21. The epicentre of the last one was located in the coast of the Adriatic Sea, so the presence of sea-layer could alter the possible mechanism of generation of the precursory anomaly to the atmosphere. The other events of January and February 2013 were characterized by a low magnitude, even if an anomaly has preceded other events of the same energy. The tectonic region of the event of 2013-1-25 is a bit different from the other events, and this could be also a possible reason for the lack of the anomaly in the leading time.

We checked the relationships for cloud anomalies related to leading time T (unit:days), which is the time in advance between the cloud anomaly and the EQ occurrence, and the cloud anomaly duration D (unit:hours) with the EQ magnitude M. The results showed that the relation

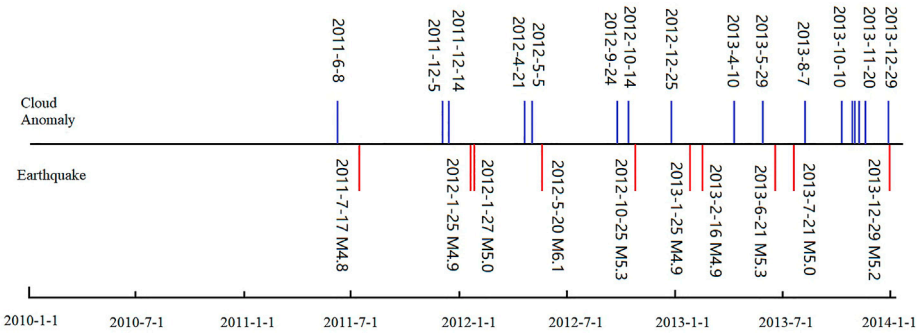

FIGURE 3 | Time series of cloud anomalies and earthquake occurrences in Italy during 2010–2013.

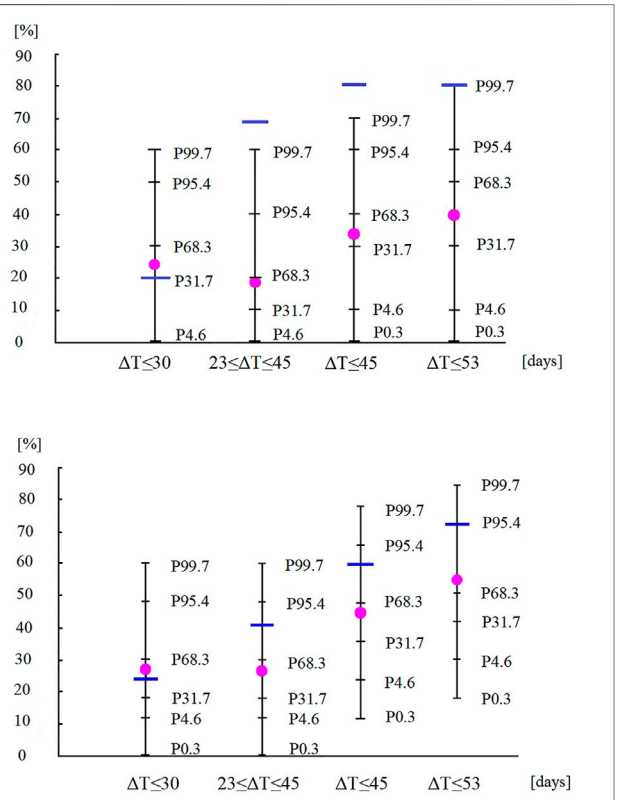

FIGURE 4 | AAR (top) in the randomly generated catalogue and EOR (bottom) in the randomly generated cloud anomalies. Magenta points denote the mean value of the simulated data; short horizontal bars indicate percentiles of simulated data and blue bars indicate the actual value of real data. Clearly the actual values of AAR and EOR are higher than those expected by chance except ΔT≤30 days.

between EQ magnitude and leading time T is not significant. This looks different from previous research results, so more investigations are needed in the future to check this point. While EQ magnitude is found to be strongly related with cloud anomaly duration, and the linear regression equation is D = 22.812M-101.52 with R^2 = 0.6992 (**Figure 5**). An interesting point is, the duration of the cloud anomaly on April 21–23, 2012, is the only one which is bigger than 2δ and 3δ compared with all the cloud duration in 2010–2013, and the earthquake that happened on 20 May 2012, is the biggest one in 2010–2013 (Guo, 2021). This means the cloud anomaly appeared on April 21–23, 2012, is related with the Emilia M6.1 earthquake with very high confidence (>99% level).

Magnitude is usually estimated with ± 0.2 uncertainty, so we also checked the case of M4.5 and M4.9 from EMSC catalogue. If M4.5 threshold is used, there are two more earthquakes that appeared compared to the M4.7 threshold. They are M4.6 in north Italy on 14:41:30, 2012–10–3, and M4.6 in north Italy on 15:01:33, 2013-6-23. The second one is the aftershock of 2013-6-21 M5.3 earthquake, and as we point out in the text, it should be clustered into one group with the main shock, so it does not affect the result. The first earthquake is a new one, so the total number will be 11 earthquakes. Because there is a cloud anomaly on 2012-9-27, which is 6 days before the earthquake, AAR will be 0.727, EOR will be 0.471, both increased. If M4.9 threshold is used, the M4.8 earthquake on 2011-7-17 will be deleted, and then the total number will be nine earthquakes. AAR will be 0.66, and EOR will be 0.35, which is very close to the result of Perrone et al. (2018).

For the USGS catalogue, if M4.7 threshold is used, the total number will be 12 earthquakes. The two new earthquakes are M4.7 in north Italy on 2012-3-5 and M4.7 in central Italy on 2012-3-15, and both have no cloud anomaly. So AAR will be 7/12 = 0.583, and EOR will not change. If M4.9 threshold is used, the M4.8 earthquake (reported by USGS) on 2013-2-16, which has no cloud anomaly, will be deleted, and then the total earthquake number will be 9. AAR is 7/9 = 0.77, EOR will not change. If M4.5 threshold is used, the total number will be 16 earthquakes, then AAR is 11/16 = 0.68, and EOR is 11/17 = 0.64. The statistics for the EMSC catalogue and USGS catalogue show that AAR and EOR are both significant for the case of 23≤ΔT≤45 days. This proves that cloud method is convincing even for different catalogues.

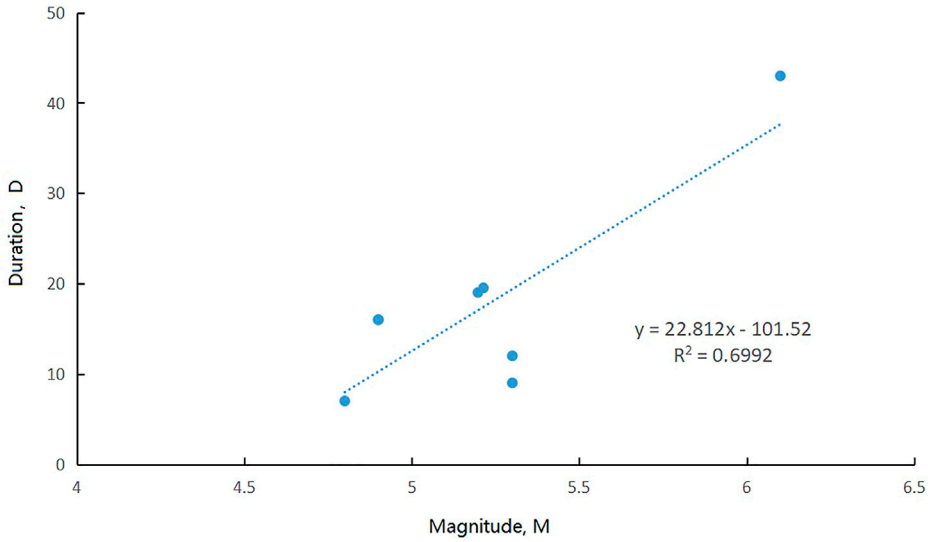

FIGURE 5 | Linear regression of cloud anomaly duration and Magnitude.

TABLE 3 | Error matrix for the statistical evaluation of the cloud anomalies 23–45 days before the M ≥ 4.7 earthquakes in Italy during 2010–2013.

		Earthquake	
		Yes	No
Cloud anomaly	Yes	7	10
	No	3	32
		Total cases 52	

TABLE 4 | Comparison of performance of three methods.

	EOR	AAR	F	ACC (%)
skt	0.4	0.4	0.167	73.9
Ionosphere	0.357	0.5	0.257	68.9
cloud	0.412	0.7	0.238	75.0

FORECAST POSSIBILITIES OF THE METHOD

Table 3 presents the error matrix for the investigated period. The total alerted time is 391 days compared with 1,461 total days, so the ratio is 26.7%. The time windows without cloud anomalies which are not followed by an earthquake is estimated as the number of not-alerted days (i.e., 1,070) divided by the width of the alerted window (23 days) and subtracting the three not-predicted earthquakes. Based on this table it is possible to define the overall accuracy of the method as the sum of the total correct case (earthquake preceded by cloud anomaly in the proper time + absence of cloud anomaly and earthquake) divided by the total case (Fawcett, 2006), and it is equal to 75% which indicates that the method is better than a prediction made by chance that would give 50% of accuracy.

To compare the performance of cloud method and other methods, we selected two research reports made by Piscini et al. (2017) and Piscini et al. (2017). Perrone et al. (2018) analysed skin temperature (skt), total column water vapour, and total column of ozone changes before five earthquakes in central Italy between July and October from 1994 to 2016. Perrone et al. (2018) analysed ionospheric anomalies and 15 earthquakes with M ≥ 6.0 in the Greece area from 2003 to 2015. The EOR, AAR, the False alarm rate (F) and the overall accuracy (Acc) of these three methods are listed in **Table 4**. The false alarm rate is the number of anomalies without a following earthquake divided by the total alarm; the closer to 0, the better the value. In our case F = 10/(10 + 32) = 0.238.

Table 4 shows that all the three methods provide similar EOR ranging from 0.357 to 0.412, and similar overall accuracy ranging from 68.9% to 75%. The false alarm rate of cloud method (0.238) is similar to that of ionosphere method (0.257), but a little higher than that of skt method (0.167). A clear difference is that the AAR of cloud method is bigger than that of the other two methods. It means that cloud method shows a better performance. If these three methods are combined together, as Piscini et al. (2017) did and combined three kinds of climate data, the final performance will increase greatly.

Japan scientists Orihara et al. (2012) used Greece VAN method (Varotsos et al., 1986) to monitor the telluric current signals observed in Kozu-Shima Island of Japan. They got 19 anomalies and 23 earthquakes in 1,139 days, and 11 quakes were preceded by a telluric current anomaly. The average earthquake frequency for this area was 1,139/23 = 49.52 days. They found that the best correlation existed for the case of $\Delta T \leq 30$ days, so the time ratio is 30/49.52 = 0.606. Our method got 17 anomalies and 10 earthquakes in 1,461 days in Italy, and seven earthquakes were preceded by cloud anomalies for the case of $23 \leq \Delta T \leq 45$ days. The average earthquake frequency was 1,461/10 = 146.1 days. Our

leading time interval was 23 days, and then the ratio was 23/146.1 = 0.157. It was much smaller than the alarm window of Japan scientists' telluric current method (0.606). This means cloud method used a shorter leading time interval and gave a better performance than telluric current method.

DISCUSSION

Thomas et al. (2015) studied the relation between clouds and earthquakes in Italy with Kuiper test method, and they considered that there was no significant relation between clouds and $M \geq 5.0$ earthquakes. In their research they set an integer M5.0 as threshold without reasonable reason, and this subjective data selection strategy would lead to different conclusion; another problem was that Kuiper test will underestimate the result when many aftershocks appeared. Here we used EOR and AAR model and proved that clouds anomaly had significant relation with $M \geq 4.7$ earthquakes in the Italy land area. These two models are widely accepted by the seismic community, and the threshold is selected based on previous studies which are widely used in thermal anomaly research, so the result is convincing.

Preseismic clouds could be mixed with orographic clouds. Someone may consider that when water vapor travels from sea to Italy land area, it climbs up the mountains and the clouds form when the temperature decreases. Satellite data show that the altitude of preseismic clouds is about 10,000 m, while the Italy Appenin mountains are just about 2000 m high (for example, the highest Appenin Mount is 2,492 m). If the water vapor climbs up the mountains from sea surface to 2000 m, then it cannot rush to an altitude of about 10,000 m. So a new physical mechanism needs to be involved, and the seismic source could be one. Scientists have put forward some possible mechanisms, for example, Japanese scientists Teramoro and Ikeya (2000) used 4 kv/m electric field in a Wilson's cloud chamber and produced some linear clouds. American scientists (Freund et al., 2007; Freund, 2010) found that electronic charge carriers would be activated when rocks were stressed, and this would create an electric field which could be strong enough to ionize air molecules. The airborne ions could act as condensation nuclei for water droplets and then lead to fogs and clouds. British scientists (Harrison et al., 2014) used Atmospheric Lithosphere-Ionosphere Charge Exchange (ALICE) model to show that the global circuit conduction current can connect surface air ionisation changes to the properties of the cloud above in semi-fair weather directly. Pulinets et al. (2015) proposed a LAI (Lithosphere-Atmosphere-Ionosphere) coupling model and tried to explain this phenomenon by a complex chain of sub-processes starting from the release of ionized particles from the stressed fault. They considered that radon gas would emit from activated faults, and the vertical electric field above the faults supports the linear structure of cluster ion flows which leaded to the formation of anomalous linear clouds. All these studies from different countries provide some possible physical mechanism which connected active fault, electric field, and cloud anomaly.

CONCLUSION

In this paper we used 4 year satellite data and a statistics model and provide a strong evidence that clouds had significant relation with earthquakes in the Italy land area in 2010–2013. Our result showed that when the leading time interval was set to $23 \leq \Delta T \leq 45$ days, seven of the total 10 earthquakes were preceded by cloud anomalies. The methods alerted a relative short time window (26.7%) and gave an overall accuracy equal to 75%. The disadvantage of this method was that the cloud anomaly was very long and it cannot estimate the epicenter location accurately. So here we suggested combing some other geophysical data and method such as VAN method (Varotsos et al., 1986), latent heat flux method (Dey and Singh, 2003), satellite thermal method (Pulinets et al., 2014), magnetic method (De Santis et al., 2017), etc. to increase the prediction accuracy. For example, Qin et al. (2012) found thermal anomaly appeared in north Italy on 12 May 2012, and if combined with the cloud anomaly which appeared on April 23, 2012, then the prediction accuracy could be promoted greatly. In future development, cloud method could be applied to other areas to test where and if it can be applied.

DATA AVAILABILITY STATEMENT

The original contributions presented in the study are included in the article/**Supplementary Material**, further inquiries can be directed to the corresponding author.

AUTHOR CONTRIBUTIONS

The author confirms being the sole contributor of this work and has approved it for publication.

FUNDING

This work was supported by Natural Science Foundation of Henan (182300410141).

ACKNOWLEDGMENTS

Four reviewers gave valuable comments and suggestions on this paper. Their kind help is greatly appreciated.

SUPPLEMENTARY MATERIAL

The Supplementary Material for this article can be found online at: https://www.frontiersin.org/articles/10.3389/feart.2022.812540/full#supplementary-material

REFERENCES

De Santis, A., Balasis, G., Pavón-Carrasco, F. J., Cianchini, G., and Mandea, M. (2017). Potential Earthquake Precursory Pattern from Space: the 2015 Nepal Event as Seen by Magnetic Swarm Satellites. *Earth Planet. Sci. Lett.* 461, 119–126. doi:10.1016/j.epsl.2016.12.037

Dey, S., and Singh, R. P. (2003). Surface Latent Heat Flux as an Earthquake Precursor. *Nat. Hazards Earth Ssyst. Sci.* 3, 749–755. doi:10.5194/nhess-3-749-2003

Fawcett, T. (2006). An Introduction to ROC Analysis. *Pattern Recognition Lett.* 27, 861–874. doi:10.1016/j.patrec.2005.10.010

Freund, F. (2010). Toward a Unified Solid State Theory for Pre-earthquake Signals. *Acta Geophys.* 58 (5), 719–766. doi:10.2478/s11600-009-0066-x

Freund, F. T., Takeuchi, A., Lau, B. W. S., Al-Manaseer, A., Fu, C. C., Bryant, N. A., et al. (2007). Stimulated Infrared Emission from Rocks: Assessing a Stress Indicator. *eEarth* 2, 7–16. doi:10.5194/ee-2-7-2007

Guo, G. (2021). A Retrospective Analysis about the Italy Emilia M6.0 Earthquake Prediction. *Ojer* 10, 68–74. doi:10.4236/ojer.2021.102005

Guo, G. M., and Yang, J. (2013). Three Attempts of Earthquake Prediction with Satellite Cloud Images. *Nat. Hazards Earth Syst. Sci.* 13, 91–95. doi:10.5194/nhess-13-91-2013

Guo, G., and Wang, B. (2008). Cloud Anomaly before Iran Earthquake. *Int. J. Remote Sensing* 29, 1921–1928. doi:10.1080/01431160701373762

Harrison, R. G., Aplin, K. L., and Rycroft, M. J. (2014). Brief Communication: Earthquake-Cloud Coupling through the Global Atmospheric Electric Circuit. *Nat. Hazards Earth Syst. Sci.* 14, 773–777. doi:10.5194/nhess-14-773-2014

Mansouri Daneshvar, M. R., Tavousi, T., and Khosravi, M. (2014). Synoptic Detection of the Short-Term Atmospheric Precursors Prior to a Major Earthquake in the Middle East, North Saravan M 7.8 Earthquake, SE Iran. *Air Qual. Atmos. Health.* 7, 29–39. doi:10.1007/s11869-013-0214-y

Matsumoto, M., Nishimura, T., and Mersenne, T. A. (1998). Mersenne Twister. *ACM Trans. Model. Comput. Simul.* 8 (1), 3–30. doi:10.1145/272991.272995

Morozova, L. I. (1997). Dynamics of Cloudy Anomalies above Fracture Regions during Natural and Anthropogenically Caused Seismic Activities. *Fizika Zemli* 9, 94–96.

Orihara, Y., Kamogawa, M., Nagao, T., and Uyeda, S. (2012). Preseismic Anomalous Telluric Current Signals Observed in Kozu-Shima Island, Japan. *Proc. Natl. Acad. Sci. U S A.* 109, 19125–19128. doi:10.1073/pnas.1215669109

Perrone, L., De Santis, A., Abbattista, C., Alfonsi, L., Amoruso, L., Carbone, M., et al. (2018). Ionospheric Anomalies Detected by Ionosonde and Possibly Related to Crustal Earthquakes in Greece. *Ann. Geophys.* 36, 361–371. doi:10.5194/angeo-36-361-2018

Piscini, A., De Santis, A., Marchetti, D., and Cianchini, G. (2017). A Multi-Parametric Climatological Approach to Study the 2016 Amatrice-Norcia (Central Italy) Earthquake Preparatory Phase. *Pure Appl. Geophys.* 174 (10), 3673–3688. doi:10.1007/s00024-017-1597-8

Pulinets, S. A., Morozova, L. I., and Yudin, I. A. (2014). Synchronization of Atmospheric Indicators at the Last Stage of Earthquake Preparation Cycle. *Res. Geophys.* 4 (1), 45–50.doi:10.4081/rg.2014.4898

Pulinets, S. A., Ouzounov, D. P., Karelin, A. V., and Davidenko, D. V. (2015). Physical Bases of the Generation of Short-Term Earthquake Precursors: A Complex Model of Ionization-Induced Geophysical Processes in the Lithosphere–Atmosphere– Ionosphere–Magnetosphere System. *Geomagnetism and Aeronomy* 55 (4), 540–558. doi:10.1134/s0016793215040131

Qin, K., Wu, L. X., De Santis, A., and Cianchini, G. (2012). Preliminary Analysis of Surface Temperature Anomalies that Preceded the Two Major Emilia 2012 Earthquakes (Italy). *Ann. Geophys.* 55, 823–828. doi:10.4401/ag-6123

Shou, Z. H. (1999). Earthquake Clouds, a Reliable Precursor. *Sci. Utopya* 64, 53–57.

Teramoro, K., and Ikeya, M. (2000). Experiment Study of Cloud Formation by Intense Electric fields. *J. Appl. Phys.* 5, 2876–2881. doi:10.1143/JJAP.39.2876

Thomas, J. N., Masci, F., and Love, J. J. (2015). On a Report that the 2012 M 6.0 Earthquake in Italy Was Predicted after Seeing an Unusual Cloud Formation. *Nat. Hazards Earth Syst. Sci.* 15, 1061–1068. doi:10.5194/nhess-15-1061-2015

Tronin, A. A., Hayakawa, M., and Molchanov, O. A. (2002). Thermal IR Satellite Data Application for Earthquake Research in Japan and China. *J. Geodynamics* 33, 519–534. doi:10.1016/s0264-3707(02)00013-3

Tronin, A. A. (2000). Thermal IR Satellite Sensor Data Application for Earthquake Research in China. *Int. J. Remote Sensing* 21, 3169–3177. doi:10.1080/01431160050145054

Varotsos, P., Alexopoulos, K., Nomicos, K., and Lazaridou, M. (1986). Earthquake Prediction and Electric Signals. *Nature* 322, 120. doi:10.1038/322120a0

Wu, L. X., Li, J. P., and Liu, S. J. (2009). "Space Observed Two Abnormal Linear Clouds before Wenchuan Earthquake," in Proceedings of the 3rd IASME/WSEAS International Conference of Geology and Seismology. February 24-26, 2009. Cambridge, United Kingdom, 138–143.

Conflict of Interest: The author declares that the research was conducted in the absence of any commercial or financial relationships that could be construed as a potential conflict of interest.

frontiers in Earth Science

ORIGINAL RESEARCH
published: 04 March 2022
doi: 10.3389/feart.2022.823540

Variation of Thermal Infrared Brightness Temperature Anomalies in the Madoi Earthquake and Associated Earthquakes in the Qinghai-Tibetan Plateau (China)

Xing Yang[1], Tie-bao Zhang[1], Qian Lu[1], Feng Long[1], Ming-jian Liang[2], Wei-wei Wu[2], Yue Gong[1], Jia-xi Wei[3] and Jia Wu[4]*

[1]Sichuan Earthquake Administration, Chengdu, China, [2]Chengdu Institute of the Tibetan Plateau Earthquake Research, CEA, Chengdu, China, [3]Chengdu Earthquake Monitoring Center Station, Chengdu, China, [4]Xichang Earthquake Monitoring Center Station, Xichang, China

OPEN ACCESS

Edited by:
Giovanni Martinelli, National Institute of Geophysics and Volcanology, Italy

Reviewed by:
Zheming Shi, China University of Geosciences, China
Dedalo Marchetti, Jilin University, China

***Correspondence:**
Tie-bao Zhang
81621214@qq.com

Specialty section:
This article was submitted to Environmental Informatics and Remote Sensing, a section of the journal Frontiers in Earth Science

Received: *27 November 2021*
Accepted: *17 February 2022*
Published: *04 March 2022*

Citation:
Yang X, Zhang T-b, Lu Q, Long F, Liang M-j, Wu W-w, Gong Y, Wei J-x and Wu J (2022) Variation of Thermal Infrared Brightness Temperature Anomalies in the Madoi Earthquake and Associated Earthquakes in the Qinghai-Tibetan Plateau (China). Front. Earth Sci. 10:823540. doi: 10.3389/feart.2022.823540

We processed MODIS data received from ground receiving stations into the spatial range of the Qinghai-Tibetan Plateau (China) and the eastern margin of the plateau, and then 283 K was set as the threshold value to remove the area covered by clouds. The monthly background field was calculated based on 17 years' data, then we obtained the spatial Brightness Temperature anomaly of the current month by deducting the background field. Furthermore, the Brightness Temperature anomaly curves for secondary tectonic blocks in the plateau were calculated. The data indicated that since June 2020, the Brightness Temperature radiation within the Qinghai-Tibetan Plateau began to increase abnormally, starting from the western part of the study area and expanding eastward to cover the entire plateau. In January 2021, such an anomaly was seen again, extending to the Sichuan-Yunnan Block in the easternmost part of the study area in april. With the ongoing anomaly, a series of moderate and strong earthquakes occurred in the Qinghai-Tibetan Plateau, and finally, on 22 May 2021, the *M*7.4 earthquake struck the Madoi County. Moreover, according to the internal Brightness Temperature time series curves of the different secondary tectonic blocks, the Brightness Temperature has increased simultaneously since the beginning of 2020. A twofold standard deviation was found in the middle-east segment of the Bayanhar Block and the Qiangtang Block in October 2020, and an almost twofold standard deviation was found in March, while a twofold standard deviation was found in the Sichuan-Yunnan Block in april 2021. The occurrence of earthquakes in the plateau before the Madoi earthquake coincided with an upward trend of the time series curve. The spatial anomaly of Brightness Temperature over the Qinghai-Tibetan Plateau disappeared and the Brightness Temperature time series curve dropped drastically after the Madoi earthquake. The development of spatial anomaly of Brightness Temperature and the time series curve both coincide with the occurrence of earthquakes and are consistent with the generation of tectonic stress in the Qinghai-Tibetan Plateau. Our study showed that thermal infrared Brightness Temperature radiation reasonably reflects regional stress development and enables the detection of anomalies prior to moderate and strong earthquakes.

Keywords: MODIS, brightness temperature, radiation anomaly, spatial and temporal anomalies, time series analysis

INTRODUCTION

Since the 1980s, thermal infrared data collected by an observation of the satellite platform was used to obtain abnormal information prior to earthquakes (Gorny et al., 1988). Significant thermal infrared radiation anomalies are usually recognized prior to moderate and strong earthquakes all over the world. Compared with conventional methods used to obtain information on earthquake anomalies, data collection *via* satellites is not limited by time and space, and they provide data with high spatial and temporal resolution worldwide. Moreover, satellite detection is less affected by ground factors, such as human activities or the stability of observation instruments on the ground, thus providing reliable and continuous observation results. Satellites can also be used to collect earthquake anomalies through a model integrating multiple means, multiple parameters, and multiple layers. As a consequence, ground surface parameters including temperature, outgoing long-wave radiation, and thermal infrared radiation can be detected (Ouzounov et al., 2004, Ouzounov et al., 2007; Tronin et al., 2002, Tronin et al., 2004; Rawat et al., 2011). Besides those ground surface parameters, atmospheric water vapor, CO_2, CH_4, CO, and other parameters can be monitored (Cui et al., 2011; Dey et al., 2004; Feng et al., 2020; Hayer et al., 2016; Weiyu et al., 2018; Wang et al., 2015; Zhong et al., 2020). The analysis of ground surface parameters prior to earthquakes in different areas revealed that temperature rise occurred in a large area around the epicenter and its vicinity several months to a week before the onset of the earthquake (Cervone et al., 2006; Tronin et al., 2002, Tronin et al., 2004; Pulinets et al., 2006; Xiong et al., 2010). Furthermore, significant anomalies in outgoing long-wave radiation were observed (Gruber et al., 1984; Ouzounov et al., 2007; Rawat et al., 2011; Kane, 2008; Zhang et al., 2017). Among the atmospheric parameters, the concentrations of CO_2, CH_4, and other gases increased in the seismic breeding zone prior to the earthquake due to underground gas overflow within this region. Such an anomaly often occurred several months to several weeks before the earthquake, and in some areas, a sudden rise in the impending stage was recorded (Corradini et al., 2010; Pardini et al., 2017; Theys et al., 2019; Feng et al., 2020).

With the increase of the monitored parameters, research methods for the reasonable interpretation of the data have been developed. Among them, eddy field, wavelet maxima, and power spectrum methods are used widely (Gruber et al., 1984; Saraf et al., 2008; Xiong et al., 2010). Based on the eddy field method, information about abnormal processes in the studied region can be obtained when the spatial resolution of data is low. For example, the outgoing longwave radiation data of NOAA(National Oceanic and Atmospheric Administration) documented different degrees of anomalies before many earthquakes worldwide (Gruber et al., 1984; Saraf et al., 2008; Xiong et al., 2010). The Wavelet Maxima method can be used to collect clear anomalies in the time domain. based on this method, interference phenomena caused by non-earthquake factors can be excluded, and the time of an anomaly result from the earthquake can be determined accurately (Cervone et al., 2004, Cervone et al., 2005; He et al., 2014; Saradjian et al., 2011; Xiong et al., 2010). The power spectrum method enables to analyze the data spectrum, which is a reliable method that was applied to monitor earthquakes for example in the eastern margin of the Qinghai-Tibetan plateau in China (Zhong et al., 2020).

The above methods and data have been successfully used and provided reasonable results in the study of earthquake anomalies all over the world. However, most studies are limited by the duration of available data. Usually, the data used in the studies are collected within 3–5 years or even within a shorter period. The limited time often complicates the modeling of a solid background field of the studied seismic breeding area. In this research, we take into account a long duration of time and try to use the Brightness Temperature (BT) as the parameter to find anomalies before earthquakes. Even thermal infrared brightness temperature was used in previous studies to detect the anomalies before earthquakes. However, only few studies have used BT data collected by Moderate-resolution Imaging Spectroradiometer (MODIS). The satellite of the MODIS sensor has operated in the orbit for more than 20 years, producing an enormous number of observation results, which requires huge storage space and supports from a long-time follow-up analysis. In the present study, the major *M7.4* Madoi earthquake on 22 May 2021, and several moderate to strong earthquakes in the Qinghai-Tibetan Plateau from June 2020 (**Table 1**), were analyzed with BT data, collected by MODIS for nearly 17 years, to detect the variation of BT in two dimensions (space and time) and determine the possible anomalies. Based on the data we propose a refined model for the evolution of the Madoi earthquake.

Data and Methodology

Dataset

Moderate-resolution Imaging Spectroradiometer (MODIS) is a sensor on the TERRA and AQUA satellites. TERRA was launched in 1999 and AQUA in 2002. The orbital altitude of both satellites is 705 km, with a coverage area (Swath Dimensions) of 2,330 km^2. The spatial resolution ranges from 250 to 1,000 m and the observed waveband length is from 0.405 to 14.385 μm. The two satellites can observe both the atmosphere and ground surface.

Data Processing

In 2004, our research team established the satellite ground receiving station to constantly receive data from MODIS. The ground radio antenna could receive the satellite data on time every day, and the ground equipment also includes other receiving and data processing devices. We developed a software system equipped with geometric correction, radiometric correction, and other functions that enables the complete data clipping, splicing, and other operations and the conversion of the original data into thermal radiation BT. In the present study, we focus on earthquakes that occurred in the Qinghai-Tibetan Plateau (from June 2020 to May 2021). As the Qinghai-Tibetan Plateau was extruded by the Indian plate, the plateau migrated eastward and the stress was concentrated on the eastern margin of the Qinghai-Tibetan Plateau. The study area of this research covers the entire Qinghai-Tibetan Plateau (70°–110°E, 20°–45°N) and its eastern margin (90°–110°E,

TABLE 1 | Data of moderate and strong earthquakes in the Qinghai-Tibetan Plateau (2020.06–2021.05).

Time	Epicenter	Magnitude	Longitude	Latitude	Focal depth (km)
2020-06-26	Hetian	*M*6.4	82.33°E	35.73°N	10
2020-07-23	Nima	*M*6.6	86.81°E	33.19°N	10
2021-03-19	Biru	*M*6.1	92.74°E	31.94°N	10
2021-03-30	Shuanghu	*M*5.8	87.68°E	34.38°N	10
2021-05-21	Yangbi	*M*6.4	99.87°E	25.67°N	8
2021-05-22	Madoi	*M*7.4	98.34°E	34.59°N	17

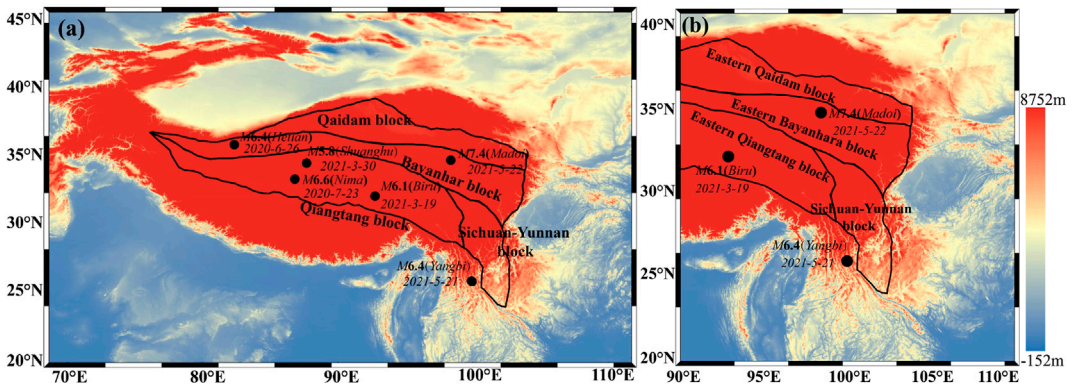

FIGURE 1 | Distribution of earthquakes (active from 2020.06 to 2021.05) with $M \geq 5.8$ in **(A)** the Qinghai-Tibetan Plateau and **(B)** its eastern margin.

20°–40°N; **Figure 1**). Because the plateau's move creates different secondary tectonic blocks, we only take the eastern margin of the Plateau (90°–110°E, 20°–40°N) as the time series tracking area. The schematic map of the two study areas and the distribution of earthquakes with $M \geq 5.8$ that occurred during the studied period is presented in **Figure 1**, and the information related to earthquakes is summarized in **Table 1**.

Brightness temperature is the temperature at which a black body in thermal equilibrium with its surroundings would have to be in order to duplicate the observed intensity of a grey body object at a frequency ν. The BT is not a temperature as ordinarily understood. It characterizes radiation, and depending on the mechanism of radiation can differ considerably from the physical temperature of a radiating body (Bates et al., 1996; Wu et al., 2013). In the BT conversion **formula (1)**, T_b is the Brightness Temperature, T is the actual temperature, C_2 is the Planck constant, λ is the wavelength, $\varepsilon_{\lambda,T}$ is the brightness ratio when the wavelength is λ.

$$T_b = \frac{C_2 T}{C_2 - \lambda T \cdot \ln \varepsilon_{\lambda,T}} \tag{1}$$

Eight wave bands, including 1–2, 20–23, and 31–32, were selected in the beginning of our study for BT inversion. Our data indicate that the 21-band provided the best response effect to the anomalies before the earthquake in the subsequent experiments where the historical earthquakes in the target areas were summarized. The wavelength of 21-Band is 3.93–3.99 *um*, as well as the spatial resolution of Band-21 is 1,000 m. Band-21 locates in the range of thermal infrared, it is profoundly sensitive to surface infrared radiation and the temperature of the cloud's canopy. As TERRA is an optical satellite, the collected data need to be processed by cloud removal. MODIS uses the maximum value on one pixel in some time past as the observed value of the pixel on the one-phase data in the production process. This method was used as a reference in this study. The following procedure was applied to process the data: 1) The receiving station obtained the original data, which were subject to geometric and radiometric corrections in the processing system. Data of the study areas were clipped and converted into the BT data. 2) The daily data of the two study areas were obtained by splicing the clipped data. 3) After several tests, we recognize that in the process of removing clouds, multi-day data synthesized with a step size of 4 days after cloud removal could ensure the reliability of ground surface information and effectively remove cloud occlusion. 4) 283 K was set as the threshold, and cloud removal was repeatedly performed on the synthesized data of 4 days. Pixel with a lower value than the threshold was removed and only those higher than the threshold were used. After completion of this procedure, the BT data within the study areas were obtained (**Figure 2**). **Figures 2A,B** is shown by RGB format in order to highlight the cloud, the white in the Figs indicates the cloud; on the other hand, the black part in **Figure 2C** indicates the area without clouds cover, and the white is the cloud-removed area.

Methods

The Qinghai-Tibetan Plateau was uplifted (about starting in the Late Cretaceous and till to Late Eocene) after being extruded by the Indian subcontinent. Therefore, the internal ingredients and

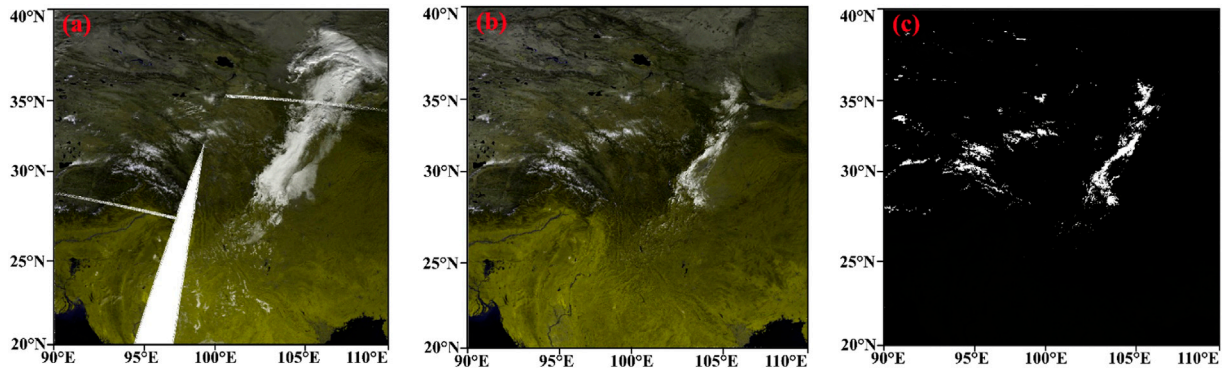

FIGURE 2 | MODIS BT Images of the eastern margin of the Qinghai-Tibetan Plateau. **(A)** Single-day data splicing, **(B)** 4-days data splicing (The white in the figures almost indicates the cloud, the green is the region without cloud and the black represents the water), **(C)** Data after cloud removal (The white region is the cloud-removed area).

materials of the Qinghai-Tibetan Plateau migrated eastward, research shows that the speed of the plate is 50–60 mm/year (Tapponnier et al., 2001; Zhang et al., 2004). This migration is also based on the background of the eastward movement of the Eurasian plate, the GPS result demonstrated that the speed of the velocity field with respect to the Eurasian plate is 45 mm/year (Wang et al., 2020). The Tectonic deformation in continental China is mainly associated with the collision between the Indian and Eurasian plates. The northward indentation of the Indian plate has resulted in a continental deformation belt which is the most active, complex, and broad in the world (Xu et al., 2016; Wang et al., 2020). This migration process caused the formation of many secondary tectonic blocks inside the plateau (Tapponnier et al., 2001; Zhang et al., 2004; Chen et al., 2010), such as the Qiangtang Block and the Bayanhar Block. The eastward migration of the Qinghai-Tibetan Plateau was stopped by the eastern continental block (Southern China Block). The migration direction, therefore, turned to the south, again causing the generation of secondary tectonic blocks, such as the Sichuan-Yunnan Block (**Figure 3**). Due to the southward turning, the secondary blocks have the characteristics of right-handed movement in the east. Due to the intense tectonic activity, this east part is prone to *M*7.0 earthquakes in the past decade, including a series of recent strong earthquakes (**Figure 3**): Wenchuan *M8.0* in 2008, Yushu *M7.1* in 2012, and *M7.0* Jiuzhaigou in 2017. The Madoi *M7.4* on 22 May 2021, the topic of the present study, and earlier moderate-strong earthquakes in the previous year (from June 2020) also occurred in this context.

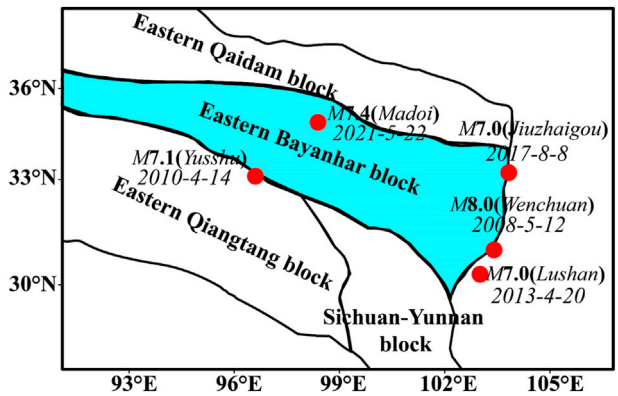

FIGURE 3 | Schematic map showing secondary tectonic blocks on the eastern margin of the Qinghai-Tibetan Plateau and the distribution of strong earthquakes after 2008.

Spatial Tracking of BT Anomalies

In the present study, we focus on the Qinghai-Tibetan Plateau and its eastern margin. Based on 17 years of data collected by the ground station with natural months as the time step, the monthly background field was calculated by the average value method, the same month's data in every year was added together then divided by 17, so finally, we have 12 monthly background fields. Subsequently, the BT anomaly was obtained after the background field was subtracted from the BT data of the study area (70°-110°E, 20°-45°N) from June 2020 to September 2021. In this way, the BT spatial anomalies in the study area were calculated, respectively. The anomaly was calculated by **formula (2)**, where S_t is the BT anomaly of the *t(th)* month, $S(x, y, t)$ represents the BT of the *t(th)* month in the entire study region, $S(x, y, t_i)$ represents the BT of the *t(th)* previous month, *i(th) is the* year, and *n* represents the number of years.

$$S_t = S(x, y, t) - \frac{\sum_{i=1}^{n} S(x, y, t_i)}{n} \quad (2)$$

Time Series Tracking of Secondary Blocks

In previous studies, some extracted data from a certain range near the epicenter for time series analysis, while others did so in the entire study area. The former failed to consider that the anomaly might not occur near the epicenter, whereas the latter might include the non-anomaly area in the calculation, thus weakening the anomaly information. Considering the

geodynamic evolution, the overall force status of the Qinghai-Tibetan Plateau varies across the area, roughly with 90°E as the boundary. Due to the extrusion of the Indian subcontinent, the stress in the west of the 90°E showed a tendency to continue with a northward movement, whereas in the east of the 90°E the stress continued in an eastward direction (Chen, YT, et al., 1996; Hui et al., 2012; Wu et al., 2020), causing the eastern edge of the Qinghai-Tibetan Plateau to become the front end of power transmission. Consequently, tectonic activity is concentrated in this area. Therefore, this area represents the cumulative development of stress prior to the earthquake and the afterward adjustment of the stress. Moreover, several secondary tectonic blocks were formed during the action of stress in the eastern margin area, including the Eastern Bayanhar Block, the Eastern Qiangtang Block, and the Sichuan-Yunnan Block (**Figure 3**). Therefore, considering these secondary tectonic blocks of the eastern part as a unit, the time series curve of BT in the unified block was calculated. Specifically, after the background field of BT was deducted based on the data of 17 years, the time series curve of BT was obtained with the twofold standard deviation as the threshold line of anomaly determination (**Formula (3)**). In the equation, $S_{i,ST}$ represents the BT difference value of the secondary block at a time i, $S_{i,obs}$ is the BT observation value of the block at the time i, and $S_{i,bag}$ is the BT background value of the block at the time i. When $S_{i,ST}$ exceeded the twofold standard deviation, it was regarded as BT anomaly information.

$$S_{i,ST} = S_{i,obs} - S_{i,bag} \tag{3}$$

Results

Characteristics of Spatial Anomaly Evolution Before Earthquakes

Figures 4A-L show the images of BT anomalies in the Qinghai-Tibetan Plateau from June 2020 to May 2021, thus 12 months in total. In this period, the Hetian *M6.4* earthquake (26 June 2020), Nima *M6.6* earthquake (23 July 2020), Biru *M6.1* earthquake (19 March 2021), Shuanghu *M5.8* earthquake (30 March 2020), Yangbi *M6.4* earthquake (21 May 2021), and Madoi *M7.4* earthquake (22 May 2021) occurred. The diagrams clearly demonstrate that the BT anomalies develop from the western part to the eastern part of the Qinghai-Tibetan Plateau, evident from the gradual increase of the BT intensity. The Hetian *M6.4* earthquake occurred in June 2020. In July 2020, BT anomalies are observed in the Indian subcontinent and the western part of the Qinghai-Tibetan Plateau, with the enhancement of more than about 4 K. The area of radiation anomaly in the western part of the Plateau alone attained around 500,000 km^2. Moreover, the Nima *M6.6* earthquake occurred at the margin of the area where BT anomalies occurred in July (**Figure 4B**). In August (**Figure 4C**), the radiation anomaly continued to develop eastward, with the radiation area further increasing up to 800,000 km^2, extending to the southern margin of the Qinghai-Tibetan Plateau and the western Kunlun Mountains. In September, BT anomalies basically occupied the entire western region of the Qinghai-Tibetan Plateau, with an area of about 1.7 million km^2 (**Figure 4D**). In October, the anomalies had covered the entire Plateau and even developed into the northern Sichuan-Yunnan Block (**Figure 4E**), occupying an area of about 3.1 million km^2. In November, the area of radiation anomaly decreased obviously and only affected some parts of the Qinghai-Tibetan Plateau (**Figure 4F**). In December, the anomalies basically disappeared (**Figure 4G**). However, since January 2021, BT radiation anomaly reappeared, covering the Qinghai-Tibetan Plateau and the Tarim Basin, covering an area of nearly 3 million km^2 (**Figure 4H**). This increase continues in February 2021, with the distribution expanding to the eastern part of the Mongolian Plateau and the Qilian Mountains (**Figure 4I**). The anomaly range basically covered half of the study areas, occupying about 6.5 million km^2. In March 2021, the enhanced radiation range was reduced, but it still dominated the Qinghai-Tibetan Plateau. In this month, Biru *M6.1* earthquake and Shuanghu *M5.8* earthquake occurred in the Plateau, with an interval of only 11 days (**Figure 4J**). By april 2021, such an anomaly disappeared in the Qinghai-Tibetan Plateau, but shifted southward to the northern part of the Sichuan-Yunnan Block, covering an area more than 300,000 km^2 (**Figure 4K**). In May 2021 the spatial BT radiation anomaly vanished but the Yangbi *M6.4* earthquake occurred in the southwestern Sichuan-Yunnan Block, and then the Madoi *M7.4* earthquake occurred in the eastern Bayankala Block almost in the same time (**Figure 4L**), with an interval of less than 5 h (on May 21 and 22, respectively).

Characteristics of the Post-earthquake Spatial Evolution

It has been mentioned in the former context that the eastern margin of the Qinghai-Tibetan Plateau (20°N~40°N, 90°E~110°E) became a center for the concentration of stress due to the tectonic evolution of the plateau. The present study was conducted to analyze the changes of the post-earthquake BT radiation in this area. **Figure 5** highlights the evolution of the regional BT anomaly in the eastern margin of the Qinghai-Tibetan Plateau from June to September 2021. The maps indicate that the BT anomalies disappeared in space since the beginning of June 2021 (**Figure 5A**). In July (**Figure 5B**), several fluctuations in its space radiation are observed, but the strength is limited, which is a common phenomenon of stress adjustment in a post-earthquake zone. From August to September (**Figures 5C,D**), the BT radiation almost disappeared. We conclude from the perspective of BT changes that the regional energy was released after the earthquakes and the stress accumulation disappeared, causing the BT radiation anomalies to disappear as well in space.

Time Series Tracking

The Eastern Bayanhar Block, the Eastern Qiangtang Block, and the Sichuan-Yunnan Block were selected to track the changes of BT in time series. **Figures 6–8** correspond to the original BT

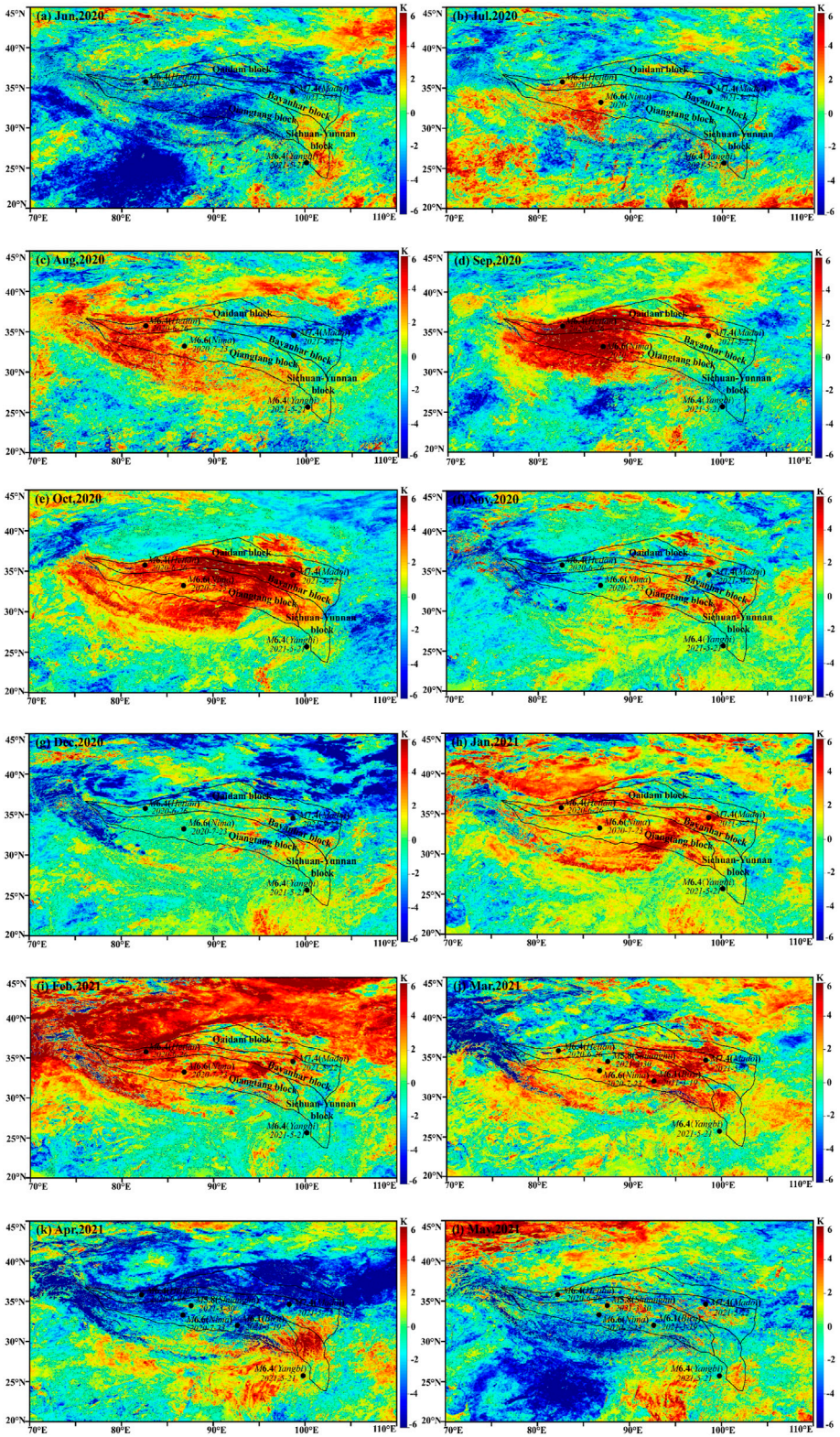

FIGURE 4 | BT anomalies and earthquakes in the Qinghai-Tibetan Plateau (2020.06**(A)**-2021.05**(L)**).

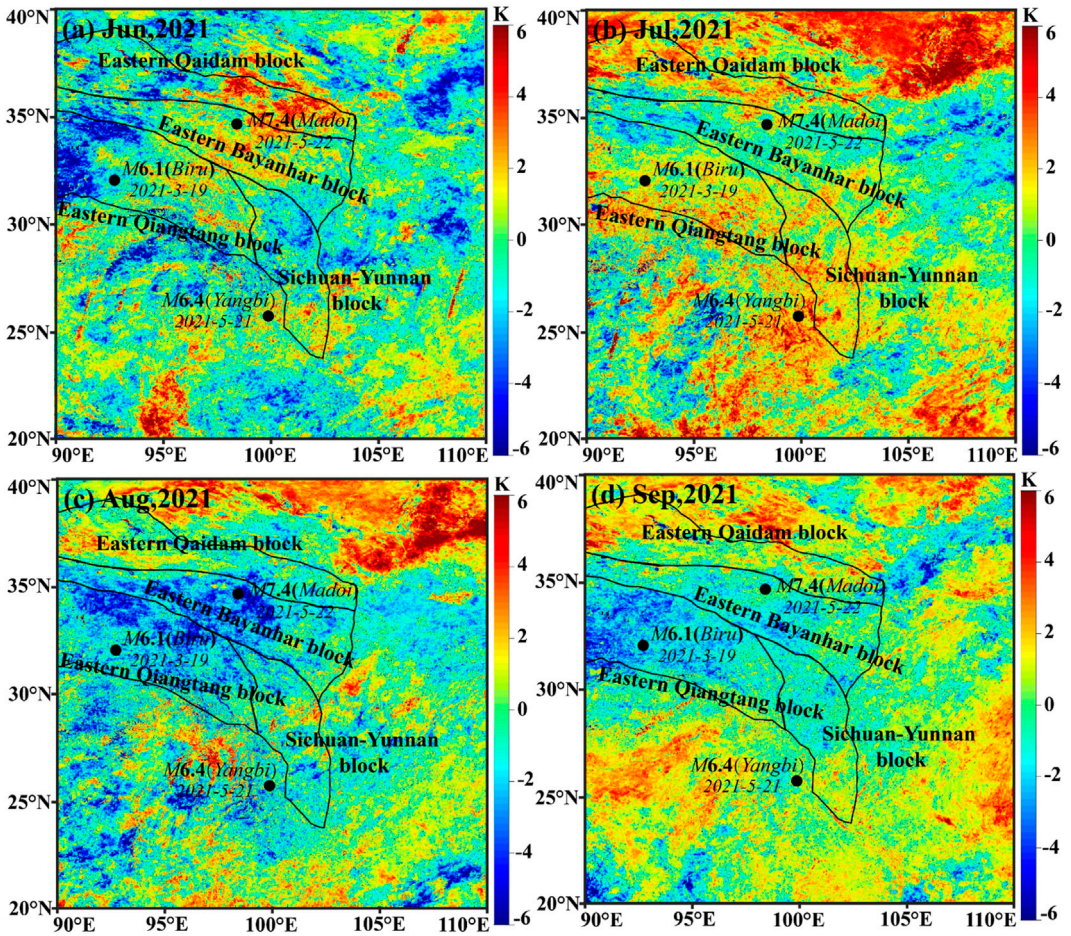

FIGURE 5 | BT anomaly in the eastern margin of the Qinghai-Tibetan Plateau (2021.06 **(A)**-2021.09 **(D)**).

data (Figure No.(a)), smoothing BT data (Figure No.(b)), the BT background field (Figure No.(c)) and the time series curve of BT anomaly in the three blocks. The original and smoothing data cover a time period from 2004 to September 2021. As the value of the BT background field was the same every year in the study period, only values during 2018–2020 were displayed. The BT anomaly was recorded from 2018 to September 2021(Figure No.(d)) and results from smoothing BT (Figure No.(b)) minus the background field (Figure No.(c)). In the diagrams, two times, one-and-a-half times, negative two times, and negative one-and-a-half times of standard deviations are marked in dotted lines. The BT anomalies occur as long as the curve exceeded two times the standard deviation. In the diagrams, Biru *M*6.1, Yangbi *M*6.4, and Madoi *M*7.4 earthquakes are marked with red pentacles.

The results in the figures reveal striking differences in the BT of the various blocks that are related to the tectonic position of the blocks. The blocks have a clear annual variation and exhibit different annual amplitudes. The overall amplitude range between 20 and 30 K, corresponding to high values in summer and low values in winter. The BT anomaly diagrams indicate that the curves exceeded the negative twofold standard deviation in early 2020 (the Bayanhar Block in late January), with its lowest point in mid-February (**Figure 6D**), and the Qiangtang Block in late January (**Figure 7D**), and then the curves increase rapidly, exceeding the twofold standard deviation in November (the Bayanhar Block reaches its maximum on November 16, and the Qiangtang Block on November 18). The roller-coaster change was formed in less than 11 months, demonstrating that BT anomalies were very prominent and the regional stress grew rapidly. Later, the BT anomaly curves of both blocks start to decrease until December 2020 but rapidly increase again after January 2021. They almost attained the threshold line-nearly twofold standard deviation in March 2021 (the Bayanhar Block reached its maximum value on March 28 and the Qiangtang Block on March 24). Two earthquakes, Biru *M*6.1 (on March 19) and Shuanghu *M*5.8 (on March 30) occurred after the internal Qiangtang Block curve increased twice. Finally, the curve decreases again and the Madoi *M*7.4 earthquake affected the Bayanhar Block about 50 days later.

The BT anomaly curve of the Sichuan-Yunnan Block (**Figure 8D**) varies from those of the Bayanhar Block and the Qiangtang Block. The curve of the Sichuan-Yunnan Block

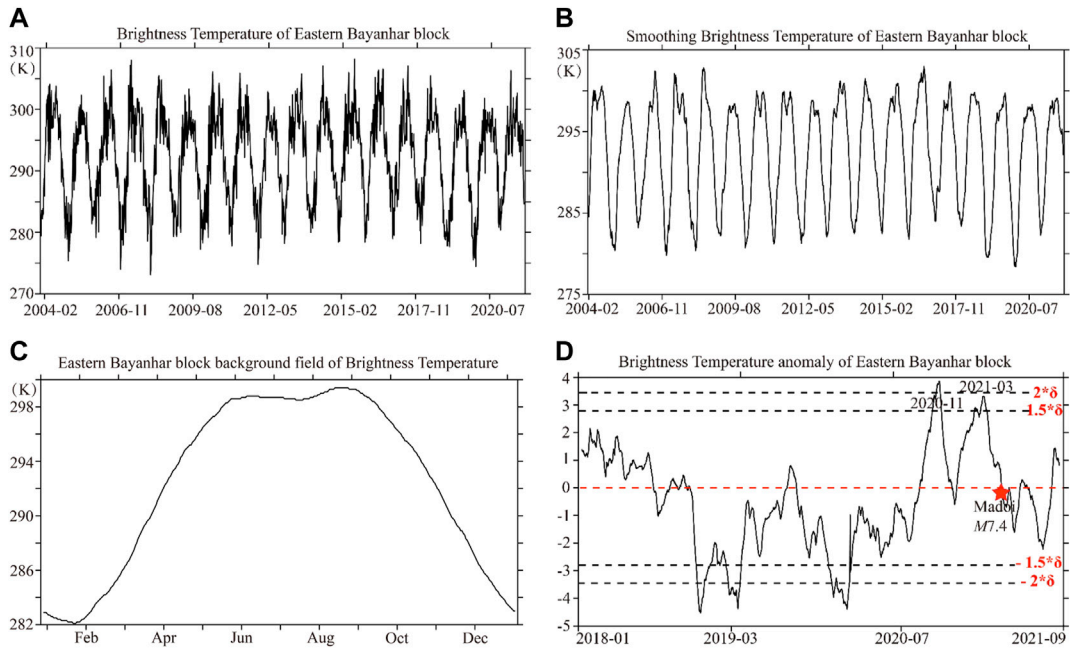

FIGURE 6 | BT in **(A)** time series, **(B)** smoothing BT **(C)** background field of BT and **(D)** BT anomaly of the Eastern Bayanhar Block.

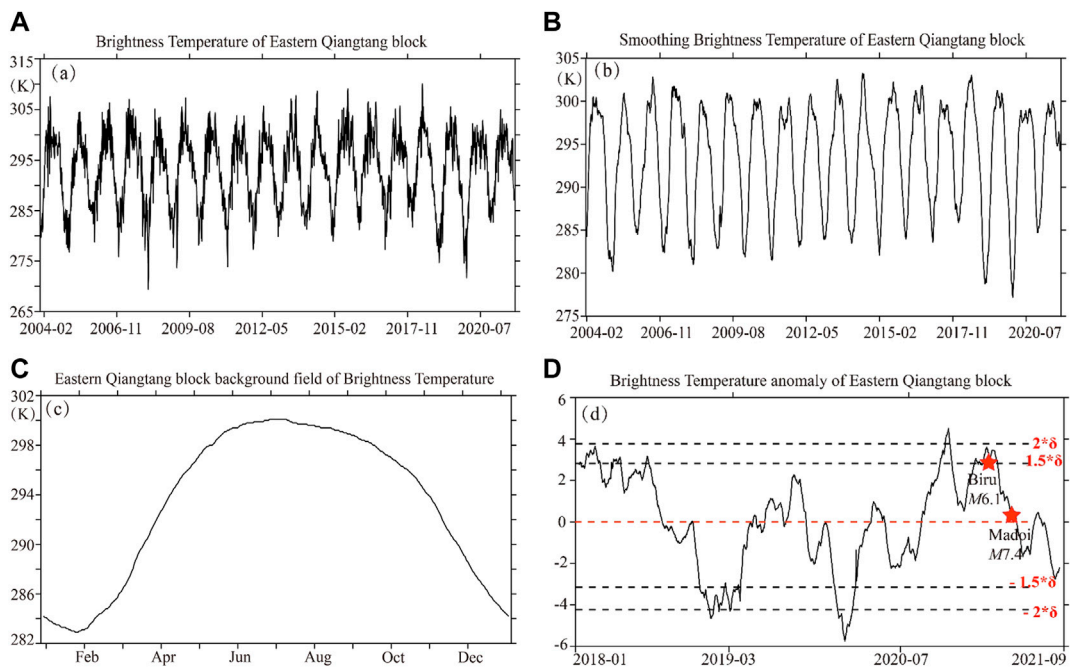

FIGURE 7 | BT in **(A)** time series, **(B)** smoothing BT **(C)** background field of BT and **(D)** BT anomaly of the Eastern Qiangtang Block.

also began to rise rapidly after approaching the negative twofold standard deviation in February 2020, and the rising trend continued until the curve exceeded the twofold standard deviation, with a time span of about 14 months. Its BT anomaly curve reached the maximum value on april 30 and exceeded the twofold standard deviation to form anomalies. Later on, the curve decreases and after 21 days, the Yangbi *M*6.4 earthquake occurred.

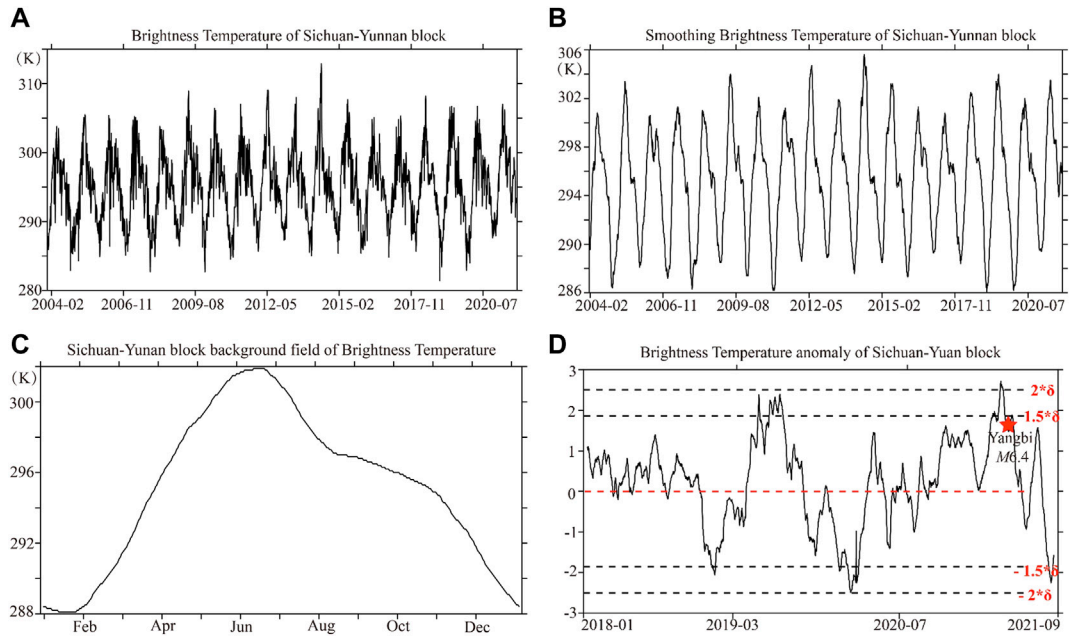

FIGURE 8 | BT in **(A)** time series, **(B)** smoothing BT **(C)** background field of BT and **(D)** BT anomaly of the Sichuan-Yunnan Block.

DISCUSSION

Link Between Spatial BT Anomalies and the Geodynamic Evolution

BT radiation anomalies document significant spatial and temporal migration in the Qinghai-Tibetan Plateau before the onset of the heavy *M*7.4 Madoi earthquake (**Figure 4**): The BT Anomalies occurred in the western Qinghai-Tibetan Plateau in July 2020 (**Figure 4B**), and then gradually spread eastward to the central plateau in August 2020, occupying the entire plateau after October 2020 (**Figures 4C–F**). From January to april 2021, the BT radiation anomalies reappeared (**Figures 3H,I**) and covered the northern Sichuan-Yunnan Block (**Figures 4J,K**. The evolution of BT radiation anomalies may be consistent with the geodynamic development of the Qinghai-Tibetan Plateau. The uplift of the Qinghai-Tibetan Plateau originated from the extrusion of the Indian subcontinent, the speed of the extrusion is about 50–60 mm/a (Tapponnier et al., 2001; Zhang et al., 2004). The plateau material was forced to migrate and later developed southward after the extrusion with the Southern China Block (Tapponnier et al., 2001; Zhang et al., 2004; Chen et al., 2010). The development of BT radiation anomalies probably corresponds to the geodynamic background and indicates the presence of a stress crush development in the Qinghai-Tibetan Plateau in the studied time interval, leading to a series of *M*6.0 earthquakes, including Madoi *M*7.4.

Correlation of BT Radiation Anomalies With Earthquakes

According to the principle of land surface thermal radiation anomalies, three major categories of theories were summarized in laboratory and practical applications through many studies: 1) Rock extrusion and burst (Saraf et al., 2008; Liu et al., 2016), 2) land surface degassing (Panda, et al., 2007; Saradjian et al., 2011) and 3) the theory of atmospheric ionization (Freund, 2000; Freund, 2002; Freund, 2003; Ouzounov et al., 2004; Pulinets et al., 2006; Ouzounov et al., 2007; Shah et al., 2018). In the seismogenic period, subsurface rocks are extruded or extended due to tectonic stress. Gradually, rocks burst internally and cause friction with other rocks externally. During the entire process, the thermal energy is accumulated and later released to spread outside from the lithosphere, and then to conduct to the air atmosphere in the form of thermal radiation. As a result, it forms the coupling of the lithosphere-atmosphere. The thermal radiation anomalies related to this process feature that with an extensive range and wide area, but can still be observed by satellites. (Eleftheriou et al., 2015; Lu et al., 2016). According to the pre-earthquake surface degassing theory, media in the lithosphere were squeezed and extended during the seismic breeding period, forcing subsurface heat source material to uprush. For example, the heat flux may rise to the surface through rocks fractures, forming an overburden layer in the form of water vapor on the land surface. Greenhouse gases, such as CO_2 and CH_4, could also rise to the surface along with rock fractures during the extrusion, and may create the regional "greenhouse effect" with water vapor and other gases on the surface. As a result, the surface temperature will increase and the surface thermal radiation will rise (Panda et al., 2007; Saradjian et al., 2011). A coupling process among lithosphere, air atmosphere, and ionosphere before strong earthquakes were reported in several studies (Freund, 2000; Freund, 2002; Freund, 2003; Ouzounov et al., 2004; Pulinets et al., 2006; Shah et al., 2018). The rock's crack or fusion, and mineral dissolution or phase transition may cause the formation of daughter isotopes

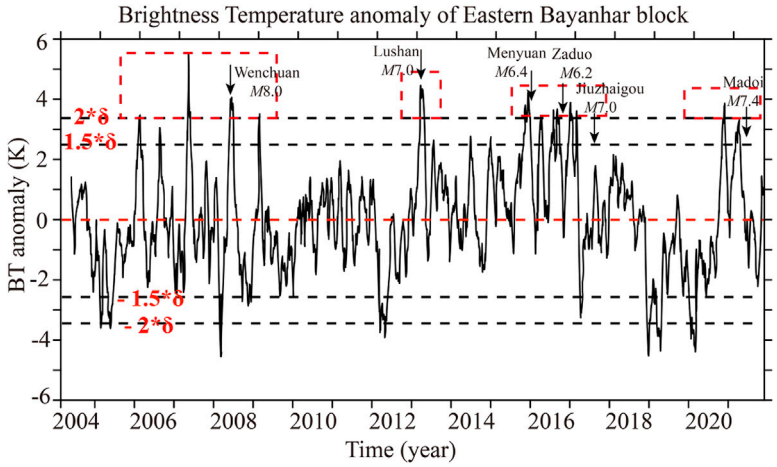

FIGURE 9 | Time series of BT anomaly of the Eastern Bayanhar block from 2004 to 2021.

from the decay of radioactive isotopes in the minerals (Chen et al., 2021a), it should be emphasized that this mechanism is a hypothesis, which originates from observations and experimental results, it needs further confirmation in the future work. however, it still remains one of the mainstream consensuses on thermal radiation anomalies' interpretation. So, the release of radon gas is used as an example; during radon gas decay, numerous α particles are produced. Positively charged α particles induce ionization in the near-surface atmosphere, which generates mass-charged ions. These ions can create hydration in the air atmosphere that reduces the relative humidity and forms an environment of high temperature and low pressure, thus creating an environment in which the total radiation is increasing (Freund et al., 2006; Freund, 2011; Walia et al., 2013; Kobayashi et al., 2015; Chen et al., 2021a; Chen et al., 2021b).

We summarized our result in **Figure 9** which shows long trend time series from 2004 to 2021 in the Eastern Bayanhar block. The main earthquakes are underlined by a black arrow and it is possible to note a systematic increase in the BT radiation before most of the events that occurred in the investigated area. Both the Madoi *M*7.4 and a series of *M*6.0 earthquakes are originated from the tectonic activities inside the Qinghai-Tibetan Plateau, as tectonic extrusion must be accompanied by stress development. This process causes the enhancement of radiation in the seismogenic zone. The reason for the production of BT radiation anomalies in the study period is probably related to a combination of multiple processes, including rock extrusion and burst, the release of subsurface greenhouse gases, and atmospheric ionization. As the BT reflects the changes of the surface radiation value, heat sources or greenhouse gases may rather reflect the changes of surface temperature, and atmospheric ionization may rather be recorded by electromagnetic detection methods. Based on these findings and the tectonic evolution of the Qinghai-Tibetan Plateau, we propose that the lithosphere extrusion and the related stress development could be as the main reason for the observed anomalies and that the other two mechanisms were rather supplementary causes.

(The red dotted line indicates the 0-value line, the black dotted lines above and below the 0-value line represent the 1.5 (negative 1.5) and 2 (negative 2) times the standard deviation respectively; the red rectangles indicate the period of the BT radiation's anomaly, and the black arrows are the corresponding earthquakes).

Correlation of Spatial and Temporal Anomalies With Seismic Events

Six moderate to strong earthquakes occurred in the interior and margin of the Qinghai-Tibetan Plateau between June 2020 and May 2021. The time and location of the seismic activity are significantly correlated with the development of BT Anomalies in space, and BT curves of the block also match the earthquake time. Therefore, we propose that the Madoi *M*7.4 earthquake and a series of earthquakes were not isolated events, but typically occurred inside the Qinghai-Tibetan Plateau under stress development.

In the beginning of 2020, the BT anomalies of the Eastern Bayanhar Block, the Eastern Qiangtang Block, and the Sichuan-Yunnan Block almost simultaneously began to rise from low values (**Figures 6D**, **7D** and **8D**). The values of the Bayanhar Block and the Eastern Qiangtang Block attained the maximum level in October 2020, exceeding the twofold standard deviation. This formed the only BT anomaly exceeding the twofold standard deviation since 2018. The BT radiation anomaly in space started in July 2020 and then gradually increased to cover the entire Qinghai-Tibetan Plateau finally (**Figures 4B–E**), which is consistent with the evolution of the time series. The Hetian *M*6.4 earthquake, Xinjiang on 26 June 2020, and the Nima *M*6.6 earthquake on 23 July 2020, occurred in the anomalous development process.

Since January 2021, BT anomalies had reappeared in the Qinghai-Tibetan Plateau, covering a larger area than before,

and the BT time series curve also started to increase again. The BT anomalies developed from the hinterland of the Qinghai-Tibetan Plateau to the northern Sichuan-Yunnan Block. In this process, the Biru *M*6.1 earthquake and the Shuanghu *M*5.8 earthquake in Tibet occurred successively on March 19 and March 30, respectively and are also displayed in the high-value segment of the time series curve (**Figures 6D**, **7D**). The BT spatial anomalies disappear in May (**Figure 4J**), and the Yangbi *M*6.4 and Madoi *M*7.4 earthquakes successively occurred on 21st and 22nd in the month. The Yangbi earthquake occurred at the southwest boundary of the Sichuan-Yunnan Block. This region marks the end of the tectonic migration and stress development of the Qinghai-Tibetan Plateau, so that stress conduction was slower than those of the Bayanhar and Qiangtang blocks. This was also the reason why the time series curve of the Sichuan-Yunnan Block started to rise and attained its peak at a lower rate compared with the other two blocks. The time series curve of the Sichuan-Yunnan Block exceeded the anomalies threshold of the twofold standard deviation in april 2021, and the Yangbi *M*6.4 earthquake occurred 21 days later.

Spatial and Temporal Development of BT Anomalies After the Earthquakes

The extensive spatial and temporal BT anomalies finally disappeared after the earthquakes (from June 2021) (**Figure 5**). Local anomalies in some time intervals were attributed to post-earthquake stress adjustment or normal annual variation, and the fluctuation of the time series curve was within the normal range after the Madoi earthquake. The adjustment to normal values of BT in time and space also demonstrated that the accumulated stress in the studied regions may have been completely released in the seismic events, and also indicated that the anomalies development of this stage might come to an end.

CONCLUSION

MODIS data were processed by splicing, cloud removal, extraction of the background field of BT, and the monthly calculation of BT anomalies with an independently developed system. The secondary tectonic blocks in the eastern margin of the Qinghai-Tibetan Plateau were modeled as one common unit to acquire the BT time series and spatial anomaly distribution of these blocks. Subsequently, the twofold standard deviation was taken as the anomaly threshold. The tracking study of the Madoi M7.4 and several previous earthquakes was conducted on this basis. The following conclusions are constrained by the new data:

(1) A strong correlation exists between earthquake occurrence and spatial anomaly of BT. The enhancement of BT radiation reflects changes in the regional stress field. The radiation anomalies of the Qinghai-Tibetan Plateau were generally consistent with stress conduction tendency on the tectonic evolution of the Qinghai-Tibetan Plateau. The BT anomalies developed from west to east and expanded its extent gradually. Meanwhile, it should be emphasized that the mechanism of the stress field and the BT variation is based on the inference of experimental results, a deep study of the stress filed goes behind the goal of this paper. In the anomaly development in 2020, the Hetian *M*6.4 and Nima *M*6.6 earthquakes occurred successively, and the Biru *M*6.1, Shuanghu *M*5.8, and Madoi *M*7.4 earthquakes occurred successively in 2021. In april 2021, BT anomalies extended into the Sichuan-Yunnan Block, and the Yangbi *M*6.4 occurred in the southwestern part of this block.

(2) A good correlation also exists between earthquake occurrence and the time series of BT. In the time series curve, covering 3 years, the phenomenon of exceeding the twofold standard deviation only occurred once in all the three blocks, and the BT anomalies in the blocks simultaneously began to rise from the beginning of the series in 2020. The BT anomalies of the Bayanhar and Qiangtang blocks exceeded the twofold standard deviation in October, and once again approached it in March 2021. The Sichuan-Yunnan Block exceeded the twofold standard deviation in april 2021, due to its location at the easternmost margin of stress development. The Hetian *M*6.4, Nima *M*6.6, Biru *M*6.1, and Shuanghu *M*5.8 earthquakes all occurred during the increase of time-series curves, whereas the Yangbi *M*6.4 and Madoi *M*7.4 earthquakes occurred during the decrease of the BT curves after they reached the maximum value.

(3) Regional BT anomalies disappear after the earthquakes and also the regional spatial BT anomalies simultaneously came to an end. Furthermore, the time series dropped to the normal range. Although the post-earthquake spatial and time series represent fluctuations on a small scale, they do not attain the abnormal standard, which might be caused by post-earthquake stress adjustment and annual variation.

(4) The occurrence of earthquakes could be in accordance with the distribution of the regional stress development. BT anomalies in space and time series reflect the development of regional stress. The time and location of earthquakes are consistent with the trend of the spatial BT anomalies and time series, indicating that the stress background of this earthquake may be consistent with that of the Qinghai-Tibetan Plateau.

Our study documents that the MODIS thermal infrared BT data is suitable to effectively obtain pre-earthquake anomalies, providing a new reference for the search of anomalies prior to earthquakes. The anomaly method, based on massive data accumulation over many years, is suitable for anomaly tracking. The results demonstrate that the study of the different parameters before earthquakes through satellites is highly promising for further research on earthquake detection.

DATA AVAILABILITY STATEMENT

The original contributions presented in the study are included in the article/supplementary material, further inquiries can be directed to the corresponding author.

AUTHOR CONTRIBUTIONS

XY, T-BZ, and QL: Software development, Methodology, Data processing, Visualization, Writing-Original draft preparation. XY, FL, M-JL, and W-WW: Data processing, Validation. XY, J-XW, and JW: Investigation.

FUNDING

This work is funded by the National Natural Science Foundation of China under Grant No. 42074082. This work is also supported by the Project of Science for Earthquake Resilience under Grant No. XH202302 and No. XH192305. This work is also supported by the Sichuan Science and Technology Project under Grant No.2020YJ0475.

ACKNOWLEDGMENTS

The authors are very grateful to NASA for providing the MODIS data. The authors would like to express gratitude to Professor Huang Fuqiong from China Earthquake Network Center(CENC) for applying to this special issue.

REFERENCES

Bates, J. J., Wu, X., and Jackson, D. L. (1996). Interannual Variability of Upper-Troposphere Water Vapor Band Brightness Temperature. *J. Clim.* 9 (2), 427–438. doi:10.1175/1520-0442(1996)009<0427:ivoutw>2.0.co;2

Cervone, G., Kafatos, M., Napoletani, D., and Singh, R. P. (2004). Wavelet Maxima Curves of Surface Latent Heat Flux Associated with Two Recent Greek Earthquakes. *Nat. Hazards Earth Syst. Sci.* 4 (3), 359–374. doi:10.5194/nhess-4-359-2004

Cervone, G., Maekawa, S., Singh, R. P., Hayakawa, M., Kafatos, M., and Shvets, A. (2006). Surface Latent Heat Flux and Nighttime LF Anomalies Prior to the Mw=8.3 Tokachi-Oki Earthquake. *Nat. Hazards Earth Syst. Sci.* 6 (1), 109–114. doi:10.5194/nhess-6-109-2006

Cervone, G., Singh, R. P., Kafatos, M., and Yu, C. (2005). Wavelet Maxima Curves of Surface Latent Heat Flux Anomalies Associated with Indian Earthquakes. *Nat. Hazards Earth Syst. Sci.* 5 (1), 87–99. doi:10.5194/nhess-5-87-2005

Chen, L., Wang, H., Ran, Y., Sun, X., Su, G., Wang, J., et al. (2010). The M S7.1 Yushu Earthquake Surface Rupture and Large Historical Earthquakes on the Garzê-Yushu Fault. *Chin. Sci. Bull.* 55 (31), 3504–3509. doi:10.1007/s11434-010-4079-2

Chen, T., Li, L., Zhang, X. X., Ma, Q. M., Li, W., Ti, S., et al. (2021b). Near-epicenter Weather Conditions Several Hours before strong Earthquakes (M_s≥6). *Nat. Hazards* 110, 57–68. doi:10.1007/s11069-021-04907-2

Chen, T., Zhang, X. X., Zhang, X. M., Jin, X. B., Wu, H., Ti, S., et al. (2021a). Imminent Estimation of Earthquake hazard by Regional Network Monitoring the Near Surface Vertical Atmospheric Electrostatic Field. *Chines J. Geophys. (In Chinese)* 64 (4), 1145–1154. doi:10.6038/cig2021O0129

Chen, Y. T., Xu, L. S., Li, X., and Zhao, M. (1996). Source Process of the 1990 Gonghe, China, Earthquake and Tectonic Stress Field in the Northeastern Qinghai-Xizang (Tibetan) Plateau. *Birkhäuser Basel* 146, 697. doi:10.1007/978-3-0348-9200-1_16

Corradini, S., Merucci, L., Prata, F., and Piscini, A. (2010). Volcanic Ash and SO2 in the 2008 Kasatochi Eruption: Retrievals Comparison from Different IR Satellite Sensors. *J. Geophys. Res. Space Phys.* 115, 13634. doi:10.1029/2009jd013634

Cui, Y. J., Du, J. G., Chen, Z., Li, J., Xie, C., Zhou, X., et al. (2011). Remote Sensing Signals of Atmospheric Physics and Chemistry Related to 2010 Yushu M_s 7.1 Earthquake. *Adv. Earth Sci.* 26 (7), 787–794. doi:10.11867/j.issn.1001-8166.2011.07.0787

Dey, S., Sarkar, S., and Singh, R. P. (2004). Anomalous Changes in Column Water Vapor after Gujarat Earthquake. *Adv. Space Res.* 33 (3), 274–278. doi:10.1016/s0273-1177(03)00475-7

Eleftheriou, A., Filizzola, C., Genzano, N., Lacava, T., Lisi, M., Paciello, R., et al. (2015). Long-term RST Analysis of Anomalous TIR Sequences in Relation with Earthquakes Occurred in Greece in the Period 2004–2013. *Pure Appl. Geophys.* 173, 285. doi:10.1007/s00024-015-1116-8

Feng, J., Chauhan, A., Ramesh, P., and Prasanjit Dash, S. (2020). Changes in Atmospheric, Meteorological, and Ocean Parameters Associated with the 12 January 2020 Taal Volcanic Eruption. *Remote Sensing* 12 (6), 1026.

Freund, F. (2002). Charge Generation and Propagation in Igneous Rocks. *J. Geodynamics* 33 (4–5), 543–570. doi:10.1016/s0264-3707(02)00015-7

Freund, F. (2011). Pre-earthquake Signals: Underlying Physical Processes. *J. Asian Earthquake Sci.* 41 (4), 383–400. doi:10.1016/j.jseaes.2010.03.009

Freund, F. T. (2003). Rocks that Crackle and Sparkle and Glow: Strange Pre-earthquake Phenomena. *J. Scientific Exploration* 17 (1).

Freund, F. (2000). Time-resolved Study of Charge Generation and Propagation in Igneous Rocks. *J. Geophys. Res.* 105 (B5), 11001–11019. doi:10.1029/1999jb900423

Freund, F. T., Takeuchi, A., Lau, B., Al-Manaseer, A., and Ouzounov, D. (2006). Stimulated Infrared Emission from Rocks: Assessing a Stress Indicator. *Eearth* 2 (1). doi:10.5194/eed-1-97-2006

Gorny, V. I., Sal'Man, A. G., Tronin, A. A., and Shilin, B. V. (1988). Outgoing Infrared Radiation of the Earth as an Indicator of Seismic Activity. *Doklady Akademii nauk SSSR* 301, 67–69.

Gruber, A., and Krueger, A. F. (1984). The Status of the NOAA Outgoing Longwave Radiation Data Set. *Bull. Amer. Meteorol. Soc.* 65 (9), 958–962. doi:10.1175/1520-0477(1984)065<0958:tsotno>2.0.co;2

Hayer, C. S., Wadge, G., Edmonds, M., and Christopher, T. (2016). Sensitivity of OMI SO2 Measurements to Variable Eruptive Behaviour at Soufrière Hills Volcano, Montserrat. *J. Volcanology Geothermal Res.* 312, 1–10. doi:10.1016/j.jvolgeores.2016.01.014

He, L. M., Wu, L. X., De Santis, A., Liu, S. J., and Yang, Y. (2014). Is There a One-To-One Correspondence between Ionospheric Anomalies and Large Earthquakes along Longmenshan Faults? *Ann. Geophys.* 32 (2), 187–196. doi:10.5194/angeo-32-187-2014

Hui, Z., Gao, Y., Shi, Y. T., Liu, X. F., and Wang, Y. X. (2012). Tectonic Stress Analysis Based on the Crustal Seismic Anisotropy in the Northeastern Margin of Tibetan Plateau. *Chin. J. Geophys.* 55 (1), 95–104.

Kane, R. P. (2008). Spatial and Temporal Characteristics of Outgoing Longwave Radiation (OLR): an Update. *Braz. J Geophys* 26 (2), 227–236. doi:10.1590/s0102-261x2008000200009

Kobayashi, Y., Yasuoka, Y., Omori, Y., Nagahama, H., Sanada, T., Muto, J., et al. (2015). Annual Variation in the Atmospheric Radon Concentration in Japan. *J. Environ. radioactivity* 146, 110–118. doi:10.1016/j.jenvrad.2015.04.007

Liu, S., Xu, Z., Wei, J., Huang, J., and Wu, L. (2016). Experimental Study on Microwave Radiation from Deforming and Fracturing Rock under Loading Outdoor. *IEEE Trans. Geosci. Remote Sensing* 54, 5578–5587. doi:10.1109/tgrs.2016.2569419

Lu, X., Meng, Q. Y., Gu, X. F., Zhang, X. D., Xie, T., and Geng, F. (2016). Thermal infrared anomalies associated with multi-year earthquakes in the Tibet region based on China's FY-2e satellite data. *Adv. Space Res.* 58. doi:10.1016/j.asr.2016.05.038

Ouzounov, D., and Freund, F. (2004). Mid-infrared Emission Prior to strong Earthquakes Analyzed by Remote Sensing Data. *Adv. Space Res.* 33 (3), 268–273. doi:10.1016/s0273-1177(03)00486-1

Ouzounov, D., Liu, D., Kang, C., Cervone, G., Kafatos, M., and Taylor, P. (2007). Outgoing Long Wave Radiation Variability from Ir Satellite Data Prior to Major Earthquakes. *Tectonophysics* 431 (1-4), 211–220. doi:10.1016/j.tecto.2006.05.042

Panda, S. K., Choudhury, S., Saraf, A. K., and Das, J. D. (2007). MODIS Land Surface Temperature Data Detects thermal Anomaly Preceding 8 October 2005 Kashmir Earthquake. *Int. J. Remote Sensing* 28 (20), 4587–4596. doi:10.1080/01431160701244906

Pardini, F., Burton, M., de' Michieli Vitturi, M., Corradini, S., Salerno, G., Merucci, L., et al. (2017). Retrieval and Intercomparison of Volcanic SO2 Injection Height and Eruption Time from Satellite Maps and Ground-Based Observations. *J. Volcanology Geothermal Res.* 331, 79–91. doi:10.1016/j.jvolgeores.2016.12.008

Pulinets, S. A., Ouzounov, D., Ciraolo, L., Singh, R., Cervone, G., Leyva, A., et al. (2006). Thermal, Atmospheric and Ionospheric Anomalies Around the Time of the Colima m7.8 Earthquake of 21 January 2003. *Ann. Geophys.* 24 (3), 835–849. doi:10.5194/angeo-24-835-2006

Rawat, V., Saraf, A. K., Das, J., Sharma, K., and Shujat, Y. (2011). Anomalous Land Surface Temperature and Outgoing Long-Wave Radiation Observations Prior to Earthquakes in India and Romania. *Nat. Hazards* 59 (1), 33–46. doi:10.1007/s11069-011-9736-5

Saradjian, M. R., and Akhoondzadeh, M. (2011). Thermal Anomalies Detection before strong Earthquakes (M > 6.0) Using Interquartile, Wavelet and Kalman Filter Methods. *Nat. Hazards Earth Syst. Sci.* 11 (4), 1099–1108. doi:10.5194/nhess-11-1099-2011

Saraf, A. K., Rawat, V., Banerjee, P., Choudhury, S., Panda, S. K., Dasgupta, S., et al. (2008). Satellite Detection of Earthquake thermal Infrared Precursors in Iran. *Nat. Hazards* 47 (1), 119–135. doi:10.1007/s11069-007-9201-7

Shah, M., Khan, M., Ullah, H., and Ali, S. (2018). Thermal Anomalies Prior to the 2015 Gorkha (Nepal) Earthquake from Modis Land Surface Temperature and Outgoing Longwave Radiations. *Geodin. Tektonofiz.* 9 (1), 123–138. doi:10.5800/gt-2018-9-1-0341

Tapponnier, P., Zhiqin, X., Roger, F., Meyer, B., Arnaud, N., Wittlinger, G., et al. (2001). Oblique Stepwise Rise and Growth of the Tibet Plateau. *Science* 294 (5547), 1671–1677. doi:10.1126/science.105978

Theys, N., Hedelt, P., De Smedt, I., Lerot, C., Yu, H., Vlietinck, J., et al. (2019). Global Monitoring of Volcanic SO2 Degassing with Unprecedented Resolution from TROPOMI Onboard Sentinel-5 Precursor. *Sci. Rep.* 9 (9), 2643. doi:10.1038/s41598-019-39279-y

Tronin, A. A., Hayakawa, M., and Molchanov, O. A. (2002). Thermal in Satellite Data Application for Earthquake Research in Japan and China. *J. Geodynamics* 33 (4-5), 519–534. doi:10.1016/s0264-3707(02)00013-3

Tronin, A. A., Biagi, P. F., Molchanov, O. A., Khatkevich, Y. M., and Gordeev, E. I. (2004). Temperature Variations Related to Earthquakes from Simultaneous Observation at the Ground Stations and by Satellites in Kamchatka Area. *Phys. Chem. Earth* 29 (4-9), 501–506. doi:10.1016/j.pce.2003.09.024

Walia, V., Yang, T. F., Lin, S.-J., Kumar, A., Fu, C.-C., Chiu, J.-M., et al. (2013). Temporal Variation of Soil Gas Compositions for Earthquake Surveillance in Taiwan. *Radiat. Measurements* 50, 154–159. doi:10.1016/j.radmeas.2012.11.007

Wang, K., He, J., Schulzeck, F., Hyndman, R. D., and Riedel, M. (2015). Thermal Condition of the 27 October 2012 Mw 7.8 Haida Gwaii Subduction Earthquake at the Obliquely Convergent Queen charlotte Margin. *Bull. Seismological Soc. America* 105, 1290–1300. doi:10.1785/0120140183

Wang, M., and Shen, Z. K. (2020). Present-day Crustal Deformation of continental China Derived from GPS and its Tectonic Implications. *J. Geophys. Res. Solid Earth* 125 (2), e2019JB018774. doi:10.1029/2019jb018774

Weiyu, M., Xuedong, Z., Liu, J., Yao, Q., Zhou, B., Yue, C., et al. (2018). Influences of Multiple Layers of Air Temperature Differences on Tidal Forces and Tectonic Stress before, during and after the Jiujiang Earthquake. *Remote Sensing Environ.* 210 (210), 159–165. doi:10.1016/j.rse.2018.03.003

Wu, W., Long, F., Liang, M., Wei, Y., Sun, W., Chen, X., et al. (2020). Spatial and Temporal Variations in Earthquake Stress Drops between the 2008 Wenchuan and 2013 Lushan Earthquakes. *Acta Geologica Sinica - English Edition* 94 (5), 1635–1650. doi:10.1111/1755-6724.14582

Wu, X., Bates, J. J., and khalsa, S. S. (2013). A Climatology of the Water Vapor Band Brightness Temperatures from NOAA Operational Satellites. *J. Clim.* 6 (7), 1282–1300.

Xiong, P., Shen, X. H., Bi, Y. X., Kang, C. L., and Chen, Y. (2010). Study of Outgoing Longwave Radiation Anomalies Associated with Haiti Earthquake. *Nat. hazards earth Syst. Sci.* 10 (10). doi:10.5194/nhess-10-2169-2010

Xu, Z., Jingsui, Y., and Zengqian, H. (2016). The Progress in the Study of continental Dynamics of the Tibetan Plateau[J]. *Geology. China* 43 (1), 1–42. (in Chinese with English abstract).

Zhang, P.-Z., Shen, Z., Wang, M., Gan, W., Bürgmann, R., Molnar, P., et al. (2004). Continuous Deformation of the Tibetan Plateau from Global Positioning System Data. *Geol* 32 (9), 809–812. doi:10.1130/g20554.1

Zhang, Y., Kang, C. L., Ma, W. Y., and Yao, Q. (2017). The Change in Outgoing Longwave Radiation before the Ludian Ms6.5 Earthquake Based on Tidal Force Niche Cycles. *Earthq. Res. China* 31, 422–430.

Zhong, M., Shan, X., Zhang, X., Qu, C., Guo, X., and Jiao, Z. (2020). Thermal Infrared and Ionospheric Anomalies of the 2017 Mw6.5 Jiuzhaigou Earthquake. *Remote Sensing* 12 (17), 2843. doi:10.3390/rs12172843

Conflict of Interest: The authors declare that the research was conducted in the absence of any commercial or financial relationships that could be construed as a potential conflict of interest.

Publisher's Note: All claims expressed in this article are solely those of the authors and do not necessarily represent those of their affiliated organizations, or those of the publisher, the editors and the reviewers. Any product that may be evaluated in this article, or claim that may be made by its manufacturer, is not guaranteed or endorsed by the publisher.

frontiers in Earth Science

ORIGINAL RESEARCH
published: 09 March 2022
doi: 10.3389/feart.2022.838299

A Continuous 13.3-Ka Paleoseismic Record Constrains Major Earthquake Recurrence in the Longmen Shan Collision Zone

Wei Shi[1], *Hanchao Jiang*[1]*, *G. Ian Alsop*[2] *and Guo Wu*[3]

[1]State Key Laboratory of Earthquake Dynamics, Institute of Geology, China Earthquake Administration, Beijing, China, [2]Department of Geology and Geophysics, School of Geosciences, University of Aberdeen, Aberdeen, United Kingdom, [3]Institute of Geology, China Earthquake Administration, Beijing, China

Thrust collision zones with low slip rates along the plate boundary are significant areas of stress accumulation and prone to develop more destructive earthquakes with longer recurrence intervals. Such regions are often classified as low seismic risk if they lack continuous records of large earthquakes, such as the eastern Tibetan Plateau before the 2008 M_w 7.9 Wenchuan earthquake. Here, we provide a continuous seismic record in the Longmen Shan thrust fault zone spanning 13,000 years based on detailed investigation of the soft-sediment deformation structures and seismites in the Lixian lacustrine sequence. The recurrence time of large earthquakes ($M \geq 8.1$) is 1,200 years, which is significantly shorter than the previous estimate of 2,000–6,000 years. The Maoxian-Wenchuan fault is the main fault that triggered the deformation in the Lixian lacustrine sediments. In addition, earthquake recurrence in the warm period is more frequent than that in the cold period, which should arouse our attention for the seismic study of tectonically active regions.

Keywords: soft sediment deformation, seismites, major earthquake recurrence time, Longmen Shan fault zone, eastern Tibetan Plateau

OPEN ACCESS

Edited by:
Yuanyuan Fu,
China Earthquake Administration, China

Reviewed by:
Yueren Xu,
China Earthquake Administration, China
Ken Ikehara,
Geological Survey of Japan (AIST), Japan
Wenjun Zheng,
Sun Yat-sen University, China

***Correspondence:**
Hanchao Jiang
hcjiang@ies.ac.cn

Specialty section:
This article was submitted to Geohazards and Georisks, a section of the journal Frontiers in Earth Science

Received: *17 December 2021*
Accepted: *14 February 2022*
Published: *09 March 2022*

Citation:
Shi W, Jiang H, Alsop GI and Wu G (2022) A Continuous 13.3-Ka Paleoseismic Record Constrains Major Earthquake Recurrence in the Longmen Shan Collision Zone. Front. Earth Sci. 10:838299. doi: 10.3389/feart.2022.838299

INTRODUCTION

Understanding fault behavior and assessing future seismic risks requires a foundation in instrumental, historical and palaeoseismic records (Berryman et al., 2012; Gomez et al., 2015; Scharer et al., 2010; Lu et al., 2020). According to a comprehensive analysis of historical and modern seismic data, no earthquake of $M \geq 7.0$ occurred in the Longmen Shan fault zone during at least 1,100–1,700 years before 2008 (**Figure 1**) (Wen et al., 2009). Moreover, the intensity of the 2008 M_w 7.9 Wenchuan earthquake greatly exceeded the largest earthquake in the history of the Longmen Shan fault zone, indicating that it is far from sufficient to accurately assess the potential seismic risk of large active fault zones with low slip rates (**Supplementary Figure S1**) based on historical earthquake records from hundreds to thousands of years (Deng, 2008; Wen et al., 2009).

Previous studies infer that the recurrence interval of large earthquakes is 2,000–6,000 years in the Longmen Shan fault zone based on GPS and seismological slip rates (Zhang et al., 2008; Zhang, 2013; Ran et al., 2014). Large earthquakes usually have a long recurrence interval that can't be covered by instrumental and historical records. This makes it extremely important to get a long and continuous palaeoseismic record for assessing fault activities and future seismic risks.

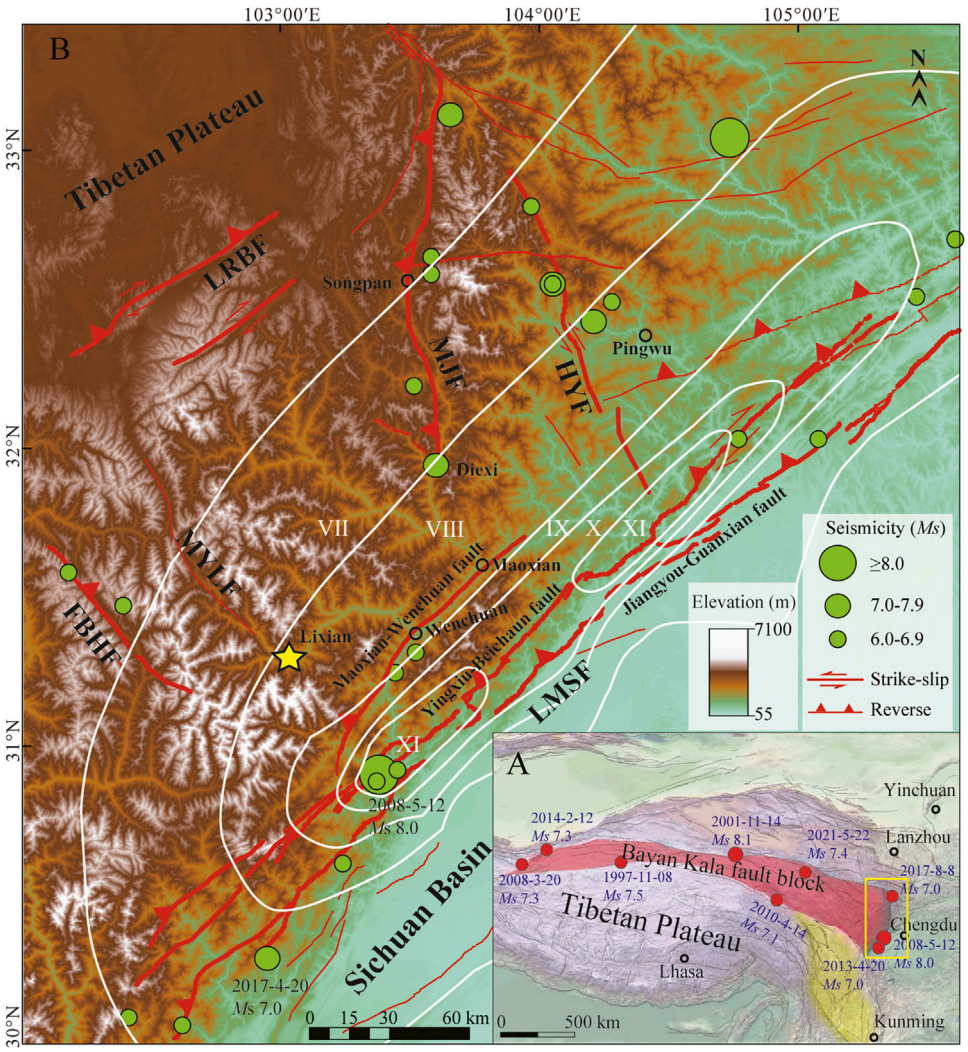

FIGURE 1 | Tectonic setting of the eastern margin of Tibetan Plateau **(A)** Epicenters distribution for $M_s \geq 7.0$ earthquakes in the Bayan Kala fault block since 1995 (Deng et al., 2014). Yellow box shows the extent of the B diagram **(B)** Major active faults (Xu et al., 2009) and the seismicity of the eastern margin of Tibetan Plateau. Seismicity data are from the China Earthquake Data Center (http://data.earthquake.cn/data). White line represents seismic intensity of Wenchuan earthquake. LMSF, Longmen Shan fault; LRBF, Longriba fault; HYF, Huya fault; MJF, Minjiang fault; MYLF, Miyaluo fault; FBHF, Fubianhe fault. The yellow star represents the Lixian section.

Paleoseismological trenching at suitable sites can extend the record for surface rupturing earthquakes to the past few thousand years (Moernaut, 2020), but continuity is not guaranteed. Lacustrine paleoseismology can capture long continuous records of strong seismic shaking, which integrate the activity of all significant seismic sources in a region and allow a reliable determination of recurrence patterns (Moernaut, et al., 2018; Ghazoui et al., 2019; Lu et al., 2020; Oswald et al., 2021), including soft-sediment deformation (SSD, co-seismic) and seismites (post-seismic). Among them, *in-situ* SSD structures can record a seismic event (Xu et al., 2015; Jiang et al., 2016; Lu et al., 2017, 2020; Zhong et al., 2019; Zhang et al., 2021; Fan et al., 2022). Some seismites overlay the SSD, others lack an underlying SSD but are temporally correlated with a historic earthquake (Lu et al., 2017).

In the eastern margin of the Tibetan Plateau, the geomorphological features of alpine valleys (**Supplementary Figure S1**) cause the serious absence of Quaternary sediments and thus paleoseismic records, which leads to poor research on the recurrence model of regional earthquakes. This brings severe challenges to the seismic risk assessment. Fortunately, the 13.3-ka-long continuous lacustrine sequence at Lixian (31.44°N, 103.16°E; 1867 ± 7 m a.s.l.) represents a precious chance to reveal palaeoseismic events, because previous studies have shown that the SSD structures and/or coarse-silt event layers in the lacustrine sediments in the tectonically active regions point to seismic genesis (Jiang et al., 2014, 2016, 2017; Liang and Jiang, 2017). However, there is a lack of quantitative analysis of event layers and seismic intensity in the eastern Tibetan Plateau.

In this study, our target is to link the SSD structures and/or seismites in the Lixian lacustrine sequence, which were published by Jiang et al. (2016, 2017), with the earthquake magnitude based on the existing fluid dynamics modeling. Recurrence mode of regional earthquakes and its controlling factors are addressed. This is of great scientific significance for assessment of the seismic risk in the tectonically active regions which are characterized by geomorphology of alpine valley and absence of Quaternary deposits.

GEOGRAPHIC AND GEOLOGIC SETTINGS

The Longmen Shan fault zone extends ~500 km from NE to SW and is composed of three groups of oblique, high-angle, listric-reverse faults (**Figure 1B**, **Supplementary Figure S1**) (Zhang et al., 2010). It separates the Tibetan Plateau from the Sichuan Basin, making it the most significant geomorphologic gradient zone in China. GPS measurements produce a short-term slip-rate of 1–2 mm yr^{-1} (**Supplementary Figure S1**) (Zhang et al., 2010), which is consistent with the long-term denudation rates by thermochronology analysis of zircon and apatite during the Late Cenozoic (Kirby et al., 2002).

Since the beginning of the 21st century, the major earthquakes in inland China are mainly distributed around the Bayan Kala block (**Figure 1A**), indicating that it is currently the main active block of strong earthquakes (Deng et al., 2010, 2014), and shows signs of gradually migrating towards the east. The 2008 Wenchuan *M*w 7.9 earthquake occurred on the Longmen Shan fault zone, the easternmost margin of the Bayan Kala block, and triggered surface rupture of 240 km on Yingxiu-Beichuan fault and 72 km on Pengxian-Guanxian fault (Xu et al., 2009), and >56, 000 landslides, covering a total area of >396 km^2 (Dai et al., 2011; Li et al., 2014; Xu et al., 2014). This brings severe challenges to the seismic risk assessment in the eastern margin of the Tibetan Plateau.

The geomorphological features of alpine valleys characterize the eastern margin of the Tibetan Plateau, which leads to less preservation of the Quaternary sediments. Instead, Paleozoic to Mesozoic bedrock outcrop widely. The bedrock is mainly composed of Silurian phyllite, quartz schist, Triassic phyllite, metamorphic sandstone and the Neoproterozoic Pengguan complex in the middle section of Longmen Shan fault zone.

The study area is poorly covered by vegetation and dominated by a windy and semi-arid climate (Shi et al., 2020; Xu et al., 2020; Wei et al., 2021). The high wind speeds occur in April (average 4.9 m/s) while the low ones occur in July (average 3.7 m/s). The highest instantaneous wind speed can reach 21 m/s (Liu, 2014). The mean annual precipitation (MAP) ranges from 500 to 850 mm, and 75% of the precipitation falls in the rainy seasons of May to October (Ding et al., 2014). Such a windy and semi-arid climate is apt for widespread transport of dust particles, given that moderate to strong earthquakes usually generate dust storms (Jiang et al., 2017).

MATERIALS AND METHODS

Earthquake Indicators and Paleoseismic Events

Linking SSD structures with earthquakes is commonly based in tectonically active areas, deformation of fine grained material, vertical repeatability, lateral traceability, separation by non-deformed layers, occurrence of SSD types simulated in laboratory, and exclusion of gravity collapse (Sims, 1975; Owen and Moretti, 2011; Jiang et al., 2016). According to these six criteria, seismic events can be recognized from SSD structures in the lacustrine sediments. Intriguingly, the SSD layers are always covered by coarse-silt layers in the Lixian sequence (Jiang et al., 2017). Based on the sedimentological analysis of high-resolution grain-size proxies, such as end-member analysis, C-M (C: one percentile, M: median diameter) diagram, Sahu value (Sahu, 1964), and so on, these layers are caused by earthquakes that triggered dust storms and massive landslides and then changed the source of dust particles (**Figure 3**) (Jiang et al., 2017). As a result, the Lixian section displays a much higher deposition rate of 1.75 mm/yr than that of the southern Chinese Loess Plateau (~0.08 mm/yr, Ding et al., 1994). This analysis is corroborated by continuously fine-grained (mean grain size: 15.9 μm) deposition at the Lixian lakeshore instead of coarse-grained sediments usually caused by fluvial flow (**Supplementary Figure S2**). Therefore, SSD structures and coarse-silt layers are used as sedimentological indicators of seismic events (Jiang et al., 2016, 2017).

Seismic shaking with different intensity can trigger the different types of SSD structures of the water-saturated sediments, and the stronger earthquakes usually result in stronger deformation (Rodrı´guez-Pascua et al., 2000; Wetzler et al., 2010; Lu et al., 2020). Accordingly, SSD of similar types in different regions probably correspond to the same triggering mechanism and intensity conditions. On this basis, fluid dynamics modeling is used to obtain the peak ground acceleration (PGA) required to trigger the typical types of deformation (Wetzler et al., 2010; Lu et al., 2020).

Peak Ground Acceleration

Previous studies indicate that earthquakes with different intensity can lead to different types of SSD structures, and the fluid dynamics modeling are used to obtain the PGA required to trigger different types of SSD structure (Wetzler et al., 2010; Lu et al., 2020). The lower-bounding magnitude of SSD is *M*w ≥ 5.3 with PGA ≥0.13 g Modified Mercalli Intensity (MMI) ≥ VI½ in the Dead Sea (Lu et al., 2020).

In this study, we collectively analyzed the SSDs in the Lixian section. The clastic dyke and micro-faults are cross-layer and often occur locally in the strata (Jiang et al., 2016), so continuity is not guaranteed, and the age is uncertain. The clastic gravel in Lixian section is composed of bedrock debris, which is possibly triggered by bedrock landslides induced by earthquakes of different intensity (Jiang et al., 2016). We eliminate these SSDs in the whole Lixian sequence. In

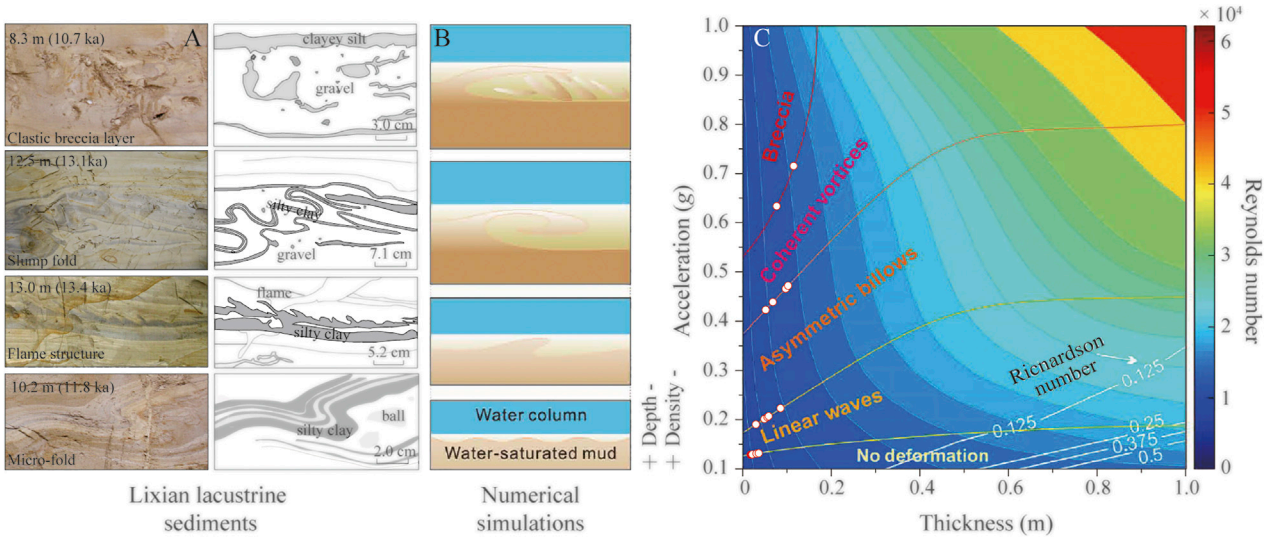

FIGURE 2 | SSD structures in the Lixian lacustrine sequence and the numerical simulation **(A)** Typical structures from the Lixian section outcrops (jiang et al., 2016) **(B)** Schematic diagrams of the four structures from the numerical simulations (Lu et al., 2020) **(C)** Quantitative estimation of the accelerations that are needed to initiate the four structures with different thicknesses (Lu et al., 2020). The circle represents different thickness and types of SSD in the Lixian section.

addition, ball-and-pillow structure in Jiang et al. (2016) are named according to deformation patterns, which cannot clearly reflect the strength of the deformation. Corresponding to the fluid dynamics modeling, the ball-and-pillow structures exhibit minimal deformation, so we redefined them as "micro-folds". The micro-folds can reflect the initial stage of the flame structures and slump folds (Jiang et al., 2016). As the deformation continues to intensify, clastic breccia layers are formed when the original rock strata break up.

As mentioned above, four typical types of SSDs, i.e. micro-folds, flame structures, slump folds and clastic breccia layers are identified corresponding to linear waves, asymmetric billows, coherent vortices and intraclast breccia layer, respectively (**Figure 2A,B**) (Jiang et al., 2016; Lu et al., 2020). We project the different types and thicknesses of SSD into the acceleration-thickness diagram to get the PGAs required to trigger different types of SSD in the Lixian section.

PGA- MMI Relations

The degree of ground shaking during earthquakes can be determined by the documented PGA and MMI (Bilal and Askan, 2014). In various earthquake studies, MMI is inferred from regional datasets, peak ground-motion data, isoseismic maps, and earthquake damage reports (Worden et al., 2012), especially in paleoseismic studies. Du et al. (2019) established the relationship between MMI and PGA in the Longmen Shan fault zone based on 34 moderate to large earthquakes. In this study, we use this relationship to infer the MMI information of the paleoseismic records in the Lixian section.

The equation is expressed as

$$\mathrm{MMI} = 3.311 \log \mathrm{PGA} - 0.354 \quad (1)$$

Intensity (I) - Magnitude (*M*) - Epicentral Distance (R) Relations

Establishing a seismic attenuation relationship is an important action in regional evaluation of seismic risk (Lei et al., 2007). Due to the complex tectonic background in China, there are significant differences in seismic attenuation relationships established in different regions.

Lei et al. (2007) established a seismic attenuation relationship based on 96 recent destructive earthquakes in Southwest China as follows.

$$\text{Long axis}: \ I_a = 7.3568 + 1.2780M - 5.0655lg(R_a + 24) \quad (2)$$

$$\text{Short axis}: \ I_b = 3.9502 + 1.2780M - 3.7567g(R_b + 9) \quad (3)$$

where I is the intensity of the MMI and R is the epicentral distance.

Considering that the Wenchuan earthquake intensity isoseismal map is distributed along the strike of the Longmen Shan fault zone (NE-SW), and the Lixian section is located on its short axis (**Figure 1B**). In this study, we use the short-axis relationship to study the seismic record of the Lixian section.

B Value and Completeness of Magnitude

The b value is the most important parameter in the magnitude-frequency relationship (Gutenberg-Richter distributions) (Wesnousky, 1995), and plays an important role in seismicity studies and seismic hazard analysis. In order to obtain a reliable complete earthquake catalog and b value, we use the empirical relations (Lei et al., 2007; Du et al., 2019) to obtain the fault distribution range and epicenter distance that triggered the lowest-degree deformation in the Lixian section based on the upper limit of potential source earthquake. We extract the seismic

data (6,435 data from 1970 to 2020) within the range of 95 km away from the Lixian section.

The minimum completeness magnitude (*Mc*) is identified by the methods of cumulative number of earthquakes plotted against time and maximum curvature (Woessner and Wiemer, 2005). On this basis, the maximum likelihood method is used to fit the corresponding seismicity parameters (b value).

RESULTS

Magnitude Constraint for SSD

In the Lixian section, we identified 17 SSD layers (**Supplementary Table S1**). Due to the absence of paleoseismic records from the middle Holocene (~6.0 ka) to present in the Lixian section, the 2008 M_w 7.9 Wenchuan earthquake provided a favorable condition for the magnitude limitation of large earthquakes in this study. Analysis of empirical equation and inversion suggests that the instrumental data (PGA = 0.21–0.38, Liu and Li, 2009) around the Lixian section correspond to the magnitudes of 7.9–8.5 and MMI of Ⅶ–Ⅷ of the Wenchuan earthquake, by taking R = 50 km (epicentral distance). The above results are consistent with the actual data (M_w of 7.9, MMI of Ⅷ–Ⅸ). These results increase the reliability of the empirical equation applied in the eastern margin of the Tibetan Plateau.

In this study, six layers of micro-folds, five layers of flame structures, four layers of slump folds and two layers of clastic breccia have been identified in the Lixian lacustrine sequence (**Supplementary Table S1**, **Figure 2A**). According to the distribution of different types of the Lixian SSD strcutures in the acceleration-thickness diagram (**Figure 2C**), the PGA for triggering SSD is ≥0.13g, ≥ 0.19g, ≥ 0.43 g and ≥0.63 g (**Supplementary Table S2**). Because the projection points are on the boundary of different deformation types, we obtained the lower boundary of acceleration that can reflect the triggering of typical deformation on the eastern margin of the Tibetan Plateau. According to the regional empirical equation (Du et al., 2019), we constrain the intensity of the four typies of SSD paleoearthquake records with MMI ≥ Ⅵ½, ≥ Ⅶ, ≥ Ⅷ½ and ≥ Ⅸ (**Supplementary Table S2**).

According to the regional empirical attenuation relations and regional geological survey, the middle segment of Longmen Shan fault zone is the main fault that triggered deformations in the Lixian lacustrine sequence, while the Miyaluo fault can only trigger the low-degree deformations (micro-folds and flame structures) (**Supplementary Text S1**). In this study, the minimum epicentral distance triggering deformation in the Lixian section is limited to $R_{min} \geq 10$, and the $R_{max} \leq 95$ km (**Supplementary Table S3**). According to the regional empirical equation (Lei et al., 2007; Du et al., 2019), the six layers of micro-folds (MMI ≥ Ⅵ½, PGA ≥0.13) and five layers of flame structures (MMI ≥ Ⅶ, PGA ≥0.19) recorded in the Lixian lacustrine sequence correspond to magnitudes of $M \geq 5.9$, 6.3 ($R_{min} \geq$ 10 km) and $M \geq 6.8$, 7.2 ($R \geq 30$ km), respectively (**Table 1**). Previous studies show that SSD can be triggered by $M_w > 5.7$ in or near isoseismic lines with MMI ≥ VII (Monecke et al., 2006). Multiple faults in the region considered are likely to trigger low-degree deformations in the Lixian lacustrine sequence. Therefore, MMI ≥ Ⅵ½ ($M \geq 5.9$) are taken as the lower-boundary conditions for triggering the deformation in the Lixian lacustrine sequence, by taking $R_{min} \geq 10$ km.

Four layers of slump folds (MMI ≥ Ⅷ½) and two layers of clastic breccia layers (MMI ≥ Ⅸ) recorded in the Lixian section correspond to PGA of 0.43 and 0.63, respectively, which are probably a response to the larger seismic shaking in the middle segment of the Longmen Shan fault zone. According to the regional empirical equation (Lei et al., 2007; Du et al., 2019), the MMI ≥ Ⅷ½ and Ⅸ earthquake events correspond to $M \geq 8.1$ and 8.6, by taking $R_{min} \geq 30$, respectively (**Table 1**). The trigger conditions for slump folds ($M \geq 8.1$, MMI ≥ Ⅷ½) are consistent with the actual data of the Wenchuan earthquake (M_w of 7.9, MMI of Ⅷ - Ⅸ), which well constrain the largest earthquake magnitude of the Lixian section. Because only two layers of clastic breccia are recorded in the Lixian lacustrine sequence which are less representative (**Figure 2C**), and the $M \geq 8.6$ is much larger than the potential source magnitude (M = 8.0) in the eastern margin of the Tibetan Plateau (**Supplementary Figure S3**), the clastic breccia layers in this study are divided into slump folds. Thus, $M \geq 8.1$ is the highest magnitude recorded by SSD structures in the Lixian lacustrine sequence.

Magnitude Constraint for Coarse-Silt Layers

Besides the SSD layers in the study area, there are also many coarse-silt layers, among which 17 directly overlie the SSD layers, indicating that deformation developed at the sediment surface (e.g. Alsop et al., 2022) (**Figure 4A**) and 46 layers exist independently (**Figure 4B**, **Supplementary Table S4**). These coarse-silt layers are caused by earthquakes, through which many more sources of clastic particles increased instantly and supplied plenty of dust particles for the study area (**Figure 3**) (Jiang et al., 2017). Generally, the thickness of the seismic event layers recorded by lacustrine sediments can be correlated with the seismic intensity, and further used to infer the regional palaeoseismic intensity (Moernaut et al., 2014).

The SSD thickness in the Lixian section has a good correlation (coefficient of 0.67) with seismic intensity, while the correlation weakens between thickness of coarse-silt layers that overlie SSD and seismic intensity with a low coefficient of 0.30 (**Figure 4C,D**). Intriguingly, when MMI is ≤ Ⅵ½, the thickness of coarse-silt layers are less than 10 cm (**Figure 4D**); when MMI is > Ⅵ½, the coarse-silt layers become thicker with the increase of intensity. The thickest is up to 19 cm (MMI ≥ Ⅷ½). Therefore, the thickness ≥19 cm of coarse-silt layer is linked with MMI ≥ Ⅷ½ event, and the 10–19 cm layer is linked with MMI ≥ Ⅶ event in this study.

In addition, the China seismic intensity scale shows that MMI of Ⅵ can produce slight damage, and MMI ≥ Ⅶ is a destructive earthquake (http://www.gb688.cn/bzgk/gb/index). The boundary condition for deformation of linear waves in the Lixian section is MMI ≥ Ⅵ½ (PGA ≥0.13 g), which is sufficient to produce geomorphic destruction. Therefore, 35 event layers of coarse

TABLE 1 | Magnitude constraint for paleosesmic events in the Lixian section.

Epicentral distance (R; to Lixian, km)	Earthquake indicators	Acceleration[a] (*g*)	Intensity[b] (MMI)	Magnitude[c] (M_{min})
≥10	Micro-folds	≥0.13	≥ VI½	≥5.9
	Flame structures	≥0.19	≥ VII	≥6.3
≥30	Micro-folds	≥0.13	≥ VI½	≥6.8
	Flame structures	≥0.19	≥ VII	≥7.2
	Slump folds	≥0.43	≥ VIII½	≥8.1
	Clastic breccia layers	≥0.63	≥ IX	≥8.6

[a]*Data are obtained from* ***Supplementary Figure S4C****.*
[b]*Based on MMI, 3.311 log PGA, 0.354 (Du et al., 2019).*
[c]*Based on* I_b = 3.9502 + 1.2780*M* - 3.7567 g (R_b + 9) *(Lei et al., 2007).*

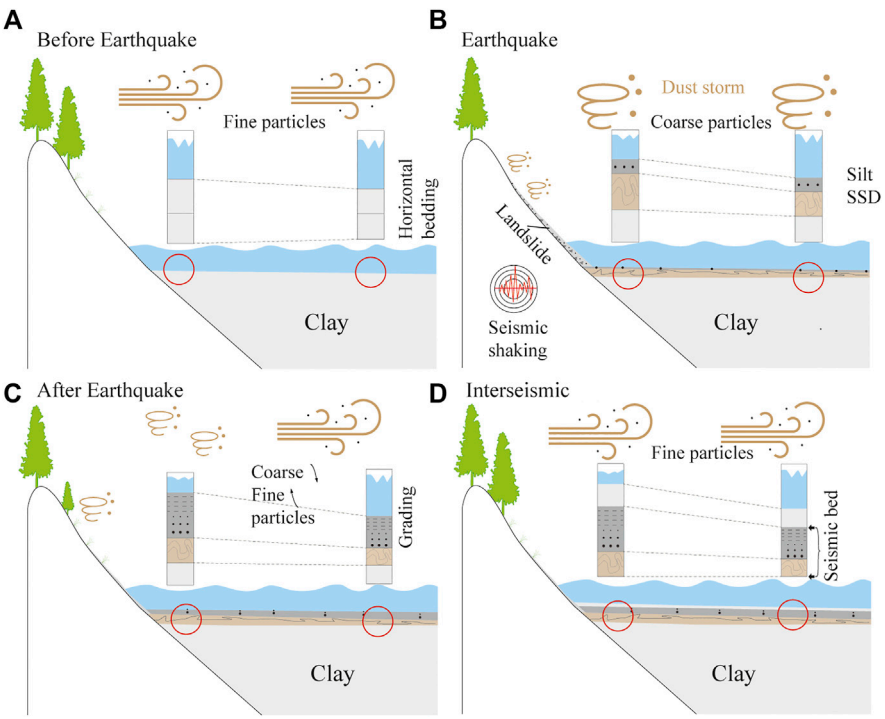

FIGURE 3 | Conceptual model of seismic layers **(A)** Background dust deposition before earthquake, with horizontal bedding **(B)** The earthquake shaking not only causes deformation of the water-saturated sediments but also provides abundant fresh coarse particles through dust storms, large quantities of landslides and surface loosening **(C)** As the landscape and vegetation restore, coarse particles decrease while fine particles increase **(D)** The source of lake sediments restores to its pre-earthquake level, and a seismic event layer is recorded.

particles (5–10 cm) occurring independently correspond probably to the moderate-strong earthquakes with MMI ≥ VI½.

DISCUSSION

A 13.3-Ka-Long Earthquake Record

Considering that the aftershocks of the 2008 Wenchuan earthquake are too many to represent the long-term seismic activity in the study area, the space-time window method (Gardner and Knopoff, 1974) is used to delete the fore- and aftershocks. Based on the analysis of seismic data from 1970 to 2020 (**Supplementary Figure S4A**), the quality of seismic records after 1986 (**Supplementary Figure S4B**) is high with M_c of 3.5 and b value of 1.06 (**Figure 5F**).

The frequency-magnitude relationship shows that the moderate-strong earthquakes ($M \geq 5.9$) and the strong earthquakes ($M \geq 6.3$) records in the Lixian section extends the fitting line of Gutenberg-Richter relationship from 5.3 to 6.3 with b value of 1.06 (**Figure 5F**), which indicates that the palaeoseismic records revealed by this study make up for the vacancy of the regional moderate-strong earthquakes and increase their completeness. The large earthquakes ($M \geq 8.1$) are much more frequent than in the fitting line of Gutenberg-Richter relationship (**Figure 5F**), which possibly indicate regional characteristic

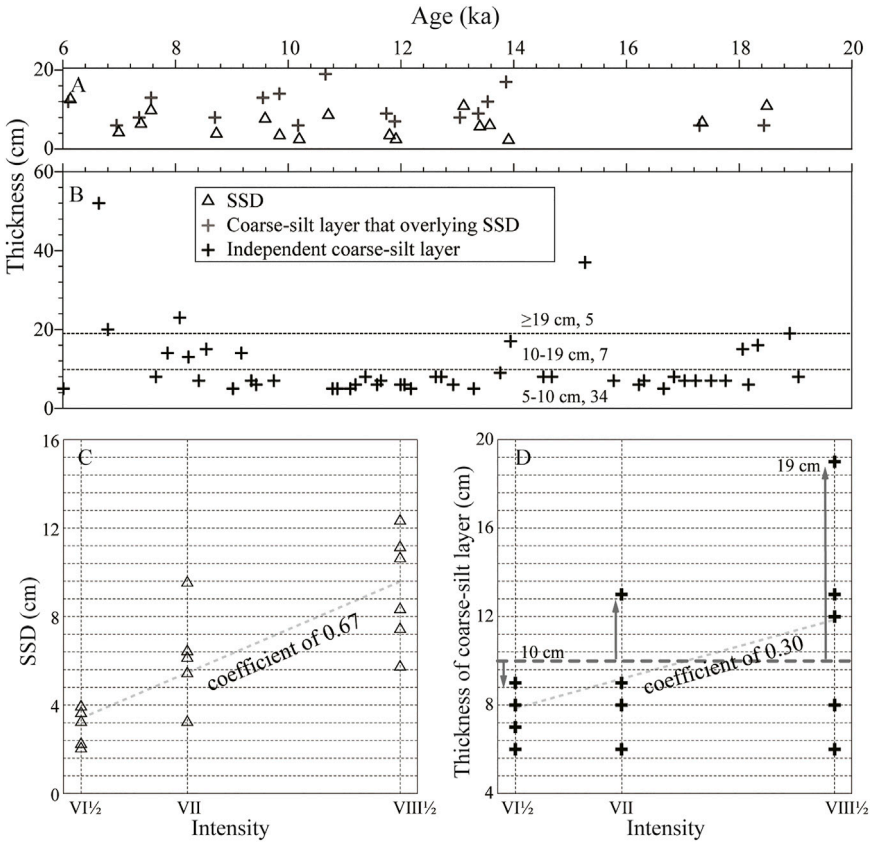

FIGURE 4 | Thickness variations and analysis of the SSD structures and coarse-silt layers with time **(A)** Distribution characteristics of the SSD structures and overlying coarse-silt layers, and **(B)** the independent coarse-silt layers **(C)** Correlation of SSD structure and **(D)** its overlying coarse-silt layers with MMI, note that the SSD thickness has better correlation with seismic intensity that than its overlying coarse-silt layers.

earthquakes (Wesnousky, 1995). Nevertheless, the significantly low b values (0.5–1.2) in Mianzhu-Maoxian of the middle-north segment of the Longmen Shan fault zone reflect the sliding state of frequent moderate-small earthquakes under the relatively high stress (Yi et al., 2006; Yi et al., 2008; Yang and Zhang, 2010), and strong earthquakes are most likely to occur in the future. This is consistent with many strong earthquakes in the middle segment of Longmen Shan fault zone revealed by this study, which implies that the magnitude constraint for strong seismic shaking events in this study is appropriate.

Earthquake Recurrence Models and Trigger Mechanism

Linear interpolation was carried out based on the existing optically stimulated luminescence (OSL) dating results (**Supplementary Figure S5**, Jiang et al., 2016) to define the timing of paleoseismic events in the Lixian section. The 63 moderate-strong earthquakes of MMI ≥ VI½ ($M \geq 5.9$) in the Lixian lacustrine record have a mean recurring time of 210 years (**Figure 5A** and **Table 2**). The mean recurring time of strong earthquakes of MMI ≥ VII ($M \geq 6.3$) is about 600 years. The large earthquakes of MMI ≥ VIII½ ($M \geq 8.1$) have the longest recurring time of 1,200 years.

The dimensionless coefficient of variation (COV) is a commonly used parameter in describing earthquake recurrence model, which includes "quasi-periodic" (COV ≤0.7), random (COV ≈1) and "clustered" (aperiodic, COV >1) (Kagan and Jackson, 1991; Berryman et al., 2012; Griffin et al., 2020; Moernaut, 2020). For intraplate settings, a Poisson or clustered recurrence model seems the most appropriate, while plate boundaries generally show quasi-periodic or weakly periodic of recurrence intervals (Williams et al., 2019; Moernaut, 2020). The MMI ≥ VI½, ≥ VII and ≥ VIII½ events recorded in the Lixian section have the COV of 0.66, 1.06, 0.77, respectively (**Table 2**; **Figure 5**). In the following, we discuss the recurrence models and trigger mechanism of these three types earthquake.

The Longmen Shan fault zone is developed along the eastern margin of the Tibetan Plateau, which is the plate boundary between the Bayan Kala fault block and Sichuan Basin (**Figure 1**). It has a low slip rate (**Supplementary Figure S1**) (Zhang, 2013). The recurrence interval of the 13.3-ka-long large earthquake records of MMI ≥ VIII½ ($M \geq 8.1$) follows the Weibull distribution (**Figure 5**) with a small COV (0.77), which reflects the weak quasi-periodic recurrent model of the plate boundary

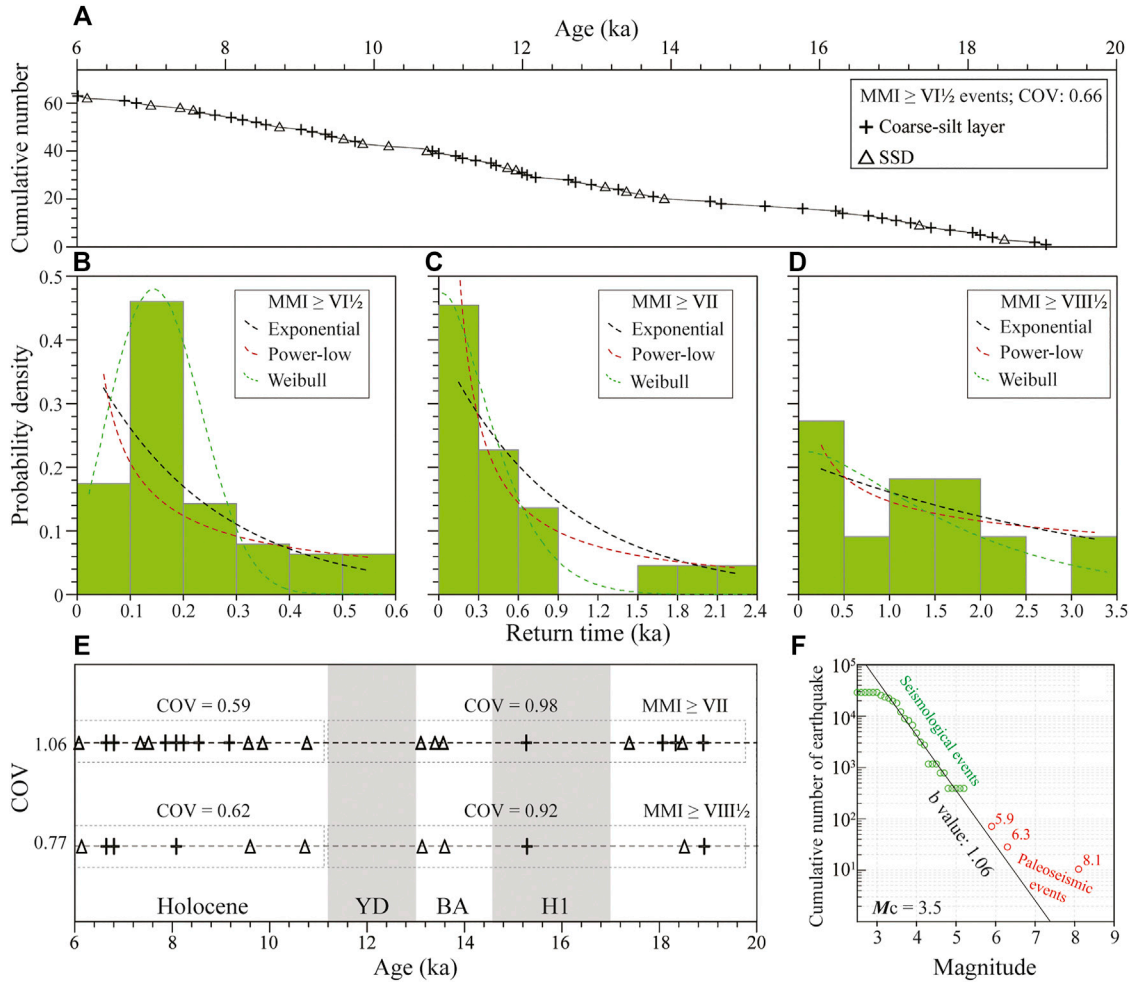

FIGURE 5 | Recurrence time statistics of seismites and magnitude constraint for strong seismic shaking events during 6.0–19.3 ka **(A)** Temporal distribution of moderate (MMI ≥ VI½) seismic shaking events **(B–D)** Histograms for return times of MMI ≥ VI½, ≥ VII, and ≥ VIII½ events. We plot difference distribution types (exponential, power-law and Weibull) for each dataset **(E)** Temporal distributions of strong and large earthquakes of the Lixian section **(F)** Magnitude-frequency distribution of modern (green colored) and paleoseismic (red colored) of the Lixian section during 6.0–19.3 ka.

TABLE 2 | Statistical analysis of recurrence times for the referred records.

		MMI ≥ VI½ events	**MMI ≥ VII events**	**MMI ≥ VIII½ events**
Magnitude (*M*)		≥5.9	≥6.3	≥8.1
PGA		≥0.13 g	≥0.18 g	≥0.43 g
Time period		6.0–19.3 ka	6.0–19.3 ka	6.0–19.3 ka
Number of events		63	22	11
Mean recurrence time (year)		210	600	1,200
COV		0.66	1.06	0.77
Fitting of return time distribution (R^2)	Weibull	0.82	0.95	0.48
	Exponential	0.76	0.92	0.38
	Power-law	0.57	0.98	0.41
Earthquake recurrence model		quasi-periodic	random	quasi-periodic

(Williams et al., 2019; Moernaut, 2020). The 1,200 years of recurrence interval of large earthquakes in the Lixian section is much shorter than 2,000–6,000 years inferred previously (Zhang et al., 2008; Zhang, 2013; Ran et al., 2014), which indicates the continuous lacustrine sequence are of great scientific significance in revealing a continuous paleoseismic record and assessing the seismic risk. The 2008 M_w 7.9 Wenchuan earthquake occurred in the middle segment of Longmen Shan fault zone, which is the

seismogenic fault that possibly triggered the high-degree deformations in the Lixian lacustrine sequence. In addition, the isolated and geometrically simple plate boundary faults exhibit relatively regular recurrence patterns (quasi-periodic) (Berryman et al., 2012). Therefore, the weak quasi-periodic recurrent model of large earthquakes recorded in the Lixian section may respond to the periodic accumulation and release of energy in the Longmen Shan fault zone caused by the mutual compression of the Tibetan Plateau and South China block (Zhang et al., 2003). In contrast, the MMI ≥ VI½ ($M \geq 5.9$) earthquake records also show the stronger quasi-periodic (the Weibull distribution and COV of 0.66) (**Figure 5**), which may be due to the combined effect of multiple faults (Longmen Shan fault zone, Minjiang fault and Miyaluo fault, **Supplementary Figure S4**) leading to more frequent seismic records (**Supplementary Text S1**).

The MMI ≥ VII ($M \geq 6.3$) earthquake records follow a power-law distribution with a COV of 1.06, which indicate a random (Poisson) recurrence model in the in-plate (Williams et al., 2019; Moernaut, 2020). The additive influence of different active seismic sources can result in an overall Poisson recurrence process (Gomez et al., 2015), and the strong stress interactions on the complex fault geometry and other active faults in the vicinity can lead to irregular seismic cycles (Visini and Pace, 2014). Therefore, the random recurrence model of 13.3-ka-long earthquake events of MMI ≥ VII ($M \geq 6.3$) is a superposition response to the multiple active seismic sources of the middle segment of Longmen Shan fault zone and Miyaluo fault (**Supplementary Text S1**).

The number of MMI ≥ VII ($M \geq 6.3$) and MMI ≥ VIII½ ($M \geq 8.1$) earthquakes recorded in the Lixian section during the last deglaciation (11.6–18.0 ka) is significantly less than that in the early Holocene (6.0–11.6 ka). The most critical aspect is that only one earthquake is recorded during the Younger Dryas (YD, 11.6–12.9 ka) and Heinrich 1 (H1, 14.6–17.8 ka) (**Figure 5E**). Entering the Holocene, the number of earthquakes in the Lixian section increases significantly (**Figure 5**) and shows a "quasi-periodic" earthquake recurrence model (COV of 0.59 and 0.62), while a random recurrence model fits for the last deglaciation (COV of 0.98 and 0.92). The frequency of earthquake recurrence in Bølling-Allerød (BA) and Holocene (warm period) is more frequent, but much less in YD and H1 (cold period), which reflects the obvious correlation between earthquake occurrence and climate change in the Longmen Shan fault zone. This is comparable with the behavior of strong earthquakes ($M > 7$) in Japan, more frequent in spring and summer (warm) than in autumn and winter (cold) (Heki, 2003). The increase in pore-fluid pressure caused by groundwater recharge can trigger seismic activity by reducing the effective normal stress on the fault (Heki, 2003; Christiansen et al., 2005; Montgomery-Brown et al., 2019), and is deserving of further investigation in the future.

CONCLUSION

We attempt to correlate the soft sediment deformation and seismic records in Lixian lacustrine sediments with earthquake intensity to discuss recurrence interval and recurrence models of regional paleoseismic events. We find that the MMI ≥ VI½ ($M \geq 5.9$, $R_{min} \geq 10$ km) is the lower-boundary condition for triggering deformation in the Lixian lacustrine sediments. The clastic breccia layer corresponds to the maximum earthquake magnitude ($M \geq 8.1$, MMI ≥ VIII½) recorded in the Lixian section. The recurrence time of large earthquakes ($M \geq 8.1$) is 1,200 years in the Longmen Shan collision zone. The Maoxian-Wenchuan fault is the main fault that triggered the slump folds and clastic breccia layers in the Lixian lacustrine sediments. In addition, the frequency of large earthquake recurrence in the warm period is more frequent than that in the cold period.

DATA AVAILABILITY STATEMENT

The original contributions presented in the study are included in the article/**Supplementary Material**, further inquiries can be directed to the corresponding author.

AUTHOR CONTRIBUTIONS

WS: Conceptualization, Methodology, Validation, Formal analysis, Investigation, Data Curation, Writing-Original Draft, Writing-Review and Editing, Visualization. HJ: Methodology, Investigation, Resources, Writing-Review and Editing, Project administration, Funding acquisition. GA: Writing- Review and Editing. GW: Methodology, Investigation.

FUNDING

This study is supported by the National Nonprofit Fundamental Research of China Institute of Geology China Earthquake Administration (IGCEA 2126, 1906), the National Natural Science Foundation of China (41572346).

SUPPLEMENTARY MATERIAL

The Supplementary Material for this article can be found online at: https://www.frontiersin.org/articles/10.3389/feart.2022.838299/full#supplementary-material

REFERENCES

Alsop, G. I., Marco, S., and Levi, T. (2022). Recognising Surface Versus Sub-Surface Deformation of Soft-Sediments: Consequences and Considerations for Palaeoseismic Studies. *J. Struct. Geol.* 154, 104493. doi:10.1016/j.jsg.2021.104493

Berryman, K. R., Cochran, U. A., Clark, K. J., Biasi, G. P., Langridge, R. M., and Villamor, P. (2012). Major Earthquakes Occur Regularly on an Isolated Plate Boundary Fault. *Science* 336 (6089), 1690–1693. doi:10.1126/science.1218959

Bilal, M., and Askan, A. (2014). Relationships between Felt Intensity and Recorded Ground-Motion Parameters for Turkey. *Bull. Seismol. Soc. Am.* 104 (1), 484–496. doi:10.1785/0120130093

Christiansen, L., Hurwitz, S., Saar, M., Ingebritsen, S., and Hsieh, P. (2005). Seasonal Seismicity at Western United States Volcanic Centers. *Earth Planet. Sci. Lett.* 240 (2), 307–321. doi:10.1016/j.epsl.2005.09.012

Dai, F. C., Xu, C., Yao, X., Xu, L., Tu, X. B., and Gong, Q. M. (2011). Spatial Distribution of Landslides Triggered by the 2008 M_s 8.0 Wenchuan Earthquake, China. *J. Asian Earth Sci.* 40 (4), 883–895. doi:10.1016/j.jseaes.2010.04.010

Deng, Q. D., Gao, X., Chen, G. H., and Yang, H. (2010). Recent Tectonic Activity of Bayan Kala Fault-Block and the Kunlun-Wenchuan Earthquake Series of the Tibetan Plateau. *Earth Sci. Front.* 17 (5), 163–178. in Chinese. CN/Y2010/V17/I5/163

Deng, Q. D., Cheng, S. P., Ma, J., and Du, P. (2014). Seismic Activities and Earthquake Potential in the Tibetan Plateau. *Chin. J. Geophys.* 57 (5), 2025–2042. in Chinese. doi:10.6038/cjg20140701

Deng, Q. D. (2008). Some Thoughts on the M_s 8.0 Wenchuan, Sichuan Earthquake. *Seismol. Geol.* 30 (4), 811–827. in Chinese. doi:10.3969/j.issn.0253-4967.2008.04.001

Ding, Z., Yu, Z., Rutter, N. W., and Liu, T. (1994). Towards an Orbital Time Scale for Chinese Loess Deposits. *Quat. Sci. Rev.* 13 (1), 39–70. doi:10.1016/0277-3791(94)90124-4

Ding, H. R., Ma, G. W., Ni, S. J., Shi, Z. M., Zhao, G. H., Yan, L., et al. (2014). Study on Sediment Discharge Increase Caused by Wenchuan Earthquake Landslide and Heavy Rainfall in the Upper Reaches of the Min River. *J. Sichuan Univ.* 46 (3), 49–55. in Chinese. doi:10.15961/j.jsuese.2014.03.006

Du, K., Ding, B., Luo, H., and Sun, J. (2019). Relationship between Peak Ground Acceleration, Peak Ground Velocity, and Macroseismic Intensity in Western China. *Bull. Seismol. Soc. Am.* 109 (1), 284–297. doi:10.1785/0120180216

Fan, J. W., Xu, H. Y., Shi, W., Guo, Q. Q., Zhang, S. Q., Wei, X. T., et al. (2022). A ~28-kyr Continuous Lacustrine Paleoseismic Record of the Intraplate, Slow-Slipping Fuyun Fault in Northwest China. *Front. Earth Sci.* 10, 828801. doi:10.3389/feart.2022.828801

Gao, M. T. (2015). *Teaching Book of Seismic Zoning Map of China*. GB 18306–2015. Beijing: China Zhijian Publishing House. in Chinese.

Gardner, J. K., and Knopoff, L. (1974). Is the Sequence of Earthquakes in Southern California, with Aftershocks Removed, Poissonian? *Bull. Seismol. Soc. Am.* 64 (5), 1363–1367. doi:10.1785/BSSA0640051363

Ghazoui, Z., Bertrand, S., Vanneste, K., Yokoyama, Y., and Beek, P. (2019). Potentially Large post-1505 Ad Earthquakes in Western Nepal Revealed by a lake Sediment Record. *Nat. Commun.* 10 (1), 2258. doi:10.1038/s41467-019-10093-4

Gomez, B., Corral, Á., Orpin, A. R., Page, M. J., Pouderoux, H., and Upton, P. (2015). Lake Tutira Paleoseismic Record Confirms Random, Moderate to Major And/or Great Hawke's Bay (New Zealand) Earthquakes. *Geology* 43 (2), 103–106. doi:10.1130/G36006.1

Griffin, J. D., Stirling, M. W., and Wang, T. (2020). Periodicity and Clustering in the Long-Term Earthquake Record. *Geophys. Res. Lett.* 47, e2020GL089272. doi:10.1029/2020GL089272

Heki, K. (2003). Snow Load and Seasonal Variation of Earthquake Occurrence in Japan. *Earth Planet. Sci. Lett.* 207 (1-4), 159–164. doi:10.1016/S0012-821X(02)01148-2

Jiang, H., Mao, X., Xu, H., Yang, H., Ma, X., Zhong, N., et al. (2014). Provenance and Earthquake Signature of the Last Deglacial Xinmocun Lacustrine Sediments at Diexi, East Tibet. *Geomorphology* 204 (1), 518–531. doi:10.1016/j.geomorph.2013.08.032

Jiang, H., Zhong, N., Li, Y., Xu, H., Yang, H., and Peng, X. (2016). Soft Sediment Deformation Structures in the Lixian Lacustrine Sediments, Eastern Tibetan Plateau and Implications for Postglacial Seismic Activity. *Sediment. Geol.* 344, 123–134. doi:10.1016/j.sedgeo.2016.06.011

Jiang, H., Zhong, N., Li, Y., Ma, X., Xu, H., Shi, W., et al. (2017). A Continuous 13.3-ka Record of Seismogenic Dust Events in Lacustrine Sediments in the Eastern Tibetan Plateau. *Sci. Rep.* 7 (1), 15686. doi:10.1038/s41598-017-16027-8

Kagan, Y. Y., and Jackson, D. D. (1991). Long-term Earthquake Clustering. *Geophys. J. Int.* 104 (1), 117–134. doi:10.1111/j.1365-246X.1991.tb02498.x

Kirby, E., Reiners, P. W., Krol, M. A., Whipple, K. X., Hodges, K. V., Farley, K. A., et al. (2002). Late Cenozoic Evolution of the Eastern Margin of the Tibetan Plateau: Inferences from40Ar/39Ar and (U-Th)/He Thermochronology. *Tectonics* 21, 1. doi:10.1029/2000TC001246

Lei, J. C., Gao, M. T., and Yu, Y. X. (2007). Seismic Motion Attenuation Relations in Sichuan and Adjacent Areas. *Acta Seismol. Sin.* 29 (5), 500–511. in Chinese. doi:10.1007/s11589-007-0532-y

Li, G., West, A. J., Densmore, A. L., Jin, Z., Parker, R. N., and Hilton, R. G. (2014). Seismic Mountain Building: Landslides Associated with the 2008 Wenchuan Earthquake in the Context of a Generalized Model for Earthquake Volume Balance. *Geochem. Geophys. Geosyst.* 15 (4), 833–844. doi:10.1002/2013GC005067

Liang, L. J., and Jiang, H. C. (2017). Geochemical Composition of the Last Deglacial Lacustrine Sediments in East Tibet and Implications for Provenance, Weathering and Earthquake Events. *Quat. Int.* 430, 41–51. doi:10.1016/j.quaint.2015.07.037

Liu, Q., and Li, X. (2009). Preliminary Analysis of the Hanging wall Effect and Velocity Pulse of the 5.12 Wenchuan Earthquake. *Earthq. Eng. Eng. Vib.* 8 (2), 165–177. doi:10.1007/s11803-009-9043-2

Liu, M. (2014). *Research on the Risk Stone under Wind Loading with Wind Tunnel Test in the Min River Valley*. master thesis. Sichuan: Chengdu University of Technology, 1–95. in Chinese.

Lu, Y., Waldmann, N., Ian Alsop, G., and Marco, S. (2017). Interpreting Soft Sediment Deformation and Mass Transport Deposits as Seismites in the Dead Sea Depocenter. *J. Geophys. Res. Solid Earth* 122, 8305–8325. doi:10.1002/2017JB014342

Lu, Y., Wetzler, N., Waldmann, N., Agnon, A., and Marco, S. (2020). A 220,000-Year-Long Continuous Large Earthquake Record on a Slow-Slipping Plate Boundary. *Sci. Adv.* 6 (48), eaba4170. doi:10.1126/sciadv.aba4170

Moernaut, J., Daele, M. V., Heirman, K., Fontijn, K., Strasser, M., Pino, M., et al. (2014). Lacustrine Turbidites as a Tool for Quantitative Earthquake Reconstruction: New Evidence for a Variable Rupture Mode in South central Chile. *J. Geophys. Res. Solid Earth* 119 (3), 1607–1633. doi:10.1002/2013JB010738

Moernaut, J., Van Daele, M., Fontijn, K., Heirman, K., Kempf, P., Pino, M., et al. (2018). Larger Earthquakes Recur More Periodically: New Insights in the Megathrust Earthquake Cycle from Lacustrine Turbidite Records in South-central Chile. *Earth Planet. Sci. Lett.* 481, 9–19. doi:10.1016/j.epsl.2017.10.016

Moernaut, J. (2020). Time-Dependent Recurrence of strong Earthquake Shaking Near Plate Boundaries: a lake Sediment Perspective. *Earth-Sci. Rev.* 210, 103344. doi:10.1016/j.earscirev.2020.103344

Monecke, K., Anselmetti, F. S., Becker, A., Schnellmann, M., Sturm, M., and Giardini, D. (2006). Earthquake-induced Deformation Structures in lake Deposits: a Late Pleistocene to Holocene Paleoseismic Record for central Switzerland. *Eclogae Geol. Helv.* 99 (3), 343–362. doi:10.1007/s00015-006-1193-x

Montgomery-Brown, E. K., Shelly, D. R., and Hsieh, P. A. (2019). Snowmelt-triggered Earthquake Swarms at the Margin of long valley Caldera, California. *Geophys. Res. Lett.* 46, 3698–3705. doi:10.1029/2019GL082254

Oswald, P., Strasser, M., Hammerl, C., and Moernaut, J. (2021). Seismic Control of Large Prehistoric Rockslides in the Eastern Alps. *Nat. Commun.* 12 (1), 1059. doi:10.1038/s41467-021-21327-9

Owen, G., and Moretti, M. (2011). Identifying Triggers for Liquefaction-Induced Soft-Sediment Deformation in Sands. *Sediment. Geol.* 235 (3-4), 141–147. doi:10.1016/j.sedgeo.2010.10.003

Ran, Y. K., Chen, W. S., Xu, X. W., Chen, L. C., Hu, W., and Li, Y. B. (2014). Late Quaternary Paleoseismic Behavior and Rupture Segmentation of the Yingxiu-Beichuan Fault along the Longmen Shan Fault Zone, China. *Tectonics* 33 (11-12), 2218–2232. doi:10.1002/2014TC003649

Rodrı´guez-Pascua, M. A., Calvo, J. P., De Vicente, G., and Gómez-Gras, D. (2000). Soft-sediment Deformation Structures Interpreted as Seismites in Lacustrine Sediments of the Prebetic Zone, SE Spain, and Their Potential Use as Indicators of Earthquake Magnitudes during the Late Miocene. *Sediment. Geol.* 135 (1-4), 117–135. doi:10.1016/S0037-0738(00)00067-1

Sahu, B. K. (1964). Depositional Mechanisms from the Size Analysis of Clastic Sediments. *J. Sediment. Res.* 34, 73–83. doi:10.1306/74D70FCE-2B21-11D7-8648000102C1865D

Scharer, K. M., Biasi, G. P., Weldon, R. J., and Fumal, T. E. (2010). Quasi-periodic Recurrence of Large Earthquakes on the Southern San Andreas Fault. *Geology* 38 (6), 555–558. doi:10.1130/g30746.1

Shi, W., Jiang, H. C., Mao, X., and Xu, H. Y. (2020). Pollen Record of Climate Change During the Last Deglaciation from the Eastern Tibetan Plateau. *PLoS One* 15 (5), e0232803. doi:10.1371/journal.pone.0232803

Sims, J. D. (1975). Determining Earthquake Recurrence Intervals from Deformational Structures in Young Lacustrine Sediments. *Tectonophysics* 29 (1-4), 141–152. doi:10.1016/b978-0-444-41420-5.50020-4

Visini, F., and Pace, B. (2014). Insights on a Key Parameter of Earthquake Forecasting, the Coefficient of Variation of the Recurrence Time, Using a Simple Earthquake Simulator. *Seismol. Res. Lett.* 85 (3), 703–713. doi:10.1785/0220130165

Wei, X. T., Jiang, H. C., Xu, H. Y., Fan, J. W., Shi, W., Guo, Q. Q., et al. (2021). Response of Sedimentary and Pollen Records to the 1933 Diexi Earthquake on the Eastern Tibetan Plateau. *Ecol. Indicat.* 129, 107887. doi:10.1016/j.ecolind.2021.107887

Wen, X. Z., Zhang, P. Z., Du, F., and Long, F. (2009). The Background of Historical and Modern Seismic Activities of the Occurrence of the 2008 M_s 8.0 Wenchuan, Sichuan, Earthquake2008. *Chin. J. Geophys.* 52 (2), 444–454. in Chinese.

Wesnousky, S. G. (1995). The Gutenberg - Richter or Characteristic Earthquake Distribution, Which Is it? *TransL. World Seismol.* 84 (6), 1940–1959. doi:10.1007/BF00807992

Wetzler, N., Marco, S., and Heifetz, E. (2010). Quantitative Analysis of Seismogenic Shear-Induced Turbulence in lake Sediments. *Geology* 38 (4), 303–306. doi:10.1130/G30685.1

Williams, R. T., Davis, J. R., and Goodwin, L. B. (2019). Do large Earthquakes Occur at Regular Intervals through Time? A Perspective from the Geologic Record. *Geophys. Res. Lett.* 46 (14), 8074–8081. doi:10.1029/2019GL083291

Woessner, J., and Wiemer, S. (2005). Assessing the Quality of Earthquake Catalogues: Estimating the Magnitude of Completeness and its Uncertainty. *Bull. Seismol. Soc. Am.* 95 (2), 684–698. doi:10.1785/0120040007

Worden, C. B., Gerstenberger, M. C., Rhoades, D. A., and Wald, D. J. (2012). Probabilistic Relationships between Ground-Motion Parameters and Modified Mercalli Intensity in California. *Bull. Seismol. Soc. Am.* 102 (1), 204–221. doi:10.1785/0120110156

Xu, H. Y., Jiang, H. C., Liu, K., and Zhong, N. (2020). Potential Pollen Evidence for the 1933 M7.5 Diexi Earthquake and Implications for Post-Seismic Landscape Recovery. *Environ. Res. Lett.* 15, 094043. doi:10.1088/1748-9326/ab9af6

Xu, H. Y., Jiang, H. C., Yu, S., Yang, H. L., and Chen, J. (2015). OSL and Pollen Concentrate ^{14}C Dating of Dammed Lake Sediments at Maoxian, East Tibet, and Implications for Two Historical Earthquakes in AD 638 and 952. *Quat. Int.* 371, 290–299. doi:10.1016/j.quaint.2014.09.045

Xu, X., Wen, X., Yu, G., Chen, G., Klinger, Y., Hubbard, J., et al. (2009). Coseismic Reverse- and Oblique-Slip Surface Faulting Generated by the 2008 Mw 7.9 Wenchuan Earthquake, China. *Geology* 37 (6), 515–518. doi:10.1130/G25462A.1

Xu, C., Xu, X. W., Yao, X., and Dai, F. C. (2014). Three (Nearly) Complete Inventories of Landslides Triggered by the May 12, 2008 Wenchuan Mw 7.9 Earthquake of China and Their Spatial Distribution Statistical Analysis. *Landslides* 11 (3), 441–461. doi:10.1007/s10346-013-0404-6

Yang, N., and Zhang, Y. Q. (2010). Tission-track Dating for Activity of the Longmen Shan Fault Zone and Uplifting of the Western Sichuan Plateau. *J. Geomech.* 16 (4), 259–371. doi:10.1017/S0004972710001772

Yi, G. X., Wen, X. Z., Wang, S. W., Long, F., and Fan, J. (2006). Study on Fault Sliding Behaviors and strong-earthquake Risk of the Longmen Shan-Minshan Fault Zones from Current Seismicity Parameters. *Earthquake Res. China* 22 (2), 117–125. in Chinese. doi:10.3969/j.issn.1001-4683.2006.02.001

Yi, G. X., Wen, X. Z., and Su, Y. J. (2008). Study the Potential strong-earthquake Risk for the Eastern Boundary of the Sichuan-Yunnan Active Faulted-Block, China. *Chin. J. Geophys.* 56 (6), 1719–1725. in Chinese. doi:10.3321/j.issn:0001-5733.2008.06.012

Zhang, P. Z., Deng, Q. D., Zhang, M. G., Ma, J., Gan, W. J., Wei, M., et al. (2003). Active Tectonic Blocks and strong Earthquakes in the Continent of China. *Sci. China* 46 (2 Suppl. ment), 13–24. doi:10.1360/03dz0002

Zhang, P. Z., Xu, X. W., Wen, X. Z., and Ran, Y. K. (2008). Slip Rates and Recurrence Intervals of the Longmen Shan Active Fault Zone, and Tectonic Implications for the Mechanism of the May 12 Wenchuan Earthquake, 2008, Sichuan, China. *Chin. J. Geophys.* 51 (4), 1066–1073. in Chinese. doi:10.3321/j.issn:0001-5733.2008.04.015

Zhang, P. Z., Wen, X. Z., Shen, Z. K., and Chen, J. H. (2010). Oblique, High-Angle, Listric-Reverse Faulting and Associated Development of Strain: the Wenchuan Earthquake of May 12, 2008, Sichuan, China. *Annu. Rev. Earth Planet. Sci.* 38 (1), 353–382. doi:10.1146/annurev-earth-040809-152602

Zhang, P. Z. (2013). Beware of Slowly Slipping Faults. *Nat. Geosci.* 6 (5), 323–324. doi:10.1038/ngeo1811

Zhang, S. Q., Jiang, H. C., Fan, J. W., Xu, H. Y., Shi, W., Guo, Q. Q., et al. (2021). Accumulation of a Last Deglacial Gravel Layer at Diexi, Eastern Tibetan Plateau and its Possible Seismic Significance. *Front. Earth Sci.* 9, 797732. doi:10.3389/feart.2021.797732

Zhong, N., Jiang, H. C., Li, H. B., Xu, H. Y., Shi, W., Zhang, S. Q., et al. (2019). Last Deglacial Soft-Sediment Deformation at Shawan on the Eastern Tibetan Plateau and Implications for Deformation Processes and Seismic Magnitudes. *Acta Geol. Sin.* 93 (2), 430–450. doi:10.1111/1755-6724.13773

Conflict of Interest: The authors declare that the research was conducted in the absence of any commercial or financial relationships that could be construed as a potential conflict of interest.

Publisher's Note: All claims expressed in this article are solely those of the authors and do not necessarily represent those of their affiliated organizations, or those of the publisher, the editors and the reviewers. Any product that may be evaluated in this article, or claim that may be made by its manufacturer, is not guaranteed or endorsed by the publisher.

frontiers in Earth Science

ORIGINAL RESEARCH
published: 24 March 2022
doi: 10.3389/feart.2022.830317

Acceleration of Deep Slip Along the Longmenshan Fault Plane Before the 2008 *M*8.0 Wenchuan Earthquake

Jing Zhao[1,2], *Zhengyi Yuan*[1], *Jinwei Ren*[3], *Zaisen Jiang*[3], *Qi Yao*[3], *Zhihua Zhou*[1], *Chong Yue*[1], *Jun Zhong*[1] *and Anfu Niu*[1]*

[1]China Earthquake Networks Center, Beijing, China, [2]Institute of Geology, China Earthquake Administration, Beijing, China, [3]Institute of Earthquake Forecasting, China Earthquake Administration, Beijing, China

The first step toward earthquake forecasting is the identification of variables whose spatio-temporal variation can be connected with pre-seismic crustal deformation. Four periods of campaign Global Positioning System (GPS) observations around the Longmenshan fault zone (LFZ) provide important insights in crustal deformation and deep fault slip before the 2008 *M*8.0 Wenchuan earthquake. By using TDEFNODE to invert the coupling fraction and dynamic slip deficit rate of the Longmenshan fault plane before the Wenchuan earthquake, we show that under a background of strong coupling, the compressive slip deficit rate perpendicular to fault increased slightly at first and then decreased; a value of ~1.5–3.6 mm/a along the central–southern segment from 1999 to 2001 increased to ~1.9–3.9 mm/a from 2001 to 2004, and then decreased to ~1.1–2.6 mm/a from 2004 to 2007. The dextral slip deficit rate parallel to fault was ~6 mm/a from 1999 to 2004, before increasing significantly to ~9.5 mm/a from 2004 to 2007, when the compressive slip deficit rate decreased. At the same time, large-scale GPS velocity profiles show that compressive shortening deformation in the Eastern Tibet Block, perpendicular to fault, increased slightly from 2001 to 2004, and then decreased from 2004 to 2007. Meanwhile, the dextral shear deformation parallel to fault near the LFZ increased significantly from 2004 to 2007. These findings are in good agreement with those calculated using repeating earthquake sequences, indicating that the deep slip rate of the Longmenshan fault plane may have accelerated several years before the Wenchuan earthquake. Our results demonstrate that GPS data can record pre-seismic preparatory processes, and have the potential for use in medium-term large earthquake forecasting.

Keywords: wenchuan earthquake, longmenshan fault zone, fault coupling fraction, GPS velocity profiles, acceleration process of deep slip rate, pre-seismic preparatory processes, earthquake forecasting

OPEN ACCESS

Edited by:
Giovanni Martinelli, National Institute of Geophysics and Volcanology, Italy

Reviewed by:
Mattia Crespi, Geodesy and Geomatics Division—DICEA Sapienza University of Rome, Italy
Alexis Rigo, UMR8538 Laboratoire de géologie de l'Ecole Normale Supérieure (LG-ENS), France
Vladimir Kostoglodov, National Autonomous University of Mexico, Mexico

***Correspondence:**
Anfu Niu
Nafcsb2004@seis.ac.cn

Specialty section:
This article was submitted to Solid Earth Geophysics, a section of the journal Frontiers in Earth Science

Received: *07 December 2021*
Accepted: *21 February 2022*
Published: *24 March 2022*

Citation:
Zhao J, Yuan Z, Ren J, Jiang Z, Yao Q, Zhou Z, Yue C, Zhong J and Niu A (2022) Acceleration of Deep Slip Along the Longmenshan Fault Plane Before the 2008 M8.0 Wenchuan Earthquake. Front. Earth Sci. 10:830317. doi: 10.3389/feart.2022.830317

INTRODUCTION

The 2008 *M*8.0 Wenchuan earthquake occurred on the listric Longmenshan fault zone (LFZ) at the boundary between the Eastern Tibet Block and South China Block. Retrospective studies into anomalies that occurred before the Wenchuan earthquake have improved our understanding of large continental thrust earthquakes. In particular, estimations of stress and strain variation from geophysical observations have revealed pre-seismic preparatory processes. Li et al. (2011) investigated deep slip rate along the ruptured Longmenshan fault plane using repeating earthquake data. The measured *in situ* deep slip rate varied from 3.5 to 9.6 mm/a for a depth range of 4–18 km, and appeared

to increase with depth. Repeating earthquake data from around the world show that the acceleration of the deep slip rate can occur on different time scales before large earthquakes (Kato et al., 2016; Uchida et al., 2016). Using repeating earthquake data, Chen and Li (2018) found that the Hongkou–Wenchuan and Beichuan segments of the LFZ began to show signs of deep slip acceleration to varying degrees in around 2006. Using Global Positioning System (GPS) velocity fields during 1999–2004 and 2004–2007, Jiang et al. (2009) generated profiles across the LFZ, which showed that dextral shear deformation parallel to the LFZ along a span of 500 km to the west side of the LFZ increased during 2004–2007 compared with that during 1999–2004; Zou et al. (2015) also considered that the northeastward movement of the Eastern Tibet Block accelerated relative to the South China block during 2004–2007, which increased the dextral shear deformation of the LFZ. However, these results only relate to surface velocity; as such, there is a need to obtain the acceleration of the deep slip rate via inversion methods using GPS velocity fields.

Pre-seismic preparatory processes are closely related to the coupling fraction and slip deficit rate of the seismogenic fault. The distribution characteristics of the coupling fraction are important basis for assessing the background of seismic risk (Moreno et al., 2010; Loveless and Meade, 2011). Generally, during the seismogenic stage, the coupling fraction of the seismogenic fault will increase before gradually stabilizing (Savage and Prescott, 1978; Meade and Hager, 2005). GPS observations have resulted in an enormous quantity of data that have substantially increased our capacity to investigate earthquake-related processes. Based on GPS velocity fields, the coupling fraction of a fault plane can be obtained by negative dislocation inversion. Spatio-temporal variation of the fault slip deficit rate obtained by inversion can be used to calculate the rate of fault strain energy accumulation (McCaffrey et al., 2013; Li et al., 2021). When the seismogenic fault is strongly coupled, the acceleration of deep slip along the fault plane is an important index to judge the urgency of seismic risk (Kato and Nakagawa, 2014; Uchida et al., 2016; Chen and Li, 2018). By constructing a three-dimensional multi-fault model of the LFZ and its surrounding faults, we used the GPS velocity fields of 1999–2001, 2001–2004, 2004–2007, and 1999–2007 to invert the spatio-temporal evolution distribution of coupling fraction and slip deficit rate of the Longmenshan fault plane before the 2008 *M*8.0 Wenchuan earthquake using the TDEFNODE negative dislocation method (McCaffrey, 2002; McCaffrey, 2009). Variation in the deep slip rates before the earthquake were analyzed; moreover, based on GPS velocity profiles across the LFZ, the evolution of large-scale surface deformation before the earthquake was analyzed according to velocity components perpendicular and parallel to the LFZ. Finally, the dynamic deep–shallow deformation characteristics of the LFZ before the earthquake were comprehensively analyzed based on the deep inversion and surface profile results.

DATA AND METHODOLOGY

GPS Velocities

We performed inversions of four periods of GPS velocity fields: 1999–2001 (160 stations), 2001–2004 (153 stations), 2004–2007 (169 stations), and 1999–2007 (203 stations), with the latter set as the background result, and the first three as dynamic results (**Figure 1**). The GPS velocity fields were processed using the GAMIT/GLOBK software (Herring et al., 2006), and the computation refers to Wang (2009). The magnitudes of the GPS velocities depend on the reference frame. In this study, in order to observe the relative movement of different blocks more obviously, we have made the GPS velocities be with respect to the South China Block, which causes the GPS velocities to be much smaller than that in the International Terrestrial Reference Frame (ITRF). The gray ellipses represent the errors of GPS velocity fields. The eastern and northern median errors of the GPS velocity fields are 1.3 mm/a and 1.1 mm/a in 1999–2001, 2.0 mm/a and 2.0 mm/a in 2001–2004, 1.4 mm/a and 1.4 mm/a in 2004–2007, and 1.1 mm/a and 1.1 mm/a in 1999–2007.

The results of four periods of GPS velocity fields show that, compared with the South China Block, stations in the Eastern Tibet Block exhibited obvious northeastward movement; moreover, the velocity field of 2004–2007 also showed increase northeastward movement. These results indicate deformation across the LFZ was dominated by dextral shear with a certain amount of compressive shortening, and dextral shear increased from 2004 to 2007. At the same time, from northwest to southeast, the velocities of GPS stations in the Eastern Tibet Block gradually decreased, while the velocities of those in the LFZ were gradually close to that of stations in the South China Block. Compared with the South China Block, stations in the Sichuan–Yunnan Block exhibited significant clockwise rotation, indicating left-lateral strike-slip motion dominates the Xianshuihe–Anninghe–Zemuhe–Xiaojiang fault zones, while tensile and compressive motions are relatively weak.

Methodology

Fault locking theory assumes that the movement of GPS stations inside a block includes the block rotation, permanent strain inside the block, and surface elastic deformation at block boundaries due to fault coupling. The principle is as follows:

$$\begin{aligned} \boldsymbol{V}_i(\boldsymbol{X}) &= \sum_{b=1}^{B} H(\boldsymbol{X} \in \Delta_b)\left[{}_R\boldsymbol{\Omega}_b \times \boldsymbol{X}\right] \cdot \boldsymbol{i} + \dot{\varepsilon}_{ii}\Delta\boldsymbol{X}_i + \dot{\varepsilon}_{ij}\Delta\boldsymbol{X}_j \\ &\quad - \sum_{k=1}^{F}\sum_{n=1}^{N_k}\sum_{m=1}^{2}\phi_{nk}G_{im}(\boldsymbol{X},\boldsymbol{X}_{nk})\left[{}_h\boldsymbol{\Omega}_f \times \boldsymbol{X}_{nk}\right] \cdot \boldsymbol{m} \end{aligned} \tag{1}$$

where $\boldsymbol{X}$ is the position of the GPS station, B is the number of blocks, Δ_b is the subset of the model domain within block b (H = 1 if the point $\boldsymbol{X}$ is contained within block b, H = 0 otherwise), ${}_R\boldsymbol{\Omega}_b$ is the Euler pole of block b relative to the reference frame, $\boldsymbol{i}$ is the unit vector in i direction (x or y), $\dot{\varepsilon}$ is the uniform strain rate inside the block, F is the number of faults, N_k is the number of nodes defining fault k, $\boldsymbol{X}_{nk}$ is the position of node n on fault k, ϕ_{nk} is the coupling fraction at node n on fault k, ${}_h\boldsymbol{\Omega}_f$ is the Euler pole of the footwall block f of fault relative to the hangingwall block h, $\boldsymbol{m}$ is the unit vector in m direction on fault plane (downdip or along strike), and $G_{im}(\boldsymbol{X},\boldsymbol{X}_{nk})$ is the response function giving the i component of velocity at surface station $\boldsymbol{X}$ due to a unit slip velocity along fault plane at node $\boldsymbol{X}_{nk}$ in the

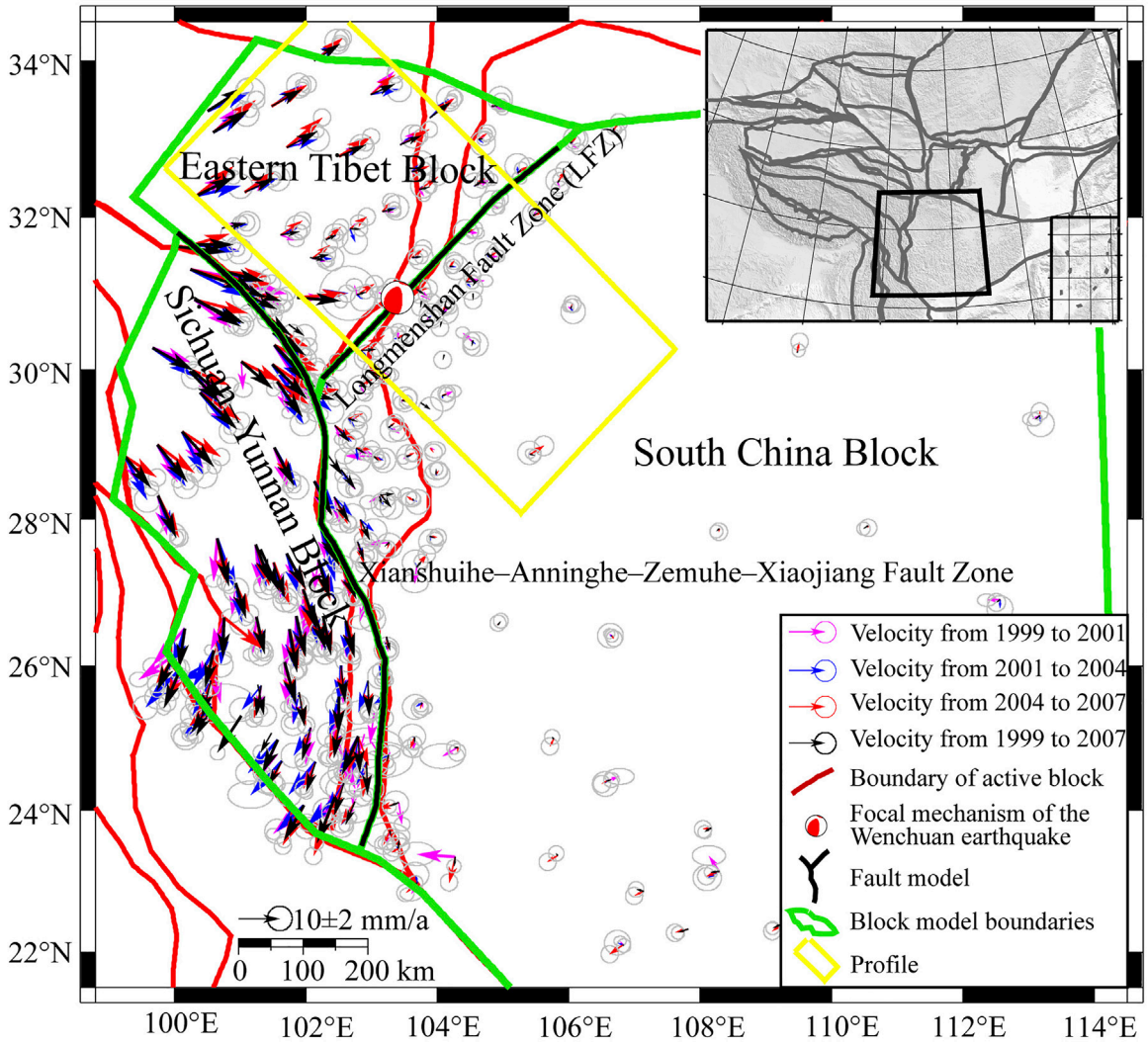

FIGURE 1 | Global Positioning System (GPS) velocity fields of the study region with respect to the South China Block during 1999–2001, 2001–2004, 2004–2007, and 1999–2007. The gray ellipses represent the errors of GPS velocity fields, and error ellipses represent 70% confidence. The insert map shows the regional position of study area. The focal mechanism of the Wenchuan earthquake is derived from Global CMT Web Page (https://www.globalcmt.org/CMTsearch.html).

m direction (Savage et al., 2001; McCaffrey, 2002; McCaffrey, 2009; Zhao et al., 2013; Zhao et al., 2021). $\boldsymbol{V}_i(\boldsymbol{X})$ is the input GPS velocity fields in i direction; $\sum_{b=1}^{B} H(\boldsymbol{X} \in \Delta_b)[{}_R\boldsymbol{\Omega}_b \times \boldsymbol{X}] \cdot \boldsymbol{i}$ represents the velocity caused by block rotation, $\dot{\varepsilon}_{ii}\Delta\boldsymbol{X}_i + \dot{\varepsilon}_{ij}\Delta\boldsymbol{X}_j$ represents the velocity caused by uniform strain inside the block, and $\sum_{k=1}^{F}\sum_{n=1}^{N_k}\sum_{m=1}^{2}\phi_{nk}G_{im}(\boldsymbol{X},\boldsymbol{X}_{nk})[{}_h\boldsymbol{\Omega}_f \times \boldsymbol{X}_{nk}] \cdot \boldsymbol{m}$ represents the velocity caused by fault coupling. The unitless coupling fraction ϕ_{nk} is a purely kinematic quantity. When it equals 0, the fault is fully creeping at a long-term slip rate; when it equals 1, the fault is completely coupled and accumulating strain to be released during transient slip events (Thomas et al., 2014); when it is between 0 and 1, the fault is partly coupled (McCaffrey et al., 2007).

Based on the theoretical model of fault locking, TDEFNODE is a Fortran-based program to model elastic lithospheric block movement and deformation using data such as GPS and InSAR velocity fields (https://robmccaffrey.github.io/TDEFNODE/manual/tdefnode_manual.html#cite). Block motions are specified by Euler rotation poles and interseismic backslip is applied along fault planes that separate blocks (McCaffrey, 2002; McCaffrey, 2009), based on the routines of Okada (1985), Okada (1992). The Euler rotation poles, permanent strain inside blocks, and spatial distribution of coupling fraction and slip rate on fault planes are estimated by simulated annealing and grid search. When building the three-dimensional model, faults are specified by longitude-latitude-depth coordinates of nodes along the fault planes. The coupling fraction and fault slip rate at each node are estimated by TDEFNODE; we then divided the fault plane between fault nodes into smaller patches (4 km along strike by 1 km downdip) and used bilinear interpolation to obtain smooth distribution results. The slip deficit rate of fault plane between two blocks is the product of the coupling

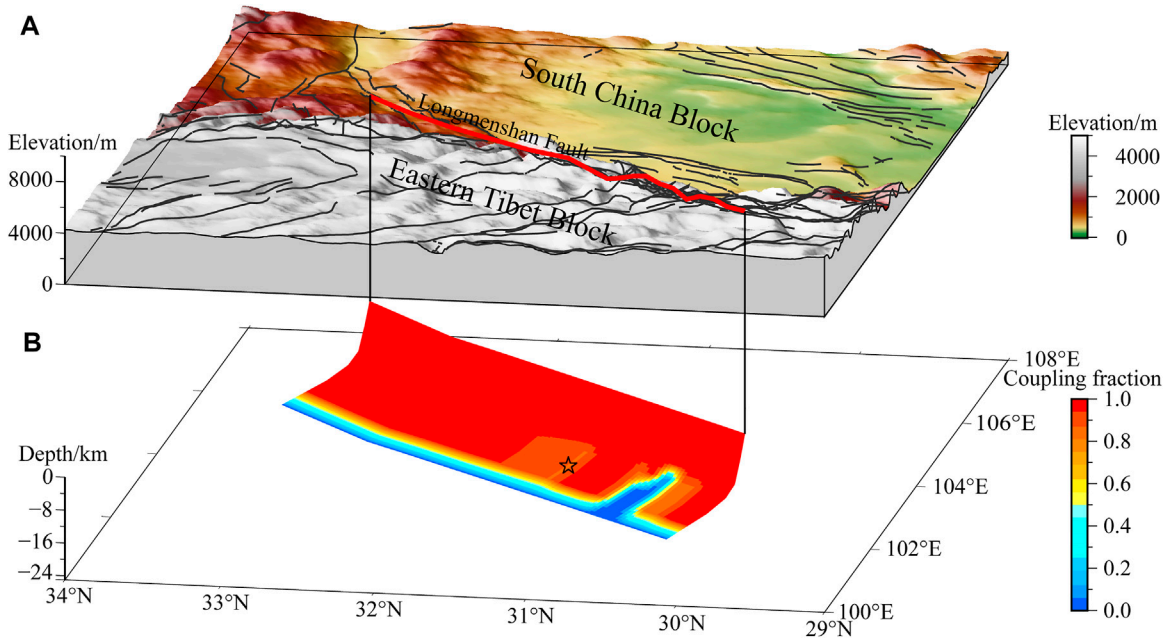

FIGURE 2 | (A) Topographic map of the area around the Longmenshan fault zone (LFZ) and **(B)** spatial distribution of the coupling fraction during 1999–2007. The thin black lines in **(A)** denote the faults, and the thick red line denotes the surface trace of the LFZ. The black star in **(B)** denotes the Wenchuan earthquake source location (Liu et al., 2008).

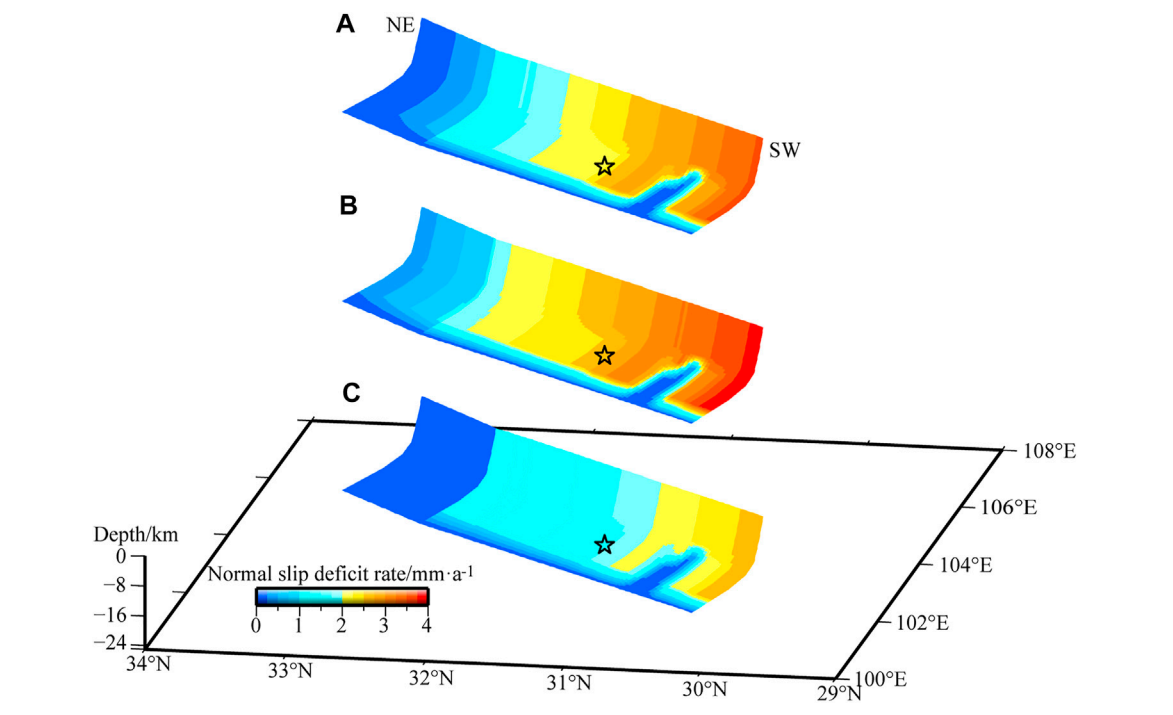

FIGURE 3 | Spatial distribution of fault-normal slip deficit rates during **(A)** 1999–2001, **(B)** 2001–2004, and **(C)** 2004–2007 along the Longmenshan fault plane. The black star denotes the Wenchuan earthquake source location.

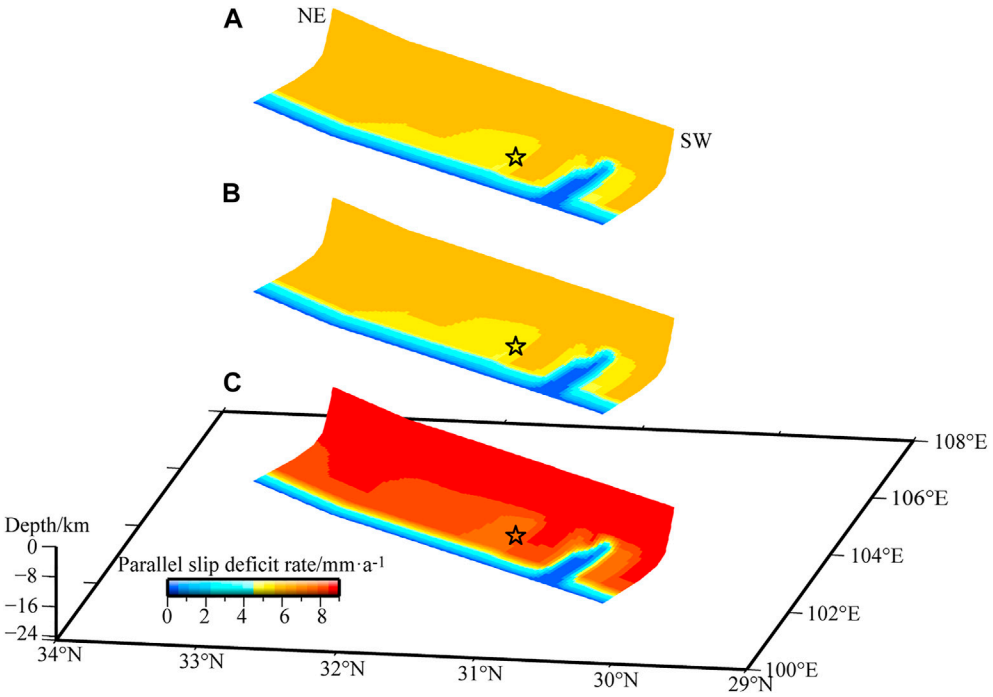

FIGURE 4 | Spatial distribution of fault-parallel slip deficit rates during **(A)** 1999–2001, **(B)** 2001–2004, and **(C)** 2004–2007 along the Longmenshan fault plane. The black star denotes the Wenchuan earthquake source location.

fraction and the fault slip rate (McCaffrey, 2002; McCaffrey et al., 2007; Zhao et al., 2020).

During the inversion, the value of the uncertainty scaling factor f was applied to the four-stage GPS velocity fields. The inversion estimates the parameters that minimize the reduced chi-squared statistic:

$$\chi_n^2 = \left[\sum_{i=1}^{n} (r_i / f\sigma_i)^2\right] \Big/ dof \quad (2)$$

where r_i is the residual, σ_i is the error of GPS velocity, and dof is the degrees of freedom (McCaffrey, 2002; Zhao et al., 2020; Zhao et al., 2021).

Three-Dimensional Model

The crust of the Qinghai-Tibet Plateau migrates eastward and is blocked by the Sichuan Basin (Huang et al., 2021). The high-elevation LFZ is formed at the junction of the two blocks (**Figures 1**, **2A**), resulting in a huge difference in crustal thickness on either side. Referring to the boundaries of active block (Deng et al., 2003), our three-dimensional model included the Longmenshan, Xianshuihe, and Anninghe–Zemuhe–Xiaojiang fault zones, which divide the study area into the Sichuan–Yunnan Block, Eastern Tibet Block, and South China Block (**Figure 1**). As the area surrounded by the Xianshuihe, Anninghe–Zemuhe–Xiaojiang, Jinshajiang, and Honghe fault zones shares similar movement and deformation characteristics, we regarded it as one block (Gan et al., 2007; Thatcher, 2007). The Eastern Tibet Block is enclosed by the Xianshuihe, Longmenshan, and East Kunlun fault zones (Meade, 2007; Hao et al., 2014).

According to results of previous studies (Weimin Wang et al., 2008; Wang et al., 2011; Zhang et al., 2008; Zhu, 2008; Du et al., 2009; Xu et al., 2009), the Longmenshan fault plane is a listric structure. The total length of the fault plane is 479 km and the total width is 78 km (**Figure 2B**). We adopted seven depth contours along strike at 0.1, 6, 12, 15, 18, 20, and 22.5 km; the dip angles between the contours were set to 55°, 50°, 20°, 10°, 7°, and 7° from the surface to the bottom of the fault plane (Zhao et al., 2020).

RESULTS

Coupling Fraction

By gradually changing the uncertainty scaling factor f, we identified the f value needed for the optimal solution, of which $\chi_n^2 \approx 1$. After multiple trials, f during 1999–2007 was set to 2.5 and $\chi_n^2 = 1.017$. We then fixed f for the other three periods. Subsequently, the inversion for 1999–2001 included 160 stations and $\chi_n^2 = 0.859$; the inversion for 2001–2004 included 153 stations and $\chi_n^2 = 0.276$ (partly because of the larger errors as described above); and the inversion for 2004–2007 included 169 stations and $\chi_n^2 = 0.558$.

The coupling fraction of the optimal model from 1999 to 2007 (**Figure 2B**) shows that most of the Longmenshan fault plane was strongly coupled along both the strike and dip directions. Only the focal location of the Wenchuan earthquake was partly coupled

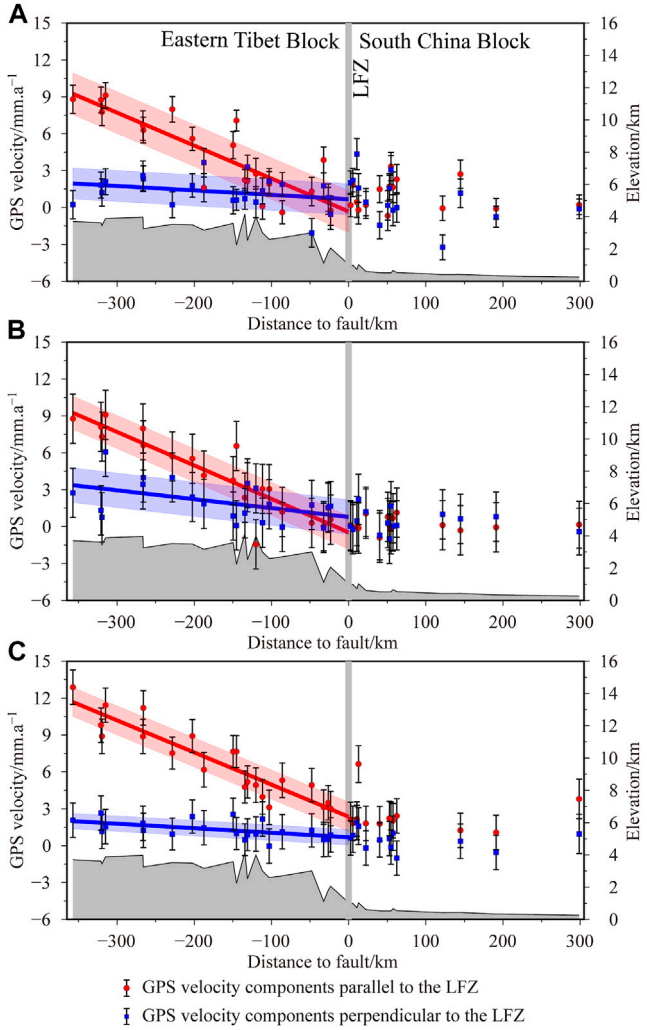

FIGURE 5 | Global Positioning System (GPS) velocity profiles across the Longmenshan fault zone (LFZ) during **(A)** 1999–2001, **(B)** 2001–2004, and **(C)** 2004–2007. The topographic profiles are in each figure. The red lines and the blue lines are linear fitting results of the dextral shear rates and compressive shortening rates in the Eastern Tibet Block with one standard deviation, respectively.

with coupling fraction of ~0.88. The only creeping section is a southwestern segment of ~20 km wide and 12–22.5 km deep (Zhao et al., 2018).

Fault-Normal and Fault-Parallel Slip Deficit Rates

Using the GPS velocity fields of 1999–2001, 2001–2004, and 2004–2007, the coupling fraction of each period was fixed as the background value of 1999–2007 (**Figure 2B**); then, only the fault-normal and fault-parallel slip deficit rates of the fault plane were inverted to obtain the spatio-temporal evolution process.

Under the strong coupling of the Longmenshan fault plane, the fault-normal compressive deficit rates of the three periods showed an obvious decreasing trend from southwest to northeast, indicating the southwestern segment of the LFZ was subjected to the strongest compression before the Wenchuan earthquake, and compression weakened northeastward. On a temporal scale, the slip deficit rate of the central–southern segment was ~1.5–3.6 mm/a from 1999 to 2001, before increasing slightly to ~1.9–3.9 mm/a from 2001 to 2004. Then, from 2004 to 2007, it significantly decreased to ~1.1–2.6 mm/a (**Figure 3**). The fault-normal compressive deficit rates in the northeastern segment of the fault plane were small during all three periods, indicating this segment was dominated by strike-slip movement.

The fault-parallel dextral deficit rates in three periods were uniformly distributed along the whole fault plane, with weak variations along strike and dip directions. Only the creeping area of the southwestern segment had a slip deficit of 0 mm/a. In terms of temporal evolution, the fault-parallel dextral deficit rate was ~6 mm/a during 1999–2001 and 2001–2004, after which it increased rapidly to ~9.5 mm/a from 2004 to 2007 (**Figure 4**).

The dynamic results of the fault-normal and fault-parallel slip deficit rates during the three periods show that taking the values of 1999–2001 as a baseline, the fault-normal slip deficit rate began to increase slightly from 2001 to 2004, while the fault-parallel slip deficit rate did not change. Subsequently, from 2004 to 2007, the fault-normal slip deficit rate decreased significantly, while the fault-parallel slip deficit rate increased rapidly. This suggests that the accumulation of fault-normal compressive strain energy during 2004–2007 was limited, but that there was rapid accumulation of fault-parallel dextral shear strain energy.

Velocity Profiles

To further analyze the surface continuous deformation characteristics on both sides of the LFZ, a 650 km long velocity profile across the LFZ (**Figure 1**) was constructed from the three periods of GPS velocity fields; then, dynamic velocity projection results both perpendicular and parallel to the LFZ were obtained (**Figure 5**).

The results show that internal deformation of the South China Block and the LFZ were weak before the earthquake. Large scale uniform deformation occurred within the Eastern Tibet Block, and the dextral shear deformation parallel to the LFZ was higher than the compressive shortening deformation perpendicular to the LFZ. A linear model was used to calculate the dextral shear rates and compressive shortening rates over a 357 km span of the Eastern Tibet Block, on the western side of the LFZ. The results for 1999–2001 (**Figure 5A**) show that the compressive shortening rate was ~1.28 mm/a, equivalent to strain rate of 0.36×10^{-8}/a, and the dextral shear rate was ~9.57 mm/a, equivalent to strain rate of 2.68×10^{-8}/a. The results for 2001–2004 (**Figure 5B**) show compressive shortening rate of ~2.58 mm/a, equivalent to strain rate of 0.72×10^{-8}/a, and dextral shear rate of ~9.72 mm/a, equivalent to strain rate of 2.72×10^{-8}/a. The results for 2004–2007 (**Figure 5C**) show compressive shortening rate of ~1.31 mm/a, equivalent to strain rate of 0.37×10^{-8}/a, and dextral shear rate of ~9.32 mm/a, equivalent to strain rate of 2.61×10^{-8}/a.

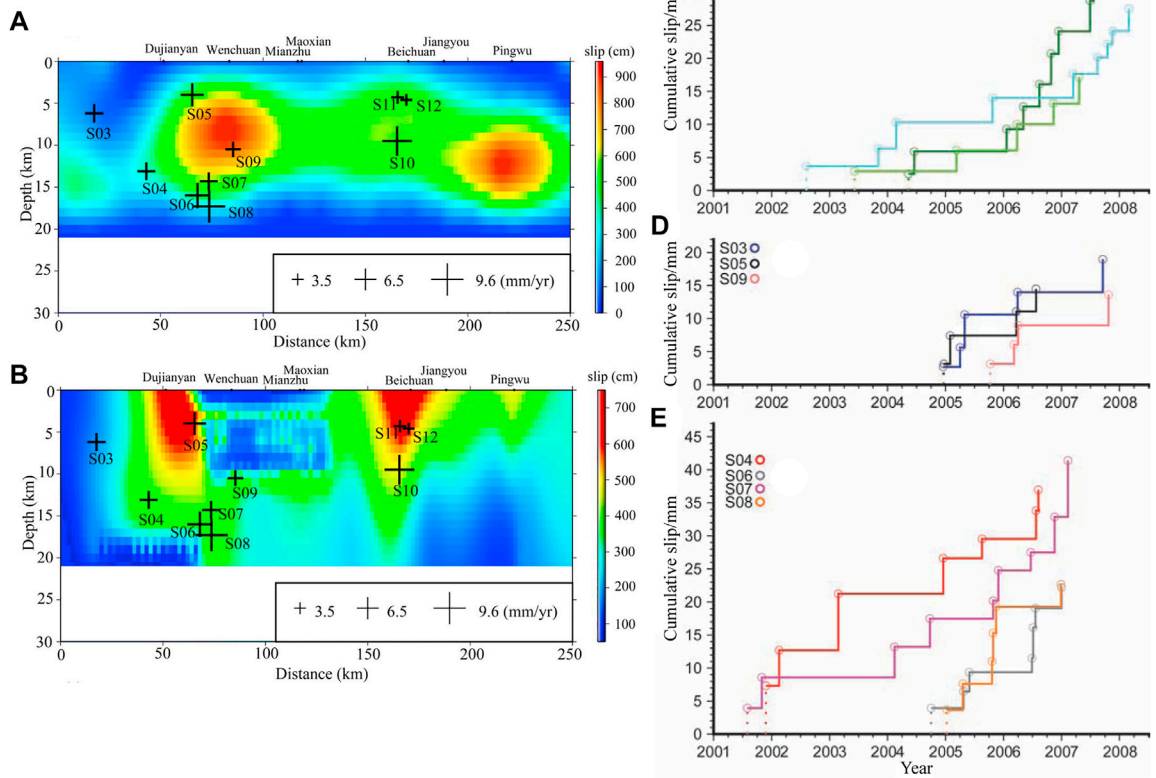

FIGURE 6 | Estimated slip rates shown together with **(A)** coseismic slip inverted from teleseismic waveform data and **(B)** coseismic slip inverted from geodetic data. **(C–E)** Cumulative slip calculated from the 10 repeating earthquake sequences in the Longmenshan fault zone (LFZ). The sizes of the crosses in **(A)** and **(B)** are proportional to the slip rate (Li et al., 2011; Chen and Li, 2018).

Comparison of the three periods shows that compressive shortening strain did not change significantly near the LFZ and was essentially distributed horizontally. Meanwhile, GPS stations inside the Eastern Tibet Block recorded significantly increase of crustal shortening strain from 2001 to 2004, followed by weakening from 2004 to 2007. This is broadly consistent with the result that the fault-normal compressive deficit rate increased at first and then decreased. Although the dextral shear strain inside the Eastern Tibet Block did not increase during 2004–2007, the dextral shear rate near the LFZ was significantly enhanced. Within a range of ~100 km to the west of the LFZ, northeastward shear during the first two periods was essentially 0, while it increased obviously during 2004–2007 (Jiang et al., 2009). This may indicate that the dextral movement of the whole Eastern Tibet Block increased from 2004 to 2007, and under the background of fault strong coupling, the dextral shear deformation of part of the South China Block near the LFZ also increased (**Figure 5C**). This is consistent with the result of the rapidly increase of fault-parallel dextral deficit rate from 2004 to 2007.

DISCUSSION

Acceleration Process of Deep Slip Along the Longmenshan Fault Plane

Interseismic surface horizontal slip rates of the LFZ inferred from GPS (Shen et al., 2005; Gan et al., 2007; YanZhao Wang et al., 2008) and geological data (Ma et al., 2005; Zhou et al., 2006) before the 2008 *M*8.0 Wenchuan earthquake are very slow (<2–3 mm/a; Zhang et al., 2010). However, the low slip rate observed at the surface may not reflect the state of accumulated strain at depth, where the devastating Wenchuan earthquake nucleated (Chen and Li, 2018). The deep rate (6–9.5 mm/a) derived in this study from the inversion of GPS velocities is two to three times higher than the above GPS and geological rates, but similar to the slip rate estimated over a depth range of 4–18 km using repeating earthquakes (3.5–9.6 mm/a; Li et al., 2011). At the same time, Zhao et al. (2008) calculated the accumulated Benioff strain using the earthquake catalogue, while Chen et al. (2015) conducted a two-dimensional viscoelastic finite-element simulation; both showed that the deep slip rate along the

Longmenshan fault plane is higher than the shallow near-surface slip rate.

Chen and Li (2018) analyzed 10 repeating earthquake sequences detected in the central and northern segments of the LFZ (**Figure 6**), and found that the S06 and S07 sequences at 14–16 km depth near Hongkou–Wenchuan (**Figure 6C**) and the S10–12 sequences at 4.3–9.5 km depth near Beichuan (**Figure 6E**) exhibited different degrees of medium-term slip acceleration in around 2006. This is consistent with our results, in which the dextral slip deficit rate increased rapidly to ~9.5 mm/a from 2004 to 2007. Both indicate that the deep slip rate of the Longmenshan fault plane may have accelerated before the Wenchuan earthquake. This may reflect a deformation response to a high stress state caused by increased tectonic loading of the Eastern Tibet Block before the Wenchuan earthquake; that is, lateral shear deformation increased in the northeastern direction after the accumulation of thrust elastic strain reached its limit in the seismogenic region. At the same time, the slip variation may not be a dominant factor until the long-term elastic strain accumulation on the fault reaches a sufficient level to be released in one large earthquake.

Regional Pre-Seismic Deformation Does Not Correspond to Coseismic Displacement

The elastic strain released by a large earthquake is accumulated for a long time before the earthquake. Therefore, the inter-seismic deformation field and coseismic deformation field should exhibit reverse and complementary magnitudes (Jiang et al., 2009; Wu et al., 2015). Based on our analysis, before the Wenchuan earthquake, the thrust component of the central and southwestern segments of the LFZ was large, while that of the northeastern segment, which is mainly strike-slip, was small. This is consistent with the basic characteristics of field measurement of the Wenchuan earthquake, which was dominated by a thrust rupture at the focal location with the strike-slip component becoming larger northeastward (He et al., 2011), until it became a fully strike-slip rupture (Xu et al., 2009; Wang et al., 2011). However, before the Wenchuan earthquake, the relative movement and deformation of the regional crust did not correspond to the coseismic displacement field in terms of magnitude. The coseismic displacement field showed that compressive strain release consistent with elastic rebound also occurred in the Sichuan Basin, to the east of the LFZ (Jiang et al., 2009; Wang et al., 2011; Wu et al., 2015), while no compressive strain accumulation was observed in the three periods before the earthquake (**Figure 5**). The coseismic displacement field mainly shows compressive strain release on both sides of the rupture zone (Jiang et al., 2009; Wang et al., 2011; Wu et al., 2015), while large scale deformation of the Eastern Tibet Block was mainly dextral shear deformation before the earthquake (**Figure 5**).

This mismatch may be due to the long process of strain accumulation before large earthquakes. Immediately prior to the Wenchuan earthquake, the seismogenic area near the LFZ was at a stalemate, with significant deformation restricted after elastic compressive deformation of the crust reached its limit. In other words, the crustal deformation of strain accumulation corresponding to the strain release displayed in the coseismic displacement had occurred earlier, but was not observed completely because the GPS observation time was too short. This indicates that multi-year observations before earthquakes cannot fully represent inter-seismic processes. At the same time, it highlights the need for encompassing longer timescales when investigating seismogenic deformation fields before large earthquakes (Jiang et al., 2009).

CONCLUSION

In this study, we used four periods of GPS velocity fields to analyze the spatio-temporal dynamics of deep slip rate and surface deformation in the LFZ before the 2008 *M*8.0 Wenchuan earthquake. Before the earthquake, the Longmenshan fault plane was strongly coupled. The fault-normal slip deficit rate increased from 2001 to 2004, and then decreased from 2004 to 2007; meanwhile, the fault-parallel slip deficit rate increased substantially during 2004–2007, indicating that the deep slip rate of the fault plane may have accelerated. GPS velocity profiles confirm this phenomenon, which may indicate that thrust elastic strain in the seismogenic region of the Wenchuan earthquake struggled to accumulate after reaching the limit and was more conducive to dextral shear deformation under the enhancement background of large-scale NE-trending crustal movement. The results of this study have important implications for medium-term forecasting of large continental thrust earthquakes, which may require observations over long timescales.

DATA AVAILABILITY STATEMENT

The raw data supporting the conclusion of this article will be made available by the authors, without undue reservation.

AUTHOR CONTRIBUTIONS

JiZ designed the research and wrote the manuscript. ZY created some figures. JR, ZJ, and QY performed data interpretation and edited the manuscript. ZZ, CY, and JZ edited the manuscript. AN analyzed the results and edited the manuscript.

FUNDING

This work was supported by the National Key Research and Development Program of China (Grant numbers 2018YFC1503606, 2018YFE0109700, and 2017YFC1500502) and the National Natural Science Foundation of China (Grant number 11672258).

ACKNOWLEDGMENTS

We are grateful to three reviewers for constructive comments and suggestions. We thank Min Wang for providing GPS velocity field datasets. English language editing was performed by Tornillo Scientific.

REFERENCES

Chen, Q. F., and Li, L. (2018). Deep Deformation of the Longmenshan Fault Zone Related to the 2008 Wenchuan Earthquake. *Chin. Sci. Bull.* 63, 1917–1933. (in Chinese with an English abstract). doi:10.1360/n972018-00362

Chen, Q. F., Hua, C., Li, L., and Cheng, J. (2015). Viscoelastic Simulation of Deep Tectonic Deformation of the Longmenshan Fault Zone and its Implication for strong Earthquakes. *Chin. J. Geophys.* 58, 4129–4137. (in Chinese with an English abstract). doi:10.6038/cjg20151120

Deng, Q. D., Zhang, P. Z., Ran, Y. K., Yang, X. P., Min, W., and Chu, Q. Z. (2003). Basic Characteristics of Active Tectonics of China. *Sci. China Ser. D-earth Sci.* 46 (4), 356–372. doi:10.1360/03ys9030

Du, F., Wen, X. Z., Zhang, P. Z., and Wang, Q. L. (2009). Interseismic Deformation across the Longmenshan Fault Zone before the 2008 *M*8.0 Wenchuan Earthquake. *Chin. J. Geophys.* 52 (11), 2729–2738. (in Chinese with an English abstract). doi:10.3969/j.issn.0001-5733.2009.11.007

Gan, W. J., Zhang, P. Z., Shen, Z. K., Niu, Z., Wang, M., Wan, Y., et al. (2007). Present-day Crustal Motion with the Tibetan Plateau Inferred from GPS Measurements. *J. Geophys. Res.* 112, B08426. doi:10.1029/2005jb004120

Hao, M., Wang, Q., Shen, Z., Cui, D., Ji, L., Li, Y., et al. (2014). Present Day Crustal Vertical Movement Inferred from Precise Leveling Data in Eastern Margin of Tibetan Plateau. *Tectonophysics* 632, 281–292. doi:10.1016/j.tecto.2014.06.016

He, H., Wei, Z., Chen, C., and Shi, F. (2011). On-site Determination of Slip Vectors along the Longmenshan Fault during the M_w 7.9 Wenchuan, China, Earthquake of May 12, 2008. *J. Asian Earth Sci.* 41, 274–282. doi:10.1016/j.jseaes.2011.02.015

Herring, T. A., King, R. W., and McClusky, S. C. (2006). *GPS Analysis at MIT, Release 10.3*. Cambridge: Massachussetts Institute of Technology.

Huang, Z. C., Ji, C., Wu, H. T., Shi, Y. T., Geng, J. Q., Xu, M. J., et al. (2021). Review on the Crustal Structures and Deformations in the southeastern Margin of the Tibetan Plateau. *Rev. Geophy. Planet. Phys.* 52 (3), 291–307. (in Chinese with an English abstract). doi:10.19975/j.dqyxx.2021-005

Jiang, Z. S., Fang, Y., Wu, Y. Q., Wang, M., Du, F., and Ping, J. J. (2009). The Dynamic Process of Regional Crustal Movement and Deformation before Wenchuan M_S8.0 Earthquake. *Chin. J. Geophys.* 52 (2), 505–518. (in Chinese with an English abstract).

Kato, A., Fukuda, J. i., Kumazawa, T., and Nakagawa, S. (2016). Accelerated Nucleation of the 2014 Iquique, Chile M_w 8.2 Earthquake. *Sci. Rep.* 6, 24792. doi:10.1038/srep24792

Kato, A., and Nakagawa, S. (2014). Multiple Slow-Slip Events during a Foreshock Sequence of the 2014 Iquique, Chile M_w 8.1 Earthquake. *Geophys. Res. Lett.* 41, 5420–5427. doi:10.1002/2014gl061138

Li, L., Chen, Q. f., Niu, F., and Su, J. (2011). Deep Slip Rates along the Longmen Shan Fault Zone Estimated from Repeating Microearthquakes. *J. Geophys. Res.* 116, B09310. doi:10.1029/2011jb008406

Li, Y. C., Nocquet, J. M., Shan, X. J., and Song, X. G. (2021). Geodetic Observations of Shallow Creep on the Laohushan-Haiyuan Fault, Northeastern Tibet. *J. Geophys. Res. Solid Earth* 126, e2020JB021576. doi:10.1029/2020jb021576

Liu, Q. Y., Chen, J. H., Li, S. C., Li, Y., Guo, B., Wang, J., et al. (2008). The M_S8.0 Wenchuan Earthquake: Preliminary Results from the Western Sichuan mobile Seismic Array Observations. *Seismol. Geol.* 30 (3), 584–596. (in Chinese with an English abstract).

Loveless, J. P., and Meade, B. J. (2011). Spatial Correlation of Interseismic Coupling and Coseismic Rupture Extent of the 2011 M_W= 9.0 Tohoku-Oki Earthquake. *Geophys. Res. Lett.* 38, L17306 (17). doi:10.1029/2011gl048561

Ma, B. Q., Su, G., and Hou, Z. (2005). Late Quaternary Slip Rate in the central Part of the Longmenshan Fault Zone from Terrace Deformation along the Minjiang River. *Seismol. Geol.* 27, 234–242. (in Chinese with an English abstract).

McCaffrey, R. (2002). "Crustal Block Rotations and Plate Coupling,". *Plate Boundary Zones*. Editors S. Stein and J. T. Freymueller (Washington D.C.: AGU Geodynamics Series), 30, 101–122.

McCaffrey, R., King, R. W., Payne, S. J., and Lancaster, M. (2013). Active Tectonics of Northwestern U.S. Inferred from GPS-Derived Surface Velocities. *J. Geophys. Res. Solid Earth* 118 (2), 709–723. doi:10.1029/2012jb009473

McCaffrey, R., Qamar, A. I., King, R. W., Wells, R., Khazaradze, G., Williams, C. A., et al. (2007). Fault Locking, Block Rotation and Crustal Deformation in the Pacific Northwest. *Geophys. J. Int.* 169, 1315–1340. doi:10.1111/j.1365-246x.2007.03371.x

McCaffrey, R. (2009). Time-dependent Inversion of Three-Component Continuous GPS for Steady and Transient Sources in Northern Cascadia. *Geophys. Res. Lett.* 36 (7), 1–5. doi:10.1029/2008gl036784

Meade, B. J., and Hager, B. H. (2005). Block Models of Crustal Motion in Southern California Constrained by GPS Measurements. *J. Geophys. Res. Solid Earth* 110 (B3), 1–19. doi:10.1029/2004jb003209

Meade, B. J. (2007). Present-day Kinematics at the India-Asia Collision Zone. *Geol* 35 (1), 81–84. doi:10.1130/g22924a.1

Moreno, M., Rosenau, M., and Oncken, O. (2010). 2010 Maule Earthquake Slip Correlates with Pre-seismic Locking of Andean Subduction Zone. *Nature* 467 (7312), 198–202. doi:10.1038/nature09349

Okada, Y. (1992). Internal Deformation Due to Shear and Tensile Faults in a Half-Space. *Bull. Seismol. Soc. Am.* 82 (2), 1018–1040. doi:10.1785/bssa0820021018

Okada, Y. (1985). Surface Deformation Due to Shear and Tensile Faults in a Half-Space. *Bull. Seismol. Soc. Am.* 75 (4), 1135–1154. doi:10.1785/bssa0750041135

Savage, J. C., Gan, W., and Svarc, J. L. (2001). Strain Accumulation and Rotation in the Eastern California Shear Zone. *J. Geophys. Res.* 106 (B10), 21995–22007. doi:10.1029/2000jb000127

Savage, J. C., and Prescott, W. H. (1978). Asthenosphere Readjustment and the Earthquake Cycle. *J. Geophys. Res.* 83 (B7), 3369–3376. doi:10.1029/jb083ib07p03369

Shen, Z. K., Lü, J. N., Wang, M., and Bürgmann, R. (2005). Contemporary Crustal Deformation Around the Southeast Borderland of the Tibetan Plateau. *J. Geophys. Res. Solid Earth* 110, B11409. doi:10.1029/2004jb003421

Thatcher, W. (2007). Microplate Model for the Present-Day Deformation of Tibet. *J. Geophys. Res. Solid Earth* 112 (B1). doi:10.1029/2005jb004244

Thomas, M. Y., Avouac, J. P., Champenois, J., Lee, J. C., and Kuo, L. C. (2014). Spatiotemporal Evolution of Seismic and Aseismic Slip on the Longitudinal Valley Fault, Taiwan. *J. Geophys. Res. Solid Earth* 119 (6), 5114–5139. doi:10.1002/2013jb010603

Uchida, N., Iinuma, T., Nadeau, R. M., Bürgmann, R., and Hino, R. (2016). Periodic Slow Slip Triggers Megathrust Zone Earthquakes in Northeastern Japan. *Science* 351, 488–492. doi:10.1126/science.aad3108

Wang, M. (2009). *Analysis of GPS Data with High Precision and Study on Present-Day Crustal Deformation in China*. Beijing: Institute of Geology, China Earthquake Administration. (in Chinese with an English abstract).

Wang, Q., Qiao, X. J., Lan, Q. G., Jeffrey, F., Yang, S. M., Xu, C. J., et al. (2011). Rupture of Deep Faults in the 2008 Wenchuan Earthquake and Uplift of the Longmen Shan. *Nat. Geosci.* 4, 634–640. doi:10.1038/ngeo1210

Weimin Wang, W. M., Zhao, L. F., Li, J., and Yao, Z. X. (2008). Rupture Process of the M_S8.0 Wenchuan Earthquake of Sichuan, China. *Chin. J. Geophys.* 51 (5), 1403–1410. (in Chinese with an English abstract).

Wu, Y., Jiang, Z., Zhao, J., Liu, X., Wei, W., Liu, Q., et al. (2015). Crustal Deformation before the 2008 Wenchuan M_s8.0 Earthquake Studied Using GPS Data. *J. Geodynamics* 85, 11–23. doi:10.1016/j.jog.2014.12.002

Xu, X., Wen, X., Yu, G., Chen, G., Klinger, Y., Hubbard, J., et al. (2009). Coseismic Reverse- and Oblique-Slip Surface Faulting Generated by the 2008 M_w 7.9 Wenchuan Earthquake, China. *Geology* 37 (6), 515–518. doi:10.1130/g25462a.1

YanZhao Wang, Y., Wang, E., Shen, Z., Wang, M., Gan, W., Qiao, X., et al. (2008). GPS-constrained Inversion of Present-Day Slip Rates along Major Faults of the Sichuan-Yunnan Region, China. *Sci. China Ser. D-earth Sci.* 51, 1267–1283. doi:10.1007/s11430-008-0106-4

Zhang, P. Z., Wen, X. Z., Shen, Z. K., and Chen, J. H. (2010). Oblique, High-Angle, Listric-Reverse Faulting and Associated Development of Strain: The Wenchuan Earthquake of May 12, 2008, Sichuan, China. *Annu. Rev. Earth Planet. Sci.* 38, 353–382. doi:10.1146/annurev-earth-040809-152602

Zhang, P. Z., Xu, X. W., Wen, X. Z., and Ran, Y. K. (2008). Slip Rates and Recurrence Intervals of the Longmen Shan Active Fault Zone, and Tectonic Implications for the Mechanism of the May 12 Wenchuan Earthquake, 2008, Sichuan, China. *Chin. J. Geophys.* 51 (4), 1066–1073. (in Chinese with an English abstract).

Zhao, J., Ren, J. W., Liu, J., Jiang, Z. S., Liu, X. X., Liang, H. B., et al. (2020). Coupling Fraction and Relocking Process of the Longmenshan Fault Zone Following the 2008 M_w7.9 Wenchuan Earthquake. *J. Geodynamics* 137, 101730. doi:10.1016/j.jog.2020.101730

Zhao, J., Ren, J. W., Jiang, Z. S., Liu, X. X., Niu, A. F., Yan, W., et al. (2018). Fault Locking and Deformation Characteristics in Southwestern Segment of Longmenshan Fault. *J. Seismol. Res.* 41 (2), 216–225. (in Chinese with an English abstract).

Zhao, J., Wu, Y. Q., Jiang, Z. S., Niu, A. F., Liu, J., Wang, L. F., et al. (2013). Fault Locking and Dynamic Deformation of the Longmenshan Fault Zone before the 2013 Lushan M_S7.0 Earthquake. *Acta Seismol, Sin.* 35 (5), 681–691. doi:10.3969/j.issn.0253-3782.2013.05.007

Zhao, J., Zhan, W., Ren, J. W., Jiang, Z. S., Gu, T., Liu, J., et al. (2021). GPS Time Series Inversion of the Healing Process of the Middle Segment of the Longmenshan Fault after the 2008 Wenchuan Earthquake. *Acta Geodaetica et Cartographica Sinica* 50 (1), 37–51. (in Chinese with an English abstract). doi:10.11947/j.AGCS.2021.20200047

Zhao, Y. Z., Wu, Z. L., Jiang, C. S., and Zhu, C. Z. (2008). Present Deep Deformation along the Longmenshan Fault by Seismic Data and Implications for the Tectonic Context of the Wenchuan Earthquake. *Acta Geol. Sin.* 82, 1778–1787. (in Chinese).

Zhou, R. J., Li, Y., Densmore, A. L., and Ellis, M. A. (2006). Active Tectonics of the Eastern Margin of the Tibet Plateau. *J. Mineral. Petrol.* 26 (2), 40–51. doi:10.19719/j.cnki.1001-6872.2006.02.007

Zhu, J. S. (2008). The Wenchuan Earthquake Occurrence Background in Deep Structure and Dynamics of Lithosphere. *J. Chengdu Univ. Technol. Sci. Technol. Ed.* 35 (4), 348–356. (in Chinese with an English abstract).

Zou, Z. Y., Jiang, Z. S., Wu, Y. Q., Wei, W. X., Fang, Y., and Liu, X. X. (2015). Dynamic Characteristics of Crustal Movement in north-south Seismic belt from GPS Velocity Field before and after the Wenchuan Earthquake. *Chin. J. Geophys.* 58 (5), 1597–1609. (in Chinese with an English abstract). doi:10.6038/cjg20150512

Conflict of Interest: The authors declare that the research was conducted in the absence of any commercial or financial relationships that could be construed as a potential conflict of interest.

Publisher's Note: All claims expressed in this article are solely those of the authors and do not necessarily represent those of their affiliated organizations, or those of the publisher, the editors and the reviewers. Any product that may be evaluated in this article, or claim that may be made by its manufacturer, is not guaranteed or endorsed by the publisher.

frontiers | Frontiers in Earth Science

ORIGINAL RESEARCH
published: 21 June 2022
doi: 10.3389/feart.2022.881884

Evolution Characteristics and Mechanism of the Load/Unload Response Ratio Based on Strain Observation Before the Jiuzhaigou M_S7.0 Earthquake

Chong Yue[1,2], Ping Ji[1], Yali Wang[1], Huaizhong Yu[1], Jin Cui[3], Chen Yu[1] and Yuchuan Ma[1]*

[1]China Earthquake Networks Center, Beijing, China, [2]Key Laboratory of Earthquake Dynamics, Institute of Geology, China Earthquake Administration, Beijing, China, [3]Seismological Bureau of Ningxia Hui Autonomous Region, Yinchuan, China

Strain observation is the most intuitive observation equipment to monitor stress change in the crust. Strain equipment near the epicenter area of the Jiuzhaigou earthquake (JZGEQ) provides a lot of reliable pre-seismic and post-seismic data for the study of stress change. In this study, the load/unload response ratio (LURR) method is used to study the stress state of rocks by calculating the ratio of strain observation during the loading phase and unloading phase. Results show that the LURR method based on strain observation is an effective method to describe the dynamic change of the constitutive relationship of the rocks in the crust. Different from the strain observation, the LURR anomaly evolution process is more continuous regardless of the time series curve or spatial and temporal distribution characteristics. The LURR curves of different stations begin to increase above 1.0 gradually from 6 months to 1 year prior to the occurrence of the JZGEQ, reaching the maximum value in 1–3 months before the JZGEQ, and subsequently return to a low level. The maximum value of the LURR anomalies decreases with the distance from the epicenters. At the same time, the spatial and temporal evolution characteristics of the LURR anomalies show us the process of "extension—enhance—weaken" in the epicenter of JZGEQ and its peripheral area prior to the earthquake. The concentration areas of the aforementioned LURR anomalies are all distributed in the pre-seismic normal stress-loading zone, which indicates that the faults are in the process of decoupling, and microfracture may exist in the stage of rock dilatancy.

Keywords: strain observation, LURR, Jiuzhaigou earthquake, normal stress, earth tide

OPEN ACCESS

Edited by:
Giovanni Martinelli, National Institute of Geophysics and Volcanology, Italy

Reviewed by:
Alexey Lyubushin, Institute of Physics of the Earth (RAS), Russia
Cataldo Godano, University of Campania Luigi Vanvitelli, Italy

****Correspondence:***
Chong Yue
yuechong@seis.ac.cn

Specialty section:
This article was submitted to Solid Earth Geophysics, a section of the journal Frontiers in Earth Science

Received: *23 February 2022*
Accepted: *10 May 2022*
Published: *21 June 2022*

Citation:
Yue C, Ji P, Wang Y, Yu H, Cui J, Yu C and Ma Y (2022) Evolution Characteristics and Mechanism of the Load/Unload Response Ratio Based on Strain Observation Before the Jiuzhaigou M_S7.0 Earthquake. Front. Earth Sci. 10:881884. doi: 10.3389/feart.2022.881884

1 INTRODUCTION

On 8 August 2017, an *M*s7.0 Jiuzhaigou earthquake (JZGEQ) occurred in Sichuan province in China (103.82°E, 33.2°N) with a depth of ~9 km. The result of the global centroid moment tensor (GCMT, see Data and Resources) solution (Ekström et al., 2012) shows that the rupture of JZGEQ is mainly dominated by strike-slip motion, and the rupture also contains ~10% of thrusting non-double-couple (NDCP) components (Sun et al., 2018). The strike of JZGEQ is 165° to the SSE direction, and the dip angle is 85°. JZGEQ occurred on the hidden fault named Shuzheng fault in the north of the Huya fault, and the post-seismic geological survey shows that there is no surface rupture around the

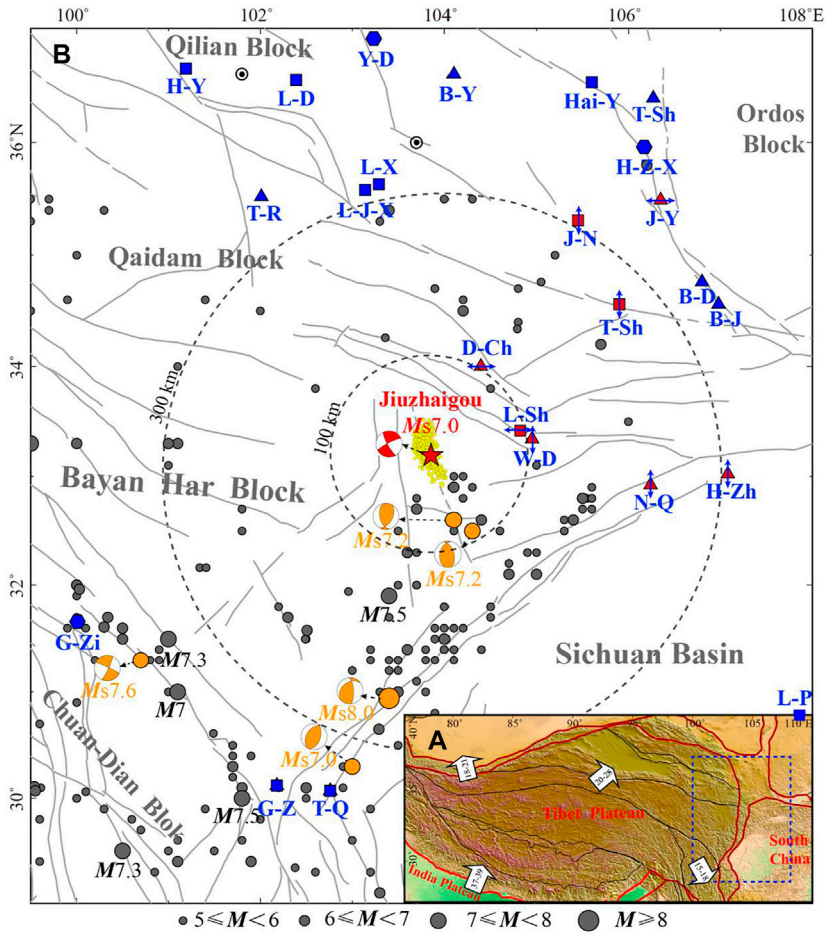

FIGURE 1 | (A) Location diagram of the study area. Red lines: primary block boundary; Black lines: secondary block boundary; Black arrow: movement direction of the plate; Blue dotted rectangle: location of **Figure 1B**. **(B)** Regional tectonic setting, historical earthquake, and strain observation stations distribution around JZGEQ. Gray dots: seismic events above *M*s5 in the study area since 1900s; Orange dots: Seismic events above *M*s7 since 1970s; Focal mechanism: epicenter events above *M*s7 since 1970s (cite from GCMT); Gray circle: epicentral distance of 100 and 300 km; Triangle: cave strainmeter station; Square: four-gauge borehole strainmeter station; Hexagonal: volumetric borehole strainmeter station; Red icon: stations in **Figure 2**; Blue arrow: direction of the strain observation; L-Sh: Liang-Shui station; W-D: Wu-Du station; D-Ch: Dang-Chang station; N-Q: Ning-Qiang station; H-Zh: Han-Zhong station; T-Sh: Tian-Shui station; J-N: Jing-Ning station; B-J: Bao-Ji station; B-D: Ba-Du station; J-Y: Jing-Yuan station; L-J-X: Liu-Jia-Xia station; L-X: Lin-Xia station; T-R: Tong-Ren station; H-Z-X: Hai-Zi-Xia station; T-Sh: Tan-Shan station; Hai-Y: Hai-Yuan station; B-Y: Bai-Yin station; Y-D: Yong-Deng station; L-D: Le-Du station; H-Y: Huang-Yuan station; G-Zi: Gan-Zi station; G-Z: Gu-Zan station; T-Q: Tian-Quan station; L-P: Liang-Ping station.

epicenter (Nie et al., 2018). The northeastern margin of the Tibet Plateau is the junction of the Qaidam block, the Bayan Har block, and the Yangtze block (**Figure 1A**). Therefore, the rupture processes of the Huya fault are highly complex (Sun et al., 2018; Liu et al., 2019), and several major seismic events have occurred in the history.

In the northeastern margin of the Tibet Plateau, a large number of strain observation instruments have been deployed by the China Earthquake Administration (**Figure 1B**). As the most intuitive observation equipment to explore stress change in the crust, aforementioned equipment provides a large number of practical and reliable data for the complete record of stress adjustment in the region before and after JZGEQ. However, it is quite difficult to identify the damage process of rock media prior to the occurrence of the earthquake directly by strain observation. Domestic and foreign scholars tried to use GNSS to study the large-scale stress adjustment before and after strong earthquakes above M7, which further promoted the understanding of seismic phenomena and physical processes (Wang et al., 2001; Shen et al., 2009; Wang and Shen, 2020). However, due to the limitation of GNSS observation time, regional stress adjustment results cannot be obtained in real time. Wang et al. (2020) tried to solve the time problem by using the continuous observation of GNSS, who recorded the pre-seismic anomalies related to the Lushan *M*s7.0 earthquake. The strain transition characteristics within a period of less than two and half years can be used as an observable and identifiable precursor to forecast an impending earthquake. However, the ambiguous anomalies and the uncertain time scales still make it difficult to predict the rupture degree of rocks in the crust, and we

still need to explore the physics mechanism of earthquake preparation.

In this study, we find that the load/unload response ratio (LURR) method based on strain observation may be used to solve the physical processes related to earthquake preparation. The LURR notion is proposed by Yin (1987) by calculating the Benioff strain of small earthquakes during the loading phase and unloading phase. Then, the method is continuously applied and developed by different scholars (Zhang et al., 2004; Yu et al., 2015; Liu and Yin, 2018), and the calculating data are developed from the seismic catalog to the groundwater level. Previous studies show that the LURR time series can reflect the change of stress state in the heterogeneous brittle system (Yin et al., 1995; Yin et al., 2000). According to the mechanical experiment results of rock, when it is in the elastic stage, the responses during the loading and unloading phases are almost the same. As a result, LURR during this period is about 1.0 (**Supplementary Figure S1**). However, when the force of the system exceeds the elastic limit of the rock, the responses during the loading and unloading phases will not be equal, and LURR during this period will exceed 1.0. This difference in the responses reflects the damage of a loaded material, and many results also prove that the LURR time series have the phenomenon of abnormal enhancement before large earthquakes (Yu et al., 2006; Yu and Zhu, 2010; Liu and Yin, 2018). Therefore, the LURR value may be served as a useful parameter to evaluate rock rupture and provide a basis for the future seismic risks in this region. However, most of the studies use the seismic catalog or groundwater level as input data, as the most intuitive way to monitor stress change, few scholars use the strain data directly for the LURR calculation. As a result, by using the LURR method based on strain observation, we try to identify the response difference of earth tide during the loading phase and unloading phase, so as to determine the stress state of the source medium.

2 THE STRAIN OBSERVATION SYSTEM AND METHODS

2.1 The Strain Observation System

Limited by the observation conditions, the strain observation stations are mostly distributed in the north and south boundaries of the Bayan Har block, especially in the north side. There are three types of strain observation stations, including the cave strainmeter stations (the triangles in **Figure 1**), the four-gauge borehole strainmeter stations (the squares in **Figure 1**), and the volumetric borehole strainmeter stations (the hexagonals in **Figure 1**). The cave strainmeter instrument generally contains two directions of observation [i.e., North–South (NS) direction and East–West (EW) direction], and the observation instrument is mostly tens of meters long in the cave. The four-gauge borehole strainmeter instrument contains data in four observation directions [i.e., NS direction, North–East (NE) direction, EW direction, and the North–West (NW) direction] in one borehole, and each direction is 45° away from each other. In this study, we name them according to the observed directions so as to achieve the purpose of differentiation. The volumetric borehole strainmeter instrument mainly monitors the volume change of the cavity installed in the borehole, and it has only one kind of observation data. The depth of the borehole is generally less than 200 m. Although the observation methods of the three types of strain observation instruments are not the same, both of them can obtain the variations of strain caused by stress changes. As the most intuitive physical quantity in the process of rocks from elastic deformation to instability and then to damage, the strain observation is easier to catch the anomalies prior to the earthquake.

It can be inferred from the epicentral distance in **Figure 1** that there is only one station (i.e., L-Sh station) within 100 km and five stations (i.e., L-Sh, W-D, D-Ch, N-Q, and T-Sh station) within 300 km. In terms of geographical location, more stations are located in the northeast side of the epicenter, and fewer stations are located in the south side of the epicenter. Therefore, the uneven distribution of stations makes it difficult to monitor the pre-seismic and post-seismic stress transition of JZGEQ. First, we comb the pre-seismic and post-seismic strain observation data of surrounding stations and find that the strain observation data of the eight stations close to the epicenter in **Figure 1** show obvious pre-seismic and post-seismic transitions. Then, we display the results of the most significant transitions in the observed data, and through the time point of strain transition, we can draw a conclusion related to epicentral distance. All the pre-seismic strain transitions of the five stations within 300 km from the epicenter occurred from 1 to 2 years prior to JZGEQ, and the larger the epicentral distance, the earlier the transition time. In contrast, the post-seismic stress transitions mainly occur at the stations with epicentral distances above 300 km. These results indicate that there are significant pre-seismic and post-seismic stress adjustments in the aforementioned areas, which are captured by the strain observation instruments, especially the pre-seismic strain transitions of the stations within 300 km from the epicenter, it is quite important for the study of the pre-seismic abnormal characteristics. However, it is still uncertain to determine the rupture degree of source media from the strain observation curves alone. In addition, it is difficult for us to give further details on epicentral distances, as there are no stations between 250 and 300 km. Therefore, since the strain observation can observe the pre-seismic strain transition caused by the stress change induced by JZGEQ, we need a method to extract pre-seismic anomalies caused by rock rupture and other phenomena in the process of seismogenetic from strain observation.

On the other hand, we also find that not all the items of the strain stations within the range of 300 km are significantly changed before the occurrence of JZGEQ. Thus, we draw the direction of strain observation in **Figures 1**, **2**, and the results show that the directions with the most significant strain transitions are mostly perpendicular to or large-angle oblique to the surrounding faults. This phenomenon may be related to the rupture mode of JZGEQ, which will be further analyzed in the discussion sections.

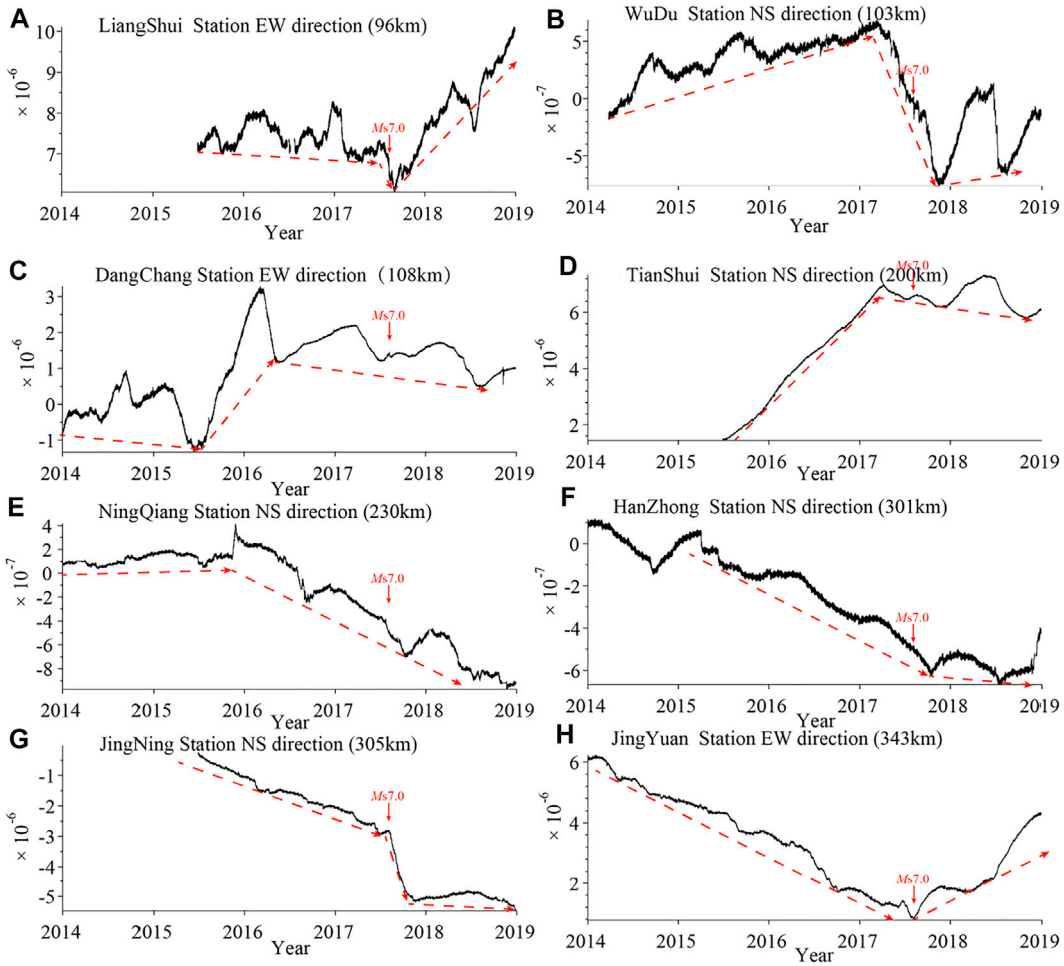

FIGURE 2 | Time series curves of strain observations at eight stations near the epicenter.

2.2 Methods

Yin et al. (2000) used the Benioff strain of small earthquakes as the loading/unloading response in the LURR calculations in different tectonic settings (California, United States, and Kanto region, Japan). Yu et al. (2021) proposed a new attempt by using water levels as calculation data and achieved a good application effect. The results of the studies prove that LURR anomalies are relatively significant prior to different earthquakes, that is, the stress accumulation before an earthquake in the seismogenic region will lead to the change of the Benioff strain and water level. As a result, our approach is founded on the premise that the cracks generated by the establishment of the criticality of an earthquake may change the strain observation during the loading and unloading phases induced by earth tide. As shear stress can usually produce cracks in rock (Byerlee 1978), in this study, like other scholars (Yin et al., 2008; Yu et al., 2015; Yu et al., 2020), stress change of source media is determined by using the Coulomb failure stress (CFS) caused by earth tide in the tectonically preferred slip direction on certain slip surface (refer the calculation process in the supplement for details). The loading phase and unloading phase will be distinguished by the angle between the tidal-effective shear stress and the tectonic-effective shear stress. When the angle is less than 90°, it will be a loading phase. When the angle is greater than 90°, the two shear stress cancel each other and will be in the unloading phase. The LURR method can be simply defined as $Y = \frac{X+}{X-}$, where "+" and "−" refer to the loading phase and unloading phase, and X is the response rate (Yin et al., 1995; Yin et al., 2000). We calculate the loading (1.0)/unloading (−1.0) state of each strain observation data and the values of strain recorded during the corresponding time period. In this study, we take the hourly value of strain observation as the input data. Then, LURR is calculated by the average values of strain recorded in corresponding periods:

$$Y = \frac{\left(\sum_{i=1}^{N+} H_i\right)/(N+)}{\left(\sum_{i=1}^{N-} H_i\right)/(N-)}, \quad (1)$$

where H_i is strain observation at the *ith* record, and $N+$ or $N-$ represents the numbers of records during the loading phase and

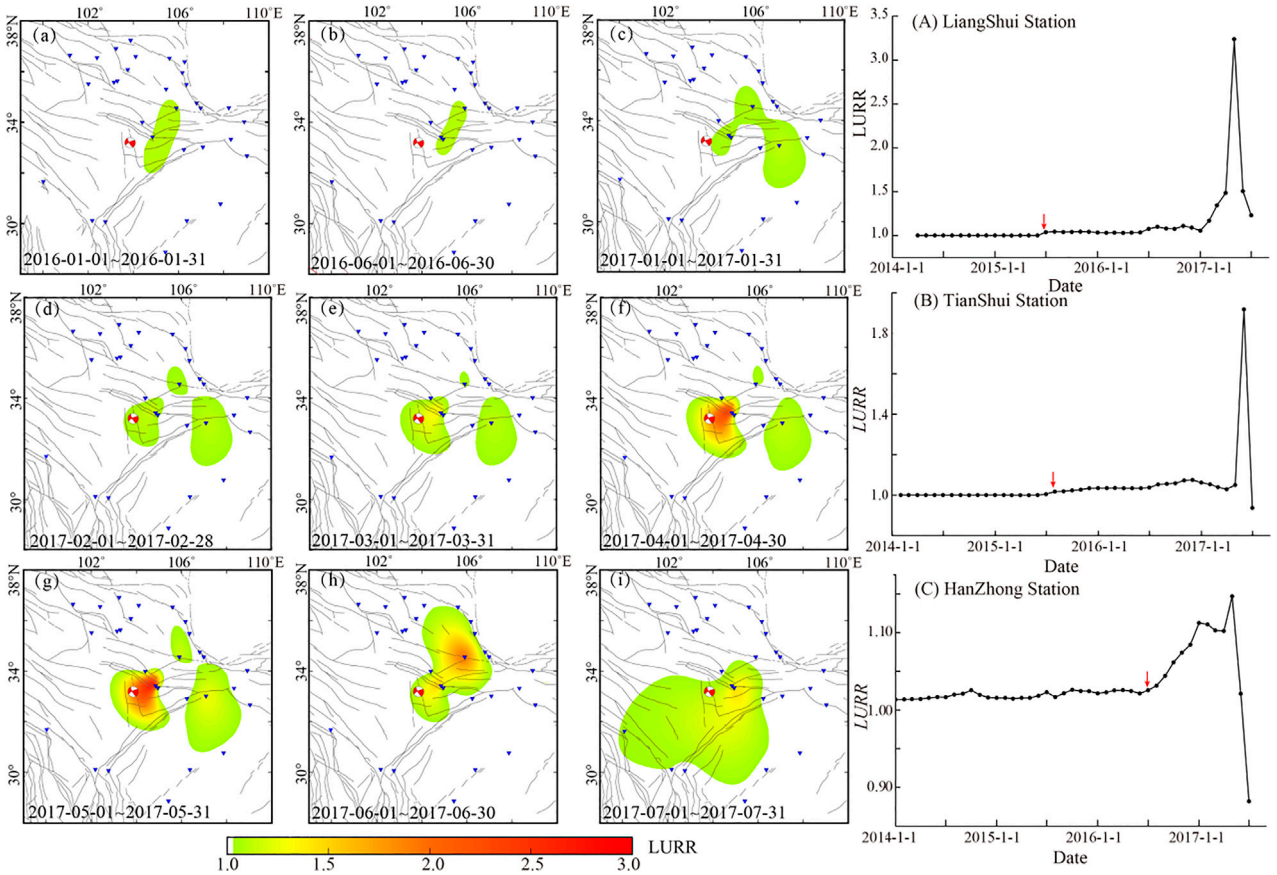

FIGURE 3 | LURR spatial distribution **(a–i)** and LURR time series of different stations **(A–C)**. **(a–i)** Spatial distribution of some periods from January 2016 to July 2017; Blue triangle: strain stations; Red focal mechanism solution: JZGEQ; Gray lines: fault. **(A–C)** LURR time series results for the L-Sh station, T-Sh station, and H-Zh station, respectively. Parameters for LURR evaluation are as follows: strike = 151, dip = 85, rake = 0, and depth = 15 km (Sun et al., 2018); Red arrow: start time of the anomaly.

unloading phase, respectively. The time window used to calculate the LURR value typically contains multiple loading–unloading cycles (Yu et al., 2021).

The strain observations may be affected by monitoring instruments and environmental impact, which will lead to some types of errors. Therefore, the following procedure is needed to preprocess the strain data in order to improve the quality of the LURR calculation. First, data with an observation period longer than 3 years are selected to ensure the stability of the instrument. Then, linear interpolation is performed for the missing data in the strain observation sequences. Finally, remove data extremes from the strain observation sequences, like the "step-change" caused by the instrument adjustment. These preprocessing procedures are quite important because short-term non tidal changes may directly affect the LURR calculation results. A total of 32 stations (13 cave strainmeter stations, 12 four-gauge borehole strainmeter stations, and seven volumetric borehole strainmeter stations) with 81 items of strain observation data are obtained, and part of the processed data is shown in **Figure 2**.

3 APPLICATION TO STRAIN DATA

We calculated the LURR time series results of 81 items and obtained the spatial distribution results of different stations by further interpolation, as shown in **Figure 3**. The calculation time window length is 1 month, the sliding step length is 1 month, and the friction coefficient is 0.4 (Yu et al., 2020; Yu et al., 2021). The selection of time window should not only consider the stability of calculation results but also identify anomalies before an earthquake. By comparing different time windows, we finally determined the time window to 1 month (**Supplementary Figure S2**).

By comparing the LURR time series obtained from strain observations at different stations (**Figures 3A–C**), we can find significant anomalies prior to JZGEQ. The LURR value of the three stations fluctuates around 1.0 in the initial period (January 2014–July 2016). Then, the LURR value begins to increase above 1.0 gradually from 6 months to 1 year before the occurrence of JZGEQ, reaching the maximum value in 1 to 3 months before the earthquake and subsequently returning to a low level prior to the earthquake. The trend of the LURR time series is similar to that of

the previous calculation of LURR using small earthquakes and groundwater level (Yin et al., 2000; Yu et al., 2021), which indicates that the LURR method based on strain observation can better extract the pre-seismic anomalies. On the other hand, under the influence of station distribution, epicentral distance, and observation instruments, there are still noticeable differences between the LURR curves. We also find this phenomenon that the magnitude of LURR anomalies decreases with the epicentral distance, the shorter the epicentral distance, the greater the LURR value. The LURR peak value of the L-Sh station before JZGEQ is 3.2, about 96 km away from the epicenter.

The LURR spatial distribution of all the stations in **Figures 3a–i** shows that the northeast margin of the Tibet plateau, a region with relatively concentrated stress, has witnessed LURR anomalies since 2016, which proves that microfracture caused by stress enhancement may exist in this region. After January 2017, the range of the LURR anomalies began to expand gradually. The T-Sh station located in the northern margin of the XiQinLing fault and H-Zh station located in the QingChuan fault show the phenomenon of increasing LURR successively. This means that during this period of time, the cracks gradually extend from the epicenter of JZGEQ to the peripheral area, and this dilatancy phenomenon is consistent with the process of the "linear elasticity—dilatation" stage with the increase of load before the rock reaches the peak stress (Wawersik and Brace, 1971; Scholz and Sykes, 1973). Subsequently, the LURR anomalies magnitude of stations near the epicenter of JZGEQ begins to increase significantly, indicating that the rupture of the rocks near the epicenter began to intensify. JZGEQ occurs as the magnitude of the anomalies decreases. From the temporal and spatial evolution characteristics of the LURR anomalies, we can clearly see the process of "extension—enhance—weaken" in the epicenter and its peripheral area before the occurrence of the JZGEQ.

4 DISCUSSION

In view of the pre-seismic stain transition and the LURR anomalies mainly concentrated in the northeast of the epicenter, and the directions with the most significant transition are mostly perpendicular to or large-angle oblique to the surrounding faults. In order to explore the relationship between pre-seismic anomalies and the seismogenesis mechanism. We further calculate the stress change induced by JZGEQ, especially the normal stress changes, based on the slip model of JZGEQ.

4.1 The Normal Stress Changes Induced by the JZGEQ

After JZGEQ, numerous academic institutions have employed far-field body wave inversion to analyze the rupture process. The GCMT solution shows that the rupture of JZGEQ is mainly dominated by strike-slip motion, and the rupture also contains ~10% of thrusting NDCP components. With the continuous application of GNSS, InSAR, and other geodetic data, the improvement of the ground deformation constraints has gradually modified and refined the seismic rupture model (Sun et al., 2018; Liu et al., 2019; Zheng et al., 2020). Liu et al. (2019) unified the slip model into one fault, and Zheng et al. (2020) divided the rupture fault into northern and southern parts according to the distribution of aftershocks. Sun et al. (2018) analyzed multiple InSAR data pairs covering the Jiuzhaigou region and adopted an MPNT inversion to the teleseismic data set. Finally, a fault model with three segments is obtained (**Figures 4A,B**). The rupture propagates bilaterally on the main fault plane (Segment 1), resulting in three concentrated slip zones in **Figure 4C**, and Segment 2 is a thrusting segment with a slip amount of about 2 m. In this study, we use this fault model with three segments to calculate the stress changes of the surrounding faults caused by JZGEQ.

In order to obtain the stress changes around the stations induced by JZGEQ, we collect focal mechanism solutions of historical earthquakes (cite from GCMT) and the achievements in the study area (Kirby et al., 2007; Ren et al., 2013a; Ren et al., 2013b; Cheng et al., 2018) to determine the main receiving fault rupture parameters (mainly for dip and rake angles of faults). The strike parameters of faults are calculated based on the surface outcrop results. The calculated receiving faults are shown in **Figure 5B**, and the rupture parameters are shown in **Table 1**. As aforementioned, the directions with the most significant transitions are mostly perpendicular to or large-angle oblique to the surrounding faults. This means that stress changes perpendicular to the faults has a more significant effect on strain observations. Therefore, we use the aforementioned slip model (Sun et al., 2018) to calculate the normal stress changes of faults induced by JZGEQ through PSGRN/PSCMP software (Wang et al., 2006). As we all know that most strain observations are surface observations (with depths less than 200 m), so we mainly calculate the normal stress changes of faults at the surface. The parameters of the lithospheric stratification in this study are shown in **Table 2** (Cheng et al., 2018; Yue et al., 2021).

According to the Coulomb rupture criterion, the Coulomb stress change (△CFS) caused by seismic dislocation on a particular fault is:

$$\triangle CFS = \Delta\tau + \mu(\Delta\sigma_n + \Delta P), \tag{2}$$

where $\Delta\tau$ is the shear stress change (take the sliding along the strike as positive), $\Delta\sigma_n$ denotes the normal stress change (make the fault unlock as positive), ΔP represents the pore pressure change of the fault (compression is positive), and μ is the friction coefficient (range from 0 to 1). In the actual calculation process, △CFS is proposed to calculate the absolute value of the shear stress on a fault (Shi and Cao, 2010). By merging the second half of **Eq. 2**, they introduce the "effective" friction coefficient (including the pore fluid and the medium characteristics on the fault), and the calculation formula becomes:

$$\triangle \mathrm{CFS} = \Delta\tau + \mu'\Delta\sigma_n, \tag{3}$$

where μ' basically ranges from 0 to 0.75, and the value is generally selected as 0.4 in previous studies (Freed and Lin, 1998; Freed and Lin, 2001; Lei et al., 2013; Shao et al., 2016).

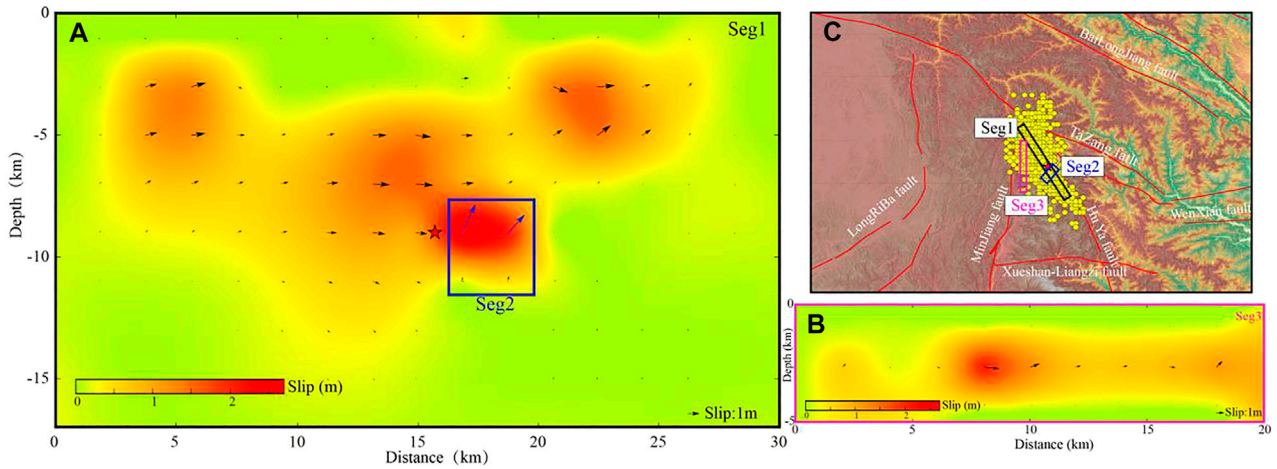

FIGURE 4 | Fault plane solution geometry and slip distribution (Sun et al., 2018). **(A)** Slip distribution on Segment 1 and Segment 2. Red pentagram: epicenter of JZGEQ. **(B)** Slip distribution on Segment 3. **(C)** Three fault segments are plotted in black, blue, and pink boxes, respectively. The distribution of aftershock seismicities is plotted as yellow filled dots. Slip directions are plotted with arrows for every subfault, respectively.

We calculate the co-seismic normal stress change distribution results of the source area (**Figure 5A**) and receiving faults **Figure 5B**. The receiving fault parameters in the source area are consistent with the JZGEQ rupture parameters in the study of Sun et al. (2018) (strike 151, dip 85, and rake 0). First of all, the calculation results of the source area show that the rupture of JZGEQ forms a significant negative normal stress change zone in the northeast and southwest directions of the main rupture zone. That means that the earthquake produced significant normal stress release in two directions perpendicular to the rupture fault, especially in the northeast side. The accumulation of normal stress between different faults may be adjusted with the variation of the earthquake preparation process, and this transition is likely to be captured by strain observation. This may be the reason why the strain transitions appear mainly in the northeast of the epicenter. Because of no strain observation in the southwest direction of the epicenter, we further calculate the normal stress changes of faults around the strain stations in the northeast side. The distribution of the receiving faults with negative normal stress changes is consistent with the direction of the source area, like GGS-DS-F, LT-DC-F, XQL-F, TY-GCS-F, LPS-F, HN-YG-G, and QC-F, which are mainly distributed in the northeast direction of the earthquake. As a result, the red strain stations marked in **Figure 1B** with significant pre-seismic and post-seismic strain transitions have excellent consistency with the calculated faults with negative normal stress changes, which indicates that the pre-seismic or post-seismic transitions observed by the strain stations are closely related to JZGEQ. That further means the LURR anomalies based on the strain observations are mainly due to the continuous cracks caused by the increase of normal stress before JZGEQ in those areas. This is consistent with the results obtained by other scholars based on the Benioff strain that the pre-seismic anomalies are distributed in the northeast of the epicenter (Yu et al., 2020).

4.2 Difference of Anomaly Characteristics

Due to the special seismogenic mechanism of this earthquake, the normal stress increases in the northeast of the epicenter before JZGEQ, namely, the faults are in the process of decoupling, and microfracture may exist in the stage of rock dilatancy. The observed results in those area is quite similar to the significant tensile pulses of ground stress normal to the fault zone in Douhe and Zhaogezhuang stations before the *M*7.8 Tangshan, China, earthquake in 1976 (Qiu et al., 1998). Their calculation results display that when the fracture front passes through the measuring point, the stress normal to the fracture will first rise and then drop. When the stress is at an angle of 30°, the observed change is not obvious. The strain equipment near the epicenter of JZGEQ provides lots of reliable pre-seismic and post-seismic data for the study of stress change. However, the anomaly characteristics of strain curves are different from those of LURR. The strain observation curves show pre-seismic or post-seismic transition, reflecting the effect of regional stress adjustment to a certain extent. Through the strain observation curves, we can better capture the general area of the future earthquake. But it is still difficult to predict the rupture degree of rocks in the crust. Assuming that the stations are densely distributed, we can even catch the rapid change of the strain before an earthquake at the stations close to the epicenter (such as L-Sh and W-D stations). However, considering the station density, it is difficult for us to accurately predict the rupture degree of source media by using only one or two strain observation curves, so as to accurately predict the time and location of the earthquake. In contrast, the LURR anomaly evolution process is more continuous regardless of time series curve or spatial and temporal distribution characteristics. The LURR anomalies mostly appear 6 months to 1 year before the occurrence of JZGEQ, then the amplitude of the anomalies gradually increases with time, and the earthquake occurs after the anomaly reaches the peak and falls back. The temporal and spatial distribution of the LURR anomalies also shows an evolution process of "extension—enhance—weaken" over time, which is consistent with the process of the "linear elasticity–dilatation" stage with the increase

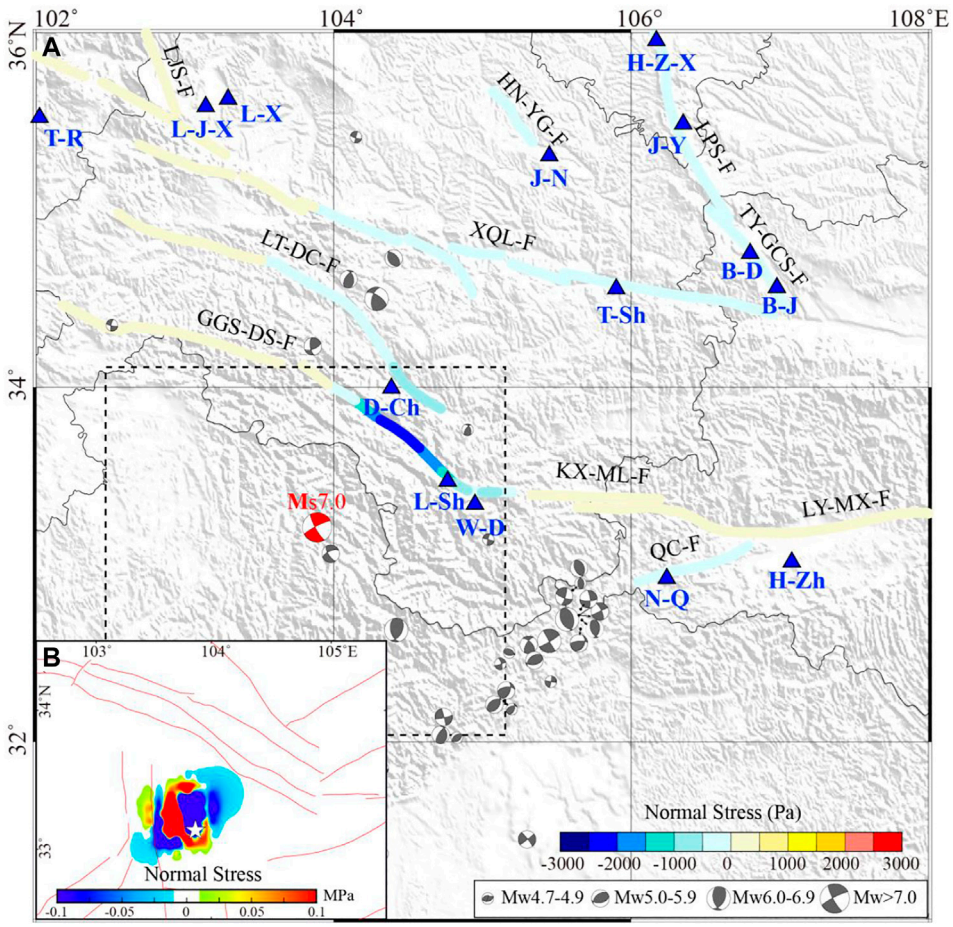

FIGURE 5 | Surface co-seismic normal stress changes induced by JZGEQ. **(A)** Results of the source area. White pentagram: epicenter of JZGEQ; Red lines: faults. **(B)** Results of the receiving faults. Blue triangle: strain stations; Gray focal mechanism solution: history earthquake since 1976 (cite from GCMT), including four sizes, 4.7 ≤ MW < 4.9, 5 ≤ MW < 5.9, 6 ≤ MW < 6.9, and MW > 7; Red focal mechanism solution: JZGEQ; The colored lines: receiving faults; GGS-DS-F: GuangGaiShan–DieShan fault; LT-DC-F: LinTan-DangChang fault; KX-ML-F: KangXian-Mianlue fault; QC-F: QingChuan fault; LY-MX-F: LueYang–MianXian fault; XQL-F: North margin of XiQinLing fault; TY-GCS-F: TaoYuan-GuiChuanSi fault; LPS-F: East margin of LiuPanShan fault; HN-YG-F: HuiNing-YiGang fault; LJS-F: LaJiShan fault.

TABLE 1 | Receiving fault rupture parameter in this study.

No.	Fault name	Strike (degree)	Dip (degree)	Rake (degree)
1	GGS-DS-F	155–175	81	–14
2	LT-DC-F	275–325	66	37
3	KX-ML-F	265–270	75	20
4	QC-F	240–265	70	180
5	LY-MX-F	90–115	55	10
6	XQL-F	275–305	70	40
7	TY-GCS-F	305–325	70	60
8	LPS-F	325–355	70	60
9	HN-YG-F	305–335	60	60
10	LJS-F	110–117	50	45

TABLE 2 | Parameters of the lithospheric-layered structure model.

No.	Depth/km	V_P/km·s^{-1}	V_S/km·s^{-1}	ρ/kg·m^{-3}	η/Pa·s
1	0	4.8	2.771	2,600	—
2	4	4.8	2.771	2,600	—
3	4	5.9	3.406	2,700	—
4	10	5.9	3.406	2,700	—
5	10	5.9	3.406	2,850	—
6	30	5.9	3.406	2,850	—
7	30	6.3	3.579	3,000	6.30×10^{18}
8	50	6.3	3.579	3,000	6.30×10^{18}
9	50	7.12	4.110	3,100	6.30×10^{18}
10	70	7.12	4.110	3,100	6.30×10^{18}
11	70	8.2	4.734	3,320	1.00×10^{20}
12	100	8.2	4.734	3,320	1.00×10^{20}

of load before the rock reaches the peak stress (Wawersik and Brace, 1971; Scholz and Sykes, 1973). The LURR method based on strain observation is an effective method to describe the dynamic change of the constitutive relationship of the source media in the crust. When we identify the rock rupture process caused by stress loading using the LURR method based on strain observation, we should pay more attention to the future seismic risk in these areas. Earthquake usually occurs after the recovery of the LURR anomaly.

5 CONCLUSION

The strain stations near the epicenter area of JZGEQ show us obvious pre-seismic and post-seismic transitions, which may be related to the significant enhancement of normal stress in the northeast direction of the epicenter before the earthquake. By calculating the ratio between the strain observations during the loading phase and the unloading phase induced by earth tides, anomalies might be found before JZGEQ. From the LURR curves, anomalies of LURR above 1.0 begin to appear in the surrounding stations successively from 6 months to 1 year prior to the occurrence of JZGEQ. The anomalies reach their peak value in 1–3 months before JZGEQ and eventually fall back to about 1.0 prior to the earthquake. In addition, the evolution characteristics of the LURR spatial and temporal anomalies are consistent with the process of the "linear elasticity—dilatation" stage with the increase of load before the rock reaches the peak stress, which proves that the LURR method based on strain observation is an effective way to describe the dynamic change of the constitutive relationship of the source media in the crust. The analysis of the anomalies in the corresponding LURR time series may help us estimate the location and time of an earthquake in the future.

DATA AVAILABILITY STATEMENT

The original contributions presented in the study are included in the article/**Supplementary Material**; further inquiries can be directed to the corresponding author.

AUTHOR CONTRIBUTIONS

CY: conceptualization, writing—original draft, and writing—review and editing. PJ, YW, and HY: manuscript revision. JC: data processing. CYu and YM: software and methodology. All authors have read and agreed to the published version of the manuscript.

FUNDING

This work was supported by the Joint Funds of the National Natural Science Foundation of China (U2039205) and the Spark Program of Earthquake Technology of CEA (XH20070Y and XH22040D).

ACKNOWLEDGMENTS

Authors thank Dr. Liu Yue (Institute of Earthquake Forecasting, China Earthquake Administration) for her help in the calculation process, Wang et al. (2006) for sharing PSGRN/PSCMP software, and Sun et al. (2018) for sharing the slip model in the article.

SUPPLEMENTARY MATERIAL

The Supplementary Material for this article can be found online at: https://www.frontiersin.org/articles/10.3389/feart.2022.881884/full#supplementary-material

REFERENCES

Byerlee, J. (1978). Friction of Rocks. *Pageoph.* 116, 615–626. doi:10.1007/bf00876528

Cheng, J., Yao, S. H., Liu, J., Yao, Q., Gong, H. L., and Long, H. Y. (2018). Viscoelastic Coulomb Stress of Historical Earthquakes on the 2017 Jiuzhaigou Earthquake and the Subsequent Influence on the Seismic Hazards of Adjacent Faults. *Chin. J. Geophys.* 61 (5), 2133–2151. (in Chinese). doi:10.6038/cjg2018L0609

Ekström, G., Nettles, M., and Dziewoński, A. M. (2012). The Global CMT Project 2004-2010: Centroid-Moment Tensors for 13,017 Earthquakes. *Phys. Earth Planet. Interiors.* 200-201, 1–9. doi:10.1016/j.pepi.2012.04.002

Freed, A. M., and Lin, J. (2001). Delayed Triggering of the 1999 Hector Mine Earthquake by Viscoelastic Stress Transfer. *Nature* 411 (6834), 180–183. doi:10.1038/35075548

Freed, A. M., and Lin, J. (1998). Time-dependent Changes in Failure Stress Following Thrust Earthquakes. *J. Geophys. Res.* 103 (B10), 24393–24409. doi:10.1029/98jb01764

Kirby, E., Harkins, N., Wang, E., Shi, X., Fan, C., and Burbank, D. (2007). Slip Rate Gradients along the Eastern Kunlun Fault. *Tectonics* 26 (2), TC20101–TC201016. doi:10.1029/2006tc002033

Lei, X. L., Ma, S. L., and Su, J. R. (2013). Inelastic Triggering of the 2013 Mw6.6 Lushan Earthquake by the 2008 Mw7.9 Wenchuan Earthquake. *Seismol. Geol.* 35 (2), 411–422. (in Chinese). doi:10.3969/j.issn.0253-4967.2013.02.019

Liu, G., Xiong, W., Wang, Q., Qiao, X., Ding, K., Li, X., et al. (2019). Source Characteristics of the 2017 Ms 7.0 Jiuzhaigou, China, Earthquake and Implications for Recent Seismicity in Eastern Tibet. *J. Geophys. Res. Solid Earth.* 124, 4895–4915. doi:10.1029/2018JB016340

Liu, Y., and Yin, X.-c. (2018). A Dimensional Analysis Method for Improved Load-Unload Response Ratio. *Pure Appl. Geophys.* 175 (2), 633–645. doi:10.1007/s00024-017-1716-6

Nie, Z., Wang, D.-J., Jia, Z., Yu, P., and Li, L. (2018). Fault Model of the 2017 Jiuzhaigou Mw 6.5 Earthquake Estimated from Coseismic Deformation Observed Using Global Positioning System and Interferometric Synthetic Aperture Radar Data. *Earth Planets Space.* 70, 55. doi:10.1186/s40623-018-0826-4

Qiu, Z. H., Zhang, B. H., Huang, X. N., and Ge, L. (1998). On the Cause of Ground Stress Tensile Pulses Observed before the 1976 Tangshan Earthquake. *Bull. Seismol. Soc. Am.* 88 (4), 989–994. doi:10.1785/BSSA0880040989

Ren, J., Xu, X., Yeats, R. S., Zhang, S., Ding, R., and Gong, Z. (2013b). Holocene Paleoearthquakes of the Maoergai Fault, Eastern Tibet. *Tectonophysics.* 590 (1), 121–135. doi:10.1016/j.tecto.2013.01.017

Ren, J., Xu, X., Yeats, R. S., and Zhang, S. (2013a). Millennial Slip Rates of the Tazang Fault, the Eastern Termination of Kunlun Fault: Implications for Strain Partitioning in Eastern Tibet. *Tectonophysics.* 608 (1), 1180–1200. doi:10.1016/j.tecto.2013.06.026

Scholz, C. H., Sykes, L. R., and Aggarwal, Y. P. (1973). Earthquake Prediction: A Physical Basis. *Science.* 181, 803–810. doi:10.1126/science.181.4102.803

Shao, Z., Xu, J., Ma, H., and Zhang, L. (2016). Coulomb Stress Evolution over the Past 200years and Seismic Hazard along the Xianshuihe Fault Zone of Sichuan, China. *Tectonophysics.* 670, 48–65. doi:10.1016/j.tecto.2015.12.018

Shen, Z.-K., Sun, J., Zhang, P., Wan, Y., Wang, M., Bürgmann, R., et al. (2009). Slip Maxima at Fault Junctions and Rupturing of Barriers during the 2008 Wenchuan Earthquake. *Nat. Geosci.* 2 (10), 718–724. doi:10.1038/ngeo636

Shi, Y. L., and Cao, J. L. (2010). Some Aspects in Static Stress Change Calculation: Case Study on Wenchuan Earthquake. *Chin. J. Geophys.* 53 (1), 102–110. (in Chinese). doi:10.1002/cjg2.1473

Sun, J., Yue, H., Shen, Z., Fang, L., Zhan, Y., and Sun, X. (2018). The 2017 Jiuzhaigou Earthquake: A Complicated Event Occurred in a Young Fault System. *Geophys. Res. Lett.* 45, 2230–2240. doi:10.1002/2017GL076421

Wang, M., and Shen, Z. K. (2020). Present-Day Crustal Deformation of Continental China Derived from GPS and its Tectonic Implications. *J. Geophys. Res. Solid Earth.* 125 (2), e2019JB018774. doi:10.1029/2019JB018774

Wang, Q., Xu, X., Jiang, Z., and Suppe, J. (2020). A Possible Precursor Prior to the Lushan Earthquake from GPS Observations in the Southern Longmenshan. *Sci. Rep.* 10, 20833. doi:10.1038/s41598-020-77634-6

Wang, Q., Zhang, P.-Z., Freymueller, J. T., Bilham, R., Larson, K. M., Lai, X. a., et al. (2001). Present-day Crustal Deformation in China Constrained by Global Positioning System Measurements. *Science.* 294 (5542), 574–577. doi:10.1126/science.1063647

Wang, R., Lorenzo-Martín, F., and Roth, F. (2006). PSGRN/PSCMP-a New Code for Calculating Co- and Post-seismic Deformation, Geoid and Gravity Changes Based on the Viscoelastic-Gravitational Dislocation Theory. *Comput. Geosciences.* 32 (4), 527–541. doi:10.1016/j.cageo.2005.08.006

Wawersik, W. R., and Brace, W. F. (1971). Post-failure Behavior of a Granite and Diabase. *Rock Mech.* 3 (2), 61–85. doi:10.1007/bf01239627

Yin, X.-C., Chen, X.-z., Song, Z.-p., and Yin, C. (1995). A New Approach to Earthquake Prediction: The Load/Unload Response Ratio (LURR) Theory. *Pageoph.* 145, 701–715. doi:10.1007/bf00879596

Yin, X.-C., Zhang, L.-P., Zhang, Y., Peng, K., Wang, H., Song, Z., et al. (2008). The Newest Developments of Load-Unload Response Ratio (LURR). *Pure Appl. Geophys.* 165, 711–722. doi:10.1007/s00024-008-0314-z

Yin, X. C. (1987). A New Approach to Earthquake Prediction. *Earthq. Res. China.* 3, 1–7. (in Chinese). doi:10.1007/978-3-540-47571-2_2

Yin, X. C., Wang, Y. C., Peng, K. Y., Bai, Y. L., Wang, H. T., and Yin, X. F. (2000). Development of a New Approach to Earthquake Prediction: Load/Unload Response Ratio (LURR) Theory. *Pure Appl. Geophys.* 157, 2365–2383. doi:10.1007/pl00001088

Yu, H.-z., Zhou, F., Cheng, J., Wan, Y.-g., and Zhang, Y.-x. (2015). The Sensitivity of the Loa/Unload Response Ratio and Critical Region Selection before Large Earthquakes. *Pure Appl. Geophys.* 172 (8), 2203–2214. doi:10.1007/s00024-014-0903-y

Yu, H.-Z., and Zhu, Q.-Y. (2010). A Probabilistic Approach for Earthquake Potential Evaluation Based on the Load/Unload Response Ratio Method. *Concurr. Comput. Pract. Exper.* 22, 1520–1533. doi:10.1002/cpe.1509

Yu, H., Yu, C., Ma, Y., Zhao, B., Yue, C., Gao, R., et al. (2021). Determining Stress State of Source Media with Identified Difference between Groundwater Level during Loading and Unloading Induced by Earth Tides. *Water.* 13, 2843. doi:10.3390/w13202843

Yu, H., Yu, C., Ma, Z., Zhang, X., Zhang, H., Yao, Q., et al. (2020). Temporal and Spatial Evolution of Load/unload Response Ratio before the M7.0 Jiuzhaigou Earthquake of Aug. 8, 2017 in Sichuan Province. *Pure Appl. Geophys.* 177, 321–331. doi:10.1007/s00024-019-02101-x

Yu, H. Z., Shen, Z. K., Wan, Y. G., Zhu, Q. Y., and Yin, X-C. (2006). Increasing Critical Sensitivity of the Load/Unload Response Ratio before Large Earthquakes with Identified Stress Accumulation Pattern. *Tectonophysics.* 428 (1-4), 87–94. doi:10.1016/j.tecto.2006.09.006

Yue, C., Qu, C. Y., and Niu, A. F. (2021). Analysis of Stress Influence of Qinghai Maduo Ms7.4 Earthquake on Surrounding Faults. *Seismol. Geol.* 43 (5), 1041–1059. (in Chinese). doi:10.3969/j.issn.0253-4967.2021.05.001

Zhang, Y., Xiang-Chu, Y., and Peng, K. (2004). Spatial and Temporal Variation of LURR and its Implication for the Tendency of Earthquake Occurrence in Southern California. *Pure Appl. Geophys.* 161, 2359–2367. doi:10.1007/978-3-0348-7875-3_17

Zheng, A., Yu, X., Xu, W., Chen, X., and Zhang, W. (2020). A Hybrid Source Mechanism of the 2017 Mw 6.5 Jiuzhaigou Earthquake Revealed by the Joint Inversion of Strong-Motion, Teleseismic and InSAR Data. *Tectonophysics.* 789, 228538. doi:10.1016/j.tecto.2020.228538

Conflict of Interest: The authors declare that the research was conducted in the absence of any commercial or financial relationships that could be construed as a potential conflict of interest.

Publisher's Note: All claims expressed in this article are solely those of the authors and do not necessarily represent those of their affiliated organizations, or those of the publisher, the editors, and the reviewers. Any product that may be evaluated in this article, or claim that may be made by its manufacturer, is not guaranteed or endorsed by the publisher.

frontiers | Frontiers in Earth Science

ORIGINAL RESEARCH
published: 12 July 2022
doi: 10.3389/feart.2022.903955

S-Wave Attenuation Variation and its Impact on Ground Motion Amplitudes During 2016–2017 Central Italy Earthquake Sequence

Aybige Akinci, Irene Munafò and Luca Malagnini*

Istituto Nazionale di Geofisica e Vulcanologia, Rome, Italy

A very energetic seismic sequence struck the central Apennines, Italy, in 2016–2017, with a series of damaging earthquakes, three of them with moment magnitudes M ≥ 5.9, and five of them with M ≥ 5.0, occurred over a few months between 24 August 2016, and late 2017. Several studies explained the phenomenon of a cascading earthquake sequence with fluid movements that provoked the rupture of different parts of the fault segments at different times and locations (e.g., Miller, Nature, 2004, 427, 724–727; Gabrielli, Frontiers in Earth Science, section Structural Geology and Tectonics, 2022; Malagnini, Frontiers in Earth Science, section Solid Earth Geophysics, 2022). In this study, we investigated the variation of crustal S-wave attenuation in terms of the frequency-dependent quality factor Q(*f*) before and after the main events (including the Amatrice, Visso, and Norcia sub-sequences, hereafter, AVN, and periods before and after the AVN multi-mainshock sequence). The spectral characteristics of regional attenuation in the central Apennines, as well as of the earthquake sources of the AVN sequence, are derived through regression analysis using a large set of seismograms; Q(*f*) is modeled, together with the bilinear geometrical spreading, g(r), using a widely used tool, namely, random vibration theory, RVT (Cartwright and Longuet-Higgins, 1956). The primary objective of this effort was to examine how the variability of crustal anelastic attenuation would impact the earthquake-induced ground motions. The latter is quantified in terms of peak ground accelerations (PGAs), peak ground velocities (PGVs), and pseudo spectral accelerations (PSAs) at 0.3 and 2 s . Here, we showed that the main events of the AVN sequence strongly affect crustal S-wave attenuation, including its frequency dependence. However, the effects of 1/Q(*f*) fluctuations on earthquake-induced ground motions are small and have a negligible impact on the seismic hazard.

Keywords: seismic wave attenuation, earthquake ground motion, stochastic ground motion simulations, seismic hazard, central Italy seismic sequence

OPEN ACCESS

Edited by:
Giovanni Martinelli, National Institute of Geophysics and Volcanology, Italy

Reviewed by:
Ortensia Amoroso, University of Salerno, Italy
Jing Ba, Hohai University, China

****Correspondence:***
Aybige Akinci
aybige.akinci@ingv.it

Specialty section:
This article was submitted to Solid Earth Geophysics, a section of the journal Frontiers in Earth Science

Received: *24 March 2022*
Accepted: *22 June 2022*
Published: *12 July 2022*

Citation:
Akinci A, Munafò I and Malagnini L (2022) S-Wave Attenuation Variation and its Impact on Ground Motion Amplitudes During 2016–2017 Central Italy Earthquake Sequence. Front. Earth Sci. 10:903955. doi: 10.3389/feart.2022.903955

1 INTRODUCTION

The central Apennines is one of Italy's most seismically active areas, with a long history of earthquakes which have strongly influenced seismic hazard and risk-related studies in Italy (Akinci et al., 2009). The recent sequences that occurred between 2009 and 2017 caused widespread building collapses due to the closeness of the causative fault to heavily populated

urban areas, and to the elevated vulnerability of old edifices in cobblestone. In the 5 months following the 24 August 2016 Amatrice earthquake, nine seismic events with magnitude M > 5.0 occurred in the area. The most significant event of the sequence (M6.3) occurred in the vicinity of the town of Norcia and was preceded, 4 days earlier, by an M5.9 foreshock near Visso. The long sequence provided us with a massive set of seismological data (three events with magnitude larger than 5.9, up to a maximum magnitude of 6.3, see Malagnini and Munafò (2018), and http://eqinfo.eas.slu.edu/Eq. c/Eq. c_mt/MECH.IT/). The highest PGA values (~0.8 g for the M6.3 Norcia and M6. 0 Amatrice earthquakes) were recorded in the near-source area, and were the largest ever documented during an Italian earthquake. The attenuation characteristics of the crust have always been thought to play a significant role in refining seismic hazards for the study area (Lombardi et al., 2005; Akinci et al., 2009).

Several studies in the central Apennines demonstrated the effect of fluid migration along with relatively high-permeability faults, and the possible occurrence of earthquake, including triggered ones, due to an increased pore-pressure from the diffusion of over-pressured fluids (Miller et al., 2004; Lucente et al., 2010; Malagnini et al., 2012; ; Chiarabba et al., 2020; Akinci et al., 2020; Gabrielli et al., 2022; Malagnini et al., 2022).

It has long been understood that seismic attenuation has the potential to be a relevant source of information about the Earth's interior. It is an important parameter that could greatly improve our understanding of subsurface processes, integrating the seismic velocity and conceding more detailed outcomes (Jackson and Anderson, 1970; Cormier 2011). Attenuation of seismic waves is strongly affected by rock permeability, pore fluids, and saturation levels (Winker and Nur, 1982; Malagnini et al., 2019; Gabrielli et al., 2022; Malagnini et al., 2022). Elevated seismic attenuation is usually observed at active faults in the brittle crust (Rietbrock, 2001).

Malagnini et al. (2022) investigated the seismic attenuation variation as a function of time and frequency before, during, and after the central Apennines seismic sequence of 2016–2017; they concluded that it is the variations in crustal rock's permeability that drive the observed changes in seismic attenuation. Following Muir-Wood and King (1993), they hypothesized that the coseismic stress drop of a normal-faulting earthquake causes a sudden closure of such cracks, which translates into a sudden decrease in permeability and seismic attenuation. However, Malagnini et al. (2022) did not assess the ground motion parameters induced by the mainshocks of the sequence, parameterizing the seismic wave attenuation, earthquake source, as well as the distortions introduced by subsurface heterogeneities at the recording sites.

Gabrielli et al. (2022) attempted separating scattering and absorption contributions to the total attenuation of coda waves and provided images of their spatial (2D) and temporal variations in different frequency bands during the AVN seismic sequence. Their coda attenuation tomography demonstrated an evident variation between the pre-sequence and the sequence time windows, before and after the three mainshocks of the AVN sequence.

Here, we investigated the anelastic attenuation of S-wave, expressed in terms of a frequency-dependent seismic quality factor Q(f). We also intend to better understand the attenuation characteristics of the crust, and to explore its variability as a function of frequency and time during the central 2016–2017 earthquake sequence. Our main objective was to examine the sensitivity of peak ground acceleration (PGA), peak ground velocity (PGV), and pseudo spectral accelerations (PSAs) at 0.3 and 2 s to the temporal variability of crustal attenuation.

Here, we separated crustal attenuation from source excitation and site response; we performed that by exploiting the theoretical framework of random vibration theory (RVT, see Cartwright and Longuet-Higgins, 1956; Malagnini et al., 2019; Malagnini et al., 2022), which allows using the peak values of narrowband-filtered time histories, instead of the noisier Fourier amplitudes (details in Malagnini and Dreger, 2016). We investigated the events registered between 1 January 2016, and 29 March 2018. We modeled the empirical propagation and excitation terms related to frequency-dependent quality factor, a geometric spreading function, a stress drop parameter, and an operator to account for site effects during the sequence (coseismic and post-seismic periods). For this purpose, we considered velocity seismograms recorded before and after the three main events (including the mainshocks), corresponding to different time windows. Regressions were carried out using large amounts of waveforms from the study area, from earthquakes with magnitudes ranging between M2.0 and M6.3.

First of all, we obtained the scaling relationships for high-frequency ground motion throughout the inversion technique that has been introduced by Raoof et al. (1999). This approach is widely and successfully used for regionalized ground motion studies in many parts of the world (Morasca et al., 2006; Akinci et al., 2006; Malagnini et al., 2007; Malagnini et al., 2011; D'Amico et al., 2012; Akinci et al., 2013; Akinci et al., 2014; D'Amico et al., 2018). Second, the regional attenuation and source scaling were parameterized to describe the observed ground motions as a function of distance, frequency, and seismic moment (or moment magnitude).

A simple grid-search was adopted to perform in order to optimize the attenuation parameters in our scaling model. The earthquake-induced ground motions for the M6.3 Norcia earthquake are obtained by a stochastic finite-fault simulation approach based on dynamic corner frequencies (Motazedian and Atkinson 2005; Boore 2009), which makes use of the parameters obtained here, describing frequency-dependent attenuation, source excitation, and site responses. Finally, comparing simulations and actual recordings, we show the variability of seismic ground motion, and consequently of seismic hazard, in the study region.

2 DATASET

We used weak- and strong-motion data from central Italy (Italy), including the AVN seismic sequence ($2.0 \leq M \leq 6.3$). We selected the focal depths and the hypocentral distances of

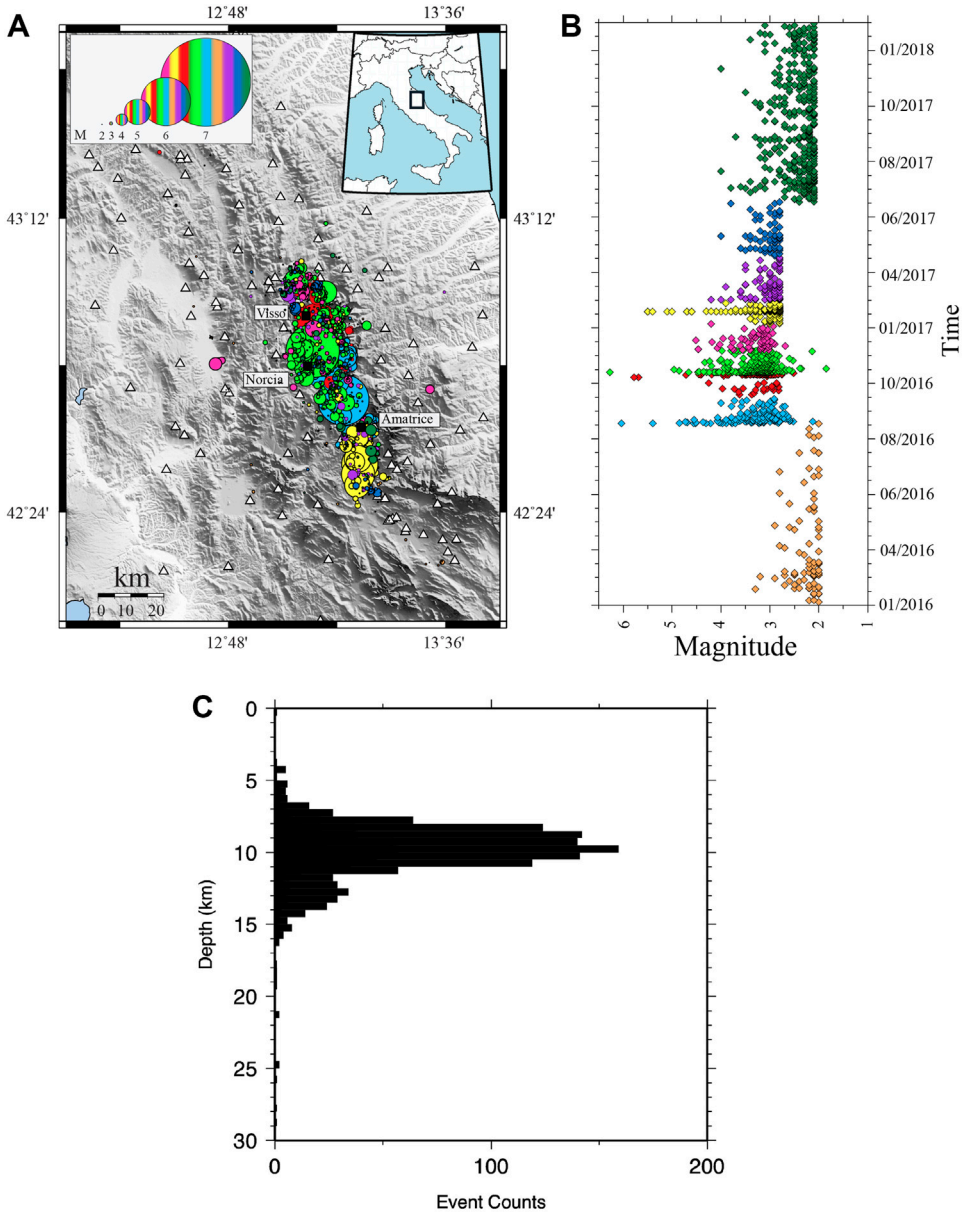

FIGURE 1 | (A) Map shows the seismicity distribution in the central Apennines area, earthquakes are shown as colored dots as a function of the time period, where the size of the circle represents the magnitude of the quake. Black squares indicate the main cities in the area, white triangles represent the seismic stations belonging to the National Accelerometric Network (RAN) and the National INGV Seismic Network (RSN). **(B)** We divided the sequence into nine phases as given in **Table 1**. **(C)** Focal depth of the selected events.

the events with similar locations from those shallower than 20 km and shorter than 100 km, respectively, distributed along an 80 km long NW-SE-oriented fault system. Almost all the focal mechanisms dominated by normal faulting agree with the extensional tectonic regime in the central Apennines (Zhong et al., 2018; Buttinelli et al., 2021). The dataset contains 1,445 selected events and more than 20,000 recordings between 1 January 2016 and 29 March 2018. This dataset covers more than 2 years of recorded seismicity, including the AVN sequence where three M ≥ 5.9 events occurred over a few months between August 24 and 30 October 2016 (Chiaraluce et al., 2017).

The locations of selected events (dots) and the seismic stations (triangles) are shown in **Figure 1A**. The distribution of seismicity is indicated with different colors corresponding to the time frames according to the following event start and end dates. These dates during the sequence (24 August 2016–30 January 2017) are selected before and after main events to have a similar time window, approximately a month, at each phase and to have a sufficient number of earthquakes to analyze. However, for the

TABLE 1 | S-wave attenuation values obtained in this study as a function of selected time phases and related information.

Time	Number of events	$Q(f) = Q_0 f^n$	Main event
Phase_I January 2016–23 August 2016 Pre-sequence	87 (~8 months)	$95 \pm 30\ f^{0.50\pm0.12}$	M3.2
Phase_II 24 August 2016–25 September 2016 Amatrice sequence	130 (~1 month)	$115 \pm 45\ f^{0.50\pm0.12}$	M6.0 Amatrice mainshock
Phase_III 30 September 2016–29 October 2016 Visso sequence	98 (~1 month)	$55 \pm 5\ f^{0.80\pm0.025}$	M5.9 Visso mainshock
Phase_IV 30 October 2016–28 November 2016 Norcia sequence	339 (~1 month)	$75 \pm 15\ f^{0.65\pm0.1}$	M6.3 Norcia mainshock
Phase_V 29 November 2016–01 January 2017	67 (~1 month)	$75 \pm 5\ f^{0.65\pm0.05}$	M4.3
Phase_VI 02 January 2017–30 January 2017 Capitignano sequence	176 (~1 month)	$85 \pm 5\ f^{0.60\pm0.05}$	M5.5
Phase_VII 03 February 2017–30 March 2017	83 (~2 months)	$70 \pm 15\ f^{0.70\pm0.12}$	M4.2
Phase_VIII 01 April 2017–10 June 2017	71 (~2 months)	$75 \pm 10\ f^{0.70\pm0.1}$	M4.0
Phase IX 11 June 2017–29 March 2018	408 (~9.5 months)	$95 \pm 20\ f^{0.50\pm0.1}$	M4.0

pre- and after sequences (after the Capitignano sequence), we selected events recorded in eight and 2 months, since the frequency of earthquake occurrence decreases over time. Hereinafter, we presented the selected phases in detail.

- January 1 through 23 August 2016: 87 events with M > 3.2 (hereafter phase-I, pre-sequence).
- August 24 through 25 September 2016 (the M6 Amatrice sequence): 130 events with 3.0 ≤ M ≤ 6.0 including the Amatrice mainshock of 24 August 2016, at 1:36:32 UTC (hereafter phase-II, the Amatrice sequence).
- September 30 through 29 October 2016 (the M5.9 Visso sequence): 98 events with 3.0 ≤ M ≤ 5.9 including the Visso mainshock of October 26 at 19:18:08 UTC (hereafter phase-III, the Visso sequence).
- October 30 through 29 November 2016 (the Norcia M6.3 sequence): 339 events with 3.0 ≤ M ≤ 6.33 including the Norcia mainshock of October 30 at 06:40:18 UTC (hereafter phase-IV, the Norcia sequence).
- 29 November 2016 through 1 January 2017: 67 events with 3.0 ≤ M ≤ 4.7 (hereafter phase-V).
- 1 January 2017 through 30 January 2017: 176 events recorded with 3.0 ≤ M ≤ 5.5 (hereafter phase-VI, the Capitignano sequence).
- 3 February 2017 through 30 March 2017: 83 events recorded with 3.0 ≤ M ≤ 4.7 (hereafter phase-VII).
- April 1, 2017 through 10 June 2017: 71 events with magnitudes 3.0 ≤ M ≤ 4.0 (hereafter phase-VIII).
- 11 June 2017 through 29 March 2018: 408 events with 2.0 ≤ M ≤ 4.0 (hereafter phase-IX).

Figure 1B shows the event distributions over the nine time windows, each of them presented with a different color. It should be noted that the minimum magnitude in the various periods is variable, that is, M3.0 during the period of the sequence and M2.0 before and after the sequence. The number of events belonging to different time phases is given in **Table 1**, together with the maximum magnitude registered in each time period. **Figure 1C** shows the distribution of the focal depths in our dataset, all within 15 km. We gathered seismograms registered by both the accelerometric stations of the Italian strong-motion network (RAN Rete Accelerometrica Nazionale) and the 24-bit broadband weak-motion seismological stations of the Digital Seismic Network run by the Istituto Nazionale di Geofisica e Vulcanologia (INGV). Strong- and weak-motion recordings were downloaded from the ITACA (ITalian ACcelerometric Archive) website or from the European Strong Motion, ESM database, and from the European Integrated Data Archive (EIDA) repository, respectively.

3 METHOD AND DATA ANALYSIS

Our method has been widely and successfully used to determine crustal attenuation, source-, and site-related parameters from recorded seismograms (Akinci et al., 2014; Malagnini and Dreger, 2016; Munafò et al., 2016; Malagnini et al., 2019). These studies demonstrated that the observed seismic attenuation varies significantly from region to region. Regression results can be utilized for estimating earthquake-induced ground motions (i.e., peak acceleration and peak velocity), given a moment magnitude and a hypocentral distance. Rather than regressing Fourier amplitudes, our technique maximizes the signal-to-noise

ratio (SNR) by analyzing peak values of narrow bandpass–filtered time histories. Our method is based on a tool called random vibration theory (RVT), developed by Cartwright and Longuet-Higgins (1956). A suitable set of constraints is used for decoupling the attenuation parameters from source and site terms, and for producing a smooth attenuation function; see Malagnini and Dreger (2016) for details.

First of all, we visually examined all the seismograms and picked the P and S arrival times for quality control. For each phase described earlier, peak ground velocities were measured in selected narrow frequency bands from 0.5 to 22.5 Hz; in each time window and for each central frequency, peak values were subsequently regressed to obtain a frequency-dependent attenuation function, a set of excitation terms, and of site responses. The 16 narrow frequency bands were centered at a set of frequencies f_c = 0.5, 0.75, 1.25, 1.75, 2.50, 3.50, 5.0, 6.5, 8.5, 10.50, 12.50, 14.50, 16.50, 18.50, 20.50, and 22.5 Hz; the bandwidth around each central frequency went from $1/\sqrt{2}\,f_c$ to $\sqrt{2}\,f_c$; filters were causal eight-pole Butterworth, high-pass and low-pass, respectively.

The peak values of the S-waves from the *i*th source, recorded at the *j*th site, at a hypocentral distance r and around a central frequency f_c , are measured on the filtered waveforms, $a_{peak}(r_{ij}, f_c)$, and can be defined as A_{ij} $(f_c, r)=\log_{10}[a_{peak}(r, f_c)]$. RVT allowing the use of the convolution theorem over peak values (instead of Fourier amplitudes) in our measurements were cast in a matrix form at each frequency band.

$$A_{ij}(f_c, r) = \mathrm{SRC}_i\left(f_c, r_{fix}\right) + \mathrm{Path}\left(f_c, r, r_{fix}\right) + \mathrm{Site}_j(f_c). \quad (1)$$

The reference distance r_{fix} is chosen within the range of observed distances. In order to stabilize inversions in **Eq. 1** and to bring a physical meaning to source and site terms, two constraints are applied; $\mathrm{Path}(r = r_{fix})=0$ at any f_c, and $\Sigma \mathrm{Site}_j(f_c)=0$. It is important to note that the $\mathrm{Site}_j(f_c)$ term in **Eq. 1** indicates the *i*th individual component of the ground motion. So the horizontal source spectrum is relative to the reference distance $r_{fix,}$ and to the average network site.

We arbitrarily chose a reference distance r_{fix} = 40 km. Such a hypocentral distance is chosen to be well inside the range of examined distances: it should be far from the source so that errors in source depth do not significantly alter hypocentral distances, and not so far to be in the range of supercritical reflections from the Moho. Furthermore, a smoothing constraint was implemented to the propagation term Path (f_c, r, r_{fix}), establishing a condition of minimum roughness with a null second derivative.

The crustal path term is described in terms of a piece-wise linear continuous function (in loglog).

$$\mathrm{Path}\left(f_c, r, r_{fix}\right) = \sum_{n=1}^{Nnodes} L_n Path_n \quad (2)$$

L_n (r) is a linear interpolation function, n is the nodes for the distance segments, and $Path_n$ is the value of the attenuation term at the hypocentral distance of the n-th node. We regularly sampled the dataset over a logarithm scale, choosing a regular length for each node.

Finally, regressions were performed over the selected central frequencies using an L1-norm inversion, as Bartels and Conn (1980) reported. The results are presented individually for all terms being SRC_i (f_c, r_{fix}), Path (f_c, r, r_{fix}), and Site_j (f_c) (**Eq. 1**). The effective signal duration is determined from a time window, including the 5% and 75% of seismic energy following the S-wave arrival. The effective time duration is an important parameter for the ground-motion prediction. It can play an essential role for earthquake damage potential and engineering purposes, notably in evaluating liquefaction and the inelastic deformation, as well as the energy dissipation of the short-period buildings (Bommer and Martinez-Pereira 1999).

4 GROUND MOTION MODELING AND PARAMETERIZATIONS

In order to quantify the regression results concerning the geometrical spreading, the frequency-dependent Q(*f*), the source scaling, and the site effects, each term in **Eq. 1** is modeled using RVT and/or stochastic time-domain simulations (Boore, 1983; Boore and Joyner, 1997). Following RVT, the peak value of the narrow bandpass–filtered seismograms is used instead of the Fourier amplitude included in the same frequency band. The narrow band-pass filters are needed to make the seismograms somewhat "stationary" as prescribed by RVT, yet they cannot be too narrow in order to allow the existence of meaningful peaks.

Clearly, the use of peak values maximizes the signal-to-noise ratios of our results. Moreover, knowing the effective duration of ground motion within a specified bandwidth near a specific center frequency, RVT allows the application of the convolution theorem to peak values. Together with the Parseval's equality, we can switch between time and frequency domains and write the matrix form for the linear inversion of the peak values (**Eq. 1**). In brief, given a stationary, random time history of length T, RVT enables a measure of its peak value following $a_{peak} \approx \xi a_{RMS}$, where a_{RMS} is the root mean square value of the time history calculated in the time window starting at the onset of S-waves, and having a duration T. The parameter ξ can be calculated from the spectral moments of the time history. The band-pass filtering procedure delivers non-zero Fourier amplitudes only between the two-corner frequencies ($1/\sqrt{2}\,f_c$ and $\sqrt{2}\,f_c$), and the following equation holds (Malagnini and Dreger, 2016):

$$a_{RMS}(f_i) = \sqrt{\frac{\int_0^T a^2(t, f_i)dt}{T}} = \sqrt{\frac{\int_{f_{1i}}^{f_{2i}} \hat{a}^2(f)df}{T}}. \quad (3)$$

In our study, we assume that the filtered seismogram is different from zero between the S-wave arrival time (elapsed time t = 0), and an elapsed time t = T. In turn, the effective duration of the ground motion (T) is estimated for each seismogram and for each central frequency. In other words, we have an effective duration which is a function of the central frequency and of the hypocentral distance:

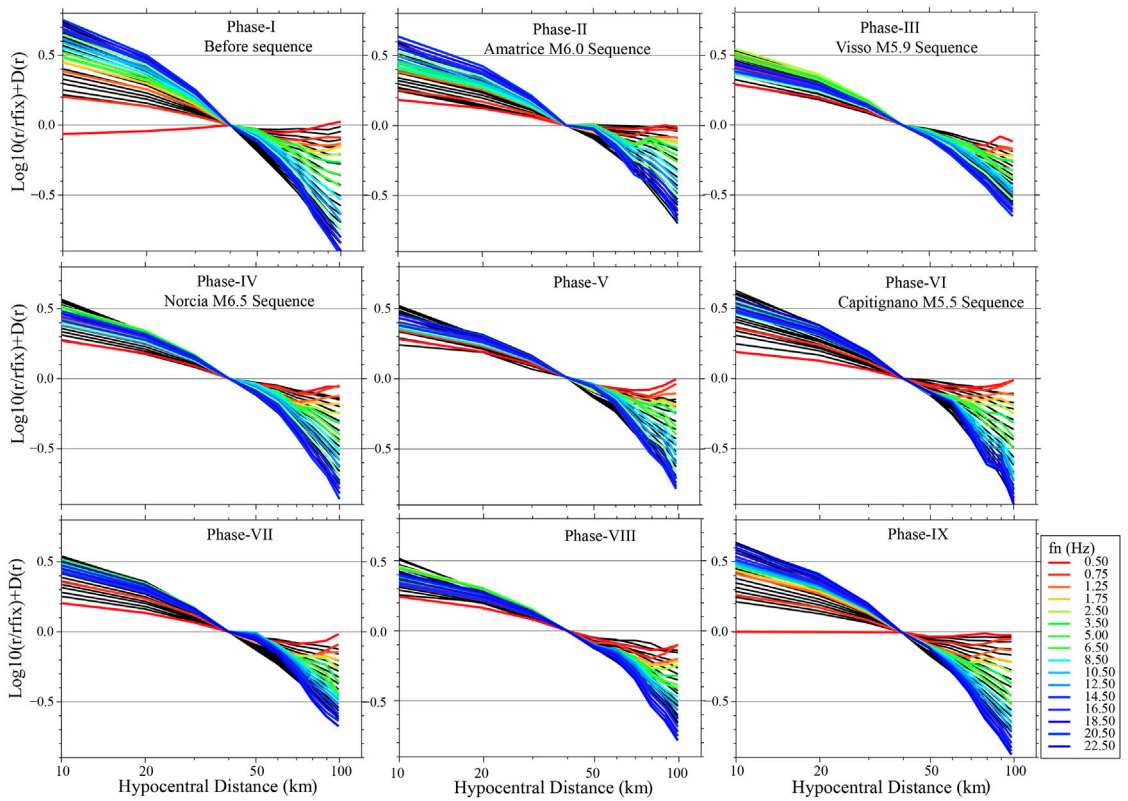

FIGURE 2 | Empirical regional attenuation, $Path_{emp}$ (r, r_{fix}, f_k) curves experienced by the narrow-band filtered amplitudes of the ground motion, at the 16 central frequencies of 0.5, 0.75, 1.25, 1.75, 2.50, 3.50, 5.0, 6.5, 8.5, 10.50, 12.50, 14.50, 16.50, 18.50, 20.50, and 22.5 Hz that are shown by colored lines at each selected time periods. Black lines in the background are obtained with the attenuation model, $Path_{theo}$ (r, r_{fix}, f_k). All lines are normalized by a 1/r decay (the horizontal dashed lines represent the 1/r decay). The reference hypocentral distance is 40 km.

$T = T(f_c, r)$. Finally, once we develop an attenuation/excitation model for the region under investigation, as well as an effective duration function, RVT can be applied to estimate peak values as a function of earthquake size and hypocentral distance, such as, peak accelerations and velocities, and/or response spectra (see for details Malagnini and Dreger, 2016; Lavrentiadis et al., 2021).

4.1 Attenuation Parameters

We modeled the empirically-based attenuation term ($Path_{emp}(r, r_{fix}, f_c)$) by specifying both the crustal anelastic attenuation, represented by the quality factor $Q(f) = Q_o(f/ f_{ref})^n$, and the geometrical spreading g(r). The latter is modeled as a piecewise continuous function of the hypocentral distance (r). The role of the reference frequency f_{ref}=1.0 Hz is just to keep the non-dimensional nature of the attenuation parameter.

$$Path_{theo}(r, r_{fix}, fc) = \log10\left[\left(g(r)/g\left(r_{fix}\right)\right)\left(exp - \pi f\left(r - r_{fix}\right)/\beta Q(f)\right)\right]. \quad (4)$$

Equation 4 reveals the effects of frequency-dependent geometrical spreading and anelastic attenuation, relying, for each frequency, on the average velocity structure along the propagation pathway and rock's physical properties (Aki, 1980). It should be noted that the theoretical attenuation term described in (**Eq. 4**) is also normalized to zero at the reference distance r_{fix}.

Figure 2 presents the regressed empirical attenuation peak velocity amplitudes (colored curves), and the theoretical attenuation curves (black curves) obtained from the RVT-based modeling. The results are relative to the nine time windows that correspond to the nine phases described earlier (prior to, and during the sequence). The L2 norm grid search through the parameter space of the geometrical spreading g(r) and the quality factor $Q(f)$ (the 1-Hz attenuation parameter Q_o and the exponent n defining its frequency dependence) gives us the optimal theoretical attenuation models ($Path_{theo}(r, r_{fix}, f_c)$), defined by minimizing the RMS-value of the residuals in each phase of the sequence. For this purpose, we used the observed durations as a function of distance and frequency (**Supplementary Figure S1**). The residual between the inverted attenuation curves, $Path_{emp}$ (r, r_{fix}, f_k) (**Figure 2** colored lines) and for the theoretical model curves, $Path_{theo}$ (r, r_{fix}, f_k) (**Figure 2** black lines) were calculated to determine our preferred ground-motion propagation model for each of the nine subsets as:

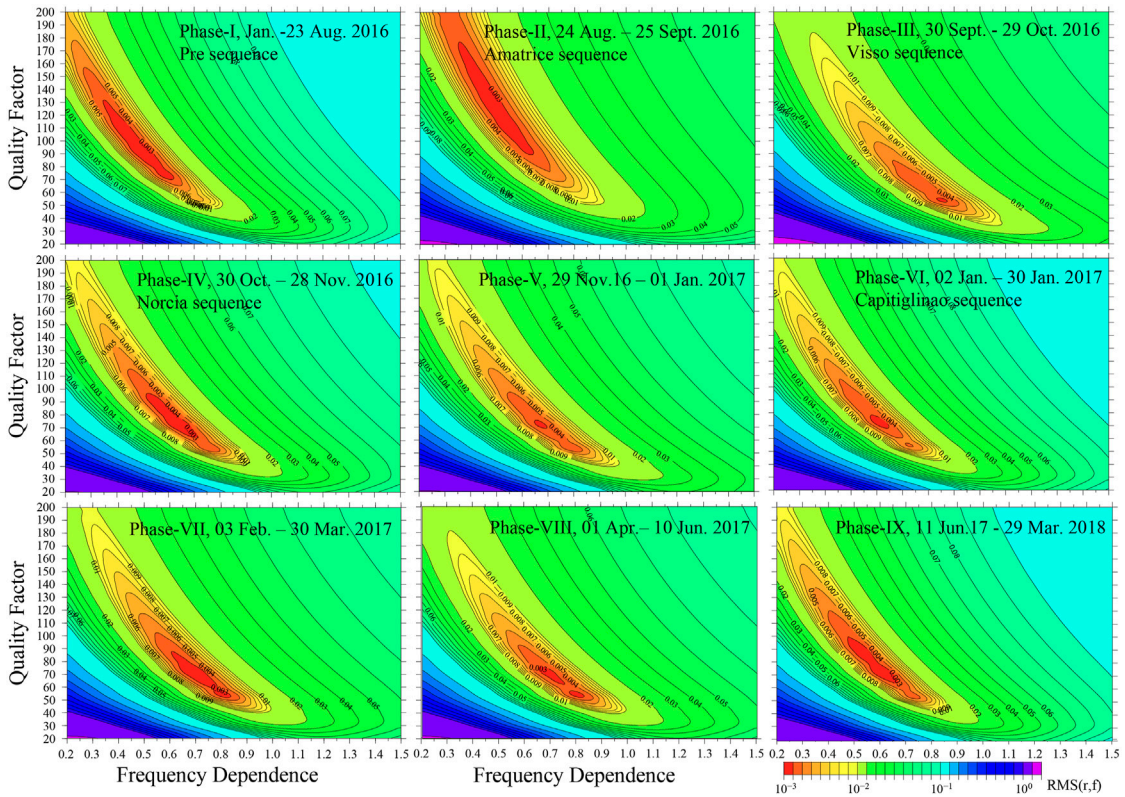

FIGURE 3 | Residuals (rms(dist)) obtained from comparing empirical log10($Path_{emp}(r, r_{fix}, f_c)$) and theoretical log10($Path_{theo}(r, r_{fix}, f_c)$) of the horizontal components, plotted as a function of Q_0 and n.

$$RMSE = \sqrt{\frac{\sum_{k,i}\left(Path_{emp}\left(r, r_{fix}, f_k\right) - Path_{theo}\left(r, r_{fix}, f_k\right)\right)^2}{\sum_{k,i}\sigma\left(f_k\right)}}, \quad (5)$$

where $\sigma(f_k)$ values are these emerging from the regression results; f_k = 0.5, 0.75, . . . and 22.5 Hz; values of i are 10, 20, 30, 40, 50, 60, 70, 80, 90, and 100 km. Finally, we obtained the solution with the minimum *RMSE* at all chosen time windows.

We allowed the quality factor, Q(f) to vary between 20 and 200 and the frequency dependence coefficient, n between 0.2 and 1.5, and the exponent α of the geometrical spreading, $g(r)=r^{-\alpha}$, to vary between 0.3 and 1.2 for distance before and after the r_{fix} = 40 km in terms $Path_{theo}$ (r, r_{fix}, f_k) (**Eq. 4**) using merged datasets. Using the dataset before the sequence, optimum results were obtained for $Q(f)=75f^{0.6}$, $g(r)=r^{-1.1}$ for distances between 5 and 40 km, and $g(r)\sim r^{-0.5}$ for distances greater than 40 km. For shorter distances, $r^{-1.1}$ describes body-wave crustal propagation, whereas for distances beyond 40 km, $g(r)\sim r^{-0.5}$ describes the propagation of a wavefield dominated by surface waves. These coefficients are very close to those calculated in the central Apennines by Malagnini et al. (2011). The optimal functional form g(r) obtained pre-sequence was fixed in all the grid searches performed on the subsequent phases, and only the parameters Q_o and n were altered. **Figure 3** presents the residuals calculated varying Q_o, n, and geometrical spreading coefficient, g(r), in the nine subsets of data, from 1 January 2016 to 29 March 2018, where the best-fit values are indicated. The best-fit attenuation parameters are presented in **Table 1** and **Figure 4**. Errors are estimated using the F distribution at the 90 percent confidence level. We consider the solutions with normalized residuals (concerning the minimum value) are smaller than 1.3–1.5 from the misfit values in **Figure 3** (for details Mayeda et al., 1992; Del Pezzo and Bianco, 2010).

4.2 Source and Site Parameters

The seismic sources of our dataset are modeled following the Brune's (1970), Brune (1971) single-corner frequency spectral model, with the static stress parameter that is a function of the earthquake's magnitude following the equation:

$$\mathrm{SRC}\left(f_c, r_{fix}\right) = log_{10}\left[s(f,M)V(f)g(r_{fix})\,exp\left[- \left(\pi f_c r_{fix}\right)/\left(\beta Q(f)\right)\right] exp\left(-\pi f k_{eff}\right)\right], \quad (6)$$

where $s(f, M) = R_{\Theta\Phi}FN\,M_o\,4\pi\rho\beta^3\,(2\pi f)S(f)$ is the Fourier velocity spectra, $R_{\Theta\Phi}$ is the average radiation pattern, 0.55, F is the free-surface amplifications, 2.0, and $N = 0.707$ is the partition of energy into two horizontal recorded components (Boore and Boatwright 1984). $S(f)$ is basically the single corner frequency Brune crack model with corner frequency, $f_0 = 0.491(\Delta\sigma_{Brune}M_o)^{1/3}$, $\Delta\sigma_{Brune}$ is

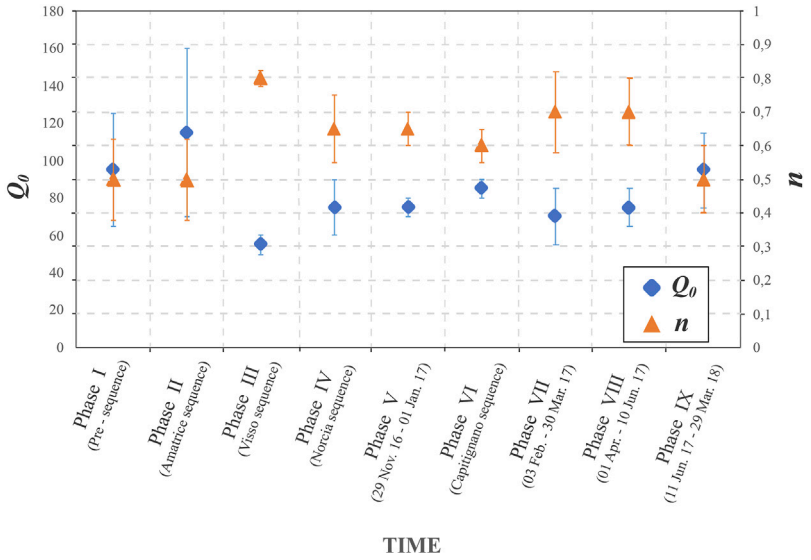

FIGURE 4 | Frequency-dependent Q as $Q(f) = Q_0\,(f/f_{ref})^n$, f_{ref} = 1 Hz. The Q_0 (blue dots) and the frequency dependence of the attenuation, n (orange triangles) and their standard errors as a function of nine time phases include Amatrice, Visso, and Norcia earthquake sequences (for the details see **Table 1**).

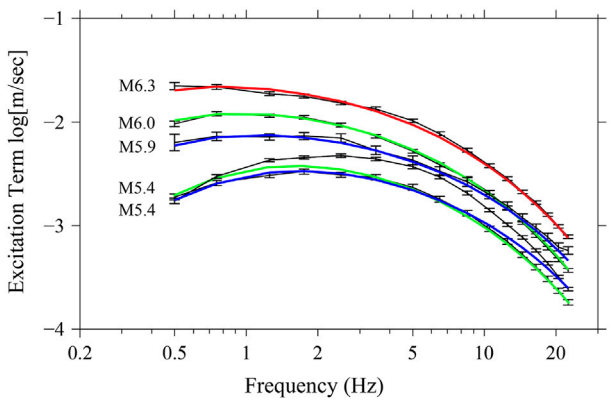

FIGURE 5 | Empirical (black) and theoretical (colored) excitation spectra at 40 km distance obtained for the peak of the filtered amplitudes derived from RVT synthetics in the frequency range from 0.5 to 22.5 Hz. The green, blue, and red lines show the predicted excitation terms obtained by using **Eq. 6**, at the moment magnitudes corresponding to those calculated for the plotted events M6.0 and M5.4 with $Q(f)=115 \pm 45f^{0.50\pm0.12}$, events M5.9 and M5.4 with $Q(f) = 55 \pm 5f^{0.8 \pm 0.025}$, and M6.3 Norcia earthquake with $Q(f)=70 \pm 15f^{0.65\pm0.1}$, respectively.

the stress-drop parameter in units of Pa, and M_0 is the seismic moment. The parameter ρ is the crustal average density and β is the shear wave velocity at the source of 3.5 km/s.

The term $exp(-\pi f\kappa_{eff})$ is a simplified version of the more correct functional form: $<V(f)\ exp(-\pi f\kappa_0)>_{avg}$, where $V(f)$ represents the site amplification relative to hard rock. The term κ_{eff} presents the average high-frequency attenuation in the very shallow crust directly beneath each site associated with the parameter κ_0 and the frequency-dependent site amplification, (f) (Boore, 1983; Anderson and Hough, 1984; Boore and Joyner, 1997). **Supplementary Figure S2** presents the site terms from the regression on horizontal filtered peak amplitudes. Because the constraint: $\Sigma Site_j\ (f_c) = 0$ was employed to the horizontal component site terms at the stations, we may render the excitation terms that present the average site of the network, 40 km away from the hypocenter. The site term is averaged over all the stations since the constraints adopted for the regression present an average value inferred from the network sites. As a result, the average effect of all the network sites is mapped on the source term (and this is why the average network site effect is included in **Eq. 6**). Since the site terms continue to trade-off with the observed excitation terms (as seen in **Eq. 6**), they do not have a functional utility in the existing form, although to look at the behavior of all the individual site terms allows the detection of instrument- or digital amplification-related malfunctions. For the definition of predictive relationships for the ground motion, the most useful site descriptions are represented by the generic site models by Boore and Joyner (1997).

The inverted excitation terms determined by the regression analysis are presented in **Figure 5** (black curves) for each M > 5.5 earthquakes in the database. Theoretical (RVT) curves using the Brune spectral model are presented in the same figure (colored curves) at a distance r_{fix} = 40 km, including the effects of propagation to reference distance due to geometrical spreading and frequency-dependent attenuation parameter. In order to fit the theoretical excitations to the empirical ones, we used a stress drop parameter and the generic rock site amplification factor (the term $V(f)exp(-\pi f\kappa_{eff})$ in **Eq. 6**).

The optimized attenuation parameters for each phase were used to determine the source-related parameters from the best visual fit between inverted and theoretical excitation spectra. The

fit for the earthquakes, excellent at all frequencies, is obtained from the following values of the Brune stress drop: $\Delta\sigma$ = 15 and 20 MPa for magnitudes M6.0 and M6.3, respectively. Our modeling effort indicates a clear trend for the stress parameter, which steadily increases with magnitude. This behavior together with the retrieved stress drops is in agreement with those obtained by Malagnini and Munafò (2018).

The high-frequency parameter κ_{eff} is estimated as κ_{eff} = 0.035 s by fitting the high-frequency part of the spectra of small earthquakes since it is independent of the earthquake size. The soil site category NEHRP B/C boundary site condition with V_{s30} of 760 ms^{-1} is used as the representative generic rock site type amplification in the study area to model the SRC (f_c, r_{fix}), excitation terms. Finally, we employed this path and source scaling parameters to estimate a series of ground motion parameters in the study region.

5 RESULTS

5.1 Temporal Variability of Averaged Seismic Attenuation

Our results (**Table 1** and **Figure 4**) provide homogeneous estimates of averaged S-wave quality factor Q(f) for each of the nine selected time windows, showing that the seismic attenuation was not constant over time during the earthquake sequence.

Before the sequence (phase-I, between 1 January 2016 and 23 August 2016), the attenuation term is modeled using a frequency-dependent quality factor, $Q(f) = 95 \pm 30f^{0.5 \pm 0.12}$, together with the geometrical spreading defined by the following bilinear relationship: $g(r)=r^{-1.1}$, for r ≤ 40 km and $r^{-0.5}$ for distances larger than 40 km.

During the 2016–2017 earthquake sequence, we observed some fluctuations in the attenuation and frequency dependence over the time windows. The attenuation of seismic waves decreases while its frequency dependence increases: $Q(f) = 115 \pm 45f^{0.50 \pm 0.12}$ in phase-II (from the 24th August Amatrice earthquake, M6.0 until the 25th September 2016, just before the Visso earthquake).

In phase-III (from the 30th September, Visso earthquake, M5.9 until the 29th October 2016 just before the Norcia earthquake), both the attenuation parameter and its frequency dependence change: $Q(f) = 55 \pm 5f^{0.80 \pm 0.025}$. This behavior is evident in **Figure 2**, where all attenuation curves for the different frequency ranges of S-wave decrease with distance similarly, presenting a high-frequency dependence of attenuation.

In the phase-IV from the 30th October, Norcia earthquake, M6.3 until the 28th November 2016, the attenuation parameter Q_o increases, whereas its frequency dependence decreases slightly, $Q(f) = 75 \pm 15f^{0.65 \pm 0.12}$.

During the phases V, VI, VII, and VIII from the end of November 2016 until the 11th June 2017, we retrieved similar attenuation values to the previous one as in the fourth one, being $Q(f)=75f^{0.65}$ with slight fluctuations on the Q(f) and its degree of the frequency dependence. This latest variation in attenuation is quite different from those observed during the Amatrice, Visso, Norcia sequence, suggesting that the major events strongly influenced the attenuation parameters. Finally, from June 2017 to the end of March 2018, we determined $Q(f) = 95 \pm 20f^{0.5 \pm 0.1}$, similar to the one obtained for the phase-I.

5.2 Investigating the Effects of Seismic Attenuation on Ground Motion Parameters

Utilizing the S-wave seismic attenuation and the source scaling, together with the duration of the ground motions revealed in this study, we produced high-frequency synthetic seismograms. To evaluate the impact of the variation of the seismic attenuation on the ground motion in the central Apennines, we analyzed several ground motion parameters, PGA, PGV, and two PSAs at 0.3 and 2 s for the M6.3, Norcia earthquake of 30 October 2016, as being the largest earthquake occurred during the seismic sequence and probably the best-recorded large earthquake in Italy. The attenuation parameters, together with the source and site-related parameters (**Table 2**) obtained for the phases II, III, and IV, correspond to Amatrice, Visso, and Norcia earthquake sequences and are introduced for the ground motion simulations through a finite fault stochastic method as given in the **Supplementary Appendix A** (Motazedian and Atkinson, 2005; Boore, 2009). In this way, we demonstrated the relative implication of this parameter to the ground motion parameters (PGA, PGV, and PSA at 0.3 and 2 s).

5.2.1 Comparisons Between Observed and Simulated Ground Motions

In this section, we compared the simulated accelerations and velocities with the 30 October 2016 Norcia earthquake's observed ground motions registered by numerous digital stations of temporary and permanent seismic networks expanded shortly after the Amatrice earthquake. We used ground motions recorded at 98 stations located on different site conditions, classified as A, B, C, and D, in accordance with the NTC18 norms. The generic site amplification curves were accounted for in the simulations from different soil classes prescribed by the Italian NTC18 seismic design code: site class-A, -B, -C, and -D following Pischiutta et al. (2021a), Pischiutta et al. (2021b) (**Table 2**). **Figure 6** shows the comparison of the PGAs, and PGVs, PSA at 0.3 and 2 s of the simulated ground motions using three different attenuation parameters with those of the records observed during the M6.3 Norcia earthquake and the reference GMM model (dashed lines) is adopted from Bindi et al. (2011) for three different types of site classes following the Eurocode8, EC8, (CEN 2003).

In general, we observed a good compromise between the observed data from the strong-motion recordings and the simulated ground motions from three different attenuation functions, up to a distance of 90 km. The compatibility between observed and predicted data remains the same also at shorter distances, even if the near-field results are governed mainly by source effects, such as directivity. On the other hand, intermediate and longer distances are governed by the path effects such as the frequency-dependent quality factor Q(f)

TABLE 2 | Model parameters for the finite-fault simulation of the 30 October 2016, M6.3 Norcia Italy earthquake.

Factor	Parameter	Representative value	Reference
Source	Fault plane	Length 34 km; width 15 km; strike 155°; dip 47°; depth 9.5 km	Scognamiglio et al. (2018)
	Slip distribution	Random slip per sub-fault	Scognamiglio et al. (2018)
	Stress drop	20 MPa for M6.3 15 MPa for M6.0 13 MPa for M5.4	This study and Malagnini and Munafò (2018)
	Moment magnitude	M6.3	Malagnini and Munafò (2018)
	Shear-wave velocity (β)	3.7 ± 0.1 km/s	
	Density (ρ)	2.8 g/cm^3	
	Pulsing percentage	50%	Motazedian and Atkinson (2005)
	Rupture velocity	0.8β	Scognamiglio et al. (2018)
Path	Quality factor, $Q_o\ f^{\eta}$	Q_0 = 115, η = 0.50 Phase II Q_0 = 55, η = 0.80 Phase III Q_0 = 75, η = 0.65 Phase IV	This study
	Path duration	Path distance (in km) and path duration (in s), slope 0.05	This study
	Geometric spreading	$r^{-1.1}$ r < 40 km; $r^{-0.5}$ r > 40 km	This study
Site	Site amplification	Italian seismic design code (NTC-18)	Pischiutta et al. (2021a)
	Kappa (κ)	0.025, 0.035, and 0.045 s for site classes A, B, and C Boore and Joyner (1997)	Pischiutta et al. (2021b)

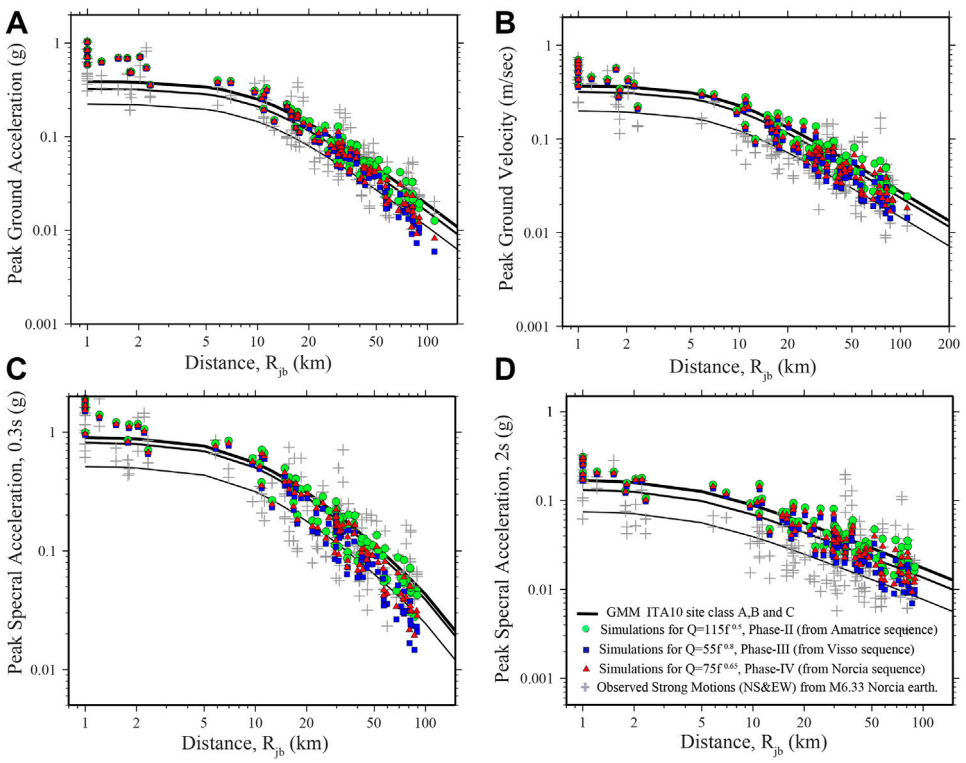

FIGURE 6 | (A) Predictions of peak ground acceleration (PGA) for the Norcia mainshock (M6.3) (colored symbols) and comparison with the observed data (gray crosses). Solid black lines refer to Bindi et al. (2011) for sites, A, B, and C classes. Simulation are generated using 1) three different attenuation parameters; Q(f)=105$f^{0.5}$ hase-II, from the Amatrice earthquake sequence; Q(f)=55$f^{0.8}$ phase-III, from the Visso earthquake sequence; Q(f)=75$f^{0.65}$ phase-IV, from the Norcia earthquake sequence and, and 2) geometrical spreading coefficient g(r)=1.0, R < 40 km and g(r)=0.5 for R > 40 km, 3) a stress drop parameter $\Delta\sigma$ = 20 MPa and 4) κ_0 = 0.025s, 0.035s and 0.045s for sites, A, B, and C classes **(B,C,D)** same as in frame (a) but for peak ground velocity (PGV), pseudo spectral accelerations at 0.3 and 2 s.

and its frequency dependence. The estimated high-frequency ground motion parameters decay faster (blue squares in **Figure 6**) during the Visso sequence with Q(f) = 55 ± 5$f^{0.80\ \pm\ 0.025}$ compared to those estimated from the Amatrice (green circles) and Norcia (red triangles) sequence attenuation functions, both being less frequency-dependent, Q(f) = 115 ±

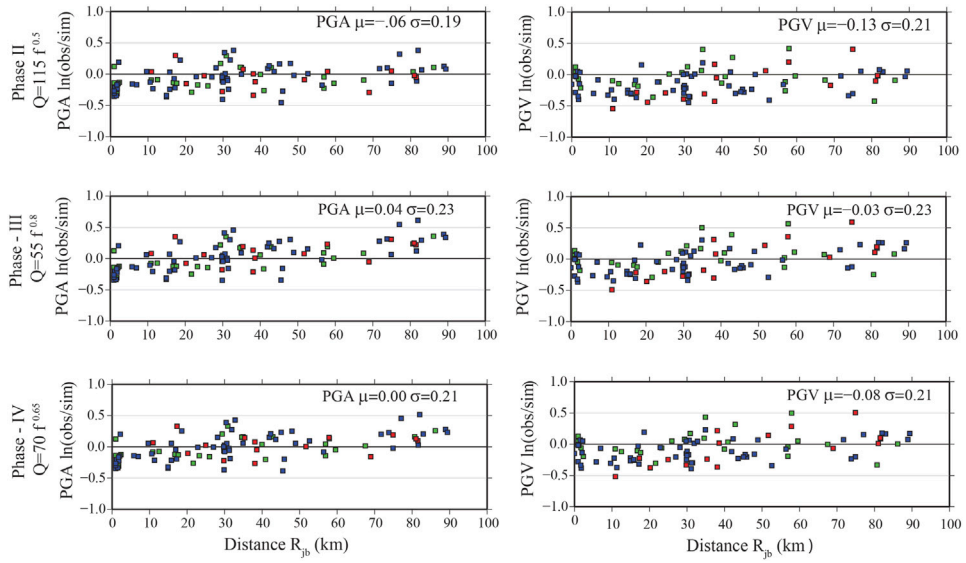

FIGURE 7 | Residuals between ground motion parameters observed on data recordings and simulated time-series for the M6.3 Norcia earthquake as a function of distance for three attenuation functions: peak ground acceleration (PGA) and peak ground velocity (PGV).

$45f^{0.50 \pm 0.12}$ and $Q(f) = 75 \pm 15f^{0.65 \pm 0.12}$, respectively. This trend is more evident in the case of the PSA at 0.3s, where high-frequency ground motions attenuate quickly as a function of distance compared to PSA at 2s.

Nevertheless, **Figure 6** quickly notes that the observed peak ground motions are more scattered than the simulations. This indicates that our simulations cannot capture the total variability of 3-D wave propagation effects (impedance gradients, source radiation pattern, trapped waves, etc.,) through a high-frequency stochastic simulation approach. The observed discrepancy between the recorded (much scattered) and the simulated ground motions (less varied) may also be caused by the insufficient representation of soil amplification factors taken into account in our study (Ojeda et al., 2021; Pitarka et al., 2021).

5.2.2 Residuals Between Observed and Simulated Ground Motions

To get an insight into attenuation variability on the simulated ground motions, we calculated residuals R_{jos} between observed and simulated values at each distance R_{jb}, related to station j as $R_{jos} = \ln(Y_{jobs}/Y_{jsim})$, where Y_{jobs} is the observed ground motion parameter, and Y_{jsim} is derived from simulations at each station's distance. We calculated the average values (μ) and standard deviations (σ) from the residuals. The residuals between observed and simulated ground motion parameters, PGA and PGV, as a function of distance, are plotted in **Figure 7** for three different site classes (A, B, and C, given with different colors). The residuals of the spectral acceleration parameters at 0.3 and 2 s are presented in **Supplementary Figure S3**. We observed that, for most stations, the residuals vary between −0.5 and 0.5. The most considerable variation of the R_{osj} ratio, with increasing residuals, is observed at larger distances, $R_{jb} > 50$ km. This deviation becomes evident at high frequencies (PSA at 0.3 s) since the frequency dependence of three attenuation parameters is quite peculiar. The histograms in **Figure 8** clearly demonstrate the impact of variation of the attenuation on ground motion parameters; it is very little where the σ is almost invariant around 0.19–0.21 in the case of PGA, while it is 0.21-0-23 for PGV. The median values for the PGA are −0.06, 0.04, and 0.0 for three periods (phases II, III, and IV). The best fit between observed and simulated was captured at phase IV (Norcia sequence), resulting in μ=0.0 and a small σ value. Similarly, we obtained small σ and μ for all of the ground motion parameters, where we used the attenuation function of the Norcia sequence for our simulations. The largest standard deviation and median values determined in the case of the spectral acceleration at 2 s may be caused by the limitations of our approach of the high-frequency stochastic finite-fault approach implemented in this study, which could not wholly capture the longer period effects. In fact, such effects mainly caused by the 3D earth structure cannot be thoroughly simulated with stochastic techniques (Pitarka et al., 2021).

6 DISCUSSION AND CONCLUDING REMARKS

We carried out a regression analysis to separate path, source, and site effects in different time windows during the 2016–2017 AVN seismic sequence in the central Apennines. The frequency-dependent attenuation parameters and the geometrical spreading function are calculated using a grid-search over a thousand combinations of the attenuation parameters. We found that the crustal attenuation and its frequency dependence are affected by transients induced by the main events and quantify the impact of the seismic wave

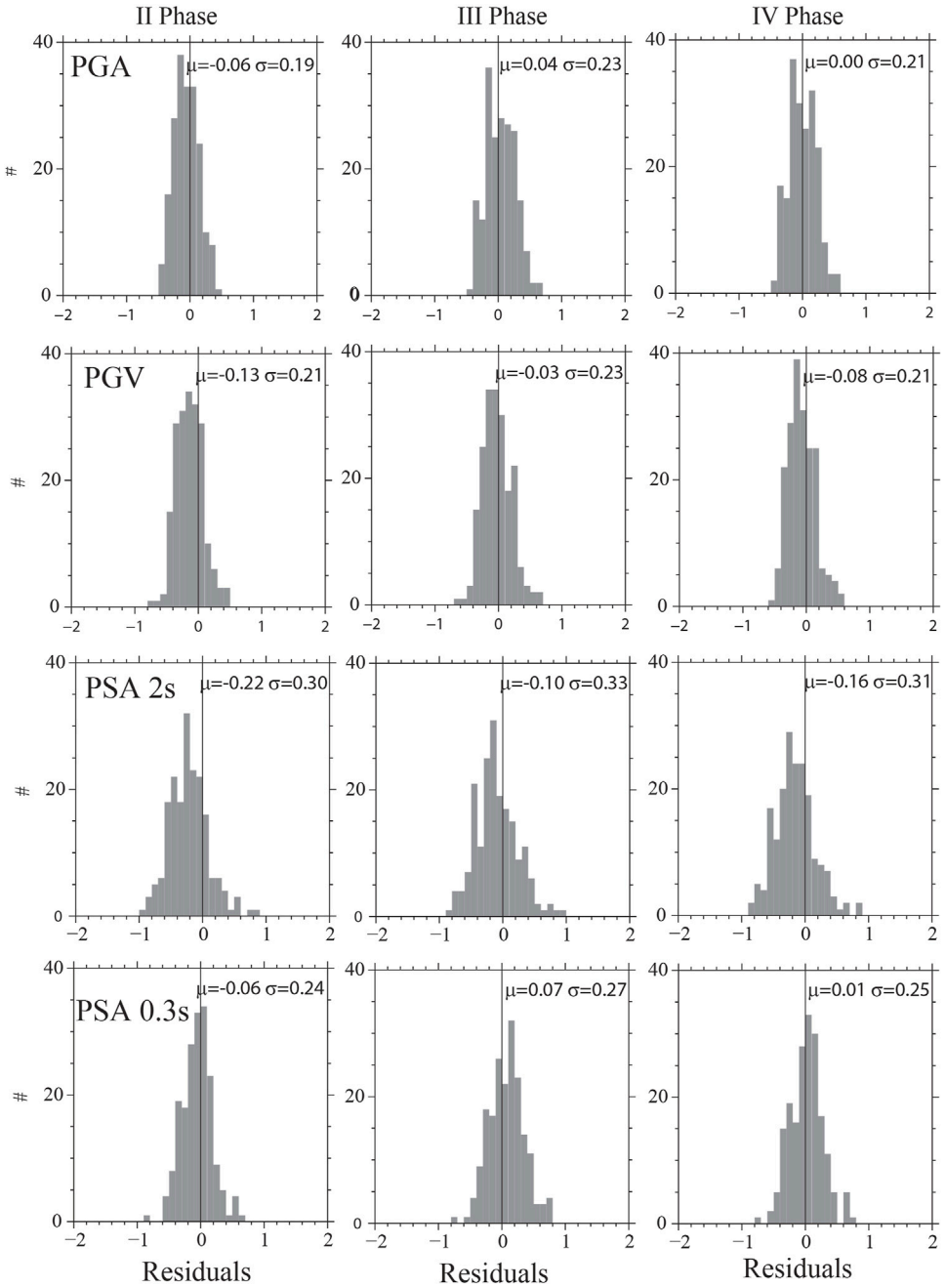

FIGURE 8 | Residuals (observed-predicted) of PGA, PGV, and PSA at 0.3 and 2 s calculated for the M6.3 Norcia earthquake. To predict the earthquake-induced ground motion, we used attenuation parameters obtained using the dataset belonging to phases II, III, and IV of the seismic sequence based on a stochastic finite-fault dynamic corner frequency method.

attenuation variability on the ground-motion hazard in the study region.

In general, we observed that the quality factor (Q_o) is changing between 55 ± 5 and 115 ± 45, and its frequency dependence (n) varies from 0.50 ± 0.025 to 0.80 ± 0.12 over different periods, including Amatrice, Visso, and Norcia earthquake sequences.

Our modeling also indicates a clear trend for the stress-drop parameter, $\Delta\sigma$, which constantly increases for increasing magnitude being 20 and 15 MPa for M6.3 and M6.0, respectively. These spectral parameters are used to explore the impact of attenuation variability on the seismic hazard through stochastic finite-fault simulations and compared against the observed ground motions for the 2016 Norcia main-shock.

The residuals calculated between the observed and simulated PGA's and PGV's for distances up to 100 km offer a quantitative assessment of the effects of the attenuation variability on the

earthquake-induced ground motion parameters. When compared to the observed data, our simulations indicate that both the mean values and the standard deviations of PGA, PGV, and PSA at 0.3 and 2 s do not show substantial variations and oscillate slightly over the three time windows (σ = 0.19–0.21, μ = 0.13–0.04) while Q (f) = $Q_o(f/f_{ref})^n$ strongly vary over time, both in amplitude and in frequency dependence. The reason that we observed slight variations on the ground motion parameters for the three different time windows during the AVN earthquake sequence including the Amatrice, Visso, and Norcia main events, is that the attenuation parameter Q(f) does not vary significantly, and provides similar values with the low-end parameter Q_o = 55, which is associated with a high frequency dependence (n = 0.8) and the high-end parameter Q_o = 115, which is associated with a low-frequency dependence (n = 0.45). This variation of attenuation is determined over several time windows as the average values for the study region and may indicate the randomness of the natural phenomenon presented in the stochastic uncertainties. However, the attenuation parameter may present a spatial variation in the studied area and may have a different impact on ground motion variation, which we did not investigate.

The main goal of this study was related to practical purposes for investigating the seismic attenuation variations in the ground motion analysis. In the end, we decided to briefly comment on the temporal variation of attenuation and possible connection with inferred material properties and/or physical states of a medium even if it is out of the scope of this study (e.g., temperature, stress, and water saturation). In fact, it is generally affirmed that bulk permeability and fluid content modulate the seismic attenuation in rocks (Winker and Nur, 1982; Malagnini and Parsons, 2020; Malagnini et al., 2022). When rock permeability reduces due to crack closure, seismic attenuation decreases (Toksöz et al., 1979). Finally, it is the fault zones that may exhibit high seismic attenuation due to a massive volume of fracturing and fluid content (Ma et al., 2020; Gabrielli et al., 2022; Ma et al., 2022).

For example, Chun et al. (2004) have noted variations in P wave attenuation within a fault region following the 1989 M7.0 Loma Prieta earthquake. This change was interpreted as being generated by coseismic and postseismic variations in permeability and fluid saturation along the fault. Previous studies in the Parkfield area reported a temporal change in attenuation associated with the 2004 M6.0 Parkfield earthquake. Attenuation increased immediately after the earthquake and then slowly decreased over several years (Allmann and Shearer, 2007; Chun et al., 2010; Kelly et al., 2013; Malagnini et al., 2022). Furthermore, numerous studies in the central Apennines investigated the impact of fluid migration along with faults network and the likely earthquake occurrence, triggering seismicity and seismic wave attenuation variations due to increased pore-pressure from the diffusion of over-pressured fluids (Miller et al., 2004; Lucente et al., 2010; Malagnini et al., 2012; Chiarabba et al., 2020; Akinci et al., 2020; Gabrielli et al., 2022; Malagnini et al., 2022).

The attenuation characteristics observed in the present study agree with those remarked in different regions worldwide. For example, high seismic attenuation is observed during the Visso sequence (phase-III), possibly due to increased fracture density and fluid flow across the seismogenic zones. Moreover, in this period, the frequency dependence of attenuation also increased, being $\sim f^{0.8}$, with that of the previous $\sim f^{0.5}$. This change could be linked to the fluid saturation and distribution during earthquake sequence since the transformation of energy into heat in solid is relatively independent of frequency while it is proportional to frequency in fluids as demonstrated by Toksöz et al. (1979) and Tisato and Quintal, (2013) and Tisato and Quintal, (2014).

Our results may provide a valuable framework for understanding the physical parameters that define crustal wave propagation and their impact on the amplitudes of the ground motions observed during the earthquake sequence in Central Italy. We remark that the main events of the sequence strongly influence the crustal S-wave attenuation and frequency dependence, while their effect on the induced ground motion is minimal.

DATA AVAILABILITY STATEMENT

Publicly available datasets were analyzed in this study. These data can be found here: Seismic waveforms were retrieved from the European Integrated Data Archive (EIDA) repository at ORFEUS—EIDA (orfeus-eu.org) and from the Italian Accelerometric Archive at http://itaca.mi.ingv.it (last accessed June 2016). Many of the plots were generated using the Generic Mapping Tools, version 4.2.1 (www.soest.hawaii.edu/gmt, last accessed December 2008; Wessel and Smith, 1998).

AUTHOR CONTRIBUTIONS

AA, IM, and LM worked together for this manuscript. LM, IM, and AA collected and preprocessed the recordings. AA performed the regression analysis to detect the propagation path attenuation and the source spectra and calculated stochastic simulations for the M6.3 Norcia 2016 earthquake. AA and IM prepared the figures. All authors participated to drafting this article.

FUNDING

This work has been partially carried out in the framework of the project Pianeta Dinamico/2020–2021 supported by Ministero dell'Istruzione, dell'Università e della Ricerca (MIUR).

SUPPLEMENTARY MATERIAL

The Supplementary Material for this article can be found online at: https://www.frontiersin.org/articles/10.3389/feart.2022.903955/full#supplementary-material

REFERENCES

Aki, K. (1980). Attenuation of Shear Waves in the Lithosphere for Frequencies from 0.05 to 25 Hz. *Phys. Earth Planet. Interiors* 21, 50–60. doi:10.1016/0031-9201(80)90019-9

Akinci, A., D'Amico, S., Malagnini, L., and Mercuri, A. (2013). Scaling Earthquake Ground Motions in Western Anatolia, Turkey. *Phys. Chem. Earth, Parts A/B/C* 63, 124–135. doi:10.1016/j.pce.2013.04.013

Akinci, A., Galadini, F., Pantosti, D., Petersen, M., Malagnini, L., and Perkins, D. (2009). Effect of Time Dependence on Probabilistic Seismic-Hazard Maps and Deaggregation for the Central Apennines, Italy. *Bull. Seismol. Soc. Am.* 99, 585–610. doi:10.1785/0120080053

Akinci, A., Malagnini, L., Herrmann, R. B., Gok, R., and Sørensen, M. B. (2006). Ground Motion Scaling in the Marmara Region, Turkey. *Geophys. J. Int.* 166, 635–651. doi:10.1111/j.1365-246x.2006.02971.x

Akinci, A., Malagnini, L., Herrmann, R. B., and Kalafat, D. (2014). High-frequency Attenuation in the Lake Van Region, Eastern Turkey. *Bull. Seismol. Soc. Am.* 104, 1400–1409. doi:10.1785/0120130102

Akinci, A., Pezzo, E. D., and Malagnini, L. (2020). Intrinsic and Scattering Seismic Wave Attenuation in the Central Apennines (Italy). *Phys. Earth Planet. Interiors* 303 (303), 106498. doi:10.1016/j.pepi.2020.106498

Allmann, B. P., and Shearer, P. M. (2007). Spatial and Temporal Stress Drop Variations in Small Earthquakes Near Parkfield, California. *J. Geophys. Res.* 112, 1–17. (B04305). doi:10.1029/2006JB004395

Anderson, J. G., and Hough, S. R. (1984). A Model for the Shape of the Fourier Amplitude Spectrum of Acceleration at High Frequencies. *Bull. Seism. Soc. Am.* 74 (5), 1969–1993.

Bartels, R. H., and Conn, A. R. (1980). Linearly Constrained Discrete I 1 Problems. *ACM Trans. Math. Softw.* 6, 594–608. doi:10.1145/355921.355930

Beresnev, I. A., and Atkinson, G. M. (1998). FINSIM--a FORTRAN Program for Simulating Stochastic Acceleration Time Histories from Finite Faults. *Seismol. Res. Lett.* 69, 27–32. doi:10.1785/gssrl.69.1.27

Bindi, D., Pacor, F., Luzi, L., Puglia, R., Massa, M., Ameri, G., et al. (2011). Ground Motion Prediction Equations Derived from the Italian Strong Motion Database. *Bull. Earthq. Eng.* 9 (6), 1899–1920. doi:10.1007/s10518-011-9313-z

Bommer, J. J., and Martínez-pereira, A. (1999). The Effective Duration of Earthquake Strong Motion. *J. Earthq. Eng.* 3, 127–172. doi:10.1080/13632469909350343

Boore, D. M., and Boatwright, J. (1984). Average Body-Wave Radiation Coefficients. *Bull. Seismol. Soc. Am.* 74, 1615–1621. doi:10.1785/bssa0740051615

Boore, D. M. (2009). Comparing Stochastic Point-Source and Finite-Source Ground-Motion Simulations: SMSIM and EXSIM. *Bull. Seismol. Soc. Am.* 99, 3202–3216. doi:10.1785/0120090056

Boore, D. M., and Joyner, W. B. (1997). Site Amplifications for Generic Rock Sites. *Bull. Seism. Soc. Am.* 87, 327–341. doi:10.1785/bssa0870020327

Boore, D. M. (2003). Simulation of Ground Motion Using the Stochastic Method. *Pure Appl. Geophys.* 160, 635–676. doi:10.1007/pl00012553

Boore, D. M. (1983). Stochastic Simulation of High-Frequency Ground Motions Based on Seismological Models of the Radiated Spectra. *Bull. Seismol. Soc. Am.* 73, 1865–1894.

Brune, J. N. (1971). Correction. *J. Geophys. Res.* 76, 5002.

Brune, J. N. (1970). Tectonic Stress and the Spectra of Seismic Shear Waves from Earthquakes. *J. Geophys. Res.* 75, 4997–5009. doi:10.1029/jb075i026p04997

Buttinelli, M., Petracchini, L., Maesano, F. E., D'Ambrogi, C., Scrocca, D., Marino, M., et al. (2021). The Impact of Structural Complexity, Fault Segmentation, and Reactivation on Seismotectonics: Constraints from the Upper Crust of the 2016-2017 Central Italy Seismic Sequence Area. *Tectonophysics* 810, 228861. doi:10.1016/j.tecto.2021.228861

Cartwright, D. E., and Longuet-Higgins, M. S. (1956). The Statistical Distribution of the Maxima of a Random Function. *Proc. R. Soc. Lond.* A237, 212–232.

CEN (2003). *(pr) EN 1998-1-Eurocode 8: Design of Structures for Earthquake Resistance—Part 1: General Rules, Seismic Actions and Rules for Buildings*. European Committee Standardization: Brussels. Draft No 6, Doc CEN/TC247/SC8/N335, January 2003.

Chiarabba, C., Buttinelli, M., Cattaneo, M., and De Gori, P. (2020). Earthquakes Driven by Fluid Overpressure: The Apennines Normal Faulting System Case. *Tectonics* 39. doi:10.1029/2019TC006014

Chiaraluce, L., Di Stefano, R., Tinti, E., Scognamiglio, L., Michele, M., Casarotti, E., et al. (2017). The 2016 Central Italy Seismic Sequence: A First Look at the Mainshocks, Aftershocks, and Source Models. *Seismol. Res. Lett.* 88 (3), 757–771. doi:10.1785/0220160221

Chun, K.-Y., Henderson, G. A., and Liu, J. (2004). Temporal Changes inPwave Attenuation in the Loma Prieta Rupture Zone. *J. Geophys. Res.* 109, B0231715. doi:10.1029/2003JB002498

Chun, K.-Y., Yuan, Q.-Y., and Henderson, G. A. (2010). Precursory Rise of P-Wave Attenuation before the 2004 Parkfield Earthquake. *Bull. Seismol. Soc. Am.* 100 (2), 509–521. doi:10.1785/0120090104

Cormier, V. F. (2011). "Seismic, Viscoelastic Attenuation," in *Encyclopedia of Solid Earth Geophysics. Encyclopedia of Earth Sciences Series*. Editor H. K. Gupta (Dordrecht: Springer), 1279–1290. doi:10.1007/978-90-481-8702-7_55

D'Amico, S., Akinci, A., and Pischiutta, M. (2018). High-frequency Ground-Motion Parameters from Weak-Motion Data in the Sicily Channel and Surrounding Regions. *Geophys. J. Int.* 214, 148–163. doi:10.1093/gji/ggy107

D'Amico, S., Akinci, A., and Malagnini, L. (2012). Predictions of High Frequency Ground-Motion in Taiwan Based on Weak-Motion Data. *Geophys. J. Int.* 189, 611–628. doi:10.1111/j.1365-246X.2012.05367.x

Del Pezzo, E., and Bianco, F. (2010). Two-layer Earth Model Corrections to the MLTWA Estimates of Intrinsic- and Scattering-Attenuation Obtained in a Uniform Half-Space. *Geophys. J. Int.* 182, 949–955. doi:10.1111/j.1365-246X.2010.04648.x

Gabrielli, S., Akinci, A., Ventura, G., Napolitano, F., Del Pezzo, E., and De Siena, L. (2022). Fast-Changes in Seismic Attenuation of the Upper Crust Due to Fracturing and Fluid Migration: the 2016-2017 Central Italy Seismic Sequence. *Front. Earth Sci. Sect. Struct. Geol. Tect.* 10, 1–18. doi:10.3389/feart.2022.909698

Jackson, D. D., and Anderson, D. L. (1970). Physical Mechanisms of Seismic-Wave Attenuation. *Rev. Geophys.* 8, 1–63. doi:10.1029/rg008i001p00001

Kelly, C. M., Rietbrock, A., Faulkner, D. R., and Nadeau, R. M. (2013). Temporal Changes in Attenuation Associated with the 2004 M6.0 Parkfield Earthquake. *J. Geophys. Res. Solid Earth* 118, 630–645. doi:10.1002/jgrb.50088

Lavrentiadis, G., Abrahamson, N. A., and Kuehn, N. M. (2021). A Non-ergodic Effective Amplitude Ground-Motion Model for California. *Bull. Earthq. Eng.*, 1573–1456. doi:10.1007/s10518-021-01206-w

Lombardi, A. M., Akinci, A., Malagnini, L., and Mueller, C. H. (2005). Uncertainty Analysis for Seismic Hazard in Northern and Central Italy. *Ann. Geophys.* 48, 853–865. doi:10.4401/ag-3239

Ma, R., Ba, J., CarcioneCarcione, J. M., and Lebedev, M. (2022). PP-Wave Scattering by Randomly Distributed Aligned Cracks in Fractal Media. *Geophys. J. Int.* 229 (2), 900–914. doi:10.1093/gji/ggab450

Ma, R., Ba, J., Lebedev, M., Gurevich, B., and Sun, Y. (2020). Effect of Pore Fluid on Ultrasonic S-Wave Attenuation in Partially Saturated Tight Rocks. *Int. J. Rock Mech. Min. Sci.* 147, 104910. doi:10.1016/j.ijrmms.2021

Malagnini, L., Akinci, A., Mayeda, K., Munafo', I., Herrmann, R. B., and Mercuri, A. (2011). Characterization of Earthquake-Induced Ground Motion from the L'Aquila Seismic Sequence of 2009, Italy. *Geophys. J. Int.* 184 (1), 325–337. doi:10.1111/j.1365-246x.2010.04837.x

Malagnini, L., Dreger, D. S., Bürgmann, R., Munafò, I., and Sebastiani, G. (2019). Modulation of Seismic Attenuation at Parkfield, before and after the 2004 M 6 Earthquake. *J. Geophys. Res. Solid Earth* 124, 5836–5853. doi:10.1029/2019JB017372

Malagnini, L., and Dreger, D. S. (2016). Generalized Free-Surface Effect and Random Vibration Theory: a New Tool for Computing Moment Magnitudes of Small Earthquakes Using Borehole Data. *Geophys. J. Int.* 206, 103–113. doi:10.1093/gji/ggw113

Malagnini, L., Lucente, F. P., De Gori, P., Akinci, A., and Munafo', I. (2012). Control of Pore Fluid Pressure Diffusion on Fault Failure Mode: Insights from the 2009 L'Aquila Seismic Sequence. *J. Geophys. Res.* 117, 1–15. doi:10.1029/2011JB008911

Malagnini, L., Mayeda, K., Uhrhammer, R., Akinci, A., and Herrmann, R. B. (2007). A Regional Ground-Motion Excitation/Attenuation Model for the San Francisco Region. *Bull. Seismol. Soc. Am.* 97 (3), 843–862. doi:10.1785/0120060101

Malagnini, L., and Munafò, I. (2018). On the Relationship between M_L and M_w in a Broad Range: An Example from the Apennines, Italy. *Bull. Seism. Soc. Am.* 108, 1018–1024. doi:10.1785/0120170303

Malagnini, L., Parsons, T., Munafò, I., Mancini, S., Segou, M., and Geist, E. (2022). Crustal Permeability Changes Observed from Seismic Attenuation: Impacts on Multi-Mainshock Sequences. *Front. Earth Sci. Sect. Solid Earth Geophys.* (under review). doi:10.1002/essoar.10507597.1

Malagnini, L., and Parsons, T. (2020). Seismic Attenuation Monitoring of a Critically Stressed San Andreas Fault. *Geophys. Res. Lett.* 47, 1–11. doi:10.1029/2020GL089201

Mayeda, K., Koyanagi, S., Hoshiba, M., Aki, K., and Zeng, Y. (1992). A Comparative Study of Scattering, Intrinsic, and Coda Q^{-1} for Hawaii, Long Valley, and Central California between 1.5 and 15.0 Hz. *J. Geophys. Res.* 97, 6643–6659. doi:10.1029/91jb03094

Miller, S. A., Collettini, C., Chiaraluce, L., Cocco, M., Barchi, M., and Kaus, B. J. P. (2004). Aftershocks Driven by a High-Pressure CO2 Source at Depth. *Nature* 427, 724–727. doi:10.1038/nature02251

Morasca, P., Malagnini, L., Akinci, A., Spallarossa, D., and Herrmann, R. B. (2006). Ground-Motion Scaling in the Western Alps. *J. Seismol.* 10, 315–333. doi:10.1007/s10950-006-9019-X

Motazedian, D., and Atkinson, G. M. (2005). Stochastic Finite-Fault Modeling Based on a Dynamic Corner Frequency. *Bull. Seismol. Soc. Am.* 95, 995–1010. doi:10.1785/0120030207

Muir-Wood, R., and King, G. C. P. (1993). Hydrological Signatures of Earthquake Strain. *J. Geophys. Res.* 98 (B12), 22035–22068. doi:10.1029/93jb02219

Munafò, I., Malagnini, L., and Chiaraluce, L. (2016). On the Relationship betweenMwandMLfor Small Earthquakes. *Bull. Seismol. Soc. Am.* 106, 2402–2408. doi:10.1785/0120160130

Ojeda, J., Akinci, A., Tinti, E., Arriola, S., and Ruiz, S. (2021). Hybrid Broadband Strong-Motion Simulation to Investigate the Near-Source Characteristics of the M 6.5, 30 October 2016 Norcia, Italy Earthquake. *Soil Dyn. Earthq. Eng.* 149, 106866. doi:10.1016/j.soildyn.2021.106866

Pio Lucente, F., De Gori, P., Margheriti, L., Piccinini, D., Di Bona, M., Chiarabba, C., et al. (2010). Temporal Variation of Seismic Velocity and Anisotropy before the 2009 MW6.3 L'Aquila Earthquake, Italy. *Geology* 38, 1015–1018. doi:10.1130/g31463.1

Pischiutta, M., Akinci, A., Tinti, E., and Herrero, A. (2020a). Broad-band Ground-Motion Simulation of 2016 Amatrice Earthquake, Central Italy. *Geophys. J. Int.* 224, 1753–1779. doi:10.1093/gji/ggaa412

Pischiutta, M., Akinci, A., Tinti, E., and Herrero, A. (2021b). Erratum: Broad-Band Ground-Motion Simulation of 2016 Amatrice Earthquake, Central Italy. *Geophys. J. Int.* 226 (3), 1695. doi:10.1093/gji/ggab163

Pitarka, A., Akinci, A., De Gori, P., and Buttinelli, M. (2021). Deterministic 3D Ground-Motion Simulations (0–5 Hz) and Surface Topography Effects of the 30 October 2016 Mw 6.5 Norcia, Italy, Earthquake. *Bull. Seism. Soc. Am.* 112 (1), 262–286. doi:10.1785/0120210133

Raoof, M., Herrmann, R. B., and Malagnini, L. (1999). Attenuation and Excitation of Three-Component Ground Motion in Southern California. *Bull. Seism. Soc. Am.* 89, 888–902. doi:10.1785/bssa0890040888

Rietbrock, A. (2001). P Wave Attenuation Structure in the Fault Area of the 1995 Kobe Earthquake. *J. Geophys. Res.* 106, 4141–4154. doi:10.1029/2000jb900234

Scognamiglio, L., Tinti, E., Casarotti, E., Pucci, S., Villani, F., and Cocco, M. (2018). Complex Fault Geometry and Rupture Dynamics of the Mw 6.5, 30 October 2016, Central Italy Earthquake. *J. Geophys. Res.* 123 (4), 2943–2964.

Tisato, N., and Quintal, B. (2014). Laboratory Measurements of Seismic Attenuation in Sandstone: Strain versus Fluid Saturation Effects. *Geophysics* 79, WB9–WB14. doi:10.1190/GEO2013-0419.1

Tisato, N., and Quintal, B. (2013). Measurements of Seismic Attenuation and Transient Fluid Pressure in Partially Saturated Berea Sandstone: Evidence of Fluid Flow on the Mesoscopic Scale. *Geophys. J. Int.* 195, 342–351. doi:10.1093/gji/ggt259

Toksöz, M. N., Johnston, D. H., and Timur, A. (1979). Attenuation of Seismic Waves in Dry and Saturated Rocks: I. Laboratory Measurements. *Geophysics* 44, 681–690. doi:10.1190/1.1440969

Wessel, P., and Smith, W. H. F. (1998). New, Improved Version of Generic Mapping Tools Released. *Eos Trans. AGU* 79 (47), 579. doi:10.1029/98EO00426

Winkler, K. W., and Nur, A. (1982). Seismic Attenuation: Effects of Pore Fluids and Frictional-Sliding. *Geophysics* 47, 1–15. doi:10.1190/1.1441276

Zhong, S., Xu, C., Yi, L., and Li, Y. (2018). Focal Mechanisms of the 2016 Central Italy Earthquake Sequence Inferred from High-Rate GPS and Broadband Seismic Waveforms. *Remote Sens.* 10 (4), 512. doi:10.3390/rs10040512

Conflict of Interest: The authors declare that the research was conducted in the absence of any commercial or financial relationships that could be construed as a potential conflict of interest.

Publisher's Note: All claims expressed in this article are solely those of the authors and do not necessarily represent those of their affiliated organizations, or those of the publisher, the editors, and the reviewers. Any product that may be evaluated in this article, or claim that may be made by its manufacturer, is not guaranteed or endorsed by the publisher.

frontiers | Frontiers in Earth Science

TYPE Original Research
PUBLISHED 01 September 2022
DOI 10.3389/feart.2022.917635

OPEN ACCESS

EDITED BY
Andrea Cannata,
University of Catania, Italy

REVIEWED BY
Tim Greenfield,
University of Cambridge,
United Kingdom
Wei Peng,
National Taiwan Normal University,
Taiwan

*CORRESPONDENCE
Lisheng Xu,
xuls@cea-igp.ac.cn

SPECIALTY SECTION
This article was submitted to Solid Earth Geophysics,
a section of the journal
Frontiers in Earth Science

RECEIVED 11 April 2022
ACCEPTED 11 August 2022
PUBLISHED 01 September 2022

CITATION
Zhou Y, Xu L, Wu J, Li C, Fang L and Pan Z (2022), Seismicity of the repeating earthquake clusters in the northern Xiaojiang fault zone and its implications. *Front. Earth Sci.* 10:917635. doi: 10.3389/feart.2022.917635

Seismicity of the repeating earthquake clusters in the northern Xiaojiang fault zone and its implications

Yun Zhou[1], Lisheng Xu[1]*, Jianping Wu[1], Chunlai Li[1], Lihua Fang[1] and Zhengyang Pan[2]

[1]Institute of Geophysics, China Earthquake Administration, Beijing, China, [2]Institute of Earthquake Forecasting, China Earthquake Administration, Beijing, China

The Xiaojiang fault zone (XJF), located at the southeastern margin of the Tibetan plateau, has been frequently struck by destructive earthquakes throughout history. Some studies showed that repeating earthquakes may be used to estimate fault slip rates and even to monitor the pre-slip prior to large asperity. This study focuses on the repeating earthquakes recorded by a high-density seismic array in the northern section of the XJF, a segment ruptured by the 1733 Dongchuan M7.8 earthquake. Using the waveform cross-correlation and relocation techniques, we processed the continuous seismic recordings from seismic stations of the array and confirmed 27 clusters of repeating earthquakes. The repeaters are located in three relatively independent sub-areas, areas A, B, and C. Area A is close to the source areas of the 2014 Ludian Ms6.5 and the 2020 Qiaojia Ms5.0 earthquakes; by analyzing the recurrence intervals of repeating clusters, we found that the Ludian earthquake had an insignificant triggering effect on surrounding events, while the triggering effect from the Qiaojia earthquake was obvious. The clusters in area B were located very close to the northernmost tip of the XJF, which should be associated with an asperity preparing for a large earthquake on the northern XJF. Together with a repeating cluster identified in a previous study and the seismicity pattern revealed by our seismic array, we determined the geometry of the asperity and slip rate, which further helps to estimate a potential Mw7.1 earthquake for the asperity, where no M>7 earthquakes have occurred since the 1733 Dongchuan M7.8 earthquake. The clusters in area C are more like human-induced earthquakes because they are concentrated during the daytime when local people are at work, and, thus, they cannot be used for the study of tectonic deformation. This study clearly indicates that the repeating earthquakes can be triggered by a moderate earthquake nearby and also that repeating earthquakes can be used to estimate fault slip rates and outline locked asperities.

KEYWORDS

repeating earthquakes, asperity, Xiaojiang fault, seismic risk, slip rate

Introduction

The northward thrusting of the Indian plate has led to the uplift of the Tibetan plateau and lateral extrusion of materials (Molnar and Tapponnier, 1975), and GPS observations indicate that the southeastern plateau is moving eastward and simultaneously rotating clockwise around the Eastern Himalaya Syntaxis (Shen et al., 2005). There are complex tectonics and frequent activity of strong earthquakes in the southeastern boundary of the Tibet Plateau (Wang and Burchfiel, 2000; Xu et al., 2003). The Xiaojiang fault (XJF) zone, one of the segments of the boundary, has played an important role in regulating regional tectonic movement (Wang and Burchfiel, 2000). This active fault is connected to the Zemuhe fault at its northern end and extends more than 400 km to the south (Li, 1993). On the basis of field observations, the fault can be divided into three parts: the northern, central, and southern segments. The northern segment has a strike of approximately 335° and is represented by a single fracture, while in the middle segment, the fault begins to separate into two north–south-striking fault strands from Dongchuan (Li, 1993; Figure 1). In history, XJF has produced a number of middle-to-large earthquakes since 1500 (Shen et al., 2003; Zhang et al., 2003; Wen et al., 2008). For example, the 1733 Dongchuan M7.8 earthquake occurred on the northern XJF, resulting in thousands of casualties (Wang et al., 2017); the 1833 Songming M8 earthquake took place in the middle section of the XJF, which killed more than 6,700 people and injured at least 5,000 people

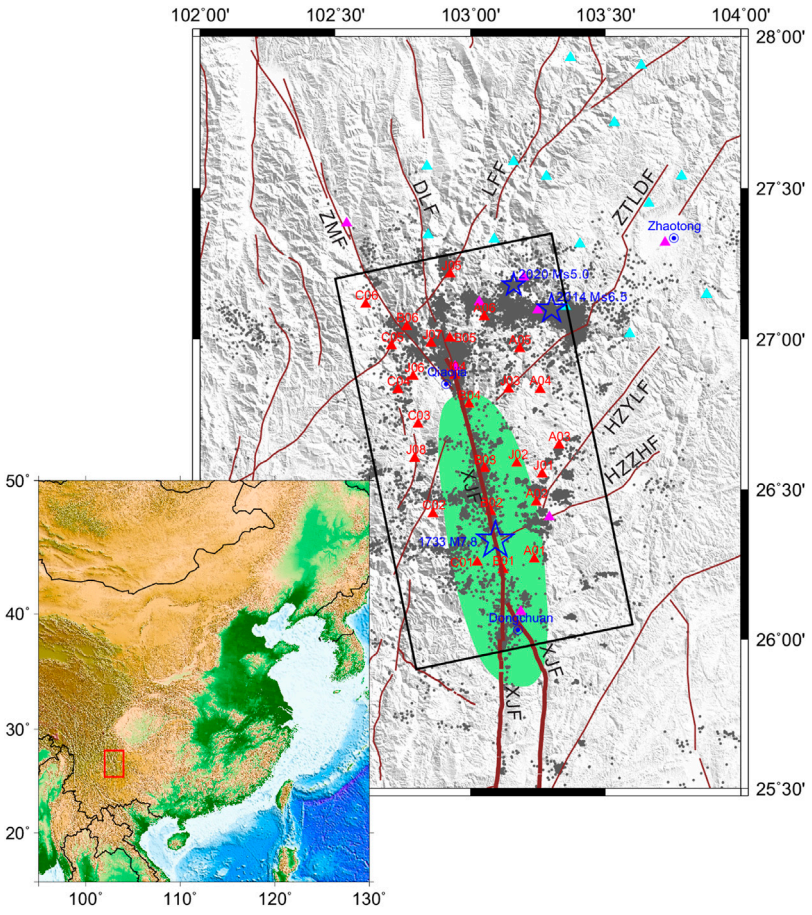

FIGURE 1
Broadband seismic array and the seismic events recorded in the northern XJF, which is emphasized with thick brown lines. The black rectangle represents the study area. Red, cyan, and magenta triangles are seismic stations of Qiaojia array, Zhaotong array, and regional network (Fu et al., 2021), respectively; in the hypoDD-relocated process, we used data from all these stations, but only the waveforms recorded from Qiaojia array are used in the waveform correlations. The red rectangle in the inset at the lower-left corner shows the location of the main plot. Gray dots are the hypoDD-relocated events recorded from March 2012 to July 2021. The blue stars represent the epicenters of the 1733 Dongchuan M7.8 earthquake, the 2014 Ludian Ms6.5 earthquake, and the 2020 Qiaojiang Ms5.0 earthquakes, and the main rupture area of the 1733 Dongchuan M7.8 earthquake (Wen et al., 2008) is indicated with green color. The cities Qiaojia and Dongchuan are marked with blue circled dots. Note: the region of the northern XJF zone is defined by the big black box. Abbreviations: XJF, Xiaojiang fault; ZMF, Zemuhe fault; DLF, Daliangshan fault; LFF, Lianfeng fault; ZTLDF, Zaotong–Ludian fault; The information of Huize–Yiliang fault (HZYLF) and Huize–Zhehai fault (HZZHF) is from Zhuang *et al.* (2019).

(Li J. et al., 2021). During the nearly 300 years that have transpired since the M7.8 event in 1733, no M>7.0 shock has occurred in the northern XJF zone (Department of Earthquake Disaster Prevention and State Seismological Bureau, 1995).

Owing to the tectonic significance and the potential seismic hazard, the slip rate of the XJF has been one of the concerns of geo-scientists for recent decades (Chen and Li, 1988; He et al., 2002; Shen et al., 2005; Wang et al., 2008; Fu et al., 2020). For example, He et al. (2002) gave the whole XJF an estimate of 13.0–16.5 mm/a, and Wen et al. (2011) pointed out that the northern, north-middle, south-middle, and southern segments of the XJF had slip rates of 10 mm/a, 8–9 mm/a, 8 mm/a, and 4 mm/a, respectively, and Jin et al. (2019) estimated a slip rate of 9.5 ± 1.2 mm/a for the whole XJF. However, most of these results are from the observation and analysis of the earth's surface in space, and the results can only reflect the movement of the surface but lack the slip rate from a certain depth underground. So, it is not enough to analyze the information on tectonic strain accumulation activity at different depths of the fault, especially at a certain depth of the seismogenic zone.

The discovery of repeating earthquakes has provided a new technique to detect the deformation, aseismic slip, and stress accumulation in a fault zone (Vidale et al., 1994; Nadeau and McEvilly, 1999; Turner et al., 2013). Repeating earthquakes are a group of earthquakes that occur at the same fault location with nearly identical magnitudes and highly similar waveforms and source mechanisms (Schaff and Beroza, 2004). Repeating earthquakes may optionally occur on fault planes (Nadeau et al., 1995; Igarashi et al., 2003) or off faults (Igarashi, 2020); however, they reflect a common physical process, that is, silent deformation of the fault zone. Nadeau and Johnson (1998) proposed a mechanism for the occurrence of repeating earthquakes as the repeated rupture of small asperities surrounded by creeping regions, and this mechanism has been verified by some numerical simulation and experimental studies (Anooshehpoor and Brune, 2001; Sammis and Rice, 2001); so, the coseismic strain release of these repeaters can be used in estimation of the strain accumulation or fault slip in fault zones (Vidale et al., 1994; Beeler et al., 2001). Therefore, these repeaters have been called virtual creep-meter (Turner et al., 2013).

Additionally, different from conventional surface observation such as GPS, InSAR, and geological investigations, repeating earthquakes are able to facilitate the direct observation of the deep behavior of fault zones (Nadeau and McEvilly, 2004; Waldhauser et al., 2004). Nadeau and McEvilly (1999) successfully estimated the slip rates of faults at different depths to describe the deformation behavior of deep faults by using seismic moments and intervals of repeating earthquakes in the Parkfield area of the SanAndreas fault. Also, the slip rates in the depth of the fault zone revealed by repeating earthquakes were about 2–3 times those from GPS and geological investigations in the Longmenshan fault zone, where the 2008 Wenchuan M7.9 earthquake occurred unexpectedly (Li et al., 2011). More importantly, repeating earthquakes were often found in proximity with the potential large-size asperities surrounded by stable creeping regions (Lay and Kanamori, 1980; Vidale et al., 1994; Kato and Hirasawa, 1997; Sammis and Rice, 2001).

The repeating earthquakes along the XJF were investigated by Li et al. (2013). In their study, the 1999–2011 seismic recordings from the Yunnan Seismic Network (YSN) were processed, and 29 groups of repeaters were selected by the techniques of waveform correlation and precise earthquake location. The estimates of the slip rates at depths of 3–12 km based on the repeating earthquakes ranged from 1.6–10.1 mm/a, indicating a variation with depths. These results were an important reference for us to continue the work on repeating earthquakes of XJF. However, the seismic stations used in this study were quite sparse, which may lead to missing some of the micro-earthquakes, large errors of event locations, or incomplete statistics of repeaters. In addition, due to the lack of seismic stations in the northern XJF, this study has not yet identified repeating earthquakes that can be used to estimate slip rates in the northern XJF (Li et al., 2013).

To understand the present deformation characteristics of the northern XJF, we set up a broadband seismic array (Qiaojia array) with around 15 km spacing between stations in 2012 (Figure 1). Since then, the array has been kept in good operation and has recorded more than 20,000 earthquakes. In this study, we have focused on the seismicity of the repeating earthquakes which have occurred since 2012, after which no research works involved repeating earthquakes following Li et al. (2013), and discussed their possible implications.

Data and methods

Since March 2012, the Qiaojia array has comprised 26 broadband stations (Figure 1) and has been kept in good operation. The array produced continuous 3-component recordings at a 100 Hz sampling rate. In this study, we processed the continuous recordings from March 2012 to July 2021, during which a total of 26,836 events were recorded, with magnitudes ranging from ML -0.7 to 6.5. Combined with the data recorded from seismic stations of the Zhaotong array and regional network (Figure 1), 22,093 events were successfully relocated using the double-difference location method (Waldhauser and Ellsworth, 2000), with 18,969 events appearing within the black box (Figure 1). The relocation improved the uncertainties of latitude, longitude, and depth to be less than 0.257, 0.241, and 0.424 km, respectively.

The identification and confirmation of repeating earthquakes usually depend on waveform similarity (Uchida, 2019). Therefore, we approximate the time window when candidate phases could appear using the theoretical arrival time of P waves calculated using the TAUP program (Crotwell et al., 1999) and

on the local velocity model (Wang et al., 2003). We filtered the vertical component between 1 and 10 Hz as used in previous studies (Li et al., 2011; Schmittbuhl et al., 2016). In order to select high-quality waveforms, we used the recording between 1 and 6 s after the P wave arrival time as the signal and the recording between 1 and 6 s before the P wave arrival time as the noise, calculated the SNR (signal-to-noise ratio), and selected the data with SNR >5 for subsequent processing.

On the basis of the abovementioned works, we selected repeating earthquakes by using the technique of cross-correlation (CC). In this process, we used waveform data recorded from 26 stations of the Qiaojia array. We performed the CC-analysis of all the event signals from the same station, and the event pairs would be identified as repeaters only when the normalized CC value exceeded 0.8. Considering that the P and S phases both are generally included to pass through the CC analysis (Uchida et al., 2003) and that the epicentral distances involved are less than 150 km (Figure 1), we windowed the event signals to be 1s before and 14s after P arrivals and allowed a time shift of no more than 0.5s because of the time errors of P arrivals. After the repeaters were identified, we applied the Hierarchical Clustering algorithm to group the repeaters into clusters and ensured the CC between two repeaters in the same cluster reached a certain threshold (Myhill et al., 2011). In particular, referring to the threshold used in a relevant study (Zhang et al., 2022), we set the thresholds conditionally. The CC values must be either no less than 0.8 at two stations or more than 0.9 at one station. In addition, we guaranteed the time interval between the first and final events in each of the clusters to be more than one year so that the slip rates would be calculated as exactly as possible.

Confirmation of the repeaters

The repeating clusters obtained according to the abovementioned steps still require further quality control. In order to certify the events in the same cluster are real repeaters, we adopted the simplified technique proposed by Li *et al.* (2011). According to the technique, two repeaters should meet the condition of $\Delta t_{s-p} \leq (r + r')/8.6$, where r and r' represent the rupture radius of the two repeaters, and Δt_{s-p} is the time difference between P and S arrivals. This means that the rupture areas of the two repeaters should be overlapping. Having noticed that most of the events involved in this study had a magnitude range from M1 to M2, we set a threshold of 0.012 s here based on a rupture radius of 50 m (equivalent to the rupture radius of an M2 earthquake). In order to measure as accurately and precisely as possible the time difference between the P and S arrivals and further the Δt_{s-p}, we re-sampled the event signals at a rate of 500 Hz, cut the P and S arrivals with a 0.5s-wide window, and then calculated the time difference for two repeater candidates by means of the CC analysis. After all the values of Δt_{s-p} were prepared, we compared these values with the threshold and removed those which did not meet the condition. To investigate the triggering effect of the 2014 Ludian M6.5 and the 2020 Qiaojia M5.0 earthquakes on repeating events, we selected repeating clusters spanning at least the Ludian or Qiaojia earthquakes within 45 km of the Ludian earthquake. We did not need to look for the repeating events related to the 2020 Qiaojia Ms5.0 earthquake because the distance between these two main shocks is ~25 km (Fu et al., 2021), and for an Ms5.0 earthquake, only the clusters within 15 km need to be considered (Chen et al., 2010), which indicates that the clusters related to Qiaojia earthquake have been included. In other areas, we selected repeating clusters in which the intervals between the first and last event in each group are more than one year.

In this way, we confirmed 27 multiplets, including a total of 132 events (Figure 2). We checked the CC values among the repeaters in the same cluster and found that all of them are larger than 0.91, and most of them are larger than 0.93. Figure 3 shows a comparison of the complete P and S arrivals at station J07 from cluster R14, which is composed of seven repeaters. The waveforms of all 27 clusters are shown in Supplementary Figures S1–S3.

The confirmed repeaters appear to be distributed in three sub-areas, A, B, and C, as shown in Figure 2. The repeaters in area A seem to be related to the 2014 Ludian Ms6.5 earthquake and the 2020 Qiaojia Ms5.0 earthquake, the two clusters in area B could be related to the northern XJF, and those in area C may be associated with the two nearby secondary faults, which, however, are eventually interpreted to be induced by human activity (see Discussion section).

After the confirmation of the repeaters, we estimated the slip rates for repeating earthquakes. The estimation of the slip rate based on repeating earthquakes with magnitudes has been conducted in previous studies (Nadeau and McEvilly, 1999; Igarashi et al., 2003; Li et al., 2011; Li et al., 2013). First, the seismic moment was calculated using the magnitude in accordance with an empirical relationship (Abercrombie, 1996):

$$\log(M_0) = 9.8 + M_L, \tag{1}$$

where M_0 is seismic moment and M_L is magnitude. Next, the rupture size r was estimated by seismic moment and static stress drop with the circular model (Eshelby, 1957; Kanamori and Anderson, 1975):

$$r = \left(\frac{7M_0}{16\Delta\sigma}\right)^{1/3}, \tag{2}$$

where $\Delta\sigma$ is static stress drop. Here, we gave the stress drop as 3 Mpa, same as the previous study used in the XJF zone (Li et al., 2013). The slip value d was calculated on the basis of the standard crack model:

$$d = \frac{M_0}{\mu\pi r^2}, \tag{3}$$

where μ is shear modulus, set at 3×10^{10}N/m^2. Finally, the slip rate of the fault was estimated by linearly fitting the cumulative slip

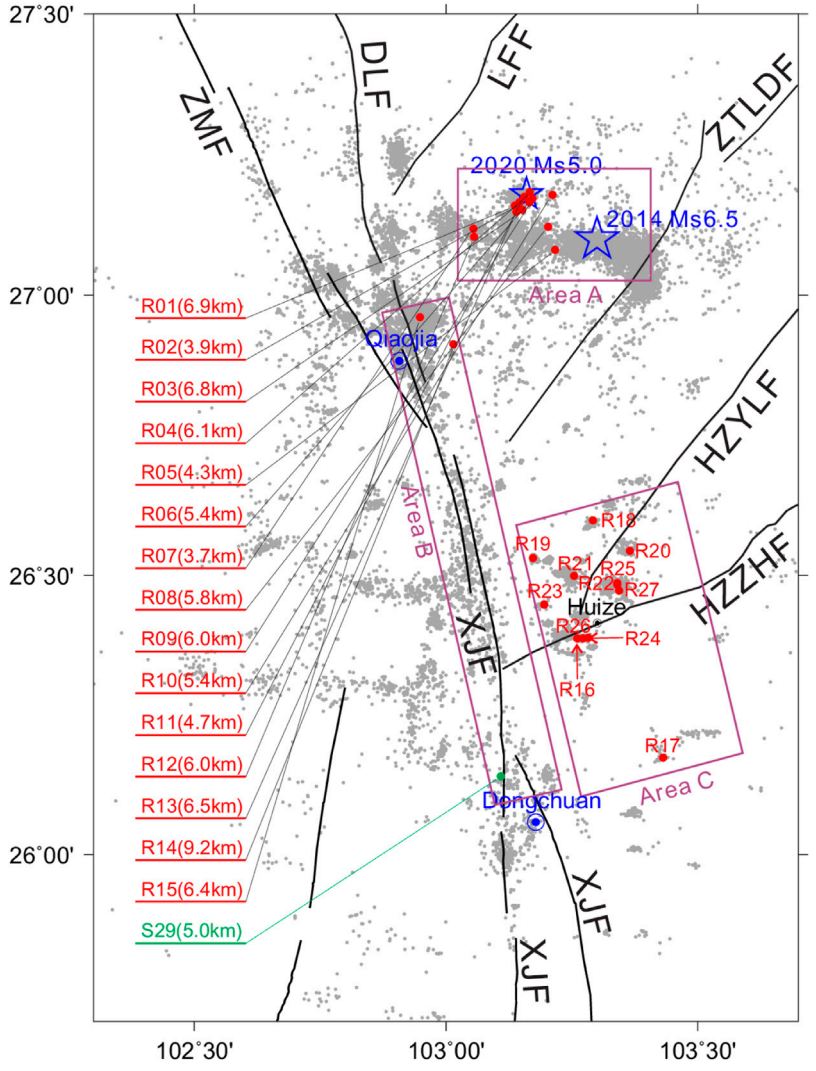

FIGURE 2
Distribution of the repeaters identified from the seismic recordings since 2012. The red dots indicate the clusters of the repeaters, and the numbers in brackets show the depths. The repeaters in area A seem to be related to the 2014 Ludian Ms6.5 earthquake and the 2020 Qiaojiang Ms5.0 earthquake, the repeaters in area B are likely to be associated with the main part of the northern XJF, and the repeaters in area C are related with human activity very probably. The S29 shows the cluster location of the repeaters from Li et al. (2013).

amounts of the repeating earthquake sequences. Considering that clusters R01–R13 in the source areas are related to the 2014 Ludian Ms6.5 and 2020 Qiaojia Ms5.0 earthquakes, and our main purpose in area A was to observe the effect of these two mainshocks on the recurrence intervals of repeating clusters; clusters R16–R27 are probably induced by human activity, so we only estimate the slip rates of clusters R14 and R15. Figure 4 presents an example of how to solve the slip rate using the repeating earthquakes, Figure 5 shows the occurrence dates of the repeating earthquakes in various clusters, and Table 1 displays the information of the various clusters. It is of note that the average depth of all the repeaters in the same cluster was adopted because they had overlapped rupture areas but different depths.

Discussion

Relationship with the 2014 Ludian Ms6.5 and 2020 Ms5.0 Qiaojia earthquakes

On 3 August 2014, an Ms6.5 earthquake occurred in Ludian, a county of Yunnan province, China. The distribution of aftershocks and the finite fault inversion (Zhang et al., 2015) both showed that this was event caused by two branches of conjugate faults, with one branch having a nearly east–west orientation, whereas the other having a nearly north–south orientation, and the major slip took place on the north–south

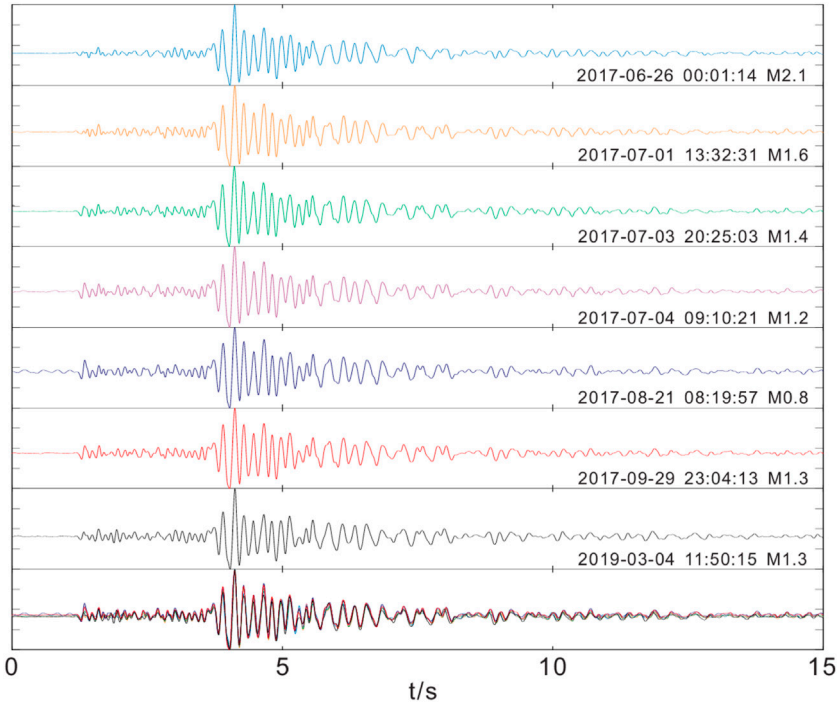

FIGURE 3
Comparison of the seismic recordings (only vertical components) of cluster R14 recorded at station J07. Each of them was normalized by its maximum amplitude. On the bottom are all the recordings of seven repeating earthquakes overlapped together to show how different they are.

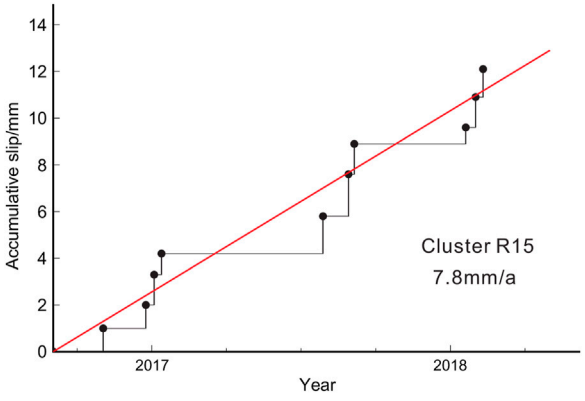

FIGURE 4
An example to illustrate how to estimate the slip rate using repeating earthquakes. The vertical axis shows the cumulative slip amounts calculated using the repeating earthquakes from cluster R15, and the horizontal axis shows the occurrence dates of the repeating earthquakes. Linearly fitting the cumulative slip values produces the red line. Note: the first event is set at the origin point.

branch and concentrated in a 15 km area, while only a minor slip occurred on the west–east branch. After that, on 18 May 2020, an Ms5.0 earthquake occurred in Qiaojia, ~20 km west of the 2014 Ludian Ms6.5 earthquake, which was located on an unmapped fault, and the aftershocks indicated a rupture length of ~5 km (Fu et al., 2021). Chen et al. (2010) studied the triggering relationship of M4-5 earthquakes on repeating events nearby, and in this research, we also investigated the triggering effect of these two earthquakes on the surrounding repeaters. Chen et al. (2010) considered five recurrence elements (Supplementary Figure S4) for analyses: 1) dt+, the time difference between a major earthquake and the first subsequent recurrence of a repeating event; 2) dt-, the time difference between a major earthquake and the most recent repeating event; 3) Tr_{cos}, the recurrence interval spanning the major event (the sum of dt+ and dt-); 4) Tr_{post}, the duration of the first full recurrence interval following the major event; and 5) Tr_{pre}, the last recurrence interval just preceding the potential trigger. These elements are divided by the average recurrence interval of a given repeating cluster to obtain the normalized values of dt+*, dt-*, Tr^*_{cos}, Tr^*_{post}, and Tr^*_{pre}. We selected six

10.3389/feart.2022.917635

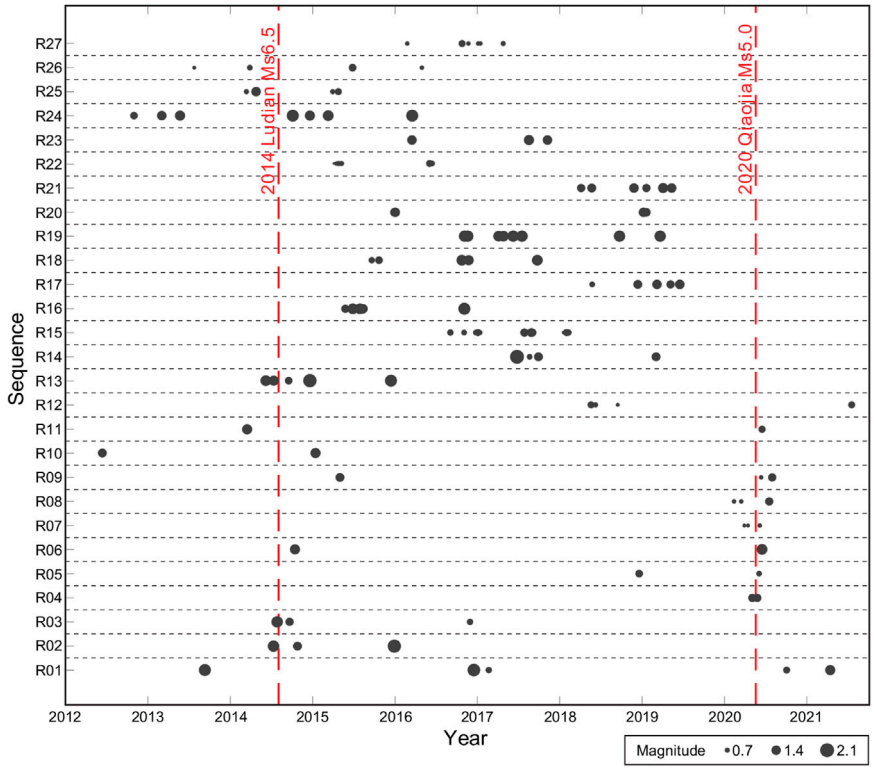

FIGURE 5
Occurrence times of the repeating earthquakes in various clusters. Two discontinuous lines indicate the dates of the 2014 Ludian Ms6.5 earthquake and the 2020 Qiaojia Ms5.0 earthquake.

TABLE 1 Information on the clusters of repeating earthquakes in areas A and B.

ID	Number	Median source location			M_L	Duration (year)	Total slip(mm)	Slip rate(mm/a)	Recurrence interval(year)
		Lon(deg)	Lat(deg)	Depth(km)					
R01	5	103.1451	27.1596	6.9	0.9–1.9	7.59	8.5	—	0.18–3.26
R02	3	103.1461	27.1656	3.9	1.3–2.0	1.47	5.9	—	0.29–1.18
R03	3	103.1448	27.1564	6.8	0.9–1.7	2.34	2.8	—	0.15–2.19
R04	3	103.1645	27.1784	6.1	0.7–1.2	0.07	2.5	—	0.01–0.06
R05	3	103.2167	27.0808	4.3	0.5–1.1	1.46	1.7	—	0.00–1.45
R06	3	103.1623	27.1697	5.4	1.0–1.6	5.67	3.9	—	0.00–5.67
R07	3	103.0547	27.1185	3.7	0.5–0.6	0.19	1.5	—	0.04–0.14
R08	3	103.2031	27.1218	5.8	0.6–1.2	0.43	2.4	—	0.09–0.34
R09	3	103.1678	27.1724	6.0	0.6–1.3	5.25	2.4	—	0.13–5.11
R10	4	103.2119	27.1788	5.4	0.8–1.5	2.59	4.6	—	0.00–2.59
R11	4	103.1556	27.1753	4.7	1.0–1.5	6.25	4.9	—	0.00–6.25
R12	4	103.0558	27.1071	6.0	0.5–1.0	3.16	2.9	—	0.05–2.84
R13	5	103.1399	27.1486	6.5	1.1–2.0	1.52	11.2	—	0.10–0.98
R14	7	103.0149	26.9126	9.2	0.8–2.1	1.69	10.9	7.5 ± 1.97	0.00–1.43
R15	11	102.9485	26.9609	6.4	0.5–1.3	1.44	12.1	7.8 ± 0.53	0.02–0.54

TABLE 2 Parameters (dt+*, dt-*, Tr^*_{cos}, Tr^*_{post}, and Tr^*_{pre}) of 6 clusters related to the Ludian earthquake.

Group	Distance(km)	dt+*	dt-*	Tr^*_{cos}	Tr^*_{post}	Tr^*_{pre}	Average recurrence(year)
R01	16.88	1.25	0.47	1.72	0.09	—	1.89
R02	17.42	0.32	0.08	0.39	1.60	—	0.73
R03	16.81	0.12	0.01	0.13	1.87	—	1.17
R10	11.79	0.52	2.47	2.99	—	0.01	0.86
R11	17.12	2.82	0.18	3.00	0.01	0.01	2.08
R13	17.09	0.33	0.14	0.48	0.68	0.25	0.38

TABLE 3 Parameters (dt+*, dt-*, Tr^*_{cos}, Tr^*_{post}, and Tr^*_{pre}) of 9 clusters related to the Qiaojia earthquake.

Group	Distance(km)	dt+*	dt-*	Tr^*_{cos}	Tr^*_{post}	Tr^*_{pre}	Average recurrence(year)
R01	2.74	0.19	1.71	1.90	0.28	0.09	1.89
R04	2.01	0.53	1.15	1.69	0.31	—	0.03
R05	12.00	0.05	1.94	1.99	0.01	—	0.73
R06	2.83	0.03	1.97	1.99	0.01	—	2.83
R07	12.91	0.53	1.00	1.53	—	0.47	0.09
R08	7.55	0.77	0.82	1.59	—	0.41	0.21
R09	2.32	0.02	1.92	1.95	0.05	—	2.62
R11	3.35	0.04	2.96	3.00	0.001	0.01	2.08
R12	12.44	1.11	1.58	2.69	—	0.25	1.05

repeating clusters within 45 km of the Ludian earthquake and nine repeating clusters within 15 km of the Qiaojia earthquake, as the influence zone caused by the mainshock is about 3–5 times its rupture dimension (Chen et al., 2010). Since the numbers of events in each cluster are generally too small to calculate some values of Tr^*_{post} and Tr^*_{pre}, we mainly studied the variation of dt+* and dt-*. Tables 2, 3 show the results.

Table 2 and Figure 6A show that five of six repeating clusters within 45 km from the Ludian earthquake are at a distance of ~17 km. The cluster R10 is 11.8 km away from the Ludian earthquake, and the dt+* and dt-* are 0.5 and 2.5, respectively. Chen et al. (2010) believe that a short dt+* along with a high dt-* indicates an obvious triggering effect and also indicates that an event occurred in a late stage of the seismic cycle, so it seems that the triggering effect of the mainshock on the nearest cluster R10 is obvious. But we have to admit that there may be some chance factors here because of the fact that cluster R10 contains four events (Table 1 and Figure 5), and three events occurred in two days (20120614–20120615). For the other five clusters, however, Figure 6B shows that the values of dt+* are greater than the values of dt-*, which indicates that the triggering effect is not obvious.

The insignificant triggering effect of the Ludian earthquake on the surrounding repeating clusters may be caused by the following reasons: 1) The epicenter of the Ludian earthquake is at the edge of our study area (Figure 1), leading us to count only the clusters in the western side; 2) The number of the clusters is relatively small (only 6) and few events in each cluster, leading to a higher chance factor in the final statistics; and 3) The clusters are relatively far away from the mainshock and are not located in the direction of the rupture caused by the mainshock, which is not conducive to triggering action.

There are nine repeating clusters within 15 km of the 2020 Qiaojia Ms5.0 earthquake. Calculations show that the pre- and post-seismic recurrence periods for these clusters are 0.40s and 0.11 years, respectively. This suggests that the Qiaojia earthquake significantly shortened the recurrence period of clusters nearby and had a triggering effect on these repeating events. Figure 5 shows that the values of dt-of four clusters (R05, R06, R09, and R11) are all greater than 1 year, but the repeating events occurred immediately after the Qiaojia earthquake, which also indicates an obvious triggering effect. Figure 6C shows that the distributions of dt+* of four in five clusters with a distance < 5 km are below 0.2, and three of them are less than 0.05. However, the distributions of dt+* of three in four clusters with a distance > 5 km are above 0.5. This indicates that the triggering effect on repeaters in the near field is generally greater than that in the far field. Figure 6D shows that the values of dt+* are all smaller than the values of dt-*, combined with the fact that the values of Tr^*_{cos} are all greater than 1 (Table 3 and Figure 6C),

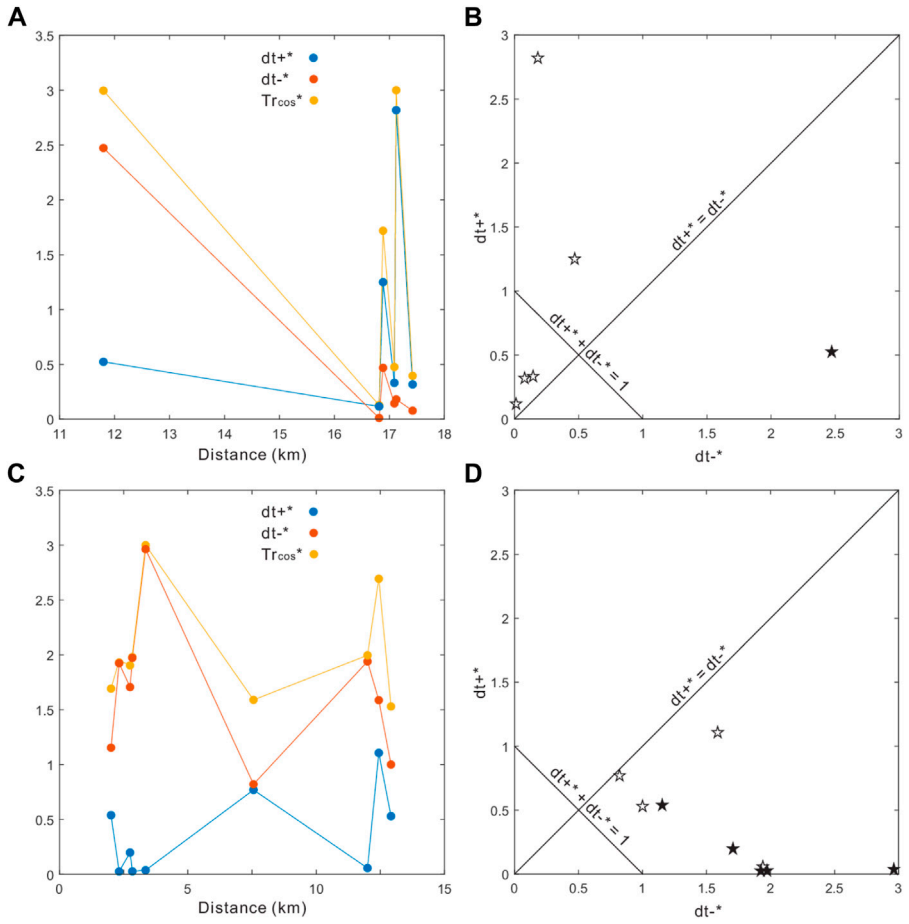

FIGURE 6
Relationship of the dt+*, dt-*, Tr^*_{cos} and the distances from the main shock. **(A)** The parameters dt+*, dt-*, Tr^*_{cos} of 6 clusters as a function of distance from the Ludian earthquake. **(B)** Plot of dt+* versus dt-* for the clusters close to the Ludian earthquake, black filled and open stars indicate the cluster R10 closest to the Ludian earthquake and the other five clusters, respectively. **(C)** The parameters dt+*, dt-*, Tr^*_{cos} of six clusters as a function of distance from the Qiaojia earthquake. **(D)** Plot of dt+* versus dt-* for the clusters close to the Qiaojia earthquake, black filled and open stars indicate the clusters for the distance range of <5 km and 5–15 km, respectively.

and we can say that only events relatively late in their respective earthquake cycle get triggered, which is similar to the results of Chen et al. (2010).

Implication to the potential seismic risk on the northern XJF

Since the 1733 Dongchuan M7.8 earthquake, no M>7 earthquakes have occurred on the northern XJF, so significant attention has been paid to this section. Based on the recurrence interval and the elapsed time of the historical strong earthquakes, Wen *et al.* (2008) delineated the northern XJF (Qiaojia–Dongchuan) as a seismic gap. By means of a three-dimensional finite element model, using the constraints of the GPS observations, the seismological crust and upper mantle models, the data of earthquake activities, tectonic stress field and fault slip rates, and the rheological property of the Sichuan–Yunnan lithosphere, and considering the influence of historically strong earthquakes since A.D. 1327, Zhu *et al.* (2016) solved for the stress distribution along the Anninghe–Zemuhe–Xiaojiang fault zone and pointed out the northern XJF (Qiaojia–Dongchuan) was one of the high-stress cumulated segments. Coincidently, as shown in Figure 7, the newest seismicity monitored by our high-density seismic array exhibited relatively sparse earthquakes on the fault plane of the northern XJF. In contrast, there is significantly more seismicity to the north, including two repeating clusters (R14 and R15). In the south, Li et al. (2013) identified a repeating earthquake swarm (S29, Figure 7). According to previous studies, repeating earthquakes usually concentrate on the fault segments with high seismicity; therefore, few repeating earthquakes were

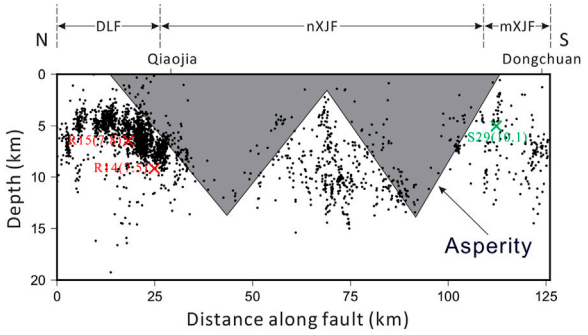

FIGURE 7
Seismicity in a 3 km-thick zone along the northern XJF. The red crosses indicate the clusters R14 and R15 of repeating earthquakes, while the black dots show the hypocenters of all the relocated events. The green cross denotes cluster S29 of repeating earthquakes identified by Li *et al.* (2013). Abbreviation: DLF, Daliangshan fault; nXJF, northern Xiaojiang fault; mXJF, middle Xiaojiang fault. The possible asperity is shown as an irregular shape.

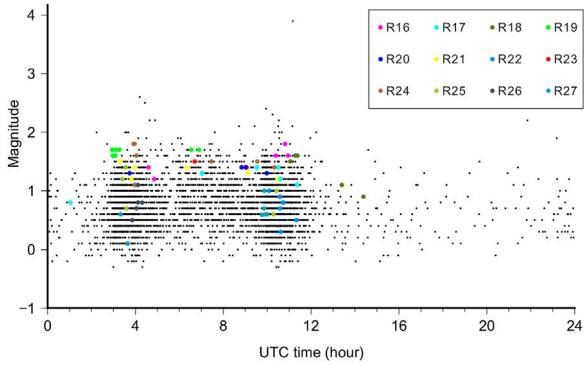

FIGURE 8
Occurrence times of the seismic events since 2012 in area C. The clusters R16–R27 are marked in various colors. Note: the UTC times plus 8 h are the local times.

distributed on the fault segments which are locked and relatively aseismic (Peng and Zhao, 2009; Deng et al., 2020; Li L. et al., 2021). Additionally, it has been found that repeating earthquakes often appear on the outer edge of asperities related to large potential earthquakes (Uchida and Bürgmann, 2019; Li L. et al., 2021). These observations are similar to the scenario exhibited in this study. Owing to the excellent monitoring capability of our seismic array, which is capable to detect and locate an event with magnitude down to Mw-0.7, we judged that the majority part of the northern XJF has been locked as an asperity, where no repeaters are identified and the seismic activity is rather weak. It was found that clusters of repeating earthquakes had once taken place in the vicinity of the rupture areas of the 2008 Wenchuan Mw7.9 and the 2013 Lushan M7.0 earthquakes on the Longmenshan fault zone (Li et al., 2011; Li, 2017), so we believe that the next large earthquake may take place between the clusters of repeating earthquakes to the north and south of the asperity.

To estimate the magnitude of the potential earthquake on the northern XJF, we defined the locked asperity, as shown in Figure 7, on the basis of the seismic distribution and the seismicity of both the repeaters and others. Based on geodetic observations, Li Y. et al. (2021) have outlined an asperity on northern XJF, which is generally consistent with our asperity. The slip rate north of the asperity in Figure 7, as clusters R14 and R15 revealed, was 7.7 mm/a (an average of 7.8 mm/a and 7.5 mm/a), which basically agrees with the rate of 6.8 mm/a estimated from near-field GPS observation (Fu et al., 2020). According to the formula of seismic moment

$$M_0 = \mu DA, \tag{4}$$

where M_0 is the seismic moment; μ is the rigidity of the medium, generally taking a value of $3*10^{10}$Pa; D is the average dislocation; and A is the fault area. Considering the shape of asperity, as shown in Figure 7, the dip angle of northern XJF is almost upright (Li Y. et al., 2021), the elapsed time of 289 years since the 1733 Dongchuan M7.8 earthquake, and the slip rate of 7.7 mm/a as estimated as earlier, we speculate that the asperity is possible of producing an earthquake with a magnitude of at least Mw7.1. We have to stress that before the operation of our network, the density of the regional seismic network was not sufficient to reflect the real seismicity of northern XJF, so we did not use the seismicity of a longer time. Considering our relatively short observation time for seismicity and the short duration for clusters R14 and R15, the final results may have a relatively large error.

The repeating clusters in the east secondary structure zone

A total of 12 clusters of repeaters are confirmed across the junction area of secondary faults southeastern to the northern XJF (area C in Figure 2). We present the earthquake waveforms of these repeating clusters (R16–R27) in Supplementary Figures S2, S3. Compared with the waveforms of other clusters (Supplementary Figures S1, S2), the waveforms of clusters R01–R15 clearly show both P and S phase arrivals, while waveforms of clusters R16–R27 do not. Also, the vertical initial motions of P waves from clusters R16–R27 are all upward, and this is the characteristic of manual blasting. Previous studies have shown that natural and artificial earthquakes can be identified by spectral analysis (Ursino et al., 2001; Allmann et al., 2008). We have also performed spectral analysis of seismic waveforms (Supplementary Figures S5–S10). The three selected events in each figure share similar magnitudes and have similar epicentral distances to the selected stations. Supplementary

Figure S5 show that the waveforms of the events in the clusters from area C are richer in low frequencies compared to the waveforms of the events in other clusters, and similar characteristics are also found in S10. However, this phenomenon is less obvious in Supplementary Figures S6–S9. Cattaneo et al. (2014) believed that studying the frequency of daytime and nighttime seismic events could provide a good reference for determining whether an earthquake is artificial or not. We also drew on this analytical approach. First, we paid attention to the occurring times of the events across this area and found a large percentage of the events occurred during daytime (UTC 0200–1200 h), as Figure 8 shows. Specifically, a total of 12 clusters of repeaters were confirmed; however, 9 clusters of them all and most of the events in the other two clusters (R09 and R17) occurred during the daytime. Cluster R27 can be taken as an example. The information in Supplementary Table S1 is from the original earthquake catalogue, and it shows the occurring time of the events in cluster R27; it can be seen that cluster R27 includes six repeating events, and five events occurred almost at UTC 09:50, and this is almost impossible for natural repeating earthquakes. Meanwhile, Supplementary Figure S11 is the histogram showing the hourly distribution of the number of events in area C, and the events were concentrated in two time periods (UTC 0300–0500h; 0900–1200 h), which corresponded to the working hours. All these seem more like an artificially set blast time. In addition, from the photos taken in the field, Supplementary Figure S12 shows the location where the cave was blasted near cluster R22, and Supplementary Figure S13 shows a stone quarry near cluster R24 (Longitude: 103.2720°; Latitude: 26.3873°) and R16 (Longitude: 103.2608°; Latitude: 26.3874°). These photos can be used as evidence for artificial earthquakes. Overall, from the waveform features and occurring times of the events in clusters (R16–R27), we believe that these events are probably induced by human activity. Or, at least, we do not think there are sufficient reasons to judge these repeating events as natural earthquakes because natural earthquakes are evenly distributed in 24 h, which is inconsistent with the phenomenon we observed.

Conclusion

By the methods of waveform cross-correlation analysis and precise seismic location, we systematically identified and confirmed the repeating earthquakes from the seismic data recorded by a high-density array from March 2012 to July 2021 in the northern XJF and reached the following conclusions:

1) A total of 27 clusters of repeaters, including 132 events, were identified and confirmed; 13 of the clusters are close to the 2014 Ludian Ms6.5 and the 2020 Qiaojia Ms5.0 earthquakes, and 2 of the clusters were located very close to the northernmost tip of the northern XJF. Furthermore, 12 of the clusters appeared off the main fault of the northern XJF and were judged to be probably caused by human activities (mining explosions). No repeaters were identified on the central part of the northern XJF.
2) Through the analysis of the relationship between the recurrence intervals of the clusters and two mainshocks, we found that the triggering effect on repeaters from the Ludian earthquake is not obvious, while the triggering effect from the Qiaojia earthquake is significant. Also, the results show that the triggering effect on repeaters in the near field is generally greater than that in the far field, and only events relatively late in their respective earthquake cycle get triggered.
3) No repeaters have occurred on the central part of the northern XJF. However, two clusters of the repeaters, confirmed in this study, together with one cluster of repeaters identified in a previous study, delineate a locked asperity. This asperity is capable of producing an Mw7.1 earthquake, as estimated on a basis of the slip rate contributed by the clusters of repeating earthquakes.
4) It is necessary to remove man-made repeaters when using seismicity for tectonic activity studies.

Data availability statement

The original contributions presented in the study are included in the article/Supplementary Material; further inquiries can be directed to the corresponding author.

Author contributions

YZ carried out data analysis and wrote the manuscript. LX conceptualized the problem and validation and participated in discussions of all aspects of the manuscript. JW and CL relocated the earthquakes. LF participated in the discussion section. ZP was involved in the analysis of the results.

Funding

This research work was supported by the National Natural Science Foundation of China (Project: 41904050 and U2139205), the Special Fund of the Institute of Geophysics, China Earthquake Administration (Grant Number: DQJB19B33) and the Special Fund of the Institute of Earthquake Forecasting, China Earthquake Administration (Grant Number: CEAIEF2022010100).

Conflict of interest

The authors declare that the research was conducted in the absence of any commercial or financial relationships that could be construed as a potential conflict of interest.

Publisher's note

All claims expressed in this article are solely those of the authors and do not necessarily represent those of their affiliated organizations, or those of the publisher, the editors, and the reviewers. Any product that may be evaluated in this article, or claim that may be made by its manufacturer, is not guaranteed or endorsed by the publisher.

Supplementary material

The Supplementary Material for this article can be found online at: https://www.frontiersin.org/articles/10.3389/feart.2022.917635/full#supplementary-material

References

Abercrombie, R. E. (1996). The magnitude-frequency distribution of earthquakes recorded with deep seismometers at Cajon Pass, southern California. *Tectonophysics* 261, 1–7. doi:10.1016/0040-1951(96)00052-2

Allmann, B. P., Shearer, P. M., and Hauksson, E. (2008). Spectral discrimination between quarry blasts and earthquakes in southern California. *Bull. Seismol. Soc. Am.* 98 (4), 2073–2079. doi:10.1785/0120070215

Anooshehpoor, A., and Brune, J. N. (2001). Quasi-static slip-rate shielding by locked and creeping zones as an explanation for small repeating earthquakes at Parkfield. *Bull. Seismol. Soc. Am.* 91, 401–403. doi:10.1785/0120000105

Beeler, N., Lockner, D., and Hickman, S. (2001). A simple stick-slip and creep-slip model for repeating earthquakes and its implication for microearthquakes at Parkfield. *Bull. Seismol. Soc. Am.* 91, 1797–1804. doi:10.1785/0120000096

Cattaneo, M., Caffagni, E., Carannante, S., and D'Alema, E. (2014). A catalogue of non-tectonic earthquakes in central-eastern Italy[J]. *Ann. Geophys.* 57 (3), 1. doi:10.4401/ag-6434

Chen, K. H., Bürgmann, R., and Nadeau, R. M. (2010). Triggering effect of M 4-5 earthquakes on the earthquake cycle of repeating events at Parkfield, California. *Bull. Seismol. Soc. Am.* 100 (2), 522–531. doi:10.1785/0120080369

Chen, R., and Li, P. (1988). Slip rates and earthquake recurrence intervals of the western branch of the Xiaojiang Fault Zone. *Seismol. Geol.* 10, 1–13.

Crotwell, H. P., Owens, T. J., and Ritsema, J. (1999). The TauP Toolkit: Flexible seismic travel-time and ray-path utilities. *Seismol. Res. Lett.* 70, 154–160. doi:10.1785/gssrl.70.2.154

Deng, Y., Peng, Z., and Liu-Zeng, J. (2020). Systematic search for repeating earthquakes along the Haiyuan fault system in northeastern Tibet. *J. Geophys. Res. Solid Earth* 125, e2020JB019583. doi:10.1029/2020jb019583

Department of Earthquake Disaster Prevention and State Seismological Bureau (1995). *The catalogue of Chinese historical strong earthquakes*. Beijing: Seismological Press, 1–514. (in Chinese).

Eshelby, J. D. (1957). The determination of the elastic field of an ellipsoidal inclusion, and related problems[J]. *Proc. R. Soc. Lond. Ser. A. Math. Phys. Sci.* 241 (1226), 376–396.

Fu, Z., Jiang, C., Yin, F., Zhang, L., Shen, X., Fang, L., et al. (2021). Preliminary report on the 18 may 2020 Ms 5.0 Qiaojia earthquake, yunnan, China. *Seismol. Res. Lett.* 92, 2122–2133. doi:10.1785/0220200233

Fu, Z., Xu, L., and Wang, Y. (2020). Seismic risk on the northern Xiaojiang fault implied by the latest and nearest GPS observations. *Pure Appl. Geophys.* 177, 661–679. doi:10.1007/s00024-019-02347-5

He, H., Yasutaka, I., Song, F., and Dong, X. (2002). Late quaternary slip rate of the Xiaojiang fault and its implication. *Seismol. Geol.* 24, 14–26.

Igarashi, T. (2020). Catalog of small repeating earthquakes for the Japanese Islands. *Earth Planets Space* 72, 73. doi:10.1186/s40623-020-01205-2

Igarashi, T., Matsuzawa, T., and Hasegawa, A. (2003). Repeating earthquakes and interplate aseismic slip in the northeastern Japan subduction zone. *J. Geophys. Res.* 108, 1. doi:10.1029/2002jb001920

Jin, H., Gao, Y., Su, X., and Fu, G. (2019). Contemporary crustal tectonic movement in the southern Sichuan-Yunnan block based on dense GPS observation data. *Earth Planet. Phys.* 3, 53–61. doi:10.26464/epp2019006

Kanamori, H., and Anderson, D. L. (1975). Theoretical basis of some empirical relations in seismology. *Bull. Seismol. Soc. Am.* 65, 1073–1095.

Kato, N., and Hirasawa, T. (1997). A numerical study on seismic coupling along subduction zones using a laboratory-derived friction law. *Phys. Earth Planet. interiors* 102, 51–68. doi:10.1016/s0031-9201(96)03264-5

Lay, T., and Kanamori, H. (1980). Earthquake doublets in the Solomon Islands. *Phys. Earth Planet. Interiors* 21, 283–304. doi:10.1016/0031-9201(80)90134-x

Li, J., Böse, M., Feng, Y., and Yang, C. (2021a). Real-time characterization of finite rupture and its implication for earthquake early warning: Application of FinDer to existing and planned stations in southwest China. *Front. Earth Sci. (Lausanne).* 9, 699560. doi:10.3389/feart.2021.699560

Li, L., Chen, Q., Niu, F., He, J., and Fu, H. (2013). Estimates of deep slip rate along the Xiaojiang fault with repeating microearthquake data. *Chin. J. Geophysics- Chin. Ed.* 56, 3373–3384.

Li, L., Chen, Q., and Niu, F. (2021b). Repeating microearthquakes and deep deformation along the major faults in the Sichuan-Yunnan region, China. *Chin. J. Geophys.* 64, 4308–4326.

Li, L., Chen, Q., Niu, F., and Su, J. (2011). Deep slip rates along the Longmen Shan fault zone estimated from repeating microearthquakes. *J. Geophys. Res.* 116, B09310. doi:10.1029/2011jb008406

Li, L. (2017). Depth-dependence of post-seismic velocity changes in and near source area of the 2013 M 7.0 Lushan earthquake revealed by S coda of repeating events. *Tectonophysics* 717, 302–310. doi:10.1016/j.tecto.2017.08.017

Li, P. (1993). *Xianshuihe-Xiaojiang fault zone*. Beijing: Seismological Press.

Li, Y., Nocquet, J. M., Shan, X., and Jian, H. (2021c). Heterogeneous interseismic coupling along the xianshuihe-Xiaojiang fault system, eastern Tibet. *JGR. Solid Earth* 126 (11), e2020JB021187. doi:10.1029/2020jb021187

Molnar, P., and Tapponnier, P. (1975). Cenozoic Tectonics of Asia: Effects of a Continental Collision: Features of recent continental tectonics in Asia can be interpreted as results of the India-Eurasia collision. *Science* 189, 419–426. doi:10.1126/science.189.4201.419

Myhill, R., McKenzie, D., and Priestley, K. (2011). The distribution of earthquake multiplets beneath the southwest Pacific. *Earth Planet. Sci. Lett.* 301, 87–97. doi:10.1016/j.epsl.2010.10.023

Nadeau, R. M., and Johnson, L. R. (1998). Seismological studies at Parkfield VI: Moment release rates and estimates of source parameters for small repeating earthquakes[J]. *Bull. Seismol. Soc. Am.* 88 (3), 790–814.

Nadeau, R. M., and McEvilly, T. V. (2004). Periodic pulsing of characteristic microearthquakes on the san Andreas fault. *Science* 303 (5655), 220–222. doi:10.1126/science.1090353

Nadeau, R. M., Foxall, W., and McEvilly, T. (1995). Clustering and periodic recurrence of microearthquakes on the San Andreas fault at Parkfield, California. *Science* 267, 503–507. doi:10.1126/science.267.5197.503

Nadeau, R. M., and McEvilly, T. V. (1999). Fault slip rates at depth from recurrence intervals of repeating microearthquakes. *Science* 285, 718–721. doi:10.1126/science.285.5428.718

Peng, Z., and Zhao, P. (2009). Migration of early aftershocks following the 2004 Parkfield earthquake. *Nat. Geosci.* 2, 877–881. doi:10.1038/ngeo697

Sammis, C. G., and Rice, J. R. (2001). Repeating earthquakes as low-stress-drop events at a border between locked and creeping fault patches. *Bull. Seismol. Soc. Am.* 91, 532–537. doi:10.1785/0120000075

Schaff, D. P., and Beroza, G. C. (2004). Coseismic and postseismic velocity changes measured by repeating earthquakes. *J. Geophys. Res.* 109 (B10). doi:10.1029/2004jb003011

Schmittbuhl, J., Karabulut, H., Lengliné, O., and Bouchon, M. (2016). Long-lasting seismic repeaters in the central basin of the main marmara fault. *Geophys. Res. Lett.* 43, 9527–9534. doi:10.1002/2016gl070505

Shen, J., Wang, Y., and Song, F. (2003). Characteristics of the active Xiaojiang fault zone in Yunnan. *J. Asian Earth Sci.* 21, 1085–1096.

Shen, Z., Lü, J., Wang, M., and Bürgmann, R. (2005). Contemporary crustal deformation around the southeast borderland of the Tibetan Plateau. *J. Geophys. Res.* 110 (B11). doi:10.1029/2004jb003421

Turner, R. C., Nadeau, R. M., and Bürgmann, R. (2013). Aseismic slip and fault interaction from repeating earthquakes in the Loma Prieta aftershock zone. *Geophys. Res. Lett.* 40, 1079–1083. doi:10.1002/grl.50212

Uchida, N., and Bürgmann, R. (2019). Repeating earthquakes. *Annu. Rev. Earth Planet. Sci.* 47, 305–332. doi:10.1146/annurev-earth-053018-060119

Uchida, N. (2019). Detection of repeating earthquakes and their application in characterizing slow fault slip. *Prog. Earth Planet. Sci.* 6, 40–21. doi:10.1186/s40645-019-0284-z

Uchida, N., Matsuzawa, T., Hasegawa, A., and Igarashi, T. (2003). Interplate quasi-static slip off Sanriku, NE Japan, estimated from repeating earthquakes. *Geophys. Res. Lett.* 30. doi:10.1029/2003gl017452

Ursino, A., Langer, H., Scarfi, L., and Di Grazia, G. (2001). Discrimination of quarry blasts from tectonic microearthquakes in the hyblean plateau (southeastern sicily)[J]. *Ann. Geophys.* 44 (4), 703–722.

Vidale, J., Ellsworth, W., Cole, A., and Marone, C. (1994). Variations in rupture process with recurrence interval in a repeated small earthquake. *Nature* 368, 624–626. doi:10.1038/368624a0

Waldhauser, F., Ellsworth, W. L., Schaff, D. P., and Cole, A. (2004). Streaks, multiplets, and holes: High-resolution spatio-temporal behavior of Parkfield seismicity. *Geophys. Res. Lett.* 31 (18), L18608. doi:10.1029/2004gl020649

Waldhauser, F., and Ellsworth, W. L. (2000). A double-difference earthquake location algorithm: Method and application to the northern Hayward fault, California. *Bull. Seismol. Soc. Am.* 90, 1353–1368. doi:10.1785/0120000006

Wang, C., Chan, W. W., and Mooney, W. D. (2003). Three-dimensional velocity structure of crust and upper mantle in southwestern China and its tectonic implications. *J. Geophys. Res.* 108, 1. doi:10.1029/2002jb001973

Wang, E., and Burchfiel, B. C. (2000). Late Cenozoic to Holocene deformation in southwestern Sichuan and adjacent Yunnan, China, and its role in formation of the southeastern part of the Tibetan Plateau. *Geol. Soc. Am. Bull.* 112, 413–423. doi:10.1130/0016-7606(2000)112<413:lcthdi>2.0.co;2

Wang, Y., Wang, E., Shen, Z., Wang, M., Gan, W., Qiao, X., et al. (2008). GPS-constrained inversion of present-day slip rates along major faults of the Sichuan-Yunnan region, China. *Sci. China Ser. D-Earth. Sci.* 51, 1267–1283. doi:10.1007/s11430-008-0106-4

Wang, Y., Zhang, X., Zhang, J., Yang, S., Han, L., and Yan, S. (2017). Seismic mountainous geo-hazard investigation of Dongchuan Ms7.8 earthquake in 1733. *South-to-North Water Transfers Water Sci. Technol.* 15, 138–144.

Wen, X., Du, F., Long, F., Fan, J., and Zhu, H. (2011). Tectonic dynamics and correlation of major earthquake sequences of the Xiaojiang and Qujiang-Shiping fault systems, Yunnan, China. *Sci. China Earth Sci.* 54, 1563–1575. doi:10.1007/s11430-011-4231-0

Wen, X., Ma, S., Xu, X., and He, Y. (2008). Historical pattern and behavior of earthquake ruptures along the eastern boundary of the Sichuan-Yunnan faulted-block, southwestern China. *Phys. Earth Planet. Interiors* 168, 16–36. doi:10.1016/j.pepi.2008.04.013

Xu, X., Wen, X., Zheng, R., Ma, W., Song, F., and Yu, G. (2003). Pattern of latest tectonic motion and its dynamics for active blocks in Sichuan-Yunnan region, China. *Sci. China Ser. D Earth Sci.* 46, 210–226.

Zhang, L., Su, J., Wang, W., Fang, L., and Wu, J. (2022). Deep fault slip characteristics in the Xianshuihe-Anninghe-Daliangshan Fault junction region (eastern Tibet) revealed by repeating micro-earthquakes. *J. Asian Earth Sci.* 227, 105115. doi:10.1016/j.jseaes.2022.105115

Zhang, P., Deng, Q., Zhang, G., Ma, J., Gan, W., Min, W., et al. (2003). Active tectonic blocks and strong earthquakes in the continent of China. *Sci. China Ser. D Earth Sci.* 46, 13–24.

Zhang, Y., Yuntai, C., Xu, L., Wei, X., Jin, M., and Zhang, S. (2015). The 2014 Mw6.1 ludian, yunnan, earthquake: A complex conjugated ruptured earthquake. *Chin. J. Geophys.* 58, 153–162.

Zhu, A., Zhang, D., and Jiang, C. (2016). Numerical simulation of the segmentation of the stress state of the Anninghe-Zemuhe-Xiaojiang faults. *Sci. China Earth Sci.* 59, 384–396. doi:10.1007/s11430-015-5157-8

Zhuang, R., Li, J., Chen, G., and Li, C. (2019). The Quaternary activity characteristics of the Huize-Zhehai fault in the Northeast area of Yunnan. *Recent Dev. World Seismol.* 7, 17–22.

frontiers | Frontiers in Earth Science

TYPE Methods
PUBLISHED 05 September 2022
DOI 10.3389/feart.2022.933066

OPEN ACCESS

EDITED BY
Ying Li,
China Earthquake Administration, China

REVIEWED BY
Zhi Chen,
China Earthquake Administration, China
Xiaocheng Zhou,
China Earthquake Administration, China

*CORRESPONDENCE
Guiping Liu,
liugp@bjseis.cn

SPECIALTY SECTION
This article was submitted to Geohazards and Georisks, a section of the journal Frontiers in Earth Science

RECEIVED 30 April 2022
ACCEPTED 04 July 2022
PUBLISHED 05 September 2022

CITATION
Yang M, Liu G, Liu Z, Ma J, Li L, Wang Z, Hua P, Xing L, Sun X, Han K, Cui B and Wu X (2022), Geochemical characteristics of geothermal and hot spring gases in Beijing and Zhangjiakou Bohai fault zone.
Front. Earth Sci. 10:933066.
doi: 10.3389/feart.2022.933066

Geochemical characteristics of geothermal and hot spring gases in Beijing and Zhangjiakou Bohai fault zone

Mingbo Yang[1], Guiping Liu[1]*, Zhe Liu[2], Jingchen Ma[2], Liwu Li[3], Zhiguo Wang[1], Peixue Hua[1], Lantian Xing[3], Xiaoru Sun[1], Kongyan Han[1], Bowen Cui[1] and Xiaodong Wu[1]

[1]Beijing Earthquake Agency, Beijing, China, [2]Beijing Institute of Geo-Engineering, Beijing, China, [3]Northwest Institute of Eco-Environment and Resources Chinese Academy of Sciences, Lanzhou, China

The Beijing and Zhangjiakou-Bohai Fault Zone is a group of NW-W orderly active fault zones with high seismic activity and abundant geothermal resources since the Cenozoic. Many violent earthquakes occurred here, where it was an important area for earthquake monitoring and research. In order to explore the temporal and spatial variation characteristics of gas geochemistry in the Zhangjiakou-Bohai Fault Zone of the capital circle, this study cited the previous two-stage survey data of 23 geothermal hot springs in the west and east of the Zhangjiakou-Bohai Fault Zone of the capital circle in 2013 and 2018. In order to fill the gap in hot spring gas geochemistry in Beijing (the middle of the Zhangjiakou-Bohai Fault Zone), 21 emergent gas samples from hot springs were collected after many field surveys from October 2020 to November 2021. The test results of 44 gas samples with chemical compositions and isotope changes of helium, neon, and carbon showed that: (1) The helium isotope ratio ($^3He/^4He$ (Rc/Ra)) of hot spring gases in the Zhangjiakou-Bohai Fault Zone ranged between 0.03 and 2.86Ra (Ra = air, $^3He/^4He = 1.39 \times 10^{-6}$), and the calculated maximum proportion of mantle-derived helium was up to 35.4%. It was revealed that although the geological fluid in the fault zone mainly came from crustal source, the mantle-derived helium was still considerable. The hot spring gases in Beijing (the middle of the Zhangjiakou-Bohai Fault Zone) were mainly composed of nitrogen, whose concentration was more than 69%, featuring a low CO_2 concentration of 0–6.1% and a $\delta^{13}C_{CO2}$ value ranging from –19‰ to –9.6‰ (vs.PDB) and showing the mixing characteristics of organic sediments and mantle sources. (2) The upwelling release of mantle-derived materials in Zhangjiakou-Bohai Fault Zone shared a good corresponding relationship with regional seismicity, which could promote the inoculation and occurrence of regional earthquakes. In the peak area, the transition zone from the western mountainous area of the Zhangjiakou-Bohai Fault Zone to the plain showed that more mantle-derived materials upwelled, and more deep fluid upwelled. The comparative analysis of regional seismicity showed that deep fluid played an important role in controlling regional seismicity in the area

with relatively strong upwelling of deep fluid in the Zhangjiakou-Bohai Fault Zone.

KEYWORDS

helium isotope, carbon isotope, gas geochemistry, Zhangjiakou-Bohai fault zone, hot spring in geothermal well

1 Introduction

The subduction of the ancient Pacific Plate is the geodynamic mechanism which leads to the thinning and destruction of the lithospheric mantle in the North China Craton. The destruction area of the North China Craton mainly occurs in the area to the east of Taihang Mountain in North China, including the integral destruction of lithospheric mantle and the strong transformation and thinning of crust as well as the obvious changes in physicochemical properties of the lithospheric mantle (Zhu et al., 2011; Feng et al., 2020).

The Zhangjiakou-Bohai Fault Zone is located at the junction of three tectonic units: the North China Basin, Yanshan Uplift, and Taihang Mountain Uplift (Xu et al., 1998), where faults are intersected and cut to form a complex seismogenic structural pattern. The Zhangjiakou-Bohai Tectonic Zone starts from the northern margin of Taihang Mountain in the west, is distributed along the junction area of Yanshan Mountain and the North China Basin, and enters the Bohai Sea in the east. It is an important NW seismic activity zone in Eastern China. In this zone, 26 earthquakes above M6 occurred (Zhao et al., 2011), and it is an active zone of typical structural faults and earthquakes.

According to the research result of the relationship between the temporal and spatial changes of helium isotope and carbon isotope in hot spring gases and fault activity in active areas such as San Andreas fault and related structures in the United States (Kulongoski et al., 2013), North Anatolia fault in Turkey (Italiano et al., 2009) and a large number of volcanic fault areas in Japan (Umeda and Ninomiya, 2009), strong fault activity areas were good channels for deep material migration. In the area with a high helium isotope ratio of hot spring gases in an active fault zone, there was usually an obvious high conductivity and low velocity area in the deep part. According to the investigation result of the temporal and spatial variations of helium isotope and carbon isotope in hot spring gases in an active fault zone, the temporal and spatial variation characteristics of mantle-derived helium and carbon dioxide in different proportions could be obtained quantitatively (Zhou et al., 2020; Zhou et al., 2021), and then the relationship between the activity of the active fault zone and mantle-derived helium and carbon dioxide in hot spring gases was further studied.

The Zhangjiakou-Bohai Fault Zone is also rich in geothermal water resources. Due to the combination of its regional geological conditions and geothermal background, it is very favorable for the storage and formation of geothermal water, and it is also one of the areas with the richest low-temperature hot water resources in China (Chen, 1988; Pang et al., 2014). Zhangjiakou-Bohai Fault Zone covers a large area, and there is no systematic and comprehensive studies and investigations on geothermal water in the whole area. Previous scholars did some intermittent research on geothermal hydrology and helium isotope distribution characteristics in the western basin-ridge structure area and the eastern basin of the Zhangjiakou-Bohai Fault Zone. Lu (2016) However, the lack of research on Beijing, which is located in the middle of the Zhangjiakou-Bohai Fault Zone, leads to the incomplete exploration of the whole Zhangjiakou-Bohai Fault Zone. In order to more comprehensively and systematically discuss whether the deep fluid upwelling and its possible temporal and spatial changes also exist in the Zhangjiakou-Bohai Fault Zone, a systematic geochemical study on hot spring gases has been conducted in the central Beijing in recent years, and basic data have been provided for future geochemical seismic monitoring of hot spring gas, mineral resources evaluation and environmental research in Beijing and the Zhangjiakou-Bohai Fault Zone.

Two groups of conjugate movement faults (NE-NEE and NW-NWW) are mainly distributed in the Zhangjiakou-Bohai Fault Zone, which together form the NW-W Zhangjiakou-Bohai Fault Zone (Chen et al., 2016) and have a certain active period (Ma et al., 2004). Strong earthquakes occurred in these fault zones where they were the areas with the most frequent strong earthquakes. The formation of the present geological structure and geomorphic pattern in the Zhangjiakou-Bohai Fault Zone originated from tectonic activity since the Archean. The Mesozoic Yanshan movement not only caused the previous strata to fold and fracture with magmatic activity but also developed a series of NE, NWW, and near EW faults (Chen et al., 2016). As the North China fault block began to disintegrate, Taihang Mountain, Yanshan Mountain, and Luxi Mountain rose, and their interior settled. This helped cultivate the early form of the structure of the North China Basin. In the Paleogene period, large-scale uneven fault depression activities occurred in the North China Basin, forming a series of staggered patterns of fault depression uplifts and depressions. The thick Cenozoic deposits in the North China Rift Basin were in contrast with the ancient bedrock outcrops in Yanshan Mountain in the north and Taihang Mountain in the southwest. The piedmont fault difference could reach several kilometers. Even in the rift basin, there were many kinds of depressions, uplifts, and secondary uplift structural units, which constituted the complex structure of the upper crust of the Zhangjiakou-Bohai Fault Zone (Zhang et al., 2007).

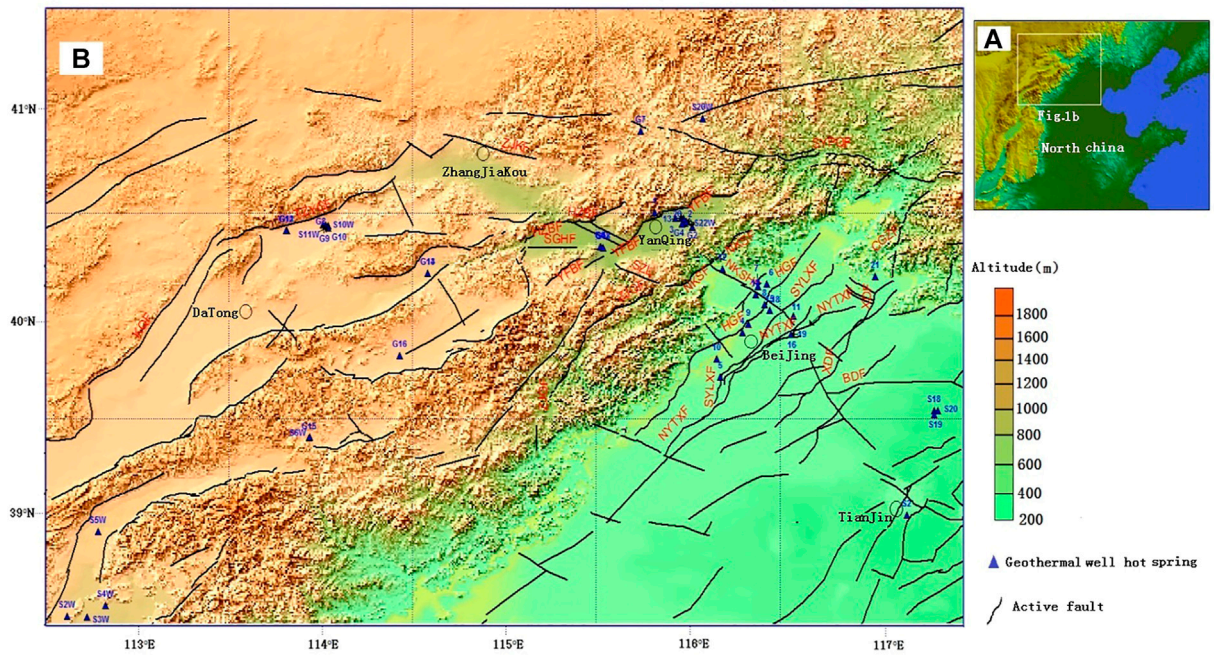

FIGURE 1
Distribution of gas sampling sites of hot springs in geothermal wells of the Zhangjiakou-Bohai Fault Zone. **(A)** Topographic map of North China. **(B)** Topographic map of the Zhangjiakou-Bohai Fault Zone and location map of sampling sites, active faults according to Xu et al. (2016).

Since the 1970s, the accuracy of earthquake location has become higher and higher. It was found that the earthquake distribution in the capital circle crossed the Yanshan Mountains, forming a very important seismic zone in the north of the North China-Zhangjiakou-Bohai Seismic Zone. Moreover, there was seismic activity in the vicinity of NE faults such as Hexiwu Fault, Liulingshan Northern Fault, Weiguang Basin Southern Margin Fault, Huangzhuang-Gaoliying Fault, and Xiadian New Fault, which formed a network distribution with the NWW Zhangjiakou-Bohai Seismic Zone (Ma et al., 2004).

Under the action of a single NEE principal compressive stress field, NWW tandem blocks moved easily, forming a NWW seismic activity intensive zone on the block boundary, while the conjugate NE or NEE faults had the structural conditions for earthquakes of moderate or strong magnitude or above. The Zhangjiakou-Bohai Fault Zone has become a structural zone closely related to earthquakes (Chen et al., 2016).

2 Measurement and experimental methods

From October 2020 to November 2021, after investigations on geothermal wells in Beijing, 21 hot spring gas samples from geothermal well were collected along the north margin of Yanji Basin, Huangzhuang-Gaoliying, Xiadian, and Nankou-Sunhe, NW faults in the Zhangjiakou-Bohai Fault Zone and related areas (Figure 1 and Supplementary Table S1).

In addition, using the previous survey work, from September 2011 to November 2012, the China Earthquake Administration predicted that it had conducted three field geological surveys in the western part of the Zhangjiakou-Bohai Fault Zone in the capital circle, investigated hot spring sites and took 18 gas samples; From July to August 2016, 24 samples of hot springs and geothermal water gas were taken from the east and west of the Zhangjiakou-Bohai Fault Zone in the capital circle (Figure 1; Supplementary Table S1).

The hot spring gas sampling container was a 500 ml glass bottle, and it was collected in the field by the drainage and gas taking method. The components of N_2, H_2, CO_2, O_2 and CH_4 in hot spring samples were measured by the Agilent Macro 490 portable gas chromatograph laboratory, and the measurement accuracy was estimated as follows: the relative standard deviation was <0.5% when the content was 1% ~ 100%, the relative standard deviation was <1% when the content was 0.01% ~ 1%, and the relative standard deviation was <0.001% ~ 0.01% (Zhou et al., 2015).

The He, Ne, and C isotopes in hot spring gas samples were analyzed by the Northwest Institute of Ecological Environment Resources, Chinese Academy of Sciences. The concentrations and isotopes of He and Ne in hot spring gases were analyzed by a Noblesse noble gas isotope mass spectrometer. When the R value

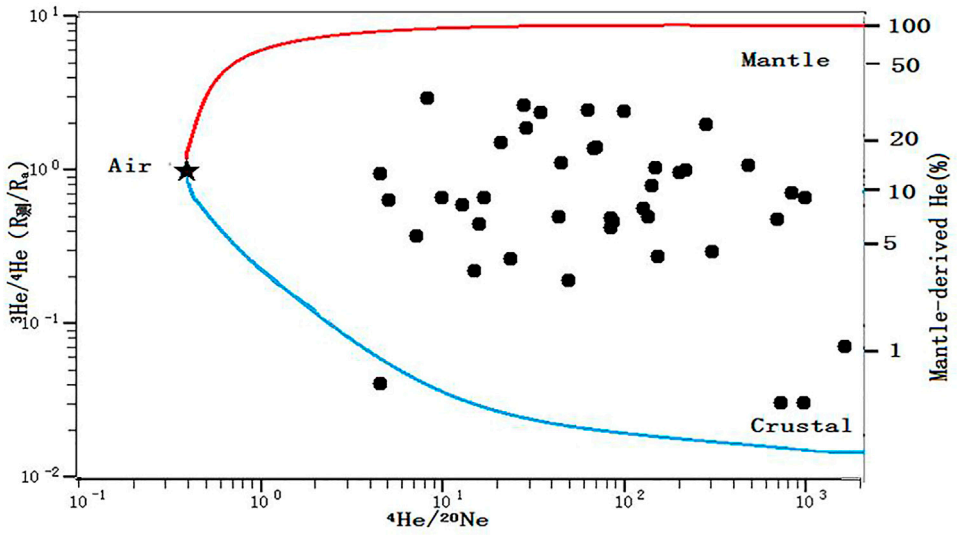

FIGURE 2
Plot of $^{3}He/^{4}He$ vs. $^{4}He/^{20}Ne$ average ratios in 44 samples of hot spring gas. Mixing lines between the atmosphere and upper mantle and the atmosphere and crust were calculated using the end members: air ($^{3}He/^{4}He$ = 1.4 × 10−6, $^{4}He/^{20}Ne$4 = 0.318), upper mantle ($^{3}He/^{4}He$ = 12 × 10−6, $^{4}He/^{20}Ne$ = 100, 000), old continental crust ($^{3}He/^{4}He$ = 0.02 × 10−6, $^{4}He/^{20}Ne$ = 100,000) (after Ozima and Podosek, 1983; Ballentine et al., 2005).

in helium isotope measurement was above 1×10^{-7}, the test error was ±10%, and the measurement data error at 1×10^{-8}~1×10^{-7} were ±15% (Cao et al., 2018). The carbon isotope ratio was analyzed by the Delta Plus XL mass spectrometer, which was manufactured by Thermo Finnigan, USA and consisted of HP6890 gas chromatography, combustion/conversion furnace, interface and the DeltaPlusXP mass spectrometer. Stable carbon isotope composition was expressed by $\delta^{13}C$; the accuracy of $^{13}C/^{12}C$ was 0.6‰ (Li et al., 2014).

3 Measurement results

He in mantle source, crust source and air had their own characteristic $^{3}He/^{4}He$ ratios, which were (1.1×10^{-5}~1.4×10^{-5}, 2×10^{-8} and 1.39×10^{-6} (Mamyrin et al., 1970; Ozima and Podosek, 1983). After atmospheric correction (Rc/Ra) of the $^{3}He/^{4}He$ value, the percentage of He in the mantle source could be calculated (Sano and Wakita, 1985).

The average proportion of helium from geothermal hot springs in Beijing's main fault zone in the Zhangjiakou-Bohai Fault Zone in this survey ranges from 0.03% to 35.4% (Supplementary Table S2).

Geothermal hot springs can be divided into two types according to the main components of the gases. In the first type, CO_2 concentration is the main component, and the average CO_2 concentration is more than 50%. In the second type, N_2 is the main component of hot springs. It can be seen from the concentration data of geothermal hot springs surveyed (Supplementary Table S2) that the main components of the gases are N_2, which is a main component of hot springs. There were a total of 21 hot springs, and the average concentration of N_2 in hot springs ranged from 63.89% to 94.74%. The average concentration range of He in all hot spring gases was 48×10^{-6}~1502×10^{-6}, that of H_2 was 265.1×10^{-6}, and that of CH4 was 0.070%~38.41%. The average distribution range of $^{3}He/^{4}He$ (Rc/R_a) was 0.24~2.86, while that of $\delta^{13}C_{CO2}$ (PDB) was -23.6‰~−2.9‰, and that of $\delta^{13}C_{CH4}$ (PDB) was -63.7‰ ~−14.1‰ (Supplementary Table S2).

Based on the previous measurement results of geothermal hot spring gases in the Zhangjiakou-Bohai Fault Zone, the average ratio of helium in mantle source of geothermal hot spring gases with helium isotope measured in 44 areas ranged from 0.03% to 35.4%, and the helium in hot spring gases mainly came from crust sources (Supplementary Table S2). However, 40 of them had obvious mantle-derived helium (>2%) (Figure 2).

4 Discussion and conclusion

4.1 Source of hot spring gases

4.1.1 He

The $^{3}He/^{4}He$ values of hot spring gas samples from Beijing and the Zhangjiakou-Bohai Fault Zone were less than 3.0Ra, showing the characteristics of typical mixed source helium. The $^{3}He/^{4}He$ ratios in mantle source, crust source and air were (1.1×10^{-5}, 2×10^{-8} and 1.39×10^{-6} (Mamyrin et al., 1970; Ozima and

Podosek, 1983; Wei et al., 2015; Mar Alonso, et al., 2021; Domokos, et al., 2021). After atmospheric correction (Rc/Ra) of the $^3He/^4He$ value, the percentage of He in the mantle source could be calculated (Sano and Wakita, 1985). The average ratio of mantle-derived helium in hot springs in Beijing and the Zhangjiakou-Bohai Fault Zone ranged from 0.03% to 35.40%. Therefore, helium in hot springs was mainly from the crust source (64.6%–99.67%) (Figure 2 and Supplementary Table S2). 40 of all 44 geothermal hot springs had obvious mantle-derived helium (>2%) (Supplementary Table S2).

It was easy to observe a large amount of mantle-derived helium in volcanic areas such as Tengchong Volcano (Zhao et al., 2012) and Wudalianchi Volcano (Xu et al., 2013). However, there were no Cenozoic active volcanoes in Beijing, so it was impossible for mantle-derived helium to be released in volcanic areas. Mantle-derived helium was diluted by helium from the crust during its upward migration along the deep fault, which was also observed in the southwest fault zone of China (Zhou et al., 2015; Zhou et al., 2020). In addition, the mantle-derived helium in the Zhangjiakou-Bohai Fault Zone could not be ^3He produced from tritium decay during nuclear bomb explosions (Yokoyama et al., 1999).

In general, Zhangjiakou-Bohai Fault Zone geothermal hot springs had obvious mantle-derived helium (>2%); this is related to the destruction of the North China Craton The subduction of the Pacific Plate led to the destruction of the North China Craton and the up welling of mantle magma, enhanced fluid metasomatism, melting and magmatism (Zhu et al., 2011), and the Zhangjiakou-Bohai Fault Zone provided a good channel for upward migration of mantle-derived helium.

The relatively high helium isotope $^3He/^4He$ value is located in the Yanfan basin-Changping area, which belongs to the transition zone from Yanshan uplift mountainous area to plain (Figure 8).

4.1.2 CO_2

The carbon isotope composition of carbon-containing compounds in hot springs contains a lot of important information (Hilton, 1996; Kulongoski et al., 2013; Babuška et al., 2016). A large number of research results showed that $\delta^{13}C_{CO2}$ of organic origin CO_2 was generally less than −10‰ and mainly distributed between −30‰ and −10‰; $\delta^{13}C_{CO2}$ of inorganic origin CO_2 was generally greater than−8‰ and mainly distributed between −8‰ and +3‰. In inorganic origin CO_2, the $\delta^{13}C_{CO2}$ value of CO_2 transformed from carbonate rock was close to that of carbonate rock, which was about 0 ± 3‰. The $\delta^{13}C_{CO2}$ value of CO_2 of volcanic magma origin and mantle origin was −6‰ ± 2‰ (Domokos et al., 2021).

Among the gases of 44 hot springs, only the central Beijing tectonic zone had complete CO_2 concentration data and carbon isotope data. There were some CO_2 concentration data in the west. The concentration of CO_2 in the hot springs of Beijing and part of the western Zhangjiakou-Bohai Fault Zone was low, ranging between 0–6.1%, and the concentration of N_2 was high, ranging between 69.18–99.42%. Carbon isotopes of CO_2 from various sources in the hot spring gases of Beijing overlapped with each other.

It can be seen from the relationship of $\delta^{13}C_{CH4}$−−$\delta^{13}C_{CO2}$ that the organic origin CO_2 in the gas of well points 11, 13, 15, 10, 12, 1, 14, 16, and 21 was mainly formed by methane oxidation (Figure 4).

In Beijing, $\delta^{13}C_{CO2}$ values vary from −19‰ to −9.6‰, which shows the characteristics of organic sediments mixed with mantle origin (mainly organic). Figure 3 shows the analytical results of Beijing hot spring gas. It is then clear that all Beijing hot spring gases are plotted within the two mixing lines. This feature strongly suggests that CO_2 in Beijing hot spring gases is released from three different sources: crustal metamorphic, mantle and organic components (Figure 3).

The $\delta^{13}C_{CO2}$ value is mainly organic, but the relatively high $\delta^{13}C_{CO2}$ value in the Yanfan basin-Nankoushanqian fault area shows that mantle-sourced CO_2 is also relatively high (Figure 4).

4.1.3 CH_4

The concentration of CH_4 in hot spring gases of the main tectonic zone of Beijing mostly varied from 0% to 6.1%. However, the XJ point of Xiji, which was located at the intersection of Zhangjiakou-Bohai Fault Zone and Xiadian Fault, was up to 27.06%. This is worthy of further study. The relationship diagram of carbon isotope$\delta^{13}C_{CH4}$–$\delta^{13}C_{CO2}$ (Figure 5) showed that the methane of hot spring sites of geothermal well No.2 and No.20 was of inorganic origin. The other hot springs were of organic origin, among which the gas CH_4 of the hot spring sites No.5, No.7, No.4, and No.19 was formed by methane-producing bacteria under strict anaerobic conditions (Domokos et al., 2021). The gas CH_4 in hot spring wells No. 3, 6, and 18 was mainly formed by carbon dioxide reduction.

4.1.4 H_2

The hydrogen in the fault zone may have the following sources: (1) As a deep source of gas, a large amount of H_2 was stored on the Earth when the Earth was formed. H_2 would escape into the atmosphere along the weak areas of the Earth (Neal and Stanger, 1983); (2) When the fracture broke, water-rock reaction occurred on the fresh silicate rock surface to produce hydrogen (Kameda et al., 2003). The more active the active fault zone was, the more developed the fresh silicate rock fracture surface in the fault zone was, and the more H_2 was produced (Kita et al., 1982); (3) U and Th elements in rocks produced high concentrations of hydrogen with water during radioactive decay (Lin et al., 2005; Donze et al., 2020); (4) A large amount of hydrogen was produced in the serpentinization process of olivine (Katayama et al., 2010; Donze et al., 2020); (5) Soil organic matters produced hydrogen during anaerobic bacterial fermentation (Libert et al., 2011). H_2 is the lowest density gas known in the

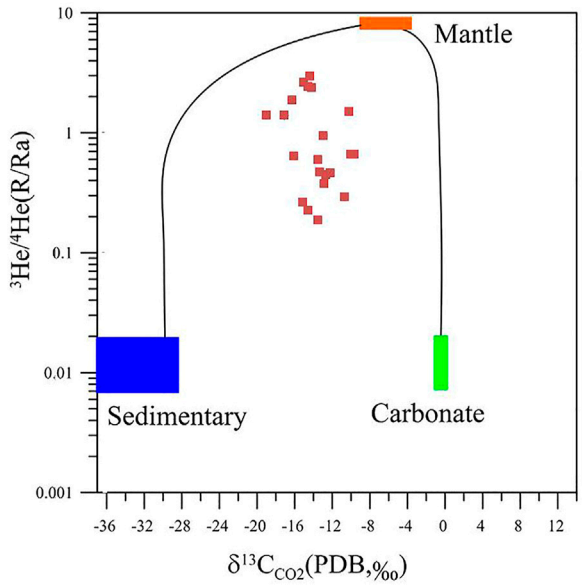

FIGURE 3
Diagram of $^3He/^4He$ (R/Ra) vs.$\delta^{13}C_{CO2}$ (PDB,‰) ratios (Mixed line according to Xu et al., 1984).

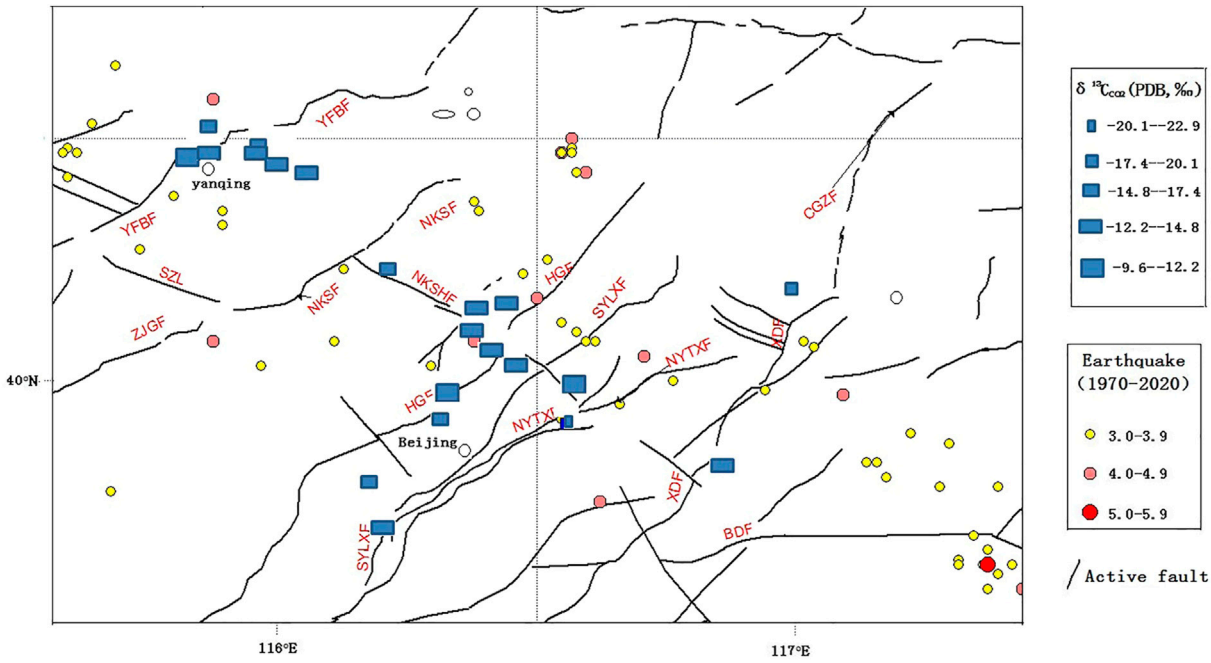

FIGURE 4
$\delta^{13}C_{CO2}$ spatial distribution map in the Zhangjiakou-Bohai Fault Zone Midwest area.

world, featuring strong diffusivity and penetrability. It is difficult to dissolve in water, slightly polluted by dissolving hydrogen in atmospheric precipitation during the upward migration of deep crust, and it is a very good tracer gas (Neal and Stanger, 1983). The survey results showed that the normal change of hydrogen concentration in Beijing was basically between 0 and 100ppm, which was a micro-concentration change (Supplementary Table S2).

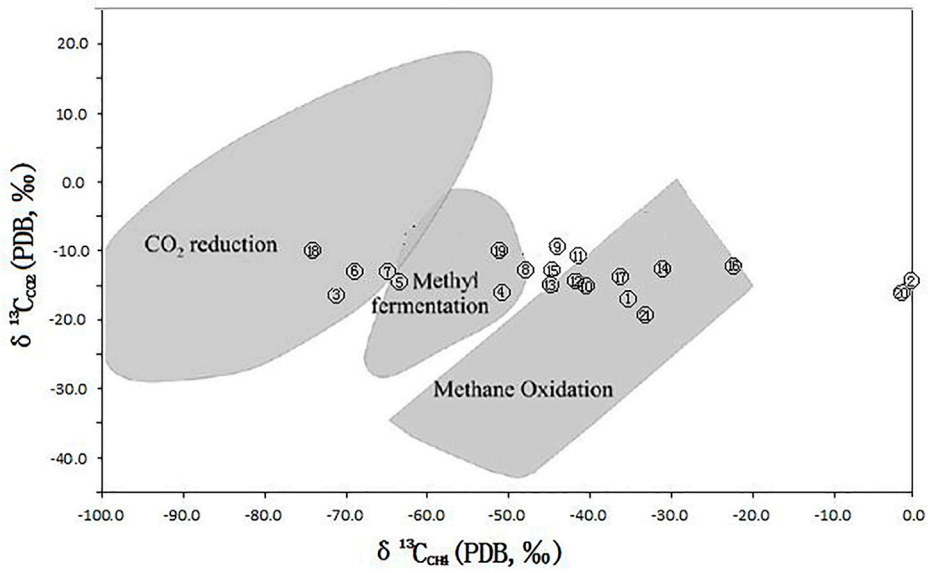

FIGURE 5
Relationship diagram of $^{13}C_{CH4}$–$\delta^{13}C_{CO2}$ (base figure according to Woltemate et al. (1984)).

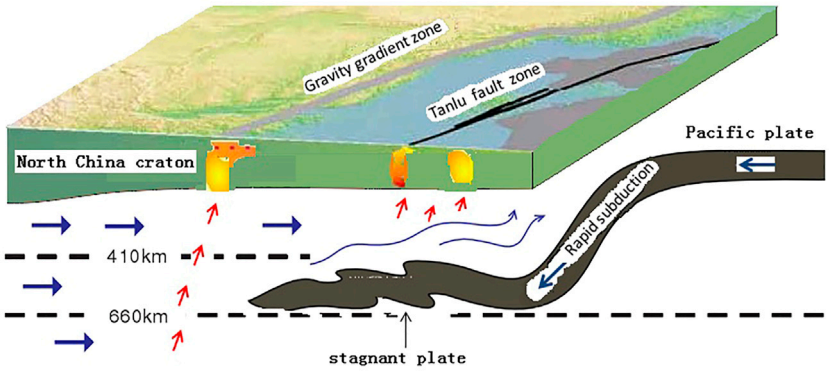

FIGURE 6
Mantle convection mechanism of destruction and transformation of the North China Craton (base map after Zhu et al., 2011).

4.2 Relationship between spatial change of the gases of hot spring in geothermal well and fault activity and seismic activity

Since the 1980s, a group of scholars have studied the upper mantle structure of the crust in North China by tomography. The present strong seismic activity and obviously low velocity of the lower crust in North China are different from other stable cratons in the world. The lithospheric structure is highly heterogeneous, which is important evidence of the destruction of the North China Craton.

The subduction of the Pacific Plate has a profound influence on the velocity structure of the North China Craton. It can be clearly seen from the topography and the distribution of gravity gradient zones that their boundary lines are parallel to the Japanese Trench and the Ryukyu Trench. The underthrust of the Pacific Plate made the upper mantle of the North China Craton form a mantle wedge-lead, and the geochemical action above the mantle wedge made the asthenosphere material rise and result in the thinning and fracture of the lithosphere (Wu et al., 2008; Zhu et al., 2011). However, the impact of the subduction of the Pacific Plate is far more than that. Geological activities such as magma intrusion, earthquakes, volcanic activity, and mineral formation caused by the destruction of the North China Craton are closely related to

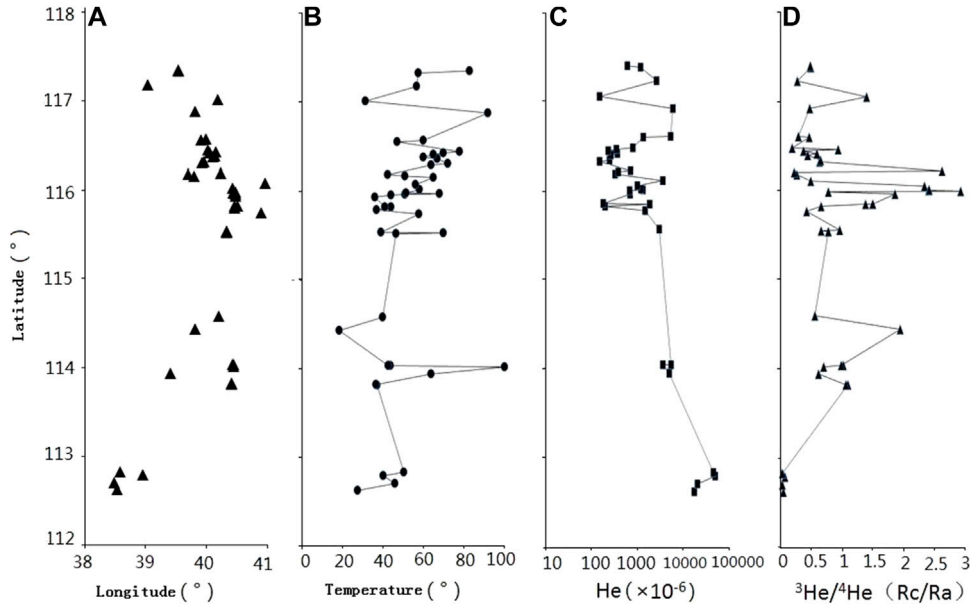

FIGURE 7
Spatial variation of hot spring water temperature; He concentration in hot spring gases and helium isotope correction value **(A)** distribution of geothermal hot spring sampling sites; **(B)** temperature; **(C)** He concentration; **(D)** helium isotope correction value.

it. The subduction of the Pacific Plate can provide evidence for the geodynamics of the Zhangjiakou-Bohai Fault Zone (Zhu and Xu, 2019) (Figure 6).

The intrusion of mantle-derived materials in the middle and upper crusts and the horizontal change of hot rock mass in the Zhangjiakou-Bohai Seismic Zone may be due to the increase in the supply of deep crustal fluids caused by the intrusion of mantle-derived materials. The long-standing fluids under the seismogenic layer of the crust will affect the structure of the fault zone, reduce the strength of the fault zone and change the regional stress field, which will lead to the concentration of stress on the fault zone and then easily cause earthquakes (Yang et al., 2018) and generate the Zhangjiakou-Bohai Fault Zone.

4.2.1 Spatial differences of helium release from deep source

The existing observation data showed that the unsteady mantle flow caused by the continuous subduction of the Pacific Plate to the East Asian continent since the Mesozoic played an important role in the overall destruction of the eastern part of the North China Craton [13, 24, 36, and 61]. The mantle magma caused by the destruction of the North China Craton invaded the crust of North China and caused the release of deep-source helium in the mantle, including the Zhangjiakou-Bohai Fault Zone. In terms of space, the trend of two large tectonic zones in Eastern China (the north-south gravity gradient zone and the Tanlu Fault Zone) also showed a correlation with the subduction of the Pacific Plate (Figure 6).

The helium isotope correction value of geothermal hot spring water in the Zhangjiakou-Bohai Tectonic Zone showed an obvious peak area from west to east (Figures 7, 8), which indicated that the Rc/Ra value in the Zhangjiakou-Bohai Fault Zone showed obvious spatial distribution differences from west to east:

This peak area (about E116° in longitude) included the Yanfan Basin-Changping Area, which was located in the transition zone from the mountainous area of the Yanshan Uplift to the plain. It was the intersection transition zone of two tectonic units with complex fault structures and active seismic activity (Li, 2021), and its highest mantle source He was 35.4%. Other areas did not have such remarkable characteristics of mantle-derived helium release. From the differences in spatial changes (Wei et al., 2015) this peak area (about E116° in longitude) was just in a transition zone. That was from the central and western parts of the North China Craton where the lithosphere was partially reformed or thinned to the eastern part of the craton (Figure 6). This transition zone was closely related to the significant changes of crust and lithosphere thickness near the boundary between the eastern part of the Craton and the central and western parts of the Craton. The gravity gradient zone between the north and the south was closely related to the sudden change in topography (Figure 6), which also indicated the particularity of this transitional zone.

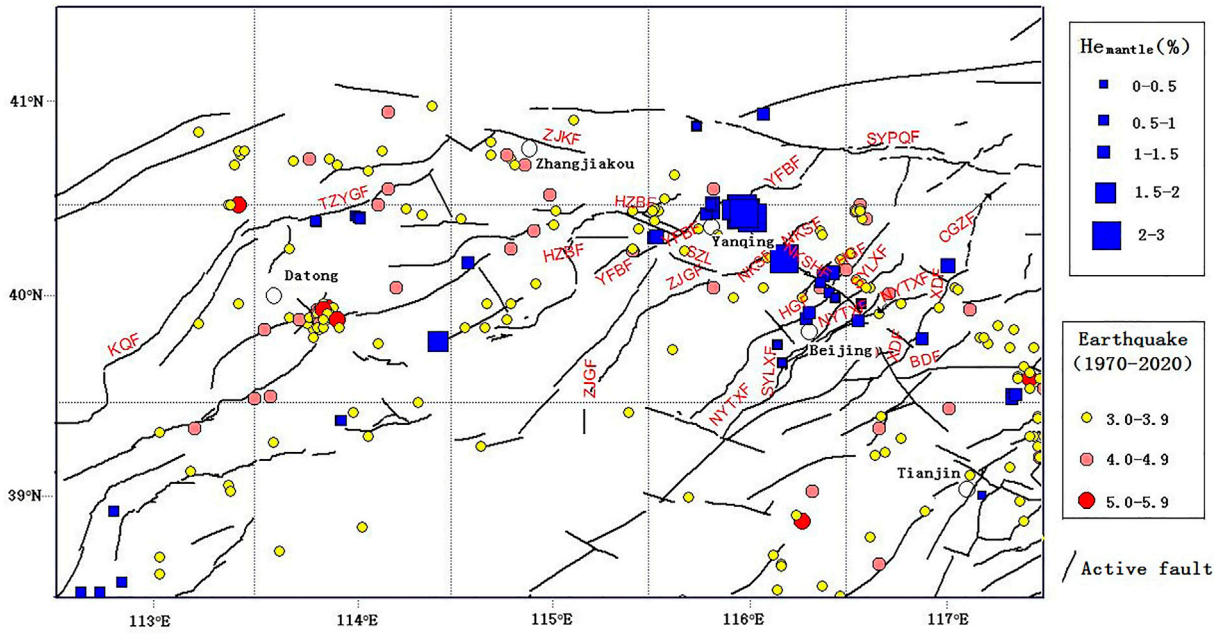

FIGURE 8
Relationship between the ratio of mantle-derived helium in geothermal wells and hot spring wells in the Zhangjiakou-Bohai Fault Zone and seismicity.

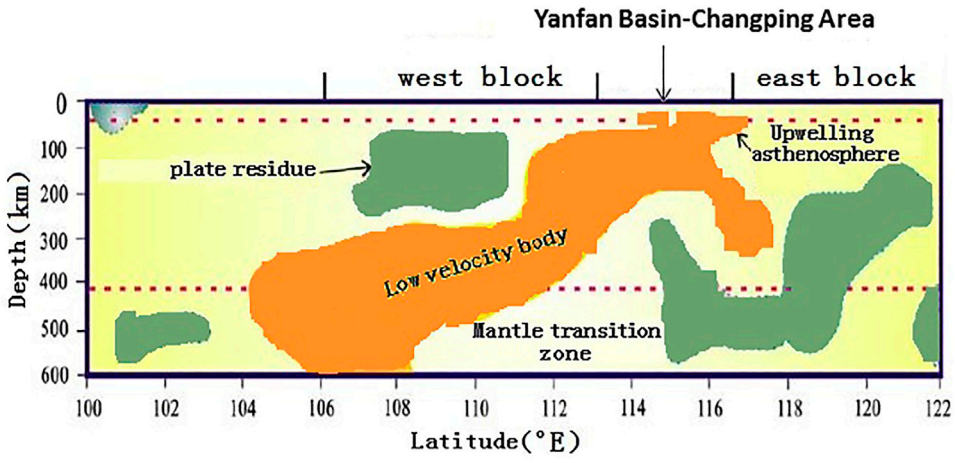

FIGURE 9
Mantle structure model of the North China Craton at 40°N latitude (base map after Santosh et al., 2010).

From the source of helium, the mantle magma caused by the destruction of the North China Craton invaded the crust of North China, and it also caused the release of deep-source helium in the mantle, including the Zhangjiakou-Bohai Fault Zone and the emergence of peak areas. Specifically, partial melting (or initial partial melting) of lithosphere or asthenosphere mantle rocks is the most effective way to release mantle-derived He (Ballentine and Burnard, 2002), and the most direct evidence is the active volcano system (or Quaternary or Cenozoic volcanic activity area) and the existence of deep melt revealed by geophysical observation. In the volcanic activity areas, mantle-derived melt can transport mantle He to the Earth's surface and atmosphere through magma eruption or intrusion. This is common in volcanic activity areas represented by mid-ocean

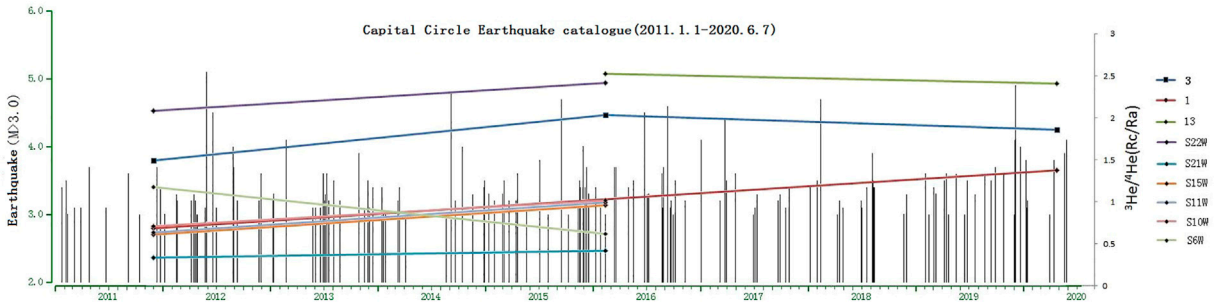

FIGURE 10
The relationship between seismic activities with percentage of mantle-derived He in hot spring gases along the Zhangjiakou-Bohai Fault Zone.

ridge and island arc volcanic areas. This area is a non-volcanic activity area, and there is an obvious low velocity anomaly in the lower mantle 70 km (Figure 9) (Santosh et al., 2010), which indicates that the deep lithospheric mantle in this area may be partially melted, which provides a material basis for the crustal displaying of mantle-derived He.

Generally, the rapid and short-range migration and other factors will cause the mantle He to be contaminated with radioactive He to a relatively low degree. However, with the distance from the Yanqing-Changping Area (the highest proportion of mantle-derived He is 35.4%) along the trend of the fault zone or the distance from the fault zone in the vertical direction, the amount of radioactive He in the crust will increase gradually, which will lead to the difference in the spatial distribution of mantle-derived materials inside and outside the fault zone.

4.2.2 The nature, scale, and attitude of the fault zone play a decisive role in the migration of mantle-derived components to the earth's surface.

According to the research, the peak area of the mantle source located at (about E116° n longitude) included the northern margin fault of the Yanji Basin, and the low-velocity bodies in the crust were found below the Machikou Depression (Gao et al., 2010). The active faults in the shallow crust that controlled these depression structures included the NEE fault in the northern margin of the Yanji Basin, the Nankou piedmont fault, and the Huangzhuang-Gaoliying fault. These faults have been active since the late Pleistocene, and they are very active. The deep faults in the Earth's crust and active faults in the shallow part of the crust that controlled the development of basins might be in a state of "convergence without intersection" (Gao et al., 2010), and these deep and shallow faults intersected with the Sunhe fault in the northwest to the south, which led to the increase in fragmentation and permeability of the fault zone and was conducive to the rapid migration of mantle-derived materials to the Earth's surface.

Therefore, the deep fault zone with high permeability and a high dip angle provided favorable structural conditions for the upwelling of mantle-derived materials in the region. This phenomenon was also observed at the intersection of Xianshuihe Fault, Longmenshan Fault and Moxi Fault in China (Zhou et al., 2017; Zhu et al., 2017; Zhou et al., 2020; Li et al., 2022; Xu et al., 2022) and in the western USA (Hu et al., 2018). The area with low P wave velocity corresponded to a higher helium isotope. In the intersection area of faults, faults developed, which provided a good channel for the upward migration of deep fluids. A large amount of mantle-derived helium migrated to the Earth's surface.

The contribution rate of mantle-derived helium in the Zhangjiakou-Bohai Fault Zone was at a medium level. Although the seismic activity was not higher than that in Sichuan-Yunnan, it still had strong activity. Especially, the Yanji Basin, which was located in the Zhangjiakou-Bohai Fault Zone with strong seismicity and high frequency, had a high value background of mantle-derived helium (Zhou, 2011; Zhang, 2013) and an abnormal high value background of soil gas concentrations of He and H_2, CO_2, and Rn (Li et al., 2009). It was worthy of further research on earthquake prediction as a key monitoring area.

4.3 Time change of helium isotope in geothermal hot spring gases

From October 2011 to November 2020, there were more than two gas helium isotope analysis data in 9 hot spring spots in the Zhangjiakou-Bohai Fault Zone, among which 8 spots showed a synchronous increase and still maintained a high value until April 2020. During this period, the earthquakes with a magnitude of 3 or above in the capital circle showed a trend of increasing activity from 2015 (Figure 10). This might be related to the increase in upwelling of deep fluid in the Zhangjiakou-Bohai Fault Zone. The rising helium isotope value of hot spring gases in this area indicated that there was an obvious upwelling of deep

fluid, which might weaken the fault to some extent (Cappa and Rutqvist, 2012; Klemperer et al., 2013; X Zhang et al., 2019) and increase the pore pressure inside the fault (Giammanco et al., 2008; Terakawa et al., 2013; Berryman, 2016). This played an important role in promoting the preparation and occurrence of earthquakes (Fulton and Saffer, 2009; Brauer et al., 2011). At present, the monitoring time interval of helium isotope in the Zhangjiakou-Bohai Fault Zone is long, and the resolution of earthquake prediction is not sufficient. It is necessary to conduct high-density long-term observations in the future and further observe the correlation between corresponding changes and earthquakes with the observation of gas concentration.

5 Conclusion

1) According to the gas composition characteristics of hot springs, the geothermal hot springs in the Zhangjiakou-Bohai Fault Zone are mainly composed of N_2. Helium in hot spring gases mainly comes from the crust source, and N_2 mainly comes from the atmosphere.
2) The existing observation data showed that Zhangjiakou-Bohai Fault Zone geothermal hot springs had obvious mantle-derived helium (>2%). This is related to the destruction of the North China Craton, the subduction of the Pacific Plate led to the destruction of the North China Craton and the up welling of mantle magma, enhanced fluid metasomatism, melting, and magmatism and Zhangjiakou-Bohai Fault Zone provided a good channel for upward migration of mantle-derived helium, the mantle magma caused by the destruction of the North China Craton invaded the crust of North China, and caused the release of deep-source helium in the mantle, including the Zhangjiakou-Bohai Fault Zone.
3) The upwelling release of mantle-derived materials in Zhangjiakou-Bohai Fault Zone has a good corresponding relationship with regional seismicity, and it may promote the preparation and occurrence of regional earthquakes. The deep faults in the Earth's crust have the deep tectonic background of seismic development.
4) There is an obvious peak in the helium isotope of geothermal hot springs of the Zhangjiakou-Bohai Fault Zone, and it is located in the transition zone from the mountainous area to the plain in the Zhangjiakou-Bohai Fault Zone- It also happens to be the North-South gravity gradient belt across North China (about E116° in longitude). From there more mantle-derived materials upwelled.

Data availability statement

The original contributions presented in the study are included in the article/Supplementary Material; further inquiries can be directed to the corresponding author.

Author contributions

MY: task management, field investigation, paper writing; GL: document collection and sorting, paper compilation; ZL, field investigation, data collection; MY: data collection and field investigation; GL: operation of tasks; PH: field survey, sampling; XS: data sorting; KH: preparation and commissioning of instruments; BC: instrument measurement; XW, preparation and coordination of field work; LL and LX participated in the analysis of gas isotope sample.

Acknowledgments

We thank the editor and two reviewers for their constructive comments and suggestions.

Conflict of interest

The authors declare that the research was conducted in the absence of any commercial or financial relationships that could be construed as a potential conflict of interest.

Publisher's note

Supplementary material

The Supplementary Material for this article can be found online at: https://www.frontiersin.org/articles/10.3389/feart.2022.933066/full#supplementary-material

Reference

Alonso, M., Pérez, N. M., Padrón, E., Hernández, P. A., Melián, G. V., Sumino, H., et al. (2021). Changes in the thermal energy and the diffuse 3He and 4He degassing prior to the 2014-2015 eruption of Pico do Fogo volcano, Cape Verde. *J. Volcanol. Geotherm. Res.* 416, 107271. ISSN 0377-0273. doi:10.1016/j.jvolgeores.2021.107271

Babuška, V., Růžek, B., and Dolejš, D. (2016). Origin of earthquake swarms in the Western Bohemian Massif: Is the mantle CO2 degassing, followed by the Cheb Basin subsidence, an essential driving force? *Tectonophysics* 668-669, 42–51. doi:10.1016/j.tecto.2015.12.008

Ballentine, C. J., and Burnard, P. G. (2002). 12. Production, release and transport of noble gases in the continental crust. *Rev. Mineral. Geochem.* 47, 481–538. doi:10.2138/rmg.2002.47.1210.1515/9781501509056-014

Berryman, J. G. (2016). Role of fluid injection in the evolution of fractured reservoirs. *Int. J. Eng. Sci.* 103, 45–58. doi:10.1016/j.ijengsci.2016.02.004

Bräuer, K., Kämpf, H., Koch, U., and Strauch, G. (2011). Monthly monitoring of gas and isotope compositions in the free gas phase at degassing locations close to the Nový Kostel focal zone in the Western Eger Rift¸ Czech Republic. *Chem. Geol.* 290 (3), 163–176. doi:10.1016/j.chemgeo.2011.09.012

Cao, C., Zhang, M., Tang, Q., Yang, Y., Lv, Z., Zhang, T., et al. (2018). Noble gas isotopic variations and geological implication of Longmaxi shale gas in Sichuan Basin, China. *Mar. Petroleum Geol.* 89, 38–46. doi:10.1016/j.marpetgeo.2017.01.022

Cappa, F., and Rutqvist, J. (2012). Seismic rupture and ground accelerations induced by CO2 injection in the shallow crust. *Geophys. J. International* 190 (3), 1784–1789. doi:10.1111/j.1365-246x.2012.05606.x

Chen, C., Jianming, H. E., Layue, L. I., and Long, D. U. (2016). Analysis of the deformation characteristics of Zhangjiakou-Bohai Fault zone and its adjacent regions based on crossfault observation data and GPS data[J]. *South china J. Seismol.* 36 (3), 17–28. doi:10.13512/j.hndz.2016.03.003

Chen, M. (1988). *North China geothermal [m]*. Beijing: Science Press.

Domokos, G., Pujol, M., Gilfillan, M., Stuart, V., and Stuart, F. M. (2021). Noble gases constrain the origin, age and fate of CO2 in the vaca muerta shale in the neuquén basin (Argentina). *Chem. Geol.* 577, 120294. ISSN 0009-2541. doi:10.1016/j.chemgeo.2021.120294

Donze, F., Truche, L., Namin, P., Lefeuvre, N., and Bazarkina, E. (2020). Migration of natural hydrogen from deep-seated sources in the são francisco basin, Brazil. *Geosciences* 10, 346. doi:10.3390/geosciences10090346

Feng, Y., Yang, J., Sun, J., and Zhang, J. (2020). Material records of North China Craton destruction induced by Mesozoic paleo Pacific plate subduction. *Sci. Sin. -Terrae.* 50, 651–662. doi:10.1360/SSTe-2019-0210

Fulton, P. M., and Saffer, D. M. (2009). Potential role of mantle-derived fluids in weakening the San Andreas Fault. *J. Geophys. Res.* 114 (B7), B07408. doi:10.1029/2008jb006087

Gao, Z., Chen, Q., Huang, J., Cheng, Q., and Li, L. (2010). Velocity structure beneath the active faults in beijing area and their seismo-tectonic characteristics. *Technol. Earthq. Disaster Prev.*, 5. 271. 280.

Giammanco, S., Palano, M., Scaltrito, A., Scarfì, L., and Sortino, F. (2008). Possible role of fluid overpressure in the generation of earthquake swarms in active tectonic areas: The case of the Peloritani Mts. (Sicily, Italy). *J. Volcanol. Geotherm. Res.* 178 (4), 795–806. doi:10.1016/j.jvolgeores.2008.09.005

Hilton, D. R. (1996). The helium and carbon isotope systematics of a continental geothermal system: results from monitoring studies at Long Valley caldera (California, U.S.A.). *Chem. Geol.* 127 (4), 269–295. doi:10.1016/0009-2541(95)00134-4

Hu, J., Badal, J., Yang, H., Li, G., and Peng, H. (2018). Comprehensive crustal structure and seismological evidence for lower crustal flow in the southeastern margin of Tibet revealed by receiver functions. *Gondwana Res.* 55, 42–59. doi:10.1016/j.gr.2017.11.007

Italiano, F., Martinelli, G., Bonfanti, P., and Caracausi, A. (2009). Long-term (1997-2007) geochemical monitoring of gases from the Umbria-Marche region. *Tectonophysics* 476, 282–296. doi:10.1016/j.tecto.2009.02.040

Kameda, J., Saruwatari, K., and Tanaka, H. (2003). H2 eneration in wet grinding of granite and single-crystal powders and implications for H2 oncentration on active faults. *Geophys. Res. Lett.* 30, 2063. doi:10.1029/2003gl018252

Katayama, I., Kurosaki, I., and Hirauchi, K. (2010). Low silica activity for hydrogen generation during serpentinization: An example of natural serpentinites in the Mineoka ophiolite complex, central Japan. *Earth Planet. Sci. Lett.* 298, 199–204. doi:10.1016/j.epsl.2010.07.045

Kita, I., Matsuo, S., and Wakita, H. (1982). H2generation by reaction between H2O and crushed rock: An experimental study on H2degassing from the active fault zone. *J. Geophys. Res.* 87 (B13), 10789–10795. doi:10.1029/jb087ib13p10789

Klemperer, S. L., Kennedy, B. M., Sastry, S. R., Makovsky, Y., Harinarayana, T., and Leech, M. L. (2013). Mantle fluids in the Karakoram fault: Helium isotope evidence. *Earth Planet. Sci. Lett.* 366, 59–70. doi:10.1016/j.epsl.2013.01.013

Kulongoski, J. T., Hilton, D. R., Barry, P. H., Esser, B. K., Hillegonds, D., and Belitz, K. (2013). Volatile fluxes through the Big Bend section of the San ndreas Fault, California: Helium and carbon-dioxide systematics. *Chem. Geol.* 339, 2–102. doi:10.1016/j.chemgeo.2012.09.007

Li, H. (2021). Earthquake mechanism analysis of cross-faults system of Zhangjiakou-bohai fault belt in North China[J]. *IOP Conf. Ser. Earth Environ. Sci.* 658 (1), 012–013. doi:10.1088/1755-1315/658/1/012013

Li, Y., Du, J., Wang, F., Zhou, X., Pan, X., and Wei, R. (2009). Geochemical characteristics of soil gas in Yanqing--Huailai basin , North China. *Act. a Seismol. Sin.* 31 (1), 82–91.

Li, Z., Wang, X., Li, L., Zhang, M., Tao, M., Xing, L., et al. (2014). Development of new method of δ13C measurement for trace hydrocarbons in natural gas using solid phase micro-extraction coupled to gas chromatography isotope ratio mass spectrometry. *J. Chromatogr. A* 1372, 228–235. doi:10.1016/j.chroma.2014.10.089

Li, Q., Zhao, C., Wang, Y., Zhou, Y., and Ran, H. (2022). Spring gas geochemistry in the weixi-qiaohou fault zone: understanding the fluid characteristics of the Western boundary of the sichuan-yunnan rhombic block. *Geochem. Int.* 60 (1), 109–121. doi:10.1134/s0016702921150027

Libert, M., Bildstein, O., Esnault, L., Jullien, M., and Sellier, R. (2011). Molecular hydrogen: An abundant energy source for bacterial activity in nuclear waste repositories. *Phys. Chem. Earth, Parts A/B/C* 36, 1616–1623. doi:10.1016/j.pce.2011.10.010

Lin, L. H., Hall, J., Lippmann-Pipke, J., Ward, J. A., Lollar, B. S., DeFlaun, M., et al. (2005). Radiolytic H2 in continental crust: Nuclear power for deep subsurface microbial communities. *Geochem. Geophys. Geosystems* 6, Q07003. doi:10.1029/2004gc000907

Lu, C. (2016). *Geochemical characteristics of fluid and its Genesis in the capital area of China*. Beijing: Institute of earthquake forecasting, CEA.

Ma, W., Xu, X., Yu, G., and Zhang, L. (2004). The relationship between seismic activity and fault activity in Beijing region. *Seismol. Geol.* 26 (2), 293–304. doi:10.1007/BF02873097

Mamyrin, B. A., Anufrier, G. S., Kamensky, I. L., and Tolstikhin, I. N. (1970). Determination of the isotopic composition of helium in the atmosphere. *Geochem. Int.* 7, 498–505.

Neal, C., and Stanger, G. (1983). Hydrogen generation from mantle source rocks in Oman. *Earth Planet. Sci. Lett.* 66, 315–320. doi:10.1016/0012-821x(83)90144-9

Ozima, M., and Podosek, F. A. (1983). *Noble gas geochemistry*. Cambridge: Cambridge University Press, 367.

Pang, Z., Huang, S., and Hu, S. (2014). Progress and Prospect of geothermal research in China(1995-2014). *Geol. Sci.* 2014 (3), 719–727.

Sano, Y., and Wakita, H. (1985). Geographical distribution of3He/4He ratios in Japan: Implications for arc tectonics and incipient magmatism. *J. Geophys. Res.* 90, 8729–8741. doi:10.1029/jb090ib10p08729

Santosh, M., Zhao, D., and Kusky, T. (2010). Mantle dynamics of the Paleoproterozoic North China Craton: A perspective based on seismic tomography. *J. Geodyn.* 49 (1), 39–53. doi:10.1016/j.jog.2009.09.043

Terakawa, T., Hashimoto, C., and Matsu'ura, M. (2013). Changes in seismic activity following the 2011 Tohoku-oki earthquake: Effects of pore fluid pressure. *Earth Planet. Sci. Lett.* 365, 17–24. doi:10.1016/j.epsl.2013.01.017

Umeda, K., and Ninomiya, A. (2009). Helium isotopes as a tool for detecting concealed active faults. *Geochem. Geophys. Geosystems* 10 (8), Q08010. doi:10.1029/2009gc002501

Wei, W., Aeschbach-Hertig, W., and Chen, Z. (2015). Identification of He sources and estimation of He ages in groundwater of the North China Plain. *Appl. Geochem.* 63, 182–189. ISSN 0883-2927. doi:10.1016/j.apgeochem.2015.08.010

Woltemate, I., Whiticar, M. J., and Schoell, M. (1984). Carbon and hydrogen isotopic composition of bacterial methane in a shallow freshwater lake. *Limnol. Oceanogr.* 29 (5), 985–992.

Wu, F., Xu, Y., Gao, S., and Zheng, J. (2008). Lithospheric thinning and destruction of the North China Craton. *Acta Petrol. Sin.* 24 (6), 1145–1174. doi:10.1016/j.sedgeo.2008.03.008

Xu, J., Song, C., and Chu, Q. (1998). Preliminary study on the seismotectonic characteristics of the Zhangjiakou Penglai fault zone. *Seismol. Geol.* 20 (2), 146–154. doi:10.1088/0256-307X/16/9/027

Xu, S., Zheng, G., Nakai, S., Wakita, H., Wang, X., and Guo, Z. (2013). Hydrothermal He and CO2 at Wudalianchi intra-plate volcano, NE China. *J. Asian Earth Sci.* 62, 526–530. doi:10.1016/j.jseaes.2012.11.001

Xu, X., Han, Z., Yang, X., Zhang, S., Yu, G., Zhou, B., et al. 2016, *Seismotectonic map of China and adjacent areas*, Beijing: Seismological Press. Data DB

Xu, S., Guan, L. F., Zhang, M. L., Zhong, J., Liu, W., and Xie, X. G (2022). Deep source gas release from Xianshui River Anning River fault zone in the eastern margin of Qinghai Tibet Plateau Chinese Science. *Chin. Sci. Earth Sci.* 52 (2), 291–308. doi:10.1360/SSTe-2021-0062

Yang, Q., Wu, Q., Sheng, Y., Gao, J., Song, J., and Di, L. (2018). Body wave imaging and seismogenic environment analysis of zhangbo seismic belt and its adjacent areas. *Chin. J.Geophys*. (in Chinese) 61 (8), 3251–3262. doi:10.6038/cjg.2018L0628

Yokoyama, T., Nakai, S., and Wakita, H. (1999). Helium and carbon isotopic compositions of hot spring gases in the Tibetan Plateau. *J. Volcanol. Geotherm. Res.* 88, 99–107. doi:10.1016/s0377-0273(98)00108-5

Zhang, W. (2013). *Geochemistry of hot spring fluid in the basin ridge tectonic area of northwest Beijing*. Beijing: Institute of earthquake forecasting,CEA.

Zhang, H., Xie, F., Jiao, Q., and Li, R. (2007). Cross-fault Deformation Observation and Crustalstress Field in Capital Circle Region. *Seismol. Geol.* 29 (4), 706–715. doi:10.3969/j.issn.0253-4967.2007.04.002

Zhang, X., Jeffrey, R. G., and He, C. (2019). A Numerical Model for the Effect of Permeability Change on Faulting During Fluid Injection[J]. *J. Geophys. Res. Solid Earth* 124, 2080.

Zhao, B., Gao, Y., Shi, Y., and Jin, H. (2011). Crustal shear wave splitting in the intersection area of yanzhangjiakou Bohai seismic belt and Shanxi seismic belt. *Chin. J.Geophys.* 54 (6), 1517–1527. (in Chinese). doi:10.3969/j.issn.0001-5733.2011.06.Oil

Zhao, C., Ran, H., and Wang, Y. (2012). Present-daymantle-derivedheliumreleaseintheTengchongvolcanicfield, Southwest China: Implicationsfortectonicsandmagmatism. *Acta Petrol. Sin.* 28 (4), 1189–1204. doi:10.1007/s11783-011-0280-z

Zhou, X. (2011). *Gas geochemistry in Western sichuan after wenchuan ms 8.0 earthquake*. Hefei: China University of science and Technology Press.

Zhou, X., Wang, W., Chen, Z., Yi, Y., Liu, L., Xie, C., et al. (2015). Hot Spring Gas Geochemistry in Western Sichuan Province, China After the Wenchuan Ms 8.0 Earthquake. *Terr. Atmos. Ocean. Sci.* 26 (4), 361–373. doi:10.3319/tao.2015.01.05.01(tt)

Zhou, X., Liu, L., Chen, Z., Cui, Y., and Du, J. (2017). Gas geochemistry of the hot spring in the Litang fault zone, Southeast Tibetan Plateau. *Appl. Geochem.* 79, 17–26. doi:10.1016/j.apgeochem.2017.01.022

Zhou, X., Wang, W., Li, L., Hou, J., Xing, L., Li, Z., et al. (2020). Geochemical features of hot spring gases in the Jinshajiang-Red River fault zone, Southeast Tibetan Plateau. *Acta Petrol. Sin.*, 36(7): 2197–2214. doi:10.18654/1000-0569/2020.07.18

Zhou, X., Yan, Y., Fang, W., Wang, W., Shi, H., Li, P., et al. (2021). Short-Term Seismic Precursor Anomalies of Hydrogen Concentration in Luojishan Hot Spring Bubbling Gas, Eastern Tibetan Plateau. *Front. Earth Sci.* 8, 586279. doi:10.3389/feart.2020.586279

Zhu, R., and Xu, Y. (2019). The subduction of the west Pacific plate and the destruction of the North China Craton. *Sci. China Earth Sci.* 62, 1340–1350. doi:10.1007/s11430-018-9356-y

Zhu, R., Chen, L., Wu, f., and liu, J. (2011). The time, scope and mechanism of the destruction of the North China Craton. *Chin. Sci. Earth Sci.* 41 (5), 583–592. doi:10.1007/s11430-011-4203-4

Zhu, J., Wang, X., Yang, Y., Fan, J., and Cheng, X. (2017). The crustal flow beneath the eastern margin of the Tibetan Plateau and its process of dynamics. *Chin. J. Geophys.* 60 (6), 2038–2057. (in Chinese with English abstract). doi:10.6038/cjg20170602

frontiers | Frontiers in Earth Science

TYPE Original Research
PUBLISHED 08 September 2022
DOI 10.3389/feart.2022.927314

OPEN ACCESS

EDITED BY
Giovanni Martinelli,
National Institute of Geophysics and Volcanology, Italy

REVIEWED BY
Maria Francesca Ferrario,
University of Insubria, Italy
Angelo De Santis,
Istituto Nazionale di Geofisica e Vulcanologia (INGV), Italy
Nilgun Sayil,
Karadeniz Technical University, Turkey

*CORRESPONDENCE
Chenhua Li,
lichdzj@163.com
Xiaocheng Zhou,
zhouxiaocheng188@163.com
Ying Li,
subduction6@hotmail.com

SPECIALTY SECTION
This article was submitted to Geohazards and Georisks, a section of the journal Frontiers in Earth Science

RECEIVED 24 April 2022
ACCEPTED 19 August 2022
PUBLISHED 08 September 2022

CITATION
Li C, Zhou X, Li J, Liu L, Su H, Li Y, He M, Dong J, Tian J, Zhou H, Gao G, Zhang C and Luo Z (2022), Hydrogeochemical characteristics of thermal springs in the Qilian–Haiyuan fault zone at the northeast Tibetan Plateau: Role of fluids and seismic activity.
Front. Earth Sci. 10:927314.
doi: 10.3389/feart.2022.927314

Hydrogeochemical characteristics of thermal springs in the Qilian–Haiyuan fault zone at the northeast Tibetan Plateau: Role of fluids and seismic activity

Chenhua Li[1]*, Xiaocheng Zhou[2]*, Jingchao Li[2], Lei Liu[3], Hejun Su[1], Ying Li[2]*, Miao He[2], Jinyuan Dong[2], Jiao Tian[2], Huiling Zhou[1], Gang Gao[4], Caiyan Zhang[4] and Zhixin Luo[2]

[1]Gansu Lanzhou Geophysics National Observation and Research Station, Earthquake Administration of Gansu Province, Lanzhou Institute of Geotechnique and Earthquake, CEA, Lanzhou, China, [2]Institute of Earthquake Forecasting, China Earthquake Administration, Beijing, China, [3]Qinghai Earthquake Agency, Xining, China, [4]Gansu Earthquake Agency, Lanzhou, China

The Qilian–Haiyuan fault zone (QHF) is located in a highly deformed and seismically active area of the northeastern margin of the Tibetan Plateau. This study investigated the major elements, strontium, hydrogen, and oxygen isotopes of 22 sites in the thermal springs along the QHF from October to November 2020. The QHF hydrochemical system is recharged by meteoric water primarily infiltrating between 2.8 and 4.4 km a.s.l. Based on quartz geothermometers, the geothermal reservoir temperature variation ranged from 25.5 to 111.3°C, and the circulation depth ranged from 1.3 to 5.6 km. In the QHF zone, the highest spring water temperature values were correlated with deep groundwater circulation circuits in areas where earthquake foci are concentrated. A conceptual model of the hydrologic cycle of thermal springs explains the spatial distribution of earthquakes associated with tectonic movements. The fluid circulation of the QHF corresponds well with the seismicity, which indicates that the hydrological characteristics of the thermal spring in a fault zone are vital in receiving information on seismic activity to assess the seismic risk of the QHF in the future.

KEYWORDS

hydrogeochemical characteristics, thermal springs, Qilian–Haiyuan fault zone, Tibetan Plateau, active seismicity

1 Highlights

- Fluid origin, reservoir temperature, and genesis of thermal waters along the Qilian–Haiyuan Fault (QHF) are constrained.
- Segmental hydrogeochemical characteristic of thermal springs in the QHF correlates well with the spatial distribution of seismic activities.

2 Introduction

The seismically active fault zones provide conduits for the upwelling of hydrothermal fluids in active tectonic settings (e.g., among many others, Arno et al., 2014; Chiodini et al., 2020). Meanwhile, geothermal fluid circulating along the fault increases increasing pore fluid pressure, triggering earthquakes and weakening the rock (e.g., among many others, Chiodini et al., 2011; Zuza and Cao, 2020). Over the years and all around the world, a large number of variations in hydrochemical parameters have been tentatively put in relation with the occurrence of earthquakes (e.g., among many others, Barberio et al., 2017; Claesson et al., 2004; Onda et al., 2018; Reddy et al., 2017; Schuessler et al., 2016; Li et al., 2021; Gori and Barberio, 2022). Previous studies have revealed that the circulation depth, reservoir temperature, and geochemistry of hydrothermal fluids are affected by fault structures involved in earthquake nucleation over variable spatial scales, including microscale fractures in dilated rocks of individual faults and kilometer-scale fault displacements across the lithosphere (e.g., among many others, Scott et al., 2020). This provides a physicochemical basis for exploring the possible relationships between fluid geochemistry and seismic activities along the active faults.

According to the official measurement of the China Seismic Network, the Ms 6.9 earthquake with a 10-km focal depth occurred in Menyuan County, Haibei Prefecture, Qinghai (37.77°N, 101.26°E) at 01:45 on 8 January 2022 (Beijing time). The earthquake resulted in a surface rupture of about 22 km due to the sinistral strike-slip motions. The Lanxin high-speed railway, passing through the fault, suffered severe damage. The earthquake occurred in the western Qilian–Haiyuan fault zone (QHF), the Lenglongling fault segment, which has been very active for many large earthquakes in history (Li et al., 2022). This could facilitate acquiring the geochemical information about the deep fluid associated with earthquakes to perform hydrological and geochemical monitoring of regions with intense seismic activities. However, previous studies have focused on the source of heat and chemical characteristics of some springs in this area. Few studies have examined the relationship between the hydrochemical characteristics of hot springs and fault activity. Such studies are essential for evaluating the geothermal energy potential along the fracture zone. This study focuses on the hydrochemical properties and origin of 22 thermal springs in the QHF. Major and trace elements, $^{87}Sr/^{86}Sr$ values, δD, and $\delta^{18}O$ values were discussed to characterize these hot springs' hydrochemical properties. The quartz geothermometers were employed to calculate their reservoir temperature and water circulation depth to reveal their possible hydrochemical evolution processes. We aimed to discuss the relationship between hot spring evolution and seismic activity through a conceptual model of the hot spring hydrology cycle, combined with the temporal variation characteristics of the chemical composition of one thermal spring continuously monitored since May 2020, prospecting its implications for future monitoring.

3 Geological and seismotectonic setting

The QHF is located on the northeastern margin of the Qinghai–Tibet Plateau. The Qilian Mountains are subjected to the continuous uplift and northeastward compressive deformation of the Tibetan Plateau (Zhang et al., 2003; Zhang et al., 2006; Lei et al., 2020), forming a series of northwest-southwest strip-like mountains controlled by late Quaternary thrust faults, strike-slip faults, and active folds, about 700 km long (Yuan et al., 2004; Yuan et al., 2013). The Qilian Shan–Hexi corridor can be regarded as a compressional zone of two strike-slip faults—the Altun Fault and Haiyuan Fault—where crustal shortening and mountain uplift caused by many thrusts and folds in the region coordinated the transition and balance between the two faults (Yuan et al., 2004; Zhang et al., 2017). Faults that developed in the region from the west to the east include the Altun Fault, Jinta South Mountain Fault, Yumu Mountain Fault, North Rim Fault of Qilian Mountains, Changma–Ebo Fault, Tuole Mountain Fault, Lenglongling Fault, and Maomao Mountain–Lahu Mountain–Haiyuan Fault (Figure 1A,B). The crustal deformation in this area is intense, and seismic activity is frequent. Since the 20th century, this area has experienced several earthquakes, such as the *M*s 8.5 Haiyuan earthquake in 1920, the *Ms* 8.0 Gulang earthquake in 1927, the *M*s 7.6 Changma earthquake in 1932, the *M*s 7.25 Shandan earthquake in 1954, and the *M*s 7 Gonghe earthquake in 1990 (Supplementary Table S1). The epicenter of the *M*s 6.9 Menyuan earthquake is located in the western segment of the Lenglongling fault zone in the middle and western segments of the generalized Haiyuan fault. The fault is a Holocene active fault with a sinistral strike-slip nature and a fault slip rate of about 4–8 mm/a. The eastern end of the fault is connected with the Gulang and Maomaoshan faults, and the western end is connected with the Tuolaishan Fault, with a total length of 130 km (Yang et al., 2022).

The thermal springs selected in this study are mainly distributed in the Northern Rim Fault of the Qilian Mountains, the Altun Fault, Yumu Mountain Fault, Lenglongling Fault, and Maomao Mountain Fault–Laohu Mountain Fault–Haiyuan Fault zone (Figure 1). The Qilian Mountains is about 1000 km long from east to west and is the birthplace of groundwater and surface water in the Hexi region (Geng, et al., 2017). The annual average precipitation and evaporation values are 298.9 and 3038.1 mm, respectively, and

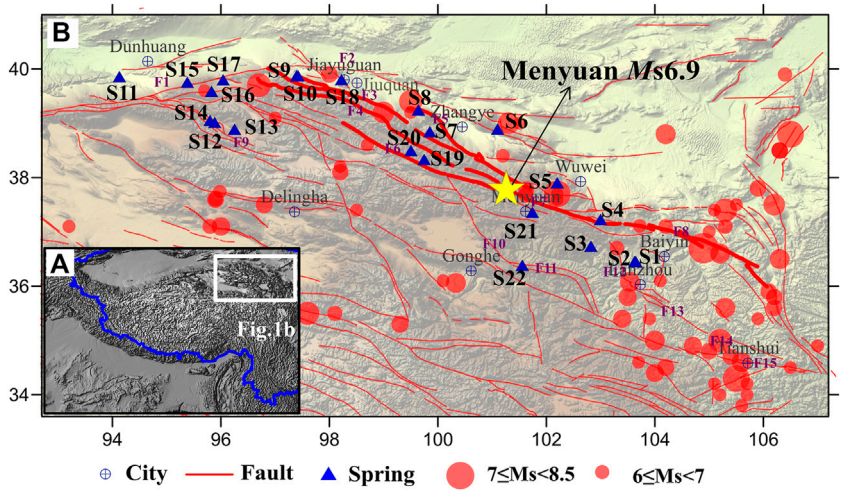

FIGURE 1
(A) Macro-regional map; **(B)** location of water sampling points and foci of large earthquakes (Ms >6), along with major fault traces (F1: Altun Fault; F2: Jinta South Mountain Fault; North Edge Fault of Qilian Mountain; F4: Changma-Ebo Fault; F5: Yumu Mountain Fault; F6: Tuole Mountain Fault; F7: Lenglongling Fault; F8: Haiyuan Fault; F9: Danghe South Mountain Fault; F10: Riyue Mountain Fault; F11: Laji Mountain Fault; F12: Zhuanglang River Fault; F13: Majie Mountain Fault; F14: Tongwei Fault; F15: Fault of north edge of West Qinling. The time of *Ms* ≥ 6 earthquake is from BC780 to 12 January 2022 (Supplementary Table S1). The blue line in Figure 1a represents the borderline. The seismicity data came from the National Earthquake Data Center of China https://data.earthquake.cn/datashare/report.shtml?PAGEID=earthquake_zhengshi).

the annual temperature ranges from −3.0 to 4.0°C. Many rivers originating from the high-altitude areas of the Qilian Mountains incise the tectonically active margin, generating strikingly steep topography and mobilizing large volumes of sediment before flowing into the arid Hexi corridor, including the Heihe River, the Shule River, and the Shiyang River (Meng et al., 2020). Rivers originating in the Qilian Mountains are the primary recharge source for groundwater in the study area. The mountain aquifers are mainly fractured, weathered rocks and in deep structural fractured zones, with direct hydraulic interaction. Water circulates fast through the fractures. Thus, groundwater is commonly connected with the surface water and is directly recharged from snow-melt and glacial ice melt (Zhao et al., 2018).

4 Material and methods

Groundwater samples were collected from 22 thermal springs along the QHF in October 2020 (Figure 1B and Supplementary Table S2). Supplementary Table S3 shows the geochemical analysis of water sampled every 3 days taken from the spring S22 since May 2021. All water samples were collected in new, colorless, polyethylene terephthalate (PET) bottles that had been rinsed with the water samples. Then, the water samples were filtered through a 0.45-μm membrane. Samples were collected in five colorless polyethylene terephthalate (PET) bottles (50 ml) for major and trace element concentrations, hydrogen and oxygen isotopes, and SiO_2 concentration analysis. Additionally, the samples were acidified with ultrapure HNO_3 for cation analysis but not acidified for anion analyses. Finally, the water samples were stored in a 4°C refrigerator, with laboratory analyses conducted within 2 weeks. The specific conductance, pH, dissolved oxygen, and temperature were measured in samples using a multiparameter probe inserted into a flow-through cell closed to the atmosphere and in springs by lowering the probe into the spring vent for *in situ* measurements. The concentrations of cations (K^+, Na^+, Mg^{2+}, and Ca^{2+}) and anions (F^-, Cl^-, Br^-, NO_3^-, and SO_4^{2-}) were measured using a Dionex ICS-900 ion chromatography system and an AS40 automatic sampler at the Earthquake Forecasting Key Lab of China Earthquake Administration, with ±2% reproducibility and 0.01 mg/L detection limits (Chen et al., 2015). The HCO_3^- and CO_3^{2-} concentrations in the thermal springs were measured by 0.05 mol/L HCl titration of 0.1% methyl orange and 1% phenolphthalein in procedures with a ZDJ-100 potentiometric titrator (within ±2% reproducibility). An inductively coupled plasma emission spectrometer Optima−5300 DV (PerkinElmer Inc.) was used to detect SiO_2. The hydrogen and oxygen isotopes were measured using a Finnigan MAT253 mass spectrometer, *via* the TC/EA method. Results were expressed as parts per thousand deviations from Vienna Standard Mean Ocean Water (V−SMOW). Precisions of ±0.2% (2 S.D.) and ±1%

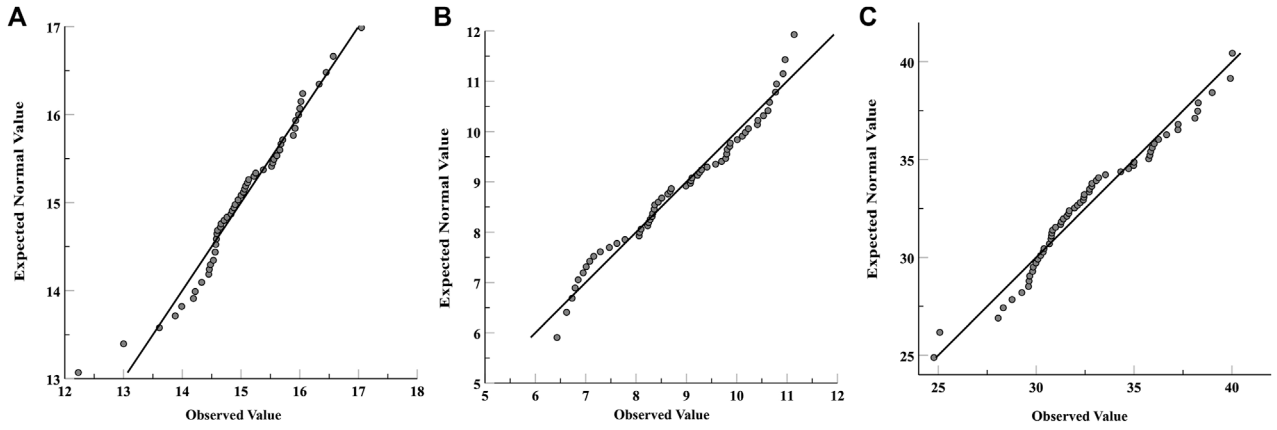

FIGURE 2
Quantile–quantile plots (Q-Q plots) of the concentration of Na^+ **(A)**, Cl- **(B),** and SO_4^{2-}- **(C)** in the S22 spring.

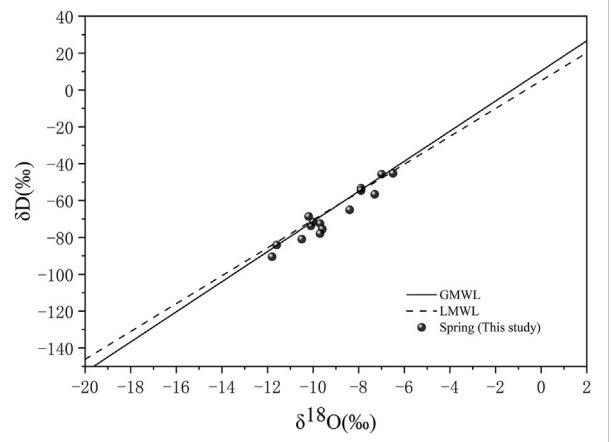

FIGURE 3
Distribution chart of δD and $\delta^{18}O$ in the water sample.

(2 S.D.) were obtained for $\delta^{18}O$ and δD in a standard water sample, respectively (Wang et al., 2010). Sr element and its isotope were analyzed at the Test Center of the Research Institute of Uranium Geology by Element XR ICP–MS (Thermo Fisher, Bremen, Germany) (Zhang et al., 2018). The data on the water chemicals were evaluated by calculating the ion balance (ib) (Baird et al., 2017). The threshold value of continuous monitoring was calculated according to the equation X+ σ and X+ 2σ (X: average value; σ: once of the standard deviation; 2σ: twice of the standard deviation, Supplementary Table S4). Additionally, since mean and standard deviation are estimated over an expected Gaussian distribution, the Gaussianity of the continuous monitoring value has been verified by the Q–Q (quantile–quantile) plots (Figure 2).

5 Results

5.1 Origin of the thermal spring water

The respective distribution ranges of the measured values of δD and $\delta^{18}O$ in the thermal spring water in the QHF are −90.4~−45.2‰ and −11.8~−6.5‰. In comparison with the global meteoric water line ($\delta D = 8.17\delta^{18}O + 10.35$) (Rozanski et al., 1993) and the meteoric water line in the northwest region of China [$\delta D = 7.56\delta^{18}O + 5.05$ ($R^2 = 0.97$)] (Huang et al., 2008), it could be observed that δD and $\delta^{18}O$ of the thermal spring water are mainly distributed near the meteoric water line (Figure 3), indicating that meteoric waters are the main recharge sources of the thermal spring. According to the relationship between $\delta^{18}O$/δD and recharge elevation ($\delta^{18}O = -0.00347ALT + 3.04$; $\delta D = -0.02585ALT + 28.28$) (Wu et al., 2020), it could be calculated that the recharge elevation is about 2.8–4.4 km (Table 1), which is close to the elevation of nearby Qilian Mountains.

5.2 Origin of water-soluble ions in thermal springs

5.2.1 Origin of the major elements

In the thermal spring water of the QHF, the main positive ions include Ca^{2+}, Mg^{2+}, and Na^+, and the main negative ions are SO_4^{2-} and HCO_3^-. The concentrations of various ions are significantly divided, and the water quality is complicated (Figure 4). In the piper chart, the water samples are mainly distributed in three areas. The water of the thermal spring points on the first zone of the piper diamond graph (S3, S4, S7, S12, S16, S21, and S22) belongs to the HCO_3–Ca·Mg type, especially distributed in the central area of the fault. The water

TABLE 1 Recharge elevation in the QHF.

No.	δ18O	δD	Recharge elevation (km)		
	(‰)		δ18O = −0.00347ALT + 3.04	δD = −0.02585ALT + 28.28	Mean
1	−10.5	−80.9	3.9	4.2	4.1
4	−7.9	−53.3	3.2	3.2	3.2
5	−9.7	−72.5	3.7	3.9	3.8
6	−10.0	−71.6	3.8	3.9	3.8
9	−10.1	−73.7	3.8	3.9	3.9
10	−9.6	−75.5	3.6	4.0	3.8
12	−9.7	−77.9	3.7	4.1	3.9
14	−11.8	−90.4	4.3	4.6	4.4
15	−11.6	−84.0	4.2	4.3	4.3
16	−8.4	−65.0	3.3	3.6	3.5
18	−7.9	−54.6	3.2	3.2	3.2
19	−7.0	−45.7	2.9	2.9	2.9
20	−6.5	−45.2	2.7	2.8	2.8
21	−7.3	−56.6	3.0	3.3	3.1
22	−10.2	−68.6	3.8	3.7	3.8

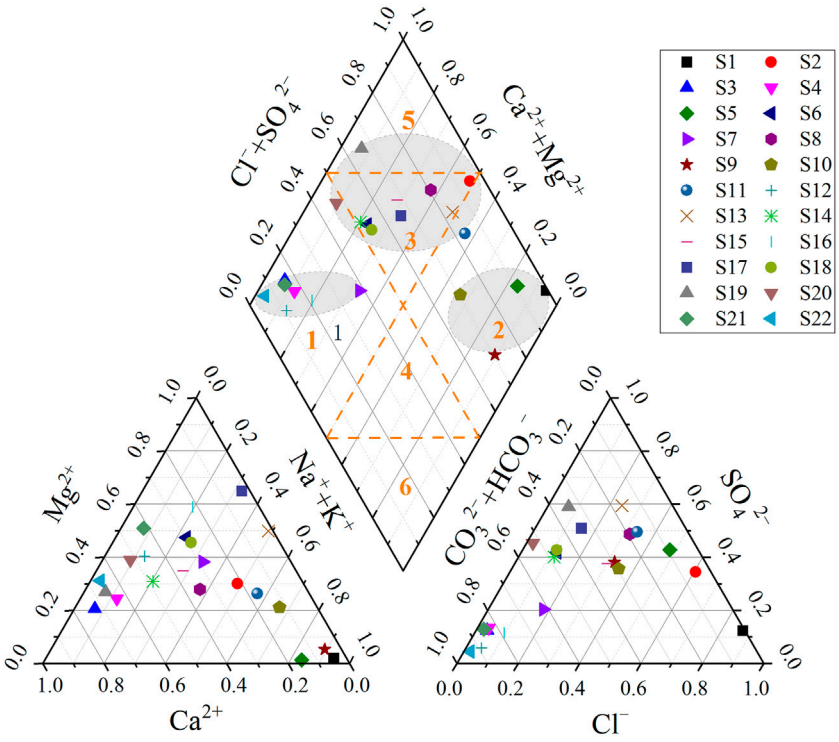

FIGURE 4
Piper trilinear nomograph for the water sample.

is mainly recharged by meteoric waters or meltwater from snow and ice from the Qilian Mountains. Geothermal water wells (deep groundwater; S1, S5, S9, and S10) in the second zone of the diamond graph, whose water belongs to the SO_4 (Cl)–Na type, mainly scatter on the northern segment piedmont fault of the Qilian Mountains, indicating that the meteoric waters or meltwater from snow and ice suffers the influence of evaporation and mutual interaction between water and rocks when passing through the basin of the Hexi corridor. Consequently, the mass concentrations of the main ions in the water are relatively high, consistent with the groundwater characteristics in the arid region of northwest China. Most other thermal spring water points are located in the third zone of the piper diamond graph. Such water belongs to the Ca–SO_4 type and scatters in the transition area between HCO_3–Ca·Mg type water and SO_4 (Cl)–Na type water (Figure 4). The results agree with previous studies, suggesting that the bedrock fissure water in the mountainous region was the belt for HCO_3–type water, the alluvial plains were the belt for the SO_4–type, and the desert and salinization areas are the belt for Cl–type water through the variation of the chemical characteristics of groundwater in the whole basin (Liu et al., 2004).

The constant elements in the thermal spring water of the Qilian Mountain Fault are closely related to the surrounding rocks, hydrodynamic force, and hydrothermal conditions. The Paleozoic strata in the research area are mainly constituted by plagioclase granite and sand–mudstone developed in the Cambrian period, fragmented rocks of monzonitic granite, and lime rocks developed in the Ordovician period, gabbro developed in the Silurian period, and diorite developed in the Devonian period and Carboniferous period. The Mesozoic strata mainly consist of quartz diorite developed in the Triassic period and Jurassic periods and granite developed in the Cretaceous period. The Precambrian strata scattered in some areas are primarily constituted by terrain developed in the Changcheng period. The rocks in the Pleistocene and Quaternary periods are mostly river flooding and windborne deposits (Su et al., 2016). Thus, the lithology of the body of the Qilian Mountain mainly comprises metamorphic rocks, tuff, sandstone, and dolomite, all of which are rich in calcium and magnesium. In the early formative period of the groundwater in the mountain, the surface water dissolved and filtered these rocks, leading to the saturation of calcite and dolomite. Consequently, the thermal spring water exposed to the central fault of the Qilian Mountain is mainly HCO_3–type water; the thermal spring water developed at the northern segment piedmont fault of the Qilian Mountain gradually transits into SO_4–type water due to the evaporation and filtering functions in the drought area; the deep circulation water within the basin of the Hexi corridor is mainly Cl–type water.

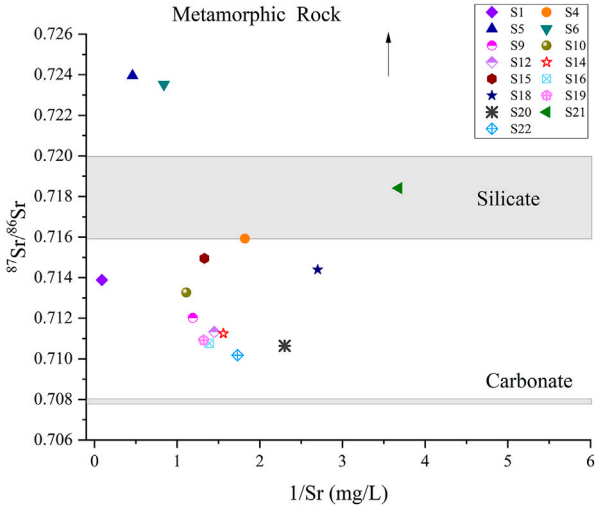

FIGURE 5
Characteristics of the Sr isotope of the thermal spring water in the Qilian Mountain Fault.

5.2.2 Sr isotope

The specific value of $^{87}Sr/^{86}Sr$ in the thermal spring is generally similar to that in the rock-forming minerals in contact with the water (e.g., Négrel et al., 1997; Capo et al., 1998; Millot et al., 2011). The constitution of the strontium isotope in spring water could reflect the lithologic characteristics of the pass-through stratum. Minerals like silicate, sulfate, and carbonate are the main sources of Sr element in the underground water, which significantly influence the specific value of $^{87}Sr/^{86}Sr$ in the underground water (Palmer and Edmond, 1992). Among them, the specific value of $^{87}Sr/^{86}Sr$ originating from weathering of sulfate and carbonate is about 0.708, whereas that originating from the weathering of aluminosilicate is generally from 0.716 to 0.720. The weathering product of metamorphic rocks has a higher specific value of $^{87}Sr/^{86}Sr$ (Wang et al., 2009; Tian et al., 2019). The value of $^{87}Sr/^{86}Sr$ in this study ranged from 0.710642 to 0.723948. Sr in the QHF mainly originates from the mixture of weathering products of silicate and carbonate rocks and weathering products of metamorphic rocks (S5, S6) (Figure 5). The value of $^{87}Sr/^{86}Sr$ of the thermal spring water in Guankou Town (S21) is 0.718415. Although it is the weathering product of silicate rock-type minerals, its chemical type is HCO_3–Mg (Ca). Therefore, it could be deduced that the water develops from the thermal spring water containing carbonate minerals after passing through the fault and silicate rocks. The water in Niuquangou (S4) had a similar situation. Previous studies believed that the metamorphic hydrothermal system formed from the landform uplift and fractures in the region of the Qilian Mountain has a high Sr isotope feature similar to that of the Himalayan region (Liu et al., 2022).

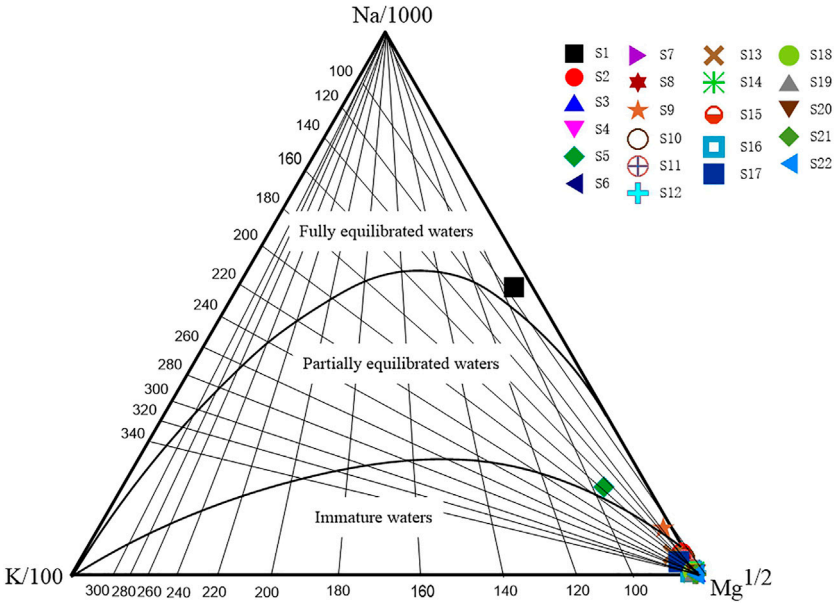

FIGURE 6
Na–K–Mg ternary diagram of the thermal spring water sample.

Moreover, the pH value of the thermal spring water in the fault zone of the Qilian Mountain ranged from 7.22 to 8.93, with a mean value of 7.85. Previous studies indicated that weak alkaline water with a pH value from 7.0 to 8.5 could easily enrich Sr^{2+} (Wang et al., 2009). The concentration of Sr^{2+} in the zone is 0.27 mg/L –11.50 mg/L, with a mean value of 1.56 mg/L, especially thermal spring S1 (NaCl-type water) has a significantly high concentration of Sr^{2+}.

5.3 Water–rock interaction of thermal springs when circulating inside the fault

Chemical equilibration was tested with a ternary diagram established using relative Na/1000, K/100, and $Mg^{1/2}$ contents (Giggenbach, 1988). The Na–K–Mg triangular plot (Figure 6) shows the S1 sample plot in the fully equilibrated water zone and S5 and S9 sample plots in the partial equilibrated water zone, located at the front rim of the fault on the north rim of the Qilian Mountain. Other thermal spring samples almost belong to immature waters, indicating that they are not fully equilibrated with the reservoir rocks.

Many chemical geothermometers are used to estimate reservoir temperatures (Fournier and Truesdel, 1973; Fournier and Potter, 1979; Fouillac and Michard, 1981; Fournier and Potter, 1982; Arnórsson, 1983; Chiodini et al., 1995). Various chemical geothermometers always yield very different reservoir temperatures because of the complex geological settings. The generally used geothermometers include a cation and SiO_2 geothermometers. The cation geothermometers were suitable to estimate the reservoir temperature of the water–rock reaction equilibrium status, although most of the thermal spring water samples did not reach the water–rock equilibrium in this study, as indicated in Figure 6 (Fouillac and Michard, 1981; Fournier and Potter, 1982; Arnórsson, 1983; Chiodini et al., 1995). Therefore, we chose the quartz geothermometers with no steam loss and calculated the circulation depth (Table 2). Li et al. (2021) gave a detailed calculation method. The results showed that the reservoir temperature of the spring samples in the QHF ranged from 25.5 to 111.3°C.

According to the reservoir temperature, the circulated depth calculation formula shown as follows is adopted

$$Z = Z_0 + (T - T_0)/T_{grad}. \quad (1)$$

Here, Z represents the circulation depth (km); Z_0 represents the depth of the constant temperature zone (km); T represents the reservoir temperature (°C); T_0 represents the temperature of the constant temperature zone (°C), namely, the local average temperature; T_{grad} represents the geothermal gradient (°C/km) reflecting the geothermal change per kilometer of the place below the constant temperature zone (Xiong et al., 1990). Based on the previous studies on groundwater in the Qilian Mountain, we selected the geothermal gradient T_{grad} of 20 C/km, the annual mean temperature T_0 in the Qilian Mountain is 0.37°C, and the

TABLE 2 Calculation of reservoir temperature and circulation depth.

No.	Temperature (°C)	SiO_2 (mg/L)	Reservoir temperature (°C)	Circulation depth (km)	Temperature difference between the spring vent and reservoir (°C)
S1	33.7	18.87	61.3	3.1	27.6
S4	6.4	7.37	29.7	1.5	23.3
S5	57.4	60.92	111.3	5.6	53.9
S6	16.3	15.40	53.9	2.7	37.6
S9	25.1	13.44	49.1	2.5	24.0
S10	13.8	11.16	42.9	2.2	29.1
S12	5.3	9.48	37.5	1.9	32.2
S14	5.9	8.33	33.4	1.7	27.5
S15	5.1	6.86	27.5	1.4	22.4
S16	3.7	20.02	63.5	3.2	59.8
S18	11.4	10.12	39.6	2.0	28.2
S19	3.7	6.41	25.5	1.3	21.8
S20	5.4	10.76	41.6	2.1	36.2
S21	7.0	6.58	26.3	1.3	19.3
S22	38.5	19.49	62.5	3.1	24.0

Z_0 is 30 m (Liu et al., 2020; Wu et al., 2020). The circulation depth along the QHF is about 1.3–5.6 km. The reservoir temperature of the thermal springs is positively associated with the circulation depth. The temperature difference between the spring vent and the reservoir indicated more mixing opportunities and a proportion of cool water during the longer groundwater circulation path (Table 2). The circulation depth of the thermal spring water in the S5 spring at the front basin of the Qilian Mountain Fault is the deepest, about 5.6 km deep, and the temperature difference is as high as 53.9°C. In contrast, the circulation depth of the thermal spring at the inter-mountain and front thrusting faults of the Qilian Mountain is shallower, about 1.5 km.

6 Discussion

6.1 The hydrological and geochemical spatial and temporal variation characteristics of the thermal spring and response to earthquakes

6.1.1 Spatial distribution characteristics of the thermal spring and earthquakes

The QHF is located in a transitional zone between the NE-striking Altyn Tagh Fault and E-striking Haiyuan Fault in the northeastern margin of the Tibetan Plateau (Meng et al., 2020), which is a focal zone with high earthquake risk. In this study, the 22 thermal springs were distributed along the four segments of the QHF, namely, the Subei segment (a), Jiayuguan–Zhangye segment (b), Wuwei–Tianzhu segment (c), and Lanzhou segment (d). The ranking of the QHF spring waters in terms of thermal reservoir temperature, circulation depth, water maturity, and water–rock interaction intensity is roughly segmented c > segment a > segment d > segment b. The historical earthquakes in the QHF used to appear and gather in segment c (Figure 7). The estimated average reservoir temperature of the thermal springs displays a southeastward increasing trend along the QHF, with an obvious high geothermal zone focusing on the Wuwei–Tianzhu segment (c). In this segment, the highest spring water temperature values are correlated with deep groundwater circulation circuits in areas where the earthquake foci are concentrated (Figure 7). Generally, the geothermal fluids potentially influence the tectonic activities of this boundary fault. Previous studies have proposed that the reactivation of faults and migration of deep fluids in the fault system may be critical controlling factors for the regional seismic activity and geothermal anomalies (Doglioni et al., 2014; Wang et al., 2018).

Deep fluid circulation and facture coupling are important triggers of earthquakes. The pore fluid overpressure in active fault systems can drive fluid flow, causing fault weakening and seismicity. Snell et al. (2020) believed that non-linear, complex feedback between fluid flow, fluid pressure, and fault deformation controls the length of an earthquake's nucleation phase and the interseismic duration period in natural faults. Zuza and Cao (2020) suggested that geothermal gradients using high-resolution earthquake-location data from California to construct

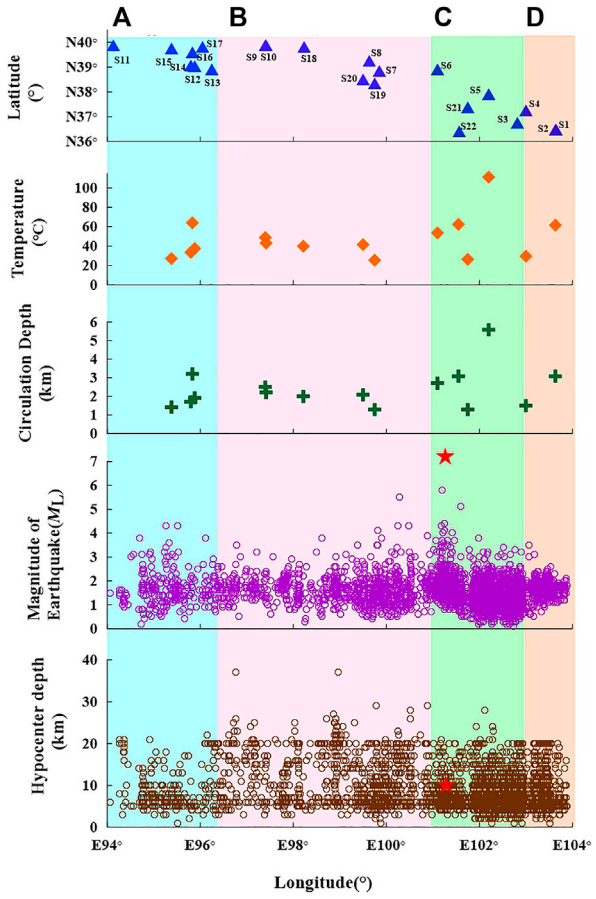

FIGURE 7
Spatial variation of water and seismic response in the QHF. **(A)** Subei segment; **(B)** Jiayuguan–Zhangye segment; **(C)** Wuwei–Tianzhu segment; **(D)** Lanzhou segment. The red star is the *Ms* 6.9 Menyuan earthquake. The duration of the earthquake data is from January 2019 to January 2022. The temperature values plotted here are estimated values by the application of the quartz geothermometer.

a topographic map of the base of the seismogenic crust mostly control the brittle-ductile transition depth. The activity of the geothermal fluid segment in the QHF is consistent with the more frequently occurring earthquake zone, which can be inferred that the distribution of geothermal anomalies in the QHF indicates localized seismic activity (Okada et al., 2015).

Moreover, most earthquakes along the QHF have focal depths ranging from 5 to 20 km, with the focal zone generally below the circulation depths of the thermal waters (1.3–5.6 km; Figure 7) but corresponding to the uppermost part of low-velocity and high-conductivity layers (Lei and Zhao, 2016). As shown in Figure 7, a comparison among fluid circulation depths and temperatures, numbers, and focal depths of earthquakes along the QHF suggests that earthquakes tend to occur beneath the regions with larger fluid circulation depths. This is consistent with the localized geothermal anomalies, suggesting potential genetic links between lithospheric thermal structure and earthquake nucleation along an active fault, similar to previous research in the southeastern and eastern Tibetan Plateau (Wang et al., 2018; Liu et al., 2022) and western North America (Wong and Chapman, 1990).

6.1.2 Temporal variation characteristics of thermal springs and response to the earthquake

The major ion concentrations of the Huangzhong Spring (S22) close to the epicenter, continuously monitored every 3 days since May 2021, did not display any obvious anomaly before the *Ms* 6.9 Menyuan earthquake (Figure 8). The absence of the anomaly might be associated with a weak correlation in stress change because the spring is not on the same structural system as the earthquake's fault. The spring is located on the Laji Mountain Fault, while the earthquake is on the Lenglongling Fault (Figure 1). However, the concentrations of SO_4^{2-} and Cl^- fluctuated abnormally in the period from January 9 to 22 after the *Ms* 6.9 Menyuan earthquake (Figure 8). Previous studies showed that the increase in the ion concentration indicated that stress accumulation promoted the development of pores within the fault zone, increasing the water–rock reaction surface (Zoback and Byerlee, 1975; Brace, 1978; Teufel, 1980; Sobolev, 1984; Claesson et al., 2007; Reddy et al., 2011; Woith et al., 2013; Chen et al., 2014; Rosen et al., 2018). Thus, we infer that the reason of no-anomaly detection at the geochemical monitoring site may be that the pre-earthquake strain accumulation in the Lenglongling Fault was not effectively transferred to adjacent faults. However, co-earthquake and post-earthquake strain release in the Lenglongling Fault was effectively transferred to the adjacent Laji Fault, which may be the cause of the post-earthquake anomaly.

Precursory changes occur in an area due to changes in the regional stress field associated with the onset of the earthquake process and the spatial pattern of these changes being non-uniform (Hauksson and Goddard, 1981; Wakita et al., 1985; Thomas et al., 1986; Utkin and Yurkov, 2010). Chen and Wang (2021) reported the major ion concentration changes in the Ganze Spring in response to the 2014 Ms 6.1 Yingjiang earthquake. Although the distance between the Ganze Spring and the epicenter was 320 km away, the spring is located in the tensile direction of the epicenter. However, no obvious hydrochemical responses in the Ganze Spring were observed during other earthquakes, which occurred within 100 km away from the Ganze Spring during the study period. For example, the 24 June 2012 *Ms* 5.7 Ninglang earthquake and the 3 March 2013 *Ms* 5.5 Eryuan earthquake indicated that earthquakes occurred in different directions of the regional stress even though they were close to the Ganze Spring. In the 1995 Kobe earthquake, for two wells within a distance of 50 m and of the same depth, one indicated changes in hydrochemistry associated with the earthquake, whereas the other did not (Wakita, 1996). These examples are related to the tectonic position of wells and the

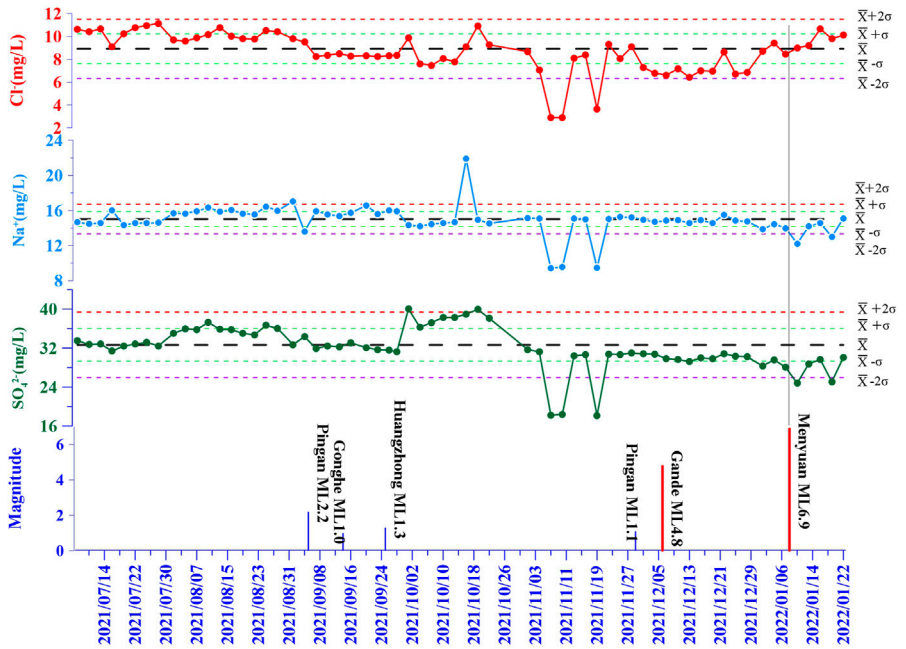

FIGURE 8
Temporal variation of water and seismic response in the S22 spring (the blue vertical line indicates the earthquakes above *Ms* 1.0 within the scope of 50 km, the red vertical line indicates the earthquakes above *Ms* 4.0 within the scope from 50 to 300 km. The duration of data monitoring is from 30 May 2021 to 22 January 2022)

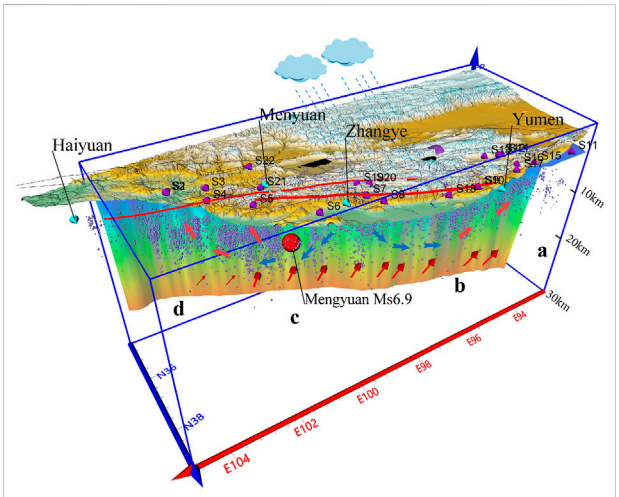

FIGURE 9
Conceptual model for the cause of formation of underground water and the hydrological geochemical circulation process.

direction of the regional stress field associated with the onset of the earthquake process. This phenomenon may be universal and similar to this study. Considering the tectonic location and distance from the epicenter, it can be inferred that the response of hot springs to seismic events is not only related to the magnitude and distance from the epicenter but is also controlled by the tectonic stress of deep major faults. To further address the spring responses to earthquakes, continuous monitoring of more hydrochemical parameters is suggested in the future, as already performed elsewhere (Pierotti et al., 2015, 2017; Gherardi and Pierotti, 2018).

6.2 The hydrogeochemical circulation model of thermal spring waters in the Qilianshan Fault

A conceptual model for the origin of the groundwater and the hydrogeochemical cycling process in the QHF was established based on previous geophysical data and this study's results (Figure 9). In the recharge area with an altitude of about 2.88–4.4 km, the meteoric waters in the Qilian mountainous area permeated into the aquifers along m4.4 km; the meteoric waters in the Qilian mountainous area permeated into the aquifers along mountain fractures and river terraces and then passed through the water–conducted zone to conduct deep circulation. When the circulation depth increases to 1.3–5.60 km and the reservoir condition reaches 25.5–111.3°C, the water would come across the water–rock reaction with rocks at different depths (like granite and igneous rock) under certain temperature and pressure conditions. Differences in the water–rock reaction degree result in partially

balanced and immature water formation. When rising to the earth's surface, such water would be mixed with shallow cool water, finally becoming exposed on the earth's surface as a thermal spring. When the crustal stress in the QHF changes, the pressure in the aquifer system and the equilibrated state of thermal spring water would be disrupted, resulting in different hydro-chemical characteristics (Claesson et al., 2007; Kima et al., 2019). Therefore, continuous monitoring could be conducted on a proper hot spring spot of the fault zone to further study the pre-seismic hydrochemical precursors.

The results of this study indicate that faults are crucial in controlling the migration of crustal fluids. These maps can improve our knowledge of earthquake hazard models including potential rupture areas for fault zones and testing existing fault-hazard models against earthquake distributions. Meanwhile, more case studies are required to understand the entire system globally.

7 Conclusion

The detailed mechanism and process of geochemical characteristic changes in the QHF were described in terms of regional groundwater flow systems by using the hydrochemical data on the 22 thermal springs. The results suggested that the surrounding thermal spring water was mainly supplied from meteoric waters of the nearby mountains with a recharge elevation of about 2.8–4.4 km. The water chemical type is primarily controlled by the lithologic features of the aquifer. The thermal spring exposed at the central fault of the Qilian Mountain is mainly the HCO_3 type, while the thermal spring water developed at the front fault of the northern rim of the Qilian Mountain gradually became SO_4 type due to evaporation and filtering functions in the drought area. Moreover, the deep circulation water within the basin of the Hexi Corridor is mainly Cl type. The $^{86}Sr/^{87}Sr$ value indicated that the thermal spring containing carbonate minerals passed through the fault and flowed through the silicate rock before exposing it from the earth's surface.

The reservoir temperature of the thermal spring in the QHF was 25.5–111.3°C, and the circulation depth was 1.3–5.6 km. The circulation depth of the thermal spring water in the S5 spring at the front basin of the QHF is the deepest, which was about 5.6 km, and the temperature difference was as high as 53.9°C. Moreover, the water–rock reaction was in a partially equilibrated state. In contrast, the circulation depth of the thermal spring at the inter-mountain and front thrusting faults of the QHF is relatively shallow, about 1.5 km. Due to the weaker water–rock reaction, most of the spring is immature water.

The circulation depth at the fault of the mountainous areas of the Qilian Mountain is shallow due to the relatively strong stress accumulation at the inter-mountain and front thrusting faults of the Qilian Mountain. The shallow fissure development results in a short water circulation path, leading to a weak water–rock reaction. However, for geothermal water in the basin on the mountain's front, the meteoric waters would pass leaching and deposits' evaporation on the basin, going through the more equilibrated water–rock reaction due to the longer circulation path.

The segmental characteristics of the fault, the hydration characteristics of the thermal springs located in different segments of the QHF, and the seismic activities are closely related. In particular, the springs in the Wuwei–Tianzhu segment had deeper recharge source and high reservoir temperatures than others. This coincided with strong tectonic and seismological activities in the Wuwei–Tianzhu segment. Thus, the spatial distribution of hot springs, the hydro-geochemical characteristics, and the influence of controlling factors are essential to further exploration of strong seismic information.

Data availability statement

The original contributions presented in the study are included in the article/Supplementary Material; further inquiries can be directed to the corresponding authors.

Author contributions

Conceptualization, CL and XZ; methodology, CL, XZ, and YL; software, JD; validation, JT; formal analysis, CL, MH, JT, and HS; investigation, CL, JL, HZ, GG, CZ, LL, and ZL; data curation, CL and XZ; writing—original draft preparation, JL; writing—review and editing, CL and XZ; visualization, CL; supervision, XZ, YL, and CL. All authors have read and agreed to the published version of the manuscript.

Funding

This research was funded by the Basic Scientific Research Fund, Science and Technology Innovation Base of Lanzhou, Institute of Earthquake Forecasting, China Earthquake Administration (grant number: 2021IESLZ05), the Science and Technology Program of Gansu Province, China (grant number: 20JR10RA500 and 21JR7RA796), Science for Earthquake Resilience, China Earthquake Administration(grant number: XH21033), Central Public-interest Scientific Institution Basal Research Fund (CEAIEF2022030205, CEAIEF20220507, CEAIEF20220213, CEAIEF2022030200, 2021IEF0101, 2021IEF1201), National Key Research and Development Project (2017YFC1500501-05, 2019YFC1509203, 2018YFE0109700) and the National Natural Science

Foundation of China (41673106, 42073063, 4193000170, U2039207), IGCP Project 724.

Acknowledgments

The authors are grateful to the Editor and reviewers for their constructive comments and suggestions.

Conflict of interest

The authors declare that the research was conducted in the absence of any commercial or financial relationships that could be construed as a potential conflict of interest.

Publisher's note

Supplementary material

The Supplementary Material for this article can be found online at: https://www.frontiersin.org/articles/10.3389/feart.2022.927314/full#supplementary-material

References

Arno, Z., Volker, O., Philippe, J., Nicholas, D., Roland, G., Art, M., et al. (2014). Analysis of induced seismicity in geothermal reservoirs - an overview. *Geothermics* 52, 6–21. doi:10.1016/j.geothermics.2014.06.005

Arnórsson, S. (1983). Chemical equilibria in Icelandic geothermal systems-Implications for chemical geothermometry investigations. *Geothermics* 12, 119–128. doi:10.1016/0375-6505(83)90022-6

Baird, R. B., Eaton, A. D., and Rice, E. W. (2017). *Standard methods for examination of water and wastewater*. 23rd ed. Camden, NJ, USAWashington, DC, USA: American Public Health Association; American Water Works Association; Water Environment Federation.

Barberio, M. D., Barbieri, M., Billi, A., Doglioni, C., and Petitta, M. (2017). Hydrogeochemicalchanges before and during the 2016 Amatrice-Norcia seismic sequence (central Italy). *Sci. Rep.* 7 (1), 11735. doi:10.1038/s41598-017-11990-8

Brace, W. F. (1978). A note on permeability changes in geologic material due to stress. *PAGEOPH* 116, 627–633. doi:10.1007/bf00876529

Capo, R. C., Stewart, B. W., and Chadwick, O. A. (1998). Strontium isotopes as tracers of ecosystem processes: Theory and methods. *Geoderma* 82, 197–225. doi:10.1016/s0016-7061(97)00102-x

Chen, L., and Wang, G. C. (2021). Hydrochemical changes of a spring due to the May 30, 2014 Ms 6.1Yingjiang earthquake, southwest China. *Environ. Pollut.* 284, 117125–125. doi:10.1016/j.envpol.2021.117125

Chen, Z., Du, J., Zhou, X., Yi, L., Liu, L., Xie, C., et al. (2014). Hydrochemistry of the hot springs in western sichuan Province related to the WenchuanMS8.0 earthquake. *Sci. World J.* 2014, 901432. doi:10.1155/2014/901432

Chen, Z., Zhou, X., Du, J., Xie, C., Liu, L., Li, Y., et al. (2015). Hydrochemical characteristics of hot spring waters in the Kangding district related to the Lushan <i>M</i>_S = 7.0 earthquake in Sichuan, China. *Nat. Hazards Earth Syst. Sci.* 15, 1149–1156. doi:10.5194/nhess-15-1149-2015

Chiodini, G., Caliro, S., Cardellini, C., Frondini, F., Inguaggiato, S., and Matteucci, F. (2011). Geochemical evidence for and characterization of CO2 rich gas sources in the epicentral area of the Abruzzo 2009 earthquakes. *Earth Planet. Sci. Lett.* 304, 389–398. doi:10.1016/j.epsl.2011.02.016

Chiodini, G., Cardellini, C., Di Luccio, F., Selva, J., Frondini, F., Caliro, S., et al. (2020). Correlation between tectonic CO2 Earth degassing and seismicity is revealed by a 10-year record in the Apennines, Italy. *Sci. Adv.* 6, eabc2938. doi:10.1126/sciadv.abc2938

Chiodini, G., Frondini, F., and Marini, L. (1995). Theoretical geothermometers andPCO2 indicators for aqueous solutions coming from hydrothermal systems of medium-low temperature hosted in carbonate-evaporite rocks. Application to the thermal springs of the Etruscan Swell, Italy. *Appl. Geochem.* 10, 337–346. doi:10.1016/0883-2927(95)00006-6

Claesson, L., Skelton, A., Graham, C., Dietl, C., Morth, M., Torssander, P., et al. (2004). Hydrogeochemical changes before and after a major earthquake. *Geol.* 32 (8), 641. doi:10.1130/g20542.1

Claesson, L., Skelton, A., Graham, C., and Morth, C. M. (2007). The timescale and mechanisms of fault sealing and water-rock interaction after an earthquake. *Geofluids* 7 (4), 427–440. doi:10.1111/j.1468-8123.2007.00197.x

Doglioni, C., Barba, S., Carminati, E., and Riguzzi, F. (2014). Fault on–off versus coseismic fluids reaction. *Geosci. Front.* 5 (6), 767–780. doi:10.1016/j.gsf.2013.08.004

Fouillac, C., and Michard, G. (1981). Sodium/lithium ratio in water applied to geothermometry of geothermal reservoirs. *Geothermics* 10, 55–70. doi:10.1016/0375-6505(81)90025-0

Fournier, R. O., and Potter, R. W. (1982). A revised and expanded silica (quartz) geothermometer. *Geoth. Res. Counc. Bull.* 11, 3–9.

Fournier, R. O., and Potter, R. W. (1979). Magnesium correction to the Na-K-Ca chemical geothermometer. *Geochim. Cosmochim. Acta* 43, 1543–1550. doi:10.1016/0016-7037(79)90147-9

Fournier, R. O., and Truesdel, A. H. (1973). Empirical Na-K-Ca geothermometer for natural waters. *Geochim. Cosmochim. Acta* 37, 1255–1275.

Geng, H., Pan, B., Huang, B., Cao, B., and Gao, H. (2017). The spatial distribution of precipitation and topography in the Qilian Shan Mountains, northeastern Tibetan Plateau. *Geomorphology* 297, 43–54. doi:10.1016/j.geomorph.2017.08.050

Gherardi, F., and Pierotti, L. (2018). The suitability of the Pieve Fosciana hydrothermal system (Italy) as a detection site for geochemical seismic precursors. *Appl. Geochem.* 92, 166–179. doi:10.1016/j.apgeochem.2018.03.009

Giggenbach, W. F. (1988). Geothermal solute equilibria: Derivationof Na-K-Ma-Ca geoindicators. *Geochim. Cosmochim. Acta* 52, 2749–2765. doi:10.1016/0016-7037(88)90143-3

Gori, F., and Barberio, M. D. (2022). Hydrogeochemical changes before and during the 2019 Benevento seismic swarm in central-southern Italy. *J. Hydrol. X.* 604, 127250. doi:10.1016/j.jhydrol.2021.127250

Hauksson, E., and Goddard, J. (1981). Radon content of groundwater as an earthquake precursor: Evaluation of worldwide data and physical basis. *J. Geophys. Res.* 86, 9397–9410. doi:10.1029/jb086ib10p09397

Huang, T., Nie, Z. H., and Yuan, L. (2008). Temperature and geographical effects of hydrogen and oxygen isotopes in precipitation in west of China. *J. arid land Resour. Environ.* 22 (8), 76–81. (In Chinese).

Kima, J., Leea, J., Petitta, M., Kim, H., Kaown, D., Park, I. W., et al. (2019). Groundwater system responses to the 2016 ML 5.8 Gyeongju earthquake, South Korea. *J. Hydrology* 576, 150–163. doi:10.1016/j.jhydrol.2019.06.044

Lei, J., Li, Y., Oskin, M. E., Wang, Y., Xiong, J., Xin, W., et al. (2020). Segmented thrust faulting: Example from the northeastern margin of the Tibetan Plateau. *J. Geophys. Res. Solid Earth* 125, e2019JB018634. doi:10.1029/2019JB018634

Lei, J., and Zhao, D. (2016). Teleseismic P-wave tomography and mantle dynamics beneath Eastern Tibet. *Geochem. Geophys. Geosyst.* 17 (5), 1861–1884. doi:10.1002/2016GC006262

Li, C. H., Zhou, X. C., Yan, Y. C., Ouyang, S., and Liu, F. (2021). Hydrogeochemical characteristics of hot springs and their short-term seismic precursor anomalies along the xiaojiang fault zone, southeast Tibet Plateau. *Water* 13, 2638. doi:10.3390/w13192638

Li, Z., Gai, H., Li, X., Yuan, D., Xie, H., Jiang, W., et al. (2022). Seismogenic fault and coseismic surface deformation of the Menyuan Ms6.9 earthquake in Qinghai,

China. *Acta Geol. Sin.* 96 (1), 330–335. (In Chinese). doi:10.19762/j.cnki.dizhixuebao.2022124

Liu, F., Cao, G., Cao, S., and Yang, Y. (2020). Research on stable isotope characteristics and recharge relationship of the main river on the southern slope of Qilian Mountains. *J. desert Res.* 40 (6), 151–161. doi:10.7522/j.issn.1000-694X.2020.00085

Liu, W., Wang, T., Gao, X., and Su, Y. (2004). Distribution and evolution of water chemical characteristics in Heihe river basin. *J. desert Res.* 24 (6), 755–762. (In Chinese).

Liu, Y., Yang, Y., Song, B., Galy, A., Zhang, F., Jin, Z., et al. (2022). Hydrothermal systems with radiogenic Sr in the North Qaidam ultrahigh-pressure metamorphic belt, NE Tibetan Plateau and implications for regional dissolved Sr budget. *Appl. Geochem.* 138, 105214. doi:10.1016/j.apgeochem.2022.105214

Meng, K., Wang, E., Chu, J. J., Su, Z., and Fan, C. (2020). Late Cenozoic river system reorganization and its origin within the Qilian Shan, NE Tibet. *J. Struct. Geol.* 138, 104128. doi:10.1016/j.jsg.2020.104128

Millot, R., Guerrot, C., Innocent, C., Negrel, P., and Sanjuan, B. (2011). Chemical, multi-isotopic (Li–B–Sr–U–H–O) and thermal characterization of Triassic formation waters from the Paris Basin. *Chem. Geol.* 283, 226–241. doi:10.1016/j.chemgeo.2011.01.020

Négrel, Ph., Fouillac, C., and Brach, M. (1997). Occurrence of mineral water springs in the stream channel of the allier river (massif central, France): Chemical and Sr isotope constraints. *J. Hydrology* 203, 143–153. doi:10.1016/s0022-1694(97)00094-2

Okada, T., Matsuzawa, T., Umino, N., Yoshida, K., Hasegawa, A., Takahashi, H., et al. (2015). Hypocenter migration and crustal seismic velocity distribution observed for the inland earthquake swarms induced by the 2011 tohoku-oki earthquake in NE Japan: Implications for crustal fluid distribution and crustal permeability. *Geofluids* 15 (1-2), 293–309. doi:10.1111/gfl.12112

Onda, S., Sano, Y., Takahata, N., Kagoshima, T., Miyajima, T., Shibata, T., et al. (2018). Groundwater oxygen isotope anomaly before the M6.6 Tottori earthquake in Southwest Japan. *Sci. Rep.* 8 (1), 4800. doi:10.1038/s41598-018-23303-8

Palmer, M. R., and Edmond, J. M. (1992). Controls over the strontium isotope composition of river water. *Geochim. Cosmochim. Acta* 56, 2099–2111. doi:10.1016/0016-7037(92)90332-d

Pierotti, L., Botti, F., D'Intinosante, V., Facca, G., and Gherardi, F. (2015). Anomalous CO2 content in the gallicano thermo-mineral spring (serchio valley, Italy) before the 21 June 2013, alpi apuane earthquake (M = 5.2). *Phys. Chem. Earth Parts A/B/C* 85 (86), 131–140. doi:10.1016/j.pce.2015.02.007

Pierotti, L., Gherardi, F., Facca, G., Piccardi, L., and Moratti, G. (2017). Detecting CO 2 anomalies in a spring on Mt. Amiata volcano (Italy). *Phys. Chem. Earth Parts A/B/C* 98, 161–172. doi:10.1016/j.pce.2017.01.008

Reddy, D. V., Kumar, D., and Purnachandra Rao, N. (2017). Long-term hydrochemical earthquake precursor studies at the Koyna-Warna reservoir site in westernIndia. *J. Geol. Soc. India* 90 (6), 720–727. doi:10.1007/s12594-017-0781-x

Reddy, D. V., Nagabhushanam, P., and Sukhija, B. S. (2011). Earthquake (M 5.1) induced hydrogeochemical and δ18O changes: Validation of aquifer breaching-mixing model in koyna, India. *Geophys. J. Int.* 184 (1), 359–370. doi:10.1111/j.1365-246X.2010.04838.x

Rosen, M. R., Binda, G., Archer, C., Pozzi, A., Michetti, A. M., and Noble, P. J. (2018). Mechanisms of earthquake-induced chemical and fluid transport to carbonate groundwater springs after earthquakes. *Water Resour. Res.* 54 (8), 5225–5244. doi:10.1029/2017wr022097

Rozanski, K., Araguas-Araguas, L., and Gonfiantini, R. (1993). *Isotopic patterns in modern global precipitation*. Washington DC: American Geophysical Union Geophysical Monograph Series.

Schuessler, J. A., Kampf, H., Koch, U., and Alawi, M. (2016). Earthquake impact on iron isotope signatures recorded in mineral spring water. *J. Geophys. Res. Solid Earth* 121 (12), 8548–8568. doi:10.1002/2016jb013408

Scott, B. E., Newell, D. L., Jessup, M. J., Grambling, T. A., and Shaw, C. A. (2020). Structural controls on crustal fluid circulation and hot spring geochemistry above a flat-slab subduction zone, Peru. *Geochem. Geophys. Geosyst.* 21, e2020GC008919. doi:10.1029/2020GC008919

Snell, T., Paola, N. P., Hunen, J. V., Nielsen, S., and Collettini, C. (2020). Modelling fluid flow in complex natural fault zones: Implications for natural and human-induced earthquake nucleation. *Earth Planet. Sci. Lett.* 530, 115869. doi:10.1016/j.epsl.2019.115869

Sobolev, G. A. (1984). "The study of failure forerunners on the big samples," in *International symposium continental seismicity and earthquake precursors* (Beijing: Seismological Press), 515–524.

Su, Q., Yuan, D. Y., and Xie, H. (2016). Geomorphic Features of the Heihe river drainage basin in Western Qilian Shan-Hexi corridor and its tectonic implications. *Seismol. Geol.* 38 (3), 560–581. (in Chinese). doi:10.3969/j.issn.0253-4967.2016.03.005

Teufel, L. W. (1980). Precursive pore pressure changes associated with premonitory slip during stick-slip sliding. *Tectonophysics* 69, 189–199. doi:10.1016/0040-1951(80)90133-x

Thomas, D., Cuff, K., and Cox, M. (1986). The association between ground gas radon variations and geologic activity in Hawaii. *J. Geophys. Res.* 9I, 12186–12198. doi:10.1029/jb091ib12p12186

Tian, J., Pang, Z., Wang, Y., and Guo, Q. (2019). Fluid geochemistry of the Cuopu high temperature geothermal system in the eastern Himalayan syntaxis with implication on its Genesis. *Appl. Geochem.* 110, 104422–104442. doi:10.1016/j.apgeochem.2019.104422

Utkin, V. I., and Yurkov, A. K. (2010). Radon as a tracer of tectonic movements. *Russ. Geol. Geophys.* 51, 220–227. doi:10.1016/j.rgg.2009.12.022

Wakita, H. (1996). Geochemical challenge to earthquake prediction. *Proc. Natl. Acad. Sci. U. S. A.* 93, 3781–3786. doi:10.1073/pnas.93.9.3781

Wakita, H., Nakamura, Y., and Sano, Y. (1985). Groundwater radon variations reflecting changes in regional stress fields. *Earthq. Predict. Res.* 3, 545–557. doi:10.1007/978-94-017-2738-9_19

Wang, P., Song, X., Han, D., Zhang, Y., and Liu, X. (2010). A study of root water uptake of crops indicated by hydrogen and oxygen stable isotopes: A case in shanxi Province, China. *Agric. Water Manag.* 97, 475–482. doi:10.1016/j.agwat.2009.11.008

Wang, Y., Chen, J., and Chen, L. (2009). *Tracing groundwater with strontium isotopic compositions in the Hexi corridor basin, northwestern China*. Berlin/Heidelberg, Germany: Springer, 184–187.

Wang, Y., Li, Q., Ran, H., Zhao, C., and Liu, Y. (2018). Geothermal and seismic activities in the southeastern Tibetan plateau: Constraints from helium isotopes. *Bull. Mineral. Geochem* 37, 652–662. (in Chinese). doi:10.19658/j.issn.1007-2802.2018.37.103

Woith, H., Wang, R., Maiwald, U., Pekdeger, A., and Zschau, J. (2013). On the origin of geochemical anomalies in groundwaters induced by the Adana 1998 earthquake. *Chem. Geol.* 339, 177–186. doi:10.1016/j.chemgeo.2012.10.012

Wong, I., and Chapman, D. (1990). Deep intraplate earthquakes in the Western United States and their relationship to lithospheric temperatures. *Bull. Seismol. Soc. Am.* 80, 589–599. doi:10.1016/0040-1951(90)90455-H

Wu, G., Liu, J., Sun, Z., Li, J., Wang, C., and Zhou, Z. (2020). Hydrogeochemical characteristics of groundwater in jiuquan yumen-suzhou area of Hexi corridor. *Water Resour. Hydropower Eng.* 51 (10), 111–118. (In Chinese).

Xiong, L., Wang, J., and Pang, Z. (1990). Circulation depth of the thermal water in Zhangzhou geothermal field. *Sci. Geol. Sin.* 4, 377–384. (In Chinese).

Yang, H., Wang, D., Guo, R., Xie, M., Zang, Y., Wang, Y., et al. (2022). Rapid report of the 8 january 2022 MS 6.9 menyuan earthquake, Qinghai, China. *Earthq. Res. Adv.* 2 (1), 100113. doi:10.1016/j.eqrea.2022.100113

Yuan, D., Ge, W. P., Chen, Z. W., Li, C., Wang, Z., Zhang, H., et al. (2013). The growth of northeastern tibet and its relevance to large scale continental geodynamics: A review of recent studies. *Tectonics* 32, 1358–1370. doi:10.1002/tect.20081

Yuan, D., Zhang, P., Liu, B., Gan, W., Mao, F., Wang, Z., et al. (2004). Geometrical imagery and tectonic transformation of Late Quaternary active tectonics in Northeastern margin of Qinghai-Xizang Plateau. *Acta Geol. sin.* 78 (2), 270–276. (In Chinese).

Zhang, H., Zhang, P., Prush, V., Zheng, D., Zheng, W., Wang, W., et al. (2017). Tectonic geomorphology of the Qilian Shan in the northeastern Tibetan Plateau: Insights into the plateau formation processes. *Tectonophysics* 706-707, 103–115. doi:10.1016/j.tecto.2017.04.016

Zhang, P., Deng, Q., Zhang, G., Ma, J., and Gan, W. (2003). Active tectonic blocks and strong earthquakes in the continent of China. *Sci. China Ser. G.* 46, 528–624. doi:10.1360/02yw0305

Zhang, P., Zheng, D., Yin, G., Yuan, D., Zhang, G., and Li, C. (2006). Discussion on Late Cenozoic growth and rise of northeastern margin of the Tibetan Plateau. *Quat. Sci.* 26 (1), 5–13. (In Chinese).

Zhang, Y., Zhang, L., Chang, Y., Fan, Z., and Guo, D. (2018). Determining trace elements in rock samples containing refractory minerals by pressurize-microwave inductively coupled plasma mass spectrometry. *Uranium Geol.* 34, 105–111. (In Chinese).

Zhao, L. J., Eastoec, C. J., Liu, X. H., Wang, L., Wang, N., Xie, C., et al. (2018). Origin and residence time of groundwater based on stable and radioactive isotopes in the Heihe River Basin, northwestern China. *J. Hydrology Regional Stud.* 18, 31–49. doi:10.1016/j.ejrh.2018.05.002

Zoback, M. D., and Bverlee, J. D. (1975). The effect of micro-crack dilatancy on the permeability of westerly granite. *J. Geophys. Res.* 80, 752–755. doi:10.1029/jb080i005p00752

Zuza, A. V., and Cao, W. (2020). Seismogenic thickness of California: Implications for thermal structure and seismic hazard. *Tectonophysics* 782-783, 782228426–782228783. doi:10.1016/j.tecto.2020.228426

frontiers | Frontiers in Earth Science

TYPE Original Research
PUBLISHED 23 September 2022
DOI 10.3389/feart.2022.928348

OPEN ACCESS

EDITED BY
Filippos Vallianatos,
National and Kapodistrian University of Athens, Greece

REVIEWED BY
Alexey Lyubushin,
Institute of Physics of the Earth (RAS), Russia
Mukesh Gupta,
Climalogik Inc., Canada

*CORRESPONDENCE
Renata Rotondi,
renata.rotondi@mi.imati.cnr.it

SPECIALTY SECTION
This article was submitted to Solid Earth Geophysics,
a section of the journal
Frontiers in Earth Science

RECEIVED 25 April 2022
ACCEPTED 25 August 2022
PUBLISHED 23 September 2022

CITATION
Rotondi R and Varini E (2022), Temporal variations of the probability distribution of voronoi cells generated by earthquake epicenters.
Front. Earth Sci. 10:928348.
doi: 10.3389/feart.2022.928348

Temporal variations of the probability distribution of voronoi cells generated by earthquake epicenters

Renata Rotondi* and Elisa Varini

Istituto di Matematica Applicata e Tecnologie Informatiche, Consiglio Nazionale delle Ricerche, Milano, Italy

The area of the cells of Voronoi tessellations has been modelled through different probability distributions among which the most promising are the generalized gamma and tapered Pareto distributions. In particular the latter has been used to model times and distances between successive earthquakes besides area and perimeter of cells generated by earthquake epicenters. In the framework of nonextensive statistical mechanics applied in geophysics, variables like seismic moment, inter-event time or Euclidean distance between successive earthquakes or length of faults in a given region have been studied through the so-called q-exponential distributions obtained by maximizing the Tsallis entropy under suitable conditions. These distributions take also the name of generalized Pareto distributions in the context of the limit distributions of excesses. In this work we consider the spatial distribution of a set of earthquakes and its temporal variations by modelling the area of Voronoi cells generated by the epicenters through a generalized Pareto distribution. Following the Bayesian paradigm we analyze the recent seismicity of the central Italy and we compare the posterior marginal likelihood of the aforementioned distributions in shifting time windows. We point out that the best fitting distribution varies over time and the trend of all three distributions converges to that of the exponential distribution in the preparatory phase for the mainshock.

KEYWORDS

voronoi tessellations, tapered Pareto distribution, generalized gamma distribution, q-exponential distribution, spatial point processes, seismic forecast, Bayesian inference, Markov chain Monte Carlo methods

Introduction

Tessellations of space for a given set of points into non-overlapping cells play an important role in the study of spatial point patterns generated by natural and social phenomena. Among many possibilities of partitions, the Voronoi tessellation is probably the most popular; it has been applied in a wide variety of disciplines such as biology, astronomy, forestry, geology and ecology (Okabe et al. (2000)). Some of the statistical properties of spatial point patterns are related to the properties of the geometrical

characteristics of the corresponding tessellation; in the case of the homogeneous Poisson point process the resulting Voronoi cells are called Poisson Voronoi (PV) cells. Even though the importance of this process has motivated many studies so far most of the results has not been obtained theoretically but through computer simulations; apart from the probability distribution of the cell length in $\mathbb{R}$, which is a Gamma (2,2) distribution, only a few moments of some characteristics of PV cells - such as the number of edges, the area, the perimeter - are known (Hinde and Miles (1980)), not their probability distributions. Fitting the histograms obtained by the simulation of some millions of PV cells Tanemura (2003) showed that the three-parameter (or generalized) gamma distribution fits quite well a wide range of probability densities of their geometrical characteristics in two- and three-dimensional spaces. With the aim to find a simpler functional form Ferenc and Neda (2007) obtained that the gamma distribution with parameters $a = b = (3\,d + 1)/2$ gives an acceptable, even if less accurate, approximation of the size distribution of PV cells in d-dimensional spaces ($d = 1, 2, 3$). Zaninetti (2009) instead investigated non-Poissonian Voronoi diagrams associated with correlated seeds; he generated seeds in polar coordinates ρ and θ in the following way: the distance ρ from the center of the region is generated according to a probability distribution chosen between the product and the ratio of two Gamma (2,2), and the polar angle θ in degrees is given by $\theta = 360\ Y$ with $Y \sim Unif\,(0, 1)$. Computer simulations provided evidence in favor of the conjecture according to which, in these cases, the area of the Voronoi cells follows the same distribution of the seeds.

In recent years some authors have begun to investigate how the properties of the cells change when boundaries are imposed to the study region. In particular Koufos and Dettmann (2019) considered PV cells located close to the boundaries of the quadrant $\mathbb{R}^+$ and obtained that the gamma distribution, with location-dependent parameters, provides a reasonably good approximation to the distribution of cell area. Gezer et al. (2021) compared the statistical properties of the area of PV cells in the infinite plane and of clipped cells in two bounded regions: the unit square and the convex hull of the points; they found that the generalized gamma distribution provides a good fit with parameters varying according to the location of the cell seed in the bounded region. It should be noted that, as the number of the points increases, the vast majority of cells are not affected by the imposition of boundaries; indeed Devroye et al. (2017) have shown that the asymptotic distribution of the Voronoi cell area is independent of the location of the seed and of the intensity measure underlying the Poisson point process.

In seismology Schoenberg et al. (2009) studied the point pattern of the earthquakes that occurred from 1984 to 2007 in Southern California through the Voronoi tessellation generated by their epicenters; they obtained that the tapered Pareto distribution, already used to describe the seismic moment (Jackson and Kagan (1999)), approximates the distribution of area and perimeter of the cells not intersecting with the boundary of the region better than the pure Pareto, log-normal and gamma distributions. This result can be explained by the spatial clustering of these events which implies many cells with a small area and some with a larger area than would be expected from a stationary point process. This behaviour is typical of heavy right-tailed distributions.

In the framework of the statistical physics a new distribution of the moment magnitude was derived from the q-exponential distribution ($1 < q < 2$) obtained by maximizing, under suitable constraints, a nonextensive generalization of the Boltzmann-Gibbs entropy given by the Tsallis entropy (Tsallis (2009); Vallianatos et al. (2015)). Following the example of Schoenberg et al. (2009) we have thought that the q-exponential distribution could describe, in addition to the earthquake size (Rotondi et al. (2022)), also the spatial properties of the seismic phenomenon such as the area of the Voronoi cells generated by the epicentral locations. This distribution also takes the name of generalized Pareto distribution in the context of the limit distributions of excesses (Bercher and Vignat (2008)); hence, hereafter, we use these two terms interchangeably.

The main aims of this work are: 1) to evaluate the fitting of the generalized Pareto distribution to the areas of Voronoi cells generated by the seismicity recorded in bounded regions of central Italy in recent years, b) to compare the performance of this distribution with that of the most promising probability distributions of the Voronoi cell area, that is, tapered Pareto and generalized gamma distributions, in time-varying windows with the same number of events. Parameter estimation is performed according to the Bayesian paradigm by applying Markov chain Monte Carlo (MCMC) methods, in particular the Metropolis-Hastings algorithm, to sample from the posterior probability distributions of the parameters (Roberts and Casella (2004)); hence the comparison is based on the ratio of the pairwise posterior marginal likelihoods of the abovementioned distributions. We will try to associate the probability distribution with the best performance to time periods characterized by a specific type of seismic activity; in particular we will notice that the likelihood of the three distributions generally assumes very different value from that of the exponential distribution apart from in a few time windows in the preparatory phase of the considered seismic crises in which the values of the four likelihoods are not significantly different.

Voronoi tessellation

Let us consider a finite number of n points $P = \{p_i \in S, i = 1, 2, \ldots, n\}$ distributed within some finite region $S \in \mathbb{R}^2$. The Voronoi tessellation partitions the region into a collection of disjoint

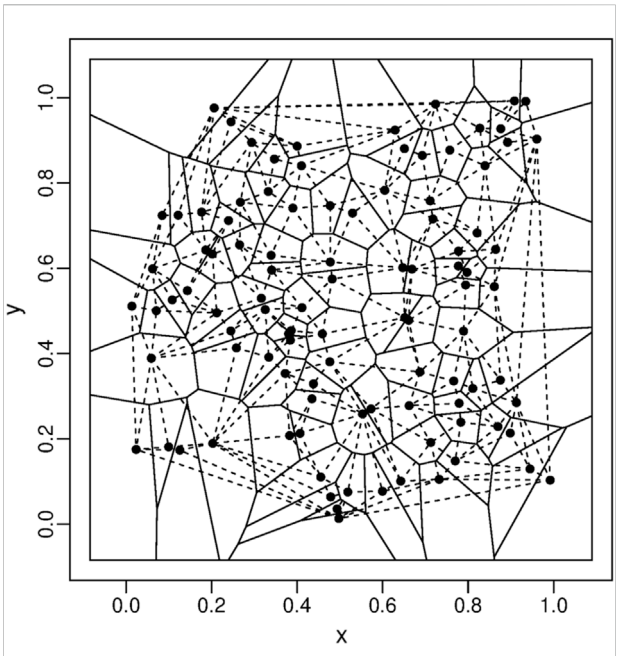

FIGURE 1
Voronoi tessellation of n =100 uniformly distributed points (black dots) bounded by the unit square and the convex hull of points; edges of the PV cells (solid lines) and Delaunay triangulation associated with the Voronoi diagram (dashed lines).

subregions $V = \{V_i, i = 1, 2, \ldots, n\}$ called Voronoi cells, which have the following properties: $V_i \cap V_j = \varnothing$ for $i \neq j$, $\cup_{i=1}^{n} V_i = S$. Each cell V_i is defined as the set (polygon) of points of S which are closer to the corresponding seed p_i than any other point in P; hence:

$$V_i = \left\{x \in S:\ \|x - p_i\| \leq \|x - p_j\| \text{ for } \quad j = 1, 2, \ldots, i-1, i+1, \ldots, n\right\}$$

where $\|\cdot\|$ denotes Euclidean distance. If we join the points p_i and p_j associated with the cells V_i and V_j that share an edge, we obtain an undirected graph called a Delaunay triangulation of the convex hull of P. Figure 1 shows an example of Voronoi tessellation of n = 100 uniformly distributed points in the unit square. In this work we have constructed Voronoi tessellations using the *deldir* library (Turner (2018)) available within R (R Core Team (2018)).

Probability distributions and Bayesian inference

We briefly present the three probability models adopted to describe the area of the Voronoi cells in a bounded region and we give the basic concepts on the Bayesian set-up we have followed in estimation and comparison of the three models. In general, let us assume that the data $\mathbf{x} = (x_1, x_2, \ldots, x_n)$ are realizations of a random variable X whose density function belongs to the parametric family $\mathcal{F} = \{f(x;\theta):\ \theta \in \Theta\}$. In the Bayesian setting the parameter θ is considered as a random variable and we express our initial beliefs about it by specifying a distribution $p_0(\theta)$, termed *prior* distribution, which supplements the information provided by data and expressed by the likelihood $\mathcal{L}(f(\mathbf{x}\,|\,\theta)) = \prod_{i=1}^{n} f(x_i;\theta)$. By applying the Bayes' theorem we can combine the two sources of information into the *posterior* distribution:

$$p(\theta\,|\,\mathbf{x}) = \frac{p_0(\theta)\,\mathcal{L}(f(\mathbf{x}\,|\,\theta))}{\int_\Theta p_0(\theta)\,\mathcal{L}(f(\mathbf{x}\,|\,\theta))\,d\theta}, \tag{1}$$

which enables us to get not only the parameter estimate, typically as the posterior mean $E_p(\theta)$, but also a measure of its accuracy by the posterior variance. These advantages however have a computational cost due to the evaluation of the integral, often high-dimensional, in (1); in fact when the prior distribution is not conjugate for the likelihood function, that integral does not have a closed-form expression and requires sophisticated numerical integration techniques. This difficulty has been tackled by the development of Markov chain Monte Carlo (MCMC) methods which produce simulated values from the posterior distribution (Roberts and Casella (2004)). In particular we apply the Metropolis-Hastings (MH) algorithm consisting of the following steps: a) generate an initial value θ_0 from $p_0(\theta)$ and set $i = 0$, b) draw a candidate $\tilde{\theta}$ from a proposal distribution $q(\theta|\theta_i)$, c) compute the acceptance probability

$$\alpha_i = min\left(1,\ \frac{\mathcal{L}\left(f\left(\mathbf{x}\,|\,\tilde{\theta}\right)\right)p_0\left(\tilde{\theta}\right)q\left(\theta_i\,|\,\tilde{\theta}\right)}{\mathcal{L}\left(f\left(\mathbf{x}\,|\,\theta_i\right)\right)p_0\left(\theta_i\right)q\left(\tilde{\theta}\,|\,\theta_i\right)}\right),$$

and accept $\tilde{\theta}$ as θ_{i+1} with probability α_i, or set $\theta_{i+1} = \theta_i$ with probability $(1 - \alpha_i)$. It can be shown that the generated sequence is a Markov chain having the posterior distribution (1) as equilibrium distribution. Since the first values of the chain are highly dependent on the starting value, we will use the sequence $\{\theta_i\}_{i=k+1}^{M+k}$, for large enough values of k and M, to estimate the posterior distribution $p(\theta|\mathbf{x})$ and to approximate the posterior marginal log-likelihood:

$$\log\mathcal{L}(f(\mathbf{x})) = \int_\Theta \log\mathcal{L}(f(\mathbf{x}\,|\,\theta))\,p(\theta\,|\,\mathbf{x})\,d\theta \approx 1\Big/M \sum_{j=k+1}^{M+k} \log\mathcal{L}\left(f\left(\mathbf{x}\,|\,\theta_j\right)\right) \tag{2}$$

that enables us to check how well the fitted model makes sense to explain the observed data. In general, given two statistical models $f_1(\cdot|\phi)$ and $f_2(\cdot|\eta)$ we can compare them by $\Delta = \log\mathcal{L}(f_1(\mathbf{x})) - \log\mathcal{L}(f_2(\mathbf{x}))$, and then, similar to the Bayes factor, we establish the degree of evidence in favor of the first model according to the value $\mathcal{K}$ of the Jeffreys scale (Kass and Raftery (1995); Gelman et al. (2004)). In the next Sections we

introduce the three probability distributions we have chosen to model the Voronoi cell area and we give some elements on their Bayesian inference.

Q-Exponential - or generalized Pareto - distribution

The probability density function of the q-exponential distribution is given by:

$$f_1(x) = \frac{1}{\beta}\left(1 - \frac{(1-q)}{(2-q)}\frac{x}{\beta}\right)^{1/(1-q)} \quad \text{for} \quad x \geq 0 \quad \beta > 0 \quad \text{and} \quad 1 < q < 2 \tag{3}$$

where q is called the entropic index and β is the generalized expectation value, that is, the mean with respect to the *escort* probability distribution (Tsallis (2009)):

$$f_q(x) = \frac{f^q(x)}{\int_0^{+\infty} f^q(x)\,dx}. \tag{4}$$

Since the q-exponential density function (3), for large x, goes to zero as a power $x^{-1/(q-1)}$ it is a fat-tailed distribution; moreover, being always bounded below by the exponential density function and having

$$\lim_{x\to+\infty} e^{tx}\bar{F}_1(x) = \lim_{x\to+\infty} e^{tx}\left(1 + \frac{q-1}{2-q}\frac{x}{\beta}\right)^{-(2-q)/(q-1)} = +\infty \quad \forall t > 0 \tag{5}$$

where $\bar{F}_1(x) = 1 - F_1(x)$, the q-exponential distribution is also heavy-tailed.

To improve the efficiency of the MH algorithm, we reparameterize the model (3) by setting $\theta = (2 - q)/(q - 1)$ with $\theta \in (0, +\infty)$. As prior distributions we adopt two lognormal distributions: θ ~Lognormal ($mean_\theta$, var_θ) and β ~Lognormal ($mean_\beta$, var_β). We emphasize that here *mean* and *var* indicate the mean and variance of the random variable and not the mean and variance of its logarithm, as in the common representation of the lognormal distribution. We also choose lognormal distributions as proposal distributions; in particular, at the $(i + 1)$-th iteration, for θ we have Lognormal $(\theta_i, (\theta_i/\kappa_1)^2)$, and for β we have Lognormal $(\beta_i, (\beta_i/\kappa_2)^2)$), with θ_i and β_i as the current value of the respective Markov chain. The values of κ_1 and κ_2 are calibrated through pilot runs on the data so that the acceptance rate of the MH algorithm is about 25–40%.

Tapered Pareto distribution

The tapered Pareto distribution has cumulative distribution function

$$F_2(x) = 1 - \left(\frac{a}{x}\right)^{\beta}\exp\left(-\frac{x-a}{\theta}\right) \qquad x \geq a \tag{6}$$

and density

$$f_2(x) = \left(\frac{\beta}{x} + \frac{1}{\theta}\right)\left(\frac{a}{x}\right)^{\beta}\exp\left(-\frac{x-a}{\theta}\right) \qquad x \geq a \tag{7}$$

where $a > 0$ is the minimum value of x, β is a shape parameter governing the power-law decrease in frequency as x increases, and θ is a parameter controlling the position of the exponential taper to zero in the frequency of large events (Vere-Jones et al. (2001)). It can be proved that the $\int_0^{+\infty} e^{tx}\,dF_2(x)$ is finite for $0 < t < 1/\theta$ (Vaičiulis and Markovich (2021)); so the tapered Pareto distribution is light-tailed.

Similarly to the q-exponential distribution we adopt the lognormal distribution both as prior distribution and as proposal distribution of the three parameters with suitable values of κ_1, κ_2 and κ_3.

Generalized gamma distribution

The generalized gamma distribution, introduced by Stacy (1962), has the following three-parameter density function:

$$f_3(x) = \frac{\beta}{\Gamma(k)}\frac{x^{\beta k-1}}{\alpha^{\beta k}}\exp\left\{-(x/\alpha)^{\beta}\right\} \qquad \beta, \alpha, k > 0 \tag{8}$$

and it includes the exponential, Weibull and gamma distributions as special cases. In this form the generalized gamma distribution presented some difficulties in maximum likelihood estimate of the parameters; to overcome these problems Prentice (1974) proposed a different but equivalent form obtained through the transformation of variable $w = \sqrt{k}\,[\beta(\log x - \log\alpha) - \log k]$. In this way we obtain the generalized gamma density function:

$$f_3(x) = \frac{\gamma\,(\gamma^{-2})^{\gamma^{-2}}}{\Gamma(\gamma^{-2})}\exp\left\{\frac{\gamma\left(\frac{\log x-\mu}{\sigma}\right) - \exp\left\{\gamma\left(\frac{\log x-\mu}{\sigma}\right)\right\}}{\gamma^2}\right\}\frac{1}{\sigma x} \tag{9}$$

where $\mu = \log\alpha + (\log k)/\beta \in (-\infty, +\infty)$ is the location parameter, $\sigma = 1/(\beta\sqrt{k}) \in (0, +\infty)$ is the scale parameter and $\gamma = 1/\sqrt{k} \in (0, +\infty)$ is the shape parameter. This parameterisation is also adopted in the *flexsurv* and *survival* libraries available within R (R Core Team (2018)) and which we use to represent the generalized gamma distribution function in the figures reported in next Sections.

As prior distributions we adopt three lognormal distributions, while we choose the proposal distributions in the MH algorithm so that, at the $(i + 1)$-th iteration, $\tilde{\mu}$ is generated from Normal $(\mu_i, (\mu_i/\kappa_1)^2)$, $\tilde{\sigma}$ from Lognormal $(\sigma_i, (\sigma_i/\kappa_2)^2)$, and $\tilde{\gamma}$ from Lognormal $(\gamma_i, (\gamma_i/\kappa_3)^2)$.

TABLE 1 Parameters of the prior distributions and κ coefficients used in the proposal distributions in MH algorithm.

		L'Aquila case			Amatrice-Norcia case		
model	**parameters**	**mean$_0$**	**var$_0$**	κ	**mean$_0$**	**var$_0$**	κ
q-exponential	θ	5	4	1.25	0.5	0.4	2
	β	1.5×10^2	2.25×10^4	2	1.5	2.25	1.5
tapered Pareto	θ	2×10^2	10^4	2	10^2	6.25×10^4	0.5
	a	0.2	0.04	2	0.2	0.04	7.5
	β	0.1	0.01	1.25	0.1	0.01	2.5
generalized gamma	μ	4	4	6	1	0.4	1
	σ	2	1	4	2	1	4
	γ	0.5	0.2	1.25	0.5	0.25	0.5

Data

The data sequences analysed in this study are drawn from the Italian National Institute of Geophysics and Volcanology (*Istituto Nazionale di Geofisica e Vulcanologia*; INGV) web services: Italian Seismological Instrumental and Parametric Database (ISIDe) working group (2016), version 1.0, accessible at http://cnt.rm.ingv.it/en/iside (ISIDe Working Group (2007)). The parameters that define each earthquake of this catalog are the origin time, the hypocenter (i.e., geographic coordinates and depth) and the size that is expressed in different units of magnitude, as local magnitude M_L, duration magnitude M_D, and moment magnitude M_w. We have applied the orthogonal regression relationships: $M_w = 1.066\ M_L - 0.164$ and $M_w = 1.718\ M_D - 1.897$ (Gasperini et al. (2013)) to convert M_L and M_D to M_w so as to construct homogenous data sets. The coordinates of the epicenters are expressed in units of latitude and longitude in the WGS84 reference system; we have converted them to planar Universal Transverse Mercator (UTM) coordinate system (in km) through the Generic Mapping Tools (GMT) (Wessel and Smith (1998)) to be consistent with the Euclidean distance used by the *deldir* library in the construction of the Voronoi tessellations.

In recent decades central Italy was hit by strong seismic activity related to L'Aquila earthquake in 2009 and Amatrice-Norcia shocks in 2016. We analyze the seismicity recorded in the corresponding seismogenic areas in the years that preceded the mainshock and in part of the aftershock period to observe how the spatial distribution of the events changes. To do that we estimate the q-exponential, tapered Pareto, and generalized gamma distributions of the Voronoi cell area for time windows of a fixed number of events that shift at each new event. In the case of the exponential probability density: $f_4(x) = \lambda \exp\{-\lambda x\}$, we adopt the conjugate Gamma (0.01, 1) distribution as prior distribution of the λ parameter so that the expected area is about 100 km^2. For the three probability models under examination Table 1 reports the parameters of the prior distributions and the κ coefficients used in the proposal distributions of the MH algorithm to obtain suitable acceptance rates.

L'Aquila case study

On 6 April 2009 (01:13:40 UTC, latitude 42.342, longitude 13.380), an M_w 6.1 earthquake struck central Italy, it was preceded by a M_w 4 shock on 30 March. The main event has been associated with the composite seismogenic source ITCS013 (Borbona-L'Aquila-Aremogna) of the Database of Individual Seismogenic Sources (DISS, version 3.2.1) (DISS Working Group (2018)), which is considered to have the potential for earthquakes of up to M_w 6.5. Considering the empirical relationships between magnitude and rupture length by Wells and Coppersmith (1992), the maximum expected rupture length in this area is about 18 km; moreover, since, according to Bowman et al. (1998), the seismic activation which precedes the major earthquakes should occur over a region with at most a characteristic length of about one order of magnitude larger than the maximum length, we consider a rectangular area centered on the epicenter, of latitude size (41.8, 43.0) degrees and longitude size (12.8, 13.8) degrees, which is included into the 33T zone of the UTM coordinate system. The events of $M_w \geq 2$ recorded by ISIDe in this area during the temporal period from 7 April 2005 to the end of July 2009 are $N = 2725$. To analyze how the spatial distribution of the events varies and to investigate if these changes are linked to different phases of the seismic cycle we consider time windows of a fixed number - $n = 100$ - of events that shift at each new event. First, we fit the three probability distributions to the $\mathbf{D^{(k)}}$ dataset of each window, $k = 1, 2, \ldots, N - n + 1$, and calculate their posterior marginal log-likelihood $\log \mathcal{L}\,(f_i(\mathbf{D^{(k)}})) = 1/m \sum_{j=1}^{m} \log f_i(\mathbf{D^{(k)}} \mid \Psi_i^{(j)})$, $\quad i = 1, 2, 3$, with $\left\{\Psi_i^{(j)}\right\}_{j=1}^{m}$ as the Markov chains of values of the parameter vectors $\Psi_1 = (\theta, \beta)$, $\Psi_2 = (\theta, a, \beta)$, and $\Psi_3 = (\mu, \sigma, \gamma)$, generated through the MH algorithm. Moreover we also compute the posterior marginal log-likelihood of the exponential distribution; all these values are associated with the time of the last event in the corresponding windows. Then, for each kth time window, we compute $i^* = \text{argmax}_{i=1,\ldots,4} \log \mathcal{L}\,(f_i(\mathbf{D^{(k)}}))$, that is the F_{i^*} probability distribution that provide the best performance among those under examination, and we evaluate the minimum

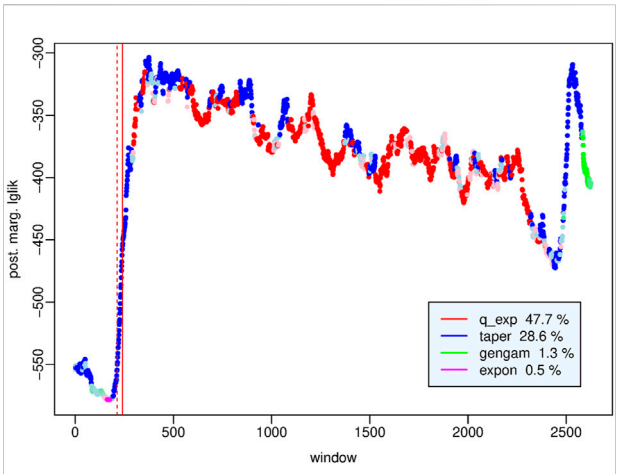

FIGURE 2
L'Aquila sequence - Posterior marginal log-likelihood of the probability distribution of Voronoi cell area that fits better than the other distributions to the dataset of each time window. The red vertical lines indicate the mainshock (solid line) and the M_w 4 30 March earthquake (dashed line) respectively.

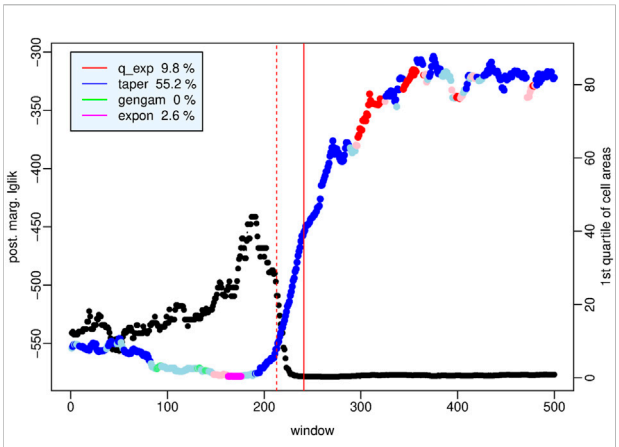

FIGURE 3
L'Aquila sequence - Magnification of Figure 2 in the period from April 2005 to 6 April 2009 (hr 8); the black dots indicate the first quartile of the set of cell areas in each time window.

discrepancy between the posterior marginal log-likelihoods of the best and of the other models given by $\Delta_{i^*}^{(k)} = \log \mathcal{L}\,(f_{i^*}(\mathbf{D}^{(\mathbf{k})}) - \max_{j\neq i^*,\ \ j=1,\ldots,4} \log \mathcal{L}\,(f_j(\mathbf{D}^{(\mathbf{k})}))$. Comparing this discrepancy with the $\mathcal{K}$ values of the Jeffreys scale (Kass and Raftery (1995)) we establish the degree of evidence in favor of the F_{i^*} model; in particular, set $\mathcal{K} = \log_e 10 = 2.3026$, $\Delta_{i^*}^{(k)} \geq \mathcal{K}$ indicates strong strength of the evidence. Figure 2 shows the value of the posterior marginal log-likelihood of the best $F_{i^*}^{(k)}$ model for this level of evidence at each time window: red dots correspond to the q-exponential probability distribution ($i^* = 1$), blue dots to the tapered Pareto distribution ($i^* = 2$), and green dots to the generalized gamma distribution ($i^* = 3$). The legend in Figure 2 reports the percentages of time windows in which $\Delta_{i^*}^{(k)} > \mathcal{K}$, that is the specific best model outperforms the others with strong evidence; this happens in about 78% of the intervals. The dots with slighter color indicate time windows in which $0 < \Delta_{i^*}^{(k)} < \mathcal{K}$, that is the evidence is less strong; in particular, from mid-September 2007 to January 2008 it is substantial ($1.1513 < \mathcal{K} < 2.3026$), then it reduces and it is worth no more than a bare mention ($0 < \mathcal{K} < 1.1513$) in favor of the exponential distribution (magenta dots) between December 2008 and January 2009, and finally it begins to increase until it returns strong in favor of the tapered Pareto distribution. In Figure 2 the red vertical lines indicate the time windows including the mainshock (solid line) and the M_w 4 30 March shock (dashed line) respectively. All this can be seen more clearly in Figure 3 which depicts magnification of the first 500 time windows of Figure 2 around the mainshock, precisely from April 2005 to 6 April 2009 (hr 8). The black dots represent the first quartile of the set of cell areas at each window. It can be noted that this quartile reaches the maximum in mid-February 2009, then it begins to decrease in correspondence to an increase of the number of small cells due to the concentration of the epicenters as the main phase approaches (De Santis et al. (2011)).

Let us examine in detail the dataset for which each probability distribution performs best in order to understand which characteristics distinguish it from the others and in which phase of the seismic cycle it is more appropriate to use it. Statistical summaries of the four sets of Voronoi cell areas are in Table 2. The q-exponential distribution provides the best fit to the events associated with the $\hat{k}$-th time window which covers few hours after the L'Aquila earthquake, that is $\hat{k} = \text{argmax}_k \Delta_{1^*}^{(k)}$; as expectable the cells of the Voronoi tessellation (top left-hand panel of Figure 4) are very small and concentrated around the epicenter of L'Aquila quake (red square) and along the rupture line, and the convex hull of the Delaunay triangulation (top right-hand panel) occupies only about 300 km^2. The bottom left histogram highlights the large number of very small area cells along with a few very large cells; the area varies in the range (0.151, 3336.13) (km^2), median is 1.89 km^2, the sample mean is approximately 120 km^2 and the third quartile is less than 6 km^2. This behaviour is well modelled by a heavy-tailed density function such as the q-exponential as also shown by the Q-Q plot in the bottom right-hand panel. The legend reports the absolute difference between sampled and theoretical quantiles for each distribution; in this case, the minimum value is obtained by the q-exponential density function.

Figure 5 refers to the period from mid-June 2009 to early July 2009 in which the tapered Pareto distribution is the best model; the seismic activity is less concentrated, in fact the area of the Voronoi cells varies in narrower range (0.0393, 1708.73) (km^2), the sample mean is still approximately 120 km^2 but the third quartile rises to 18 km^2. After about 3 months since the

TABLE 2 Statistical summaries of the sets of Voronoi cell areas (in km^2) to which each probability model fits best.

model	Min	1st Qu	Median	Mean	3rd Qu	Max
q-exponential	0.151	1.139	1.886	120.045	5.841	3336.129
tapered Pareto	0.0393	0.1475	0.794	121.270	17.946	1708.728
generalized gamma	0.0183	0.370	5.819	120.045	23.978	2195.998
exponential	0.280	35.473	75.190	118.845	169.574	591.0038

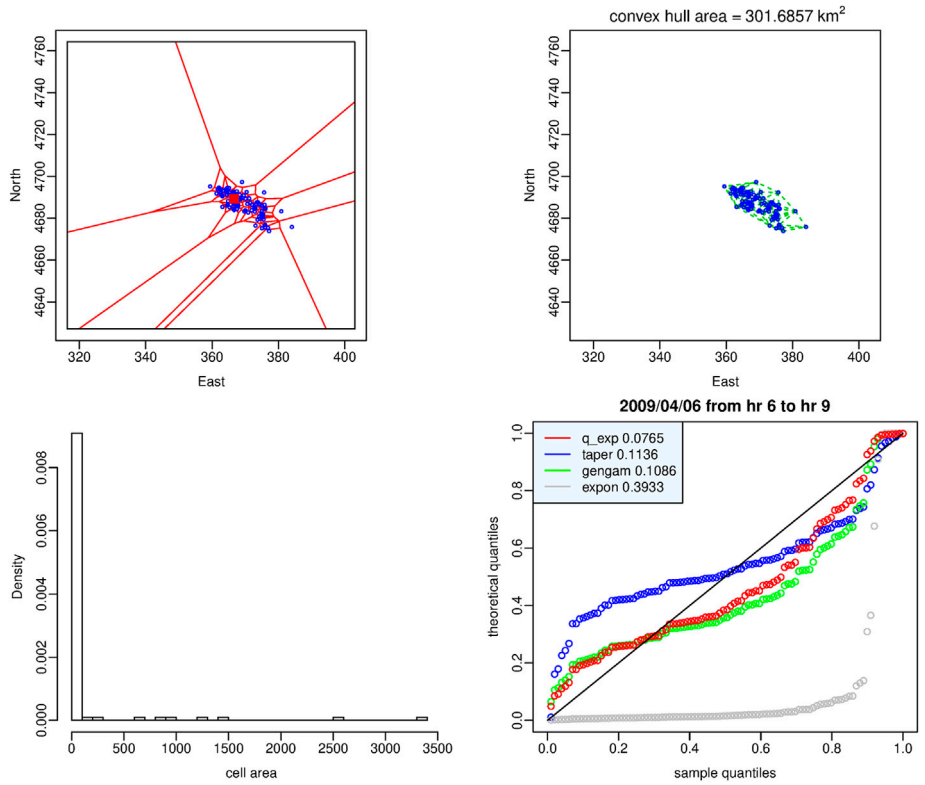

FIGURE 4
Dataset of the time window in which the q-exponential distribution provides the best fit. Top: Voronoi tessellation (left-hand panel) and Delaunay triangulation (right-hand panel). Bottom: histogram of the cell areas (left-hand panel) and Q-Q plot of the four probability distributions (right-hand panel). Red square indicates the epicenter of L'Aquila shock.

mainshock the secondary events begin to move away from its epicenter area so that the area of the convex hull is almost equal to 980 km^2. Also the Q-Q plot and the absolute difference between sampled and theoretical quantiles (bottom right-hand panel) show clear evidence in support of the tapered Pareto distribution as optimal model.

The dataset represented in Figure 6 consists of the events recorded from the end of June to mid-July 2009; the best fitting to the areas of the corresponding Voronoi tessellation is given by the generalized gamma distribution. The third quartile of the set of areas (−24 km^2) is larger than that of the previous sets but there are still many very small cells probably due to the presence of localized clusters of secondary events. Also in this case the Q-Q plot and the absolute difference between sampled and theoretical quantiles support the generalized gamma distribution as optimal model in agreement with the posterior marginal log-likelihood.

A completely different situation is represented in Figure 7; the top left-hand panel shows the Voronoi tessellation generated by the rather scattered events that occurred in the period from mid-June 2007 to the end of January 2009. In Table 2 it can be seen that the range of variability of the cell areas is considerably reduced; while maintaining roughly the same mean, the first and third quartiles vary significantly. The four probability

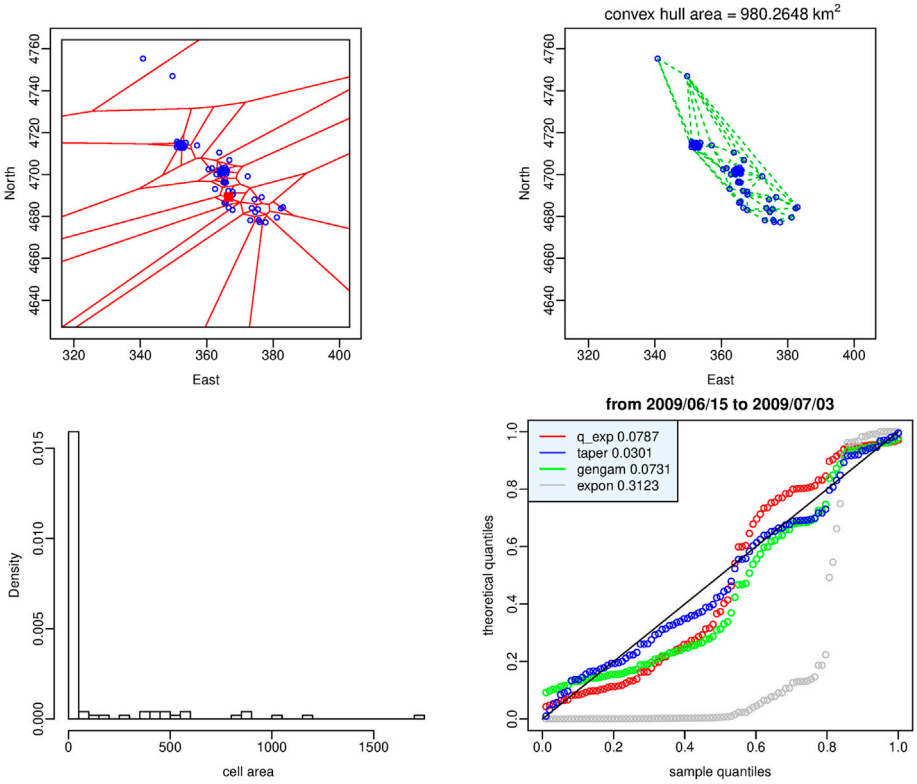

FIGURE 5
Dataset of the time window in which the tapered Pareto distribution provides the best fit. Top: Voronoi tessellation (left-hand panel) and Delaunay triangulation (right-hand panel). Bottom: histogram of the cell areas (left-hand panel) and Q-Q plot of the four probability distributions (right-hand panel). Red square indicates the epicenter of L'Aquila shock.

distributions behave similarly and fit well to the data but the posterior marginal likelihood of the exponential distribution is greater, although not substantially, than the likelihood of the other distributions.

Observing Figures 2, 3 we can conclude that there is no single optimal probability distribution of the Voronoi cell area; the distribution that provides the best performance, as well as the spatial distribution of the events, varies over time according to the phases of the seismic cycle: (i) the exponential distribution exceeds the other distributions only in the period December 2008 - January 2009 which could mark the beginning of the preparatory phase, (ii) the q-exponential distribution characterizes mainly the initial, most active part of the aftershock sequence, (iii) the tapered Pareto distribution provides the best performance in the period encompassing the mainshock and covering the main phase up to approximately the time window in which all events are aftershocks, a few hours after the mainshock, (iv) the generalized gamma distribution characterizes, together with the tapered Pareto distribution, the quiescence period and the less active part of the aftershock sequence when seismicity begins to slowly diffuse at larger distances from the fault area.

Amatrice-Norcia case study

On 24 August 2016 (01:36:32 UTC, latitude 42.698, longitude 13.234), an M_w 6 earthquake hit central Italy with its epicenter between the village of Accumoli and the town of Amatrice. After a few years of relative quiescence that followed the aftershocks of the Aquila earthquake, the Amatrice shock marked the beginning of a more complex seismic crisis than the one that had just ended; in fact, what was first believed to be the mainshock, turned out to be later as a foreshock of the strongest quake (M_w 6.5) that would have occurred at the town of Norcia on 30 October 2016 (06:40: 17 UTC, latitude 42.830, longitude 13.109). The seismic sequence lasted probably up to November 2018, and included several shocks among which there were three earthquakes with magnitudes greater than 5: on 24 August 2016, of M_w 5.3, and on 26 October 2016, of M_w 5.4 and M_w 5.9, and four earthquakes on 18 January 2017 of magnitude greater than 5: at 09:25 UTC M_w 5.1, at 10:14 UTC M_w 5.5, at 10:25 UTC M_w 5.4, and at 13:33 UTC M_w 5.0.

Since the Amatrice and Norcia earthquakes have been associated with the composite seismogenic source ITCS028

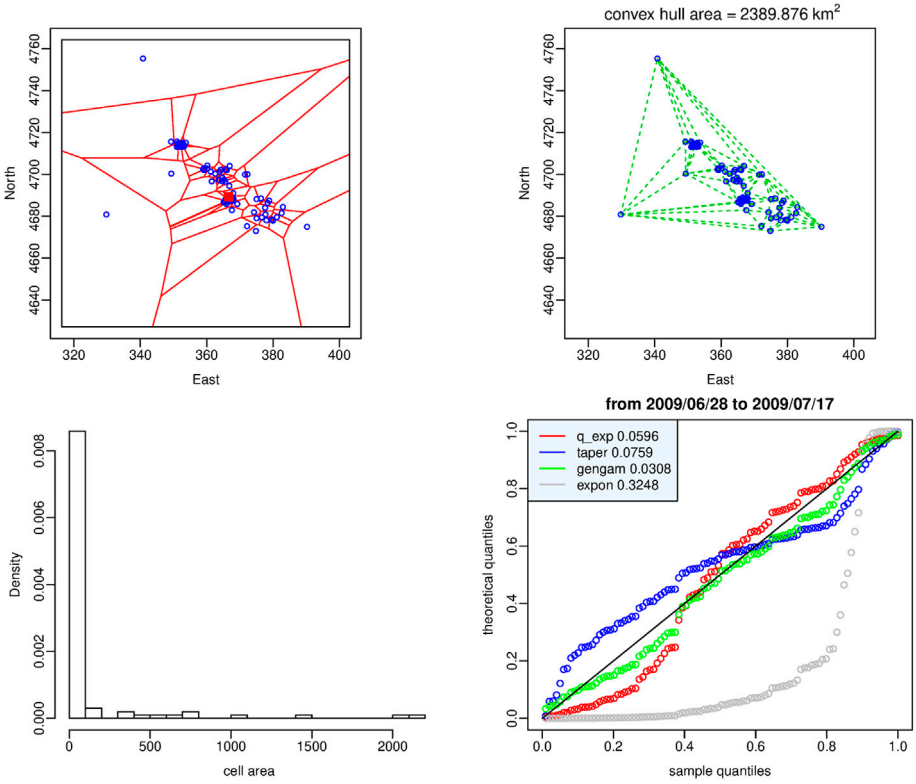

FIGURE 6
Dataset of the time window in which the generalized gamma distribution provides the best fit. Top: Voronoi tessellation (left-hand panel) and Delaunay triangulation (right-hand panel). Bottom: histogram of the cell areas (left-hand panel) and Q-Q plot of the four probability distributions (right-hand panel). Red square indicates the epicenter of L'Aquila shock.

(Colfiorito-Campotosto) of the DISS (DISS Working Group (2018)), following the same criteria adopted to select the study region in the case of L'Aquila, we choose as study area a rectangular area of latitude size (42.3, 43.2) degrees and longitude size (12.7, 13.5) degrees centered around the Amatrice - Norcia earthquakes which also includes the L'Aquila epicenter and part of its aftershocks. To examine the spatial pattern of the events also in the period between the two seismic crises we extend the period under study back to the beginning of 2009 and up to June 2018. Moreover we raise the magnitude threshold to the value $m_0 = 2.5$ to reduce the effects of possible partial incompleteness of the catalogue in the first hours after the Norcia mainshock. In this way we obtain a data set of $N = 5,062$ events drawn from ISIDe catalogue (ISIDe Working Group (2007)). Also in this case, we consider time windows of 100 events that shift at each new event. First we build the Voronoi tessellation generated by the events of each window, we fit the four probability models to each set of cell areas and then we compare the four probability distributions through pairwise differences of the respective posterior marginal log-likelihoods. Figure 8 shows, for each time window, the value of the posterior marginal log-likelihood of the model that behaves strongly better than the others; subdued colors indicate less evidence in favor of the optimal model; the vertical lines indicate the occurrence time of the Amatrice (dashed red), Norcia (solid red) and Capignano (M_w 5.5, 18 January 2018) (blue) earthquakes respectively. Figure 9 is a magnification of the same values around the Amatrice earthquake (red dashed line) from September 2010 to September 2016; black dots indicate the first quartile of the set of cell areas at each window. We note that the exponential distribution (magenta dots) outperforms the other distributions with less than substantial degree of evidence and not continuously in the period from late 2013 to February 2016, precisely up to 10 windows before the Amatrice shock; around the same time the first quartile of the sets of cell areas reaches its highest values.

The legend of Figure 8 reports the percentages of time windows in which the specific best model outperforms the others with strong evidence. Recalling that our dataset contains two aftershock sequences, the large number of windows in which the q-exponential distribution is the optimal model supports the conclusion that this heavy-tailed distribution is suitable for describing the spatial pattern of highly clustered events; in particular it outperforms the other distributions in the following time intervals: from the L'Aquila (6 April 2009) shock up to September 2009, from a few hours after the Amatrice earthquake to early November 2016, and for half a

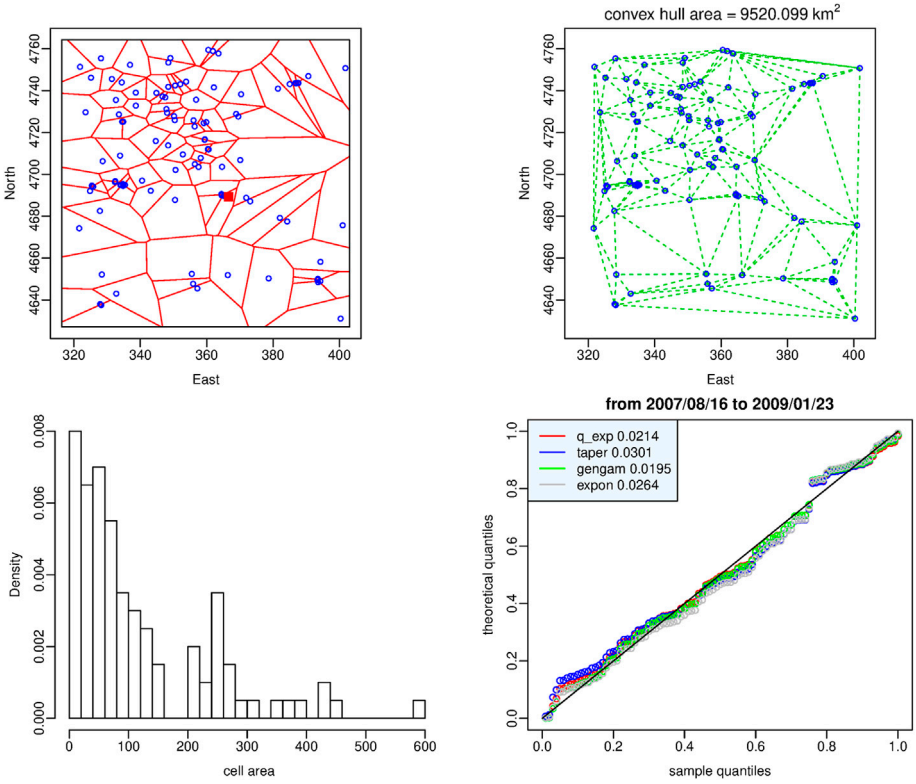

FIGURE 7
Dataset of the time window in which the exponential distribution provides the best fit. Top: Voronoi tessellation (left-hand panel) and Delaunay triangulation (right-hand panel). Bottom: histogram of the cell areas (left-hand panel) and Q-Q plot of the four probability distributions (right-hand panel). Red square indicates the epicenter of L'Aquila shock.

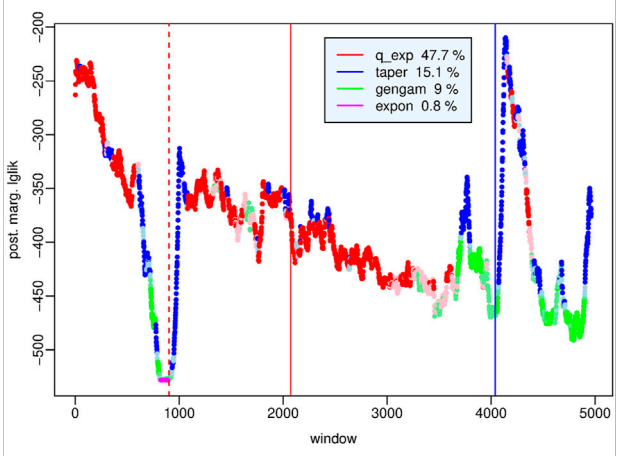

FIGURE 8
Amatrice-Norcia sequence - Posterior marginal log-likelihood of the probability distribution of Voronoi cell area that fits better than the other distributions to the dataset of each time window. The red vertical lines indicate the Amatrice (M_w 6.1) shock (dashed line) and the Norcia (M_w 6.5) mainshock (solid line) respectively; the blue vertical line indicates the Capignano (M_w 5.5) shock that occurred on 18 January 2017.

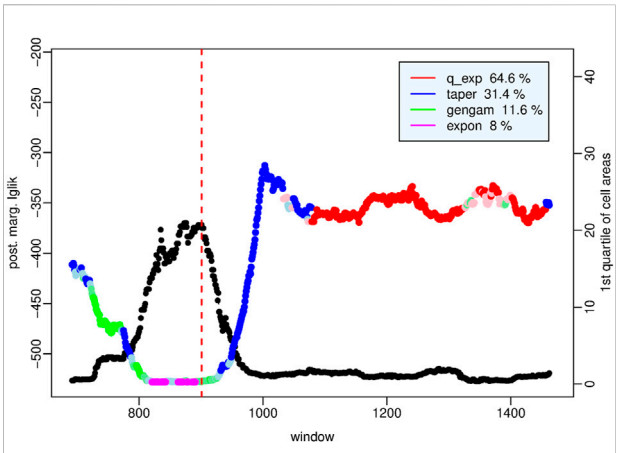

FIGURE 9
Amatrice-Norcia sequence - Magnification of Figure 8 in the period from mid-August 2009 to end of August 2016; the black dots indicate the first quartile of the set of cell areas in each time window. Red dashed vertical line indicates the Amatrice shock.

month after the Capignano (M_w 5.5, 18 January 2017) shock. The tapered Pareto distribution instead characterizes the initial phase of the activation following the Amatrice and Capignano earthquakes until all the events in the time window are triggered events; moreover, the tapered Pareto distribution, together with the generalized gamma distribution, fit to the sets of cell areas in periods of low seismic activity such as that recorded from late October 2009 to mid-2013, and when the aftershocks begin to move away from the fault area as from December 2016 to the end of the period under study.

Final remarks

In this work we have a twofold objective: to propose a new probabilistic model - the q-exponential distribution - for the Voronoi cell area that is inspired by nonextensive statistical mechanics and to compare it with the most promising probability distributions in the literature to determine if there is a single optimal distribution according to the ratio of their posterior marginal likelihoods. We have therefore examined four distributions on the whole: the q-exponential, the tapered Pareto, the generalized gamma and the simple exponential distributions. Considering two seismic sequences recorded in central Italy in the last years and associated with the L'Aquila and Amatrice-Norcia destructive earthquakes we have verified that the probability distribution that best fits to the set of the areas of Voronoi cells generated by the epicenters of a fixed number of events included into shifting time windows varies over time apparently in correspondence with the phases of a seismic cycle (De Santis et al. (2011)).

The detailed examination of the results obtained for the four probability distributions in the two case studies allows us to discriminate different regimes:

- in a preparatory phase the exponential distribution exceeds weakly the other probability distributions in a few tens of time windows which cover some months before the foreshock activity; in this period we could also say that the four distributions are all basically suitable to describe a diffuse seismicity.
- Thereafter the activity tends to concentrate around the mainshock area with an increase in the variability range of the cell areas; this implies the best performance of the tapered Pareto distribution in what we can call the main phase. This phase comprises an event, which may not be the mainshock, but is strong enough to trigger a significant sequence of secondary events.
- The period of maximum concentration of the seismicity is characterized by the outperformance of the q-exponential distribution as it has heavier tail than the other distributions; we denote this period as primary clustering phase.
- The tapered Pareto and the generalized gamma distributions instead characterize the less active part of the aftershock sequence that we denote as secondary clustering phase, in which the concentration of events diffuses to a larger area surrounding the seismogenic area. A measure of this fact is given by the area of the convex hull in the Delaunay triangulation; in the top right-hand panel of Figures 4–7 we can note that this area is increasing as the best model moves from the q-exponential distribution to the tapered Pareto distribution, then to the generalized gamma distribution and finally to the exponential one.
- The spatial pattern of events in periods of quiescence is best modelled by the generalized gamma distribution but also by the tapered Pareto distrubtion.

It will, of course, be interesting to test the results obtained through further studies on different cases and in different seismotectonic settings.

Data availability statement

The datasets analyzed for this study can be found in the Italian Seismological Instrumental and Parametric Database (ISIDe) (ISIDe Working Group (2007)) at http://iside.rm.ingv.it.

Author contributions

All authors listed have made a substantial, direct, and intellectual contribution to the work and approved it for publication.

Funding

This research is partially funded by the INGV Project "Dynamic Planet" (CUP D53J19000170001), Topic 8-PANACEA 2021, supported by The Italian Ministry of Education, Universities and Research (MIUR).

Acknowledgments

The authors thank the Editor Prof. F. Vallianatos and the two reviewers.

Conflict of interest

The authors declare that the research was conducted in the absence of any commercial or financial relationships that could be construed as a potential conflict of interest.

Publisher's note

References

Bercher, J.-F., and Vignat, C. (2008). A new look at q-exponential distributions via excess statistics. *Phys. A Stat. Mech. its Appl.* 387, 5422–5432. doi:10.1016/j.physa.2008.05.038

Bowman, D., Ouillon, G., Sammis, C., Sornette, A., and Sornette, D. (1998). An observational test of the critical earthquake concept. *J. Geophys. Res.* 103, 24359–24372. doi:10.1029/98jb00792

De Santis, A., Cianchini, G., Favali, P., Beranzoli, L., and Boschi, E. (2011). The Gutenberg-Richter law and entropy of earthquakes: Two case studies in central Italy. *Bull. Seismol. Soc. Am.* 101, 1386–1395. doi:10.1785/0120090390

Devroye, L., Györfi, L., Lugosi, G., and Walk, H. (2017). On the measure of Voronoi cells. *J. Appl. Probab.* 54, 394–408. doi:10.1017/jpr.2017.7

DISS Working Group (2018). *Database of individual seismogenic sources (DISS), version 3.2.1: A compilation of potential sources for earthquakes larger than M 5.5 in Italy and surrounding areas*. Available at: http://diss.rm.ingv.it/diss/, Istituto di Geofisica e Vulcanologia. doi:10.6092/INGV.IT-DISS3.2.1

Ferenc, J.-S., and Neda, Z. (2007). On the size distribution of Poisson Voronoi cells. *Phys. A Stat. Mech. its Appl.* 385, 518–526. doi:10.1016/j.physa.2007.07.063

Gasperini, P., Lolli, B., and Vannucci, G. (2013). Empirical calibration of local magnitude data sets versus moment magnitude in Italy. *Bull. Seismol. Soc. Am.* 103, 2227–2246. doi:10.1785/0120120356

Gelman, A., Carlin, J., Stern, H., and Rubin, D. (2004). *Bayesian data analysis*. New York: Chapman & Hall.

Gezer, F., Aykroyd, R., and Barber, S. (2021). Statistical properties of Poisson-Voronoi tessellation cells in bounded regions. *J. Stat. Comput. Simul.* 91, 915–933. doi:10.1080/00949655.2020.1836184

Hinde, A., and Miles, R. (1980). Monte Carlo estimates of the distributions of the random polygons of the Voronoi tessellation with respect to a Poisson process. *J. Stat. Comput. Simul.* 10, 205–223. doi:10.1080/00949658008810370

ISIDe Working Group (2007). *Italian Seismological Instrumental and Parametric Database (ISIDe), Istituto Nazionale di Geofisica e Vulcanologia (INGV)*.

Jackson, D., and Kagan, Y. (1999). Testable earthquake forecasts for 1999. *Seismol. Res. Lett.* 70, 393–403. doi:10.1785/gssrl.70.4.393

Kass, R., and Raftery, A. (1995). Bayes factors. *J. Am. Stat. Assoc.* 90, 773–795. doi:10.1080/01621459.1995.10476572

Koufos, K., and Dettmann, C. (2019). Distribution of cell area in bounded Poisson Voronoi tessellations with application to secure local connectivity. *J. Stat. Phys.* 176, 1296–1315. doi:10.1007/s10955-019-02343-y

Okabe, A., Boots, B., Sughara, K., and Chiu, S. (2000). *Spatial tessellations concepts and applications of Voronoi diagrams*. Chichester: John Wiley & Sons.

Prentice, R. (1974). A log gamma model and its maximum likelihood estimation. *Biometrika* 61, 539–544. doi:10.1093/biomet/61.3.539

R Core Team (2018). *R: A language and environment for statistical computing*. Vienna, Austria: R Foundation for Statistical Computing.

Roberts, C., and Casella, G. (2004). *Monte Carlo statistical methods*. Springer.

Rotondi, R., Bressan, G., and Varini, E. (2022). Analysis of temporal variations of seismicity through non-extensive statistical physics. *Geophys. J. Int.* 230, 1318–1337. doi:10.1093/gji/ggac118

Schoenberg, F. P., Barr, C., and Seo, J. (2009). The distribution of Voronoi cells generated by Southern California earthquake epicenters. *Environmetrics* 20, 159–171. doi:10.1002/env.917

Stacy, E. (1962). A generalization of the gamma distribution. *Ann. Math. Stat.* 33, 1187–1192. doi:10.1214/aoms/1177704481

Tanemura, M. (2003). Statistical distributions of Poisson Voronoi cells in two and three dimensions. *Forma* 14, 221–247.

Tsallis, C. (2009). *Introduction to nonextensive statistical mechanics. Approaching a complex world*. Springer. doi:10.1007/978-0-387-85359-8

Turner, R. (2018). *deldir: Delaunay triangulation and dirichlet (Voronoi) tessellation. R package version 0*, 1–15.

Vaičiulis, M., and Markovich, N. (2021). Estimating the parameters of a tapered Pareto distribution. *Autom. Remote Control* 82, 1358–1377. doi:10.1134/s000511792108004x

Vallianatos, F., Michas, G., and Papadakis, G. (2015). "A description of seismicity based on non-extensive statistical physics: A review," in *chapter in the book earthquakes and their impact on society* (Springer Natural Hazard, Springer).

Vere-Jones, D., Robinson, R., and Yang, W. (2001). Remarks on the accelerated moment release model: Problems of model formulation, simulation and estimation. *Geophys. J. Int.* 144, 517–531. doi:10.1046/j.1365-246x.2001.01348.x

Wells, D., and Coppersmith, K. (1992). New empirical relationships among magnitude, rupture length, rupture width, rupture area, and surface displacement. *Bull. Seism. Soc. Am.* 84, 974–1002.

Wessel, P., and Smith, W. (1998). New, improved version of generic mapping Tools released. *Eos Trans. AGU.* 79, 579. doi:10.1029/98eo00426

Zaninetti, L. (2009). Poissonian and non-Poissonian Voronoi diagrams with application to the aggregation of molecules. *Phys. Lett. A* 373, 3223–3229. doi:10.1016/j.physleta.2009.07.010

frontiers | Frontiers in Earth Science

TYPE Brief Research Report
PUBLISHED 28 September 2022
DOI 10.3389/feart.2022.902745

OPEN ACCESS

EDITED BY
Giovanni Martinelli,
National Institute of Geophysics and Volcanology, Italy

REVIEWED BY
Alexey Lyubushin,
Institute of Physics of the Earth (RAS), Russia
Paolo Plescia,
National Research Council (CNR), Italy

*CORRESPONDENCE
Shanshan Yong,
yongshanshan@pku.edu.cn

SPECIALTY SECTION
This article was submitted to Geohazards and Georisks, a section of the journal Frontiers in Earth Science

RECEIVED 23 March 2022
ACCEPTED 26 August 2022
PUBLISHED 28 September 2022

CITATION
Xie J, Yong S, Wang X, Bao Z, Liu Y, Zhang X and He C (2022), Weekly earthquake prediction in a region of China based on an intensive precursor network AETA.
Front. Earth Sci. 10:902745.
doi: 10.3389/feart.2022.902745

Weekly earthquake prediction in a region of China based on an intensive precursor network AETA

Jinhan Xie[1], Shanshan Yong[2]*, Xin'an Wang[1], Zhenyu Bao[1], Yibin Liu[1], Xing Zhang[3] and Chunjiu He[1]

[1]The Key Laboratory of Integrated Microsystems, Peking University Shenzhen Graduate School, Shenzhen, China, [2]Faculty of Engineering, Shenzhen MSU-BIT University, Shenzhen, China, [3]School of Software & MicroElectronics, Peking University, Beijing, China

Once a majority of earthquakes occur without prediction, it is very likely to have a huge impact on human society. To solve the worldwide challenging problem of earthquake prediction, our laboratory has developed a set of sensory systems to monitor the abnormal activity of geological signals before an earthquake happens in China. At present, more than 300 stations have been deployed, and the observation time has exceeded 4 years. Based on the various geological activities collected, a local correlation tracking method is used to capture signal anomalies before an earthquake, and then the ROC curve is used for the evaluation of the predictive accuracy. The method is applied in the Sichuan-Yunnan area weekly, verifying the forecast within a 91-week time frame and a 30-week time frame. The method proposed in this article has earthquake prediction ability with a rate of over 70%. It promotes and contributes to helping people avoid the fear of unpredictable earthquakes.

KEYWORDS

earthquake prediction model, ROC curve, AETA system, singular value decomposition, local correlation tracking

Introduction

Earthquake prediction is very challenging. Countries have carried out a lot of research but still have not made substantial progress. An earthquake is a major event of earth activity; before the release of huge energy, there must be some precursors in a region through various forms (Yin et al., 2004; Keilis-Borok et al., 2004; Pulinets and Ouzounov, 2011; Roger, 2010; McGuire et al., 2005; Schorlemmer and Wiemer, 2005). In Martinelli et al. (2020a) and Martinelli et al. (2020b), Martinelli et al. studied shear experiments on quartz rocks and single quartz crystals. Through their experiments, they proposed that shear-stressed quartz crystals can generate electromagnetic emissions in the LF-MF range. They also discovered that a characteristic migration of peak frequencies was observed, proportional to the evolution of the fracturing process. Those signals, observed in laboratory faults, also widely precede earthquakes and may contain precursors. In earthquake prediction, observational science should be very important. Through

long-term high-density observations, rich earthquake and precursory signal data can help us find the difference between predicted and actual earthquake occurrence.

This study selects the electromagnetic disturbance data of No.90 MX station (Figure 7A) and No.75 QW station (Figure 7B) of our system (Acoustic & Electromagnetics AI, AETA) to calculate the Pearson correlation coefficient and LCT correlation coefficient. The data window is from 14 July 2017 to 13 August 2017. From the results (Figure 7), the LCT method has a better output based on non-stationary signals. The classical correlation method cannot reasonably reflect the correlation between the electromagnetic signals from two stations (Figure 7C). If the signals from a station are obviously abnormal, this method cannot be applied to effectively find anomalies. In contrast, the use of the local cross-correlation tracking method can well reflect the correlation between the electromagnetic data of any two stations. Even if very weak signals show anomalies, this method is able to sensitively pick up the anomalies (Figure 7D). In the analysis, Figure 6 shows the epicenter at Jiuzhaigou and the five AETA stations; the LCT method was employed to calculate the correlation between AETA stations. The anomaly detected by using this method is called the LCT anomaly correspondingly. In order to show that the LCT method is able to find the correlation between AETA electromagnetic data and detect earthquake anomalies, the electromagnetic disturbance data of five AETA stations within 200 km from the epicenter are collected (Figure 8). Although the electromagnetic disturbance data from the No.43 QC station fluctuates obviously from July 15 to July 25, the signals from these five stations have all been collected in waveform (Figure 8). The electromagnetic disturbance data from each four observation stations for various precursor signals, no precursor signals, and corresponding abnormal features have been found to imply a 100% coming earthquake (Schuck, 2005). Many different non-seismic pre-earthquake A plethora of non-seismic signals have been reported, but there is great uncertainty about their origin, correlation with each other, and the impending seismic events (Freund., 2010).

Researchers have made long-term exploration and analysis of the mechanism of earthquakes. Also, put forward many theories and models. Paul and Pedersen come up with theories that the aftershock duration is consistent with models of seismicity rate variations based on rate- and state-dependent friction laws (Jónsson et al., 2003).

Moreno et al. proffered that co-seismic slip heterogeneity at the scale of single asperities should indicate the seismic potential of future great earthquakes, which thus might be anticipated by geodetic observations (Moreno et al., 2010).

Olson and Allen propounded that the frequency of radiated seismic waves within the first few seconds of rupture scales with the final magnitude of the event. Thus, the magnitude of an earthquake can be estimated before the rupture is complete (Olson and Allen, 2005). However, the models are based on overmuch assumptions, and the actual situation is significantly different from the model, which cannot provide substantial guidance for earthquake prediction.

Regarding earthquake prediction, although mechanism exploration is crucial, observational science should be the first to be concerned. Only by collecting a large number of observations, we will be able to determine whether effective precursor signals can be captured and thus make accurate predictions (Chadha et al., 2003) (Uyeda et al., 2011). Second, through long-term high-density observations, the abundant data of earthquake and precursor signals could assist us in improving the construction and demonstration of the earthquake mechanism model and finding the differences between the predictions and actual earthquake happenings.

Based on the analysis of our observational data and the models constructed by our AETA laboratory in the past 4 years, in this project, a spatio-temporal earthquake prediction model based on local cross-correlation of seismic data from our AETA stations was proposed. This new model is applied to predict weekly earthquakes with M3.50 or higher in the Sichuan-Yunnan region (22° N-34° N, 98° E-107° E) from 22 April 2019 to 24 January 2021, 21 months (91 weeks) in total. Our success rate for earthquake prediction is up to 72.50%.

Intensive precursor network AETA

The AETA (Acoustic & Electromagnetics AI) system makes use of electromagnetic disturbance and geo-acoustic signals as observation inputs. It aims to commence imminent earthquake prediction by using large-scale and high-density seismic data as well as well-developed methods from data mining, machine learning, neural network, and relevant fields. The AETA system consists of two parts: 1) the data acquisition subsystem and 2) the data analysis and prediction subsystem.

1) The data acquisition subsystem consists of many AETA stations. Each AETA station is equipped with an electromagnetic sensing probe, a geo-acoustic sensing probe, and a data terminal. Data from the sensing probes will be collected, packed, and transferred to a cloud server. 2) The data analysis subsystem includes a cloud server, a database, a client of data display, a website for data display (https://www.aeta.cn), and our software for real-time seismic prediction. The cloud sever and the database are used for feature extraction and data storage. The software is working to check the data updates and display the predicted outcomes in real time (Figure 1).

In this article, only electromagnetic data are being analyzed in the proposed model. The specifications of the electromagnetic probes are described as follows: the frequency band is 0.1 Hz–10 kHz, the spatio-temporal model of dynamic range is 0.1–1,000 nT, the sensitivity is >20 mV/nT@0.1 Hz–10 kHz, and the sampling rate for the low-frequency band (≤200 Hz) is

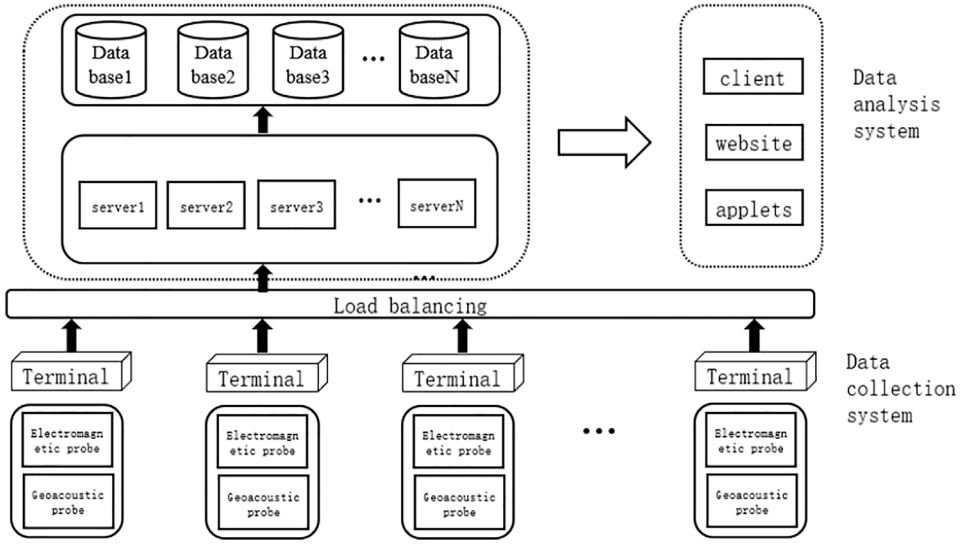

FIGURE 1
Architecture of the AETA system.

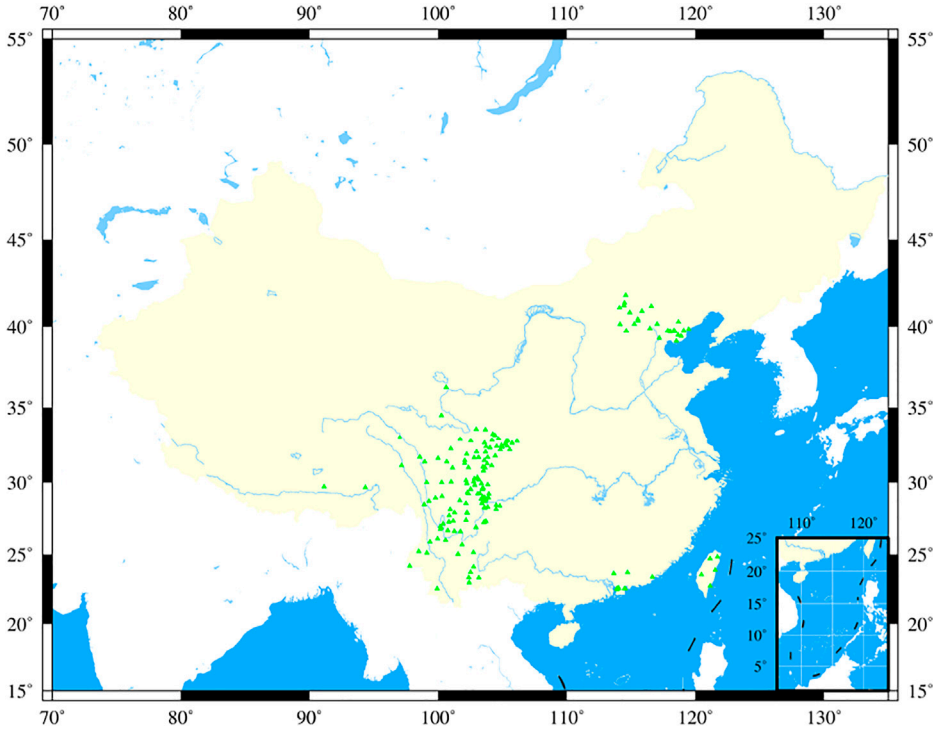

FIGURE 2
Distribution of AETA observational stations.

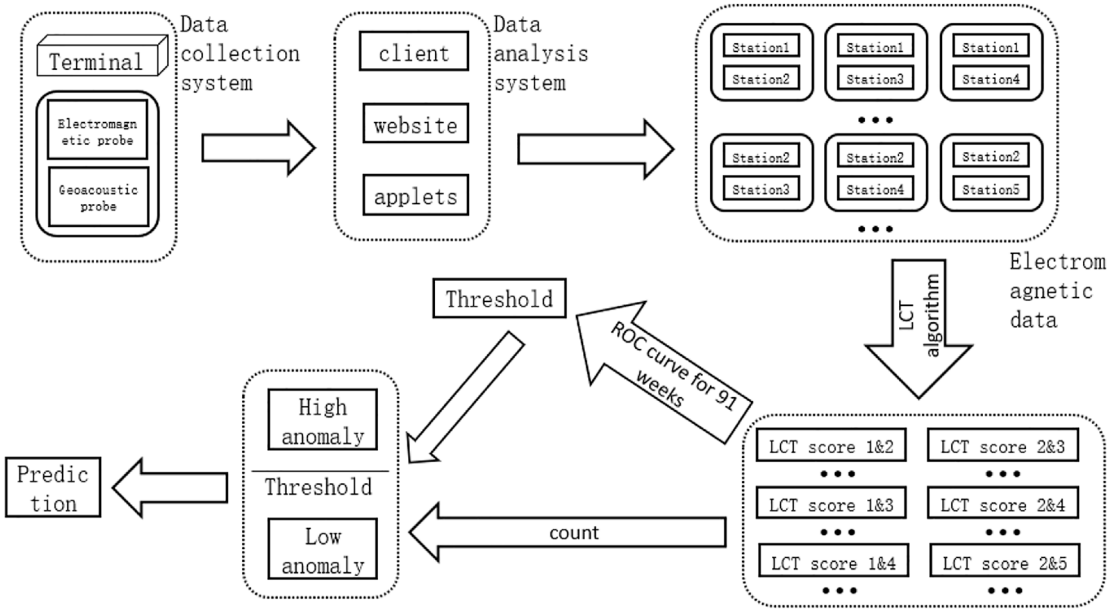

FIGURE 3
Workflow of our proposed model.

500 Hz, which is 30 kHz for the full frequency band (≤10 kHz). Its noises are within 0.1–0.2 pT/Hz@(10 Hz–1 kHz) (Guo et al., 2021).

Since January 2017, the AETA team has started constructing the observation network in China (Figure 2). Up to now, more than 300+ stations have been deployed. Most of them are located in the Sichuan-Yunnan region (more than 200 stations, namely, 22°N-34°N and 98°E-107°E) because the region has high seismicity than other places in China (Guo et al., 2021). After 4 years of observations, more than 45 TB of data has been collected, and 20 GB of new data is collected every day. In order to analyze multiple dimensional features, 95 classes of electromagnetic and geo-acoustic signals have been taken into account (Guo et al., 2021). In this article, an average of the electromagnetic data is imported into the proposed model to represent the data in the temporal domain.

Our spatio-temporal model for earthquake prediction

Based on two classes of precursor signals observed by using the AETA system, a new model to predict whether an earthquake will occur in the Sichuan-Yunnan region is proposed. The prediction will be made every Sunday, and the time frame for this prediction is the next 7 days (Figure 3). An LCT algorithm (i.e., local correlation tracking) is being applied to cope with the electromagnetic signals of the AETA system.

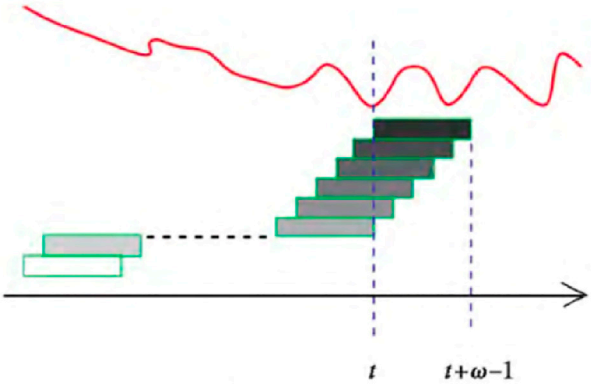

FIGURE 4
Exponential decay window.

LCT algorithm

The proposed LCT method is an improvement of the conventional linear correlation method (Verma et al., 2013). The novelty of this method is that a sliding window in the temporal domain is added, and the correlation between local covariance matrices is calculated in each time window (Schuck, 2005). The correlation calculated by this method in this study is called the LCT correlation.

Regarding time series analysis of electromagnetic signals, at first, a sliding window in the temporal domain $x_{t,\omega}$ is applied to

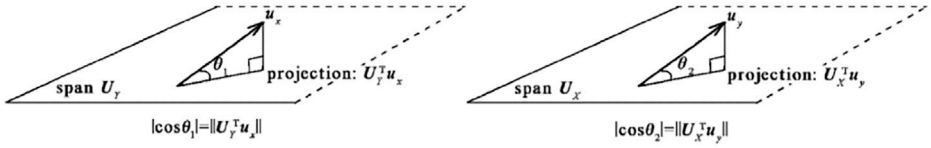

FIGURE 5
Local cross-correlation.

segment the data at time t. The window in this article is an exponential decay window, namely, at time t, all windows $x_{t,\omega}$ are multiplied by an exponential weight $\beta^{t-\tau}$. Among them, the window $x_{t,\omega}$ closer to the time t will be given a larger exponential weight, while the window far away from the time t will be assigned a smaller weight (Figure 4). Hence, the darker the color, the greater the weight, and vice versa.

Regarding any streaming data X, its local covariance matrix at time t is expressed by Eq. 1.

$$\vec{\Gamma}_t(X,\omega,\beta) = \sum_{\tau=1}^{t} \beta^{t-\tau} X_{\tau,\omega} X_{\tau,\omega}. \tag{1}$$

After calculating the covariance of the two streaming data by using Eq. 1, the local covariance matrix at time t is obtained. After a singular value decomposition (SVD) operation, local covariance matrices $\vec{\Gamma}_t(X)$ and $\vec{\Gamma}_t(Y)$ are obtained by using Eq. 2 and 3.

Among them, feature vectors corresponding to the largest eigenvalues are u_x and u_y. In Eq. 2, $U(X)$ is the left singular vector (LSV) of $\vec{\Gamma}_t(X)$, $V(X)$ is the right singular vector (RSV) of $\vec{\Gamma}_t(X)$, and Σ is the singular value matrix (SVM) of $\vec{\Gamma}_t(X)$as the same in Eq. 3.

$$\vec{\Gamma}_t(X) = U(X)\Sigma V(X)^T, \tag{2}$$

$$\vec{\Gamma}_t(Y) = U(Y)\Sigma V(Y)^T. \tag{3}$$

Similar to the principal component analysis (PCA) method (Wold et al., 1987), the first few principal components will retain most of the information. Depending on the data distribution, the first k principal components keep the principal feature vector (PFV) matrix. Therefore, the two PFV matrices Y_X and U_Y are shown in Eq. 4 and 5, respectively.

$$U_X = U(X)[:,k], \tag{4}$$

$$U_Y = U(Y)[:,k]. \tag{5}$$

Now, there are two spaces $span(U_Y)$ spanned by U_Y and $span(U_X)$ spanned by U_X. Then, multiply u_x by using U_Y at the left side and get $U_Y^T u_x$, which is a projection in space $span(U_Y)$. Similarly, multiply u_y by U_X at the left and get $U_X^T u_y$, which is a projection in space $span(U_X)$ (Figure 5). The angle between them is expressed as Eq. 6 and 7, correspondingly.

$$\theta_1 \equiv \angle\left(u_x, span(U_Y)\right) = \angle\left(u_x, U_Y^T u_x\right), \tag{6}$$

$$\theta_2 \equiv \angle\left(u_y, span(U_X)\right) = \angle\left(u_y, U_X^T u_y\right). \tag{7}$$

Thus, if two spaces have LCT correlation, θ_1 and θ_2 approach 0.00, and $\cos\theta_1$ and $\cos\theta_2$ will tend to 1.00 as shown in Eq. 8 and 9.

$$|\cos\theta_1| = \|U_Y^T u_x\| / \|u_x\| \rightarrow 1.00, \tag{8}$$

$$|\cos\theta_2| = \|U_X^T u_y\| / \|u_y\| \rightarrow 1.00. \tag{9}$$

Finally, define the local correlation $LocoScore_t$ at time t as shown in Eq. 10.

$$LocoScore_t = 0.5 \cdot (|\cos\theta_1| + |\cos\theta_2|). \tag{10}$$

In summary, the LCT method is applied to calculate the correlation between two streaming data. If there is a large LCT correlation between them, *LocoScore* should tend to 1.00. On the contrary, if the LCT correlation is small, *LocoScore* should be close to 0.00.

The analysis of earthquake data by using the LCT method

An earthquake (103.82°E, 33.2°N, M7.0) occurred in Jiuzhaigou County, Sichuan Province on 8 August 2017. There are five AETA stations whose geographic locations are near the epicenter (Figure 6 and Table 1), and the low-frequency electromagnetic data collected from these stations 1 month before the earthquake was selected for the analysis.

In order to calculate the correlation coefficient between the data from our stations, it makes use of the classical correlation method and local cross-correlation tracking method to calculate the Pearson correlation coefficient (Jacob et al., 2009).

First, select the electromagnetic disturbance data of No.90 MX station (Figure 7A) and No.75 QW station (Figure 7B) to calculate the Pearson correlation coefficient and LCT correlation coefficient. The data window is from 14 July 2017 to 13 August 2017. From the results (Figure 7), the LCT method has a better output based on non-stationary signals. The classical correlation method cannot reasonably reflect the correlation between the electromagnetic signals from two

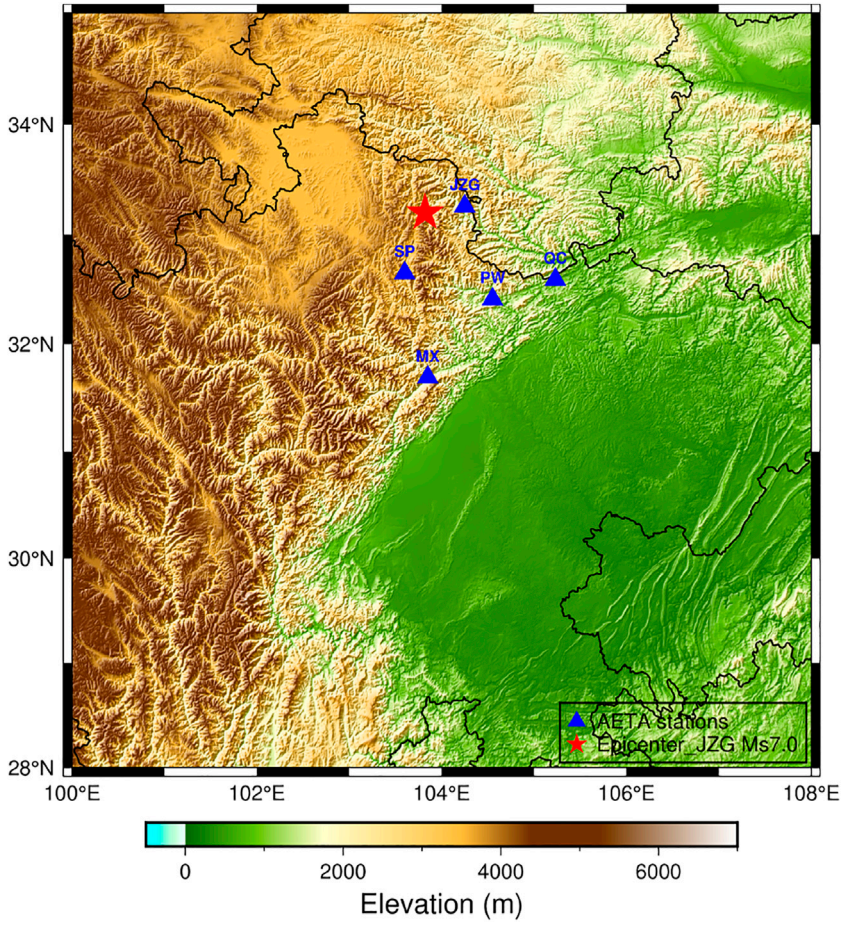

FIGURE 6
Epicenter at Jiuzhaigou and the five AETA stations.

TABLE 1 Selected five AETA stations.

No.	Station name	Abbreviation	Longitude	Latitude
90	MaoXian	MX	103.85	31.69
121	JiuZhaiGou	JZG	104.25	33.26
129	SongPan	SP	103.60	32.65
116	PingWuxian	PW	104.55	32.41
43	QingChuangxian	QC	105.23	32.59

stations (Figure 7C). If the signals from a station are obviously abnormal, this method cannot be applied to effectively find anomalies.

In contrast, the use of the local cross-correlation tracking method can well reflect the correlation between the electromagnetic data of any two stations. Even if very weak signals show anomalies, this method is able to sensitively pick up the anomalies (Figure 7D). In the analysis, the LCT method was employed to calculate the correlation between AETA stations, and the anomaly detected by using this method is called the LCT anomaly, correspondingly.

In order to show that the LCT method is able to find the correlation between AETA electromagnetic data and detect earthquake anomalies, the electromagnetic disturbance data of five AETA stations within 200 km from the epicenter are collected (Figure 8). Although the electromagnetic disturbance data from the No. 43 QC station fluctuate obviously from July 15 to July 25, the signals from these five stations have all been collected in waveform (Figure 8). The electromagnetic disturbance data from each AETA station have anomalies in the week before the earthquake.

Subsequently, the electromagnetic disturbance data from these five AETA stations were analyzed by using the LCT method, a set of *LocoScore* scores were calculated between every pair of two stations, and there were a total of C_5^2=10 sets of results. Among them, in the green box, the

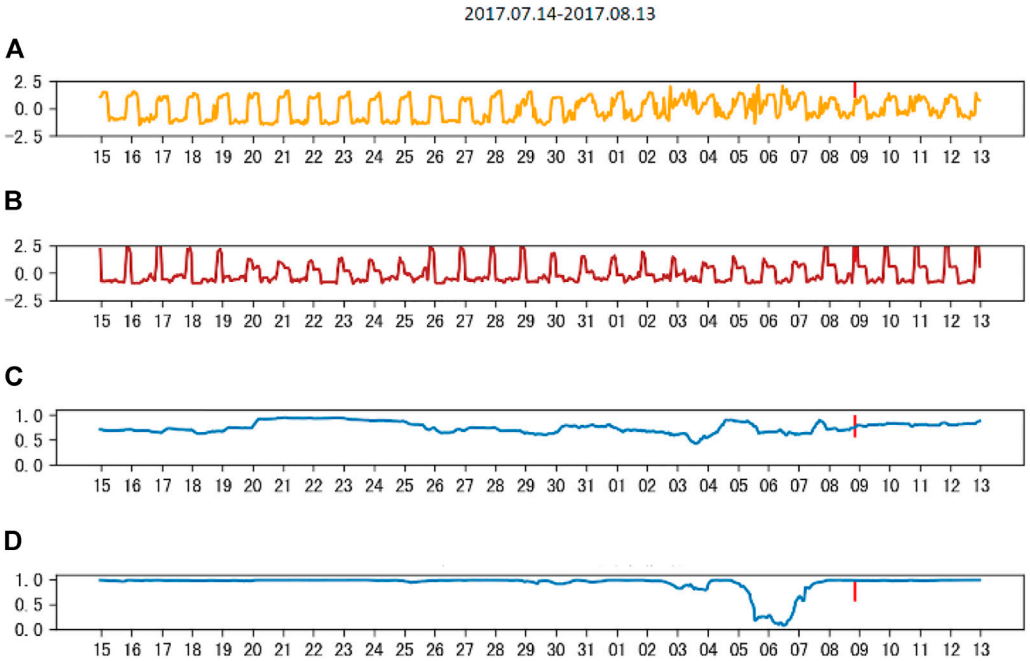

FIGURE 7
(A) Normalized electromagnetic disturbance data of MX station, **(B)** normalized electromagnetic disturbance data of QW station, **(C)** the Pearson correlation coefficient between **(A)** and **(B)**, and **(D)** LCT correlation coefficient between **(A)** and **(B)**.

LocoScore of each group was abnormal about 1 week before the earthquake (Figure 9). However, due to the fluctuations in the electromagnetic data of the No.43 QC station, the *LocoScore* related to the QC station was abnormal before July 25 (Figure 9).

From previous analysis and experimental results (Figure 9), it is found that in the long period of observations before the earthquake, *LocoScore* between the signals from every two stations is basically close to 1.00, that is, the electromagnetic signals from the stations are the same. The data have good spatial consistency. However, a week before the earthquake, *LocoScore* between every two stations showed an anomaly of less than 1.00, that is, the original spatial correlation of the electromagnetic data between the two stations was broken by the earthquake. These LCT anomalies reflect precursors related to earthquakes. Based on the analysis, applying the LCT method to AETA electromagnetic disturbance data is able to predict an earthquake.

LCT abnormal calculation

Based on the LCT algorithm, the electromagnetic data from every pair of AETA stations will be applied to an abnormal evaluation, which will be output every day.

First, define the LCT anomaly: the electromagnetic data from multiple AETA stations will be analyzed by using the LCT method to calculate the *LocoScore* of each pair of stations before the earthquake and a total of 10 days after the earthquake. According to the choice of the time window, there will be different *LocoScore* values.

There are 24 values in the *LocoScore* per hour per day for a total of $24 \times 10 = 240$ values in 10 days. Thus, define the anomaly of each day as *LocoScoreDay* (Figure 10) or day-based.

Therefore, the abnormal results of LCT will be output every day. The median of the daily *LocoScore* is selected as the outlier of the two stations per day.

Large-scale application of the LCT method

By using the LCT method of AETA, an outlier is able to be obtained from the data of the two stations every day. The outlier is between [0,1.00]. The smaller the value, the more serious the abnormal situation between the data of these two stations. There are 80 stations that were selected after removing those stations with frequent failures or with unchanged signals, and get C_{80}^{2}=3,160 LCT outliers every day. It's necessary to choose a threshold x and calculate the number of these 3,160 LCT outliers that are less than x to count the anomalies of electromagnetic signals in the Sichuan-Yunnan region on 1 day. After multiple tests, finally, the threshold is set x as 0.08. The number of outliers less than this threshold is called *Num*.

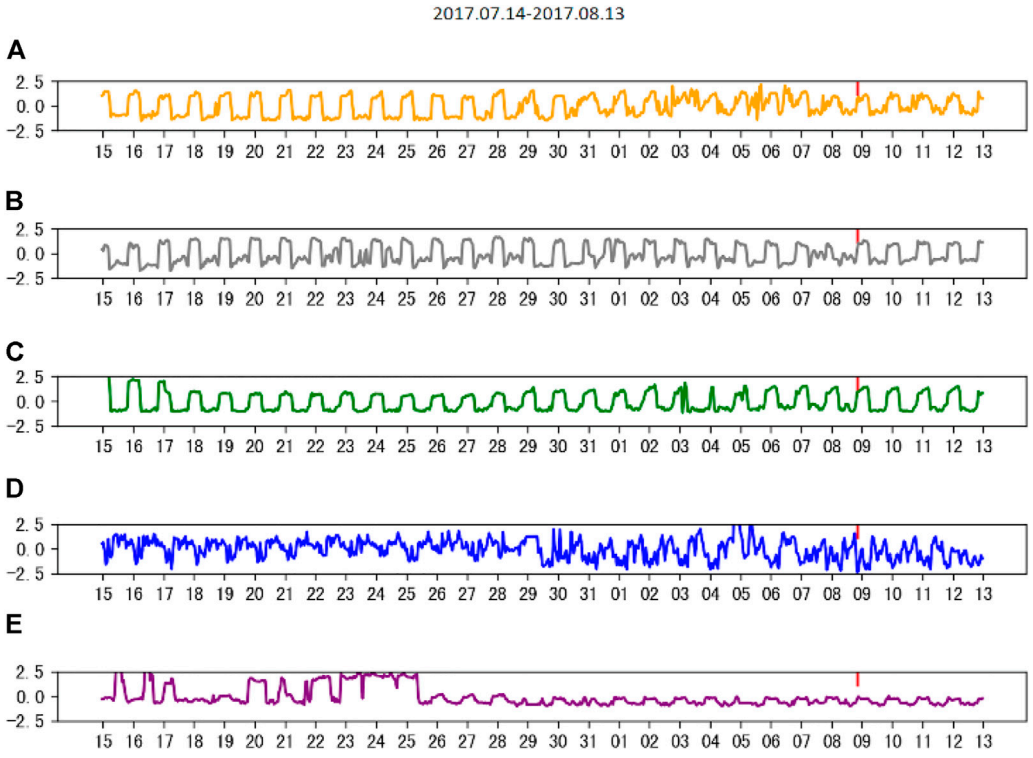

FIGURE 8
Normalized electromagnetic disturbance data from **(A)** MX, **(B)** JZG, **(C)** SP, **(D)** PW, and **(E)** QC.

The specifications in this work from the different datasets for the model were extracted.

Weekly earthquake prediction in the Sichuan-Yunnan region

The LCT anomalies were calculated based on AETA electromagnetic disturbance data for 21 months (91 weeks) in the Sichuan-Yunnan region from 22 April 2019 to 24 January 2021. During this period of time, the distribution of earthquakes and AETA stations (Figure 11). The red dots indicate the epicenter, and the blue dots show the AETA station.

The daily LCT abnormal times in the Sichuan-Yunnan area for 1 week are counted, then look for the value threshold $Val \in \mathbf{R}$ and the number threshold $Num \in \mathbf{Z}^+$ of daily anomalies, and review all of them every Sunday. If the times of LCT abnormalities whose values are lower than *Val* on a day of this week exceed *Num*, it is considered that there will be an earthquake of M3.5 or higher in the next week. Otherwise, it is predicted that there will be no earthquakes next week. For example, let's assume *Num*=20. A one-week review was conducted on Sunday (3 January 2021), and the LCT anomalies from 28 December 2020 to 3 January 2021 were counted. It is found that on 30 December 2020, the number of anomalies below 0.08 was 48. More than 20, we predict that the next week from 4 January 2021 to 10 January 2021, there will be an earthquake in the region (Table 2). A suitable *Num* will be found so that the outcome of using LCT anomalies to predict weekly earthquakes is the best. By using the ROC curve to analyze and calculate, the *Num* result is 30.

ROC curve

ROC curve refers to the receiver operating characteristic (ROC) curve. The ROC curve is a diagram composed of the false alarm probability as the horizontal axis and the hit probability as the vertical axis; the curve is drawn by different results obtained by the subjects under specific stimulus conditions due to different judgment standards (Molchan, 2010; Mirmiran et al., 2004).

The hit rate in the ROC curve is the proportion of positive samples in the test set that are correctly classified. The false-positive rate in the ROC curve is the proportion of negative samples in the test sample set that are incorrectly identified (Kamarudin et al., 2017).

For a dataset, each classification model has a ROC curve (Calì and Longobardi, 2015). The classification model follows a rule,

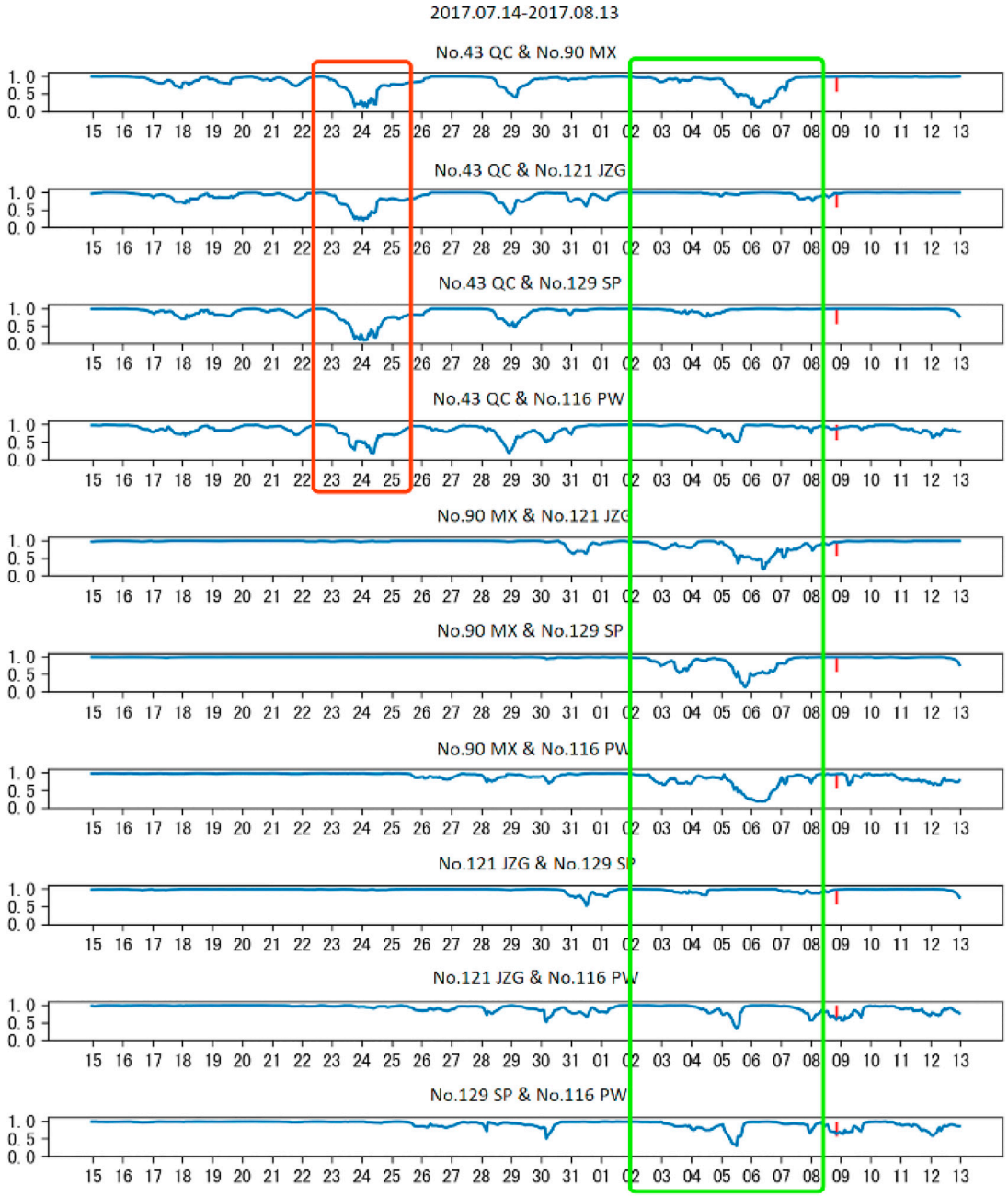

FIGURE 9
There are 10 sets of *LocoScore* scores calculated by using the LCT method.

usually, a threshold. The hit rate and false alarm rate of this threshold based on the sample set are obtained, so as to mark a point on the ROC curve, it could continuously adjust the threshold of the classification model and mark the points on the ROC map, and these points are connected to the ROC curve of this classification model based on this sample set.

For the classification results by using the LCT method, a threshold is needed to be fixed. If the threshold is exceeded, the sample is judged as an earthquake sample; otherwise, it is judged as a no-earthquake sample. We make use of the number of anomalies to make judgments. For our dataset, if the earthquake magnitude is higher than M3.5, the week is defined as a positive week, while the weeks without earthquakes are treated as negative weeks (Figure 12).

Obviously, if the threshold is 0.00, all samples are judged as positive samples. At this time, the hit rate is 1.00, and the false

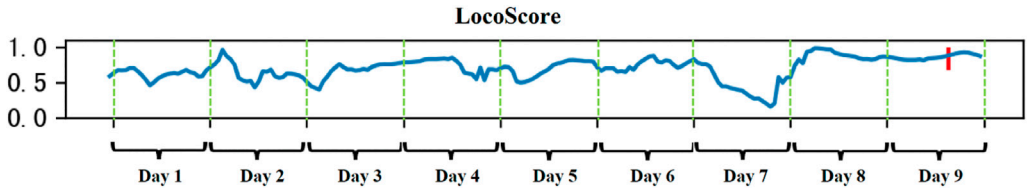

FIGURE 10
LocoScore curve.

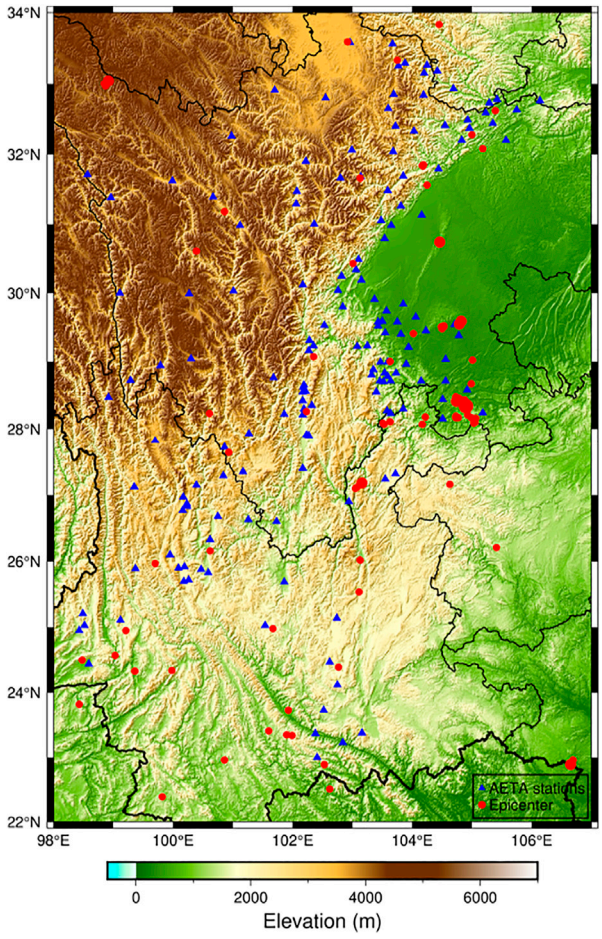

FIGURE 11
AETA stations and earthquakes in the Sichuan-Yunnan area.

alarm rate is 1.00, corresponding to the points at (1.00, 1.00) in the top-right corner. If the threshold is set at infinity, all samples are judged as negative samples. At this time, the hit rate is 0.00, and the false alarm rate is 0.00, corresponding to the points at (0.00, 0.00) in the bottom-left corner. The remaining points on the blue line correspond to other thresholds. As the threshold continues to increase, the corresponding points move along the blue line from the top-right to the bottom-left corner. A small drop in false alarm rates is a tradeoff with a drop in hit rates. The most ideal point is the point at the top-left corner. The hit rate is 1.00, and the false alarm rate is 0.00, which means this classification model completely distinguishes between positive and negative samples. The closer to the upper left corner, the better the threshold.

TABLE 2 Specifications of the original data.

Zone	Sichuan-Yunnan region
Period	2019.4–2021.1
Source	Data from AETA stations
Size	598.50 MB
Earthquakes	59
Max magnitude	M6.0

The red star and the black star (Figure 12) are the closest ones to the top-left corner. The threshold related to the red star is 8, and the threshold corresponding to the black star is 30. The coordinates of the red star are (0.50, 0.86), while those of the black star are (0.22, 0.69). The distance from (0, 1.00) is 0.52 for the red star and 0.37 for the black star. The classification result with the threshold of 30 corresponding to the black star is better.

The AUC value of the classifier for the number of abnormal points in the LCT model, which is the area under the diagonal line, is calculated easily (Kamitsuji and Kamatani, 2006; Lever et al., 2016) (Figure 12) as 0.74, far exceeding 0.50. This is a good result in earthquake prediction. With the AUC value, it can be concluded that LCT anomalies have a considerable correlation, which proves that LCT anomalies are effective in predicting earthquakes that will occur in a few days.

To sum up, first, use the LCT method to analyze the electromagnetic signals from the AETA station, get the signal anomalies between two stations every day, and count the number of abnormal values below 0.08. A weekly review is carried out every Sunday. If this week has anomalies and the number of anomalies for this week is greater than or equal to 30, it is predicted that an earthquake will occur in this region next week; otherwise, it is predicted that no earthquake will occur.

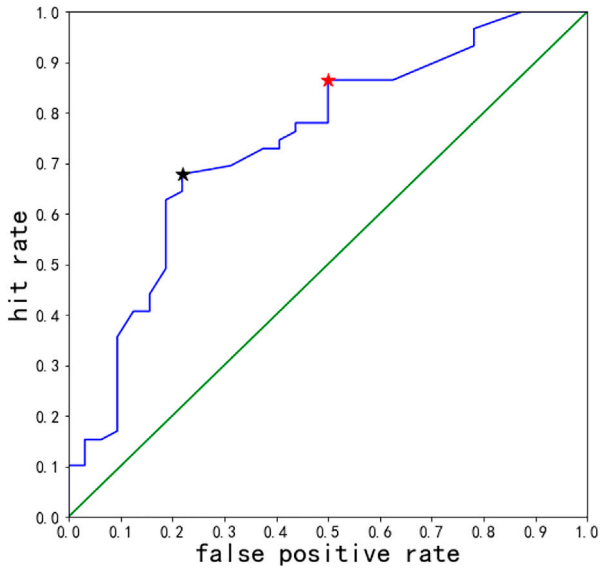

FIGURE 12
ROC curve of our method.

Prediction result analysis

The ROC curve can be used to find the optimal and sub-optimal amounts of data and draw a prediction chart based on this. Therefore, earthquakes can be predicted more intuitively (Figure 13). The abscissa is the number of weeks in chronological order, and the ordinate is the number of LCT outliers less than 0.08. The blue discount indicates the actual occurrence of earthquakes in the 91 weeks, 0 means no earthquake occurred this week, and non-zero means an earthquake occurred this week. The black horizontal line represents the threshold represented by the black star (Figure 13), which is 30. The red broken line represents the number of days with the largest number of LCT outliers of less than 0.08 this week. If the red broken line is lower than the black horizontal line, it will be predicted that there will be no earthquakes; otherwise, the occurrence of earthquakes will be predicted. Compared with the blue broken line, which indicates the actual occurrence of the earthquake, the yellow area is to indicate whether the earthquake is correctly predicted (Figure 14, Figure 13). The threshold presented by using a black horizontal line has been changed to 9, which corresponds

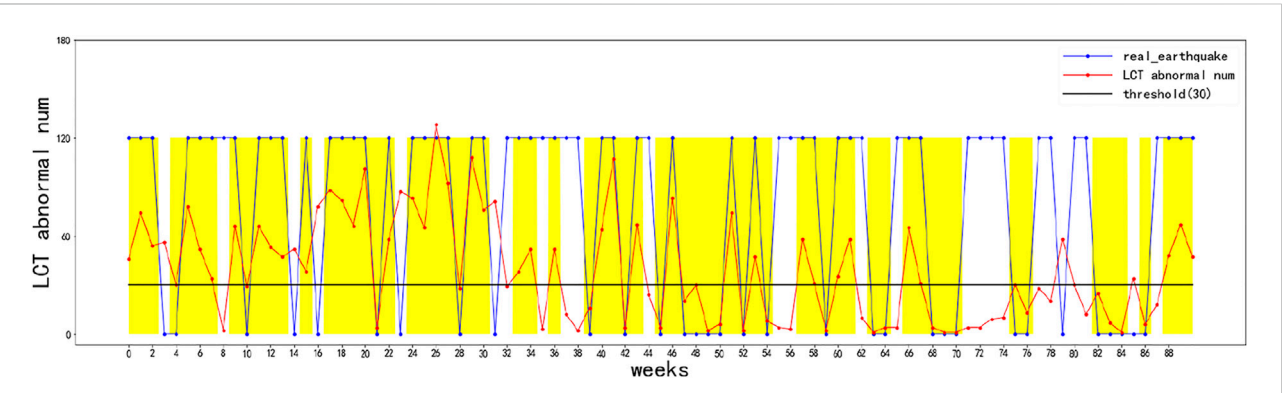

FIGURE 13
Prediction result 1.

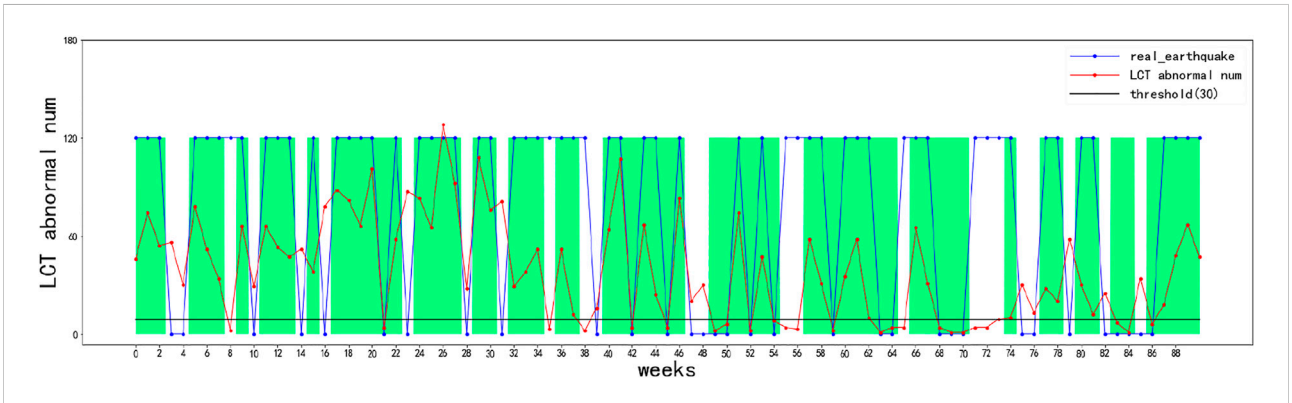

FIGURE 14
Prediction result 2.

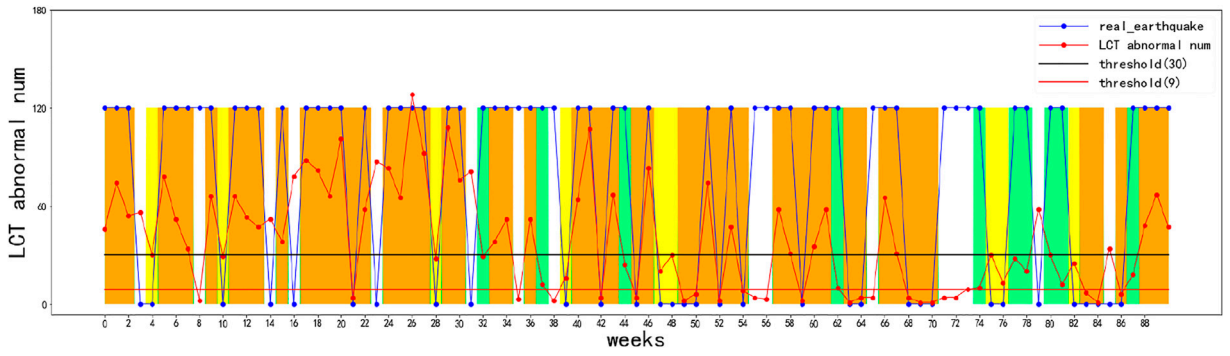

FIGURE 15
Prediction result for 91 weeks.

TABLE 3 *TP*/*FN*/*FP*/*TN* sample table.

	Forecast	
Actual	**Yes**	**No**
Yes	*TP*	*FN*
No	*FP*	*TN*

TABLE 4 Prediction result for 91 weeks.

	Prediction	
Actual	**Yes**	**No**
Yes	41	18
No	7	25

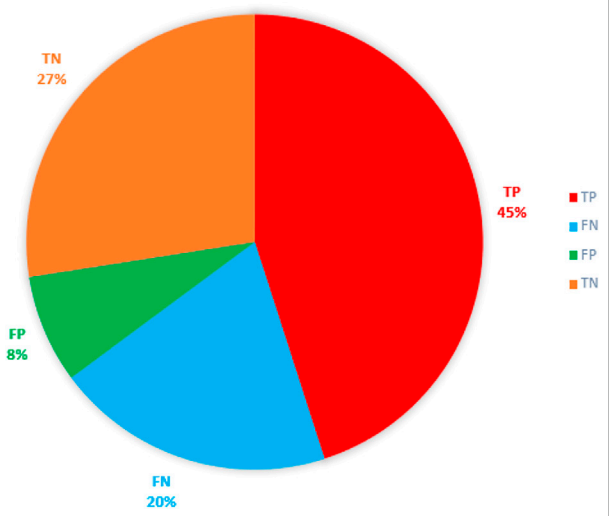

FIGURE 16
Prediction result for 91 weeks.

TABLE 5 Prediction result for 30 weeks announced in real time.

	Prediction	
Actual	**Yes**	**No**
Yes	11	4
No	7	8

to the threshold represented by the red star (Figure 12), the correct prediction time has also been replaced by a light green block, and the orange color block indicates the time if both thresholds are correctly predicted (Figure 15).

It is clear that no matter whether the threshold is 8 or 30, the number of correct predictions of earthquake occurrence far exceeds the number of incorrect predictions (Figures 13–15). This also reflects that LCT anomalies indeed predict earthquakes much more accurately, and there is definitely a greater correlation between them and earthquakes.

To verify whether there will be an earthquake prediction next week, we may get four results (Asencio-Cortés et al., 2015). In this article, we treat earthquakes as positive samples and no earthquakes as negative samples. *TP* and *TN* mean the prediction is correct. The results are shown (Table 3, Table 4 and Figure 16).

In this article, we propose the metrics to measure the quality of the forecast results.

$$P = TP/(TP + FP), \tag{11}$$

$$R = TP/(TP + FN), \tag{12}$$

$$A = (TP + TN)/(TP + TN + FN + FP), \tag{13}$$

$$F = FP/(TN + FP). \tag{14}$$

By calculating P=0.85, A=0.73, R=0.69, and F=0.23, where *TP* is a true positive or hit, *FN* is a false negative or the miss, *FP* is a false positive or false alarm, and *TN* is a true negative or correct rejection. Meanwhile, *Pre* is the precision, *Rec* is the recall, *Acc* is the accuracy, and *Fpr* is the false positive rate.

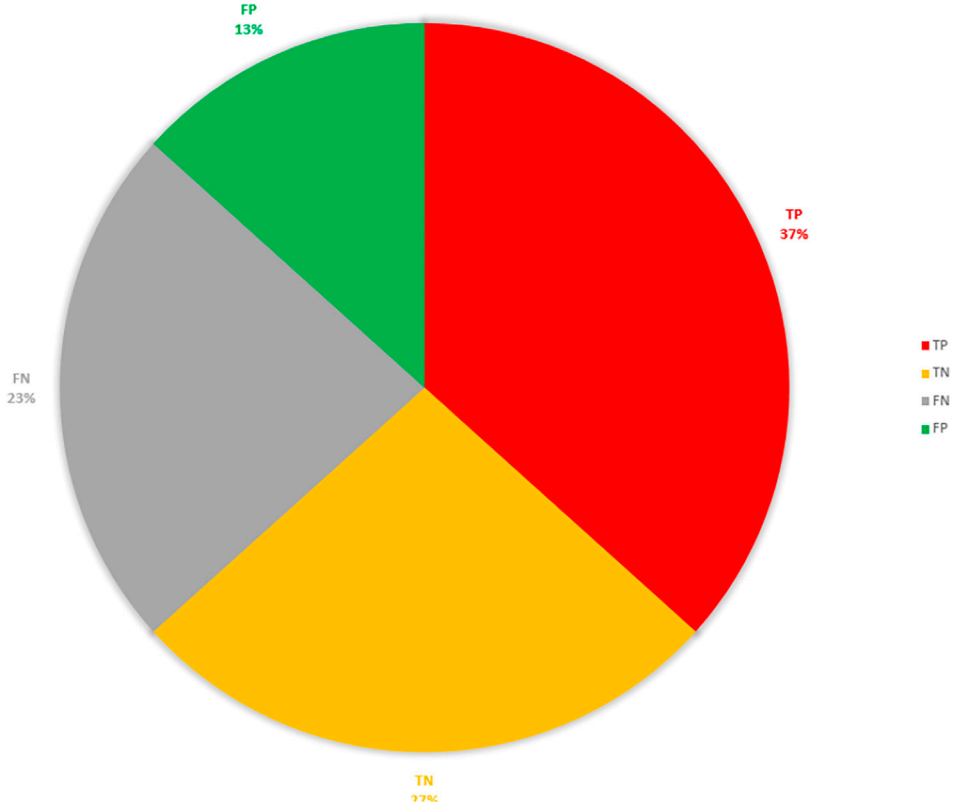

FIGURE 17
Prediction result for 30 weeks announced in real time.

The earthquake prediction results in real time for a total of 30 weeks from 1 April 2021 to 31 October 2021 can also be calculated and published on the AETA prediction platform website, open to visitors from all over the world. During the 30 weeks, there were 15 weeks of actual earthquakes in the Sichuan-Yunnan area and 15 weeks without earthquakes. The system gives 18 earthquake predictions and 12 earthquake-free predictions. The prediction results are shown in Table 5 and Figure 17.

Conclusion

Our work is designing and developing AETA systems based on the deployed stations first. Since January 2017, we have started creating an observation network in China. Up to now, more than 300 stations have been deployed. Most of them are located in the Sichuan-Yunnan region in China, with more than 200 stations, which collect a huge amount of low-frequency electromagnetic data.

Second, based on the low-frequency electromagnetic signals observed by using the AETA system, the LCT method is applied to analyze, calculate, and process the correlation between the local covariance matrices corresponding to each time window of the two streaming data. The daily anomalies by using the LCT method can be calculated. By counting the number of abnormal values below the threshold of 0.08 and conducting a weekly review every Sunday, an earthquake can be predicted to occur in the region next week.

Finally, based on the LCT abnormal analysis from the electromagnetic disturbance data of AETA, the ROC curve is employed to analyze the prediction outcomes of the LCT model in 91 weeks. Key metrics such as hit rate, false alarm rate, and AUC value are proposed. The ROC curve for earthquake prediction of each classifier was drawn, and the data of earthquakes were analyzed. It proves that the LCT anomaly and the earthquake have a considerable correlation, the optimal threshold was found, and the classification results were evaluated, respectively. Finally, four metrics are introduced to measure the LCT method based on earthquake prediction classification, which proves its excellent performance for classification.

Data availability statement

The original contributions presented in the study are included in the article/Supplementary Material; further inquiries can be directed to the corresponding author.

Author contributions

JX: data curation, formal analysis, writing—draft, software, and methodology. SY: project administration and writing—review. XW: funding acquisition, investigation, and project administration. Others: support.

Conflict of interest

The authors declare that the research was conducted in the absence of any commercial or financial relationships that could be construed as a potential conflict of interest.

Publisher's note

Supplementary material

The Supplementary Material for this article can be found online at: https://www.frontiersin.org/articles/10.3389/feart.2022.902745/full#supplementary-material

References

Asencio-Cortés, G., Martínez-Álvarez, F., Morales-Esteban, A., Reyes, J., and Troncoso, A. (2015). "Improving earthquake prediction with principal component analysis: Application to Chile," in *Hybrid artificial intelligent systems*. Editors E. Onieva, I. Santos, E. Osaba, H. Quintián, and E. Corchado (Cham: Springer International Publishing), 393–404.

Calì, C., and Longobardi, M. (2015). Some mathematical properties of the roc curve and their applications. *Ric. Mat.* 64 (2), 391–402. doi:10.1007/s11587-015-0246-8

Chadha, R. K., Pandey, A. P., and Kuempel, H. J. (2003). Search for earthquake precursors in well water levels in a localized seismically active area of reservoir triggered earthquakes in India. *Geophys. Res. Lett.* 30 (7). doi:10.1029/2002gl016694

Freund., F. (2010). Toward a unified solid state theory for pre-earthquake signals. *Acta Geophys.* 58 (5), 719–766. doi:10.2478/s11600-009-0066-x

Guo, Q., Yong, S., and Wang, X. (2021). Statistical analysis of the relationship between aeta electromagnetic anomalies and local earthquakes. *Entropy* 23 (4), 411. doi:10.3390/e23040411

Jacob, B., Chen, J., Huang, Y., and Cohen, I. (2009). *Pearson correlation coefficient*. Berlin, Heidelberg: Springer Berlin Heidelberg, 1–4.

Jónsson, S., Paul, S., Pedersen, R., and Björnsson, G. (2003). Post-earthquake ground movements correlated to pore-pressure transients. *Nature* 424 (6945), 179–183. doi:10.1038/nature01776

Kamarudin, A. N., Cox, T., and Kolamunnage-Dona, R. (2017). Time-dependent roc curve analysis in medical research: Current methods and applications. *BMC Med. Res. Methodol.* 17 (1), 53. doi:10.1186/s12874-017-0332-6

Kamitsuji, S., and Kamatani, N. (2006). Estimation of haplotype associated with several quantitative phenotypes based on maximization of area under a receiver operating characteristic (roc) curve. *J. Hum. Genet.* 51 (4), 314–325. doi:10.1007/s10038-006-0363-z

Keilis-Borok, V., Shebalin, P., Gabrielov, A., and Turcotte, D. (2004). Reverse tracing of short-term earthquake precursors. *Phys. earth Planet. interiors* 145 (1-4), 75–85. doi:10.1016/j.pepi.2004.02.010

Lever, J., Martin, K., and Altman, N. (2016). Classification evaluation. *Nat. Methods* 13 (8), 603–604. doi:10.1038/nmeth.3945

Martinelli, G., Plescia, P., and Tempesta, E. (2020). Electromagnetic emissions from quartz subjected to shear stress: Spectral signatures and geophysical implications. *Geosci. Switz.* 10, 140. doi:10.3390/geosciences10040140

Martinelli, G., Plescia, P., and Tempesta, E. (2020). pre-earthquake" micro-structural effects induced by shear stress on α-quartz in laboratory experiments. *Geosciences* 10, 155. doi:10.3390/geosciences10050155

McGuire, J. J., Boettcher, M. S., and Jordan, T. H. (2005). Foreshock sequences and short-term earthquake predictability on east Pacific rise transform faults. *Nature* 434 (7032), 457–461. doi:10.1038/nature03377

Mirmiran, P., Esmaillzadeh, A., and Azizi, F. (2004). Detection of cardiovascular risk factors by anthropometric measures in tehranian adults: Receiver operating characteristic (roc) curve analysis. *Eur. J. Clin. Nutr.* 58 (8), 1110–1118. doi:10.1038/sj.ejcn.1601936

Molchan, G. (2010). *Space—time earthquake prediction: The error diagrams*. Basel: Springer Basel, 53–63.

Moreno, M., Rosenau, M., and Oncken, O. (2010). 2010 Maule earthquake slip correlates with pre-seismic locking of Andean subduction zone. *Nature* 467 (7312), 198–202. doi:10.1038/nature09349

Olson, E. L., and Allen, R. M. (2005). The deterministic nature of earthquake rupture. *Nature* 438 (7065), 212–215. doi:10.1038/nature04214

Pulinets, S., and Ouzounov, D. (2011). Lithosphere–atmosphere–ionosphere coupling (laic) model–an unified concept for earthquake precursors validation. *J. Asian Earth Sci.* 41 (4-5), 371–382. doi:10.1016/j.jseaes.2010.03.005

Roger, B. (2010). Lessons from the Haiti earthquake. *Nature* 463 (7283), 878–879. doi:10.1038/463878a

Schorlemmer, D., and Wiemer, S. (2005). Microseismicity data forecast rupture area. *Nature* 434 (7037), 1086. doi:10.1038/4341086a

Schuck, P. W. (2005). Local correlation tracking and the magnetic induction equation. *Astrophys. J.* 632 (1), L53–L56. doi:10.1086/497633

Uyeda, S., Nagao, T., and Kamogawa, M. (2011). Earthquake precursors and prediction. *Encycl. Solid Earth Geophys.* 1, 168–178. doi:10.1007/978-90-481-8702-7_4

Verma, M., Steffen, M., and Denker, C. (2013). Evaluating local correlation tracking using co5bold simulations of solar granulation. *Astron. Astrophys.* 555, A136. doi:10.1051/0004-6361/201321628

Wold, S., Kim, E., and Paul, G. (1987). Principal component analysis. *Chemom. Intell. Lab. Syst.* 2 (1), 37–52. doi:10.1016/0169-7439(87)80084-9

Yin, X. C., Yu, H. Z., Kukshenko, V., Xu, Z. Y., Wu, Z., Li, M., et al. (2004). Load-unload response ratio (lurr), accelerating moment/energy release (am/er) and state vector saltation as precursors to failure of rock specimens. *Pure Appl. Geophys.* 161 (11), 2405–2416. doi:10.1007/s00024-004-2572-8

frontiers | Frontiers in Earth Science

TYPE Original Research
PUBLISHED 06 January 2023
DOI 10.3389/feart.2022.767586

OPEN ACCESS

EDITED BY
Giovanni Martinelli,
National Institute of Geophysics and Volcanology, Italy

REVIEWED BY
Zhonghua Hong,
Shanghai Ocean University, China
J. R. K. Kumar Dabbakuti,
K. L. University, India

*CORRESPONDENCE
Xia Chaoxu,
xiachaoxu@ies.ac.cn

SPECIALTY SECTION
This article was submitted to Geohazards and Georisks, a section of the journal Frontiers in Earth Science

RECEIVED 31 August 2021
ACCEPTED 17 August 2022
PUBLISHED 06 January 2023

CITATION
Chaoxu X, Gaozhong N, Huayue L, Xiwei F, Junxue Z, Rui Y and Xun Z (2023), Research on lethal levels of buildings based on historical seismic data.
Front. Earth Sci. 10:767586.
doi: 10.3389/feart.2022.767586

Research on lethal levels of buildings based on historical seismic data

Xia Chaoxu[1,2]*, Nie Gaozhong[1,2], Li Huayue[1,2,3], Fan Xiwei[1,2], Zhou Junxue[1,2,4], Yang Rui[1,2] and Zeng Xun[1,2]

[1]Key Laboratory of Seismic and Volcanic Hazards, China Earthquake Administration, Nanning, China, [2]Institute of Geology, China Earthquake Administration, Nanning, China, [3]China Earthquake Networks Center, Nanning, China, [4]Earthquake Administration of Guangxi Zhuang Autonomous Region, Nanning, China

Due to the influences of buildings, geographical and geomorphological environments, road conditions, etc., the probabilities and numbers of casualties in different areas after an earthquake are different. Accordingly, we propose the concept of the lethal level, which attains different grades representing the mortality rate of differing intensities. Different regions have unique lethal levels, and regional lethal levels are affected mainly by the proportion of each building type and the corresponding lethal level, as different types of buildings also have unique lethal levels. Based on data of 52 historical earthquake disasters, we constructed a lethal level calculation model and obtained the lethal level of each building type. The results reveal that the lethal level ranges of different building types are fixed and unequal; moreover, the ranges of different building types overlap each other. The lethal level range of adobe structures is 0.85–1, that of civil structures is 0.75–0.95, that of brick-wood structures is 0.6–0.9, that of brick-concrete structures is 0.33–0.6, that of wood structures is 0.2–0.35, and that of reinforced concrete structures is 0.1–0.25. Based on the lethal levels of these building types, the overall level of a region can be quantified and graded, and this classification does not depend on the geographical location or administrative boundaries. In pre-earthquake evaluation efforts, the lethal level of an area can be derived through field research. After an earthquake, the number of casualties can be quickly assessed based on the mortality rate corresponding to the intensity of the area. This approach can further provide scientific support for risk zoning and risk assessment research.

KEYWORDS

mortality rate, destruction ratio, lethal level, building types, range

Introduction

Earthquakes are geological disasters that occur abruptly and often result in casualties, property damage, the destruction of resources and the environment, and detrimental impacts on social and economic functions (Fu, 1993). The lethality of an earthquake is affected by many factors, mainly the earthquake parameters, regional environmental

factors, and building properties, among others (Feng et al., 2013). The parameters of earthquakes mainly include the magnitude, intensity, occurrence time, and focal depth, while regional environmental factors predominantly include the earthquake location, population density, percentage of personnel present, economic level, and topography of the earthquake area, and building factors include the building structure type, proportions of building types, construction year, and building style; in addition, other factors include the types of seismic fortification, earthquake prediction, secondary disasters, the efficiency of earthquake emergency rescue efforts, the ability of personnel to help each other, and traffic and road factors. Moreover, these influencing factors have different effects on the number of deaths. Nevertheless, it is not earthquakes that result in deaths but the collapse and destruction of buildings caused by the earthquake (Zhu and Yang, 1998). Hence, the number of people killed during an earthquake is related to the number of buildings that collapse and are destroyed (Ma and Zhao, 2008; Spence et al., 2008; So, 2011). Therefore, research on methods to evaluate the number of casualties based on influencing factors such as the earthquake magnitude, intensity, and building vulnerability is an important research direction.

At present, assessment methods are divided into two main categories: evaluation methods are based on seismic parameters and building vulnerability, while methods based on seismic parameters are used primarily to obtain empirical functions and models based on the earthquake magnitude, intensity, and focal depth and the number of deaths through statistical fitting and to assess the number of possible casualties induced by an earthquake (Samardjieva and Oike, 1992; Ma and Xie, 2000). For example, the death evaluation model is based on impact factors such as the magnitude and population density (Christoskov and Samardjieva, 1984; Samardjieva, 2002; Badal and Samardjieva, 2003; Badal et al., 2005). Nonetheless, although the influencing factors in these models may be the same, the final fitted models are not completely identical due to regional differences and variations in the selected historical earthquake cases (Oike, 1991; Wang et al., 2011; Ceferino et al., 2018a; Zhang et al., 2018). As another example, the empirical function method uses only the seismic parameters of historical earthquakes (Jaiswal et al., 2015); since this method considers only the impacts of the earthquake magnitude, intensity and other factors on the number of deaths, the need for basic data is small, and thus, this approach can be used to rapidly assess the number of casualties after an earthquake. However, historical seismic data are limited and are not available in all regions, especially historical data of casualties. Therefore, the current models obtained based on historical seismic data are not generally applicable, the regional application of such methods is restricted by certain limitations, and the accuracy of the evaluation results is low.

Evaluation methods based on building vulnerability rely predominantly on statistical fitting relationships between the building vulnerability and mortality rate to build a model to evaluate the resulting casualties. At present, the most commonly used casualty assessment approach is based on historical seismic data through regression fitting to obtain the building vulnerability function (Miyakoshi et al., 1998; Goncharov and Frolova, 2011; Alel and Pahang, 2013). Scholars have also carried out research on various alternative methods (Miyakoshi et al., 1998; Alexander, 2011), including research on the relationship between building damage and casualties (Okada and Takai. 1999; Ferreira et al., 2011), new classification methods of building damage (Spence et al., 2011), new methods for assessing the vulnerability of various types of buildings (Pomonis et al., 2011), and methods based on the population size, intensity, building type, proportions of building types and level of damage. (Zhize and He, 1996; So and Spence, 2013). However, the existing research methods on the vulnerability of buildings have an excessively high demand on the requirement for basic data, and there are many research methods to choose from, which also introduces certain limitations in the evaluation methods.

At the same time, various other casualty assessment methods are available, such as the casualty assessment model based on performance-based earthquake engineering (PBEE) (Ceferino et al., 2018b; Pang et al., 2020), which has achieved good success in various applications, such as the proposed model adopting the FEMA P-58 framework for risk assessment.

Furthermore, because different methods require different types of basic data, the accuracy of the results also varies. Assessment methods based on the vulnerability of buildings fully consider the impact of the destruction of the building on the number of deaths, which greatly improves the accuracy of the evaluation results. However, the actual numbers of casualties caused by the 2014 Ludian (3 August 2014, Ludian County,

TABLE 1 Building types and proportion data in Ludian earthquake and Jinggu earthquake area.

Area	Building types and proportion (%)				
	Reinforced-concrete structure	Brick-concrete structure	Wood structure	Brick-wood structure	Civil structure
Ludian	0.33	17.82		1.41	80.44
Jinggu	0.86	18	81.14		

Civil structure: The construction materials of civil structures are mainly bamboo, wood, rammed earth, straw, hay, adobe bricks and tiles. It is a structure with wood as beam and tile or hay as cover. Bamboo strips replace steel bars as connections, clay (some will also be mixed with straw) instead of concrete as walls.

TABLE 2 52 historical earthquake data selected in this paper.

No.	Location	Longitude	Latitude	Date	Time	Magnitude (Mw)	Focal depth (km)	Population density (person/km^2)	Destruction ratio	Death (person)	Injury (person)
1	Lijiang, Yunnan	27.18	100.13	19960203	19:14	7	10	57.42	0.1429	309	17,057
2	Yibin, Sichuan	29.04	104.41	19960228	19:21	5.4	15	42.00	0.0637	1	37
3	Jiashi, Xinjiang	40	76.8	19960319	23:00	6.9	11	20.31	0.1762	24	128
4	Baotou, Neimenggu	40.8	109.43	19960503	11:32	6.4	20	22.75	0.1283	26	453
5	Lijiang, Yunnan	26.9	100.06	19960702	15:05	5.2	10	124.32	0.0673	2	57
6	Lijiang, Yunnan	27.12	100.19	19960925	3:24	5.7	15	42.07	0.1105	1	141
7	Baiyu, Sichuan	30.6	99.5	19961221	16:39	5.5	25	4.53	0.1981	2	60
8	Jiashi, Xinjiang	39.6	77.4	19970121	9:47	6.4	33	57.44	0.1373	12	44
9	Jiashi, Xinjiang	39.5	76.9	19970301	14:04	6	22	131.98	0.0491	1	6
10	Jiashi, Xinjiang	39.7	76.8	19970411	13:34	6.6	17	57.33	0.1399	8	62
11	Zhangbei, Hebei	41.1	114.3	19980110	11:50	6.2	10	88.00	0.5304	49	11,439
12	Jiashi, Xinjiang	39.9	77.9	19980827	17:03	6.6	11	50.00	0.0794	3	13
13	Ninglang, Yunnan	27.3	100.9	19981119	19:38	6.2	10	40.16	0.4331	5	1487
14	Wenxian, Gansu	32.9	104.9	19990415	14:29	4.7	8	88.60	0.1361	1	30
15	Chengjiang, Yunnan	24.5	102.8	19991125	0:40	5.2	10	207.00	0.1151	1	12
16	Anxian, Sichuan	31.4	104.4	19991130	16:24	5	26	363.00	0.0600	1	2
17	Yaoan, Yunnan	25.5	101.1	20000115	7:37	6.5	30	123.04	0.3548	7	2,528
18	Neixiang, Henan	33.1	112	20000429	11:54	4.7	16	10.33	0.3160	1	28
19	Wuding, Yunnan	25.8	102.2	20000821	21:25	5.1	8	93.76	0.1142	2	292
20	Yajiang, Sichuan	29.4	101.1	20010223	8:09	6	10	4.70	0.0825	3	154
21	Shidian, Yunnan	24.48	99.01	20010410	11:13	5.9	10	196.15	0.1600	3	235
22	Yanyuan, Sichuan	27.6	100.9	20010524	5:10	5.8	5	21.23	0.1500	1	39
23	Shidian, Yunnan	24.8	99.1	20010608	2:03	5.3	5	208.09	0.0767	1	15
24	Yongsheng, Yunnan	26.2	100.6	20011027	13:35	6	15	138.41	0.1737	1	220
25	Yumen, Gansu	39.8	97.3	20021214	21:27	5.9	15	19.85	0.2071	2	350
26	Bachu-Jiashi,Xinjiang	39.5	77.2	20030224	10:03	6.8	25	30.67	0.3612	268	4,853
27	Jiashi, Xinjiang	39.4	77.3	20030504	23:44	5.8	26	49.29	0.1489	1	3
28	Dayao, Yunnan	26	101.2	20030721	23:16	6.2	6	101.90	0.0971	16	793
29	Balinzuoqi, Neimenggu	43.9	119.7	20030816	18:58	5.9	15	36.46	0.2323	4	1064
30	Dayao, Yunnan	26	101.3	20031016	18:28	6.1	5	84.30	0.1623	3	57
31	Minle, Gansu	38.4	101.2	20031025	20:41	6.1	18	58.87	0.2312	10	46
32	Minxian, Gansu	34.7	103.9	20031113	10:35	5.2	12	165.95	0.2166	1	133

(Continued on following page)

10.3389/feart.2022.767586

TABLE 2 (*Continued*) 52 historical earthquake data selected in this paper.

No.	Location	Longitude	Latitude	Date	Time	Magnitude (Mw)	Focal depth (km)	Population density (person/ km^2)	Destruction ratio	Death (person)	Injury (person)
33	Ludian, Yunnan	27.2	103.6	20031115	2:49	5.1	10	415.91	0.0440	4	94
34	Zhaosu, Xinjiang	43.01	83.5	20031201	9:38	6.1	18	10.34	0.1046	10	47
35	Dongwuzhumuqinqi, Neimenggu	45.4	118.2	20040324	9:53	5.9	30	2.91	0.0943	1	5
36	Yibin, Sichuan	29.01	104.56	20040617	5:25	4.7	5	322.13	0.1708	1	9
37	Ludian, Yunnan	27.2	103.6	20040810	18:26	5.6	10	353.50	0.1627	4	597
38	Minxian, Gansu	34.7	103.9	20040907	20:15	5	33	105.80	0.1793	1	36
39	Shuangbai, Yunnan	24.7	101.5	20041226	15:30	5	7	72.44	0.1152	1	20
40	Lindian, Heilongjiang	46.9	125	20050725	23:43	5.1	15	88.85	0.5179	1	11
41	Pingguo, Guangxi	23.6	107.5	20051027	19:18	4.6	16	152.50	0.0693	1	3
42	Jiujiang, Jiangxi	29.7	115.7	20051126	8:49	5.7	10	638.10	0.1798	13	775
43	Wenxian, Gansu	33.1	105	20060621	0:52	5	15	93.70	0.0783	1	19
44	Yanjin, Yunnan	28	104.2	20060722	9:10	5.1	9	169.85	0.1462	22	114
45	Yanjin, Yunnan	28	104.2	20060825	13:51	5.1	7	194.47	0.1147	2	67
46	Ninger, Yunnan	23	101.1	20070603	5:34	6.4	5	74.75	0.1635	3	419
47	Yingjiang, Yunnan	24.9	97.8	20080821	20:24	5.9	7	78.78	0.0918	5	130
48	Panzhihua, Sichuan	26.2	101.9	20080830	16:30	6.1	10	131.52	0.1974	41	1010
49	Dangxiong, Xizang	29.8	90.3	20081006	16:30	6.6	8	10.17	0.1565	10	60
50	Yaoan, Yunnan	25.6	101.1	20090709	19:19	6	10	115.44	0.1001	1	372
51	Rongchang, Chongqing	29.22	105.27	20090808	21:26	4	11	626.01	0.1020	2	1
52	Suining, Sichuan	30.3	105.7	20100131	5:36	5	10	571.96	0.0831	1	16

10.3389/feart.2022.767586

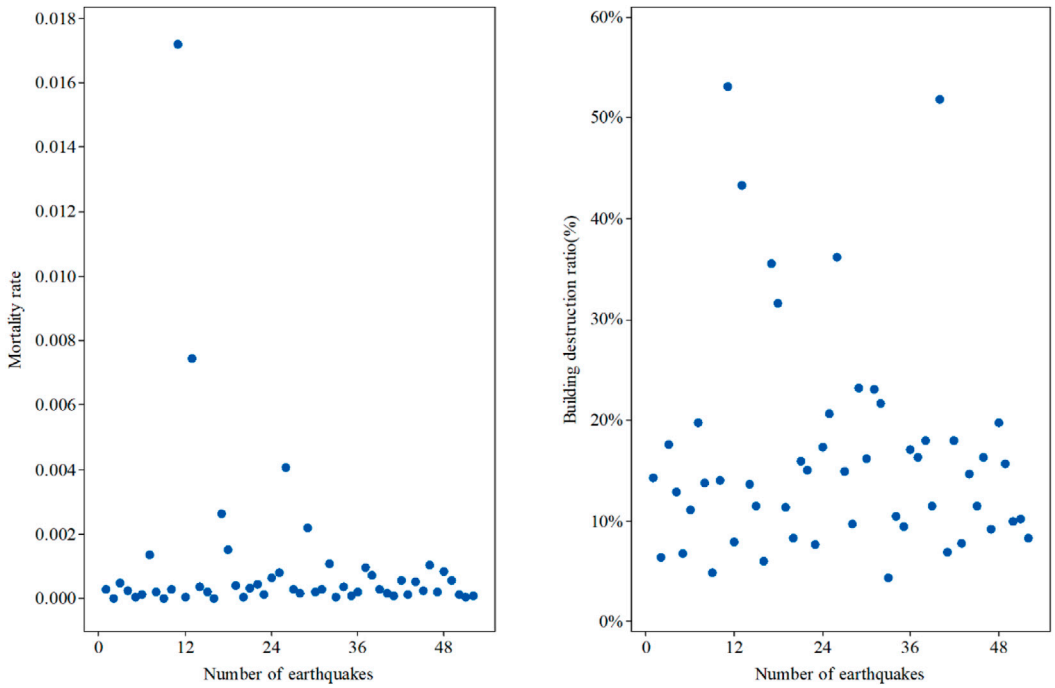

FIGURE 1
Distribution of the mortality rate and the proportion of building destruction of 52 earthquakes.

Zhaotong City, Yunnan Province, Mw6.5, the focal depth is 12 km) and Jinggu (7 October 2014, Jinggu Dai and Yi Autonomous County, Pu'er City, Yunnan Province, Mw6.6, the focal depth is 5 km) earthquakes differed enormously (617 versus 1, respectively), even though the magnitudes of the two earthquakes, the population densities, and the geomorphological environments were all similar. Table 1 describes the proportions of various types of buildings in these two earthquake areas. Both of the affected areas contain relatively equal proportions of reinforced concrete structures and brick-concrete structures, but the Ludian earthquake area is dominated by civil structures (characterized by the use of bamboo strips instead of steel bars and clay instead of concrete for the walls of houses; some walls are mixed with straw with wood being used as beams and tile or hay employed as the cover), while the Jinggu earthquake area is dominated by wood structures. The vulnerability matrices of various types of buildings are almost identical, and the proportions of damaged buildings are the same, but there was a considerable difference in the number of deaths.

The above example reveals that the probability of death is different after the collapse and severe damage of different types of buildings. Accordingly, we hypothesized that we can quantify the difference in the possibility of death caused by such buildings to obtain the correlation between building destruction and the probability of death. By investigating this relationship, we can carry out research on a method to evaluate the deaths caused by earthquakes.

Data

The data sources for this study are the 1996–2000 and 2001–2005 versions of the Assessment and Compilation of Earthquake Disaster Loss in Mainland China, the 2006–2010, 2011, 2012, 2013, and 2014 versions of the Earthquake Disaster Assessment Report published by the China Earthquake Administration. At the same time, we referenced some scholars' relevant literature on the statistics of earthquake casualties and obtained the proportions of various types of buildings during 52 historical earthquakes. The data mainly include the numbers of casualties and injuries and the proportions of destroyed buildings. Damage to buildings is divided into five main classifications: basically intact, minor damage, moderate damage, severe damage and destruction, as shown in Table 2. We mainly use data on the proportions of destroyed buildings for each earthquake to conduct a comparative analysis of the mortality rate, where the extent of the studied region refers mainly to the intensity zone delineated for each earthquake. At the same time, we also collected the proportion data of various types of buildings in each earthquake area. The results are shown in Table 4.

As shown in Figure 1, the proportions of buildings destroyed in historical earthquakes are generally concentrated in less than 30% of the affected area. The distribution characteristics of the proportions of buildings destroyed during earthquakes in different regions with different magnitudes are obviously similar. Similarly, the distribution of the mortality rate is relatively fixed and generally concentrated in

TABLE 3 52 historical earthquake data grouping and the number of equations.

Group	Building type	Number of earthquake	Number of groups	Permutations	Earthquake		
					No.	Date	Location
1	Adobe structure, Civil structure, Brick-wood structure, Brick-concrete structure	6	1	C_6^4 =15	1	19990415	Wenxian, Gansu
					2	20030224	Bachu, Xinjiang
					3	20030504	Jiashi, Xinjiang
					4	20031115	Ludian, Yunnan
					5	20040810	Ludian, Yunnan
					6	20060621	Wenxian, Gansu
2	Civil structure, Brick-wood structure, Brick-concrete structure, Reinforced concrete structure, Wood structure	6	1	C_6^5 =6	1	19960228	Yibin, Sichuan
					2	19980827	Jiashi, Xinjiang
					3	19991125	Chengjaing, Yunan
					4	20010223	Yajiang, Sichuan
					5	20031113	Minxian, Gansu
					6	20040617	Yibin, Sichuan
3	Civil structure, Brick-wood structure, Brick-concrete structure	6	2	2× C_6^3 =40	1	19970121	Jiashi, Xinjiang
					2	19970301	Jiashi, Xinjiang
					3	19970411	Jiashi, Xinjiang
					4	20031201	Zhaosu, Xinjiang
					5	20040324	Dongwuzhumuqinqi, Neimenggu
					6	20040907	Minxian, Gansu
					7	19980110	Zhangbei, Hebei
					8	20030816	Balinzuoqi, Neimenggu
					9	20050725	Lindian, Heilongjiang
					10	20051027	Pingguo, Guangxi
					11	20090808	Rongchang, Chongqing
					12	20100131	Suining, Sichuan
4	Civil structure, Brick-wood structure, Brick-concrete structure, Reinforced concrete structure	28	4	4× C_7^4 =140	1	19960203	Lijiang, Yunnan
					2	19960319	Jiashi, Xinjiang
					3	19960503	Baotou, Neimenggu
					4	19960702	Lijiang, Yunnan
					5	19960925	Lijiang, Yunnan
					6	19961221	Baiyu, Sichuan
					7	19981119	Ninglang, Sichuan
					8	19991130	Anxian, Sichuan
					9	20000115	YaoanYunnan
					10	20000429	Neixiang, Henan
					11	20000821	Wuding, Yunnan
					12	20010410	Shidian, Yunnan
					13	20010524	Yanyuan, Sichuan
					14	20010608	Shidian, Yunann
					15	20011027	Yongsheng, Yunan
					16	20021214	Yumen, Gansu
					17	20030721	Dayao, Yunnan
					18	20031016	Dayao, Yunnan
					19	20031025	Minle, Gansu
					20	20041226	Shuangbai, Yunnan
					21	20051126	Jiujiang, Jiangxi

(Continued on following page)

TABLE 3 (*Continued*) 52 historical earthquake data grouping and the number of equations.

Group	Building type	Number of earthquake	Number of groups	Permutations	Earthquake		
					No.	Date	Location
					22	20060722	Yanjin, Yunnan
					23	20060825	Yanjin, Yunnan
					24	20070603	Ninger, Yunnan
					25	20080821	Yingjiang, Yunnan
					26	20080830	Panzhihua, Sichuan
					27	20081006	Dangxiong, Xizang
					28	20090709	Yaoan, Yunnan
Total		52	8	201			

the range below 0.001. In general, the distributions of the mortality rate and proportion of destroyed buildings correspond to each other. However, there is no one-to-one positive correlation between the proportion of destroyed buildings and the mortality rate. Hence, if a death assessment model is constructed based only on data of the proportion of destroyed buildings, large errors are inevitable. Based on an analysis of historical earthquakes, it was found that the destruction of buildings is not the only factor responsible for deaths; secondary geological disasters and various other factors are also responsible, and among them, building collapse is the dominant cause of casualties during earthquakes (Jaiswal et al., 2011). Thus, to comprehensively express the number of deaths caused by these factors, we introduced the concept of the lethal level (LL) (Nie et al., 2020; Xia et al., 2020; Nie et al., 2021), which represents the comprehensive possibility or level of various factors that cause death after a building is destroyed and other reason. It is expressed by the predominant mortality rate at a certain level under various intensities.

After an earthquake, the factors resulting in the death of people are very complicated; these factors include building damage, collapsing walls, collapsing gatehouses, falling wall hangings, rolling stones, landslides, fires, and inadequate treatment, etc. Therefore, to comprehensively describe the possible extent and number of deaths caused by earthquakes in various disaster areas, a novel concept needs to be introduced, that is, the regional LL, the weight of each factor varies among different disaster areas; for example, in plain areas, it is directly related to the possibility of death after the destruction of a building, whereas in mountainous areas, it may include the possibility of death after building damage and the possibility of death from rolling stones and post seismic landslides. The casualties induced by landslides and rockfalls exceed the casualties caused by building destruction, and the number of deaths in areas with inconvenient traffic conditions and complex distributions of buildings can even increase due to transportation interruptions and inadequate treatment.

The best indicator of the LL is the mortality rate caused by an earthquake, and the effects of the various lethal factors of an earthquake are comprehensively reflected in the mortality rate of the disaster area. In other words, after an earthquake, if an area is in a different intensity range, then its corresponding death rate is different, or the same area (county or township) may be in a different intensity range, so the corresponding death rate of the same area is also different, different LLs correspond to mortality rates of differing intensity. Thus, it is crucial to quantify the mortality rate within a region. Then, after an earthquake, regardless of the intensity range within an area, given the level of that area, a mortality rate must correspond to the intensity. Therefore, one of the main purposes of this article is to develop a method to quantify the LL of an area.

Materials and methods

The analysis of historical earthquake data reveals that data can be obtained on the mortality rate and the proportion of buildings destroyed in the historical earthquake area. Thus, we can construct a model to obtain the regional LL which based on various types of data, such as the proportion of damaged buildings, the mortality rate etc. The overall seismic capacity of a region are affected mainly by the types and proportions of buildings (as different types of buildings have different seismic capacities due to variations in building materials), construction methods and building quality. In other words, different types of buildings have different capacities to cause death after being damaged, therefore, we can obtain the LL of each building type according to the overall level of each historical earthquake area and the proportion data of each type of building.

Lethal level model

For historical earthquakes, many factors comprehensively account for the causes of death, the destruction of buildings is the main factor; other factors include the occurrence time of the earthquake and the population density. This article presents an evaluation model of casualties based on the proportion of damaged buildings proposed by Yin Zhiqian (Yin, 1991), we

TABLE 4 52 historical earthquake building destruction proportion, mortality rate, lethal level and proportion of each type of building.

Location	Date	Destruction proportion	Mortality rate	Lethal level	Proportion of each type of building (%)					
					Adobe	Civil	Brick-wood	Brick-concrete	Reinforced-concrete	Wood
Lijiang, Yunnan	19960203	0.1429	0.000287	0.7583		85.43	5.96	5.83	2.77	
Yibin, Sichuan	19960228	0.0637	0.000015	0.7051		68.00	2.00	14.00	5.00	11.00
Jiashi, Xinjiang	19960319	0.1762	0.000507	0.8422		93.19	1.71	5.00	0.10	
Baotou, Neimenggu	19960503	0.1283	0.000262	0.5817		46.85	8.75	19.81	24.60	
Lijiang, Yunnan	19960702	0.0673	0.000055	0.8428		89.00	5.00	5.00	1.00	
Lijiang, Yunnan	19960925	0.1105	0.000132	0.8514		86.90	7.00	5.00	1.10	
Baiyu, Sichuan	19961221	0.1981	0.001378	0.7124		65.42	12.58	12.00	10.00	
Jiashi, Xinjiang	19970121	0.1373	0.000235	0.5691		32.34	18.82	48.85		
Jiashi, Xinjiang	19970301	0.0491	0.000029	0.5978		32.34	18.82	48.85		
Jiashi, Xinjiang	19970411	0.1399	0.000294	0.7839		79.19	8.74	12.07		
Zhangbei, Hebei	19980110	0.5304	0.017174	0.8251		53.00	40.00	7.00		
Jiashi, Xinjiang	19980827	0.0794	0.000067	0.6897		40.66	39.74	5.33	3.00	11.27
Ninglang, Yunnan	19981119	0.4331	0.007460	0.7641		71.76	11.92	9.48	6.83	
Wenxian, Gansu	19990415	0.1361	0.000381	0.7118	10.00	61.00	3.00	26.00		
Chengjiang, Yunnan	19991125	0.1151	0.000226	0.6668		59.02	1.38	19.09	10.51	10.00
Anxian, Sichuan	19991130	0.0600	0.000014	0.7055		0.00	80.77	10.18	9.06	
Yaoan, Yunnan	20000115	0.3548	0.002630	0.6775		77.96	8.93	10.08	3.04	
Neixiang, Henan	20000429	0.3160	0.001526	0.4577		10.00	10.00	70.00	10.00	
Wuding, Yunnan	20000821	0.1142	0.000425	0.8126		91.56	4.21	2.94	1.29	
Yajiang, Sichuan	20010223	0.0825	0.000051	0.4641		10.00	4.00	40.00	5.00	41.00
Shidian, Yunnan	20010410	0.1600	0.000355	0.7605		77.94	12.78	6.77	2.51	
Yanyuan, Sichuan	20010524	0.1500	0.000464	0.7439		50.00	37.00	8.00	5.00	
Shidian, Yunnan	20010608	0.0767	0.000151	0.8335		85.31	9.33	4.28	1.08	
Yongsheng, Yunnan	20011027	0.1737	0.000641	0.855		92.87	3.32	2.91	0.90	
Yumen, Gansu	20021214	0.2071	0.000832	0.6555		16.85	44.65	35.05	3.45	
Bachu-Jiashi,Xinjiang	20030224	0.3612	0.004086	0.8167	10.00	85.00	3.00	2.00		
Jiashi, Xinjiang	20030504	0.1489	0.000298	0.8182	10.00	86.39	1.22	2.40		
Dayao, Yunnan	20030721	0.0971	0.000172	0.7312		77.24	11.40	10.15	1.21	
Balinzuoqi, Neimenggu	20030816	0.2323	0.002221	0.7372		38.56	53.44	8.00		
Dayao, Yunnan	20031016	0.1623	0.000212	0.7977		91.66	5.48	2.55	0.31	
Minle, Gansu	20031025	0.2312	0.000295	0.3739		25.28	32.57	28.03	14.11	
Minxian, Gansu	20031113	0.2166	0.001108	0.7074		30.97	10.00	10.00	10.00	39.03
Ludian, Yunnan	20031115	0.0440	0.000057	0.8809	83.91	4.00	7.34	4.75		
Zhaosu, Xinjiang	20031201	0.1046	0.000364	0.5793		54.02	25.89	20.10		
Dongwuzhumuqinqi, Neimenggu	20040324	0.0943	0.000113	0.5937		18.64	35.50	45.87		
Yibin, Sichuan	20040617	0.1708	0.000207	0.4321		15.00	10.00	30.00	35.00	10.00
Ludian, Yunnan	20040810	0.1627	0.000965	0.9286	82.48	3.00	7.73	6.79		
Minxian, Gansu	20040907	0.1793	0.000730	0.716		30.87	54.13	15.00		
Shuangbai, Yunnan	20041226	0.1152	0.000308	0.7069		60.04	15.30	18.14	6.52	
Lindian, Heilongjiang	20050725	0.5179	0.000193	0.7608		71.69	21.93	6.38		
Pingguo, Guangxi	20051027	0.0693	0.000090	0.5357		10.00	44.60	45.40		
Jiujiang, Jiangxi	20051126	0.1798	0.000588	0.6508		69.68	0.16	29.28	0.88	
Wenxian, Gansu	20060621	0.0783	0.000152	0.8197	8.56	67.58	3.00	20.86		
Yanjin, Yunnan	20060722	0.1462	0.000523	0.7603		62.01	13.02	18.13	6.84	

(Continued on following page)

TABLE 4 (*Continued*) 52 historical earthquake building destruction proportion, mortality rate, lethal level and proportion of each type of building.

Location	Date	Destruction proportion	Mortality rate	Lethal level	Proportion of each type of building (%)					
					Adobe	Civil	Brick-wood	Brick-concrete	Reinforced-concrete	Wood
Yanjin, Yunnan	20060825	0.1147	0.000263	0.7167		60.02	16.14	12.61	11.23	
Ninger, Yunnan	20070603	0.1635	0.001047	0.5479		25.13	22.62	32.31	19.94	
Yingjiang, Yunnan	20080821	0.0918	0.000197	0.5903		42.65	39.03	17.49	0.84	
Panzhihua, Sichuan	20080830	0.1974	0.000834	0.713		73.73	5.06	11.21	10.00	
Dangxiong, Xizang	20081006	0.1565	0.000577	0.7416		39.39	45.75	10.61	4.25	
Yaoan, Yunnan	20090709	0.1001	0.000140	0.6173		66.04	10.69	19.29	3.98	
Rongchang, Chongqing	20090808	0.1020	0.000074	0.5597		36.93	0.00	63.07		
Suining, Sichuan	20100131	0.0831	0.000087	0.537		1.02	49.35	49.63		

selected the influencing factors such as the percentage of personnel present, the population density etc. To constructed the model, as shown in Eq. 1:

$$logRD = 12.479 \times \left(P_t \times \rho \times RA \times \alpha\right)^{0.1} - 13.3 \qquad (1)$$

where RD is the mortality rate of the earthquake (the ratio of the number of casualties to the total population), RA is the proportion of collapsed and destroyed buildings in the earthquake area, α is the overall LL in the earthquake area, ρ is the population density in the earthquake area, and P_t is the average occupancy rate of personnel (i.e., the average proportion of personnel in buildings during the earthquake). Among them, the average occupancy rate mainly refers to the research of relevant scholars: during the daytime, the average occupancy rate is 0.75, whereas at night, the occupancy rate is set as 1 (Xu et al., 2008; Wei et al., 2017).

Lethal levels of different types of buildings

For a historical earthquake, the regional LL is affected mainly by the proportions of various types of buildings in the region and their unique LLs. Therefore, based on the proportion of each type of building, a method for calculating the LL of each building is established, as shown in Eq. 2:

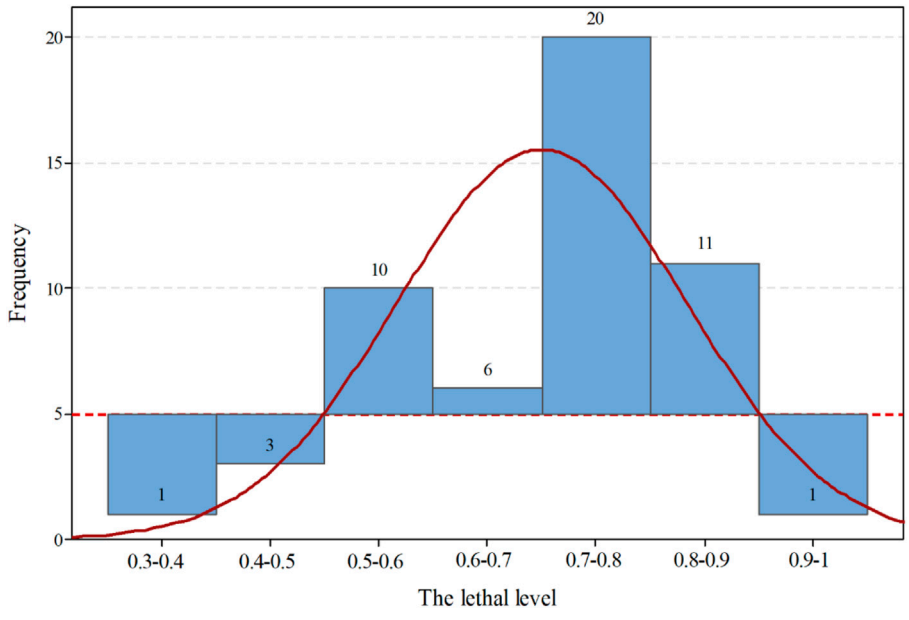

FIGURE 2
The frequency distribution of the regional lethal level of 52 historical earthquakes.

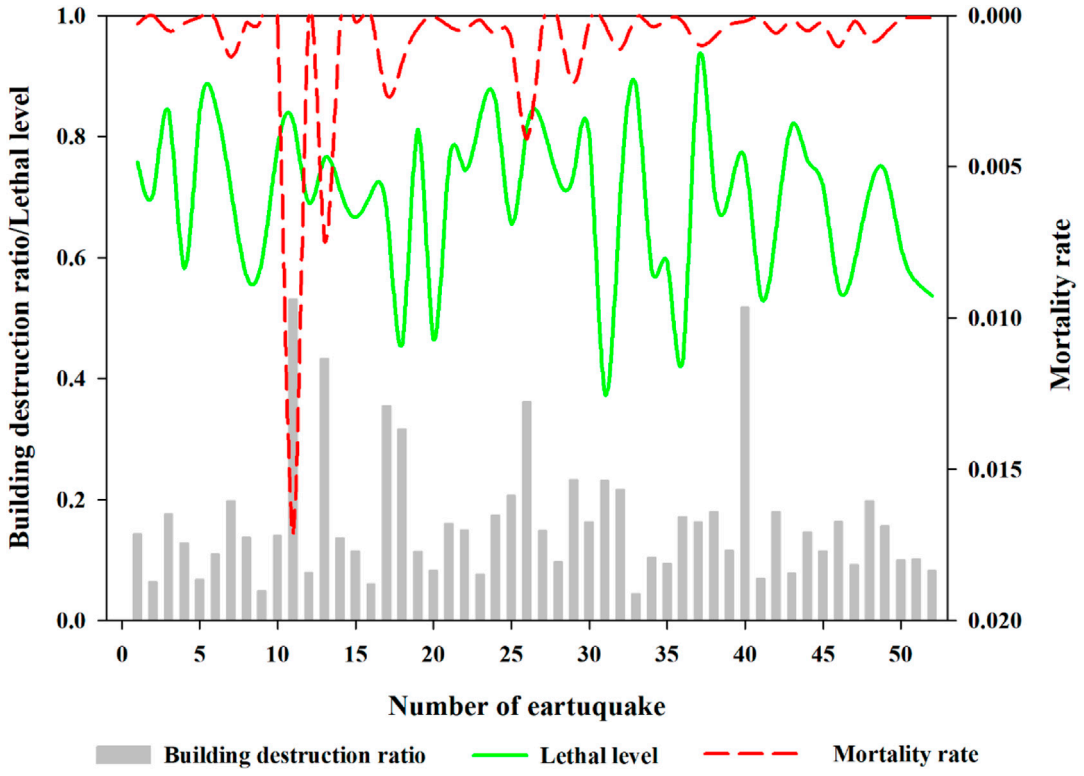

FIGURE 3
Comparative analysis of building destruction ratio, lethal level and mortality rate.

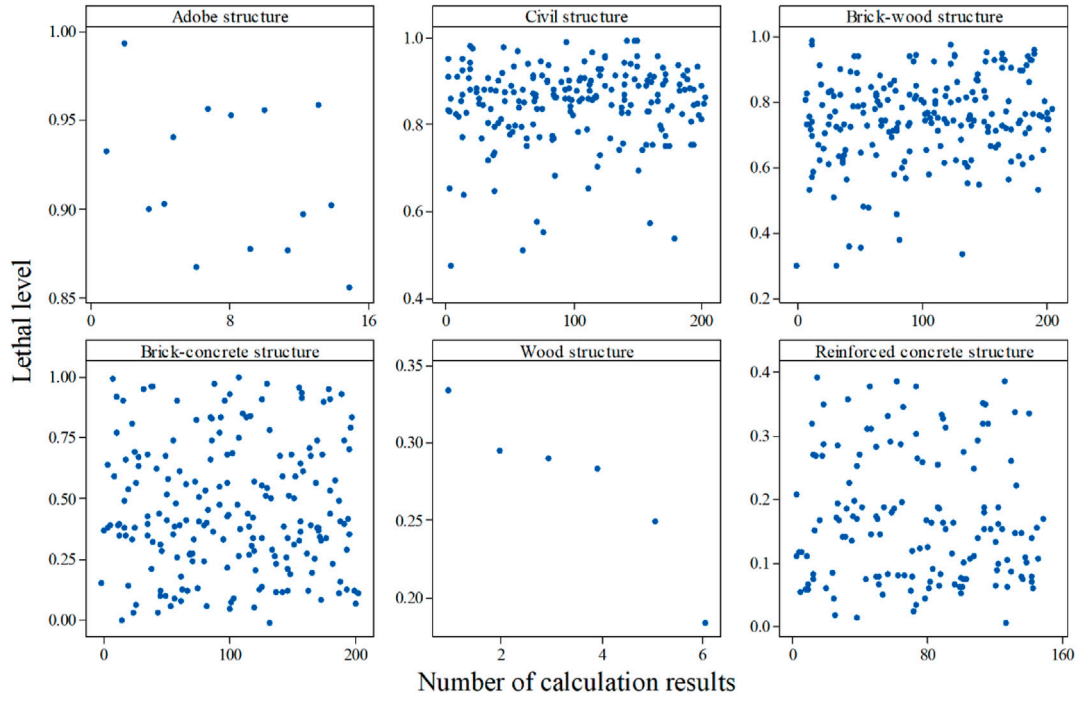

FIGURE 4
Calculation results of lethal level of different types of buildings.

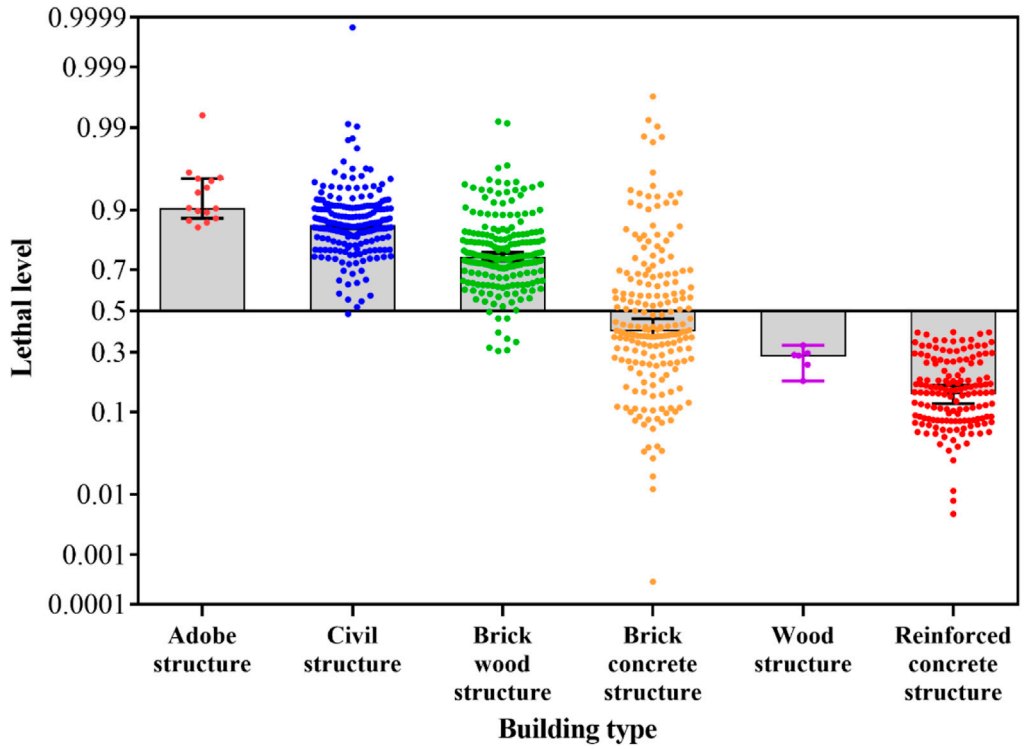

FIGURE 5
Different types of buildings lethal level distribution characteristics.

$$\alpha = \sum_{i=1}^{i\,max} (\beta_i \times \lambda_i) \tag{2}$$

where α refers to the overall LL of the historical earthquake area,β_i refers to the proportion of the i-th type building in the earthquake area,λ_i refers to the LL of the i-th type of building in the earthquake area, and i_{max} is determined mainly based on the actual number of types of buildings in the earthquake area.

The above formula is a multivariate linear equation, the regional LL (y_1-y_n which refer to the α) and the proportions of various types of buildings (a_1-a_q which refer to theβ) are known quantities in this equation, the calculation of the LL of each building type is actually the process of solving the multivariate linear equation based on each earthquake area:

$$\begin{aligned} &a_1x_{11} + \cdots + a_jx_{1j} + \cdots + a_qx_{1q} = y_1,\\ &a_1x_{21} + \cdots + a_jx_{2j} + \cdots + a_qx_{2q} = y_2,\\ &\vdots\\ &a_1x_{i1} + \cdots + a_jx_{ij} + \cdots + a_qx_{iq} = y_i,\\ &\vdots\\ &a_1x_{n1} + \cdots + a_jx_{nj} + \cdots + a_qx_{nq} = y_n, \end{aligned} \tag{3}$$

where a_1-a_q denote the proportions of different types of buildings in different earthquake areas, x_{11}-x_{nq} denote the LLs of those different types of buildings in different earthquake areas, and y_1-y_n denote the overall LLs in different earthquake areas. Among them, since a_1-a_q represents the proportional data of various types of buildings, it is obtained based on the actual collection results, the specific results are shown in Table 4.

In fact, if there are 4 building types in the area, then a quaternary linear equation is constructed, in theory, four historical earthquake data can be used to solve the equation system, which will inevitably lead to abnormal results. In order to avoid this situation, we arrange and combine the historical seismic data with the same building type, so as to obtain as many calculations results as possible, and to some extent avoid the result error caused by single data.

Results

The number of building types varies among different earthquake regions, therefore, we use the number of building types as a grouping standard, if different regions have the same building type, it will into one group, in this way, according to the number of building types, different multivariate linear equations can be constructed, in this study, 52 historical earthquakes are

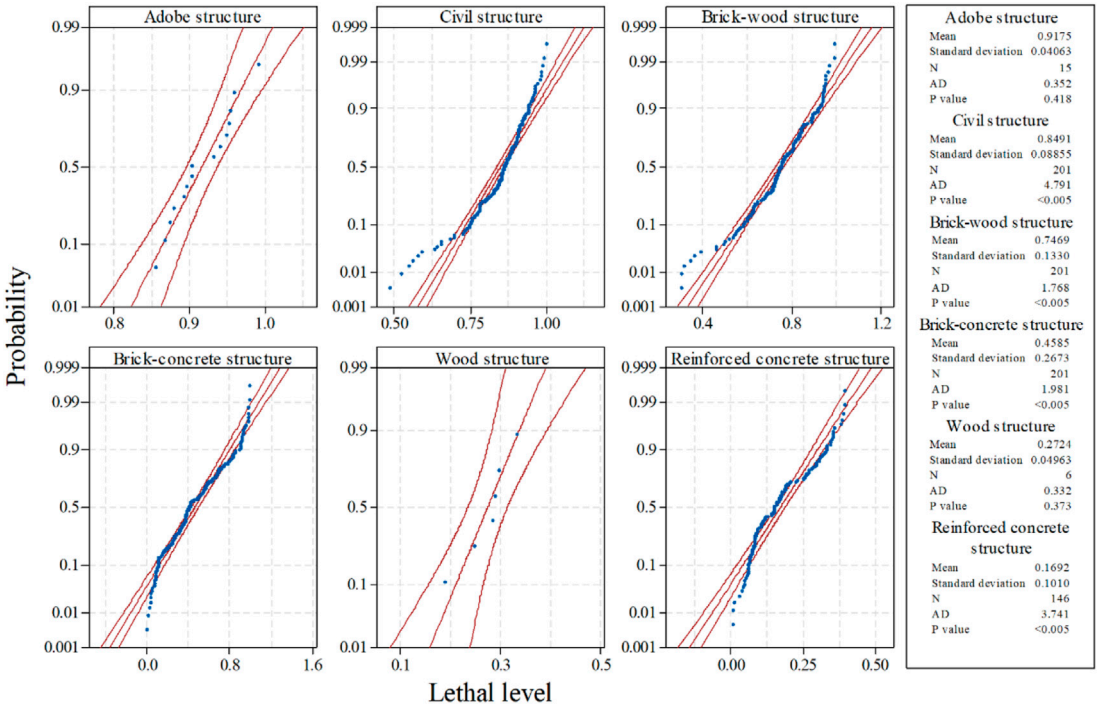

FIGURE 6
95% confidence interval distribution of lethal level of different types of buildings.

first grouped according to the building type, as shown in Table 3, the first group includes 6 earthquakes (2 in Gansu, 2 in Xinjiang, and 2 in Yunnan), the location distribution is mainly in the northwest region of China and the building types are adobe, civil, brick-wood and brick-concrete structures, there are 4 types of buildings, then quadratic linear equations can be constructed, and since the number of historical earthquakes is 6, a total of 15 quadratic linear equations are obtained, and each equation system can be calculated, the results of these 4 types of buildings, which may be a discrete result or a centralized distribution result, corresponding, the second group includes 6 earthquakes (3 in Sichuan, 1 in Xinjiang, 1 in Yunnan, and 1 in Gansu), and the

TABLE 5 95% confidence interval index parameters of building lethal level.

Indicator name	Index of indicators (building type)					
	Adobe structure	Civil structure	Brick wood structure	Brick concrete structure	Reinforced concrete structure	Wood structure
Sample size	15	201	201	201	146	6
Mean value	0.9175	0.8491	0.7469	0.4585	0.1692	0.2724
standard deviation	0.040629	0.088548	0.132954	0.267283	0.101018	0.049626
Sampling mean error	0.028729	0.051123	0.076761	0.069012	0.039622	0.031386
Confidence	0.95	0.95	0.95	0.95	0.95	0.95
Degrees of freedom	15	201	201	201	146	6
Two-sided quantile of t distribution	2.48988	1.971837	1.971837	1.971837	1.976346	2.446912
Allowable error	0.071531	0.100807	0.151360	0.136081	0.078308	0.076799
Lower limit	0.845975	0.748337	0.595503	0.322454	0.090908	0.195633
Upper limit	0.989038	0.949951	0.898223	0.594616	0.247523	0.349231

TABLE 6 Lethal level range and influencing factors of various types of buildings.

Building structure type			
Building type	**Secondary classification**	**Influencing factors**	**Lethal level range**
Reinforced-concrete structure	RCa	Construction measures, foundation type, construction time, height	0.1–0.25
	RCb		
Wood structure	Wa	Construction measures, foundation type, construction time, structural style	0.2–0.35
	Wb		
Brick-concrete structure	Ba(Fortified)	Construction measures, foundation type, construction time, purpose, height	0.33–0.6
	Bb(Non-Fortified)		
Brick-wood structure	BWa	Construction measures, foundation type, construction time, structural style	0.6–0.9
	BWb		
Civil structure		Construction measures, foundation type, construction time, building materials	0.75–0.9
Adobe structure		Wall type, foundation type, construction time, building materials	0.85–1

building types include civil, brick-wood, brick-concrete, reinforced concrete and wood structures, a total of 6 fourth-order linear equations are obtained, the third group includes 12 earthquakes (divided into 2 regional groups: 6 earthquakes in Xinjiang, Gansu, Sichuan and Chongqing in the west and 6 earthquakes in Hebei, Heilongjiang and Guangxi in the east), and the building types include civil, brick-wood and brick-concrete structures, altogether, the two earthquakes groups yield 40 third-order linear equations, the fourth group includes a total of 28 earthquakes divided into 4 groups according to their spatial distribution (each group has 7 earthquakes; three groups include earthquakes mainly in Yunnan Province, while the other group includes earthquakes in Sichuan, Xizang, Xinjiang, Neimenggu, and Jiangxi), and the building types include civil, brick-wood, brick-concrete, and reinforced concrete structures, these four groups yield 140 quadratic linear equations. Solve different multivariate linear equations separately, and the result obtained is the lethality level of different building types.

As shown in Table 4, an analysis of the calculation results reveals that the LLs among the earthquake areas are significantly different even if the proportion of destroyed buildings and the mortality rate are similar, for instance, even if the proportion of destroyed buildings is high, the corresponding LL is not necessarily high, in other words, for different areas, the overall proportion of destroyed buildings may be the same, but the LLs in different areas may differ greatly.

As shown in Figure 2, the distribution characteristics of the LL are obvious with values mainly within 0.5–0.9, in particular, there are 20 earthquake areas with 0.7–0.8, and these areas are distributed mainly in 3 regions: Yunnan Province, Sichuan Province and Gansu Province, considering the geographical distribution in the 52 historical earthquake areas, the distribution does not depend on the spatial distribution of historical earthquakes, the regional LL of historical earthquakes in the same Province may be different, but in different Provinces may be similar.

Furthermore, Figure 3 shows the distributions of the proportion of destroyed buildings, mortality rate and LL in each of the 52 historical earthquake areas, the main distribution interval of the proportion of destroyed buildings is concentrated within 0.1–0.3, the larger the proportion of destroyed buildings is, the higher the mortality rate, but this relationship is not absolute. In fact, there is a situation where the proportion of destroyed buildings is large but the mortality rate is relatively small, nevertheless, the mortality rate is positively correlated with the LL.

A comparative analysis of the correlations between these three parameters demonstrates that the proportions of destroyed buildings are similar between the two earthquakes, but due to the obvious difference in the regional LL, the mortality rates of the two earthquakes vary, the proportions of destroyed buildings in the two earthquake areas also differ considerably, but due to the large difference in the LL between the two areas, the overall mortality rates of the two earthquakes may be the same, this finding confirms that the it is one of the main influencing factors of the mortality rate, and it can reflect the comprehensive level of an earthquake area.

Generally, for the same earthquake area, although the impact fields of earthquakes at different times are not completely the same, since earthquakes at different times are basically within the scope of an administrative area, the basic physiology (such as the geography and geological landforms) in an area will not change substantially, and thus, there should be no major differences in the LL in the same area at different times, however, we found a significant difference in the same area, for example, among the 6 earthquakes that occurred in Jiashi, Xinjiang, from 1996 to 2003, the LLs were 0.8422, 0.5691, 0.5978, 0.7839, 0.6897, and 0.8182; thus, the difference in the same area at different times reached 0.2731, similarly, for the earthquakes that occurred in

Lijiang, Yunnan, on 3 February 1996, 2 July 1996, and 25 September 1996, the LLs were 0.7583, 0.8428, and 0.8514, respectively, and the difference reached 0.0931, for the earthquakes that struck Minxian, Gansu Province, on 13 November 2003, and 7 September 2004, it were 0.7074 and 0.716, respectively, and the difference reached 0.0086, for the earthquakes that occurred in Wen County, Gansu Province, on 15 April 1999, and 21 June 2006, it were 0.7118 and 0.8197, respectively, with a difference of 0.1079, for the earthquakes that occurred in Yibin, Sichuan, on 28 February 1996, and 17 June 2004, it were 0.7051 and 0.4321, respectively, and the difference reached 0.273. We postulate that such different in the same areas may be due to the different types and proportions of buildings in those areas because the types and proportions of buildings in an area may change with economic development over time, but the geography and landforms in the same area will not undergo remarkable change.

As shown in Figure 4, the results of the 6 building types show relatively obvious distribution interval characteristics, although the distribution intervals of adobe and wood structures are less obvious due to the relatively small number of these buildings, nevertheless, the calculated LLs of adobe structures are concentrated above 0.85, those of wood structures are distributed between 0.15 and 0.35, those of civil structures are between 0.5 and 1, those of brick-wood structures are between 0.3 and 0.9, those of brick-concrete structures have a scattered distribution ranging from 0 to 1, and those of reinforced concrete structures are between 0 and 0.4, in other words, even for earthquakes with different occurrence times, regional environments, and magnitudes, the LLs of the same type of buildings are relatively similar, consequently, there are no significant differences in the LL of the same building type among the different areas.

As shown in Figure 5, the distributions of the LLs of various types of buildings are relatively concentrated within certain ranges, according to the average values of the LL of various types of buildings, adobe structures have the highest LLs, followed by civil structures and brick-wood structure, the distribution of the brick-concrete structures is more scattered, and the concentration distribution interval is relatively insignificant, reinforced concentrate structures exhibit have the lowest, and the distribution intervals are relatively concentrated, moreover, the number of wood structures is relatively small, but the overall distribution interval is relatively concentrated between those of brick-concrete structures and reinforced concentrate structures.

As shown in Figure 6, from the calculation results of 95% confidence intervals of the LLs of the 6 building types reveals the following: the average LL of adobe structures is 0.9175, and the standard deviation is 0.04063; the civil structures is 0.8491, and the standard deviation is 0.08855; the brick-wood structures is 0.7469, and the standard deviation is 0.133; the brick-concrete structures is 0.4585, and the standard deviation is 0.2673; the reinforced concrete structures is 0.1692, and the standard deviation is 0.101; and the wood structures is 0.2724, and the standard deviation is 0.04963, in addition, the distributions of the average values are relatively concentrated, the average LLs of adobe and wood structures are relatively less abundant, but they can still reflect the distribution trends of these two types of buildings, that is, the calculation results based on the 95% confidence interval can better reflect the concentrated partial range of the LL of each type of building.

As shown in Table 5, according to the calculated results of each building type, we obtained the sample mean, standard deviation, sampling average error and allowable error of each building type, based on the mean and allowable error, the lower and upper confidence limits of each building type were obtained, we define these lower and upper confidence limits as the upper and lower limits of the LL interval of each building type, the interval range of the LLs of adobe structures is within 0.85–1, that of civil structures is within 0.75–0.95, that of brick-wood structures is within 0.6–0.9, that of brick-concrete structures is within 0.33–0.6, that of wood structures is within 0.2–0.35, and that of reinforced concrete structures is within 0.1–0.25, these distribution interval ranges can further represent the main concentrated distribution areas of various types of buildings, however, the distributions of the building typologies are regionally dependent (Pavic et al., 2019; Pavic et al., 2020a; Pavic et al., 2020b), and it should be noted that the LL range corresponding to each type of building obtained in this article is just a theoretically calculated range of values based on each type, moreover, the same building types even have different structure and properties among different regions/cities/municipalities; therefore, to determine the actual LLs of buildings in earthquake areas, it is still necessary to construct a corresponding model for calculations based on this interval.

As shown in Table 6, we determined the range of LLs for each type of building, at the same time, based on a large amount of field investigation experience, we found that each type of building has different factors affecting its LL, including the construction style, building materials, building age, construction measures, building height, building use, cement type, foundation type, etc., in other words, for each type of building, the different details of its construction are responsible for the differences in the LL, but the actual values of various buildings should be within the ranges corresponding to the above types of structures.

Discussion

Based on an analysis of historical earthquakes, the magnitude, population density, geographical and geomorphological environment, and proportion of damaged buildings are similar between the two earthquakes, but there is a considerable difference in the number of casualties, earthquake-induced deaths are affected not only by the proportion of damaged buildings but also by the combined effects of regional geological features, road traffic, and

incidental factors, we constructed a matrix of mortality rates based on the LL and intensity (Xia et al., 2020); in fact, it represents different intensities, and the corresponding mortality rate is different, so for different regions, different LLs correspond to personnel mortality rates with intensities of VI-XI, its different to the casualty assessment method by the United States Geological Survey (USGS) which has only one component of the mortality rate by intensity for a country, if we can obtain the LL of an area prior to an earthquake, then after the earthquake, we can select the corresponding mortality rate for evaluation and calculation, this also provides another possibility for rapidly assessing earthquake casualties.

The LL of an area is affected by many influencing factors, of which buildings are dominant, which means that different types of buildings have unique LLs, it is an extension of the vulnerability level, which is concerned mainly with the probability that different buildings will cause different damage states after an earthquake, and different damage levels correspond to the mortality rate, however, for different buildings, even is the proportion of damaged buildings is the same, the mortality rate still varies, therefore, this article employs historical earthquake data to quantitatively calculate the LLs of various types of buildings.

The LLs of different historical earthquake areas far from one another may be similar, but those of areas adjacent to each other may be quite different; hence, the LL does not depend on the geographical location, theoretically, for different earthquakes located in the same area, even at different times, the geological and geomorphological conditions within the area will not change significantly, furthermore, the population size and density will not vary considerably, thus, without a large difference in the earthquake magnitude, the main mechanism responsible for the differences in the LL in the same area may be the impacts of buildings in the area, an analysis of the building types and their proportions in each earthquake area reveals that the main cause of changes in the regional LL is the differences between the building types and their proportions.

The earthquakes that occur in different time periods in the same area, building types undergo certain changes after their restoration and reconstruction, inevitably leading to differences in regional LLs, for example, for the Jiashi earthquake in Xinjiang on 19 March 1996, the buildings in the earthquake area were predominantly adobe structures (composing 93.19% of all structures), whereas brick-concrete structures accounted for only 5%, and the LL was 0.8422, the buildings in the same earthquake area on 21 January 1997, were likewise dominated by adobe and brick-concrete structures, but their proportions were 45.84% and 38.01%, respectively; the proportion of the latter was relatively large, which caused the LL of the area to change significantly (0.5691), in other words, the influences of building types and proportions in an area are the main reason for the differences in the LL; therefore, the unique LL of a region can be comprehensively reflected by the building types, the proportions of buildings, the LLs of the various types of buildings.

Moreover, for a given building type, differences in the building materials, construction methods, and building quality cause the LL to differ, in other words, the actual LLs of buildings of the same type in different areas may be greatly different; nevertheless, regardless of this difference, the range of change should be within (should not exceed) the range corresponding to that type of building, the type of building, construction materials, construction time, etc., all affect the value, and the weights of these impacts are vary, based on these weights, the actual LL of a building can be quantitatively calculated.

The LLs of different building types have unique concentrated distribution interval ranges that are not equal, some buildings have small ranges, such as civil structures, whereas others have large ranges, such as brick-concrete structures, in addition, the LL ranges of different building types overlap, for example, the range of wood structures is 0.2–0.35, and that of brick-concrete structures is 0.33–0.6, generally, the wood structures is higher than that of a brick-concrete structure, but the lower limit of the interval range of brick-concrete structures is lower than the upper limit of wooden structures, which is also consistent with the actual survey situation, for example, the LL of a high-quality brick-concrete structure with a complete building structure may be lower than that of a wood structure of poor quality that is older in age, therefore, the actual LL of each type of building in each area needs to be determined according to its actual situation.

Conclusion

This paper proposed the concept of the LL and constructs a calculation model for determining the regional LL, based on data of 52 historical earthquakes, the LLs of the types of buildings in different regions were obtained, based on theoretical calculations and field survey experience, we obtained the ranges of LLs for various types of buildings, thereby providing a theoretical basis for the field investigation and quantitative calculation for buildings in different areas.

Based on historical earthquakes, the LL of each building type is within an interval range; that is, even among the same type of buildings, due to differences in the building structure, quality, and age, etc., their actual LLs diverge, in addition, the interval ranges of different types of buildings are not equivalent, and these ranges overlap with each other, hence, the LL of one type of building is not necessarily lower than that of another type of building, these quantitative results can also reduce errors caused by classifications based solely on building types.

By calculating and determining the LLs of buildings, it is possible to quantitatively calculate the LL of a region, the quantitative result of this calculation reflects the probability of casualties for the whole region, different LLs represent a group of dominant mortality rates of various intensities, based on the

different LLs of regions, it is possible to achieve the zonation of regions, and these zones is not limited to simple administrative divisions or geographic boundaries, instead, it is a quantitative metric of the overall capacity of an area, which reduces the need to acquire detailed building data, it can intuitively reflect the overall earthquake resistance of an area and can also provide support for the risk assessment of casualties.

This paper used mainly historical seismic data to determine the LLs of buildings and obtained the ranges of different types of buildings, these findings provide insight into and a method for quantitatively calculating the seismic capacity of buildings, subsequent studies will need to introduce methods to determine the LLs of various other types of buildings.

Data availability statement

The original contributions presented in the study are included in the article/Supplementary Material, further inquiries can be directed to the corresponding author.

Author contributions

XC, LH, ZJ, YR, and ZX directed and performed field experiments, processed data and produced some figures. FX processed data and produced some figures. NG oversaw the complete project and provided guidelines. XC prepared the first draft manuscript. All authors were involved in the final manuscript preparation. All authors read and approved the final manuscript.

Funding

This work was jointly supported by the National Nonprofit Fundamental Research Grant of China, Institute of Geology, China Earthquake Administration (Grant No. IGCEA2106) and the National Natural Science Foundation of China (Grant No. 42071337) and the National Natural Science Foundation of China (Grant No. 41907397).

Conflict of interest

The authors declare that the research was conducted in the absence of any commercial or financial relationships that could be construed as a potential conflict of interest.

Publisher's note

All claims expressed in this article are solely those of the authors and do not necessarily represent those of their affiliated organizations, or those of the publisher, the editors and the reviewers. Any product that may be evaluated in this article, or claim that may be made by its manufacturer, is not guaranteed or endorsed by the publisher.

References

Alel, M. N. A. (2013). "Estimation of life casualties for seismic vulnerability assessment in Bukit Tinggi," in Geocon 2013 Proceedings, 30 Jun 2014 (Johor Bahru: GEOCON2013).

Alexander, D. E. (2011)."Mortality and morbidity risk in the L'aquila, Italy earthquake of 6 April 2009 and lessons to be learned," in *Human casualties in earthquakes*. Editors R. Spence, E. So, and C. Scawthorn. (Dordrecht: Springer), 29. doi:10.1007/978-90-481-9455-1_13

Badal, J., and Samardjieva, E. (2003). *Prognostic estimations of casualties caused by strong seismic impacts*. Nice, France: EGS-AGU-EUG Joint Assembly.

Badal, J., Zquez-Prada, M. V., and Gonz-lez, R. (2005). Preliminary quantitative assessment of earthquake casualties and damages. *Nat. Hazards (Dordr).* 34 (3), 353–374. doi:10.1007/s11069-004-3656-6

Ceferino, L., Kiremidjian, A., and Deierlein, G. (2018a). Regional multiseverity casualty estimation due to building damage following a Mw 8.8 earthquake scenario in Lima, Peru. *Earthq. Spectra* 34 (4), 1739–1761. doi:10.1193/080617eqs154m

Ceferino, L., Kiremidjian, A., and Deierlein, G. (2018b). Probabilistic model for regional multiseverity casualty estimation due to building damage following an earthquake. *ASCE-ASME J. Risk Uncertain. Eng. Syst. Part A Civ. Eng.* 4 (3), 04018023. doi:10.1061/ajrua6.0000972

Christoskov, L., and Samardjieva, E. (1984). An approach for estimation of the possible number of casualties during strong earthquakes [J]. *Bulg. Geophys J.* 4, 94–106.

Feng, T., Hong, Z., Wu, H., Fu, Q., Wang, C., Jiang, C., et al. (2013). Estimation of earthquake casualties using high-resolution remote sensing: A case study of dujiangyan city in the may 2008 wenchuan earthquake. *Nat. Hazards (Dordr).* 69 (3), 1577–1595. doi:10.1007/s11069-013-0764-1

Ferreira, M., Oliveira, C., and Sá, F. (2011). "Estimating human losses earthquake models: A discussion [M], human casualties in earthquakes," in *Advances in natural and technological hazards research*. Dordrecht: Springer.

Fu, Z. (1993). A preliminary study on establishment of probabilistic vulnerability matrix of life from earthquakes [J]. *Earthq. Res. china* 3, 205–210.

Goncharov, S., and Frolova, N. (2011). *Casualty estimation due to earthquakes: Injury structure and dynamics*. Dordrecht: Springer.

Jaiswal, K., Wald, D., and D'Ayala, D. (2011). Developing empirical collapse fragility functions for global building types. *Earthq. spectra* 27 (3), 775–795. doi:10.1193/1.3606398

Jaiswal, K., Bausch, D., Chen, R., Bouabid, J., and Seligson, H. (2015). Estimating annualized earthquake losses for the conterminous United States. *Earthq. Spectra* 31 (1), S221–S243. doi:10.1193/010915EQS005M

Ma, Y., and Xie, L. (2000). Research on the estimation method of earthquake casualties[J]. *Earthq. Eng. Eng. Vib.* 20 (4), 140–147. doi:10.3969/j.issn.1004-4574.2000.03.013

Ma, Y., and Zhao, G. (2008). *Earthquake disaster risk analysis and management*. Beijing: Science Press.

Miyakoshi, J., Hayashi, Y., and Tamura, K. (1998). "Damage ratio functions of building using damage data of the 1995 hyogo-ken nanbu earthquake," in 7th International Conference on Structural Safety and Reliability (ICOSSAR '97), Kyoto, Japan, November 24–28, 1997. 1, 349–354.

Nie, G., Xia, C., and Fan, X. (2020). Classification of anti-lethal level based on historical earthquake death data[J]. *Chin. J. Geol.* 55 (4), 1298–1314. doi:10.12017/dzkx.2020.078

Nie, G., Xia, C., Fan, X., and Li, H. (2021). Research on the lethal level of buildings based on historical seismic data[J]. *Chin. J. Geol.* 56 (4), 1250–1266. doi:10.12017/dzkx.2021.068

Oike, K. (1991). "A discussion on the relation between the magnitude and the number of the dead by earthquakes [M]," in Proc of the International Seminar on Earthquake (Tsukuba: Prediction and Hazard Mitigation Technology), 333–341.

Okada, S., and Takai, N. (1999). Classifications of structural types and damage patterns of buildings for earthquake field investigation [J]. *Nihon. Kenchiku. Gakkai. Kozokei. Ronbunshu.* 64 (524), 65–72. doi:10.3130/aijs.64.65_5

Pang, W., Majdalaweyh, S., Safiey, A., Rokneddin, K., Prabhu, S., Javanbarg, M., et al. (2020). A probabilistic casualty model to include injury severity levels in seismic risk assessment. Report.

Pavić, G., Bulajić, B., and Hadzima-Nyarko, M. (2019). The vulnerability of buildings from the osijek database [J]. *Front. Built Environ.* 5 (66), 1–14. doi:10.3389/fbuil.2019.00066

Pavić, G., Hadzima-Nyarko, M., and Bulajić, B. (2020a). A contribution to a UHS-based seismic risk assessment in Croatia—a case study for the city of osijek. *Sustainability* 12 (5), 1796–1824. doi:10.3390/su12051796

Pavić, G., Hadzima-Nyarko, M., Bulajić, B., and Jurković, Ž. (2020b). Development of seismic vulnerability and exposure models – a case study of Croatia. *Sustainability* 12 (3), 973–1024. doi:10.3390/su12030973

Pomonis, A., Kappos, A., and Karababa, F. (2011). "Seismic vulnerability and collapse probability assessment of buildings in Greece [M]," in S. R., S. E., S. C., Human Casualties in Earthquakes, 08 December 2010 (Dordrecht: Advances in Natural and Technological Hazards Research), 153–170.

Samardjieva, E. (2002). Estimation of the expected number of casualties caused by strong earthquakes. *Bull. Seismol. Soc. Am.* 92 (6), 2310–2322. doi:10.1785/0120010112

Samardjieva, E., and Oike, K. (1992). Modelling the number of casualties from earthquakes [J]. *J. Nat. disaster Sci.* 14 (1), 17–28.

So, E. (2011). *Challenges in collating earthquake casualty field data*. Dordrecht: Springer.

So, E., and Spence, R. (2013). Estimating shaking-induced casualties and building damage for global earthquake events: A proposed modelling approach. *Bull. Earthq. Eng.* 11 (1), 347–363. doi:10.1007/s10518-012-9373-8

Spence, R., So, E., and Cultrera, G. (2008). "Earthquake loss estimation and mitigation in europe: A review and comparison of alternative approaches [C]," in The 14th World Conference on Earthquake Engineering, 12/10/2008-18/10/2008 (Beijing, China: World Conference on Earthquake Engineering).

Spence, R., So, E., Jenkins, S., Coburn, A., and Ruffle, S. (2011). "A global earthquake building damage and casualty database," in *Human casualties in earthquakes*, Editor Spence, R., So, E., and Scawthorn, C.(Dordrecht: Springer), 29. doi:10.1007/978-90-481-9455-1_5

Wang, H. X., Niu, J. X., and Wu, J. F. (2011). ANN model for the estimation of life casualties in earthquake engineering. *Syst. Eng. Procedia* 1, 55–60. doi:10.1016/j.sepro.2011.08.010

Wei, B., Nie, G., Su, G., Sun, L., Bai, X., and Qi, W. (2017). Risk assessment of people trapped in earthquake based on km grid: A case study of the 2014 ludian earthquake, China. *Geomat. Nat. Hazards Risk* 8 (2), 1289–1305. doi:10.1080/19475705.2017.1318795

Xia, C., Gaozhong, N., Xiwei, Z., and Junxue, P. (2020). Research on the rapid assessment of earthquake casualties based on the anti-lethal levels of buildings. *Geomat. Nat. Hazards Risk* 11 (1), 377–398. doi:10.1080/19475705.2019.1710581

Xu, J., Fuquan, W., and Zhang, L. (2008). Preliminary study on evaluating the number of casualties and trapped victims by an earthquake - a case study of Zhangzhou City, Fujian Province [J]. *J. Seismol. Res.* 31 (4), 382–387. doi:10.3969/j.issn.1000-0666.2008.04.014

Yin, Z. (1991). Research on earthquake disaster loss prediction [J]. *Earthq. Eng. Eng. Vib.* 4, 89–98.

Zhang, Y., Lin, Q., Liu, Y., and Wang, Y. (2018). The quick assessment model of casualties for asia based on the vulnerability of earthquake [J]. *Nat. Hazards Earth Syst. Sci. Discuss.* 1–22. doi:10.5194/nhess-2018-21

Zhize, F., and He, J. (1996). Earthquake casualty prediction research: —taking lunan area as an example [J]. *J. Seismol.* 000 (1), 58–62.

Zhu, J., and Yang, M. (1998). Prediction and facts about the casualties caused by the earthquake: The relationship between house destruction and the number of deaths[J]. *Seismol. Sci. Technol. Inf.* 000 (004), 32–37.

Frontiers in Earth Science

Investigates the processes operating within the major spheres of our planet

Advances our understanding across the earth sciences, providing a theoretical background for better use of our planet's resources and equipping us to face major environmental challenges.

Discover the latest Research Topics

See more →

Frontiers

Avenue du Tribunal-Fédéral 34
1005 Lausanne, Switzerland
frontiersin.org

Contact us

+41 (0)21 510 17 00
frontiersin.org/about/contact